# Sound Propagation Over Rigid Porous Layers

## Thesis

# Sound Propagation Over Rigid Porous Layers

Thesis submitted by

**Craig Howorth** B.Sc.

**for the degree of**

**Doctor of Philosophy**

**July 1991**

Department of Engineering Mechanics
Faculty of Technology
Open University
Milton Keynes
England

Date of submission: 31 July 1991
Date of award: 3 May 1991

## Abstract

The work studies two related topic areas namely:

1. the measurement of the acoustical characteristics of rigid porous materials, that is the impedance and propagation constant;
2. the propagation of sound over the surface of a hard backed layer of such a material.

A review of impedance measurement leads to the selection of an indirect method which is employed successfully on a wide range of surfaces. A numerical comparison of impedance models follows including a one–parameter semi–empirical model, a phenomenological model and a microstructural model which relates several physical parameters of a material to the acoustical properties of a surface. The models differ in their prediction of the acoustical properties of a low porosity material. A numerical comparison of the solutions of point source propagation in the presence of a porous media indicates that the 'extended' Weyl van der Pol approximation is reliable over short source receiver distances. The study is extended to examine the phenomenon of the acoustical surface wave. Three experimental techniques are used to produce new evidence for the existence of such a wave which shows good agreement with the theoretical predictions. The indirect method is used to obtain impedances and model parameters for a wide variety of surfaces varying from soils to fibreglass and which are compared with the results of an impedance technique and with standing wave tube measurements.

The indirect method of impedance measurement is employed together with the microstructural model and the propagation model examined earlier in studies of the acoustical properties of porous road surfaces. It proves possible to use the indirect method both to determine the microstructural parameters and to classify the acoustical properties of such a pervious surface when the sound source is either a loudspeaker point source or a vehicle. The results of the parameter determination are validated by a series of non–acoustical measurements. With regard only to the excess attenuation provided by these surfaces, optimum combinations of material parameters are suggested which should lead to the production of a low noise road surface for many types of vehicle and tyre tread patterns.

## Acknowledgements

The completion of this work would not have been possible without the help and assistance of many people. Firstly I would like to thank Dr Keith Attenborough for his continuous help and advice during the supervision of this work. Thanks are also due to Dr Nick Heap for discussions relating to the direction of the work and for helping solve the many problems associated with new experimental techniques. I am also grateful to the technical staff of Engineering Mechanics who helped build and construct whatever equipment was necessary and to Dr Charles Don for helping to implement the impulse method of impedance measurement. I would also like to thank the members of the acoustics group, especially Dr. Jeanette Brooks, for their support and advice and for providing a stimulating atmosphere in which to work. Thanks are also due to the staff of the Open University academic computing service, for their initial advice on ForTran programming and for many hours spent solving problems with graphics or word processing packages.

I would also like to acknowledge the support of the Science and Engineering Research Council and the Transport and Road Research Laboratory who have acted as sponsors for this work. Special thanks are due to Paul Nelson and Phil Abbot who arranged for the laying of the test track and for the chance to visit the Cadre Noir at Saumur, France.

Finally my most sincere thanks are due to my family who have helped, encouraged and supported me not only through these PhD studies but from before my first spoken word.

Take care of the sense , and the sounds will take care of themselves Alice in Wonderland *Lewis Carroll (1832 - 1898)*

# Contents

# List of Figures

# List of Tables

# Sound Propagation over Rigid Porous Layers

Craig Howorth
Open University

# Chapter 1

# Introduction

## 1.1 Overview of the thesis

Since the early work of Parkin and Scholes [1] and [2] there has been a noticeable increase in the amount of time devoted to the study of the theory of sound propagation over a porous media with particular attention paid to the ground effect. In many cases alternative formulations have been provided to supercede earlier work. The result is a wealth of information but little indication as to the applicability and practical improvements offered by the various theoretical developments.

The aim of this work is to study the acoustics of sound propagation from a spherical source over rigid porous materials. These are materials in which the acoustical energy is carried by a wave propagating in the fluid filled interstices. It is also presumed that the sound wave travels above the porous surface in the absence of wind and temperature gradients. This study may be divided into two related parts.

- Evaluation of the acoustical properties of the material, namely the acoustic impedance and propagation constant.
- Study of wave propagation in the presence of such a medium.

Both parts of the study are used in determining an optimum porous road surface for the reduction of noise propagating from a vehicular source. The initial chapter, the introduction, outlines the aim of this work, details the

structure of the thesis and provides a review of the basic acoustical terms and procedures used in the following chapters. The next two chapters address the problem of characterization and determination of the acoustical properties of the material. A study of the methods of evaluating the characteristic impedance and complex propagation constant is followed by examination of rigid porous material theory and it's applicability to modelling the acoustical properties of a porous surface. A comparison is made between the impedance models developed to date.

The problem of modelling point to point propagation of broadband sound in the presence of such a surface is considered in chapter 4. Predictions for several of the most recent asymptotic series expansion solutions are compared to those obtained by a more accurate numerical integration solution the form of which was suggested by Chandler–Wilde [3]. Comparison is also made with predictions of a formulation developed from asymptotic approximations of Weyl [4] and Van der Pol [5]. This approximation is found to have wide applicability even when used to represent propagation over an externally reacting hard–backed layer. Particular attention is paid to the phenomenon of the acoustical surface wave. The existence of such a wave is indicated under certain conditions but has eluded convincing experimental verification. The study of the surface wave results in a series of experimental measurements that when compared to the theory indicate the presence of the surface wave above a lattice layer fixed to a rigid backing. Chapter 6 combines the study of rigid porous materials with the solution to the point to point propagation problem to develop the indirect method of impedance measurement. The data resulting from application of this technique over several surfaces are compared with data provided by impulse and tube techniques.

The penultimate chapter consolidates the work studied so far in a study of the acoustical characteristics of porous tarmacadam road surfaces and their influence on sound propagation. The indirect method of measuring impedance developed in chapter 6 is used together with the microstructural model to evaluate the impedance model parameters. The results of this

acoustical surveying procedure are supported by a series of non–acoustical measurements of the material properties. The study of the sound propagation over the porous road surfaces confirms the accuracy of the modified Weyl van der Pol formulation. Validation of the impedance and propagation models is followed by an optimization procedure which suggests the ideal surface to reduce the noise propagated from a range of road traffic sources. The work is concluded by a review of the findings of the study and by suggestions for further work.

## 1.2 Review of fundamental acoustical concepts used in the study of sound propagation

The acoustic wave radiating from a point source will be represented using equation 1.1.

$$p(r,t) = \frac{A}{r} e^{-\imath(\omega t - k_0 r)} \tag{1.1}$$

where $p$ is the acoustic pressure at a time $t$ and distance $r$. The angular frequency $\omega = 2\pi f$ where f is the frequency of the acoustic wave. The wave number is given by $k_0 = \frac{\omega}{c_0}$, $c_0$ being the speed of sound in the fluid in which the wave is travelling, normally air. The reflection of the wave from a boundary is dependent on the normalized surface impedance and, for an externally reacting medium, on the complex propagation constant. The normalized relative characteristic impedance is defined as the ratio of pressure and normal velocity at the surface of a semi–infinite medium divided by the characteristic impedance of air ( the product of the density and the velocity). This impedance is a complex number whose real and imaginary parts are termed the resistance and reactance respectively. If the medium is semi-infinite the characteristic impedance is equal to the normalized surface impedance. It should be noted that De Bie and Greonewoud [6] termed this impedance the specific acoustic impedance and defined the characteristic impedance as the impedance of a material that can be measured at any place in the medium. The bulk propagation constant ($k_b$) will be required

when there is significant acoustical energy transmitted in directions other than normal to the surface of the material. The real and imaginary parts of the propagation constant are termed the phase and attenuation constant respectively. If the acoustic wave impinging on a surface of a semi–infinite medium is refracted towards the normal such that there is no significant lateral wave propagation, the materials properties are encompassed in the characteristic impedance and the medium is classed as being locally reacting. If this is not the case then both the impedance and bulk propagation constant are required and the material is classed as externally reacting or has the properties of extended reaction.

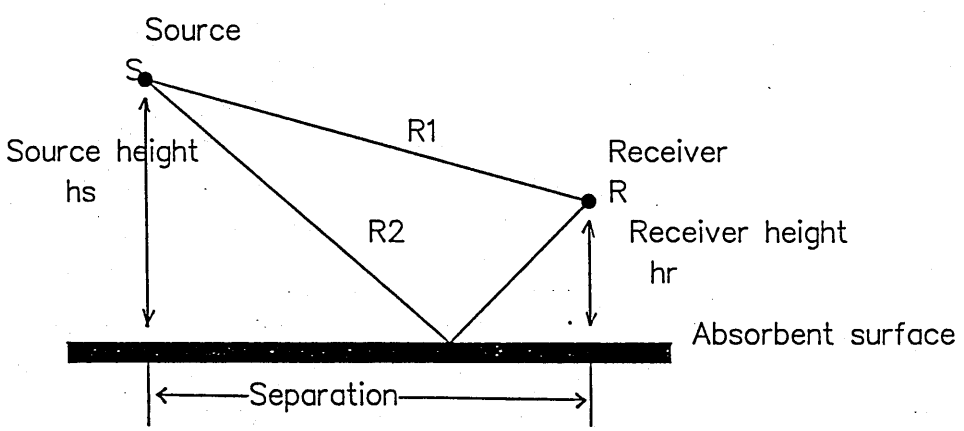


**Figure 1.1** Geometry of point sound source and receiver above a flat absorbing ground

Consider the simple source–receiver geometry shown in figure 1.1. The sound received at the receiver may be classed as coming from two waves; a direct wave and a wave reflected from the surface of the material. This may be expressed as shown in equation 1.2.

$$p_t = p_d + Q\, p_r \tag{1.2}$$

where $Q$ is the spherical wave reflection coefficient. The reflected wave may be decomposed into a specularly reflected wave and a ground wave which, in turn, in some cases may include a surface wave. If the source and receiver are a great distance from the surface of the material the plane wave reflection coefficient $R_p$ may be used. Given by $R_p = |R_p|e^{i\phi}$. The phase change on reflection from the surface is represented by the term $\phi$. When the phase difference between the two acoustic waves is $\pi$ radians ( 180 ° degrees) there exists destructive interference. The conditions for this interference depend on the source receiver geometry, on the impedance of the material, through the plane wave reflection coefficient, and on the frequency of the propagating wave. The condition for a pressure minimum is given by equation 1.3

$$(2n+1)\pi = \frac{2\pi}{\lambda}(R2 - R1) + \phi \tag{1.3}$$

If the extreme cases of a pressure release boundary ($\phi = \pi$) and a perfectly reflecting surface ($\phi = 0$) are considered it is seen that as the impedance of the surface increases the location of the minimum shifts to a higher frequency. For most porous materials the surface acts as a pressure release boundary at high frequencies and thus the frequency location of the higher order dips will be dependant mainly on the source receiver geometry and their associated path lengths $R1$ and $R2$. The excess attenuation is used as a measurement of the wave interference it is defined as the quotient of the total wave impinging on the receiver and the direct component, see equation 1.4

$$\text{Excess Attenuation} = 20.0 \times \log\left|\left(\frac{p_t}{p_d}\right)\right| \tag{1.4}$$

The excess attenuation for a two surfaces with low and high impedances is shown in figure 1.2. Note also an increase in the effect of the destructive interference with an increase in the impedance of the material.

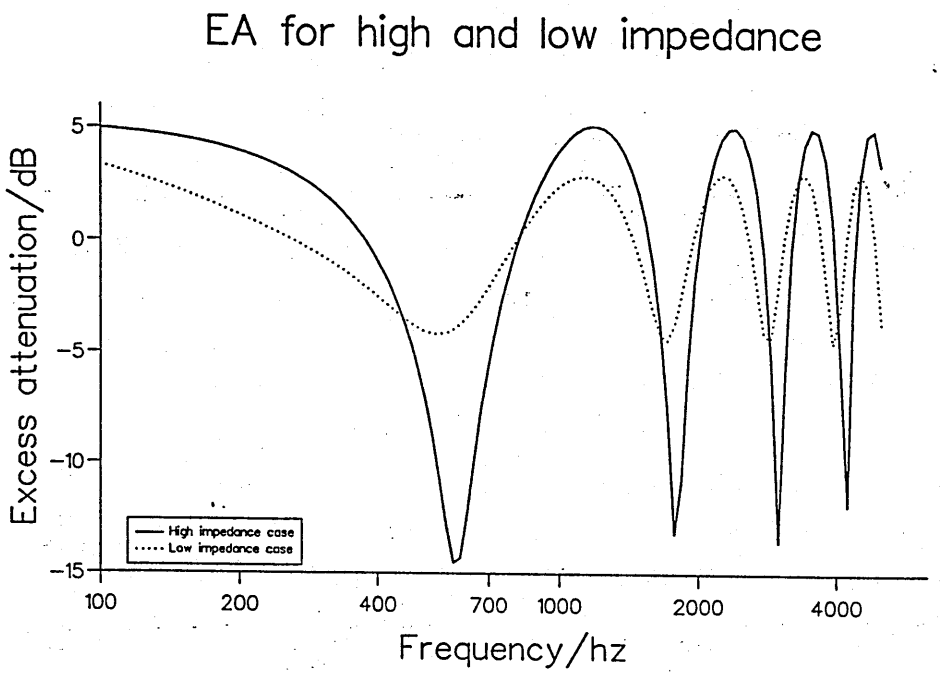


**Figure 1.2** Excess attenuation spectra for low and high impedance materials

# Chapter 2

# Review of methods of measuring the acoustical properties of a material

## 2.1 Introduction

Chapter 1 discussed the nature of the acoustic impedance of a surface and why it should be measured when considering sound propagation. Before one can measure the acoustic impedance of a ground surface it is necessary to subject the various methods of measurement to critical examination and determine which methods are most appropriate and to chose a particular method for further investigation. One of the earliest reviews by Beranek [7] in 1940 and updated in 1949 [8] subdivided the methods into three classes:

1. Surface methods; where data taken near the surface was considered when the sample was exposed to a plane wave sound field.
2. Transmission line methods; which by analogy with electromagnetic wave theory involve data taken at some distance from the surface.
3. Comparison methods; again the basis of the techniques used stems from electrical circuit theory where known and unknown impedances are compared in a bridge system. Due to the difficulty in developing a reliable acoustic standard impedance the method has not been developed since the original work of Schuster [9] and Robinson [10]. This method is not considered here.

Gately and Cohen [11] reviewed methods of evaluating acoustic filters in 1969 and Dean [12] in 1974 examined in–situ wall impedance measurements in flow ducts. Kilmer [13] also in 1974 investigated the properties of composite acoustic absorbers. He divided the methods of impedance measurement into the same three categories as Beranek.

It was not until Singh's review [14] that all modern impedance measurement techniques were considered. This comparatively short review suggested seventeen different groups. Many of the methods investigated however could easily have been reorganized into fewer larger categories. Space also precluded any in–depth criticism of the methods used. He did however cover the digital instrumentation methods and pulse techniques which had become possible after Beranek's review due to the improvement in digital electronics and instrumentation techniques. Heap [15] extended the basic categories of Beranek and Kilmer to include three more classes which would incorporate the methods introduced with the advances in signal processing and computational facilities.

1. Indirect methods; used at oblique angles of incidence. The pressure above a surface is compared to theoretical predictions. Adjustment either of impedance or of a range of parameters in an impedance model is used to gain agreement between theoretical and practical measurements of the pressure profile or frequency dependent excess attenuation spectrum.
2. Impulse methods; broadband pulses or bursts of swept tone are used to investigate the time separated direct and reflected sound waves. From these measurements the reflection coefficient and hence the impedance are calculated.
3. Transfer function methods which may be described as an extension of the impulse technique but with an improvement in the signal to noise ratio. The method uses the idea of a two port system, see figure 2.1. The impulse response $h(t)$ of the system in the time domain is related via the Fourier transform to the

complex transfer function $H(f)$. It is this function which is then related to the reflection coefficient.

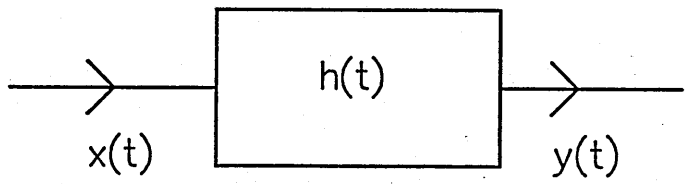


**Figure 2.1** Transfer function technique principle

The methods contained in these groups may not be appropriate for measuring the impedance of an outdoor ground surface. The ideal measurement technique should be.

1. Accurate
2. Fast
3. Simple to perform
4. Repeatable
5. May be used in–situ without destroying the ground structure.
6. May be used at all angles of incidence

Thus the ideal method should not be invasive or contained in a tube and should use a broadband or pulsed source. It should be relatively unaffected by unwanted reflections. The following review examines the techniques that have been applied or might be applied to ground surfaces.

## 2.2 Volume velocity techniques

Volume velocity techniques were developed by Cook [16] and El–Mawardi [17] for use on finite samples. These methods measure the pressure variations due to a known volume velocity source or attempt to measure the volume

velocity and then calculate the impedance form the ratio of the two variables. It is easier to design a constant volume velocity source such as the device constructed by Salava [18] than to measure the volume velocity using a hot wire anemometer as attempted by Pratt [19]. The only successful example of the application of a surface technique to measurement of the ground impedance is the Helmholtz resonator based device of Zuckerwar [20]. This is a cam driven system to be used in–situ, see figure 2.2. As can be seen this involves a Helmholtz resonator driven by a piston and located directly on to the ground surface, the instrument being first calibrated by location onto a steel plate. This is only used at normal incidence. Although his results are shown to be in agreement with the predictions of the Delany and Bazely model, see chapter 3, the resonator technique tends to under predict the real and imaginary parts of the impedance. This has been remarked by Daigle and Stinson [21]. Moreover the method is equipment intensive requiring phase matched low pass filters.

## 2.3 Transmission line methods

The most commonly used methods of measuring the impedance of a ground surface are found in the transmission line category. The standing wave tube method developed be Taylor [22] and modified by Scott [23] has been used in–situ for grassland surfaces by Prout [24], Mansbach [25] and Dahl [26]. Oura [27], Ishida [28] and Buser [29] used the method to examine the acoustical characteristics of snow. It is also possible to use the impedance tube on samples of material if the surface from which they are taken is homogeneous and if the sample, is unlikely to be damaged during the extraction process. The tube technique may also be used to examine the ideal model surfaces employed when developing the propagation model for outdoor surfaces. The method is normally used at normal incidence.

Consider the ideal case the apparatus is shown in figure 2.3. This consists of a square or circular cross sectional tube. At one end there is mounted the sample of material under investigation. At the other a loud-

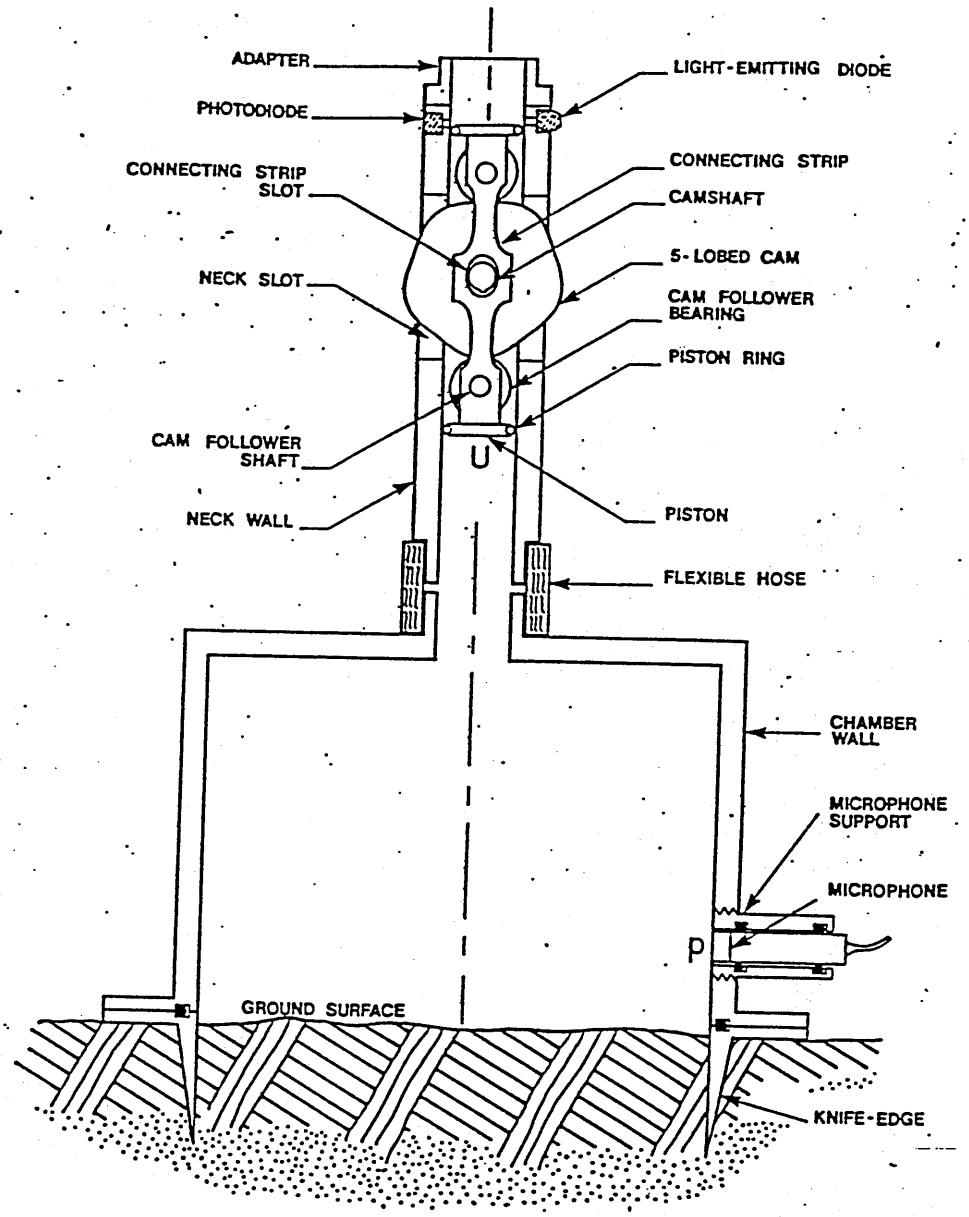


**Figure 2.2** Piston driven Helmholtz resonator for impedance measurement after Zuckerwar

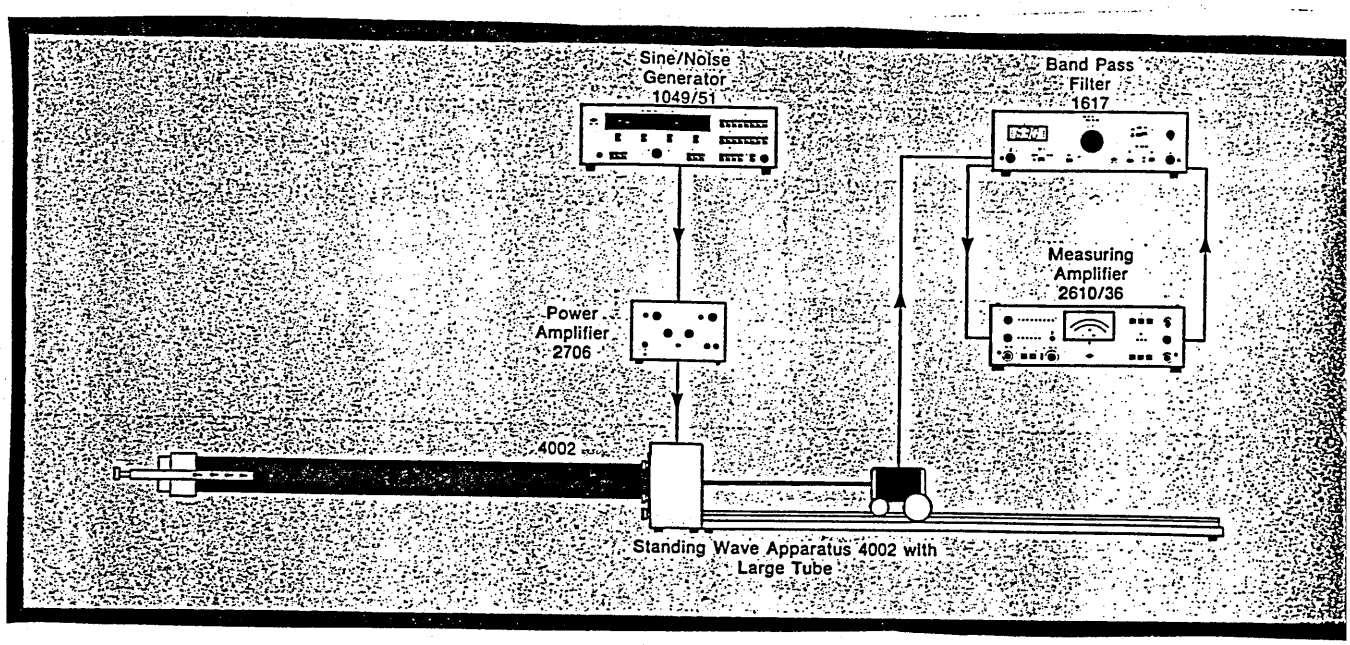


**Figure 2.3** Apparatus for Standing Wave Ratio measurement of Impedance

speaker driven by a pure tone generator. A probe microphone runs coaxially down the tube the location of the probe with respect to the sample may be measured from a rule running along side the probe. The probe is then used to measure the standing wave maxima and minima and their location relative to the surface of the sample. Consider the ideal loss–less tube with a rigid termination the wave propagation is shown in figure 2.4.

The incident and reflected waves are given,assuming the time dependance of $e^{-\imath\omega t}$ as

$$p_i(x,t) = P_0 e^{\imath(k_0 x - \omega t)}$$

$$p_r(x,t) = P_0 e^{\imath(-k_0 x - \omega t)}$$

The total pressure is found from

$$p_t(x,t) = P_0 e^{-\imath\omega t}\left[e^{\imath k_0 x} + e^{-\imath k_0 x}\right]$$

Hence

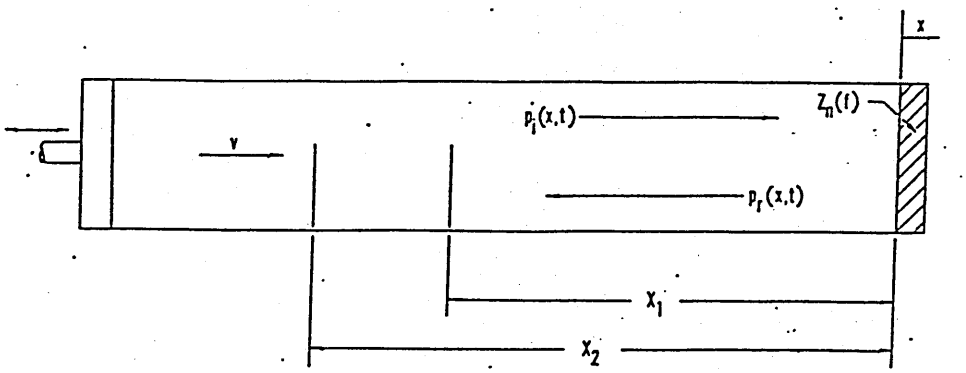


Figure 2.4 Wave propagation in loss–less tube

$$p_t(x) = 2P_0 \cos(k_0 x)$$

$$u(x) = \frac{-1}{\omega \rho_0} \frac{dp}{dx} = \frac{-2P_0}{\imath \rho_0 c_0} \sin(k_0 x)$$

Thus substituting $x = 0$, i.e. at the surface of the sample gives

$$p_t(x) = 2P_0$$

Hence the impedance is found from

$$Z_s(x) = \frac{p_t}{u} = \imath \rho_0 c_0 2 \cot(k_0 x)$$

Thus the pressure is seen to vary between $2P_0$ when $\cos(k_0 x) = 1$ and 0 when $\cos(k_0 x) = 0$. If a sample is now inserted into the tube which has a reflection coefficient of $e^{-\phi}$.

$$p_r(x) = P_0 e^{-\imath k_0 x - \phi}$$

and

$$p_t(x) = P_0 \left[ e^{ik_0 x} + e^{-ik_0 x - \phi} \right]$$

the volume velocity is given by

$$u(x) = \frac{P_0}{\rho_0 c_0} \left[ e^{ik_0 x} - e^{-ik_0 x - \phi} \right]$$

thus

$$Z_s(x) = \rho_0 c_0 \left[ \frac{e^{ik_0 x} + e^{-ik_0 x - \phi}}{e^{ik_0 x} - e^{-ik_0 x - \phi}} \right]$$

$$Z_s(0) = \rho_0 c_0 \left[ \frac{1 + e^{-\phi}}{1 - e^{-\phi}} \right]$$

If $\phi = \phi' + i\phi''$

$$R_s(0) = \frac{(\rho_0 c_0) tanh\left(\frac{\phi'}{2}\right) \left[1 + \tan^2\left(\frac{\phi''}{2}\right)\right]}{tanh^2\left(\frac{\phi'}{2}\right) + \tan^2\left(\frac{\phi''}{2}\right)}$$

$$X_s(0) = \frac{(\rho_0 c_0) tanh\left(\frac{\phi''}{2}\right) \left[tanh^2\left(\frac{\phi'}{2}\right) - 1\right]}{tanh^2\left(\frac{\phi'}{2}\right) + \tan^2\left(\frac{\phi''}{2}\right)}$$

The impedance $Z_s$ may now be found from $\phi$. Kilmer [13] has shown that

$$e^{-\phi'} = \frac{10^{\frac{L}{20}} - 1}{10^{\frac{L}{20}} + 1}$$

and

$$\phi'' = \pi(1 - 2d)$$

where $L$ is the standing wave ratio

$$L = 20 \log \left[ \frac{p_{max}}{p_{min}} \right]$$

and

$$d = \frac{x_{m1}}{x_{m2} - x_{m1}}$$

.Where $x_{mn}$ is the distance from the sample to the $n^{th}$ minima.

In practice $L$ can not be accurately measured due to the tube attenuation i.e. energy dissipation due to the air absorption, non–smooth non–rigid walls and air viscosities. If these factors introduce an additional attenuation $\alpha$,

$$p_i(x) = P_0 \left[ e^{-\imath k_0 x_1 - \alpha x_1} \right]$$

$$p_r(x) = P_0 \left[ e^{-\imath k_0 x_2 - \phi + \alpha x_2} \right]$$

$$p_t(x) = P_0 \left[ e^{-\imath k_0 x_1 - \alpha x_1} + e^{-\imath k_0 x_2 - \phi + \alpha x_2} \right]$$

$$u_x = \frac{-\imath(\imath k_0 - \alpha) P_0}{\omega \rho_0} \left[ e^{-\imath k_0 x_1 - \alpha x_1} - e^{-\imath k_0 x_2 - \phi + \alpha x_2} \right]$$

$$Z_s(0) = \frac{\omega \rho_0}{(k_0 - \alpha)} \left[ \frac{1 + e^{-\phi}}{1 - e^{-\phi}} \right] = \frac{\rho_0 c_0}{\left(1 - \frac{\alpha}{k_0}\right)} \left[ \frac{1 + e^{-\phi}}{1 - e^{-\phi}} \right]$$

i.e. an attenuation factor of $\left(\frac{k_0}{k_0 - \alpha}\right)$ has been introduced. Thus to evaluate the impedance it is necessary to know the value of the attenuation coefficient $\alpha$ and the effect of the sample $\phi$. The tube attenuation coefficient has been examined by Kirchoff [30] who put

$$\alpha = 2.77.10^{-7} \frac{f^{\frac{1}{2}}}{r} \text{ nepers/m}$$

where $f$ is the frequency of interest and $r$ is the radius of the tube in meters.

Beranek [8] measured $\alpha$ experimentally and found

$$\alpha = 3.18.10^{-7} \frac{f^{\frac{1}{2}}}{r} \text{ nepers/m.}$$

The American standard [31] uses

$$\alpha = 2.95.10^{-7} \frac{f^{\frac{1}{2}}}{r} \text{ nepers/m.}$$

Having determined $\alpha$ it now remains to find $\phi$. For a non–rigid termination it is not possible to measure $L$ at the face of the sample. Kilmer measured the SPL of any maximum ($SPL_{max}$) and that of the first and second minima ($SPL_{min1}$, $SPL_{min2}$) then he calculated

$$L_1 = SPL_{max} - SPL_{min1}$$

$$L_2 = SPL_{max} - SPL_{min2}$$

A graph of $L - L_1$ against $L_1 - L_2$ allowed the deduction of $L$ as shown in figure 2.5

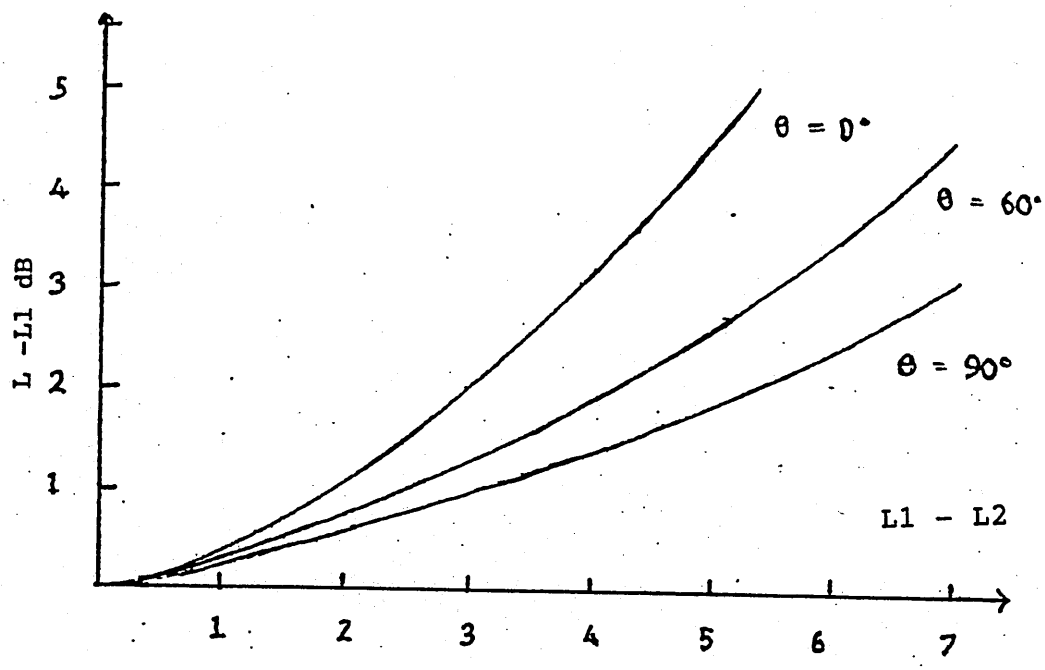


**Figure 2.5** Determination of $L$ (after Kilmer)

Morse [32] plotted the values of the SPL at the maxima and minima and extrapolated to $x = 0$ to find $L$. Ando [33] and Joffe [34] also proposed extrapolation techniques to account for the errors introduced by the tube losses. Ando examines the pressure wave in front of the sample figure 2.6.

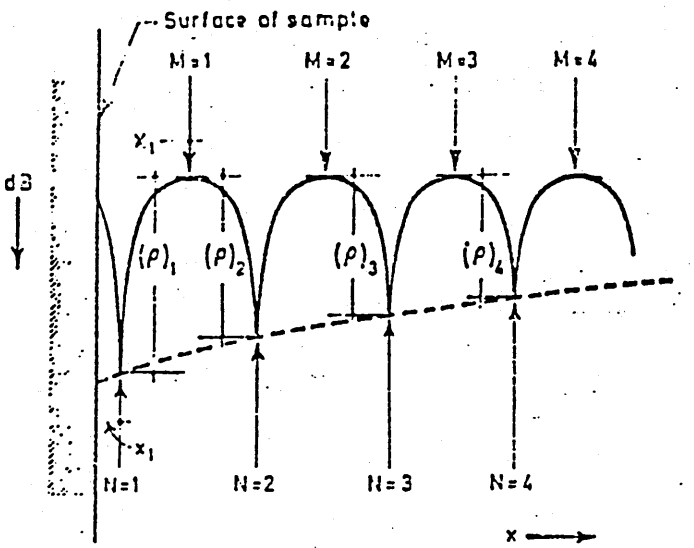


**Figure 2.6** Pressure distribution in front of sample under test

Note that the magnitude of the pressure minima falls with increasing distance from the sample due to the effect of the tube attenuation, whilst the magnitude of the maxima remains constant. Assuming $2\lambda < x_N \leq 0.1\lambda$ the reflection coefficient $|R_N|$ at $x_N$ will lie on a straight line, hence $|R_0|$ can be found at $x = 0$, figure 2.7.

The function $|R_N| = |R_0|(1-2\alpha x_N)$ is plotted against $x_N$ thus the slope of the line is $-2\alpha|R_N|$. The phase is found from

$$\phi'' = (2N+1)\pi - 2k_0 x_N + \delta_N$$

with

$$\delta_N = \sin^{-1}\left(\frac{\alpha}{2k_0}\left[\frac{e^{2\alpha x_N}}{R_N} - \frac{|R_N|}{e^{2\alpha x_N}}\right]\right)$$

It should be noted that as the attenuation constant is measured the ideal gas assumption in the calculation of $\alpha$ is no longer required. Joffe [34] uses a similar method to examine the error present on Ando's method. This method of measuring the impedance relies upon the accurate location of the

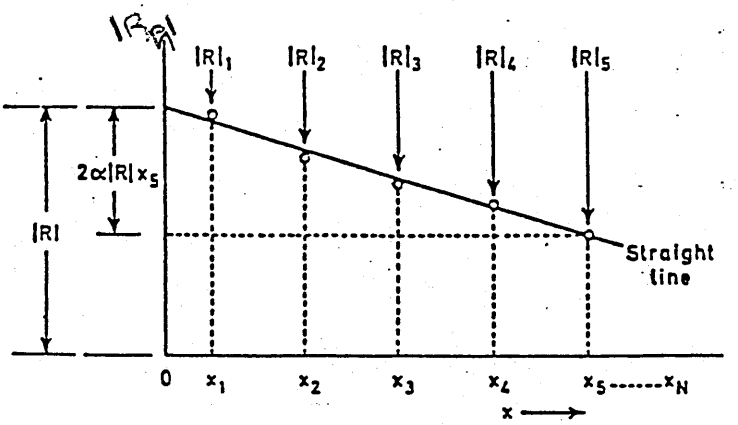


**Figure 2.7** Location of $|R_0|$ from plot of reflection coefficient

pressure minima. This usually involves the use of a probe microphone. As the pressure measured is not at the physical end of the tube but at some distance in front of the opening a probe end correction has to be introduced. Morse [32] used

$$c_e = -1.4a \leftrightarrow -1.6a$$

where $a$ is the radius of the probe tube. Ando [35] used

$$c_e = -a(0.11ka - 0.64).$$

The American standard advocates measuring the end correction using a rigid termination

$$c_e = d_1 + 0.5(d_2 - d_1)$$

where $d_i$ is the distance to the $i^{th}$ minima measured from the rigid termination.

There are several other source of error that should be considered. Location of the sample within the tube is inherent in any tube technique. If the sample is oversize, edge clamping may change the properties around the circumference of the sample. An undersize sample allows air round the sample so the impedance measured is that of the sample and the rigid termination.

Donato [36] has looked at the subject of clamping with inconclusive results. A common method is to use an undersize sample and to seal the edges with petroleum jelly. Other source of error are

1. Temperature induced frequency instabilities
2. Micro–climatic variations in the tube (especially when used outdoors in–situ [37])
3. Wave dispersion
4. Viscosity of the fluid and non–rigid tube walls. This problem has been studied by Morse and Ingard [38] who show that the velocity of sound in air differs from that in a flexible walled tube
5. Non plane wave propagation. The theory presumes plane wave propagation. Thus the upper frequency of use is determined by the tube diameter $r$. The first transverse mode which occurs at $\lambda = 3.41r$ [39] must not be excited. Though Beranek [8] states that this will not be excited by axial wave propagation and that the first transverse mode will become apparent at $\lambda = 6.82r$. The upper frequency of use is approximately 2500Hz for the large Bruel and Kjaer tube and 6500Hz for the small tube.
6. The lower frequency limit is a consequence of the need to measure two pressure minima thus the tube must have a minimum length of half a wavelength. This value is around 300Hz for the standard tube and 1KHz for the smaller tube.

Developments in signal processing have allowed the introduction of a two microphone technique pioneered by Schmidt [40] and modified by Seybert and Ross [41] and later Chung and Blaser, [42] [43]. The method has been used by Heisler, McDaniel and Dahl [44] to measure the impedance of a forest floor. The results were found to be similar to the standing wave ratio tube technique however the use of a broadband source reduced the time taken to perform the measurements. Consider the apparatus shown, figure 2.8

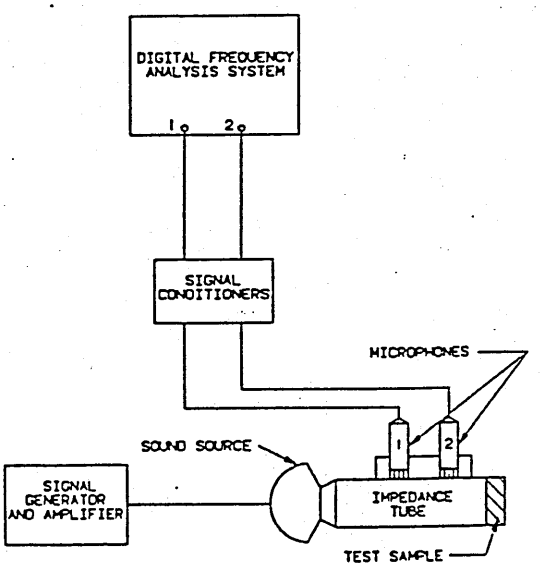


**Figure 2.8** Broadband impedance tube technique

The transfer function between the pressures at the two microphones was related to the impedance. The accuracy of the measurement may be enhanced using either of two techniques.

1) Sensor switching. This overcomes the problem of mismatch between the channels by using a transfer function in the calculations which is the geometric mean of the original transfer function and that obtained with the location of the sensors interchanged.

2) The enhancement method. The coherence function developed by Chu [45] may be used to improve the signal to noise ratio of the measurements.

The impedance was now given by

$$\frac{Z}{\rho_0 c_0} = \frac{\imath C \bar{H}_{12} \sin(k_0\, l) - \sin[k_0(l-s)]}{\cos[k_0(l-s)] - C.\bar{H}_{12} \cos(k_0 l)}$$

where $\bar{H}_{12}$ is the geometric mean of the two transfer functions and

$$C = \left[ \frac{(v^0_{23}.v^s_{23})}{v^0_{12}.v^s_{12}.v^0_{31}.v^s_{31}} \right]^{\frac{1}{2}}$$

with $v_{ij}$ the positive square root of the ordinary coherence function between microphones $i$ and $j$. The subscripts o and s refer to the original and switched sensor positions. The distance from the first microphone to the tube end is denoted by $l$. It should be noted that a third sensor is required to use this method to act as a reference. Chung et al also examined the sensor positioning and found indeterminate values of $\bar{H}_{12}$ when

$s = m\left(\frac{\lambda}{2}\right)$ m=1.2.3....

$s$ is the spacing of the microphones and hence the lower frequency limit is given by

$$s \leq \frac{c_0}{2f_m}$$

The method developed by Chung et al is now an American standard [46].

As the technique has increased in popularity the likely sources of error and various applications have been examined. Chu [47] included the attenuation coefficient into the technique and later proposed a development of the method that only required one microphone [48]. The single microphone recordings at two separate positions were related to a deterministic pseudorandom source signal. The expression for the reflection coefficient was modified to give

$$R_p(f) = \left[H_{12}(f) - e^{-s(\imath k_0+\alpha)}\left(e^{s(\imath k_0+\alpha)} - H_{12}(f)\right)^{-1}\right] e^{2L(\imath k_0+\alpha)}$$

where $\alpha$ is the attenuation coefficient, $s$ the separation between the two microphones and $L$ the distance from the sample to the first microphone. The last quantity had been kept small by Chung et al to minimize the effect of the tube attenuation.

Seybert and Soenarko [49] suggested the microphone separation should be small to give a high coherence though this will reduce the accuracy at low frequencies with the value of the transfer function tending to unity. In practice a series of microphone spacings are used to cover the frequency range of interest.

Boden and Abom expanded the work of Soenarko et al. to examine the errors inherent in the dual microphone technique first without [50] and then

with [51] a mean flow present. They concluded that the bias errors in the measurement of the transfer function would be kept to a minimum if the length of the tube was kept as small as possible. The source termination should be anechoic and the first microphone should be located as close to the sample as possible. Random error is reduced by minimizing background noise. They advised however that the microphone separation should not be below 50mm as although this improved the coherence the effect of any measurement errors became significant. The separation should be chosen so that

$$0.1\pi < k_0 s < 0.8\pi$$

Banks-Lee et al [52] studied the length–induced errors and reached the same conclusion as Boden et al. They also suggested that one sensor be located near a minimum and the other by a maximum. A modified method has been produced by Fahy [53] using a digital computer to streamline the data collection process. This uses a single microphone which is moved to sample two points of the sound field.

## Adaptations of tube techniques

Many of the techniques applied to samples of finite size mounted in a tube may also be used for in–situ measurements without a tube. Thus the SWR method was first adapted by Ingard [54], and later by Ando [55], Dickinson [37], Sides and Mulholland [56] and Klein and Cops [57]. The process requires that a probe microphone be inserted through a sample to measure the pressure field above the surface. The experiment was refined by Legouis and Nicolas [58] who examined the standing wave field above a surface produced by a continuous source. They measured the phase and amplitude gradient and used these variable parameters in the expression evaluated by Nicolas and Lemire [59]. The measured phase gradient was compared to the predicted one with the magnitude and phase of the reflection coefficient as variables so that the function

$$J(|R_N|, \phi) = \sum_{i=1}^{n} (\Delta\varphi_i - \Delta\varphi(x_i, R_N, \phi))^2$$

is minimized where

$x_i$ the distance from the source to the measurement position.

$\Delta\varphi_i$ is the measured phase gradient.

$\Delta\varphi$ is the theoretical phase gradient.

The method was adapted to determine the impedance of a grassland surface at low frequencies by Daigle and Stinson [21]. They measured the phase difference and studied the area around the first peak and trough and the distance of the first peak from the surface. They showed that the distance between the plotted phase difference first peak and its neighbouring trough, the P–V phase difference and the distance from the peak to the sample surface were sufficient to determine the reflection coefficient, see figure 2.9. These parameters have been studied as functions of the magnitude and phase of the reflection coefficient.

It is also possible to adapt the broadband techniques used in the impedance tube for use in the free–field situation, [25], [60]. To obtain the white noise spectra essential for the correlation technique Miki [60] formulated a two stage process. A signal generation mode was use to 'whiten' the source i.e. to compensate for the frequency response of the system. The measurement mode then utilized this new signal. The measurements used simultaneously emitted broadband noise and a sinusoidal signal. The pilot signal was monitored to allow for changes in the coherence due to wind and temperature gradients. The cross correlation function ($F$) between the transmitted and received signals was used to extract the direct and reflected components from which the impedance may be calculated using

$$Z_s(f) = \frac{F(x(\tau)+y(\tau))}{F(x(\tau)-y(\tau))}\left(1 - \frac{ic_0}{2\pi f(\tau+2h)}\right)$$

where $x(\tau)$ and $y(\tau)$ are the waveforms corresponding to the direct and reflected signals.

$r$ is the source to receiver separation

$h$ is the receiver height.

This method assumes the ground is a minimum phase system in which the real and imaginary parts of the impedance are related via the Hilbert transform. This may not be the case however for layered media.

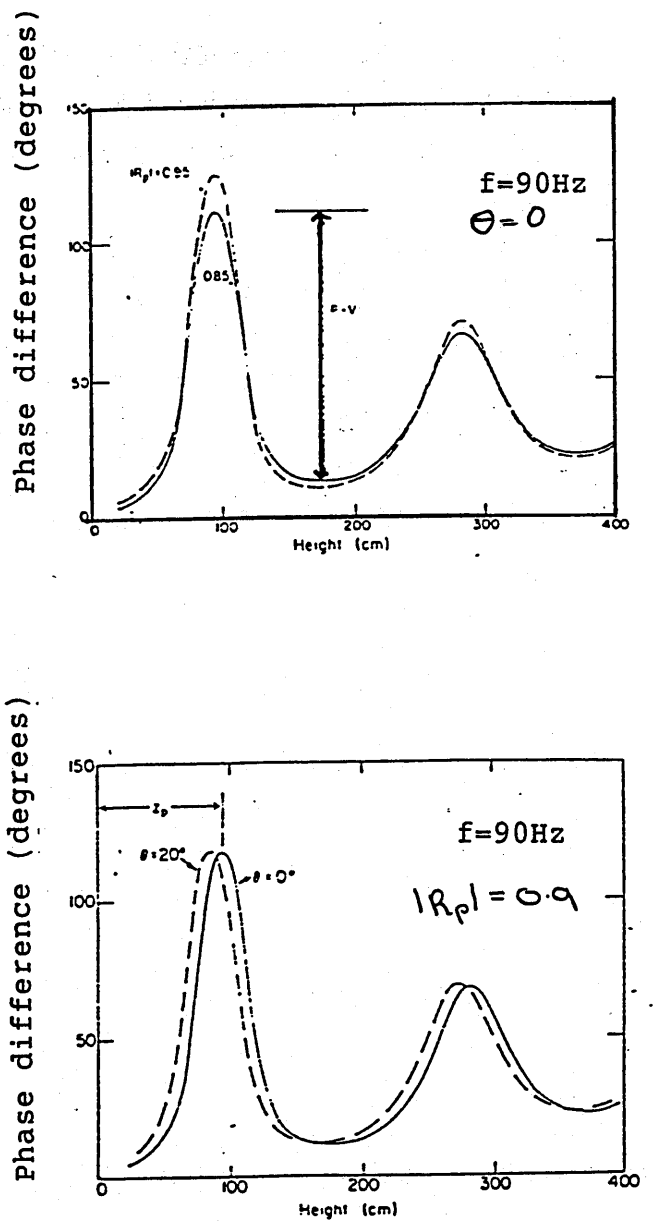


Figure 2.9 Measured values for phase gradient technique

A similar technique was used by Yamada [61] who related the power and cross spectra of a pair of vertically separated microphones to the impedance of a surface. If one considers the geometry shown in figure 2.10

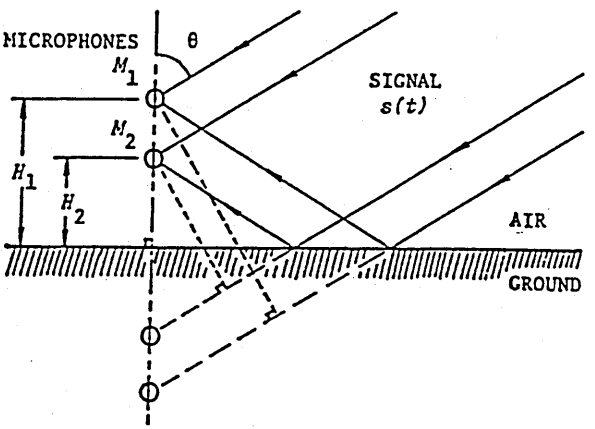


**Figure 2.10** Free field technique geometry after Yamada

The sound pressure at microphone i is given by

$y_i(t) = s(t + \Delta_{1i}) + \int_0^\infty a(T).s(t - \Delta_{1i} - \Delta_i - T)dt$

$s(t)$ is the incident sound pressure

$a(t)$ the impulse response of the system, i.e. the time domain definition of the frequency response of the system.

$\Delta_i$ is the time lag associated with the path difference between the direct and reflected waves

$\Delta_{1i}$ is the time lag associated with the path length difference between the direct waves for microphones 1 and i.

The power spectrum at microphone i is given by

$p_i(f) = P_s(f) + \left[1 + R(f)e^{-i2\pi f\Delta_i}\right]^2$

with $P_s(f)$ the power spectrum of $s(t)$, and the cross spectrum of $y1(t)$ and $y_2(t)$ is given by

$p_{12}(f) = P_s(f) + \left[1 + R^*(f)e^{i2\pi f\Delta_i}\right] . \left[1 + R(f)e^{i2\pi\Delta_2}\right] e^{-i2\pi f\Delta_{12}}$

where $*$ denotes the complex conjugate. The two equations are solved to find $R(f)$ the complex reflection coefficient and hence the impedance from

$$R(f) = e^{(\imath 2\pi f \nu_{12})} \frac{\frac{P_{12}(f)}{P_1(f)} e^{(-\imath 2\pi f \nu_{12})} - 1}{e^{(-\imath 2\pi f \nu_{12})} - \frac{P_{12}(f)}{P_1(f)}}$$

with $\nu_{12}$ the time delay between the direct and reflected signal at a point midway between $M_1$ and $M_2$.

It was suggested that the delay times are measured using a cepstral or auto–correlation technique. An alternative solution may be derived from the spectra at three microphones as used by Watanabe and Kotabe [62] for single frequency measurements. In practice once an estimation of the delay times has been found they are varied in an optimization routine to give a precise value of R(f). The optimization uses the predicted value and a measured value at a third microphone. This method is similar to the adaptation of Chung and Blaser's two microphone work to in-situ applications by Allard for fibrous absorbers. The impedance was first measured at normal incidence with an intensity probe measuring the pressure and particle velocity, [63]. The separation between the microphones used is determined by the frequency range of interest and by the sample size. The effect of the sample size on the absorption coefficient has been determined, [64] and the impedance measurement method modified accordingly. It has been shown that the method is mathematically similar to that of Chung and Blaser. The basic method is described in [65]. Consider the microphone arrangement figure 2.11.

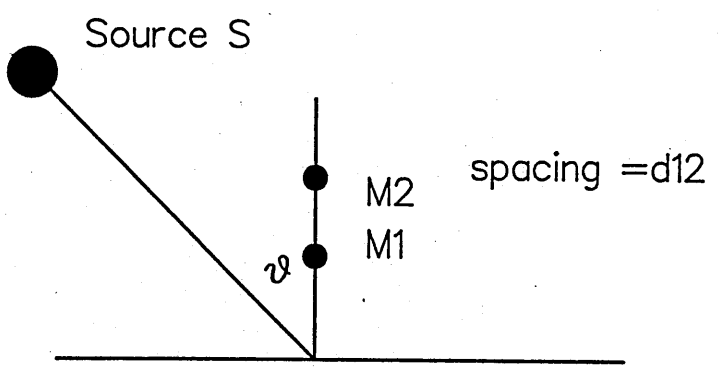


**Figure 2.11** Free field geometry after Allard

The pressure at a point $M$ midway between the two microphone is given

by

$p(x) = \frac{p_1(x)+p_2(x)}{2}$

where $p_i$ is the pressure at microphone i and the velocity is given by

$u = \frac{p_2-p_1}{\imath\omega\rho_0 d_{12}}$

$d_{12}$ is the separation between $M1$ and $M2$. Thus

$Z_M = \frac{\imath\omega\rho_0 d_{12}(p_1+p_2)}{2(p_1-p_2)}$

Thus if $H(\omega)$ is the transfer function between $p_1$ and $p_2$

$Z_M = \frac{\imath\omega\rho_0 d_{12}(H(\omega)+1)}{2(1-H(\omega))}$

If the acoustic field is assumed to be plane

$$Z_s = \frac{Z_M - \imath\rho_0 c_0 \tan\left(\frac{\omega d}{c_0}\right)}{\rho_0 c_0 - \imath Z_M \tan\left(\frac{\omega d}{c_0}\right)}$$

with $d$ the distance from $M$ to the surface of the sample. The method has been adapted for used at oblique incidence by Allard et al [66] giving

$$Z(\theta) = \frac{\rho_0 c_0}{\cos\theta} \frac{\left[\frac{Z_M - \imath\rho_0 c_0 \tan\left(\frac{\omega d\cos\theta}{c_0}\right)}{\cos\theta}\right]}{\left[\frac{\rho_0 c_0}{\theta} - \imath Z_M \tan\left(\frac{\omega d\cos\theta}{c_0}\right)\right]}$$

Where $\theta$ is the angle between the source and the normal to the surface.

This method has been used on poro–elastic [67] and anisotropic [68] materials. It was modified further by Allard and Champoux [69]. The modifications took two forms. The plane wave assumption was replaced by a spherical and then a spherically decoupled representation for the acoustic field. The latter model was shown to be preferable when compared to the theory developed by Nobile and Hayek. Hence $R$ was found from

$R = \frac{e^{\imath k_0 r_2} r_2 - H(\omega) e^{\imath k_0 r_1} r_1}{H(\omega) e^{\imath k_0 r'_1} r'_1 - e^{\imath k_0 r'_1} r'_1}$

see figure 2.12.

The impedance is then calculated from

$Z_s = \frac{1+R}{1-R}\left(1 + \frac{1}{\imath k_0 r}\right)$

The second modification was the use of an iterative procedure, (figure 2.13), using the Nobile and Hayek model. This method was used by Allard for measurements on coated surfaces [70].

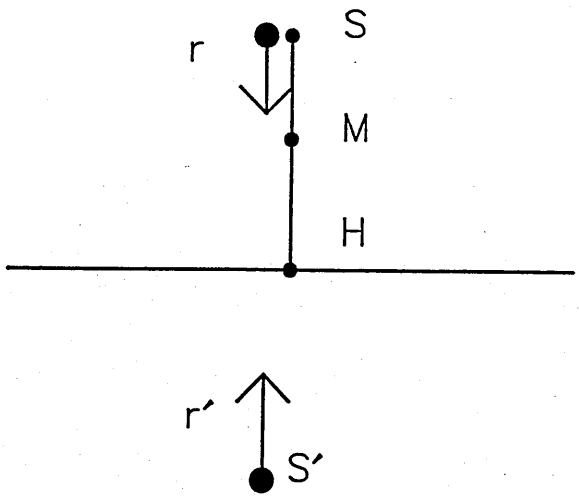


**Figure 2.12** Improvement to Allard technique

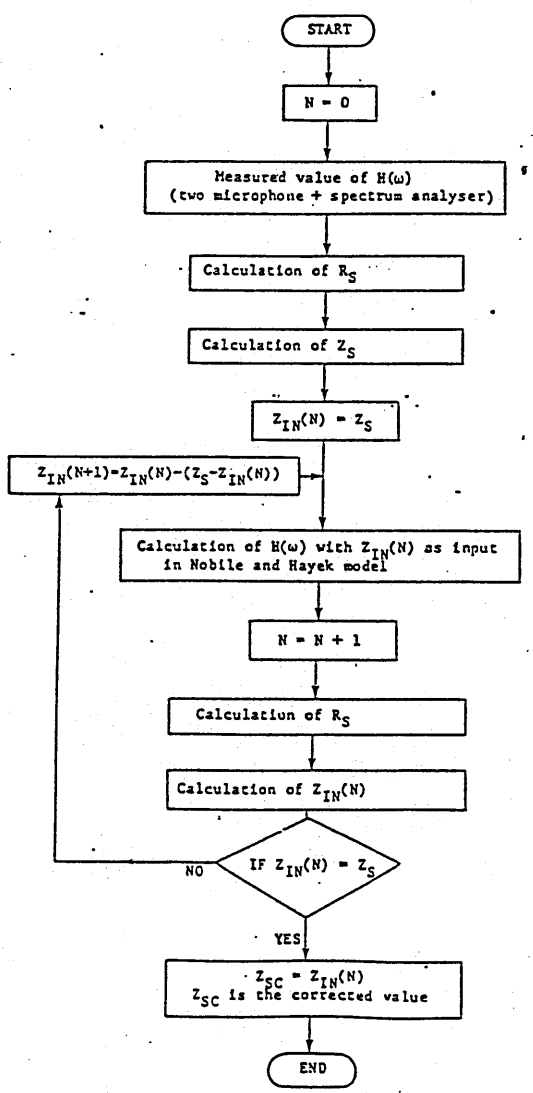


**Figure 2.13** Iterative procedure to improve Allard's free field technique

The method was studied by Champoux [71] who discusses the procedure for the calibration of the two microphones. Further sources of error were examined by Champoux et al [72] and briefly by Minten [73] who used the earlier technique on rigid backed materials.

Nobile [74] has also produced the necessary equations relating the impedance to the transfer function of a pair of vertically separated microphones. His method appears to be a less precise version of Allard's technique. as does the approach used by Vigran [75], [76] and Waddington [77], [78] which assumes plane wave propagation. Tamura [79] proposes a transfer function method relating the pressures in two planes to the direct and reflected waves via spatial Fourier transforms to find the plane wave components and then examines plane wave propagation theory to separate the direct and reflected waves. Luzzato [80] generates a transcendental equation in $k_x$ which is solved with a series of boundary conditions. The solution then being used to find the impedance. The method is claimed to be less sensitive to background noise than Allard's technique.

## 2.4 Indirect Methods

One of the more recent methods proposed for measuring impedance is the indirect method. This operates by comparing the measured sound field above the surface of interest from a point source with a numerical propagation model. The impedance is then calculated from a best fit procedure. Either the real and imaginary parts of the impedance or the parameters of a theoretical model of ground impedance are altered to gain an agreement between the theoretical and practical results.

Thomasson [81] examined the propagation from a point source over an impedance boundary and arrived at the expression for the field above a boundary assuming that the refraction index was large. He related the physical properties of the boundary to four variable parameters which were in turn related to the impedance. The four parameters were adjusted until a measured excess attenuation spectrum at short range was matched by the

prediction, and subsequently the deduced values of the parameters allowed calculation of the impedance. Several geometries were examined to enhance the accuracy of the measurements. Thomasson examined a rigidly backed layered system and proposed the variables used should be:

$$a = \frac{\rho_0 c_0 |K\rho\Omega|^{\frac{1}{2}}}{\rho} \tag{2.1}$$

$$b = \arg(K\rho)^{\frac{1}{2}} \tag{2.2}$$

$$c = \frac{\sigma}{\rho} \tag{2.3}$$

$$d = \left[|K\rho\Omega|^{\frac{1}{2}} 2\pi z_1\right] - 1 \tag{2.4}$$

$$b' = e^{-\imath b} \tag{2.5}$$

$$c' = \left[1 + \imath c(2\pi f)^{-1}\right]^{\frac{1}{2}} \tag{2.6}$$

with

$$0 < \arg(c') < \frac{\pi}{4} \tag{2.7}$$

The impedance is found from

$$Z_s = \frac{\imath}{a\left(\frac{b'}{c'}\right)\tan\left(\frac{b'c'f}{d}\right)} \tag{2.8}$$

with $c_0$ the velocity of sound in air,
$K$ the compressibility of the fluid
$\Omega$ the porosity of the layer
$\sigma$ the specific flow resistivity of the layer
$\rho$ the dynamic air density
$\rho_0$ the density of air
and
$z_1$ the layer depth

Thomasson also tried to vary three parameters but did not achieve the required results. A similar indirect process for measuring the impedance has been derived from the microstructural model [82] developed by Attenborough [83]. This approach is discussed further in chapter 6.

Bass and Bolen [84] used the real and imaginary parts of the impedance as variables to fit a series of averaged single microphone readings or to fit the spectra from two microphones simultaneously. The experimental data being compared to Donato's theoretical work. The results had a large standard deviation especially for the single microphone technique and were less reliable at frequencies less than 200Hz. Van der Heijden [85] used a sloping microphone array arranged so that the path length for the reflected wave increased by 2cm for each microphone. A pure tone source was used and the results compared to those gathered in an anechoic chamber to overcome source effects. A wide spread of data was gained for a grassland surface though a 'forest soil' gave more uniform results. Glaretas [86] , [87] extended the method applying it not only to a locally reacting surface but also to an extended reacting half space and an externally reacting rigidly backed layer. Again a large scatter of data especially at lower frequencies was found. A pair of vertically separated microphones was used with a broadband noise source. The magnitude and phase of the impedance were used as variables. To overcome phase and amplitude mismatch problems a sensor switching technique similar to that used by Chung and Blaser was employed. The frequency range of the measurements was extended by using a range of geometries. Glaretas claimed that the method was more accurate at the higher frequencies and in the frequency range spanning the first attenuation dip.

Habault [88] fitted the S.P.L for a number of geometries at one frequency varying the phase and modulus of the impedance in a locally reacting surface model. The lowest frequency being examined was 580 Hz. She also showed that the Delaney and Bazley impedance model, see chapter 3 was not applicable to all ground surfaces. This has been suggested by others, [89] [90]. The unsuitability of the Delany and Bazley formulae particularly for

cultivated soil surfaces and snow has been confirmed more recently by Hess, Attenborough and Heap [91] by using a prototype version of the indirect method described more fully in chapter 6.

## 2.5 Pulse Methods

With the improvement in digital signal theory the use of impulses or tone bursts in the measurement of the impedance of a surface in a non–anechoic environment has become a feasible. A geometry may be chosen such that the direct and reflected signals may be separated in time, captured and Fourier transformed to find the frequency response and hence the reflection coefficient and impedance.

Gately and Cohen [11] used a tone burst method in an impedance tube to evaluate the performance of acoustic filters, though a long tube was required to separate the direct and reflected signals, and each burst contained information for a single frequency only. Although this improved the signal to noise ratio the large range of frequency information contained in an impulse is lost. Louden [92] used a single pulse to measure the characteristics of a surface but suffered signal to noise ratio problems and had a poor dynamic range. Kintsl [93] measured the reflection coefficient and absorption coefficient at normal incidence using a spark discharge to form the impulse. The direct and reflected pulses were stored on an oscilloscope photographed and Fourier transformed. Davies and Mulholland [94] refined the method of Ingard and Bolt [54] to measure the impedance of a surface. The source, is assumed to be spherical and produces a signal

$$p_t(\omega) = p_d(\omega) + p_r(\omega)e^{(i\omega\tau)} \qquad (2.9)$$

where

$p_t(\omega)$ is the total signal

$p_d(\omega)$ is the direct signal and

$p_r(\omega)$ is the reflected signal. $\tau$ is the time delay between the direct and reflected signals. If $R(\omega)$ is the reflection coefficient then

$$p_r(\omega) = R(\omega)p_d(\omega)f\left(\frac{d_1}{d_2}, \theta\right) \tag{2.10}$$

Therefore

$$R(\omega) = \frac{p_t(\omega) - p_d(\omega)}{f\left(\frac{d_1}{d_2}, \theta\right).p_d(\omega)e^{-\imath\omega\tau}} \tag{2.11}$$

at $x = 0$, $f\left(\frac{d_1}{d_2}, \theta\right) = 0$ and $\tau = 0$

$$R(\omega) = \frac{p_t(\omega) - p_d(\omega)}{p_d(\omega)} \tag{2.12}$$

Davies et al [94] measured the direct signal a distance from the surface in anechoic conditions windowing out any unwanted reflections. The triggering of the impulse capture had to be closely monitored with respect to the signal sent to the loudspeaker and the geometry had to be kept constant. Errors in the triggering or geometry would lead to phase error in the calculation of the reflection coefficient. Salikuddin et al [18] used Singh and Katra's method [95] to measure the impedance of a duct. Singh generated the impulses from a microprocessor using a digital to analogue converter and loudspeaker. Thus the pulse shape could be carefully controlled during it's synthesis. Salikuddin used a spark discharge system to give a flat uniform spectra and pulse uniformity. Van der Heijden and De Bie [96] applied the Davies and Mulholland method to trays of sharp sand. A tone burst similar to that used by Yuzawa [97] was emitted from a high frequency transducer mounted vertically above the sand surface. A transducer between the speaker and surface measured the direct and reflected impulses at normal incidence. The pulses were captured, the time of arrival and the amplitude of the first two maxima and the first minima of both the direct and reflected spectra were recorded see figure 2.14. The measurements were then repeated over a rigid backing and the time delay of the pulse is found from;

$$t_r = \frac{1}{3}\sum_{n=1}^{3}(t'_n - t_n) \tag{2.13}$$

$$A_r = \frac{1}{3}\sum_{n=1}^{3}\frac{A'_n.B_n}{A_n.B'_n} \tag{2.14}$$

with $B_n$ and $B'_n$ the amplitudes from the hard surface. The phase of the reflection coefficient is found from

$$\phi = 2\pi f\left[t_r - t_b + (R_2 - R_1)\left[\frac{1}{c(20)} - \frac{1}{c(\psi)}\right]\right] \tag{2.15}$$

$c(\psi)$ is the speed of sound in air at $\psi$ degrees celsius found from

$$c(\psi) = \frac{\left(273 + \frac{\psi}{273}\right)^{\frac{1}{2}} 331.6}{1 - 0.21 \times 10^{-4} p_w h} \tag{2.16}$$

where $p_w$ is the vapour pressure at $\psi$ degrees celsius relative to barometric pressure,

$h$ is the relative humidity of air in Vol %,

$f$ is the frequency if interest,

$t_r, t_b$ are the time differences from the sand and hard backing respectively found from equation 2.13 and $R_2, R_1$ are the path lengths of the reflected and direct signals respectively.

The reflection coefficient is found from.

$$R = A_r e^{i\phi} \tag{2.17}$$

and

$$Z_s = \frac{1 + R}{(1 - R)\cos\theta\left(1 + \frac{1}{k_0 h}\right)} \tag{2.18}$$

where $\theta$ is the angle of incidence of the sound, $k_0$ is the wave number and $h$ is the distance between the source and the surface. Heijden noted the impedance changes with the grain size of the sand and the effect of the layer depth. Above 90mm at 2KHz the impedance was constant with layer depth. Errors were introduced into the phase measurement from incorrect measurement of the path lengths and into the amplitude measurements by rounding. The latter effect was noticeable particularly with an acoustically

hard surface. Attention was also paid to the sample size. Kintsl [93] related the radius of the area under investigation to the pulse length by

$$r = \frac{\sqrt{(h + l + \frac{cT_2}{2})(h + \frac{cT_2}{2})(2l + cT_2)cT_2}}{h + l + cT_2} \tag{2.19}$$

with $r$ the radius of the area under investigation,
$h$ the distance from the source to the surface,
$l$ the distance from the receiver to the surface and
$T_2$ the reflected pulse width.

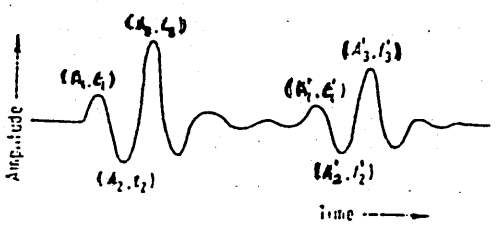


**Figure 2.14** Impulse measurements after Van der Heijden

To date the most effective use of an impulse to measure the impedance of outdoor surfaces has been made by Cramond and Don [98]. A broad band pulse is emitted from an impulse source whose design is similar to that of a firearm. The arrangement in figure 2.15 is implemented. The direct and reflected impulses are captured at A and B with a time delay of

$$T = \frac{\left[(r_2^2 + 4h_s^2)^{\frac{1}{2}} + r_2\right]}{c_0} \tag{2.20}$$

separating the direct and reflected pulses with $h_s = h_r$. The direct and reflected pulses are then frequency analysed to determine the complex reflection coefficient and the impedance is found from

$$R = \frac{\sin\theta - \frac{\rho_0 c_0}{Z_2}}{\sin\theta + \frac{\rho_0 c_0}{Z_2}} \tag{2.21}$$

for a locally reacting surface. The method assumes that the propagation is given by

$$p_t = \frac{1}{R_1}e^{-\imath k_0 R_1} + \frac{R}{R_2}e^{-\imath k_0 R_2} + (1-R)\frac{F}{R_2}e^{-\imath k_0 R_2} \qquad (2.22)$$

where the third term the ground wave is presumed to be negligible. The method has been used for angles of incidence ranging from $12^0$ to $90^0$ and does not involve any comparative measurements made over perfectly reflecting surfaces. Geometrical spreading and atmospheric absorption is accounted for using the geometries described providing the source has cylindrical symmetry.

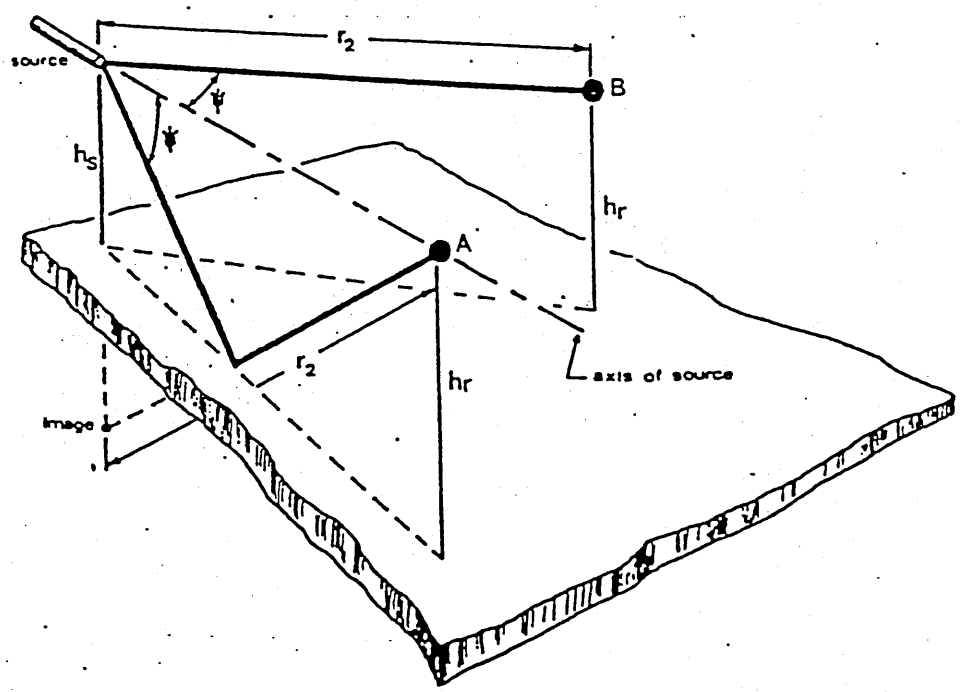


**Figure 2.15** Impulse geometry for oblique incidence after Cramond et al

The system is calibrated by placing the two microphone close to each other on the normal from the pulse source with the diaphragms perpendicular to the source receiver path. A series of pulses (at least eight) are captured to calibrate the two channels. The microphones are then moved to the chosen measurement geometry and a further series of pulses is captured. The signals are processed so that the direct and reflected signals

are captured and the rest of the pulse set gradually to zero. The starting edge of the pulses are captured and aligned and summed to produce a direct and reflected pulse which are then Fourier transformed to give the reflection coefficient and the impedance. The alignment of the pulses is crucial. The results of the measurements are reported in chapter 7. Cramond showed the pulses were repeatable and Fourier transformed the direct pulse to examine the spectrum of the measurement signal this located any areas of uncertainty in the calculated impedance. The shape of the pulses used means that there is no information below 800Hz though the signal to noise ratio is improved by using a series of impulses. The measurements may also be affected by extraneous reflections and thus the receivers should be removed from any source of unwanted reflections such as stands. The surfaces tested by Cramond et al were examined to see if they were locally reacting if so then the impedance calculated from the impulses at one angle could be used with the direct pulse to construct the reflected pulse at another angle of incidence. The grassland and carpet surface were found to be locally reacting unlike the concrete backed fibreglass which showed two distinct reflections one from the upper boundary and a second from the fibreglass concrete interface. As the technique relies on relative phase and magnitude measurements within a pulse no phase information is lost due to positional uncertainties. The neglect of the ground wave term was shown to be a reasonable assumption for the grassland and carpet surfaces but not so for the fibreglass at angles of incidence of 45°. The lowest angle of incidence that may be measured is determined by the geometry and the pulse length that may be used to prevent the pulses overlapping in the time domain. This problem may be overcome by using a shorter pulse but the signal to noise ratio would fall. An alternative method is to separate overlapping pulses using the cepstral technique described by Bolton and Gold [99], [100], and [101].

Consider the spectrum at a receiver in the time domain

$$p_t(t) = p_d(t) + \frac{R_1}{R_2} p_d(t) * h(t-\tau). \qquad (2.23)$$

Where $p_t(t)$ is the total signal, $p_d(t)$ is the direct signal and $h(t-\tau)$

the impulse response of the system delayed by a period $\tau$. $\frac{R_1}{R_2}$ accounts for the spherical spreading. The power cepstrum is defined by Hassab and Boucher [88] as the inverse Fourier transform of the natural logarithm of the squared modulus of the Fourier transform of the time history. Performing these operations on 2.23 gives us

$$|p_t(\omega)|^2 = |p_d(\omega)|^2 \left[1 + \frac{R_1}{R_2} H(\omega) e^{-\imath\omega\tau}\right] . \left[1 + \frac{R_1}{R_2} H^*(\omega) e^{\imath\omega\tau}\right] \qquad (2.24)$$

for the squared modulus. Where $H(\omega)$ if the Fourier transform of $(h(t-\tau)$. Then taking the natural logarithm gives

$$\log_e(|p_t(\omega)|^2) = \log_e(|p_d(\omega)|^2) + \log_e\left[1 + \frac{R_1}{R_2} H(\omega) e^{-\imath\omega\tau}\right] + \log_e\left[1 + \frac{R_1}{R_2} H^*(\omega) e^{\imath\omega\tau}\right] \qquad (2.25)$$

expanding the last two logarithmic terms using

$$\log_e[1+z] = z - \left(\frac{z^2}{2}\right) + \left(\frac{z^3}{3}\right) - \cdots \qquad (2.26)$$

gives

$$\hat{p}_t(t) = \hat{p}_d(t) + \frac{R_1}{R_2} h(t-\tau) - \left(\frac{R_1}{R_2}\right)^2 h(t-\tau) * \frac{h(t-\tau)}{2} + \cdots + \qquad (2.27)$$

$$\frac{R_1}{R_2} h(-t-\tau) - \left(\frac{R_1}{R_2}\right)^2 h(-t-\tau) * \frac{h(-t-\tau)}{2} + \cdots \qquad (2.28)$$

$\hat{p}_t(t)$ is the cepstrum of the total signal and $\hat{p}_d(t)$ is that of the direct signal. The impulse response modified by the spherical spreading factor occurs at the time $\tau$ which is determined by the path length difference between the direct and reflected signals. The higher order rahmonics (similar in form to harmonics) occur at intervals of $\tau$ $2\tau$ etc. Thus the impulse response may be extracted from the cepstrum and an inverse Fourier transform applied to find the reflection coefficient. It is more difficult to find the phase of the reflection coefficient which must be accurately measured to calculate the impedance. Errors arise when the impulse response is extracted from the

cepstrum using the sine squared filter. The error arises from being unable to find the delay between the window and the start of the function. This value may be found by correlation with a unit sample function or a model of the response or by examination of the impedance calculated from the technique. The extraction time was simple to find when Bolton et al used an electrical analogue to represent the surface as the behaviour of the circuit was well known but was more difficult to locate when the method was used to measure the impedance of a reticulated polyurethane foam. The source used in these practical measurements was a swept sine wave with a frequency range of twice that of the acoustical range of interest to reduce aliasing problems. This also ensures that the cepstrum of the direct term has decayed before $\tau$ and thus reduces the amount of extraction noise. The effect of the direct signal may also be removed using background subtraction that is measuring the spectrum of the direct signal in anechoic conditions and subtracting it from the log modulus of the total spectrum. This extends the validity of the low frequency data as does increasing the time period $\tau$ which allows a larger time segment to be extracted from the cepstrum, as the rahmonics are moved further away in time, and so improve the resolution of the system. The frequency dependent effects of the sound production and data collection instrumentation are accounted for using a form of inverse filtering.

## 2.6 Measurement of bulk propagation constant

To describe the acoustical properties of an extended reacting material information is required about both the characteristic impedance and the bulk propagation constant. Scott [23] measured the attenuation constant of a fibrous material by examination of the decay of the sound pressure with the distance along an impedance tube filled with steel wool. This allowed the attenuation constant i.e the imaginary part of the bulk propagation constant to be found. The change in phase of the pressure acts as a measurement of the wavelength and thus the phase constant i.e. the real part of the bulk propagation constant may also be deduced.

The bulk propagation constant may also be measured from impedance tube measurements of samples with thicknesses d and 2d. The method suggested be Ferrero and Sacerdote [102] and utilized by Pyett [103] measures the normal surface impedance for the two thicknesses. The propagation constant is then found from

$$cosh(-2\imath k_b d) = \left[\frac{R'(R-R')+X'(X-X')}{(R-R')^2+(X-X')^2}\right]+\imath\left[\frac{R'(X-X')+X'(R-R')}{(R-R')^2+(X-X')^2}\right] \tag{2.29}$$

where $R$, $X$, $R'$, and $X'$ are the real and imaginary parts of the surface impedance for the single and double thickness layers respectively. The argument of the hyperbolic cosine is best found using an iterative technique or using nomograms such as those produced by Rybner [104]. The characteristic impedance is found from

$$Z_c = Z(d,0)tanh(\imath k_b d) = Z(2d,0)tanh(2\imath k_b d) \tag{2.30}$$

It should be noted that the characteristic impedance of a sample may also be found by measuring the impedance of a quarter wavelength backed sample.

$$Z(d) = Z_c coth(-\imath k_0 d) \tag{2.31}$$

and

$$Z(\frac{\lambda}{4}) = Z_c tanh(-\imath k_0 d) \tag{2.32}$$

thus

$$Z(d).Z(\frac{\lambda}{4}) = Z_c^2 \tag{2.33}$$

Dunlop first used a flanged tube [105] and then a protruding tube [106] to measure the impedance and propagation constant of a surface using an indirect technique. A tube containing two wall mounted microphones is inserted into the sample. The two microphones measure the sound field

generated from a loudspeaker at one end. The specific acoustic impedance is then calculated using the technique suggested by Seybert and Ross [41]. The specific acoustic impedance $Z_s$ in the tube may be written in terms of the length of tube protruding into the sample $l$ and the termination impedance $Z_t$.

$\frac{Z_s}{Z_t} = \frac{Z_t cosh(kl)+Z_0 sinh(kl)}{Z_t sinh(kl)+Z_0 cosh(kl)}$

where $Z_0$ and $k$ are the impedance and propagation constant of the sample. The tube termination impedance may be approximated for a dissipative media by

$\frac{Z_t}{Z_0} = \frac{k^2a^2}{4} + \imath 0.6ka$

where $a$ is the tube radius.

$Z_0$ and $k$ are given by the Zwikker and Kosten model [107] as

$k = \frac{\imath\omega\sqrt{k_z}\left(1-\frac{\imath\delta}{2}\right)}{c_0}$

and

$Z_0 = \rho_0 c_0 \sqrt{k_z}\left(1 - \frac{\imath\delta}{2}\right)$

where $k_z$ is a structure factor and $\delta$ the phase lag between the particle velocity and pressure which characterizes the dissipative properties of the medium. These two parameters are adjusted to match the measured value of $Z$. Thus the impedance and propagation constant may be calculated.

## 2.7 Comparison of impedance measurement methods

It is important to discuss the relative merits of the various impedance measurement techniques for measuring the impedance of outdoor surfaces. As previously asserted the ideal technique should be

1. Accurate
2. Repeatable
3. Used in–situ
4. Fast
5. Simple

6. Useable over a wide range of angles

The surface methods operate using a discrete frequency and have not been adapted to oblique angles of incidence. Apart from Zuckerwar's Helmholtz resonator based device they all operate on samples cut from a larger surface. Although they could be adapted to measure acoustic parameters at oblique angles of incidence other errors inherent in the technique and the difficulty in producing a reliable constant volume velocity source do not make these methods an attractive option.

The impedance tube which is the most common finite sample transmission line technique may be used at normal incidence with relative ease. It is not easily adapted to oblique angles of incidence. Though the frequency range is restricted by the tube length for the low frequency measurements and by its diameter at the upper frequency range. The tube method may also be used to measure the propagation constant of a surface and thus may be used for measurement of the road surface characteristics at normal incidence. In practice it is difficult to use in–situ and suffers from micro–climatic changes. Thus it is not recommended for use on grassland surfaces though as the surface is locally reacting the normal incidence acoustic impedance should be a reliable measurement of the grassland's acoustical properties. Broadband tubular techniques will reduce the amount of time required to measure the impedance and the method suggested by Chung and Blaser is now in frequent use. However the tube technique has been limited to use at normal incidence.

Transmission line based free field techniques may be used in–situ and at oblique angles of incidence and remove any limitations of sample cutting, though the positioning of measurement probe may be affected if the surface area of interest is too small. The standing wave ratio method was adapted to free field use and refined by Klein and Cops [57] and Sides and Mulholland [56]. This involves a probe microphone passing through the surface to examine the field produced. Access is required to the rear of the surface. So although it may be used on large samples it is not a valid in–situ method outdoors. The method developed from this technique by Daigle and

Stinson of measuring the phase gradient may be used in–situ. However the measurement is limited to use at normal incidence and is affected by reflections from surrounding objects. Allard has been successful in producing a free field version of the broadband two microphones tube technique. The dual microphone probe may be used at oblique angles of incidence over any surface. The microphone location and positioning is critical. The method has been fully investigated as an impedance measurement technique. This method has been used to deduce the impedance of grassland surface by Waddington [78].

The experiments using an acoustic or electroacoustic bridge suffer from the need for a reliable standard and are operated at discrete frequencies. Adaptation to in–situ measurements would be difficult.

The indirect methods can be used at any angle of incidence over any surface since they are less sensitive to the effects of reflections than two–microphone transfer function and phase–gradient techniques. A reliable model for the propagation of the sound and in some cases for the acoustic impedance is required. The study in chapter 5 of the propagation models shows that they are reliable and accurate to within measurable tolerances. Work is still progressing on theories used for modelling the impedance of the surface though the microstructural model discussed in chapter 3 has been shown to provide an adequate description of the acoustical properties of many surfaces. The indirect method may be developed further still by considering the real and imaginary parts of the impedance as variables and by examination of the sensitivity of the method to the source receiver geometry. Both indirect methods are developed in chapter 6, the impedance fitting technique is preferable for the purpose of propagation modelling where a range of surfaces are considered. The parameters fitting technique is applicable to non-destructive evaluation of material parameters it does however impose a frequency dependency of the resulting impedance and hence has a limited range of use. Both the indirect method and the impulse technique developed by Cramond et al are relatively insensitive to inaccuracies in the source receiver positioning. They are both simple to use and give reliable

repeatable results. The impulse method is broadband and may be used near grazing incidence. The original method assumed that the ground wave was negligible it may be modified however to include the ground wave and hence may be used near grazing incidence on extended reacting surfaces; though pulse length will then become a limiting factor. The impulse method modified in this way has been used for comparison with the indirect method.

## 2.8 Non-acoustical measurements

Four of the five parameters of the microstructural model detailed in chapter 3 may be evaluated with ease using non-acoustical techniques. These are: flow resistivity, porosity, layer depth and tortuosity and hence grain shape, if the Bruggeman relationship, equation 2.41 is assumed. These measurements have been performed on 97mm diameter test cores taken from porous road surfaces the results of which are described in chapter 8. It should be noted that although little structural damage occurs during the cutting process the samples may deform due to softening of the binder. This effect may be reduced by keeping the samples cool.

### Flow resistivity

The flow resistivity was measured on the test cores using the flow rig shown in figure 2.16. Compressed air regulated by a series of valves passes through a narrow tube to a small chamber. The motion of the air produces a partial vacuum which is filled by air being drawn through the sample. The rate of flow is controlled by a series of meters and may range from 8.7 litres/minute to 0.1 litres/minute. A pair of micromanometers measure the pressure drop across the surface with respect to the atmospheric pressure for each flow rate. For structurally stable samples such as the road surface cores the whole range of flow rates may be used. For samples that have little structural integrity, for example soils, high flow rates must be avoided to prevent the air flow compacting and therefore changing the characteristics of the material. Measurements with low flow rates are difficult to perform due

to changes in external pressure for example from draughts. However the lowest flow rate possible should be used as it is the flow resistivity deduced from this measurement which corresponds most closely with the acoustical flow resistivity. The figures in appendix D show this effect by plotting the deduced flow resistivity against the flow rate. A consistent value of flow resistivity is obtained for low flow rates. The flow resistivity is calculated from equation 2.34.

$$R = \frac{C_1 A \Delta P}{QL} \tag{2.34}$$

where

$R$ the flow resistivity in MKS Rayls/m
$L$ the length of the sample in cm
$Q$ the flow rate in $cm^3/sec$
$\Delta P$ the pressure drop in inches $H_2O$
$C_1$ is a conversion factor equal to 2490000 for the above units

Ideally several samples of each material should be collected and studied.

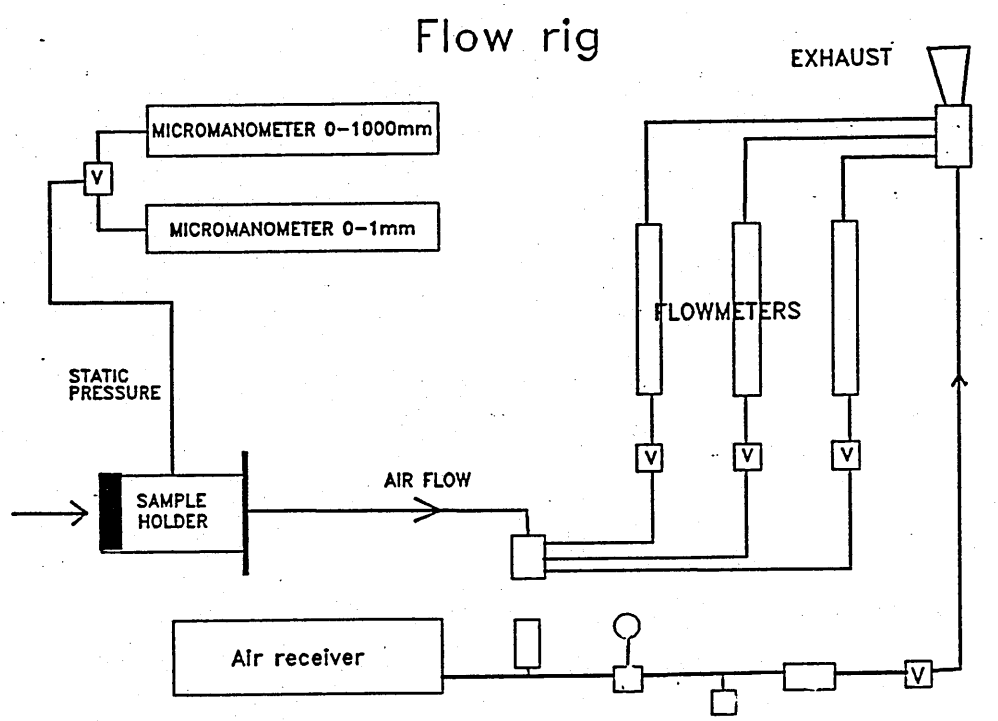


**Figure 2.16** Flow resistivity rig (V indicates location of a valve)

Flow resistivity may also be measured directly on extracted material samples using Leonards apparatus [108] or indirectly by the methods suggested by Wall [109] and Stanton [110]. Leonards apparatus is shown in figure 2.17. It consists of a balance mechanism. One arm supports a displacement cylinder (A) floating in a paraffin filled double walled cylinder (D). The material sample is placed in the holder (B) whilst a known mass is applied to the opposite pan (E). This causes the floating chamber to rise increasing the volume within the chamber and so drawing air through the material sample. The rate of air flow is monitored by timing the pointer (F). The flow resistivity (R) is then calculated from equation 2.35.

$$R = \frac{Fw\Delta t A_1}{A_2 \Delta h A_2 L} \tag{2.35}$$

$Fw$ is the force on the pan = mass $\times$ acceleration

$\Delta t$ is the average time for the pointer to move twenty graduations

$A_1$ is the area of the sample

$A_2$ is the area of the displacement cylinder

$\Delta h$ is the known length separating the twenty graduations. All values are for cgs units.

### Porosity

The porosity is defined at the ratio of the volume of inter–connected air space to the volume of the sample. The porosity of the road samples was determined using the equipment shown in figure 2.18. The cling film wrapped sample is weighed in air and then weighed in water and subsequently weighed unwrapped in water. The porosity is calculated from equation 2.36. Alternatives are the gravimetric method which was used by Hess [82] and a precision method which has been proposed recently by Champoux et al [111] based on the work of Beranek [112]. The porosity is deduced from the method involving weighing in water by using,

$$\Omega = \frac{WV - WW}{WA - WW} \tag{2.36}$$

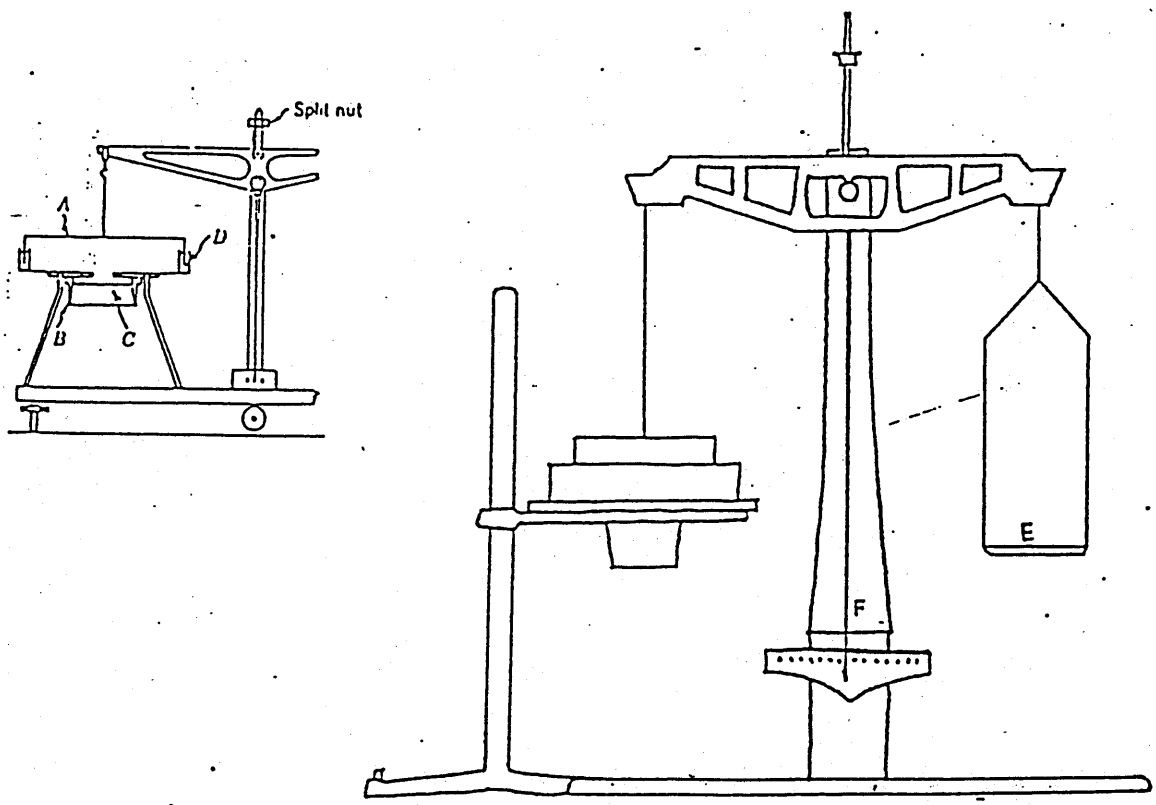


**Figure 2.17** Leonards apparatus

where

$\Omega$ is the porosity
$WV$ the weight of the sample unwrapped in water
$WW$ the weight of the sample wrapped in water
$WA$ the weight of the sample unwrapped in air

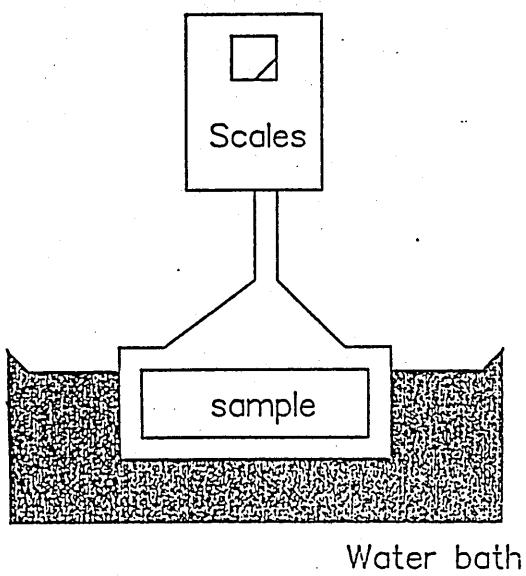


**Figure 2.18** Equipment for evaluation of porosity

If possible a suction technique should be employed to ensure that the sample is saturated. This is essential when evaluating tortuosity.

### Tortuosity

The tortuosity of a porous material is a measurement of the increased path length through the material due to the deviation from a straight line. It is possible to relate the tortuosity of a sample to the electrical conductivity of a conductive fluid saturated material. The tortuosity of a sample has been related to its porosity and formation factor by Brown [113]. Hence

$$T = F\Omega \tag{2.37}$$

where $\Omega$ is the porosity and $F$ the formation factor given by

$$F = \frac{\sigma_f}{\sigma_s} \tag{2.38}$$

where $\sigma_f$ is the conductivity of the fluid and $\sigma_s$ that of the fluid saturated sample.

$$\sigma = \frac{GL}{A} \tag{2.39}$$

where $L$ is the length of the sample, $A$ the area of the end of the sample and

$$G = \frac{I}{V} \tag{2.40}$$

a measured current $I$ flowing when an a.c. voltage $V$ is applied. Figure 2.19 shows the equipment used for the initial measurements of the fluid saturated sample. An a.c. voltage of 2 volts to 3 volts is applied across the sample and the current is measured with an $AVO$ meter. Circular electrodes of the same diameter as the sample have been found to be most effective. The sample is saturated by drawing the fluid through the sample after forming a vacuum above it. Agitation of the sample may improve the saturation process especially for small stone sizes and low porosity materials. The conductivity of the fluid is measured at similar voltages with a separate fluid–tight unit. The separation between the two plates should be easily measurable as should the radius of the sample.

To validate the method of measurement the tortuosity of glass beads ( 1.5 - 2.0 mm in diameter) was measured using a saline solution as the conductive fluid. The measured value was then compared to the theoretical tortuosity as stated by Sen, Scala and Cohen [114].

$$T = \Omega^{-\beta} \tag{2.41}$$

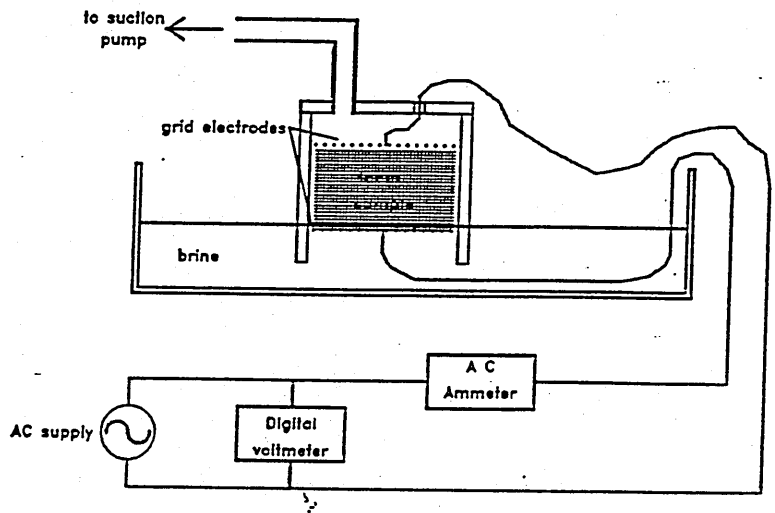


**Figure 2.19** Initial tortuosity measurement on fluid saturated sample

where $\beta$ is 0.5 for a random array of spheres with a porosity between 0.03 and 0.38. After validation of the method the tortuosity of the road surface core samples was measured. For soil crumbs $\beta = 1.0$ has been found appropriate [115].

### 2.8.1 Results of initial measurements

'Theoretical' calculations of tortuosity from porosity assume that $\beta = 1.0$ for the road samples. This however has proved to be an inaccurate first guess. It is expected that the grain shape will depend on the flakiness of the stones, that is, a measurement of the stone chip length in relation to it's width. Better agreement is gained overall if values of $\beta$ greater than 1 are used. Jackson [116] suggests that these correspond to flatter grains. $\beta$ in the table 2.1 is found from

$$\beta = -\frac{\log T(meas)}{\log \Omega(meas)} \tag{2.42}$$

| Sample | Porosity | Tortuosity (theoretical) | Tortuosity (measured) | $\beta$ |
|---|---|---|---|---|
| Glass spheres | 0.214 | 2.14 | 2.11 | 0.484 |
| TRRL area L | 0.204 | 4.9 | 4.0 | 0.872 |
| MIRA | 0.29 | 3.44 | 5.25 | 1.34 |
| WG 27 | 0.170 | 5.8 | 8.28 | 1.19 |
| Ricardos | 0.23 | 4.34 | 7.93 | 1.409 |
| Binder test cores | | | | |
| 6mm | 0.24 | 4.2 | 8.5 | 1.49 |
| 10mm | 0.23 | 4.4 | 3.18 | 0.78 |
| 20mm | 0.16 | 6.2 | 5.5 | 0.93 |

**Table 2.1** Summary of tortuosity measurements

However the theoretical value of $\beta$ for glass spheres (0.5) assuming that equation 2.41 holds is shown to be accurate. Although this simplified method gave an accurate value when used with glass beads it was found that the electrodes corroded due to the contact with the saline solution which in turn reduced the accuracy of the technique.

## Practical details

An improved method has been proposed by Champoux et al [117] who has used it with manufactured ideal samples with a known theoretical tortuosity (drilled wooden blocks) and has obtained pleasing results. The equipment used is shown in figure 2.20. Two silver–silver chloride power electrodes are used along with 99.9% silver wire measurement electrodes, [118]. Saturation of the sample is ensured by using a vacuum pump, The conductivity of the saline solution is evaluated at the same time as that of the fluid saturated sample. The distance between the measurement electrodes and the sample have been increased to ensure a uniform field. Details of the measurement rig are seen the photographs in appendix L

An alternative method for deducing tortuosity has been proposed by Nye et al [119]. This method involves gaseous diffusion and would be more applicable to structures which cannot be saturated with a conducting fluid without the structure being altered, for example soils.

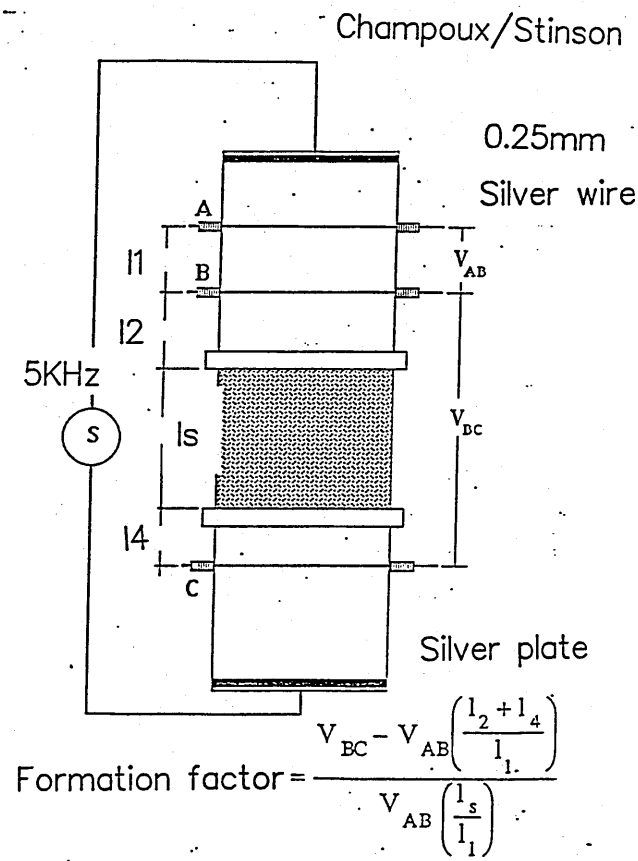


**Figure 2.20** Improved tortuosity equipment

## Chapter 3

# Models for the acoustical characteristics of rigid porous materials

Models for the acoustical properties of a material are obtained by theoretical study of the interaction of an acoustic wave with a rigid porous material. The result of such a study is a number of equations relating several physical ( non–acoustical ) parameters to the specific acoustic impedance and the bulk propagation constant of a material. Impedance models may be validated by comparison of their predictions with data collected from acoustical measurements. In this thesis the models are compared with data obtained by short range level difference and normal incidence absorption coefficient measurements ( see chapter 6 ). In some cases the physical parameters may be measured directly by non-acoustic means ( see chapter 8 ).

There follows a brief review of the impedance models derived by assuming that the porous materials have rigid frames. Particular attention is paid to three types of models; empirical, phenomenological and microstructural. The limitations of the associated equations are studied explicitly and numerically. The chapter is concluded by a closer examination of the possible effects of pore shape.

## 3.1 Review of impedance models for rigid porous media

The various impedance models may be subdivided into three categories

1. Empirical
2. Phenomenological
3. Microstructural
    a Pore based models
    b Grain based models
    c Scattering theory based models

The development of each type of model is considered briefly. Where applicable, the equations relating the physical parameters of the material to the acoustical characteristics are given and the boundaries of their validity are quoted. Only the pore based microstructural models are considered. A review of the other types may be found elsewhere [120].

### 3.1.1 Empirical impedance models

The impedance and bulk propagation constant for a range of fibrous materials was evaluated at normal incidence by Delany and Bazley [121] using a standing wave tube. The flow resistivity of each material was evaluated by measuring the volume velocity air flow for a known pressure drop across a sample of known volume. The data were analysed to yield power law relationships between the specific acoustic impedance, bulk propagation constant and the quotient of frequency and flow resistivity. Which are given in equations 3.1 to 3.5.

$$\Re(Z_c) = 1 + 0.0571C^{-0.754} \tag{3.1}$$

$$\Im(Z_c) = 0.087C^{-0.732} \tag{3.2}$$

$$\Re(\frac{k_b}{k_0}) = 1 + 0.0978C^{-0.7} \tag{3.3}$$

$$\Im(\frac{k_b}{k_0}) = 0.1819C^{-0.595} \tag{3.4}$$

with

$$C = \left[\frac{2\pi\sigma\Omega}{\omega\rho_0}\right]^{-1.0} \tag{3.5}$$

The materials used had flow resistivities between 20000 and 80000 MKS Rayls/m and porosities around 0.9. Delany and Bazley suggested that the formulae were only robust for values of $C$ in the ranges of 0.01 to 1.0. Their work was extended by Mechel [122]. New formulae were presented as a result of a comparison with the low frequency approximation of the Rayleigh model [39] although the validation could have been made by comparison to the work of Zwikker and Kosten [107], ( see section 3.1.3 ). The resulting formulae are given in equations 3.6 to 3.12.

$$\Re(Z_c) = 1 + 0.0489C^{-0.754} \tag{3.6}$$

$$\Im(Z_c) = 0.087C^{-0.731} \tag{3.7}$$

$$\Re(\frac{k_b}{k_0}) = 1 + 0.0978C^{-0.693} \tag{3.8}$$

$$\Im(\frac{k_b}{k_0}) = 0.189C^{-0.618} \tag{3.9}$$

for values of $C$ between $\frac{1}{60}$ and 1.0. For $C$ less than $\frac{1}{60}$ equations 3.10 to 3.12 apply, a porosity value of 0.95 and a tortuosity of unity were assumed.

$$\Re(Z_c) = \frac{1.403k_0}{k_b} \tag{3.10}$$

$$\Im(Z_c) = \frac{k_0}{2\pi C k_b} \tag{3.11}$$

$$\frac{k_b}{k_0} = (1.466 + \imath 0.212C^{-1})^{\frac{1}{2}} \tag{3.12}$$

Alternative formulae were presented by Bies and Hanson [90]. They suggested that the empirical relationships given in equations 3.1 to 3.5 were valid for values of $C$ greater than 1. Attenborough [120] compared the power series solutions to the high frequency approximations of the Rayleigh model and stated that the conclusions reached by Bies et al may not be correct. He also stressed that the latter workers had presumed that the material was locally reacting. Attenborough also noted that the extension of the theory to non–fibrous materials, suggested principally by Delany and Bazley [123] and later by Bies et al [90] and Chessel [89], followed from the fact that the parameter $C$ is related to the width of the viscous boundary layer at a viscous fluid–solid interface which in turn is related to pore shape. The doubts as to the validity of equations 3.1 to 3.5 for a wide range of outdoor surfaces were confirmed by Hess, Attenborough and Heap [91]. The Delany and Bazley model was compared to the microstructural model developed by Attenborough from Rayleigh ( see section 3.1.3 ) for two surface types. Noticeable differences were seen between the resulting calculated impedances and the corresponding level difference spectra. The semi–empirical model has been used extensively by Embleton et al [124], Piercy et al. [125] and De Jong et al [126] for propagation distances up to 300m. Embleton, Piercy and Daigle [127] used flow resistivity as an adjustable parameter to fit short range near–grazing angle measurements for a wide range of surfaces. The theory has been adapted to model rigidly backed layers by Talaske [128], Soom [129] and Rasmussen [130] who used the formulae given in equation 3.13 to derive the impedance of forest floors, snow and grass covered surfaces respectively.

$$Z = Z_c coth\,(-\imath k_b k_0 d) \tag{3.13}$$

### 3.1.2 Phenomenological impedance model

The phenomenological model is derived by applying a series of *ad hoc* modifications to the equations governing wave propagation in a homogeneous inviscid fluid. These modifications account for the friction between the rigid frame and the fluid supporting the acoustic wave. This results in an increased inertia and a particle velocity which is not necessarily in the same direction as the driving force. Such a model was proposed by Morse and Ingard [38]. The equations of motion, continuity and state are modified by the introduction of four parameters.

- Porosity: The ratio of the volume of the connected pores to the total volume of the material
- Flow resistivity: The resistance to the passage of air through the sample per unit thickness, defined in [131].
- Structure factor: This represents the ratio of the effective density of the air in the pores due to the incident sound wave to the equilibrium density
- Thermo–dynamic factor: This accounts for the fact that the compression of the air in the pores is neither adiabatic or isothermal. This is not accounted for in the phenomenological model used in this work

The phenomenological approach has been used by Morse and Bolt [32] who suggested a frequency dependant effective porosity to account for the thermal effects whereas Zwikker and Kosten [107] utilized an effective stiffness of the air in the pores. The model used in this work was developed by Morse and Ingard [38] who introduced a structure factor as a variable parameter although the expected ranges of validity had to be extended to gain agreement with the data collected by Morse et al [132] and Beranek [133]. They also suggested that the effective flow resistivity could be replaced by the steady flow resistivity if Poiseille type flow existed within the pores. This assumption may introduce other inaccuracies as indicated by

Scott [23] who found that the effective flow resistivity of mineral wool was frequency dependant and by Zwikker and Kosten [107] who doubted that such a flow would exist in larger pores at high frequencies.

A derivation of the phenomenological model is found in [38] which has been modified by Attenborough in [120] and [134] and in the report by Hamet [135] and is repeated here. Consider the section of material shown in figure 3.1.

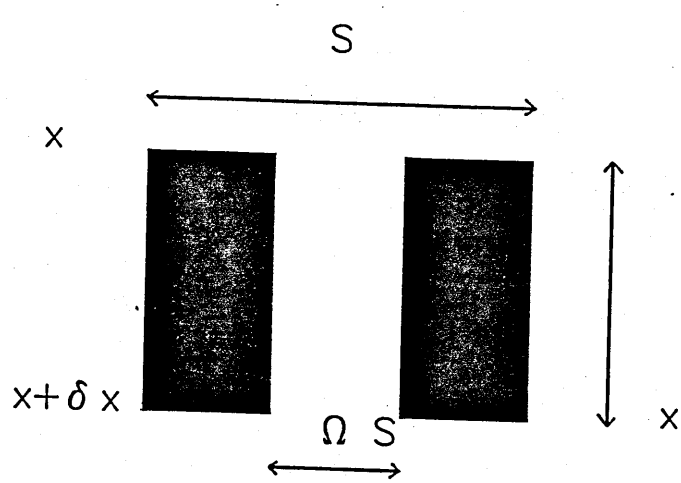


**Figure 3.1** Dimension of single pore

$L$ is the material depth
$\Omega$ the porosity
$\underline{u}(x,t)$ is the average particle velocity
$u(x,t)$ is the particle velocity perpendicular to the material surface
$\delta x$ is a small increment of distance

The equation of continuity is derived by considering that the variation in mass per unit time contained within the volume is related to the loss due to the flow traversing the surface of the volume.

$$\int_V \frac{\partial \rho}{\partial t} dV = -\int_S \rho \underline{u}\, \underline{ds} \tag{3.14}$$

Where $\rho$ is the volumetric mass of the fluid ($\rho = \rho_0 + \delta$). Where $\rho_0$ is the volumetric mass of the air at rest. Considering the flow $u$ in the direction $x$ from the infinitely small volume $S\Omega dx$

$$\int_V \frac{\partial \rho}{\partial t} dV = \frac{\partial \rho}{\partial t} \Omega S dx \tag{3.15}$$

As

$$\int_S \rho \underline{u}\, \underline{ds} = S\,(\rho u)_{x+\delta x} - S\,(\rho u)_x = S \frac{\partial (\rho u)}{\partial x} dx \tag{3.16}$$

equation 3.14 becomes

$$\Omega \frac{\partial p}{\partial t} = \frac{\partial\,(\rho u)}{\partial x} \tag{3.17}$$

Assuming linear wave propagation $u$ is small hence

$$\Omega \frac{\partial \rho}{\partial t} + \rho_0 \frac{\partial u}{\partial x} = 0 \tag{3.18}$$

and in three dimensions

$$\Omega \frac{\partial \rho}{\partial t} + \rho_0\, div(\underline{u}) = 0 \tag{3.19}$$

The equation of state is derived by considering the volumetric mass and it's variation with pressure.

$$K_P = \frac{1}{\rho_0} \frac{\partial \rho}{\partial p} \tag{3.20}$$

where $K_P$ is the compressibility. If the process is adiabatic i.e. at high frequencies then $K_P = K_S$ and hence

$$K_S = \frac{1}{\rho_0} \left( \frac{\partial \rho}{\partial p} \right)_S = \frac{1}{\rho_0 c_0^2} \tag{3.21}$$

where $c_0$ is the velocity of sound in the air. Whilst at low frequencies isothermal compressibility results in $K_P \leftrightarrow K_T$ as the air temperature remains constant.

Writing

$$K_P = \gamma_p K_S \tag{3.22}$$

gives $\gamma_p = 1$ at high frequencies and $\gamma_p = \frac{c_P}{c_v} = 1.4$ at low frequencies. The phenomenological model uses

$$\frac{dp}{d\rho} = \frac{1}{\gamma_p \rho_0 K_S} = \frac{c_0^2}{\gamma_p} \tag{3.23}$$

a frequency dependant quantity.

The dynamic equation is modified by introducing a shape factor $K$ which accounts for the increase in kinetic energy of the air due to the transverse component of the average speed and the effective increased mass of the air traversing a constriction. Consider again the small volume shown in figure 3.2

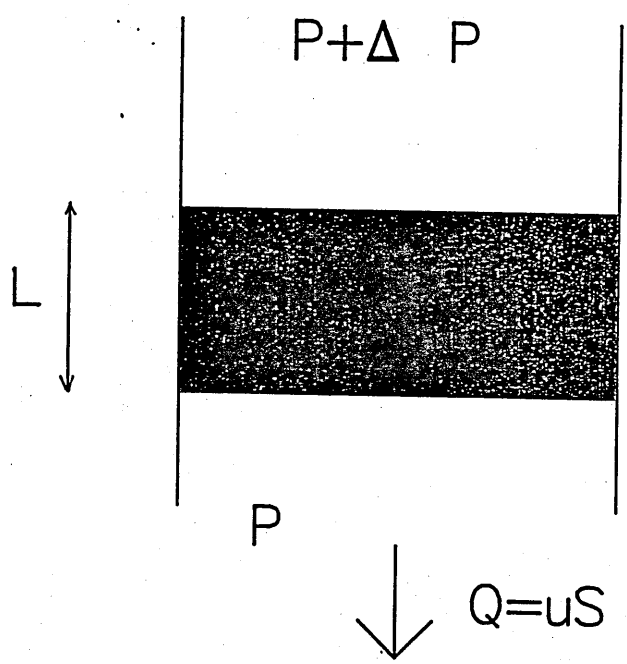


**Figure 3.2** Pressure difference across air volume in pore

If $Q$ is the outflow from the volume of thickness $L$ and is subject to a pressure differential $\Delta p$ then $\frac{\Delta p}{Q}$ can be related to a resistance to the passage of air. The specific resistance $R_S$ to the passage of air is related to the outflow per unit section.

$$R_S = \frac{1}{L}\frac{\Delta p}{u} \tag{3.24}$$

The equation of motion is given by

$$K\rho_0 \frac{\partial u_{air}}{\partial t} + R_S u = -\frac{\partial p}{\partial x} \tag{3.25}$$

where $\frac{\partial p}{\partial x}$ is the pressure gradient, $\frac{\partial u_{air}}{\partial t}$ is the acceleration of the air particles in the pores and $R_S$ the resistance to the motion of air. Relating the speed of the air in the pores to the average speed using

$$Su = S_{air}u_{air} \leftrightarrow \frac{S}{S_{air}}u = \frac{u}{\Omega} \tag{3.26}$$

Hence

$$\rho_0 \frac{K}{\Omega}\frac{\partial u}{\partial t} + R_S u = -\frac{\partial p}{\partial x} \tag{3.27}$$

or in three dimensions

$$\rho_0 \frac{K}{\Omega}\frac{\partial \underline{u}}{\partial t} + R_S u = -grad\, p \tag{3.28}$$

The equation of propagation is given by deriving an expression for the pressure in the material from combining equations 3.19, 3.23 and 3.28 to give

$$\Delta^2 p - \frac{K\gamma_p}{c_0^2}\frac{\partial^2 p}{\partial t^2} - \frac{R_S}{\rho_0 c_0}\frac{\Omega\gamma_p}{c_0}\frac{\partial p}{\partial t} = 0 \tag{3.29}$$

Given that

$$\underline{u}(\underline{x}, t) = -grad\psi(x, t) \tag{3.30}$$

from equation 3.28 leads to

$$p = \rho_0 \frac{K}{\Omega}\frac{\partial \psi}{\partial t} + R_S \psi \tag{3.31}$$

and from equation 3.29

$$\Delta^2\psi - \frac{K\gamma_p}{c_0^2}\frac{\partial^2\psi}{\partial t^2} - \frac{R_S}{\rho_0 c_0}\frac{\Omega\gamma_p}{c_0}\frac{\partial\psi}{\partial t} = 0 \tag{3.32}$$

Applying the Fourier transform to examine the frequency domain and using the convention

$$\psi(\underline{x},t) = \psi(\underline{x})e^{-\imath\omega t} \tag{3.33}$$

gives

$$p(\underline{x}) = \left(\imath\omega\rho_0\frac{K}{\Omega} - R_S\right)\psi(\underline{x}) \tag{3.34}$$

defining

$$\rho_p = \frac{\rho_0}{K\Omega} \tag{3.35}$$

which gives from equation 3.34

$$p(\underline{x}) = \imath\omega\rho_p\left(1 + \frac{\imath R_s}{\omega\rho_p}\right)\psi(\underline{x}). \tag{3.36}$$

Defining

$$\rho_e = \rho_p\left(1 + \imath\frac{R_S}{\omega\rho_p}\right) \tag{3.37}$$

as the equivalent volumetric mass gives

$$p(\underline{x}) = \imath\omega\rho_e\psi(\underline{x}). \tag{3.38}$$

The wave equation can then be written from 3.32 as

$$\Delta^2\psi = K\gamma_p\frac{\omega^2}{c_0^2}\psi - \imath\frac{\omega}{c_0}\frac{R_S}{\rho_0 c_0}\Omega\gamma_p\psi = 0. \tag{3.39}$$

Defining

$$c_p = \frac{c_0}{\sqrt{K\gamma_p}} \tag{3.40}$$

and

$$c_e = \frac{c_p}{\sqrt{1 + \imath \frac{R_S}{\omega \rho_p}}} \tag{3.41}$$

gives

$$\Delta^2 \psi + \left(\frac{\omega}{c_e}\right)^2 \psi = 0. \tag{3.42}$$

Considering propagation perpendicular to the surface of the material

$$\psi(x) = \psi_+ e^{-\imath k_e x} + \psi_- e^{\imath k_e x}. \tag{3.43}$$

Thus

$$k_e = \frac{\omega}{c_e} = \frac{\omega}{c_p}\sqrt{1 - \frac{\imath R_S}{\omega \rho_p}}. \tag{3.44}$$

The characteristic impedance is given as the ratio of the normal pressure and the particle velocity.

$$p(x) = \imath \omega \rho_e \psi(x) = p_+(x) + p_-(x) \tag{3.45}$$

and

$$u(x) = -\frac{\partial \psi}{\partial x} = u_+(x) + u_-(x). \tag{3.46}$$

Hence the characteristic impedance is given by

$$Z_c = \frac{p_+(x)}{u_+(x)} = \rho_e c_e = \rho_p c_p \sqrt{1 + \imath \frac{R_s}{\omega \rho_p}}. \tag{3.47}$$

Substituting the definitions given in equations 3.36 and 3.40 and presuming $\gamma_p = 1$ gives

$$Z_c = \frac{\sqrt{K}}{\Omega}\left[1 + \frac{\imath \Omega \sigma}{\omega \rho_0 K}\right]^{\frac{1}{2}} \tag{3.48}$$

The propagation constant $k_b$ is given by

$$k_b = \imath k_e, \tag{3.49}$$

hence

$$k_b = \Omega Z_c. \tag{3.50}$$

The model has been applied to grass covered surfaces by Bolton [100], Thomasson [136] and Donato [137]. The former researchers used formulae provided by Brekhovskikh [138] to apply the model to a multi–layer surface. Donato attempted to extend the model to allow for an exponential change in the physical characteristics with depth Attenborough [139] has shown that his resulting model assumed that the porosity increased with depth. Thomasson applied a phenomenological approach to layered locally reacting media and produced a five parameter model the fifth parameter being layer depth, ( see chapter 2 ). This model was used to deduce impedance by minimization of theoretical and measured excess attenuation. Lately the phenomenological model given in equations 3.48 and 3.50 have been used to describe the acoustical characteristics of a porous road surface by Von Meier [140], Hamet [135] and Berengier et al [141]. Although the applicability of this model to low flow resistivity surfaces (less than 5000 MKS Rayls) has been questioned by Attenborough and Howorth [142,143]. More detail of these discussions are given in chapter 8.

### 3.1.3 Microstructural pore based impedance models

The microstructural pore based model is developed from the work of Zwikker and Kosten [107]. Thermal and viscous effects are treated separately whilst considering the wave propagation in a single pore. The result is then extended to a bulk medium.

Consider a cylindrical pore, radius $R$ containing an annulus of length $\delta x$ and with a width given by outer radius $-$ inner radius $= \delta r$, as shown in figure 3.3

If the pressure drop across the annulus is given by

$$\frac{\partial p}{\partial x} dx 2\pi r \, dr. \tag{3.51}$$

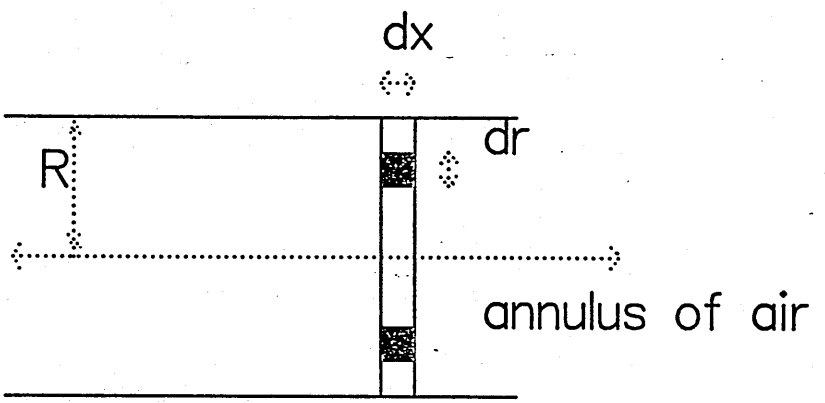


**Figure 3.3** Cylindrical pore containing small volume

The viscous drag force is given by

$$-\frac{\partial}{\partial r}\left(\mu\frac{\partial u}{\partial r}\right)dr2\pi r\,dr \tag{3.52}$$

and the inertial force is

$$2.\pi r\,dr\,dx\rho\frac{\partial u}{\partial t}. \tag{3.53}$$

Equating the driving force to the sum of the drag and inertial forces gives

$$\frac{\partial p}{\partial x}=\frac{\mu}{r}\left(r\frac{d^2u}{dr^2}+\frac{du}{dr}\right)+\omega\rho u. \tag{3.54}$$

Rearranging gives

$$u=\frac{1}{\mu K_s^2}\frac{\partial p}{\partial x}+CJ_0(K_s r) \tag{3.55}$$

where $K_s^2=(\frac{i\omega}{\nu})$. The kinematic viscosity $\nu=\frac{\mu}{\rho_0}$.

Applying the boundary conditions $u=0$ at $r=R$ leads to

$$u = \frac{1}{\mu K_s^2}\frac{\partial p}{\partial x}\left[1 - \frac{J_0(K_s r)}{J_0(K_s R)}\right]. \tag{3.56}$$

Integrating across the radius of the capillary pore

$$\frac{1}{\pi R^2}\int_0^R J_0(K_s r) 2\pi r\, dr = \frac{2}{\pi R} J_1(K_s R) \tag{3.57}$$

giving

$$\overline{u} = \frac{1}{\imath\omega\rho}\frac{\partial p}{\partial x}\left[1 - \frac{2}{\lambda_c\sqrt{\imath}}\frac{J_1(\lambda_c\sqrt{\imath})}{J_0(\lambda(c\sqrt{\imath})}\right] \tag{3.58}$$

Thus the complex density of air within a single capillary pore is given by

$$\frac{\partial p}{\partial x} = \rho_c(\omega)\frac{\partial u}{\partial t} \tag{3.59}$$

where $u$ is the average particle velocity across the pore for propagation in the $x$ direction. The dimensionless parameter $\lambda_c$ is defined as

$$\lambda_c = \left(\frac{a\omega}{\nu}\right)^{\frac{1}{2}} \tag{3.60}$$

this accounts for the viscous boundary layer at the pore wall. If the pore radius is given by $a$ . The expression for the complex density derived by Zwikker and Kosten [107] may now be written as

$$\rho_c(\omega) = \rho_0\left[1 - 2\left(\lambda_c\sqrt{\imath}\right)^{-1} T\left(\lambda_c\sqrt{\imath}\right)\right]^{-1} \tag{3.61}$$

where

$$T\left(\lambda_c\sqrt{\imath}\right) = \frac{J_1\left(\lambda_c\sqrt{\imath}\right)}{J_0\left(\lambda_c\sqrt{\imath}\right)} \tag{3.62}$$

where $J_0$ and $J_1$ are the zeroth and first order Bessel function respectively.

A similar approach may be applied to a parallel sided slit of half–width $2b$ to give the analogous expression to equation 3.62

$$\rho_s(\omega) = \rho_0 \left[1 - \left(\left(\lambda_s\sqrt{-i}\right)\right)^{-1} \tanh\left(\left(\lambda_s\sqrt{-i}\right)\right)\right]^{-1} \tag{3.63}$$

with

$$\lambda_s = b\left(\frac{\omega}{\nu}\right)^{\frac{1}{2}}. \tag{3.64}$$

Thermal effects are accounted for by considering the complex compressibility $C_c(\omega)$. If the heat energy is transported in the transverse direction only and the pressure is uniform across the pore section, then from the work of Zwikker and Kosten [107] the complex compressibility of air within the pore is given by

$$C_c(\omega) = (\gamma_p P_0)^{-1}\left[1 + 2(\gamma_p - 1)T\left(N_{PR}^{\frac{1}{2}}\lambda_c\sqrt{i}\right)\right] \tag{3.65}$$

where $N_{PR}$ is the Prandtl number. A similar result is obtained for parallel sided slits namely

$$C_s(\omega) = (\gamma_p\rho_c)^{-1}\left(1 + \frac{(\gamma_p - 1)}{N_{PR}^{\frac{1}{2}}\lambda_s(-i)^{\frac{1}{2}}}\tanh\left[N_{PR}^{\frac{1}{2}}\lambda_s(-i)^{\frac{1}{2}}\right]\right). \tag{3.66}$$

A simplification may be made by introducing the parameter

$$\lambda_p = \frac{\lambda_c}{n} = \frac{l}{n}\left(\frac{\omega}{\nu}\right)^{\frac{1}{2}} \tag{3.67}$$

where $n$ is the shape factor and $l$ the characteristic dimension of the pore. This leads to general formulae for the complex density and complex compressibility of the air in any pore, namely

$$\rho_p(\omega) = \rho_0\left[1 - 2(\lambda_p\sqrt{i})^{-1}T(\lambda_p\sqrt{i})\right]^{-1} \tag{3.68}$$

$$C_p(\omega) = (\gamma_p)^{-1}\left[1 + 2(\gamma_p - 1)\left(N_{PR}^{\frac{1}{2}}\lambda_p\sqrt{i}\right)^{-1}T\left(N_{PR}^{\frac{1}{2}}\lambda_p\sqrt{i}\right)\right]. \tag{3.69}$$

The pores in a realistic medium will not run perpendicular to the surface of the material. Hence a tortuosity $q$ is introduced to account for the

deviation of the pore path. Assuming that the pores are identical the fluid velocity averaged over a single pores cross section $< u >$ may be related to the average velocity taken over the cross section of the material $u$.

$$< u >= \frac{qu}{\Omega} \tag{3.70}$$

Presuming laminar flow exists the pressure gradient across a pore may be related to the flow resistance per unit length in a single pore $R_{SP}$.

$$-\frac{dp}{dx} = q^2 R_{SP} \frac{u}{\Omega} \tag{3.71}$$

where

$$R_{SP} = \frac{8\mu s}{l^2} \tag{3.72}$$

$s$ is the steady flow or static shape factor as detailed by Carman [115]. Assuming all the pores are identical the flow resistivity may be found for the material from equations 3.71 and 3.72.

$$R_S = \frac{8\mu q^2}{l^2 \Omega} \tag{3.73}$$

Elimination of the characteristic pore dimension for equations 3.60, 3.67 and 3.73 leads to

$$\lambda_p = \frac{1}{n}\left(\frac{8\rho_0 q^2 s\omega}{\Omega R_S}\right)^{\frac{1}{2}} \tag{3.74}$$

From equation 3.71 it is noted that the factor $\frac{q^2}{\Omega}$ relates the property of a single pore to that of the bulk medium. Hence from equations 3.59 and 3.68 a frequency dependant form for the bulk medium is given by

$$\rho_b(\omega) = \left(\frac{q^2}{\Omega}\right)\rho_p(\omega) \tag{3.75}$$

The equation of continuity is written from reference [107] as

$$-\frac{\partial u}{\partial x} = \left(\frac{\Omega}{\rho_0}\right)\left(\frac{d\rho}{dp}\right)\left(\frac{\partial p}{\partial t}\right) \tag{3.76}$$

the equation of motion is given by

$$-\frac{\partial p}{\partial x} = \rho_b(\omega)\frac{\partial u}{\partial t} \tag{3.77}$$

From equation 3.65 the wave equation is given by

$$\frac{\partial^2 p}{\partial x^2} = q^2\rho_p(\omega)C_p(\omega)\frac{\partial^2 P}{\partial t^2} \tag{3.78}$$

If a wave travelling in the positive $x$ direction is represented by the $e^{-\imath\omega t}$ time convention. The complex propagation constant is given by

$$k_b^2 = q^2\omega^2 C_p(\omega)\rho_p(\omega). \tag{3.79}$$

Considering that $(\gamma_p p_0)$ the adiabatic compressibility is equal to $(\rho_0 c_0^2)^{-1}$. Equations 3.68, 3.69 and 3.79can be used to give

$$k_b^2 = q^2\left(\frac{\omega}{c_0}\right)^2\left[1-2\left(\lambda_p\sqrt{\imath}\right)^{-1}T\left(\lambda_p\sqrt{\imath}\right)\right]^{-1}$$
$$\left[1+2(\gamma_p-1)\left(N_{PR}^{\frac{1}{2}}\lambda_p\sqrt{\imath}\right)^{-1}T\left(N_{PR}^{\frac{1}{2}}\lambda_p\sqrt{\imath}\right)\right] \tag{3.80}$$

the characteristic impedance is given by

$$Z_c = \frac{\omega\rho_b(\omega)}{k_b}. \tag{3.81}$$

It should be noted that the dynamic shape factor was derived by scaling the complex density and compressibility functions directly between the models indicated by considering a slit and a cylindrical pore. This gives rise to a dynamic shape factors that are frequency dependent. The alternative method due to Biot [144] and Allard [145] scales the complex viscosity function defined by $\rho_b(\omega) = \rho_0 + \frac{\imath\sigma_p F(\omega)}{\omega}$. This form of scaling discussed by Stinson [146] does not result in a frequency dependent factor.

The model considered in this section is based upon the work of Rayleigh [39] as detailed above. In particular we shall consider the work of Attenborough [120,134,83] who used the formulae of Smith and Greenkorn [147] as a starting point. The latter's work was based in turn on the papers of Zwikker

and Kosten [107] and Biot [144]. Viscous and thermal effects are treated separately as indicated by Zwikker et al and result in the phenomena of complex density and complex stiffness respectively. A dynamic shape factor is introduced following the work of Biot [144], Janse [148] and Smith et al [147] to allow for a pore shapes with a range of cross sections, the extreme limits being those of a circular and a slit like pore. The work is extended to apply to bulk media by use of the Dupuit relationships [115] modified to include the effect of tortuosity. Tortuosity is defined as the increased path length of the pore due to it's deviation from the normal. This results in a four parameter model given in equations 3.82 to 3.87. The four parameters used are flow resistivity ($\sigma$), porosity ($\Omega$), pore shape ($s_p$) and grain shape ($n$).

$$\rho(\lambda) = \frac{q^2}{\Omega}\rho_0 \left[1 - 2\left(\lambda\sqrt{i}\right)^{-1} T\left(\lambda\sqrt{i}\right)\right]^{-1} \tag{3.82}$$

$$K(\lambda) = \left(\frac{\gamma p_0}{\Omega}\right)\left[1 + 2(\gamma - 1)\left(N^{\frac{1}{2}}\lambda\sqrt{i}\right)^{-1} T\left(N^{\frac{1}{2}}\lambda\sqrt{i}\right)\right]^{-1} \tag{3.83}$$

$$Z_c = \frac{(\rho(\lambda)K(\lambda))^{\frac{1}{2}}}{(\rho_0 c_o)} \tag{3.84}$$

$$k_b k_o = \omega\left(\frac{\rho(\lambda)}{K(\lambda)}\right)^{\frac{1}{2}} \tag{3.85}$$

where

$$\lambda = \left(\frac{0.5}{s_p}\right)\left(\frac{8\rho_0 q^2 \omega}{\Omega\sigma}\right)^{\frac{1}{2}} \tag{3.86}$$

and

$$k_0 = \frac{\omega}{c_0} \tag{3.87}$$

The complex density and stiffness are given by $\rho(\lambda)$ and $K(\lambda)$ respectively. Also $q^2 = \Omega^{-n}$ i.e. the tortuosity is given by the Bruggeman relationship [115]. $N$ is the Prandtl number and $T = \frac{J_1}{J_0}$. $J_n$ being the $n^{th}$ order

cylindrical Bessel function. The remaining symbols are as given in appendix A. These equations are based on a microstructural model constructed from a series of cylinders, radius r with their axes normal to the surface of the material. For this ideal structure the parameter $\lambda$ and the flow resistivity may be evaluated using equations 3.88 and 3.89.

$$\lambda = r\left(\frac{\omega}{\nu}\right)^{\frac{1}{2}} \tag{3.88}$$

$$\sigma = 8\frac{\mu}{\Omega r^2} \tag{3.89}$$

where $\nu$ is the kinematic viscosity of air. A microstructure composed of straight sided slits results in equations 3.90 and 3.91,

$$\rho(\lambda) = \frac{1}{\Omega}\rho_0\left[1 - \left(\lambda\sqrt{-\imath}\right)^{-1} tanh\left(\lambda\sqrt{-\imath}\right)\right]^{-1} \tag{3.90}$$

$$K(\lambda) = \left(\frac{\gamma\rho_0}{\Omega}\right)\left[1 + (\gamma - 1)\left(N_{PR}^{\frac{1}{2}}\lambda\sqrt{-\imath}\right)^{-1} tanh\left(N_{PR}^{\frac{1}{2}}\lambda\sqrt{-\imath}\right)\right]^{-1}. \tag{3.91}$$

If $b$ is the semi-width of the slit like pores then $\sigma$ and $\lambda$ are given by equations 3.92 and 3.93.

$$\lambda = b\left(\frac{\omega}{\nu}\right)^{\frac{1}{2}} \tag{3.92}$$

$$\sigma = \frac{3\mu}{\Omega b^2}. \tag{3.93}$$

A series of approximations are made dependant on the value of $\lambda$. Hence if $\lambda \ll 1$, which corresponds low frequencies and/or high flow resistivities the characteristic impedance and bulk propagation constant are given by equations 3.94 to 3.96.

$$Z_c \approx \frac{\left[I_0\left(\frac{q^2}{\Omega}\right) + \imath\left(\frac{2s_p^2\sigma}{\pi f\rho_0}\right)\right]}{k_b} \tag{3.94}$$

$$k_b = (\gamma\Omega)^{\frac{1}{2}} \left[ \frac{aq^2}{\Omega} + \imath \left( \frac{2s_p^2\sigma}{\pi f \rho_0} \right) \right]^{\frac{1}{2}} \tag{3.95}$$

where

$$a = I_0 - \left[ \frac{(\gamma - 1)}{\gamma} \right] N. \tag{3.96}$$

$I_0$ is dependant on pore shape and varies between 1.33 for cylindrical pores and 1.2 for slit like pores. Similarly when $\lambda > 1$, i.e. a high frequency and/or low flow resistivity approximation equations 3.97 and 3.98 are used to determine the acoustical characteristics of the surface,

$$Z_c \approx \left[ (1 + 2\sqrt{\imath\lambda}) \left( 1 + \frac{2\sqrt{\imath}(\gamma - 1)}{\left(N^{\frac{1}{2}}\lambda\right)} \right)^{-1} \right]^{\frac{1}{2}} \tag{3.97}$$

$$k_b = \left[ (1 + 2\sqrt{\imath\lambda}) \left( 1 + \frac{2\sqrt{\imath}(\gamma - 1)}{\left(N^{\frac{1}{2}}\lambda\right)} \right) \right]^{\frac{1}{2}}. \tag{3.98}$$

If $\lambda \gg 1$ a further simplification results in the expressions given by equations 3.99 and 3.100,

$$Z_c \approx \left( \frac{1}{\Omega} \right) \left[ q + \frac{1}{2} \left[ 1 - \frac{\gamma - 1}{N^{\frac{1}{2}}} \right] \left( \frac{\Omega s_p^2 \sigma}{2\pi f \rho_0} \right)^{\frac{1}{2}} (1 + i) \right] \tag{3.99}$$

$$k_b = q + \frac{1}{2} \left[ 1 + \frac{\gamma - 1}{N^{\frac{1}{2}}} \right] \left( \frac{\Omega s_p^2 \sigma}{2\pi f \rho_0} \right)^{\frac{1}{2}} (1 + i). \tag{3.100}$$

The microstructural model has an advantage over the empirically and phenomenologically based models in that most of the parameters may be determined non–acoustically, see chapter 8. The exception is the pore shape factor. The microstructural model developed by Attenborough used in this study is founded upon the study of a structure composed of identical tortuous capillary pores. Microstructural pore based models are available for four pore shapes, namely parallel sided slits, circular capillaries , rectangular and equilateral triangular pore shapes. The complex density $\overline{\rho}$ and compressibility $\overline{C}$ may be calculated from equations 3.101 and 3.102 respectively [146].

Where $F(\lambda)$ and $\lambda$ are given in table 3.1 for each pore shape. It should be noted that $\lambda_T = N_{PR}\lambda$ where $N_{PR}$ is the Prandtl number.

$$\overline{\rho} = \frac{\rho_0}{F(\lambda)} \tag{3.101}$$

$$\overline{C} = \frac{(1-\gamma)F(\lambda_T)+\gamma}{\rho_0 c_0^2} \tag{3.102}$$

| Pore shape | $F(\lambda)$ | $\lambda$ |
|---|---|---|
| Parallel sided slit width 2b | $1 - \frac{tanh(\lambda\sqrt{-i})}{\lambda\sqrt{-i}}$ | $b\left(\frac{\omega}{\nu}\right)^{\frac{1}{2}}$ |
| Circular capillary radius $r$ | $1 - 2\left(\lambda\sqrt{i}\right)^{-1}\frac{J_1(\lambda\sqrt{i})}{J_0(\lambda\sqrt{i})}$ | $r\left(\frac{\omega}{\nu}\right)^{\frac{1}{2}}$ |
| Rectangle sides $2a$ and $2b$ | $\frac{64}{\pi^2}\sum_{m,n\ odd}\frac{1}{m^2n2Y_{mn}(\lambda)}$ $Y_{mn}(\lambda) = 1 + \left(\frac{i\pi^2}{\lambda^2}\right)\frac{b^2m^2+a^2n^2}{(a+b)^2}$ | $\frac{2ab}{(a+b)}\left(\frac{\omega}{\nu}\right)^{\frac{1}{2}}$ |

**Table 3.1** Dimensionless parameters for varying pore shapes

The complex density and compressibility for each pore shape are shown in figures 3.4 to 3.5, it should be noted that the imaginary parts of the complex density and compressibility have been written as negative values. Two comparisons have been made, the first uses identical values of $\lambda$ by adjusting the characteristic dimension of the pores, the second uses a flow resistivity of 100000 MKS Rayls/m and calculates the characteristic dimension using equation 3.103. The steady flow pore shape factor values (s) used are given by Carman [115], $\mu$ is the viscosity of air factor ( $\nu$ the kinematic viscosity of air ($\nu = \frac{\mu}{\rho_0}$)) and $l$ is the characteristic dimension

$$R_s = \frac{8\mu s}{l^2}\Omega \tag{3.103}$$

It is seen that there is little difference between varying pore shapes except for low values of $\lambda$. It appears that pores with equivalent characteristic dimensions will have similar flow resistivities. It would seem that pore shape alone may not be enough to distinguish between different materials. This has been shown by Attenborough [149]. He proposes an extension to the theory which develops formulae for the complex density of a material by considering a log–normal distribution of identical cylindrical or slit like pores. Low and high frequency approximations are compared to work by Norris [150] and Yamamoto and Turgut [151] to develop a structural factor that is dependant on pore shape and tortuosity and a pore shape distribution factor. The later parameter is related to the standard deviation of the size distribution. The modified model is then compared to the attenuation and phase constant measured for a sandy loam using a probe microphone technique.

## 3.2 Numerical comparison of impedance models

The impedance models for the empirical theory ( equations 3.1 to 3.5), phenomenological theory ( equations 3.48 and 3.50) and microstructural pore based theory ( equations 3.82 to 3.87) are considered. Four cases are considered to examine the ranges of validity of the models namely . The flow resistivities are in MKS Rayls/m

1. Flow resistivity=1500 , porosity=0.9, grain shape=0, pore shape=0.5
2. Flow resistivity=500000, porosity=0.9, grain shape=1.1, pore shape=0.5
3. Flow resistivity=1500, porosity=0.2, grain shape=0, pore shape=0.5
4. Flow resistivity=500000, porosity=0.2, grain shape=1.1, pore shape=0.5

These surfaces represent a selection of possible poro–rigid materials. The normalized characteristic impedance and propagation constant for each of the three model types and four surfaces is shown in figures 3.6 to 3.9. The imaginary parts of the impedance and propagation constant are written as negative values.

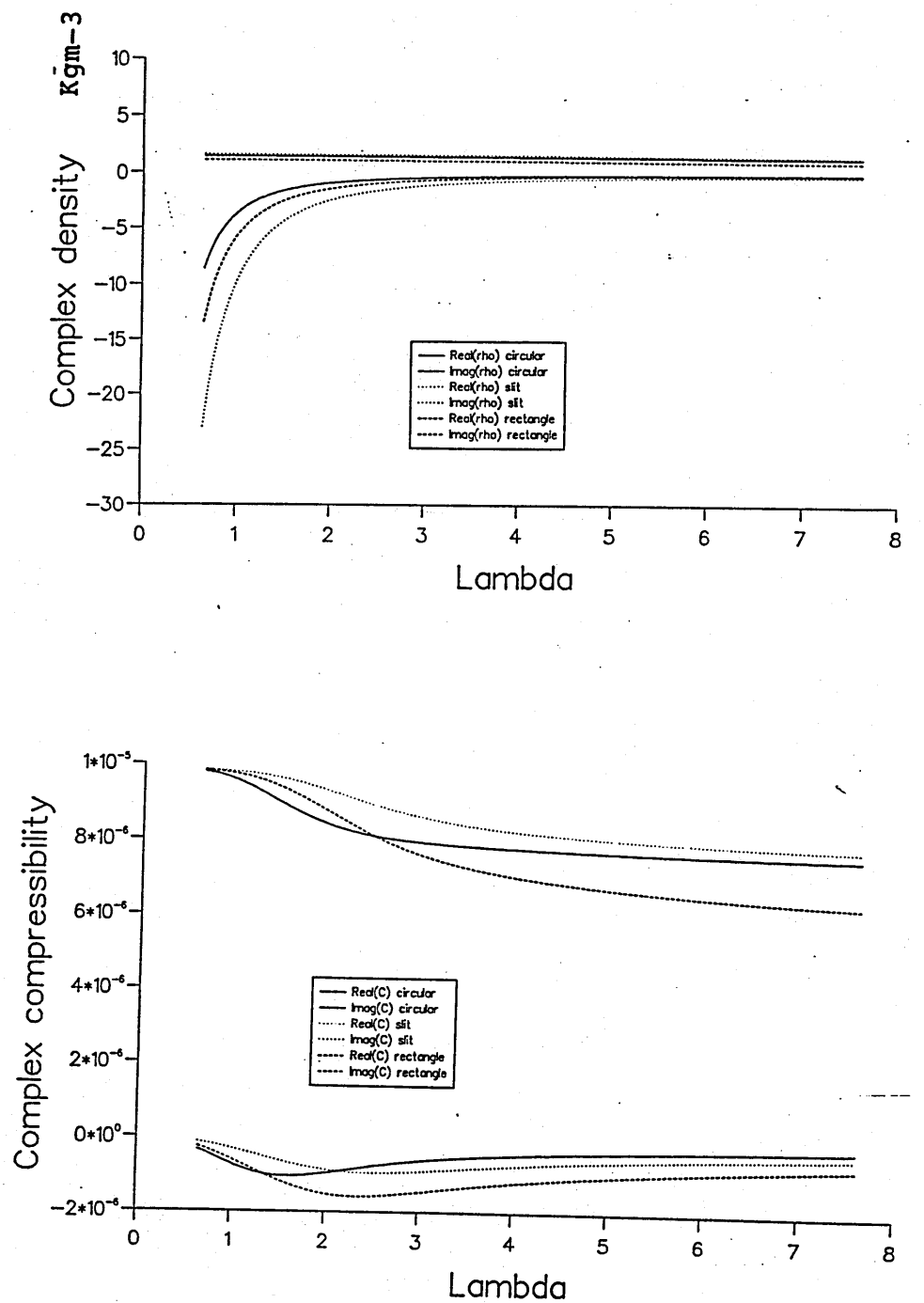


**Figure 3.4** Complex density and compressibility for pores with same dimensionless parameter.

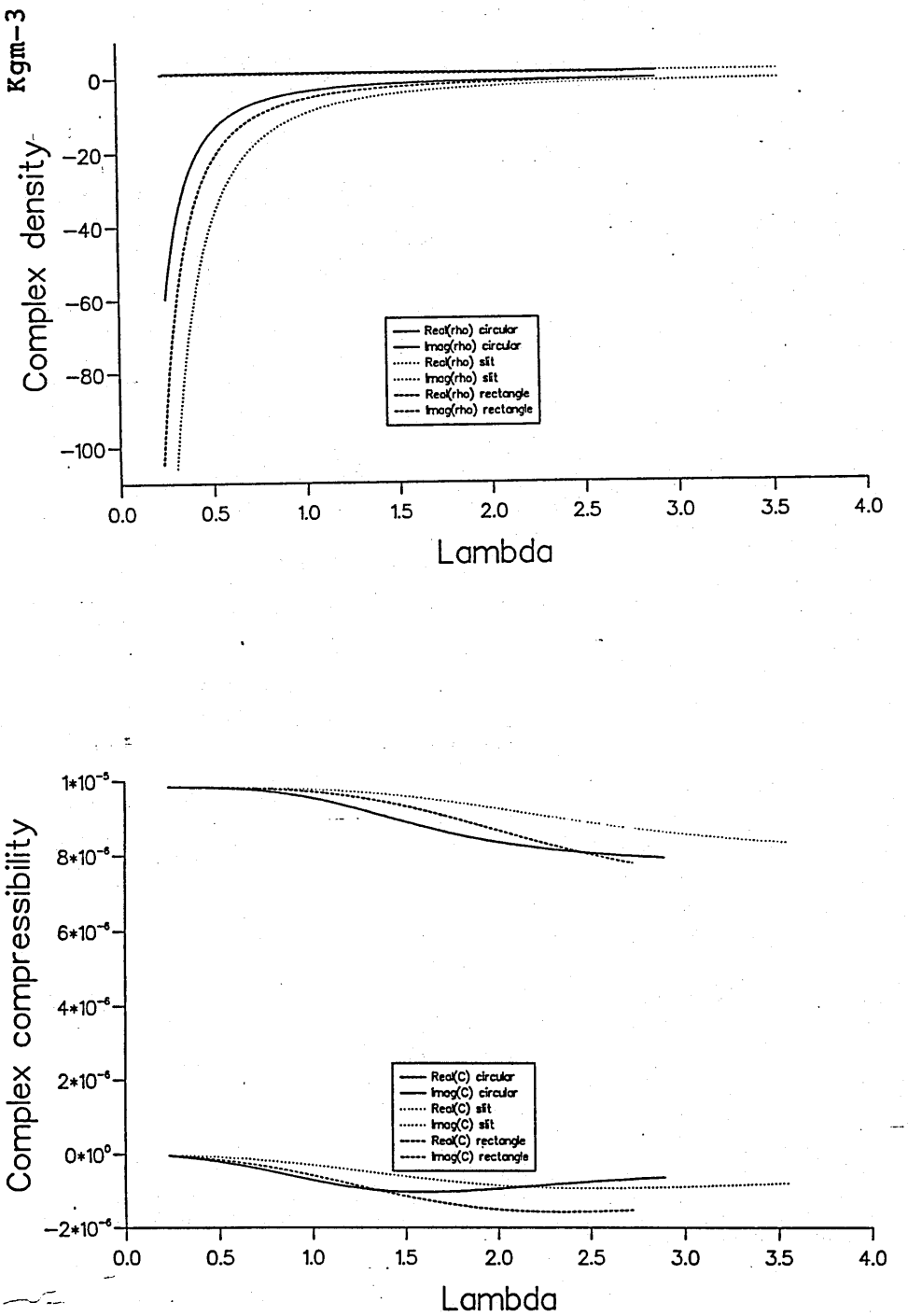


**Figure 3.5** Complex density and compressibility for pores with same flow resistivity.

If porosity is high i.e. for values of $C$ greater then $0.6 \times 10^{-2}$ consistent with materials for which the empirical model was developed, there is good agreement between the model types , although there is notably more divergence in the propagation constant calculations. However if porosity is low then the resistance and phase constant predicted by the empirical model are much less than those predicted by the alternative approaches. The deviations between the attenuation constant predicted by the empirical model and the predictions of the other models increases as the flow resistivity increases. Therefore is is important that not only the value of $C$ but the porosity of the material must be considered when examining the validity of the empirical model. For case 1, the high porosity and low flow resistivity material there is reasonable agreement between all the impedance models. This is also true for the second case. However when cases three and four are considered, i.e. for low porosity materials the empirical model over predicts the real and imaginary parts of the propagation constant.

There is also considerable variation between the oblique angle of incidence absorption coefficients calculated using the empirical phenomenological and microstructural models. This aspect is shown in figures 3.10 to 3.15. The absorption coefficient is plotted for five angles of incidence and the four cases discussed earlier on page 76.

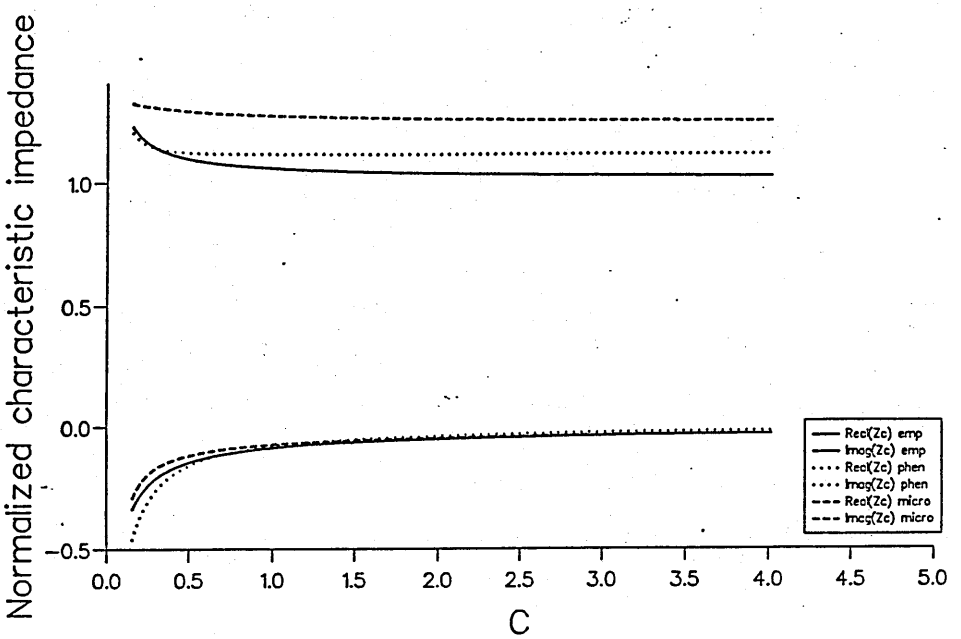


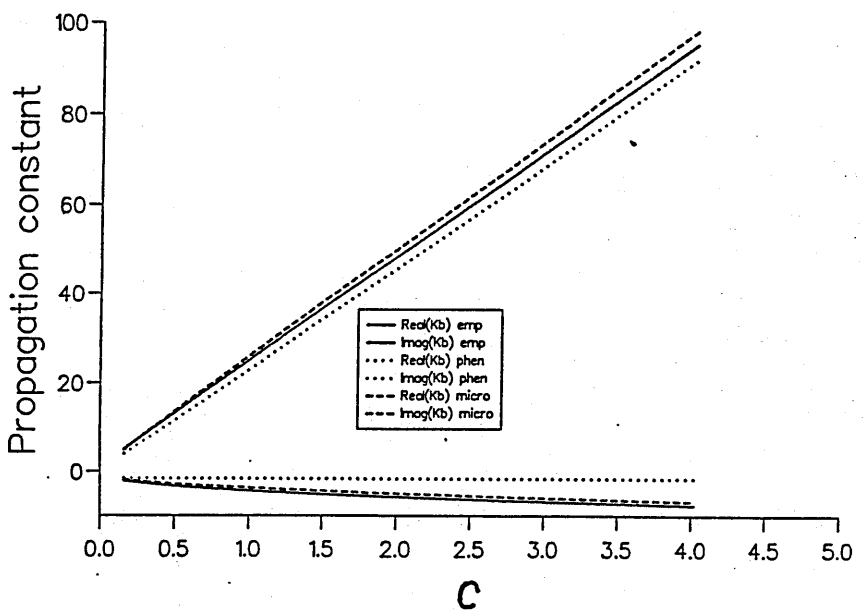


**Figure 3.6** Comparison between models for case 1

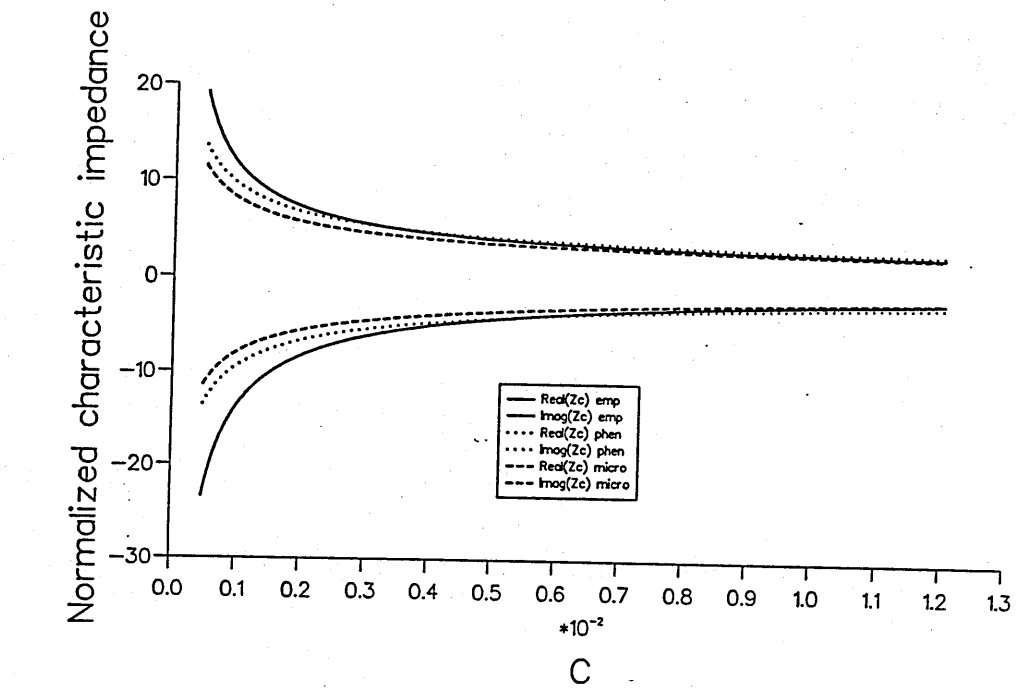


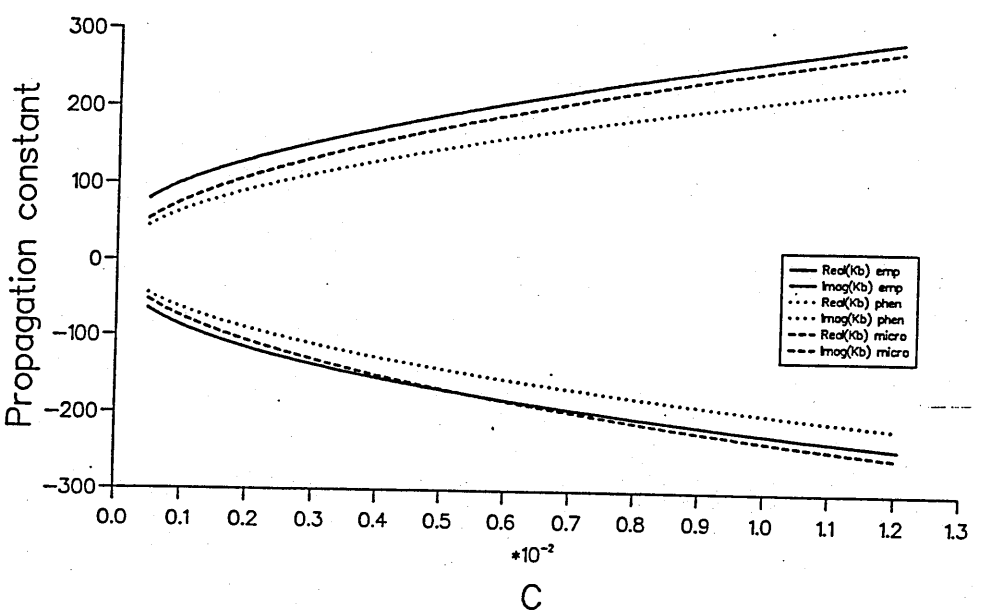


**Figure 3.7** Comparison between models for case 2

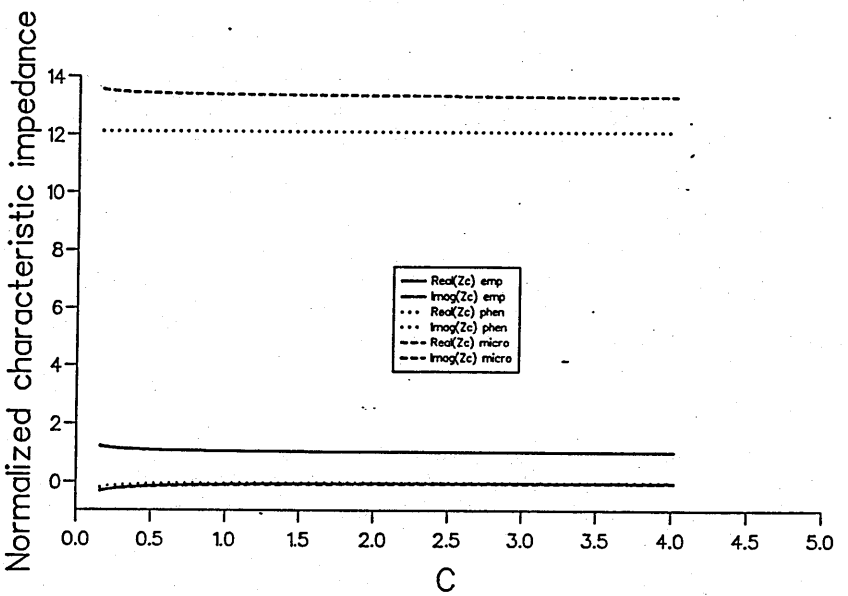


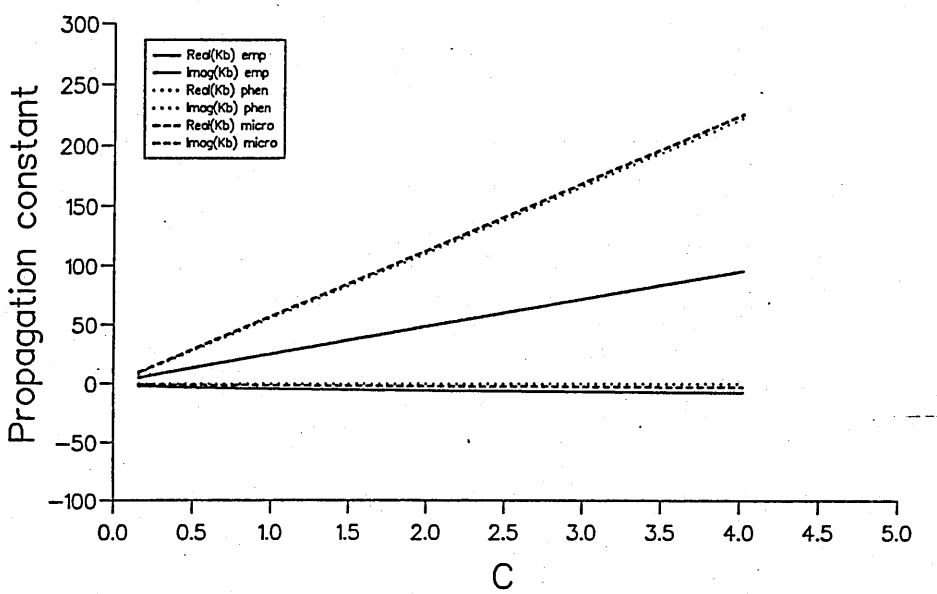


**Figure 3.8** Comparison between models for case 3

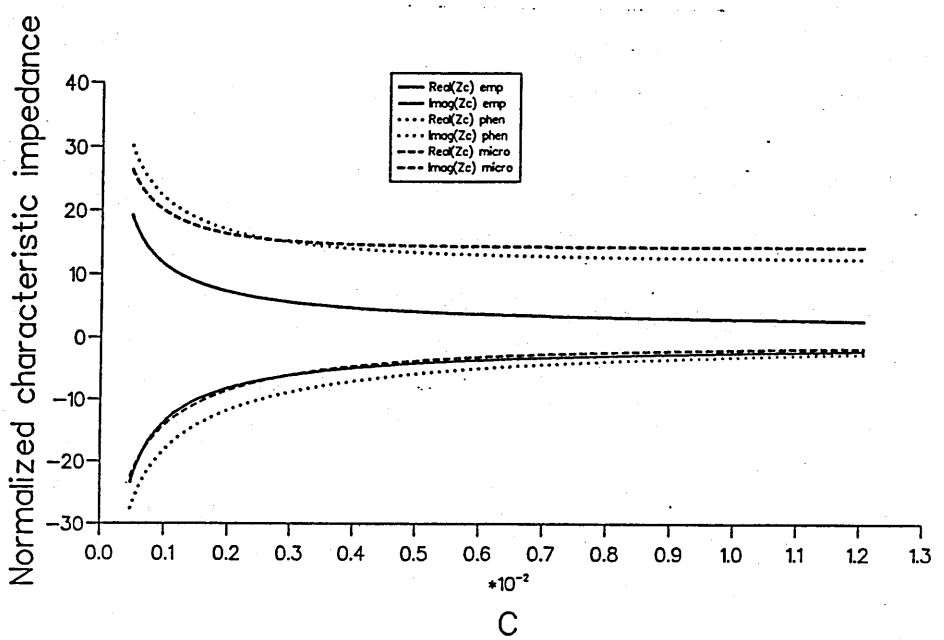


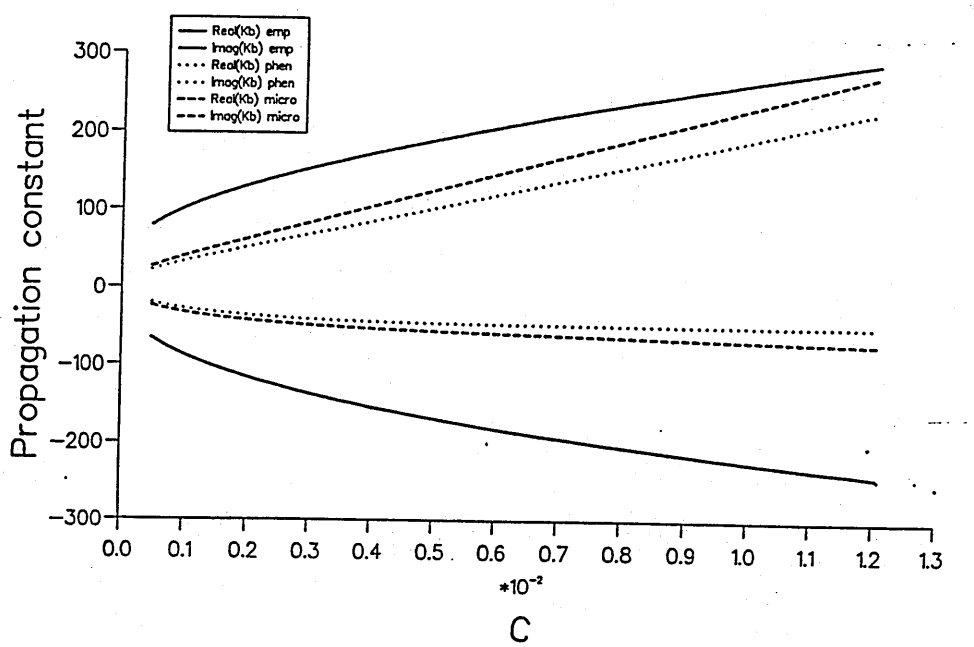


**Figure 3.9** Comparison between models for case 4

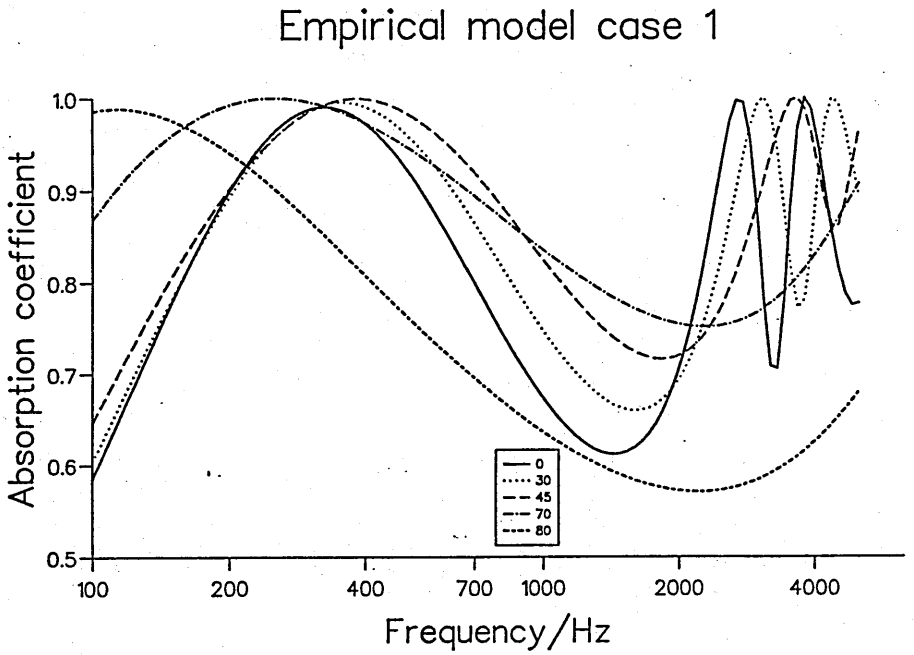


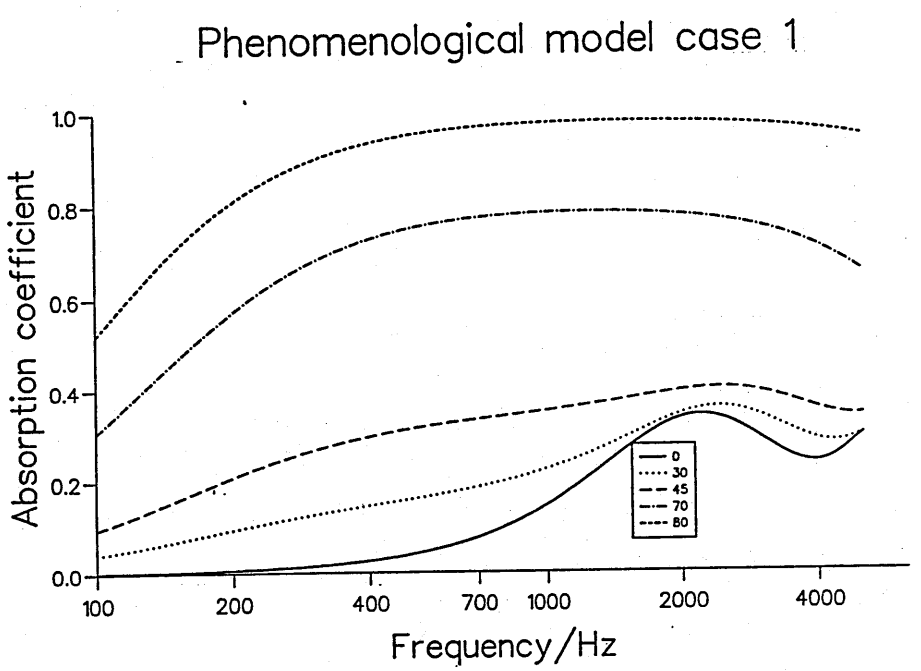


**Figure 3.10** Oblique incidence absorption coefficient for case 1.

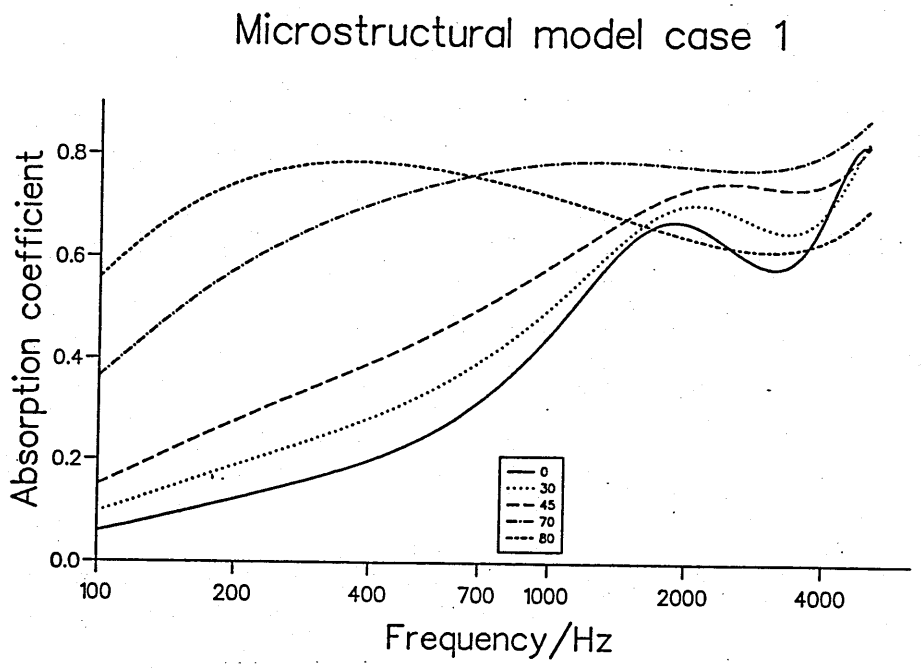


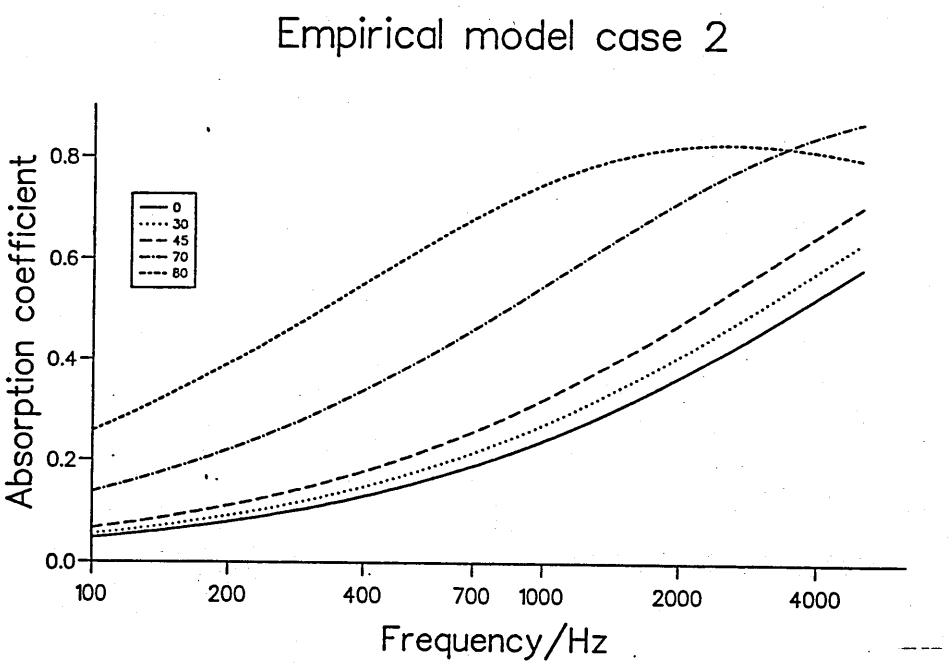


**Figure 3.11** Oblique incidence absorption coefficient for case 1/2.

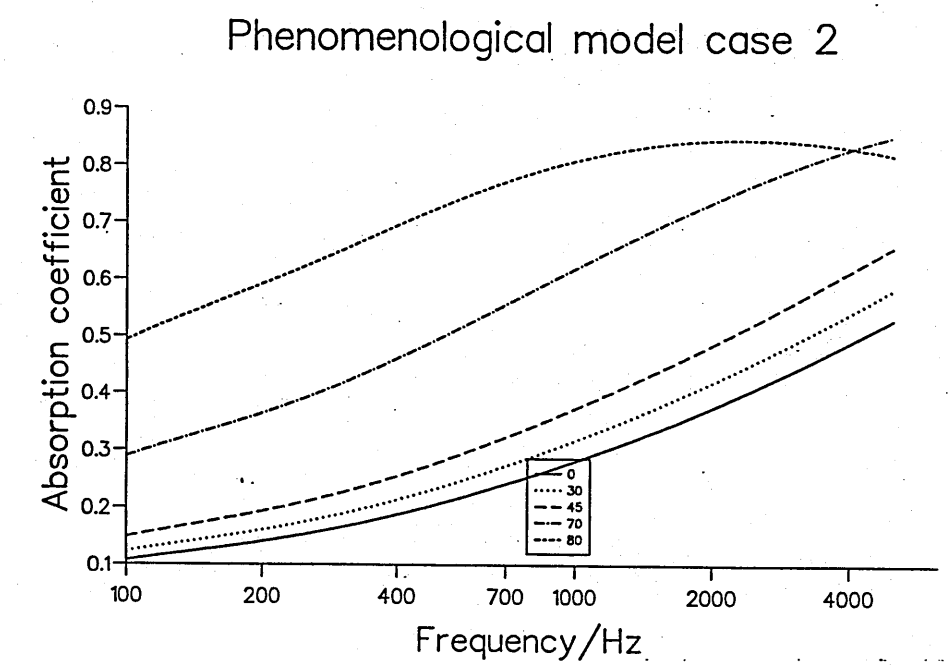


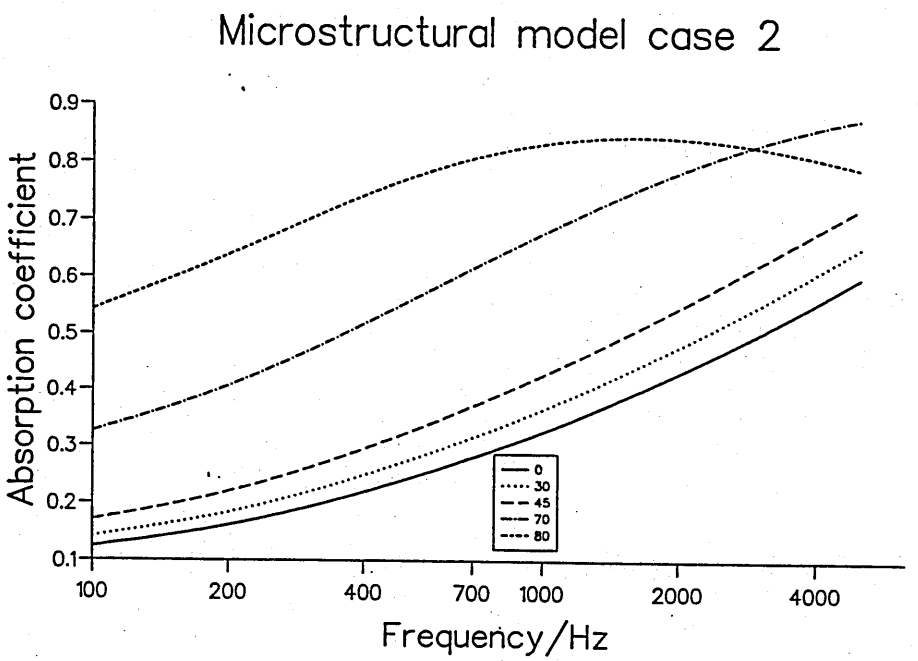


**Figure 3.12** Oblique incidence absorption coefficient for case 2.

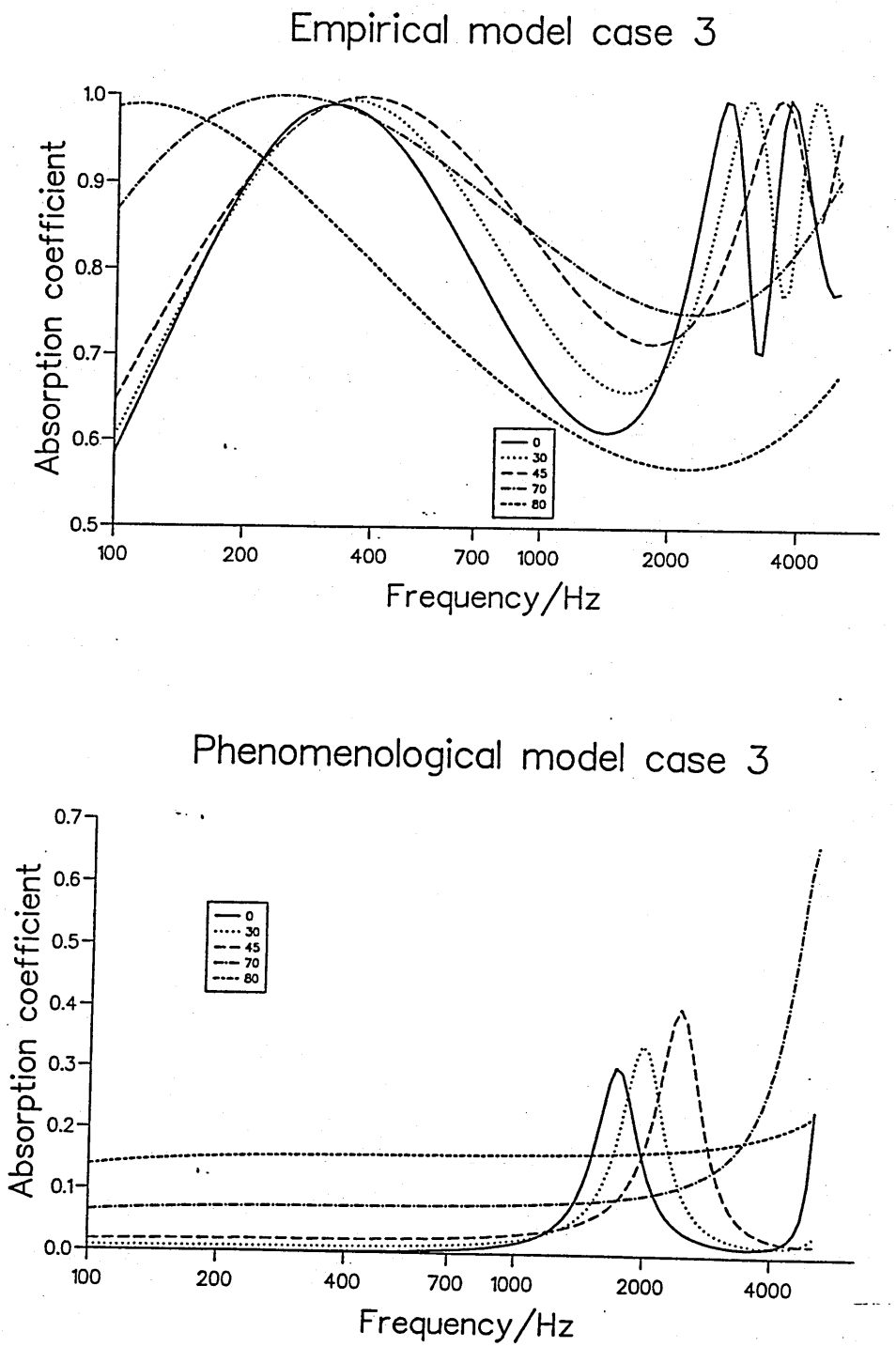


**Figure 3.13** Oblique incidence absorption coefficient for case 3.

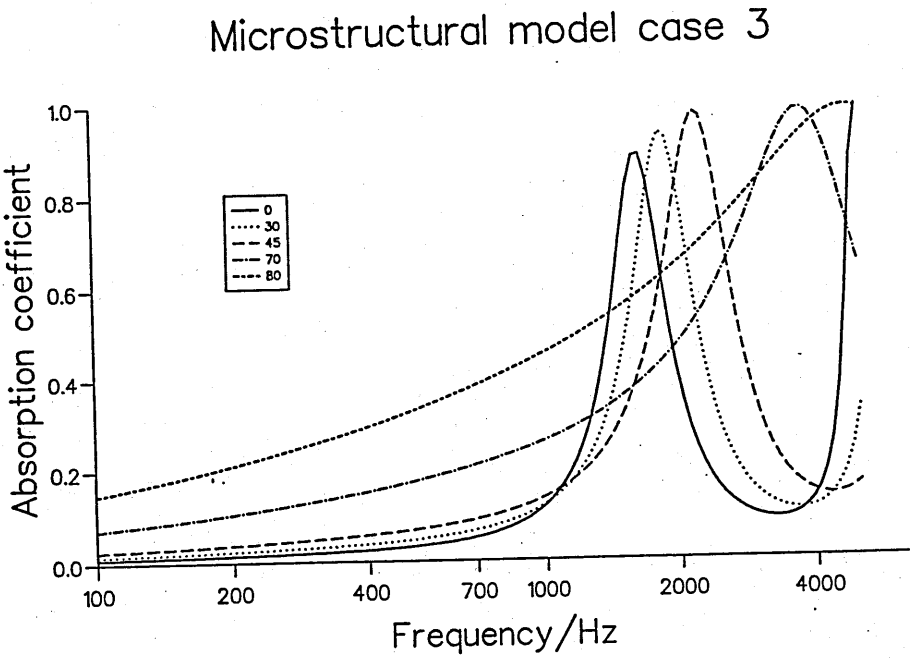


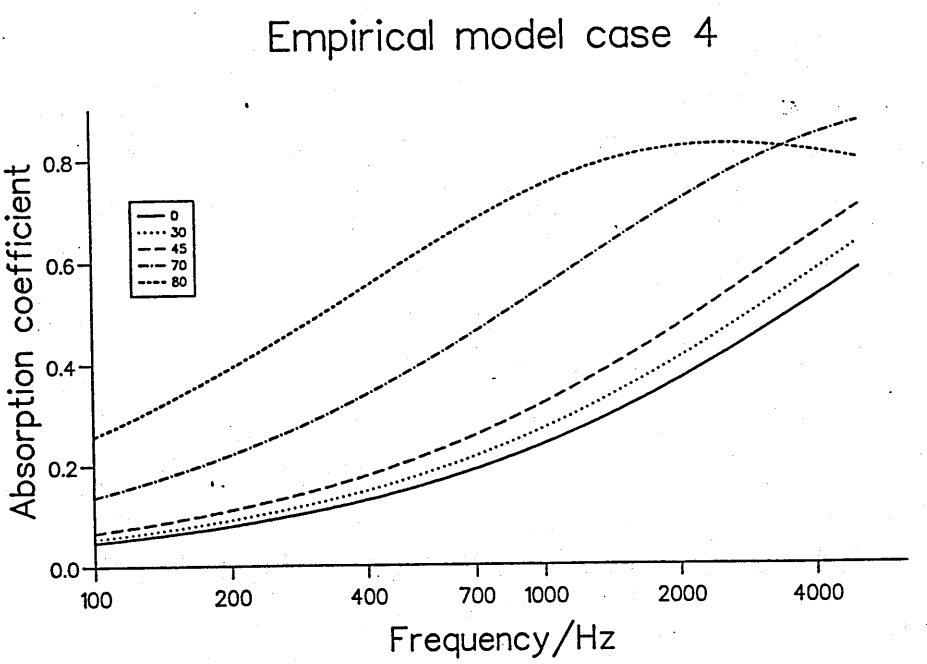


**Figure 3.14** Oblique incidence absorption coefficient for case 3/4.

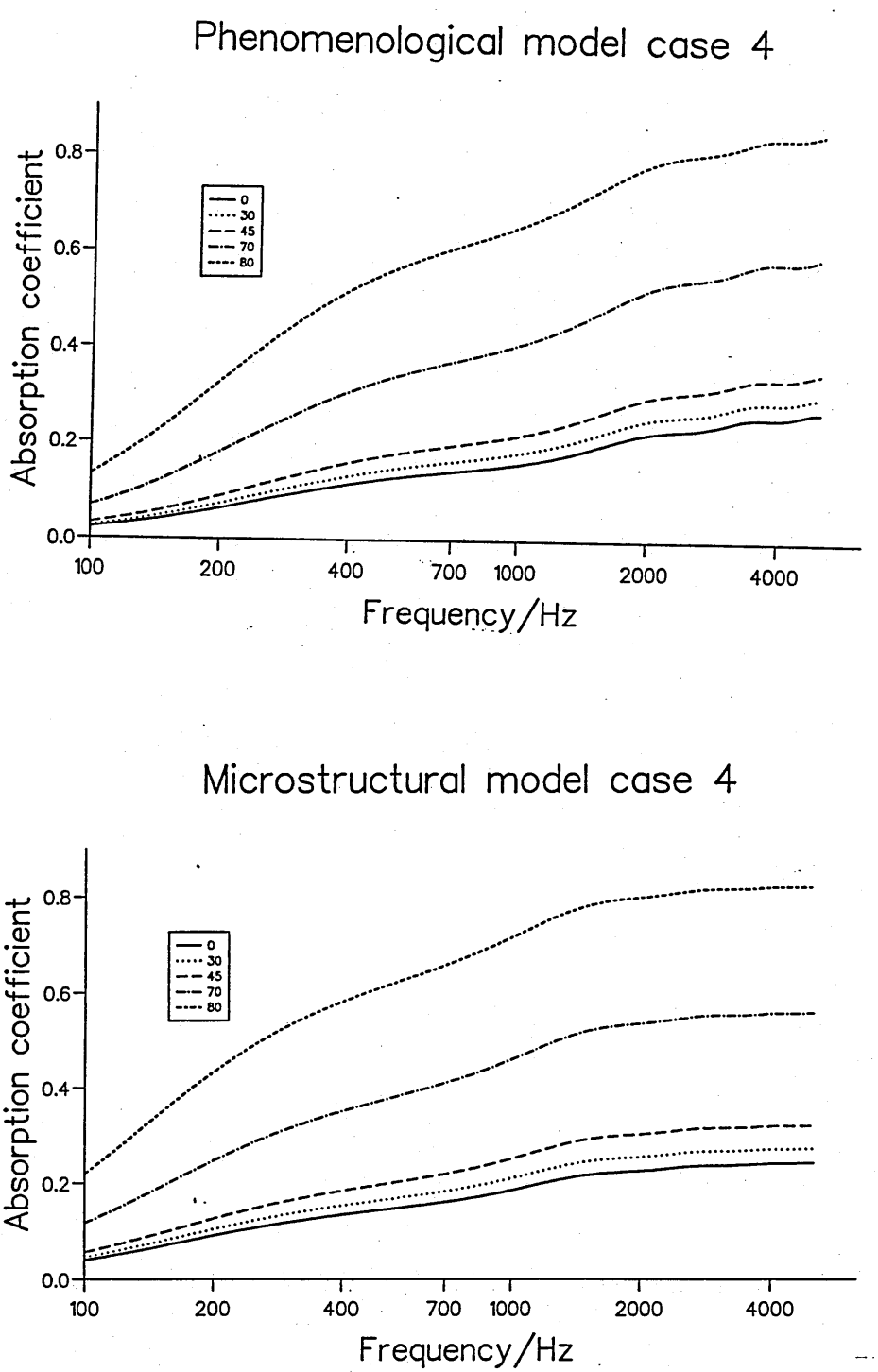


**Figure 3.15** Oblique incidence absorption coefficient for case 4.

## Chapter 4

# Propagation from a spherical source over a plane boundary

Having examined the methods of evaluating and modelling the acoustical properties of a rigid porous medium in the form of the impedance and the propagation constant the propagation from a point source over such a medium may be considered. The three dimensional wave equation may be developed for propagation through an inviscid homogeneous fluid and a general solution found. One may then account for the reflection from a plane infinite boundary and develop a general solution to the problem. The simplest case, propagation over a locally reacting medium, is considered first by defining such a material and then examining the most recent analytic approximations to the propagation problem. A range of hypothetical locally–reacting test surfaces is proposed and a numerical comparison between an accurate numerical integration using adaptive quadrature and recent asymptotic series solutions is performed. Also considered in the study is the widely used Weyl van der Pol approximate solution and the plane wave reflection coefficient approximation of this solution. The limitations of the formulations are examined. Approximate solutions for sound propagation over externally reacting media are then described and another series of hypothetical test surfaces proposed. Again a numerical comparison is performed to asses and compare the various solutions. The conclusion to the chapter suggests which propagation model is best suited to a particular situation

and considers their use in the proposed indirect method of impedance measurement.

## 4.1 The linearized acoustic wave equation

Consider the propagation of a longitudinal acoustic wave through an inviscid fluid. The fluid has an equilibrium density of $\rho_0$ and an equilibrium pressure of $\mathcal{P}_0$. The passage of the wave generates a net instantaneous density and pressure of $\rho$ and $\mathcal{P}$ respectively. If the medium is a perfect gas then the thermodynamic laws give:

$$\mathcal{P} = \rho r T_K \tag{4.1}$$

with $T_K$ the temperature in Kelvins and $r$ a gas constant. The propagation of the acoustic wave is considered to be adiabatic i.e. there is no significant transfer of thermal energy between molecules, the entropy of the system remains constant

$$\frac{\mathcal{P}}{\mathcal{P}_0} = \left(\frac{\rho}{\rho_0}\right)^{\gamma} \tag{4.2}$$

where $\gamma$ is the ratio of specific heats. A Taylor series expansion gives

$$\mathcal{P} = \mathcal{P}_0 + \left(\frac{\partial \mathcal{P}}{\partial \rho}\right)_{(\rho_0)} (\rho - \rho_0) + \frac{1}{2}\left(\frac{\partial^2 \mathcal{P}}{\partial \rho^2}\right)_{(\rho_0)} (\rho - \rho_0)^2 + \cdots \tag{4.3}$$

Assuming small amplitude acoustic waves the density fluctuations are small and hence the first term only is used.

$$\mathcal{P} - \mathcal{P}_0 = \mathcal{B}\left(\frac{\rho - \rho_0}{\rho_0}\right) \tag{4.4}$$

with $\mathcal{B} = \rho_0 \left(\frac{\partial \mathcal{P}}{\partial \rho}\right)_{(\rho_0)}$

$$p = \mathcal{B}s \tag{4.5}$$

with $p$ the acoustic pressure, i.e. $p = \mathcal{P} - \mathcal{P}_0$. Now consider the equation of continuity of mass. The rate at which the mass flows into the volume

$dx.dy.dz = dV$ is equal to the rate at which the mass within the volume increases. Consider the spatially fixed volume in figure 4.1.

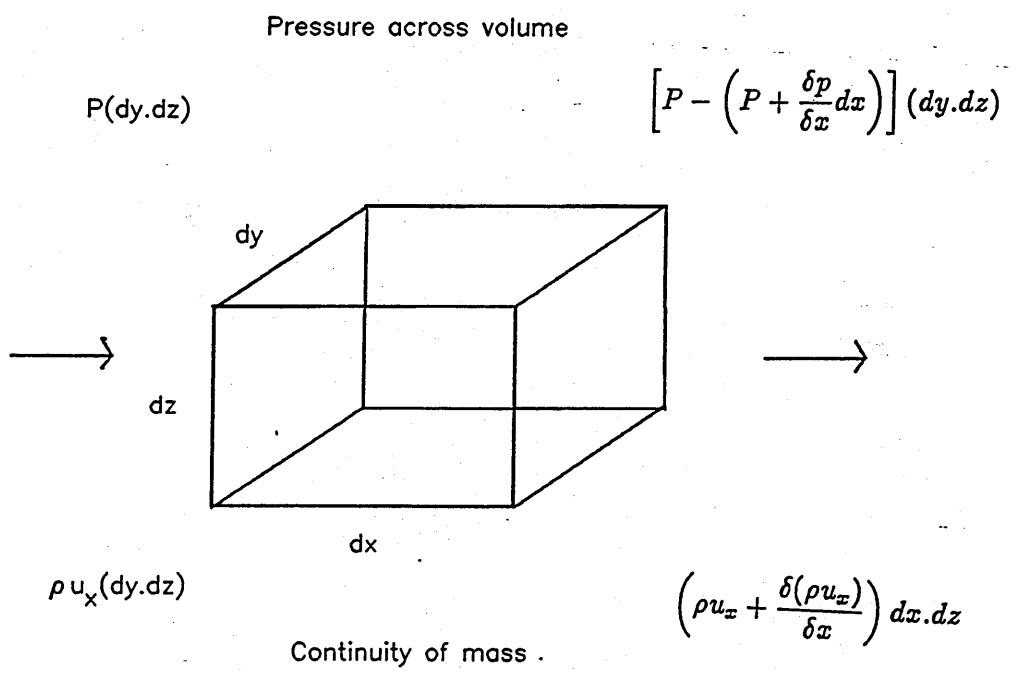


**Figure 4.1** Continuity across a fixed volume

where $\vec{u} = \frac{d\vec{\xi}}{dt} = u_x.\hat{x} + u_y.\hat{y} + u_z.\hat{z}$, the particle velocity and $\xi$ is the particle displacement form the equilibrium position, $\vec{r} = x\hat{x} + y\hat{y} + z\hat{z}$. The rate at which the mass increases is given by $\frac{\partial \rho}{\partial t}dV$. Therefore in three dimensions

$$-\left[\nabla \rho \vec{u}\right] dV = \frac{\partial \rho}{\partial t} dV \qquad (4.6)$$

$$\frac{\partial \rho}{\partial t} + [\nabla \rho \vec{u}] = 0 \tag{4.7}$$

i.e. the equation of continuity. Using $\rho = \rho_0(1+s)$ and assuming $s$ is small gives

$$\frac{\partial s}{\partial t} + \nabla \vec{u} = 0 \tag{4.8}$$

the linearized continuity equation. Applying Newton's second law to our representative volume $dV$ to derive the force equation, we have,

$$\partial \vec{f} = \vec{a} \partial m. \tag{4.9}$$

From figure 4.1 it can be seen that the pressure difference across the volume provides the force, so that

$$\partial \vec{f} = -\nabla \mathcal{P} dV. \tag{4.10}$$

At a time $t$ the particle velocity is given by $\vec{u}(x,y,z,t)$ whereas at a time $t+dt$ the element has moved to a new location and the velocity is given by $\vec{u}(x+u_x dt, y+u_y dt, z+u_z dt, t+dt)$. This may be expanded using a Taylor series expansion to give an acceleration of

$$\vec{a} = \frac{\partial \vec{u}}{\partial t} + u_x \frac{\partial \vec{u}}{\partial x} + u_y \frac{\partial \vec{u}}{\partial y} + u_z \frac{\partial \vec{u}}{\partial z} \tag{4.11}$$

$$\vec{a} = \frac{\partial \vec{u}}{\partial t} + (\vec{u}\nabla)\,\vec{u} \tag{4.12}$$

$$-\nabla \mathcal{P} dV = \rho dV \left[ \frac{\partial \vec{u}}{\partial t} + (\vec{u}\nabla)\,\vec{u} \right] \tag{4.13}$$

as $s \ll 1$ and $\vec{u}\nabla\vec{u} \ll \frac{\partial \vec{u}}{\partial t}$ and $\nabla \mathcal{P} \approx \nabla p$ (as $\mathcal{P}_0$ is constant) then Euler's equation 4.13 can be simplified to

$$-\nabla p = \rho_0 \frac{\partial \vec{u}}{\partial t} \tag{4.14}$$

Elimination of the particle velocity between equations 4.8 and 4.14 taking the divergence of 4.14 gives

$$-\nabla^2 p = \rho_0 \nabla \frac{\partial \vec{u}}{\partial t}. \tag{4.15}$$

As $\frac{\partial(\nabla \vec{u})}{\partial t} = \nabla \frac{\partial \vec{u}}{\partial t}$ from equation 4.8,taking the time derivative we get

$$\frac{\partial^2 s}{\partial t^2} + \nabla \frac{\partial^2 \vec{u}}{\partial t^2} = 0. \tag{4.16}$$

Therefore combining 4.15 and 4.16 gives

$$\nabla^2 p = \rho_0 \frac{\partial^2 s}{\partial t^2} \tag{4.17}$$

and using 4.5 to eliminate the condensation gives the three dimensional linearized wave equation

$$\nabla^2 p = \frac{1}{c^2} \frac{\partial^2 p}{\partial t^2} \tag{4.18}$$

where $c = \sqrt{\frac{E}{\rho_0}}$. To solve the equation for spherical waves the Laplacian is written in spherical coordinates

$$\nabla^2 = \frac{\partial^2}{\partial r^2} + \frac{2}{r}\frac{\partial}{\partial r} + \frac{1}{r^2 \sin\theta}\frac{\partial}{\partial \theta}\left(\sin\theta \frac{\partial}{\partial \theta}\right) + \frac{1}{r^2 \sin^2\theta}\frac{\partial^2}{\partial \phi^2}. \tag{4.19}$$

As the waves have spherical symmetry this reduces to

$$\nabla^2 = \frac{\partial^2}{\partial r^2} + \frac{2}{r}\frac{\partial}{\partial r}. \tag{4.20}$$

A study of the energy equation shows the pressure amplitude is expected to fall as $\frac{1}{r}$ thus using $rp$ as the variable gives

$$\frac{\partial^2 (rp)}{\partial r^2} = \frac{1}{c^2}\frac{\partial^2 (rp)}{\partial t^2}. \tag{4.21}$$

It can be shown that for harmonic waves the solution to this differential equation is a combination of a converging and a diverging spherical wave. The solution for the divergent wave is given as

$$p = \frac{A}{k_0 r} e^{i(\omega t - k\vec{r})}. \tag{4.22}$$

Subsequently the time dependence $e^{i\omega t}$ is assumed and is not explicitly written in the equations.

## 4.2 Reflection of the spherical wave from a plane impedance boundary

Consider the geometry shown in figure 4.2 the field at the receiver $P$ consists of a spherical diverging wave travelling form the source to the receiver along the path $R_1$ and a reflected wave travelling along the path $R_2$. Thus the total wave field at P can be written as

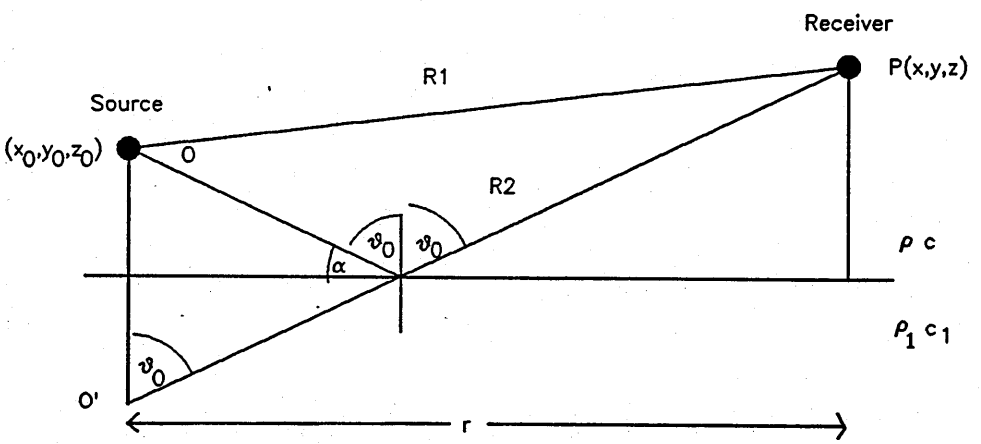


**Figure 4.2** Geometry for reflection of a spherical wave from a plane boundary

$$p_t = \frac{e^{ik_0R_1}}{k_0R_1} + p_r \tag{4.23}$$

It is the evaluation of $p_r$, the reflected wave, that leads to the various solutions to be considered here. There have been many algorithms produced, the earlier work of Rudnick [152], Ingard [153] and Donato [36] followed the study of the electromagnetic wave propagation over the earths surface by Sommerfield [154] and Wait [155]. Many of these earlier papers have been corrected or superceded. Only the results of the most common or more recent formulations will be considered in this study. Firstly the simple case of sound propagation over a locally reacting surface is considered. A locally reacting medium has a large refractive index so that the waves impinging on the surface are refracted toward the normal. There is no lateral wave propagation. The acoustical characteristics of a medium are determined by the normal impedance or reflection coefficient.

### 4.2.1 Plane wave reflection coefficient solution

The simplest solution is derived by assuming that the wave front impinging on the surface has travelled sufficiently far for the plane wave reflection coefficient to be an accurate approximation to that for spherical waves. In this case the reflected wave is given by

$$p_r = R(\theta_0)\frac{e^{ik_0R_2}}{k_0R_2} \tag{4.24}$$

with

$$R(\theta_0) = \frac{\cos\theta_0 - \beta}{\cos\theta_0 + \beta} \tag{4.25}$$

The reciprocal of the impedance, the admittance is denoted by $\beta$. This solution is termed the plane wave reflection coefficient solution (p.w.r.c.) and will be the most primitive propagation model considered here. It is expected that this model will become increasingly inaccurate as $kr$ decreases i.e. at small source receiver separations and at low frequencies. Also for small source heights where the sphericity of the wave front is more important.

A more complete study is obtained by splitting the spherical waves into a summation of plane waves. The reflection from the surface is then considered and the effect of each of the waves at the receiver is summed to gain the total field. This produces a reflected wave field term in the form of a numerical integrand. In general the solution can be written in the form

$$p_r = \frac{e^{ik_0R_2}}{k_0R_2}\left[R(\theta_0) + G\left(R(\theta_0)\right)\right] \tag{4.26}$$

The second term in equation 4.26 is known as the ground wave term and accounts for the sphericity of the wave front. It may be thought of as a diffusion of the optical image source at $O'$, i.e. waves other than those incident at $\theta_0$ are received at $P$. The sum of the two terms in the brackets is known as the spherical wave reflection coefficient.

### 4.2.2 Weyl van der Pol solution

The most commonly used solution to the above problem is known as the Weyl van der Pol solution after the similar result in electromagnetic wave propagation theory. The corresponding solution for the acoustic problem was derived by Ingard [54] and Lawhead and Rudnick [156]. The title of the solution arises from the theoretical extension of Sommerfield's work by Weyl [4] and Van der Pol [5]. The solution is found by modifying the integral for the reflecting wave and evaluating it using a method of steepest descents. Ingard neglected a pole which lies near the saddle point of the deformed path of integration and by doing so excluded the existence of the surface wave see chapter 5. The correction to give the total wave field was derived implicitly by Brekhovskikh [138] and explicitly by Donato [157]. Donato used the complex wave number as the argument of the integral whereas Ingard and Lawhead et al integrated over the complex angle of incidence. The result is a field given by

$$p_t = \frac{e^{ik_0R_1}}{k_0R_1} + Q\frac{e^{ik_0R_2}}{k_0R_2} \tag{4.27}$$

with

$$Q = R(\theta_0) + (1 - R(\theta_0))F(w) \tag{4.28}$$

With $R(\theta_0)$, the plane wave refection coefficient, given by equation 4.25. $\theta_0$ is the angle of incidence as given in figure 4.2. $\beta$ is the admittance of the locally reacting surface. $F(w)$ the boundary loss factor is given by

$$F(w) = 1 + \imath\sqrt{\pi}we^{(-w^2)}erfc(-\imath w) \tag{4.29}$$

$$w^2 \approx \frac{1}{2}(\imath k_0 R_2)(\cos\theta_0 + \beta)^2 \tag{4.30}$$

The inaccuracies in the solution will become more apparent for small values of $kr$ and for $\beta \geq 1$. Also at near normal angles of incidence.

### 4.2.3 Attenborough, Hayek and Lawther solution

The Weyl–van der Pol formulae for the acoustic problem may be derived from either the Attenborough, Hayek and Lawther solution, [158], or from the work of Chein and Soroka, [159], [160]. As these solutions are essentially the same only the more recent work by Attenborough et al shall be considered here. The solution is obtained in the form:

$$\phi_t = \frac{e^{\imath k_0 R_1}}{4\pi R_1} + \frac{e^{\imath k_0 R_2}}{4\pi R_2} + \phi_{rad} \tag{4.31}$$

The method used by Paul [161] is employed near grazing angles of incidence. The integrand for the radiated wave is rewritten using the relationship between Bessel and Hankel functions, and an exact integral solution proposed as the sum of two branch cut integrals and the residue from a pole on the upper Reimann sheet. An approximate solution is then obtained by transforming the integral around the branch cuts into paths of steepest descent in the complex angle of incidence plane. Assuming that the source and receiver separation is large compared to the sum of the source and receiver height. The location of the poles due to the reflection coefficient term is considered, only one pole may lie between the steepest descent path and the path of integration from which it was derived. This pole gives rise to

the surface wave term. The method of subtraction of the pole must be used otherwise the convergence of the series derived from the steepest descent integral will be restricted. A locally reacting boundary is considered by setting the refractive index to a value much larger than one and $|\beta| < 1$. The solution for the field above the impedance boundary is given by

$$\phi_t \simeq \frac{e^{ik_0R_1}}{4\pi R_1} + R(\theta_0)\frac{e^{ik_0R_2}}{4\pi R_2} - \frac{k_0\beta}{4}$$
$$\left[e^{(-\frac{x_0^2}{2})}erfc(-\frac{ix_0}{\sqrt{2}}) \times H_0^1\left[k_0r(1-\beta^2)^{\frac{1}{2}}\right]e^{ik_0r(1-\beta^2)^{\frac{1}{2}}}e^{ik_0R_2}\right] + V'(R) \quad (4.32)$$

with

$$\frac{(x_0)^2}{2} = ik_0R_2(1+\beta\cos\theta_0 - (1-\beta^2)^{\frac{1}{2}}\sin\theta_0)$$

and

$$V'(R) \simeq \frac{\beta}{2\pi}\frac{e^{ik_0R_2}}{R_2(\beta+\cos\theta_0)}\left[\frac{1}{\sqrt{2}}\left(\frac{1+\beta\cos\theta_0}{(1-\beta^2)^{\frac{1}{2}}\sin\theta_0}+1\right)^{\frac{1}{2}}\right. \quad (4.33)$$
$$+\frac{1}{ik_0R_2(\beta+\cos\theta_0)^2}\left[-(1-\beta\cos\theta_0) + \frac{\sin\theta_0(1-\beta^2)^{\frac{1}{2}}}{8\sqrt{2}}\right. \quad (4.34)$$
$$\left.\left.\times\left(1+\frac{1+\beta\cos\theta_0}{\sin\theta_0(1-\beta^2)^{\frac{1}{2}}}\right)^{\frac{3}{2}}\left(\frac{1+\beta\cos\theta_0}{\sin\theta_0(1-\beta^2)^{\frac{1}{2}}}+3\right)\right]\right] \quad (4.35)$$

A further approximation may be gained by putting $|\beta|^2 \ll 1$ and $\theta_0 \simeq \frac{\pi}{2}$. Giving the Weyl–van der Pol solution.

Quartararo [162], who corrected the typographical errors in the Attenborough et al paper, has suggested that when the $|\beta|^2 \ll 1$ condition is violated there may be up to two decibels difference between the fields predicted by equations 4.32 and 4.27.

### 4.2.4 Thomasson solution

Thomasson [81] began his work by examining the work of Ingard and Wenzel. He concluded that the basic mathematical method of Cauchy's integrand theorem of two complex variables, which was used by Weyl and adapted by Ingard to the acoustic case, was a suitable tool to solve the propagation problem, but it had been used incorrectly. Starting from the radiated wave term given by Wenzel, Thomasson defined an integration path that included the pole due to the reflection coefficient term. He then transformed this into a steepest descent and a branch cut integral. The contribution from the branch cut integral was termed the surface wave but Thomasson noted that this mathematical proof did not prove the physical existence of such a wave. The main results of this work was a form for the total wave field which could be evaluated numerically. Thomasson stated " with the high speed computers of today (1976) there is no need for asymptotical expansions or approximate solutions as the solution given here is numerically very efficient". The total field is given by

$$\phi_t = -\frac{e^{ik_0R_1}}{4\pi R_1} - \frac{e^{ik_0R_2}}{4\pi R_2} + \phi_{rad} \tag{4.36}$$

with

$$\phi_{rad} = \begin{cases} \phi'_{rad} + \phi_s & \Re(\gamma_0) > 0, Im(\beta) < 0 \\ \phi'_{rad} & \text{otherwise} \end{cases} \tag{4.37}$$

with

$$\phi_s = \frac{k_0\beta}{2} H_0^{(1)}\left[k_0 r\left(1-\beta^2\right)^{\frac{1}{2}}\right] e^{-\imath k_0 h\beta} \tag{4.38}$$

$h = h_r + h_s$

$$\phi'_{rad} = \frac{k_0\beta}{2\pi} e^{\imath k_0 R_2} I_1 \tag{4.39}$$

$$I_1 = \int_0^\infty e^{-k_0R_2t} \frac{1}{W^{\frac{1}{2}}} dt \tag{4.40}$$

with

$$Re\left(W^{\frac{1}{2}}\right)\begin{cases} <0 & \text{if } \Re(\gamma_0)>1, \Im(\beta)<0, t>t_1 \\ >0 & \text{otherwise} \end{cases} \tag{4.41}$$

$$\gamma_0 = -\beta\cos(\theta_0) + \left(1-\beta^2\right)^{\frac{1}{2}}\sin\theta_0 \tag{4.42}$$

$$\gamma_1 = -\beta\cos(\theta_0) - \left(1-\beta^2\right)^{\frac{1}{2}}\sin\theta_0 \tag{4.43}$$

$$W = (1+\imath t-\gamma_0)(1-\imath t-\gamma_1) \tag{4.44}$$

$$= \left[\cos(\theta_0)+\beta^2\right] + 2\imath t\left[1+\cos(\theta_0)\beta\right] - t^2 \tag{4.45}$$

$$t_1 = \frac{\Im\left[(\gamma_0-1)(\gamma_1-1)\right]}{\Re\left[(\gamma_0-1)+(\gamma_1-1)\right]} \tag{4.46}$$

$$\tag{4.47}$$

$$= \frac{-\Im(\beta)\left[\Re(\beta)+\cos\theta_0\right]}{1+\cos\theta_0\Re(\beta)} \tag{4.48}$$

with

$$\Re\left[(1-\beta^2)\right] > 0 \tag{4.49}$$

Chandler–Wilde 4.2.8 has developed this solution to give a form which may be used to generate a more exact solution. Thomasson expanded his work to include the propagation over a rigidly backed porous layer [136] and derives an asymptotic series solution despite his earlier comment, qualifying his decision by considering the propagation over a screen.

Thomasson produced another series solution by using Watson's lemma [163]. Unlike his earlier series solution the only limitation on this solution is that $k_0R_2 \gg 1$. Most other series have an additional restriction on the impedance or the geometry. The integrand of the radiated wave see $I_1$ in equation 4.40 includes in the denominator the term $W^{\frac{1}{2}}(t) = (A^2+t)(B^2-t)$. Ingard expanded this term and neglected the $t^2$ term

to put the integrand into the form of an error function. Previously Thomasson neglected $t$ compared to $B^2$ to avoid the surface wave term presuming that $|B|^2 \gg |A|^2$ which is a reasonable assumption for most practical ground surfaces. This solution however was not mathematically rigorous so instead the root $(B^2 - t)$ is expanded for small values of $t$. The remainder of the integral is

$$I_m = \int_0^\infty \frac{t^m e^{-t}}{\sqrt{A^2 + t}} dt \tag{4.50}$$

It is seen that an iterative procedure may be developed with

$$I_m = (m - \frac{1}{2} - A_2) I_{(m-1)} + \cdots + (m-1) A^2 I_{(m-2)} \text{ for } m \gg 2 \tag{4.51}$$

$$I_0 = \sqrt{\pi} e^{A^2} erfc(A) \tag{4.52}$$

and

$$I_1 = A + \left(\frac{1}{2} - A^2\right) I_0 \tag{4.53}$$

A similar procedure may be applied to the surface wave term. The resulting total field is given by

$$\phi_t = \frac{e^{ik_0 R_1}}{-4\pi R_1} + \frac{e^{ik_1 R_2}}{-4\pi R_2} + \frac{C k_0 \beta e^{ik_0 R_2}}{2\pi B} \sum_{m=0}^{\infty} \frac{(2m)! I_m}{(m!)^2 (4B^2)^m} \tag{4.54}$$
$$+ \frac{1}{4}(1 - C) k_0 \beta H_0^{(1)}(k_0 r (1 - \beta^2)^{\frac{1}{2}}) \exp[-ik_0(h_s + h_r)\beta]$$

$$W(t) = (A^2 + t)(B^2 - t) \tag{4.55}$$

$$A = [ik_0 R_2(\gamma_0 - 1)]^{\frac{1}{2}} \tag{4.56}$$

$$B = [ik_0 R_2(1 - \gamma_1)]^{\frac{1}{2}} \tag{4.57}$$

$\gamma_0$ and $\gamma_1$ are given in equation 4.42 and 4.43.

$$C = \begin{cases} +1; & -\frac{\pi}{2} \leq \arg(A) \leq \frac{\pi}{4} \\ -1; & \frac{\pi}{4} \leq \arg(A) \leq \frac{\pi}{2} \end{cases} \tag{4.58}$$

for $\Re(\gamma_0) > 1$.

### 4.2.5 Kawai, Hidaka and Nakajima solution

Kawai, Hidaka and Nakajima [164] considered another modified saddle point method to calculate the field above an impedance boundary. The integral for the reflected wave is obtained in a form suggested by Brekovskikh [138] i.e.

$$\phi_r = \frac{ik_0}{2} \int_L e^{ik(h_s+h_r)\cos\theta_0} H_0^{(1)}(kr\sin\theta_0)(R(\theta_0)-1)\sin\theta_0 d\theta_0 \tag{4.59}$$

and a steepest descent path is obtained for $k_0 R_2 \gg 1$. The effect of a pole located near to the saddle point is included by using a method of subtraction, a Taylor series expansion is utilized for the function incorporating the pole. Alternative expressions originating from [165] are given for the $F^*(w)$ term. The authors claim that their series developed from the Taylor series expansion converge faster that the Thomasson solution gained by expanding $\frac{1}{\sqrt{1-x}}$. The total field is given by

$$\phi t = \frac{e^{ik_0 R_1}}{R_1} + \frac{e^{ik_0 R_2}}{R_2} + \phi'_{rad} + \phi_s \tag{4.60}$$

with

$$\phi'_{rad} = -\frac{\beta\sin\theta_0}{\beta+\cos\theta_0}\sqrt{\frac{2\pi k_0}{R_2}} H_0^1(k_0 r\sin\theta_0) e^{(ik_0 R_2\cos^2\theta_0 + i\frac{\pi}{4})} \tag{4.61}$$

$$\times \left[1 + a\left[\frac{2(1+\beta\cos\theta_0)}{(\beta+\cos\theta_0)^2} - \frac{1}{4\sin^2\theta_0}\right][F^*(k_0 R_2 a) - 1]\right] \tag{4.62}$$

with

$$a = 1 + \beta\cos\theta_0 - \sqrt{1-\beta^2}\sin\theta_0 \tag{4.63}$$

for $\Re(\sqrt{1-\beta^2}) > 0$ and $kR_2 \gg 1$.

An expansion for the Hankel function in equation 4.60 is suggested and the series corrected so that the first two terms of the approximate series solution are identical to those of the exact solution. The surface wave term $\phi_s$ again arises when the pole is located between the original path of integration and the steepest descent path which replaces it. The pole is shown to lie between the integration paths when

$$Im(\beta) < 0 \text{ and } \Re(a) < 0 \tag{4.64}$$

$$\phi_s = \begin{cases} -2k_0\beta H_0^{(1)}(k_0 r\sqrt{1-\beta^2})e^{-\imath k_0(h_r+h_s)\beta} & \Im(\beta) < 0 \text{ and } \Re(a) < 0 \\ 0 & \text{otherwise} \end{cases} \tag{4.65}$$

is found from the residue theory. The total field obtained by using an expansion of the Hankel function and the surface wave is given by

$$\phi_t = \frac{e^{ik_0R_1}}{R_1} + \frac{e^{ik_0R_2}}{R_2} + +(R(\theta_0)) - \frac{4\beta(1+\beta\cos\theta_0)}{(\beta+\cos\theta_0)^3} a\{F^*(k_0R_2a) - 1\} + \phi_s \tag{4.66}$$

### 4.2.6 Nobile and Hayek solution

The penultimate series solution for propagation model over a locally reacting boundary is that derived by Nobile and Hayek [166] The pole is dealt with from the onset by including its effect in the reflected wave integral, this method was suggested by Van der Pol [5] and used by Lawhead and Rudnick though Nobile et al apply a different identity to account for the pole. The result is transformed to give an integral evaluated for $\Im(\beta) > 0$. This results in the following recursive formulae.

$$p_t = \frac{e^{ik_0R_1}}{R_1} + \frac{e^{ik_0R_2}}{R_2} - \frac{4ik_0\beta e^{ik_0R_2}}{(\beta+\sin\theta_0)} \sum_{n=0}^{\infty} T_n[e_0E_n + K_n] \tag{4.67}$$

$$T_n = \text{ Taylor coefficient } = \frac{1}{(2B)^n} \sum_{n=0}^{(n-2k)\geq 0} \begin{pmatrix} n-k \\ k \end{pmatrix} a_{n-k} \left(\frac{4G}{H}\right)^{n-k} \tag{4.68}$$

$$\begin{pmatrix} n-k \\ k \end{pmatrix} \text{ is the binomial coefficient} \tag{4.69}$$

$$e_0 = \frac{1}{2}\sqrt{\frac{\pi}{ik_0R_2}} e^{-\lambda^2} erfc(-i\lambda) \tag{4.70}$$

$$E_m = -BE_{m-1} + \left[\frac{(m-1)}{2ik_0r_2}\right] E_{m-2} \tag{4.71}$$

$$E_0 = 1,\ E_1 = -B \tag{4.72}$$

$$K_m = -BK_{m-1} + \left[\frac{(m-1)}{2ik_0R_2}\right] K_{m-2} \tag{4.73}$$

$$K_0 = 0.\ K_1 = \frac{1}{2ik_0R_2} \tag{4.74}$$

with

$$B = -i\sqrt{1+\beta\sin\theta_0 - \sqrt{1-\beta^2}\cos\theta_0} \text{ for } (\Re\surd > 0) \tag{4.75}$$

$$\lambda = \sqrt{ik_0R_2}\sqrt{1+\beta\sin\theta_0 - (1-\beta^2)^{\frac{1}{2}}\cos\theta_0} \tag{4.76}$$

$$G = -B^2 = 1+\beta\sin\theta_0 - \sqrt{1-\beta^2}\cos\theta_0 \tag{4.77}$$

$$H = 1+\beta\sin\theta_0 + \sqrt{1-\beta^2}\cos\theta_0 \tag{4.78}$$

$$a_m = \left[\frac{(\frac{1}{2}-m)}{m}\right] a_m - 1,\ a_0 = 1. \tag{4.79}$$

Thus we get for the first seven terms;

$$a_0 = 1,\ a_1 = \frac{-1}{2},\ a_2 = \frac{3}{8},\ a_3 = \frac{-5}{16},\ a_4 = \frac{35}{128},\ a_5 = \frac{-63}{256},\ a_6 = \frac{231}{1034} \tag{4.80}$$

### 4.2.7 Habault and Fillippi solution

The final asymptotic series solution to be considered is that of Habault and Fillippi [167]. The solution which was originally developed for propagation over an externally reacting boundary is simplified to account for a locally reacting boundary. The layer potential formulation proposed presumes that the reflected field is derived from an array of image sources whose support is a plane parallel to the media interface and passing through the optical image source. A more standard 'surface wave' representation is also presented. For the locally reacting case however both lead to the same asymptotic series solution, thus at this stage only the layer potential formulation will be considered. A two dimensional Fourier transform pair is used to generate a solution to the wave equation for a pair of homogeneous media. The resultant Fourier transform of the reflected pressure has three components, an image source and two surface sources located in the plane $z = -h_s$. An inverse transform is then applied. The coefficients of the two surface terms are then found by applying the conditions of local reaction. The solution obtained is in the form of a numerical integration. The derivation of the series expansion form this point has been evaluated by Habault in an earlier paper [168]. The Helmholtz elementary solution found in the integrand of the surface source terms is expanded into a spherical harmonic series and integrated to give a solution in the form of a series of even Hankel functions. These are then expanded to result in the series solution. The first two terms in the series solution are presented as providing an accurate representation for the far field. The field above the locally reacting surface is given by

$$p_t = -\frac{e^{ik_0 R_1}}{R_1} - \frac{e^{ik_0 R_2}}{R_2}\left[R(\theta_0) + \frac{2i}{k_0}\frac{\beta(\beta+\cos\theta_0)}{(\beta\cos\theta_0+1)^3}\frac{1}{R_2} + \cdots\right] \tag{4.81}$$

### 4.2.8 Derivation of adaptive quadrature solution

Chandler–Wilde [3] has recently made a critical review of the solutions for a field above a locally reacting plane . A precis of this review has a dual purpose here. First the radiated wave is presented as a soluble numerical integration, one form of which has previously been obtained by Thomasson. Secondly the study compares the derivation of the series solutions and will aid a better understanding of the relationship between the various representations of the total field to be examined numerically.

#### Development of more exact solution

Recalling the geometry given in figure 4.2. Let $\gamma = \cos\theta_0$, and $\rho = k_0 R_2$. Again the total field at P is given by equation 4.31 where $\phi_{rad}$ can be considered as accounting for the finite impedance if the boundary. A Hankel transform pair is applied to evaluate this radiated wave which will satisfy the boundary problem

$$(\nabla\bar{r}^2 + k_0^2)\phi_{rad} = 0. \tag{4.82}$$

The impedance boundary condition

$$\frac{\partial\phi_t}{\partial z} + \imath k_0\beta\phi_t = 0 \tag{4.83}$$

should also be satisfied at $z = 0$ with $\Re(\beta) > 0$.

Application of the inverse transform gives

$$\phi_{rad} = \frac{\imath k_0\beta}{4\pi}\int_{-\infty}^{\infty} \frac{e^{\imath(h_s+h_r)\sqrt{k_0^2-t^2}}H_0^{(1)}(tr)t}{\sqrt{k_0^2-t^2}(\sqrt{k_0^2-t^2}+k_0\beta)}dt. \tag{4.84}$$

It is possible to use the substitution $t = -u$ and the relationship between the Hankel and Bessel functions of the first type to give

$$\phi_{rad} = \frac{\imath k_0\beta}{2\pi}\int_{0}^{\infty} \frac{e^{\imath k_0(h_s+h_r)\sqrt{1-u^2}}J_0(k_0ru)u}{\sqrt{1-u^2}(\sqrt{1-u^2}+\beta)}du \tag{4.85}$$

This solution obtained by Richard's et al [169] is oscillatory and is not suitable for numerical integration.

Solution most applicable to Gauss–Laguerre integration

One uses the substitution $u = \sin\theta$ to give an integration along the path L, figure 4.3. The integrand obtained has poles at

$$\theta = \pm\cos^{-1}(-\beta) + 2n\pi \tag{4.86}$$

and a branch point singularity occurring at $\sin\theta = 0$ After checking that the branch point lies away form the proposed new path of integration, deformation of the path L to the steepest descent integral $\Gamma$, figure 4.3, gives:

$$\phi_{rad} = \frac{\imath\beta}{4\pi}\sqrt{\frac{2k_0}{r}}\int_L p(\theta)e^{\imath\rho\cos(\theta-\theta_0)}d\theta. \tag{4.87}$$

Where

$$p(\theta) = \left(\frac{k_0 r}{2}\right)^{\frac{1}{2}}(\cos\theta+\beta)^{-1}e^{-\imath k_0 r\sin\theta}\sin\theta H_0^{(1)}(k_0 r\sin\theta_0). \tag{4.88}$$

This integral may be used in a steepest descent integration if $p(\theta)$ is independent of $\rho$ i.e. when $kr\sin\theta_0$ is large. When the deformation is performed a pole is crossed if $\Re(a_+) < 0$, and $\Im(\beta) < 0$. With

$$a\pm \approx 1+\beta\gamma \mp \sqrt{1-\beta^2}\sqrt{1-\gamma^2} \tag{4.89}$$

Using the calculus of residues this gives the surface wave term $\phi_s$. Where

$$\phi_{rad} = \phi'_{rad} + \phi_s \tag{4.90}$$

$\phi'_{rad}$ is the radiated wave term after subtraction of the pole contribution. The modified radiated wave term is given by

$$\phi'_{rad} = \frac{\imath\beta}{2\pi}\sqrt{\frac{k_0}{2r}}\int_\Gamma p(\theta)e^{\imath\rho\cos(\theta-\theta_0)}d\theta \tag{4.91}$$

and

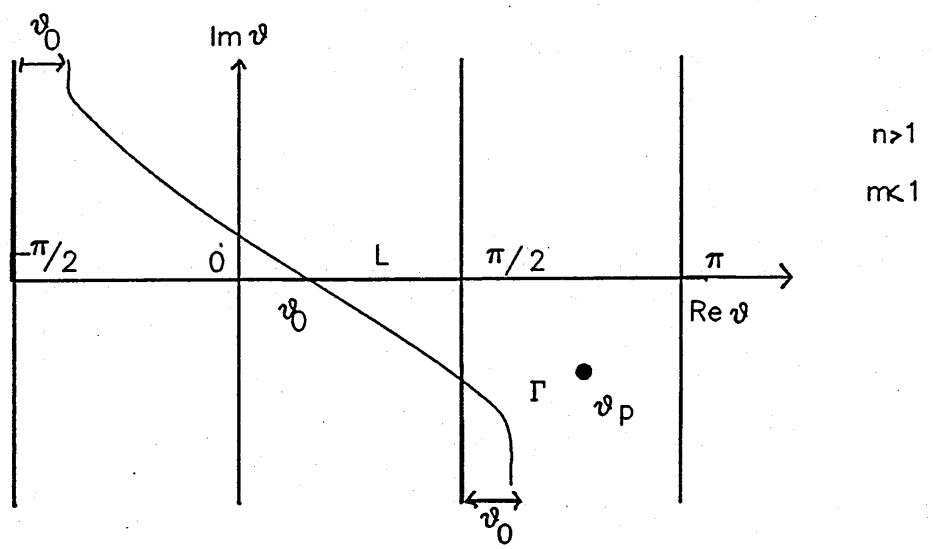


**Figure 4.3** Path of integration

$$\phi_s \approx \begin{cases} \frac{k_0\beta}{2} H_0^{(1)}(k_0 r\sqrt{1-\beta^2}e^{-\imath k_0(h_s+h_r)\beta} & \text{If } \Im(\beta) < 0 \text{ and } \Re(a_+) < 0 \\ \frac{k_0\beta}{4} H_0^{(1)}(k_0 r\sqrt{1-\beta^2}e^{-\imath k_0(h_s+h_r)\beta} & \text{If } \Im(\beta) < 0 \text{ and } \Re(a_+) = 0 \\ 0 & \text{otherwise} \end{cases} \tag{4.92}$$

Continuing the steepest descent method gives the point at which many of the asymptotic series started.

$$\phi'_{rad} = \frac{k_0\beta e^{\imath\rho}}{2\pi} \int_{-\infty}^{\infty} P(s) e^{-\rho s^2} ds \tag{4.93}$$

with

$$P(s) = \sqrt{\frac{2}{k_0 r}} \frac{p(\theta)}{\sqrt{s^2 - 2\imath}} \tag{4.94}$$

and

$$\frac{d\theta}{ds} = \frac{2\imath s}{\sin(\theta - \theta_0)} \text{ with } s = \sin\theta \tag{4.95}$$

Writing the integral in the form of a Laplace type integral gives:

$$\phi'_{rad} = \frac{k_0\beta e^{\imath\rho}}{2\pi} \int_0^{\infty} t^{-\frac{1}{2}} e^{-\rho t} f(t) ft \tag{4.96}$$

where

$$f(t) = \frac{1}{2}(P(\sqrt{t}) + P(-\sqrt{t})) = -\frac{P^*(\sqrt{t}) + P^*(-\sqrt{t})}{2\sqrt{t - 2\imath}(t - \imath a_+)(t - \imath_-)} \tag{4.97}$$

and

$$P^*(\sqrt{t}) = e^{(-\imath k_0 r \sin\theta)} H_0^{(1)}(k_0 r \sin\theta) \sin\theta((1+\imath s^2)\gamma + s\sqrt{s^2 - 2\imath}\sqrt{1-\gamma^2} + \beta) \tag{4.98}$$

It would be possible at this point to calculate $\phi'_{rad}$ numerically but the function contained within the integral is not smooth. To ensure that $f(t)$ is smooth which is essential for Gauss–Laguerre quadrature the restrictions;

$$|1-\beta| < \frac{1}{4} \text{ and } 0 \leq \gamma \leq \frac{3}{4} \tag{4.99}$$

are required. This ensures that the singularities at $\imath a_+$ and $\imath(1 \pm \gamma)$ are not between the original and deformed paths of integration. This restriction also ensures that $\phi_s = 0$. Thus Gauss–Laguerre numerical integration may be employed if $\rho$ is not too small. The solution is difficult to calculate as it contains two Hankel functions with complex arguments and can only be used when the numerical distance is small, when the pole $t = \imath a_+$ does not lie the near the real axis. Subtraction of the pole will give $\phi'_{rad}$ as a Laplace type integral and a complementary error function of a complex number. This representation however is not satisfactory if $\gamma$ tends to 1.

Solution most applicable to adaptive quadrature

Starting from equation 4.93, it is possible to apply the identity

$$\frac{1}{x} = \int_0^\infty e^{-xs} ds \text{ when } \Re(x) > 0 \text{ and } \Im(\beta) > 0 \tag{4.100}$$

to gain

$$\phi_{rad} = \frac{k_0 \beta}{4\pi} \int_{-\infty}^{\infty} \frac{e^{\imath(h_s+h_r)\sqrt{k_0^2-t^2}}}{\sqrt{k_0^2-t^2}} H_0^{(1)}(tr) t \left( \int_0^\infty e^{\imath(\sqrt{k_0^2-t^2}+k_0\beta)s} ds \right) dt \tag{4.101}$$

This form was obtained by Van der Pol [5] and Lawhead et al [156]. The order of integration is reversed and the Hankel transform of $\frac{-e^{\imath k_0 R_2}}{4\pi R_2}$ is recognized to give

$$\phi_{rad} = 2\imath k_0 \beta \int_0^\infty \left[ \frac{e^{\imath k_0 R_2}}{4\pi R_2} \right] e^{\imath k_0 \beta s} ds \text{ for } \Im(\beta) > 0 \tag{4.102}$$

An alternative form of this equation is evaluated by Rawlins [170] for $\Im(\beta) < 0$ by deforming the path of integration from the real to the imaginary axis. A further representation for $\Im(\beta) > 0$ is gained by deforming the path of integration from the imaginary axis to the real negative axis. As a branch cut is crossed in the deformation the radiated wave term is in the form of an integral along the real axis and a branch cut integral. This solution is

obtained by Thomasson [81] and by Habault and Fillipi [167], the later authors however used a layer potential formulation to reach this point. The result may be interpreted as the sum of a line of sources passing along the axis between the image source and actual source and a surface wave term. The resulting integral however is oscillatory and therefore can not be easily evaluated using numerical quadrature. A further substitution of $t = \frac{s}{R_2}$ is made to give a Laplace type integral which may be deformed into a steepest descent integral.

Using the steepest descent substitution

$$\beta s + \sqrt{1 + 2\gamma s + s^2} = 1 + \imath t \tag{4.103}$$

gives

$$s = \frac{(-(\beta + \gamma + \imath\beta t) \pm \sqrt{W(t)})}{(1 - \beta^2)} \tag{4.104}$$

with

$$W(t) \approx -(t - \imath a_+)(t - \imath a_-) = -t^2 + 2\imath t(1 + \beta\gamma) + (\beta + \gamma)^2 \tag{4.105}$$

With both real and imaginary parts of $\beta$ greater than 0 and $\Im(t) \leq 0, \Re(t) \geq 0$. Having considered the sign of $W(t)$ the path of integration is deformed to the real axis to give

$$\phi_{rad} == \frac{k_0\beta}{2\pi} e^{\imath\rho} \int_0^\infty \frac{e^{-\rho t}}{\sqrt{W(t)}} dt \text{ for } \Im(\beta) > 0 \tag{4.106}$$

This representation of $\phi_{rad}$ was obtained by Ingard [153] using the method suggested by Weyl [4]. Ingard's work was completed by Thomasson [81]. The result for any $\Im(\beta)$ and $\Re(a_+)$ is given as

$$\phi_{rad} = \frac{k_0\beta}{2\pi} e^{\imath\rho} \int_0^\infty \frac{e^{-\rho t}}{\sqrt{W(t)}} dt + \phi_s \tag{4.107}$$

with

$$\phi_s = \begin{cases} H_0^{(1)}(k_0 r\sqrt{1-\beta^2}) e^{-\imath k_0\beta(h_s+h_r)} & \text{if } \Im(\beta) < 0 \text{ and } \Re(a_+) < 0 \\ 0 & \text{otherwise} \end{cases} \tag{4.108}$$

The sign of $W(t)$ has been determined by Thomasson to be

$$\Re(\sqrt{W(t)}) = \begin{cases} < 0 & \text{if } \Im(\beta) < 0, \Re(a_+), t > t_1 \\ > 0 & \text{otherwise} \end{cases} \tag{4.109}$$

Thus the total field is given by

$$\phi_t = \begin{cases} \frac{\imath k_0 \beta}{2\pi} e^{\imath\rho} \int_0^\infty \frac{e^{-\rho t}}{\sqrt{-W(t)}} dt + \frac{k_0\beta}{2} H_0^{(1)}(k_0 r\sqrt{1-\beta^2}) e^{-\imath k_0 \beta(h_s+h_r)} & \Im(\beta) < 0, \Re(a_+) < 0 \\ \frac{k_0\beta}{2\pi} e^{\imath\rho} \int_0^\infty \frac{e^{-\rho t}}{\sqrt{W(t)}} dt & \text{otherwise} \end{cases} \tag{4.110}$$

This second solution may be solved using adaptive quadrature using a method described by Habault [171]. Both Gauss Laguerre and adaptive quadrature may be applied to equations 4.96 and 4.110. As $W(t)$ is the more simple function however equation 4.110 is used. It should be noted however that errors in this solution will arise if $|w|$ is small due to the singularity at $t = \imath a_+$. Although it would be possible to account for this by using equation 4.96 and subtraction of the pole.

As mentioned previously the integral

$$I = \int_0^\infty \frac{e^{-\rho t}}{\sqrt{W(t)}} dt \tag{4.111}$$

or its complementary value in equation 4.110 is evaluated using an automatic integrator (NAG D01AMF [172]). Such a technique involves: specification of the integral to be evaluated; the limits of integration; the tolerance and the number of functional evaluations. The method of evaluation used in this case is an iterative adaptive procedure based on the Gauss seven point Kronrod 15 point rules. In adaptive procedures evaluation points of the integral are dependant on the integrand. Successive approximations are generated until the specified tolerance is obtained. The tolerance and relative error of the routine are only a guide to the accuracy of the result. The improper integral is transformed into a bounded form using:

$$\int_A^\infty F(t)dt = \int_0^1 F\left(A + \frac{(1-x)}{x}\right) \frac{1}{x^2} dx \tag{4.112}$$

to which the Gauss–Kronrod rules are applied.

### 4.2.9 Comparison of series solutions

The series solutions are subdivided into three types by Chandler–Wilde and we shall use the same three classes.

Expansions in the inverse powers on $\rho$ The radiated wave term is found in inverse powers of $\rho$. The starting point is the equation 4.107. To which Watson's Lemma [173] may be applied. $(W(t))^{-\frac{1}{2}}$ is expanded as a series in $t$ and each term is integrated in order. The series derived in this manner by Rawlins was also gained by Habault via the layer potential representation. The first terms of the series are used to derive the equation in subsection 4.2.7. Chandler–Wilde however suggests that the series known as the correcting terms and correcting series do not converge and that the accuracy claimed by the authors will not be achieved. Richard's et al [169] also criticized the solution which they claimed would become inaccurate for small values of the numerical distance $w$.

Modified saddle point derivation The second type of solution uses equation 4.93 as a starting point and is a popular method for deriving the asymptotic series solution. The modified saddle point method of Ott is applied [174]. This method is pursued by Attenborough, Hayek and Lawther [158] and Kawai *et al.*. Equation 4.93 is written as

$$\phi_{rad} = \frac{k_0\beta}{2\pi} e^{\imath\rho} \int_0^\infty \hat{p}(s) \frac{e^{-\rho s^2}}{s^2 - \imath a_+} ds \tag{4.113}$$

with $\hat{p}(s) = p(s)(s^2 - \imath a_+)$. $p(s)$ is then expanded in a power series around the origin and the integral is performed term by term, note that $\gamma < 1$. The integrals in the form $\int_Z^\infty e^{-u^2} u^{-2n} du$ are expressed in terms of the complementary error function. This gives

$$\phi_{rad} = \frac{e^{-\imath\frac{\pi}{4}} k_0\beta\sqrt{1-\gamma^2}}{2\sqrt{2\pi}(\beta-\gamma)} e^{-\imath\rho\gamma^2} H_0^{(1)}(\rho(1-\gamma^2))^{\frac{-1}{2}} \rho\,(1 + KF^*(w)) \tag{4.114}$$

$$K = \begin{cases} 1 & \text{one term} \\ 1 + a_+\left(\frac{1}{a} - \frac{1}{4(1-\gamma^2)}\right) & \text{two terms} \end{cases} \tag{4.115}$$

Which is the equation 4.60 derived by Kawai et al. Note that a similar process was followed by Brekovskikh [138] and Donato [157]. However the replacement of the Hankel function by its asymptotic form leads to the introduction of further errors. Kawai et al recover from the introduction of these errors whilst developing 4.66 by the removal of the $\frac{1}{4\sin^2\theta_0}$ term. This solution also has the advantage of not being singular at $\gamma = 1$. Chandler–Wilde suggests an improvement to the series solution produced by Kawai in the form

$$\phi_t = \frac{e^{\imath k_0 R_1}}{4\pi R_1} + \frac{e^{\imath k_0 R_2}}{4\pi R_2}\left[R(\theta_0) - \frac{2\beta}{(\beta+\cos\theta)}\left(\frac{\imath}{8\rho} + \left(1 + \frac{a_+}{a_-} - \frac{a_+}{4} - \frac{\imath}{8\rho}\right)F(w)\right)\right] + \phi_s \tag{4.116}$$

Where $F(w) = 1 - F^*(-\imath w^2)$

This form of the solution should be more accurate in the far field at grazing angles of incidence. This will not be true however for small $\rho$ due to the unbounded $\frac{\imath}{8\rho}$ terms.

Attenborough et al followed an alternative saddle point approach and subtracted the pole from equation 4.96. The replacement of the Hankel function by it's integral representation leads to a complex integral.

Generalized Watson's Lemma The third form of solution applies the generalized Watson's Lemma as described by Clemmow [175]. The radiated wave term is in the form of equation 4.107 where

$$\sqrt{W(t)} = (\beta+\gamma)\sqrt{1 - \frac{t}{\imath a_-}}\frac{\sqrt{t+\imath a_+}}{\sqrt{\imath a_+}} \tag{4.117}$$

The $\left(1 - \frac{t}{\imath a_-}\right)^{-\frac{1}{2}}$ term is expanded using the binomial theorem to give Thomasson's recursive formulae. The formulae only requires $\rho \gg 1$ and is valid near normal incidence like many solutions gained using the second method. The Nobile and Hayek solution is derived using a process similar to that used above. The series $(a_- + 2\imath s\sqrt{a_+} - s^2)^{-\frac{1}{2}}$ in equation 4.96 is expanded in a power series of $s$ and integrated term by term. The result is the same as equation 4.96 if the first term is used and the restriction $\Im(\beta) > 0$ or $\Re(a_+) > 0$ is applied.

Finally the number of terms to be used in the Nobile and Hayek solution and in Thomasson's solution must be considered. The series are asymptotic and not convergent. The series should be terminated when it begins to diverge so the terms will be chosen such that

$$|\phi^1_{rad} - \phi^2_{rad}| > |\phi^2_{rad} - \phi^3_{rad}| \cdots |\phi^{n-1}_{rad} - \phi^n_{rad}| \qquad (4.118)$$

Where $\phi^n_{rad}$ is the value of the radiated wave for $n$ terms in the series. A further restriction of $1 \leq n \leq 10$ is made.

A summary of the relationships of the series solutions is shown in figure 4.2.9.

In summary the solutions considered in the numerical comparison are shown in table 4.1

Table 4.1 Summary of local reaction propagation models

| Solution | Equation number | Program name | Reference number |
|---|---|---|---|
| P.W.R.C. | 4.24,4.25,4.23 | PLN | M1 |
| Weyl–van der Pol | 4.27,4.28,4.29, 4.30 | WVP | M2 |
| Thomasson | 4.54 | THM | M3 |
| Attenborough et al | 4.32 | AHL | M4 |
| Kawai,Hidaka and Nakajima | 4.60 | KHN | M5 |
| Nobile and Hayek | 4.67 | NAH | M6 |
| Habault and Fillippi | 4.81 | HAF | M7 |
| Adaptive quadrature | 4.110 | TCW | M8 |
| Chandler Wilde | 4.116 | CHW | M9 |

The appropriate program listings may be found along with the associated subroutines for the calculation of the mathematical functions in appendix K. The attribute of the sound field most readily measured is the logarithm of the magnitude of the pressure. As explained in section 8.2.1 this quantity is measured as a level difference spectra. It is the difference between the adaptive quadrature technique and the series solutions in terms of the difference in level differences that is examined here. Having determined the solutions to be examined the impedances over which they are to be measured and the level difference geometries must be defined.

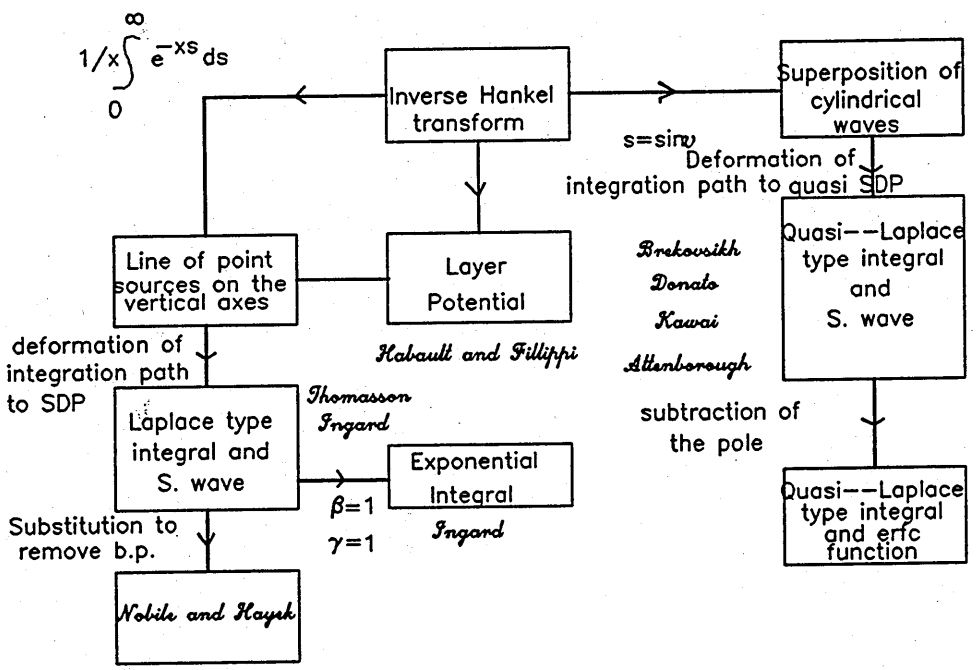


**Figure 4.4** Summary of development of series solutions

The impedances of the surfaces are produced by insertion of the various parameters into the Attenborough four parameter impedance model see Chapter 3. At this stage we shall consider two locally reacting boundaries. Surface S1B has an impedance similar to that of the outdoor grassland surface measured by Embleton [124]. The second surface (S1) has acoustical characteristics of a rigidly backed artificial grass measured by Heap [15] in a standing wave tube. This impedance is used directly in solutions considered for a locally reacting half space.

The first level difference geometry considered (G1) is a short range level difference geometry typical of that used by Hess [82] for the characterization of soils and used for the indirect method of measuring impedance developed in chapter 7. The geometry G1 is listed in table 4.2.9. The second geometry (G2) examines the accuracy of the models at near grazing angles of incidence. The geometry (G3) examines accuracy for normal incidence by considering a geometry similar to that used by Allard in his two microphone impedance measurement technique.

Table 4.2 Summary of level difference geometries

| Geometry | Upper receiver height (m) | Lower receiver height (m) | Source height (m) | Source-receiver separation (m) | Angle of incidence (°) |
|---|---|---|---|---|---|
| G1 | 0.50 | 0.05 | 0.50 | 1.50 | 56 |
| G2 | 0.10 | 0.05 | 0.10 | 7.50 | 88 |
| G3 | 0.10 | 0.05 | 1.50 | 0.00 | 0.0 |

### 4.2.10 Results and discussion of comparison of locally reacting models

The results of the numerical comparisons are shown in graphical form in appendix C. The discrepancies between the models become more noticeable as the impedance falls. Howorth [176] showed previously that the Weyl–van der Pol solution was adequate when predicting the field above a high impedance boundary at geometries similar to G1. Surface S1B has a lower impedance than S1 and a significant error is found for geometry G1. Note that in this case the error is considered significant if there is a discrepancy

greater then 1dB, below this level rounding errors in the program and instrumental errors would make it difficult to measure the difference.

The greatest disagreement is obtained at frequencies which correspond to the attenuation dips in the level difference spectra. At these frequencies the direct and reflected waves are in anti-phase and hence the ground wave term is more significant. Reducing the angle of incidence produces an increase in the error of the plane wave solution as expected and also results in errors in the Habault et al solution. This appears to be due to the lack of convergence in the correcting series and correcting terms as suggested by Chandler–Wilde. The remainder of the solutions have little error and show the same trends. It is interesting to note that the error in the Attenborough et al propagation model is reduced by increasing the source height whilst maintaining the angle of incidence (G2B), the error in the P.W.R.C. model remains constant, and the error in the Nobile and Hayek model increases. At near normal incidence little error is detected, the Attenborough et al solution is indeterminate at this angle due to the $\frac{1}{\sin\theta_0}$ term in the expression for $V'(R)$. The extension of the Kawai series produced by Chandler–Wilde has a negligible numerical effect, the differences between the two models arising from rounding errors.

It may be concluded from this study that the Weyl–van der Pol solution is an adequate representation of the propagation over a grassland media and a layered artificial grass. For the geometries considered it represents a significant improvement over the P.W.R.C. solution, though this may not be the case when the surface wave is excited (see chapter 5). Numerical errors appear in the Attenborough et al propagation model for small source heights and low impedances. The Habault solution is also as much prone to error as the P.W.R.C. model.

## 4.3 Reflection of a spherical wave from a semi–infinite plane externally reacting boundary.

An externally reacting medium will support a lateral wave and is characterized by its impedance and propagation constant. A comparison of level difference spectra over these media may be made as before. The solutions considered are:

1. Weyl van der Pol solution (M10)
2. Attenborough, Hayek and Lawther solution (M11)
3. Attenborough, Hayek and Lawther approximate solution (M12)
4. Habault and Fillipi solution (M13)
5. FFP solution (M14)

As the derivation of these solutions is similar to those for the locally reacting media only the result of the analysis shall be given here.

### 4.3.1 Weyl van der Pol solution for semi–infinite half space

The nature of the extended reacting medium is accounted for and the Weyl van der Pol solution for the locally reacting medium is modified accordingly. Such a solution is given by Embleton, Piercy and Olson [124] as

$$\phi_t = \frac{e^{\imath k_0 R_1}}{R_1} + Q\frac{e^{\imath k_0 R_2}}{R_2} \tag{4.119}$$

with

$$Q = R(\theta_0) + (1 - R(\theta_0))F(w) \tag{4.120}$$

and

$$R(\theta_0) = \frac{\cos\theta_0 - \frac{Z_1'}{Z_2'}}{\cos\theta_0 + \frac{Z_1'}{Z_2'}} \tag{4.121}$$

with

$$\frac{Z_1'}{Z_2'} = \frac{Z_1}{Z_2}\left[1 - \frac{k_2^2}{k_1^2}\sin^2\theta_0\right]^{\frac{1}{2}} \tag{4.122}$$

$F(w)$ is given by equation 4.29 and

$$w^2 \approx \frac{1}{2}(\imath k_0 R_2)\left(\cos\theta_0 + \frac{Z_1}{Z_2}\right)^2 \tag{4.123}$$

### 4.3.2 Attenborough, Hayek and Lawther 'accurate' series solution for semi-infinite half space

The solution is derived from the steepest descent method of integration to give:

$$\phi_t = \frac{e^{\imath k_0 R_1}}{4\pi R_1} + \frac{R(\theta_0)e^{\imath k_0 R_2}}{4\pi R_2} - \frac{k_0 A}{4(1-M^2)}$$
$$\left[e^{-\frac{x_0^2}{2}} erfc(\frac{-\imath x_0}{\sqrt{2}} H_0^{(1)}\left(k_0 r(1-A^2)^{\frac{1}{2}}\right) e^{-\imath k_0 r(1-A^2)^{\frac{1}{2}}} e^{\imath k_0 R_2}\right] + V'(R) \tag{4.124}$$

with

$$V'(R) = \frac{e^{\imath k_0 R_2}}{2\pi R_2}\left[\frac{A}{\sqrt{2}(1-M^2)}\left[1 + \frac{1 + A\cos\theta_0}{(1-A^2)^{\frac{1}{2}}\sin\theta_0}\right]^{\frac{1}{2}}\right. \tag{4.125}$$

$$\times \frac{1}{A + \cos\theta_0} + \frac{1}{\imath k_0 R_2}\left[\frac{F\cos\theta_0}{\cos\theta_0 + M(n^2 - \sin^2\theta_0)^{\frac{1}{2}}} + \frac{A}{\sqrt{2}(1-M^2)(A+\cos\theta_0)}\right. \tag{4.126}$$

$$\left.\left.\left(1 + \frac{1 + A\cos\theta_0}{\sin\theta_0(1-A^2)^{\frac{1}{2}}}\right)^{\frac{1}{2}} \times \left(\frac{1 + A\cos\theta_0 + (1-A^2)^{\frac{1}{2}}\sin\theta_0}{2(A+\cos\theta_0)^2} + \frac{1}{8\sin\theta_0(1-A^2)^{\frac{1}{2}}}\right)\right]\right]$$

with (4.127)

$$F = -1 - \frac{\sin^2\theta_0}{\cos\theta_0\left[\cos\theta_0 + M(n^2-\sin^2\theta_0)^{\frac{1}{2}}\right]} \quad (4.128)$$

$$\times\left[1 - \frac{\cos\theta_0}{\sin^2\theta_0}\left(\cos\theta_0 + \frac{2M\cos^2\theta_0 - 3M\sin^2\theta_0}{2(n^2-\sin^2\theta_0)^{\frac{1}{2}}} + \frac{M\cos^2\theta_0\sin^2\theta_0}{2(n^2-\sin^2\theta_0)^{\frac{3}{2}}}\right)\right] \quad (4.129)$$

$$+\left[\frac{\sin^2\theta_0}{n^2-\sin^2\theta_0}\left(\frac{(n^2-\sin^2\theta_0)^{\frac{1}{2}} + M\cos\theta_0}{M(n^2-\sin^2\theta_0)^{\frac{1}{2}} + \cos\theta_0}\right)^2\right]. \quad (4.130)$$

$$R(\theta_0) = \frac{\cos\theta_0 - \beta\left(1 - \frac{k_0^2\sin^2\theta_0}{k_2^2}\right)^{\frac{1}{2}}}{\cos\theta_0 + \beta\left(1 - \frac{k_0^2\sin^2\theta_0}{k_2^2}\right)^{\frac{1}{2}}} \quad (4.131)$$

$M = \frac{\rho_1}{\rho_2}$, $n = \frac{k_2}{k_1}$, $A = M\left[\frac{n^2-1}{1-M^2}\right]^{\frac{1}{2}}$ with $\Re(A) > 0$ and $\Im(A) < 0$.

$$\frac{x_0^2}{2} = \imath k_0 R_2\left(1 + A\cos\theta_0 - (1-A^2)^{\frac{1}{2}}\sin\theta_0\right) \quad (4.132)$$

with $\Re(x_0) > 0$.

### 4.3.3 Attenborough, Hayek and Lawther approximate series solution for semi–infinite half space

Neglecting the higher order terms in the asymptotic series used to develop the previous solution gives an approximate solution of:

$$\phi_t = \frac{e^{\imath k_0 R_1}}{R_1} + Q\frac{e^{\imath k_0 R_2}}{R_2} \quad (4.133)$$

with

$$Q = R(\theta_0) + B(1 - R(\theta_0))F(w) \quad (4.134)$$

and

$$B = \frac{\left(\cos\theta_0 + \beta\left(1 - \frac{\sin^2\theta_0}{n^2}\right)^{\frac{1}{2}}\right)(1-n^2)^{\frac{1}{2}}}{\left(\cos\theta_0 + \frac{\beta(1-n^{-2})^{\frac{1}{2}}}{(1-M^2)^{\frac{1}{2}}}\right)\left(1 - \frac{\sin^2\theta_0}{n^2}\right)^{\frac{1}{2}}} \tag{4.135}$$

$$\times \frac{\left[(1-M^2)^{\frac{1}{2}} + \beta(1-n^{-2})^{\frac{1}{2}}\cos\theta_0 + \sin\theta_0(1-\beta^2)^{\frac{1}{2}}\right]^{\frac{1}{2}}}{(1-M^2)^{\frac{3}{2}}(2\sin\theta_0)^{\frac{1}{2}}(1-\beta^2)^{\frac{1}{4}}} \tag{4.136}$$

$F(w)$ is given in equation 4.29 with

$$w^2 = \imath k_0 R_2\left(1 + \frac{\beta\cos\theta_0(1-n^{-2})^{\frac{1}{2}} - \sin\theta_0(1-\beta^2)^{\frac{1}{2}}}{(1-M^2)^{\frac{1}{2}}}\right) \tag{4.137}$$

### 4.3.4 Habault and Fillipi solution for semi–infinite half space

The asymptotic series solution is again developed from the layer potential representation to give:

$$\phi_t = \frac{e^{\imath k_0 R_1}}{4\pi R_1} - \frac{e^{\imath k_0 R_2}}{4\pi R_2}\left[\frac{Z\cos\theta_0 - K}{Z\cos\theta_0 + K} + \frac{\imath}{2k_0}R_2\left[\frac{2Z\cos\theta_0(1-k^2)}{(Z\cos\theta_0+K)^2K^3}(2-k^2\sin^2\theta_0) + \right.\right.$$
$$\left.\left.\frac{4Z\sin^2\theta_0(1-k^2)}{Z\cos\theta_0+K)^3K^2}(ZK + k^2\cos\theta_0\chi\right]\right] \tag{4.138}$$

with

$$Z = \frac{\rho_2 k_2}{\rho_0 k_0} \tag{4.139}$$

and

$k = \frac{k_0}{k_2}$, $K = \sqrt{1 - k^2\sin^2\theta_0}$, with $\Im k \leq 0$.

### 4.3.5 FFP solution

The solution to spherical wave propagation above a rigid–porous half–space may be evaluated using a fast field program. The method may be used for any layered porous material but is computationally intensive. The solution

however is more accurate for values of $kr \gg 1.$ as a result of the Hankel function approximation which it employs. The FFP solution is used in this section as a comparison for the series solutions. The details of the particular program employed which in fact is for propagation above layered porous and elastic media, are to be found in reference [177]. For this application the elastic parameters were chosen to make the surface rigid. Again the impedance and the propagation constant which describe the surface were computed from the Attenborough microstructural model. The Hankel function is replaced with a Bessel function effectively giving a discrete Fourier transform.

The externally reacting semi–infinite surface (S3) has parameters similar to those expected for snow. The input parameters to the impedance model have been determined by Hess [82] using both an indirect impedance measurement method and a buried microphone technique. These are found to be:

- flow resistivity = 2000 Rayls/m
- porosity = 0.90
- pore shape factor = 0.5
- grain shape factor = 6.0

### 4.3.6 Externally reacting rigidly backed media

The solutions considered for a rigidly backed externally reacting layer of depth ($d$) are:

1. Weyl van der Pol (modified), M15
2. Habault and Fillipi, M16
3. FFP, M17

### 4.3.7 Weyl van der Pol solution for rigidly backed medium

The Weyl van der Pol solution has been adapted for predicting propagation over a hard backed layer by Nicolas, Berry and Daigle [178]. The adaptation is effected by replacing the characteristic impedance and the plane wave reflection coefficient in the original equation by those of a finite thickness of ground. The resulting total field is given by:

$$\phi_t = \frac{e^{\imath k_0 R_1}}{4\pi R_1} + R(\theta_0)\frac{e^{\imath k_0 R_2}}{4\pi R_2} + (1 - R(\theta_0))F(w)\frac{e^{\imath k_0 R_2}}{4\pi R_2} \tag{4.140}$$

with

$$w = \frac{\imath k_0 R_2}{2}\left(\cos\theta_0 + \frac{1}{Z_0}\right)^2 \tag{4.141}$$

$$Z_0 = \left(\frac{Zc}{\left(1 - \frac{k_1^2}{k_2^2}\sin\theta_0^2\right)}\right) \times \coth\left[-\imath k_0 k_2 d\left(1 - \frac{k_1^2}{k_2^2}\sin\theta_0^2\right)\right] \tag{4.142}$$

with $Z_c$ the normalized characteristic impedance of the material.

$$R(\theta_0) = \frac{[Z_0\cos\theta_0 - 1]}{[Z_0\cos\theta_0 + 1]} \tag{4.143}$$

### 4.3.8 Habault and Fillipi solution for a rigidly backed medium

Again development is from the layer potential representation. The total field is given by:

$$p_t = -\frac{e^{ik_0 R_1}}{4\pi R_1} - \frac{e^{ik_0 R_2}}{4\pi R_2}\left[\frac{Z_h\cos\theta_0 - f}{Z_h\cos\theta_0 + f} + \frac{\imath}{2\imath k_0 R_2}\left[\frac{2Z_h\cos\theta_0}{(Z_h\cos\theta_0 + f)^2}(2f + f'\cot\theta_0 + f'') + \frac{4Z_h}{(Z_h\cos\theta_0 + f)^3}(f\sin\theta_0 + f'\cos\theta_0)(Z_h\sin\theta_0 - f')\right]\right] \tag{4.144}$$

where

$$Z_h = \frac{\imath\rho_2 k_0}{\rho_0 k_2}\tan(k_2 d) \tag{4.145}$$

$$f = \frac{K \tan(K k_2 d)}{\tan(k_2 d)} \tag{4.146}$$

$$f' = -\frac{k^2 \sin 2\theta_0}{2K \tan(k_2 h)} \left[ \tan(K k_2 d) + \frac{K k_2 d}{\cos^2(K k_2 d)} \right] \tag{4.147}$$

and

$$f'' = -\frac{k^2}{2 \tan(k_2 h)} \left[ \left( \tan(K k_2 d) + \frac{K k_2 d}{\cos^2(K k_2 d)} \right) \right. \tag{4.148}$$

$$\left. \left( \cos 2\theta_0 + \frac{k^2 \sin^2 2\theta_0}{4K^2} \right) - \frac{k^2 k_2 d \sin^2 2\theta_0}{2 \cos^2(K k_2 h)} \left( \frac{1}{K} + k_2 h \tan(K k_2 h) \right) \right] \tag{4.149}$$

$K$ and $k$ are defined in subsection 4.3.4.

In this case the surface (S4) to be considered is a typical porous macadam (see chapter 8). The parameters for the microstructural model are typically those which have been measured independently and are:

- flow resistivity = 10000 Rayls/m
- porosity = 0.15
- pore shape factor = 0.5
- grain shape factor = 1.0
- layer depth = 0.05 m

Again geometries G1 to G3 are considered.

### 4.3.9 Results and discussion of the comparison of extended reacting models

The results of the comparison of the series solution models with the more accurate F.F.P. solution are shown in appendix C together with the impedance and propagation constant of the surfaces used. As for the locally reacting half space there is no measurable discrepancies between the Weyl van der Pol series solution and the more exact solution. The formulae suggested

by Habault et al however perform less well than the other solutions. The main errors occur at low values of $k_0 R_2$ and when the field is dominated by the ground wave term. The errors are magnified at near grazing incidence. Although the Attenborough, Hayek and Lawther model is not determinate at normal angles of incidence it performs well at other angles of incidence.

The modified Weyl van der Pol form of solution performs well at short source receiver separations both for semi–infinite and rigidly backed media. Suggesting that for most ground characterization measurements this approximate asymptotic series solution is adequate for calculating point to point sound propagation. Mechel [179] suggested that any extensions of the series solutions would lead to little improvement and may increase the error due to numerical rounding errors. However comparisons given elsewhere [177] between FFP results and those due to the Attenborough et al ' accurate series ' do not support this suggestion.

# Chapter 5

# Surface waves

An interesting feature of the analytic approximation of the field above a porous boundary is the surface wave. However there is little experimental evidence as to whether this wave exists in a practical situation. The examination of the field above an impedance boundary results in an expression of the form

$$p_{tot} = p_{dir} + p_{ref} + p_{surf} \tag{5.1}$$

where

- $p_{tot}$ is the total field above the impedance boundary from the spherical source.
- $p_{dir}$ is the contribution to the total field from the direct wave.
- $p_{ref}$ is the reflected wave contribution which may be divided into a component arising from the image source and a second term accounting for the sphericity of the wave front, that is the ground wave.
- $p_{surf}$ is the surface wave contribution.

This chapter examines the nature of the surface wave, reviews the work carried out to date and presents new evidence for it's existence above a lattice layer. The phase speed, group velocity, horizontal attenuation and

vertical attenuation are calculated for a surface wave traveling over the lattice layer. These predictions are then compared to steady state and tone burst measurements made over such a surface.

## 5.1 Review of past work

Embleton and Daigle [180] suggested that the surface wave phenomenon could be explained by considering the particle motion. Away from the boundary there is horizontal particle displacement whilst for a locally reacting surface the particle motion of the air in the pores is in a vertical direction. The combination of these two vectors produces an elliptical particle motion in a layer above the boundary. This results in a reduced phase speed and consequently the wave front of a disturbance traveling near the surface is directed towards the boundary. The resultant characteristic properties of a surface wave are the exponential decay in the x and z coordinates and the reduced phase speed. The surface wave may be written in the form

$$p_s = p_0 e^{-\imath\alpha z} e^{\imath(hx-\omega t)} \tag{5.2}$$

$p_0$ includes the geometrical spreading factor which is proportional to $x^{\frac{1}{2}}$. $h = \sqrt{k_0^2 + \alpha^2}$ where $k_0$ is the wave number of the body wave. Hence the phase velocity is given by

$$c_p = \frac{\omega}{\sqrt{k_0^2 + \alpha^2}} \tag{5.3}$$

which is less than $\frac{\omega}{k_0}$ the phase velocity of the body wave. If the surface wave is travelling over a surface with normal surface impedance $Z\rho c_0$.

$$Z\rho_0 c_0 = \frac{p_s}{u_z} \text{ and } u_z = \frac{-1}{\omega\rho}\frac{\partial p_s}{\partial z} \tag{5.4}$$

this gives

$$\alpha = \frac{\omega\rho_0}{Z} \tag{5.5}$$

dividing through by $\rho_0 c_0$, gives the relative impedance in the denominator i.e.

$$\alpha = \frac{k_0}{Z} \tag{5.6}$$

The vertical attenuation is given by the imaginary part of $\alpha$ i.e.

$$\alpha_v = \frac{-k_0 X}{R^2 + X^2} \tag{5.7}$$

where the impedance has been written as the sum of the real and imaginary parts ($Z = R + \imath X$). Equations 5.3 and 5.6 then give a complex phase velocity as

$$c_p = \frac{\omega}{k_0 \sqrt{1 + \frac{1}{Z^2}}} \tag{5.8}$$

The group velocity is given by $c_g = \frac{\partial \omega}{\partial k}$ hence $c_g = c_p + k_0 \frac{\partial c_p}{\partial k}$ i.e.

$$c_g = c_p + k_0 \frac{\partial}{\partial k} \left( \frac{c_0}{\sqrt{1 + \frac{1}{Z^2}}} \right) \tag{5.9}$$

Hence if the impedance is frequency dependent the medium is dispersive and the group velocity is larger than the phase velocity. To determine the group velocity we need to consider the impedance of the surface of interest. The normal surface impedance $Z_L$ of a rigidly backed lattice work (see photograph in appendix L) is given, approximately, by considering a hard backed air layer i.e.

$$Z_L = -i \cot(k_0 L) \tag{5.10}$$

where $L$ is the depth of the lattice. This gives

$$c_g = c_p - \frac{\omega k_0 \left[ \sqrt{1 + \frac{1}{Z_L^2}} + k \left( \frac{1}{2} \left( 1 + \frac{1}{Z_L^2} \right)^{\frac{-1}{2}} \frac{(-2\imath L) Z_L cosec^2(kL)}{Z_L^4} \right) \right]}{\left( k \sqrt{1 + \frac{1}{Z_L^2}} \right)^2}. \tag{5.11}$$

The attenuation in the horizontal direction is given by the imaginary part of $h$ where

$$h^2 = k^2 + \alpha^2. \tag{5.12}$$

After substituting for $\alpha$ and taking the imaginary part it is possible to deduce that

$$\alpha_h = \frac{-kRX}{(R^2 + X^2)^2}. \tag{5.13}$$

The expressions obtained above are similar to those obtained by Donato [36] when the different time convention is accounted for.

There has been some discussion as to whether the surface wave described above could exist above an impedance boundary or whether the wave was a mathematical artefact. Some early studies into the nature of the surface wave were carried out by Brekhovskikh [181] who examined the acoustic surface wave for a comb like structure and a boundary with an elastic impedance. He also demonstrated that for a spherical wave source the surface waves are excited when the condition

$$h > \frac{k_0}{\sin\theta_0} \text{ or } z + h_s < \frac{r}{Z} \tag{5.14}$$

is satisfied. It was shown that the ratio of the energy of the surface wave $W_s$ to that of the wave in free space $W$ is given by

$$\frac{W_s}{W} = \frac{2\pi e^{-2\alpha x}}{Z} \tag{5.15}$$

The paper also includes a section on the excitation of the cylindrical surface wave and the use of a ribbed structure as a surface wave guide. Ivanov–Shits and Rozhin [182] continued Brekhovskikh work by attempting to verify experimentally the existence of the surface waves above a comb like structure. The horizontal and vertical sound field over a comb like structure were measured. The measured and theoretical values of the vertical attenuation and the phase speed were then compared. Although some agreement was obtained the experiment was not conclusive proof that the surface wave

exists. A battery of eleven speakers was used as a source this would not have acted as a point source as is studied in most literature. Furthermore the dispersive nature of the surface was not accounted for. Thomasson [136] considered the sound propagation over a rigidly backed porous layer. Measurements of the vertical and horizontal attenuation were used to derive values for the impedance of the surface which compared well with measurements made using an impedance tube. Similar measurement were performed by Donato [36] who earlier produced expressions for the surface wave term and the total field above the surface, [157]. Attenborough et al [158] however concluded that the surface wave term produced by Donato would be negated by a heavyside step function in the derivation. They produced an analytic approximation for the field above the impedance boundary which did not include the surface wave term explicitly. The surface wave term still arose however when the complementary error function had a negative imaginary argument. Raspet, Bass and Ezell, [130], [183] however found little numerical difference between the two solutions with and without an explicit surface wave. Van der Heijden and Martens [184] examined the propagation of road traffic noise over a series of grooved surfaces and concluded that the attenuation effects of the grooves could be attributed to surface wave theory.

Raspet, Ezell and Bass ,[130], [183] contested Daigle et al's statement [185] that the acoustic surface wave found over a Delaney–Bazely/Chessel, [121], [89] type surface, or a rigidly backed or some layered surfaces described by the Attenborough microstructural model, was the same type of surface wave as found in propagation over the comb like boundary. Instead they suggested that the surface wave was not an independently traveling wave but rather a response to the incident body wave. This controversy has been dispelled subsequently by Raspet and Baird [186] who applied Tolstoy's criteria [187] to the surface wave above an impedance boundary. This states that a true surface wave will propagate along a surface independently of the body wave. To achieve this criterion Raspet et al examined the surface wave when the medium in the upper half space became incompressible, i.e. the speed of sound tended to infinity whilst the density remained constant.

The result is confirmation that the surface wave above such an impedance boundary is a true surface wave.

Evaluation of the steepest descent integration used to determine the reflected wave term shows that the surface wave contributes to the total field if the pole arising from the denominator of the plane wave reflection coefficient term is encountered while deforming the path of integration to the steepest descent path. This results in the conditions for the surface wave to exist above an externally reacting boundary

$$a + \sin\delta \leq \cos\delta\sqrt{(cosh^2\theta_p'') - 1} \tag{5.16}$$

where

$$cosh^2\theta_p'' = \frac{1 + a^2 + b^2 + \sqrt{(1 + a^2 + b^2)^2 - 4a^2}}{2} \tag{5.17}$$

$$a = \Re\left\{\left[\frac{\left(\frac{c_1}{c_0}\right)^2 - \left(\frac{k_0}{k_1}\right)^2}{Z^2 - \left(\frac{k_0}{k_1}\right)^2}\right]^{\frac{1}{2}}\right\} \tag{5.18}$$

$$b = \Im\left\{\left[\frac{\left(\frac{c_1}{c_0}\right)^2 - \left(\frac{k_0}{k_1}\right)^2}{Z^2 - \left(\frac{k_0}{k_1}\right)^2}\right]^{\frac{1}{2}}\right\} \tag{5.19}$$

and $\delta = \frac{\pi}{2} - \theta_0$. The resulting surface wave is given by

$$\phi_s = 2\left(\frac{2\pi k_0}{R_2}\right)^{\frac{1}{2}}\left(\frac{c_0}{c_1}\right)^{\frac{1}{2}} e^{-\frac{i\pi}{4}} e^{ik_0R_2\cos(\theta_p - \theta_0)\frac{c_0}{c_1}} \times \frac{\cos\theta_p}{(\sin\theta_p)^{\frac{1}{2}}}\left[\frac{Z^2}{Z^2 - \left(\frac{k_0}{k_1}\right)^2}\right] \tag{5.20}$$

For outdoor sound propagation $a$, $b$ and $\delta$ are small and the conditions for the existence of the acoustic surface wave are given by Donato [157].

Daigle [188] examined the experimental evidence for the existence of the surface wave;

1. By considering the sound pressure level above a rigid surface and a porous surface it was seen that the porous surface supported

sound pressure levels greater than the 6dB found above the rigid boundary. This indicates surface wave existence.

2. By using short tone bursts the surface wave could be seen as a separate arrival though this was not the case when pulses were used.

## 5.2 Verification of the existence of acoustic surface waves

When the angle of incidence $\theta_0$ approaches 90 ° the condition for the existence of the acoustic surface wave above a locally reacting surface reduces to $X > R$. This condition is fulfilled by the surface impedance of a cubic lattice of dimension 1.27cm. Such a surface was used by Donato [36] and thus any results gained here may be compared to this earlier work. Figure 5.1 shows the theoretical impedance of the single and double depth lattice calculated from equation 5.10 and the impedance measured by the rigorous impedance tube technique suggested in chapter 2. An end correction of 3.37mm is required and the tube attenuation is found to be $3.09.10^{-7}\frac{f^{\frac{1}{2}}}{r}$ nepers/m slightly larger than that predicted by the American standard, this discrepancy is probably due to different temperature and humidity conditions inside the tube. The measurements suggest a significant increase in the reactive component of the lattice compared to the predicted values. At low frequencies a finite resistance is measured compared with the theoretical prediction of zero. It can be seen that improved agreement is obtained by reducing the effective pore depth to 0.9cm and 2.0cm for the single and double lattice respectively, see figure 5.2. Donato suggesting that the effective pore depth was 0.9cm and 2.1cm. He suggested that the anomalies arose from the clamping effect of placing the sample in the tube although latter results in this chapter indicate that the impedance tube measurements are in agreement with measurements of the surface wave. To confirm the accuracy of the impedance tube measurements the indirect technique of deducing impedance developed in chapter 6 was used. The resulting single and double

depth lattice work impedances, and the associated level difference spectra are shown in figures 5.4 to 5.7. This in turn suggests that the simple equation 5.10 does not generate the impedance of the lattice work. It presumes that the characteristic impedance is unity and ignores viscous and thermal effects at the square pore boundaries. An alternative formulation for the impedance of a material containing rectangular pores has been derived by Arnott [189] and more recently by Stinson [146]. It can be seen in figure 5.3 that this model is a more accurate representation of the lattice than the simple equation used previously, a porosity of 0.82 and a tortuosity of 1.0 are used in the calculation. The porosity is calculated from measuring the dimensions of the lattice. Since the agreement of the simple theory using a modified pore depth and the measured impedance data is rather similar to that obtained with the square pore theory the former is used in the remainder of the chapter for the numerical comparisons.

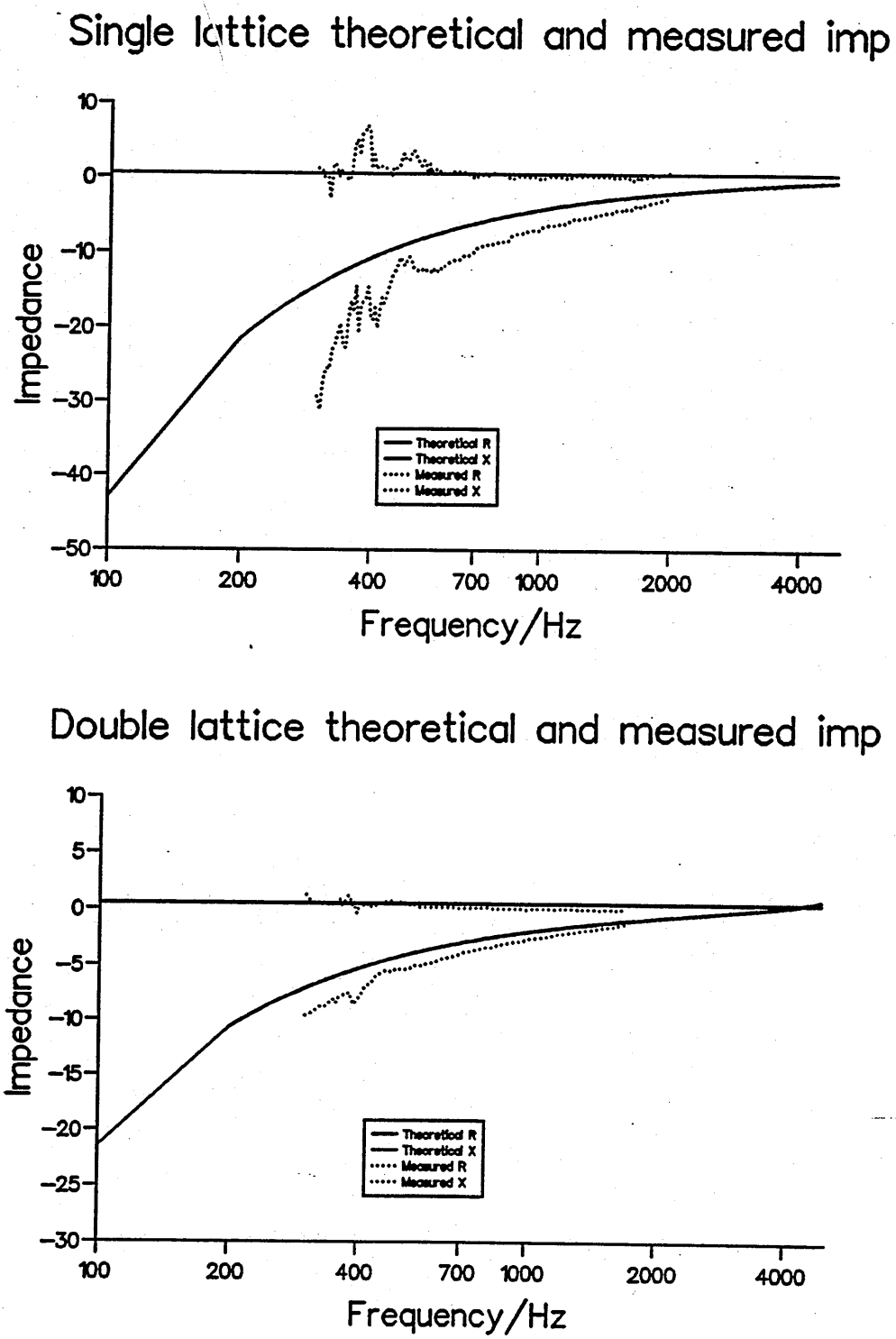


Figure 5.1 Impedance of lattice work

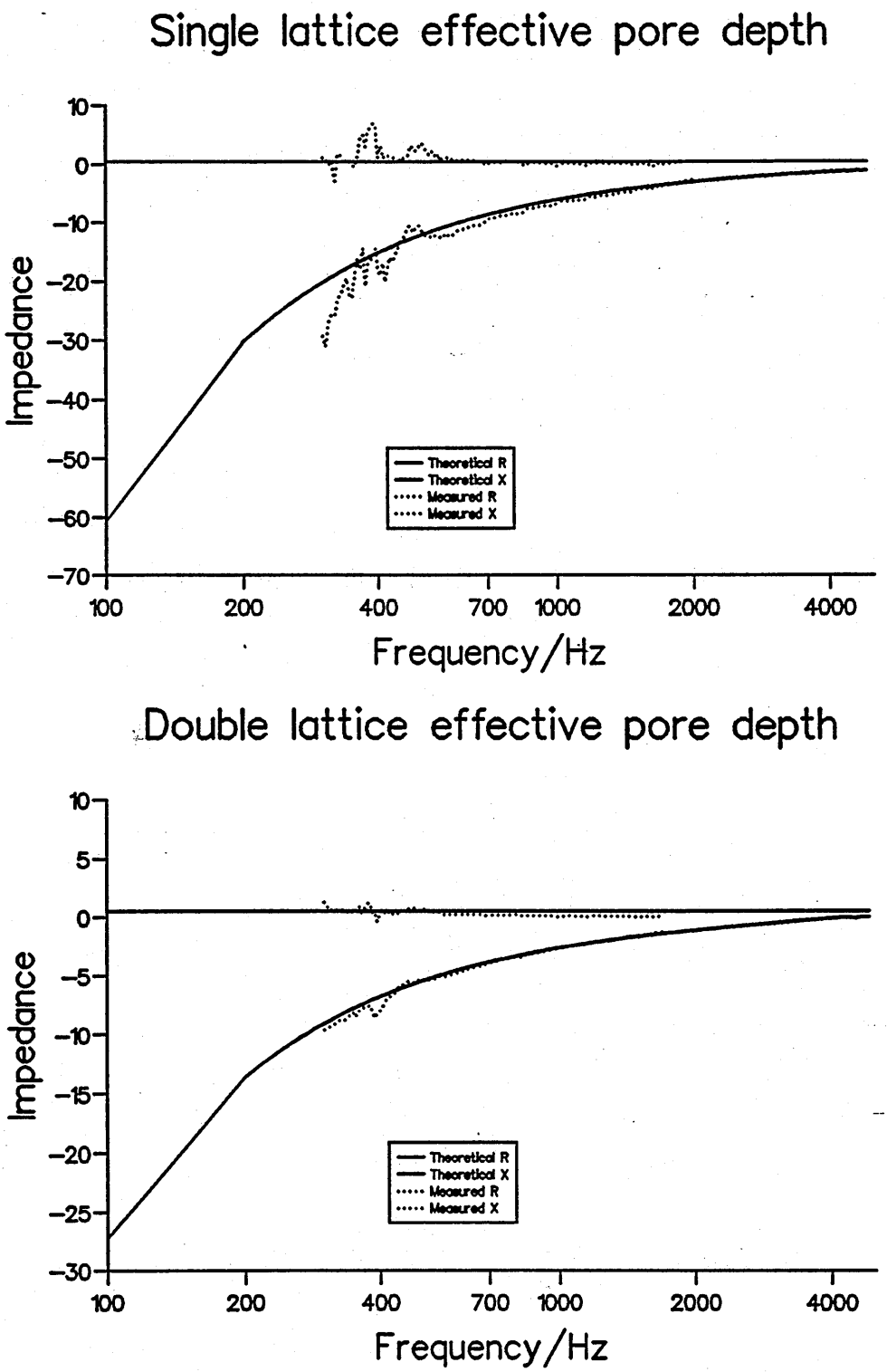


**Figure 5.2** Effective impedance of lattice work

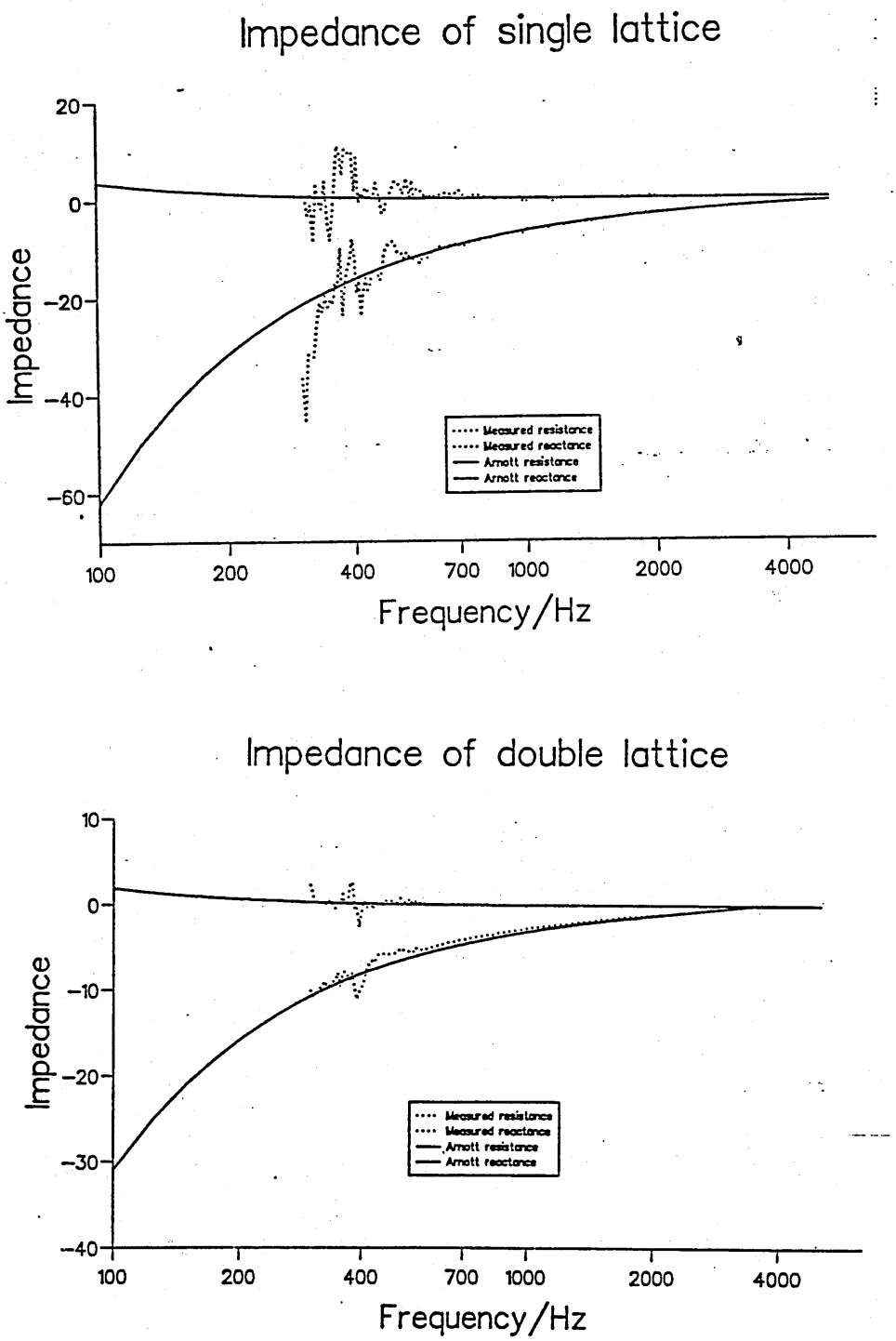


**Figure 5.3** Impedance of lattice work after Arnott

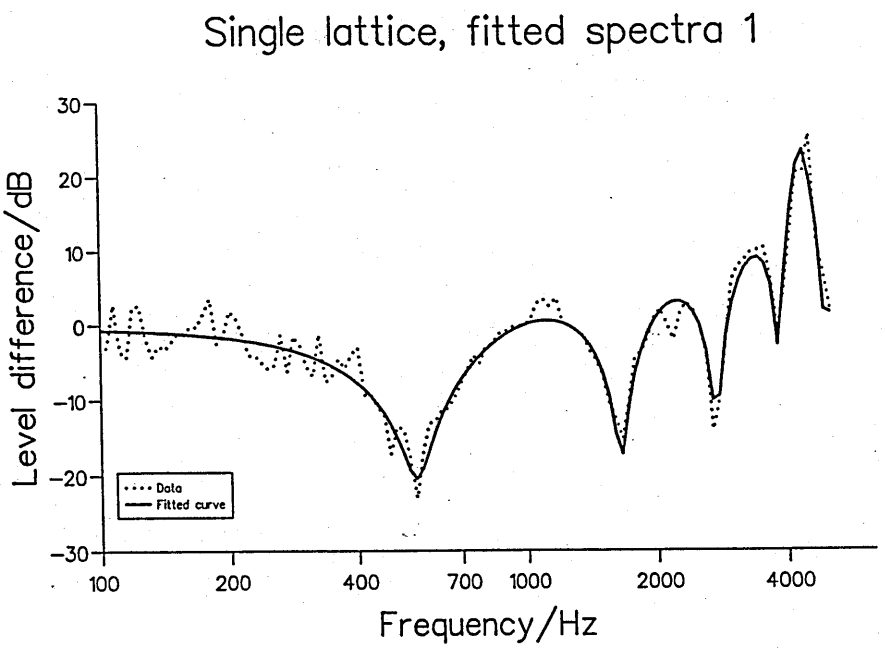


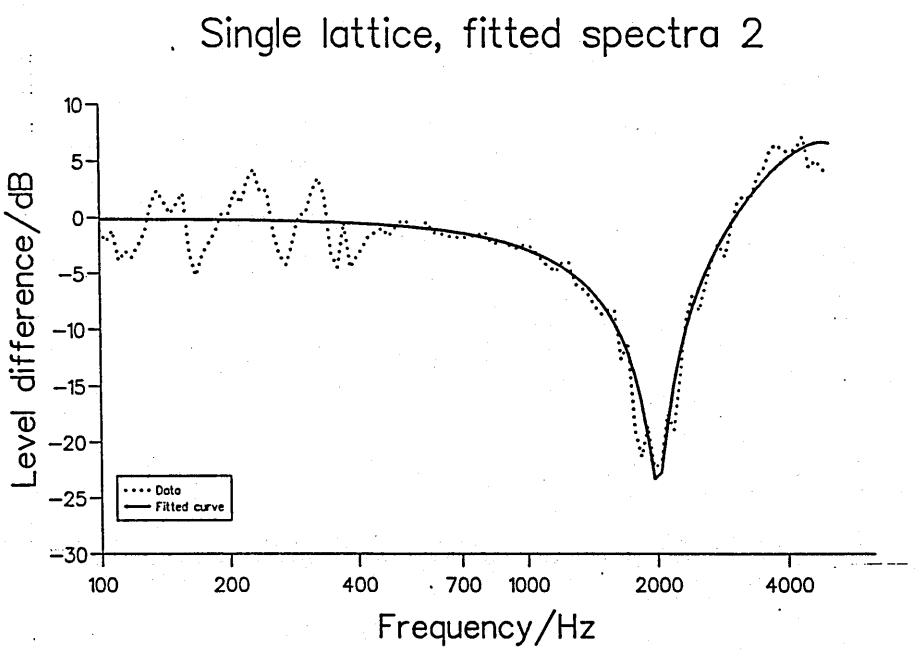


**Figure 5.4** Level difference spectra used for determination of single lattice impedance

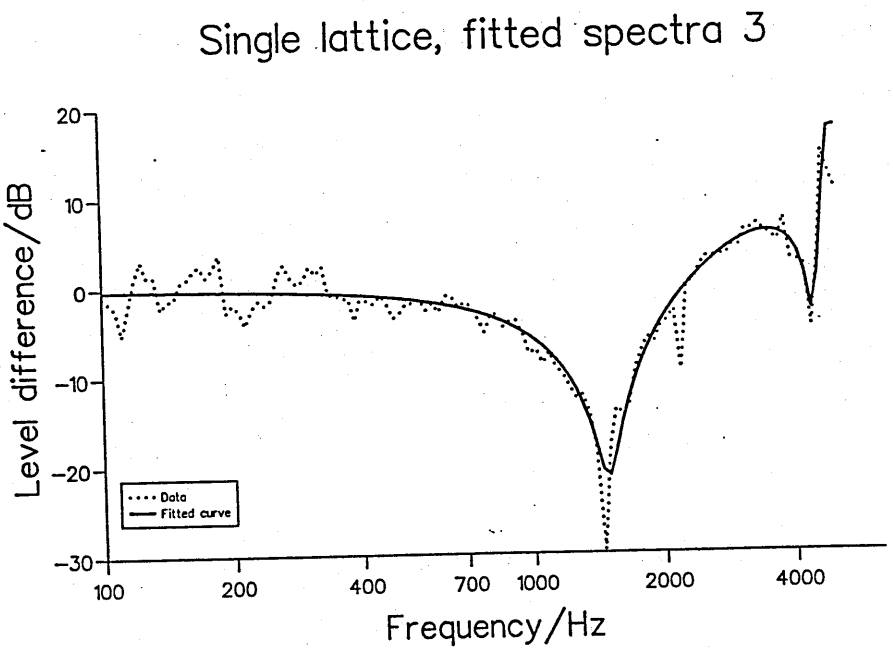


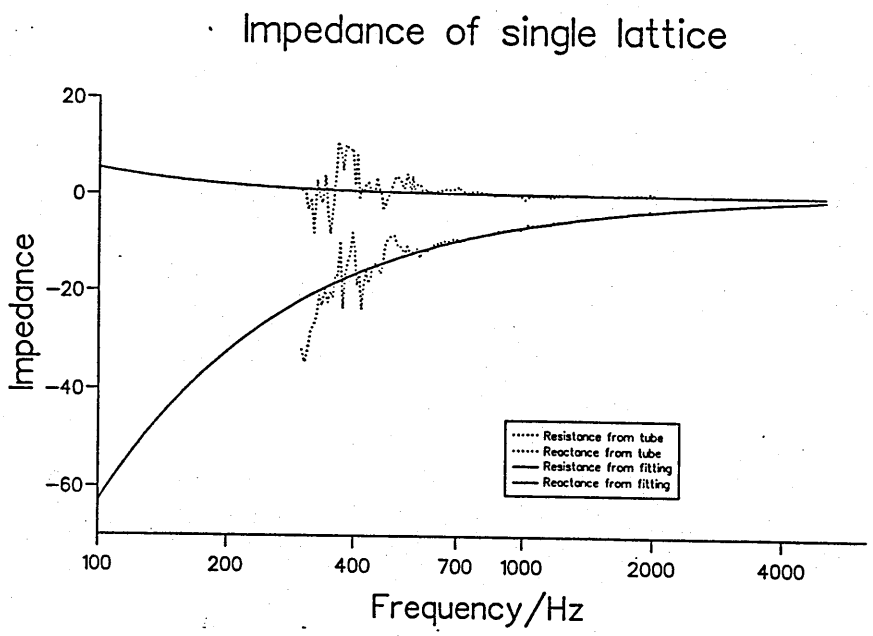


**Figure 5.5** Level difference spectrum used for determination of single lattice impedance, and resulting impedance

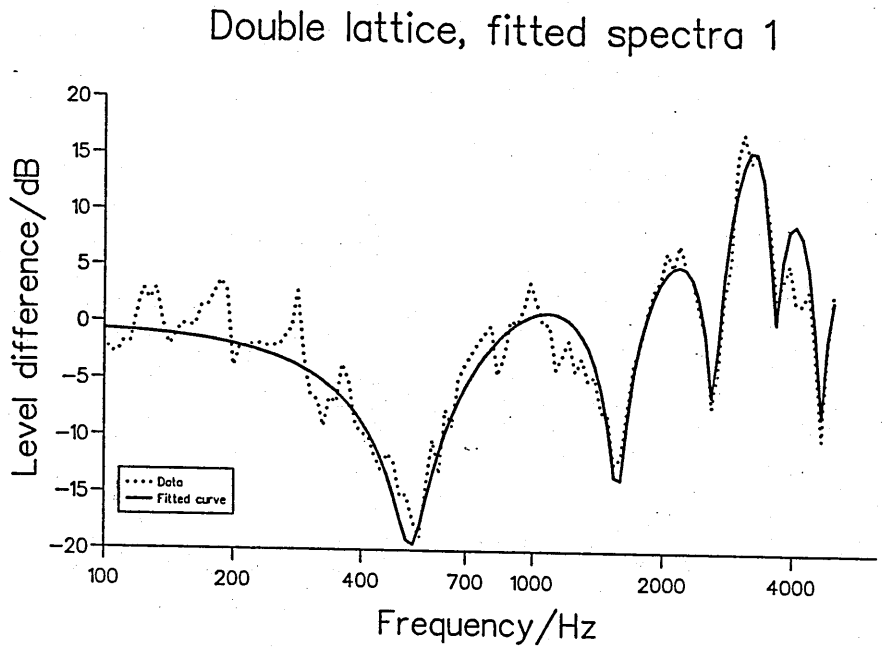


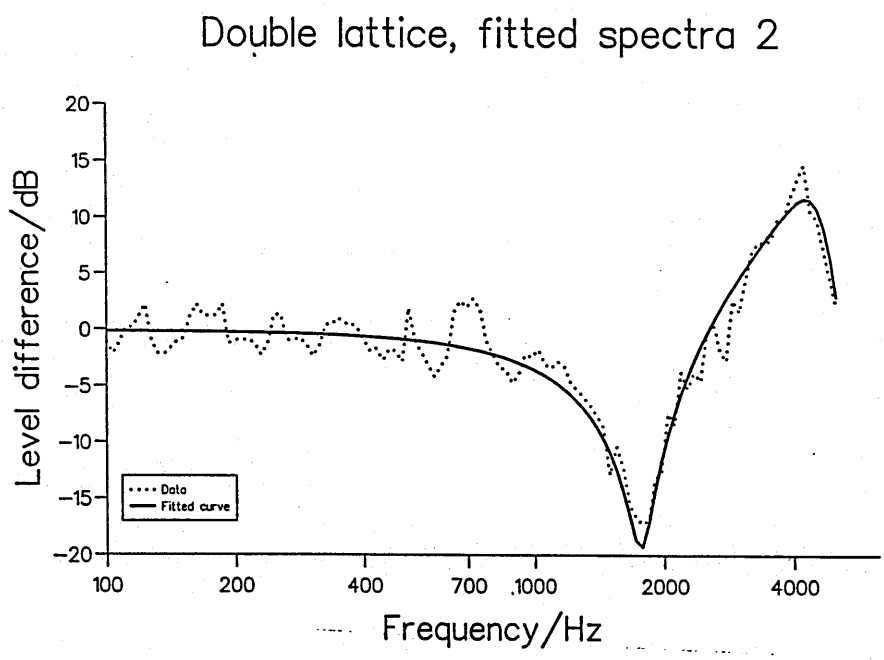


**Figure 5.6** Level difference spectra used for determination of double lattice impedance

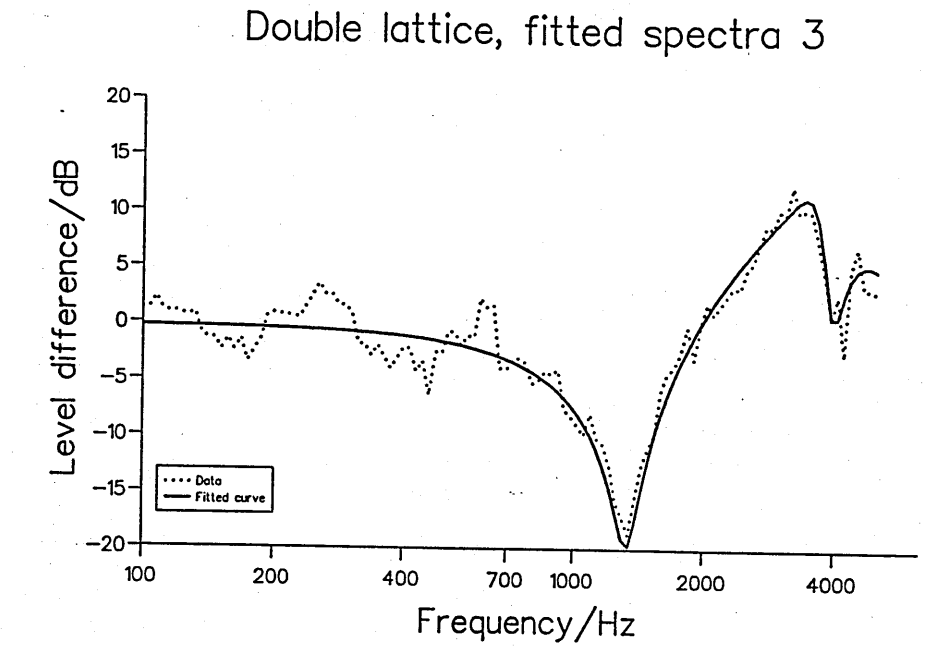


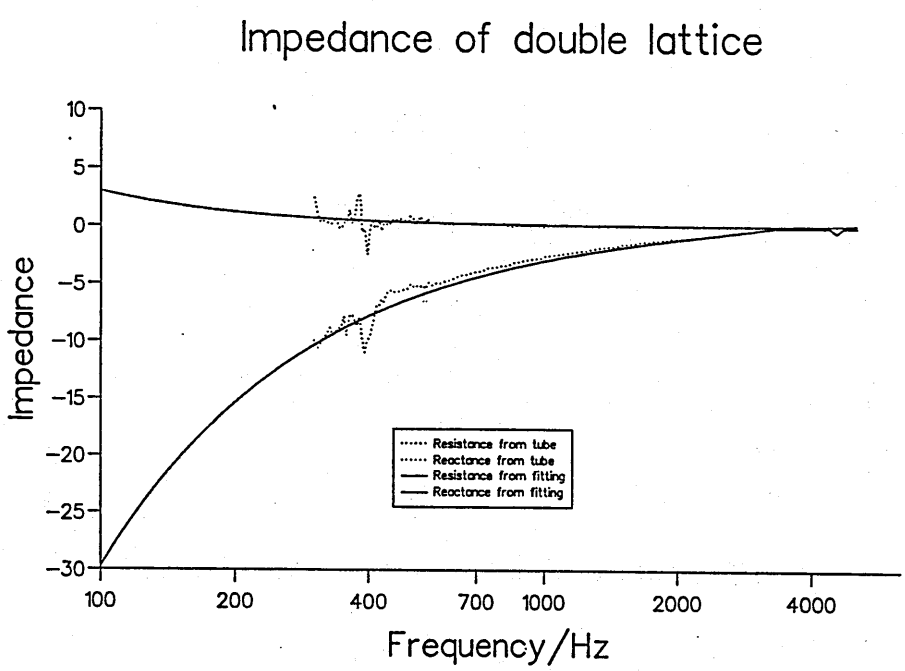


**Figure 5.7** Level difference spectra used for determination of double lattice impedance and resulting impedance

The experimental evidence for the existence of the surface waves presented here takes three forms

- Comparison of theoretical and measured values for white noise propagation from a point source above the lattice work
- Comparison of the theoretical and experimental values of vertical and horizontal attenuation
- Comparison of theoretical and practical values of phase speed

Raspet et al [186] showed that the theory presented by Attenborough et al [158] was in agreement with Donato's work [157]. That is either theory would predict the existence of the surface wave although only Donato derived an explicit term. Figure 5.8 compares the theoretical work of Attenborough and Donato with the measurements taken by Rasmussen [190] over a grass covered ground. The impedance of the ground is generated by using a flow resistivity of 425 MKS Rayls/m [190] with the theory modified by Chessel, [89] from Delany and Bazley [121]. It is seen that both theories predict the existence of a surface wave at frequencies up to 400Hz. During this study the propagation model derived by Attenborough et al is employed [158].

The excess attenuation due to sound propagation from a white noise source over a lattice was measured using a two stage process. Firstly the direct field at a number of source–receiver separations was measured in an anechoic chamber using equipment similar to that shown in figure 5.19. The source was then mounted over either the single or double lattice work which was fastened to a blockboard base. The spectrum at a number of geometries was recorded using a $\frac{1}{4}$ inch Bruel and Kjaer microphone see photographs in appendix L. The transfer function between the two sets of measurements for the same source receiver separation was evaluated to result in the excess attenuation spectra. The theoretical excess attenuation was evaluated using either the theoretical or measured values of impedance. The resulting spectra are shown in figures 5.9 and 5.10. for a double and single lattice work. The details of geometries SW1 to SW4 are given in table 5.1

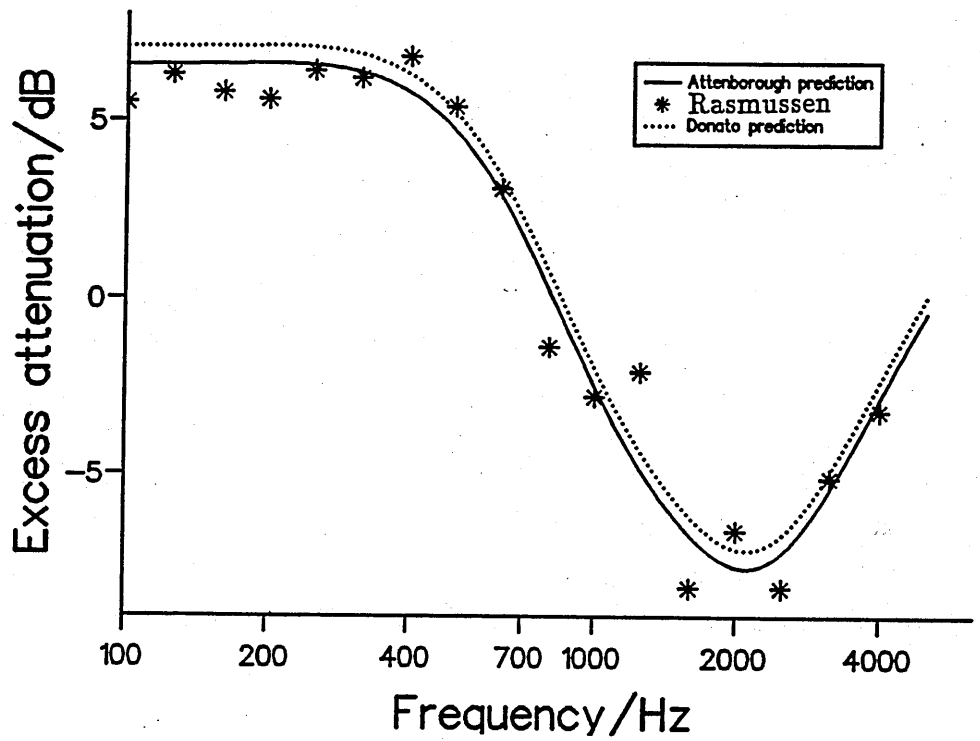


**Figure 5.8** Comparison of theory and Rasmussen data over grassland

| Geometry | Receiver height (m) | Source height (m) | Separation (m) |
|---|---|---|---|
| SW1 | 0.024 | 0.014 | 2.05 |
| SW2 | 0.024 | 0.014 | 1.00 |
| SW3 | 0.014 | 0.017 | 2.05 |
| SW4 | 0.014 | 0.017 | 1.00 |

**Table 5.1** Geometries for point source measurements

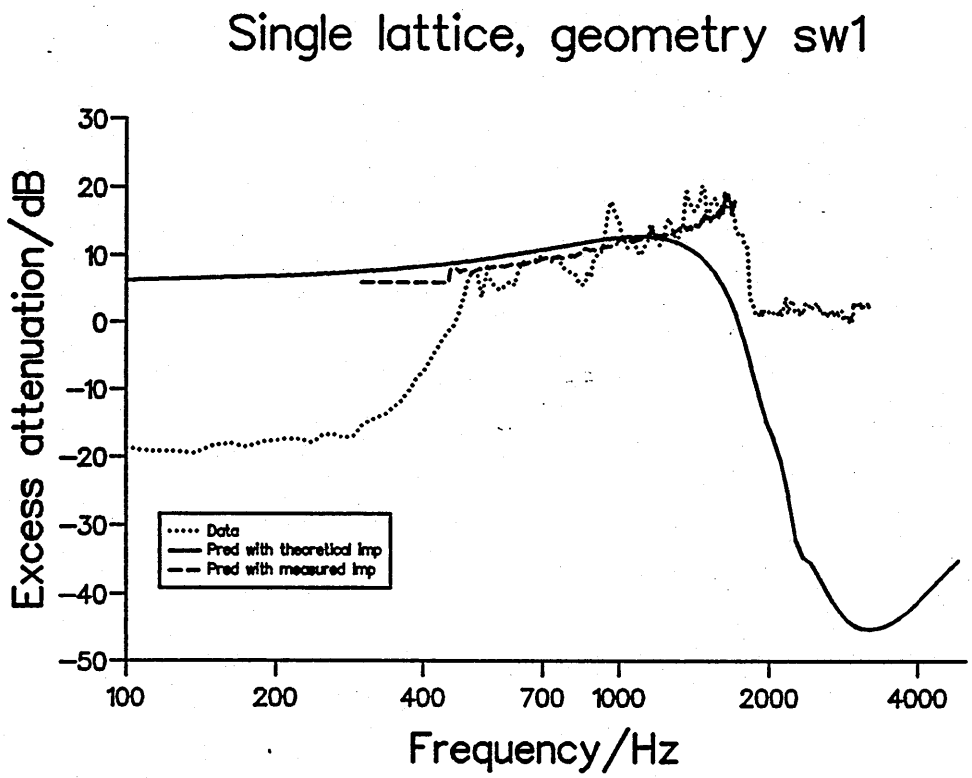


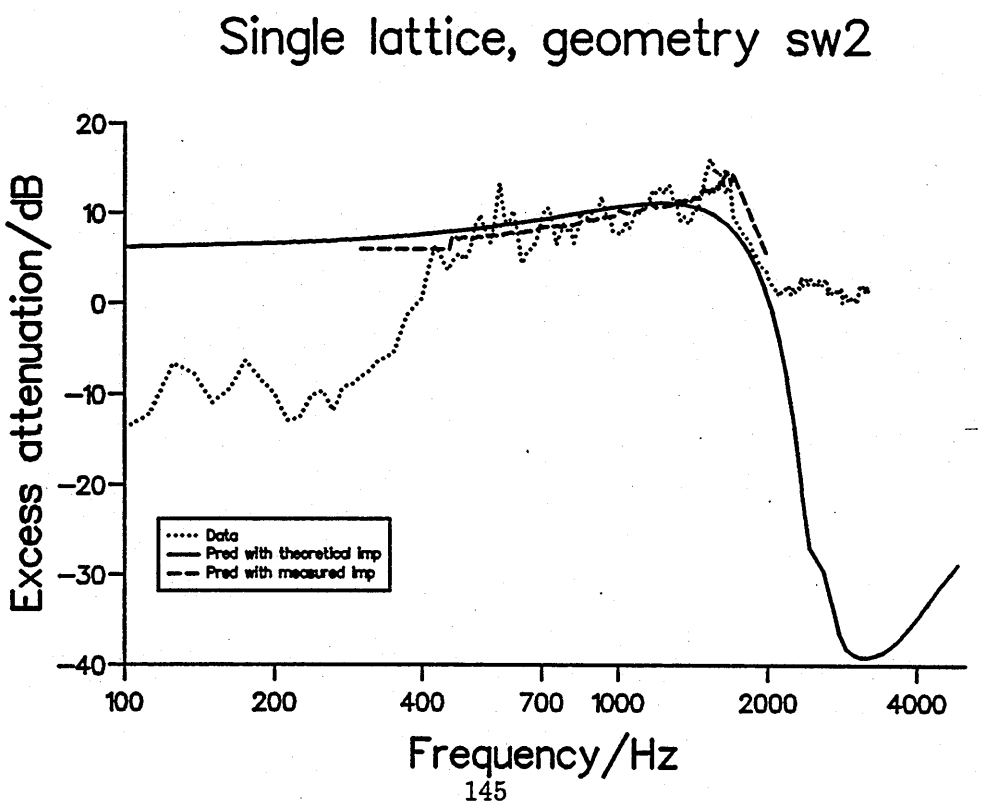




Figure 5.9 White noise propagation over single lattice

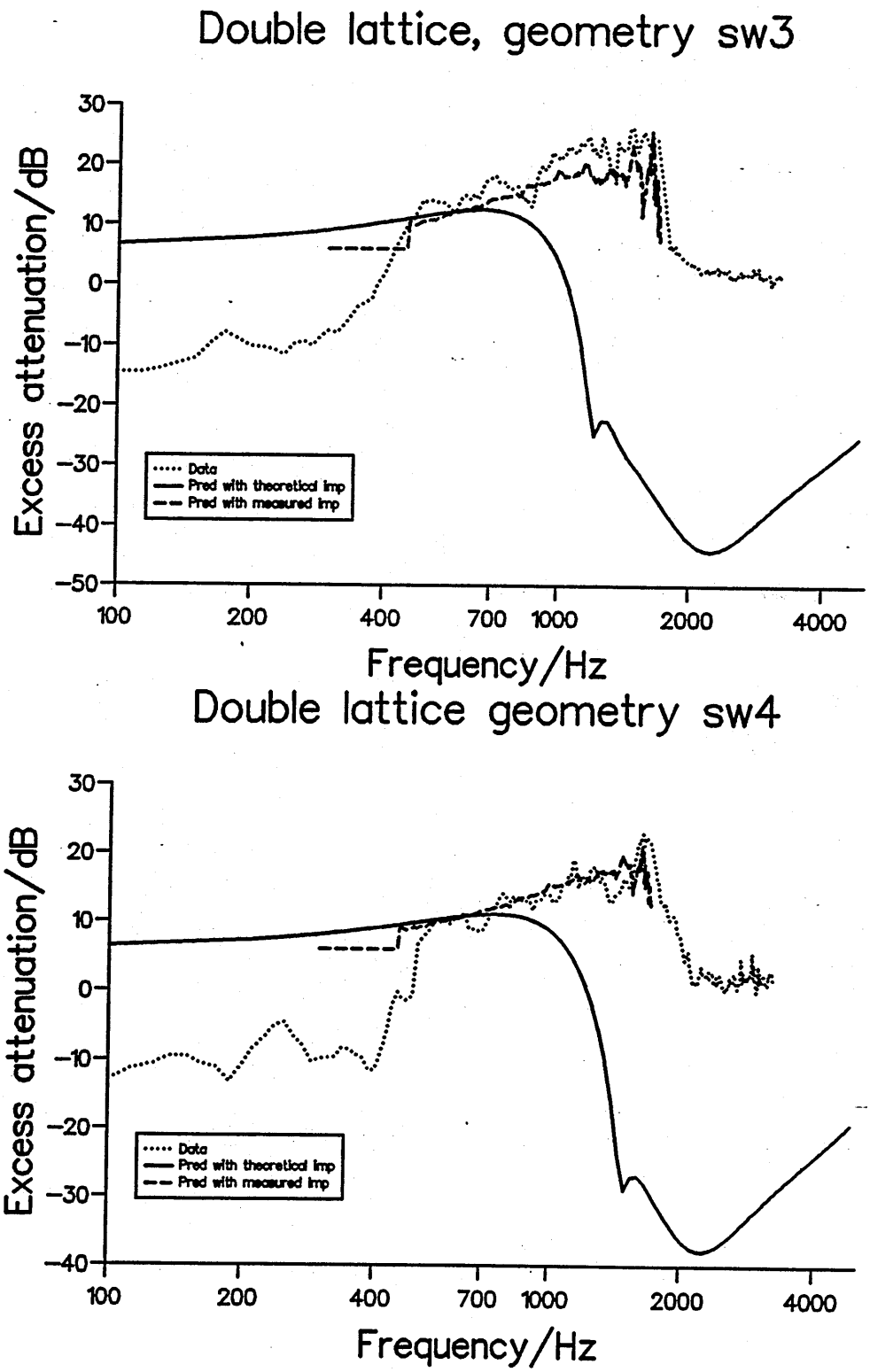


Figure 5.10 White noise propagation over double lattice

The source has little output below 400Hz and thus the data is unreliable below this frequency. However agreement between the theoretical predictions and experimental evidence is tolerable in the region 400Hz to 2KHz when the measured impedance is used. Essentially the measured impedance displays a greater reactance than that predicted by the simple equation 5.10 and the surface wave contribution to excess attenuation is very sensitive to the assumed values of reactance. As seen in figure 5.11 an increase in the reactance extends the frequency range over which the surface waves exist. Levels up to 14dB above free field are obtained between 1KHz and 2KHz. This indicates that the impedance tube has produced an accurate measurement of the acoustic impedance. The high frequency response is distorted by the presence of background noise and by unwanted reflections from the measuring equipment.

The second experiment involves measurement of the characteristic exponential decay both vertically and horizontally. Discrete microphone positions were used to asses the vertical and horizontal decay of the sound pressure level. The horizontal measurements were corrected by subtracting the effect of the cylindrical spreading. arising from the $\frac{1}{\sqrt{r}}$ factor in equation 5.20. An exponential curve is the fitted through the data points to evaluate the attenuation as seen in figure 5.12 for a single lattice at 1KHz. The measured attenuations may be compared to the values calculated using equations 5.7 and 5.13 for the vertical and horizontal attenuations respectively. The resulting data is presented in figure 5.13. The theoretical curves are produced using the impedance calculated from the modified pore depth. It is difficult to evaluate attenuations less than 3dB/cm. This along with the restrictions on high frequency measurements limits the amount of experimental data available.

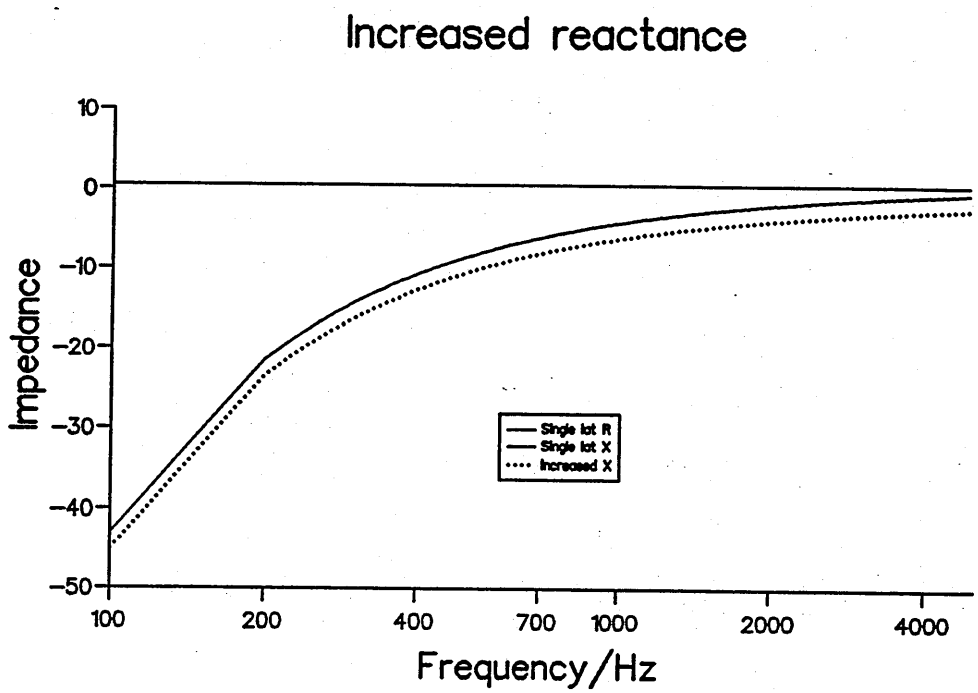


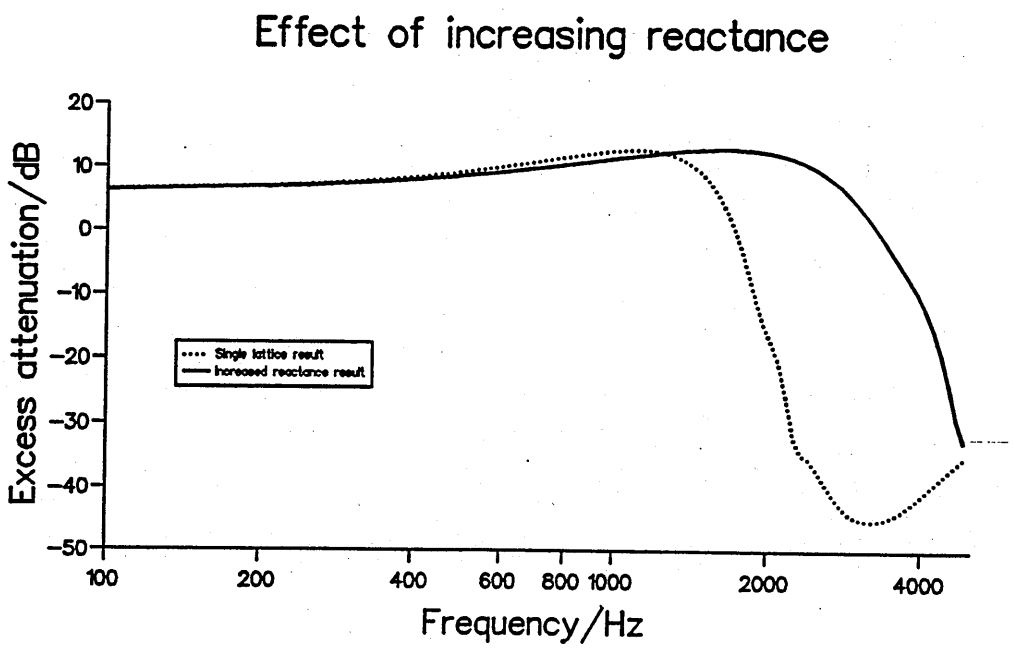


Figure 5.11 Effect of increasing reactance

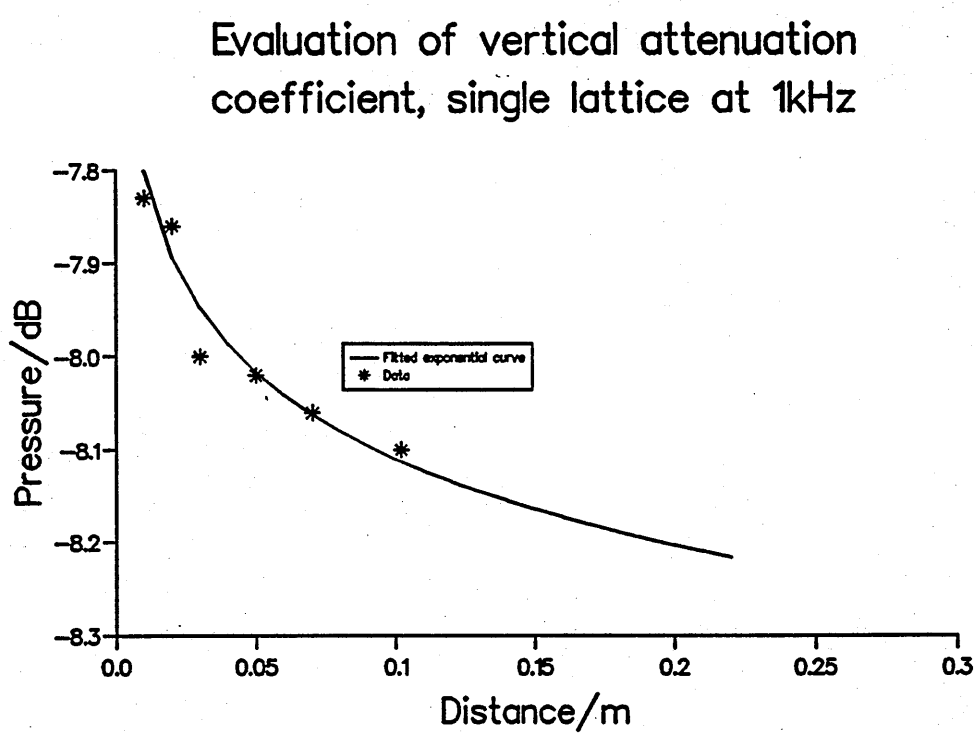


**Figure 5.12** Fitted exponential curve to derive attenuation

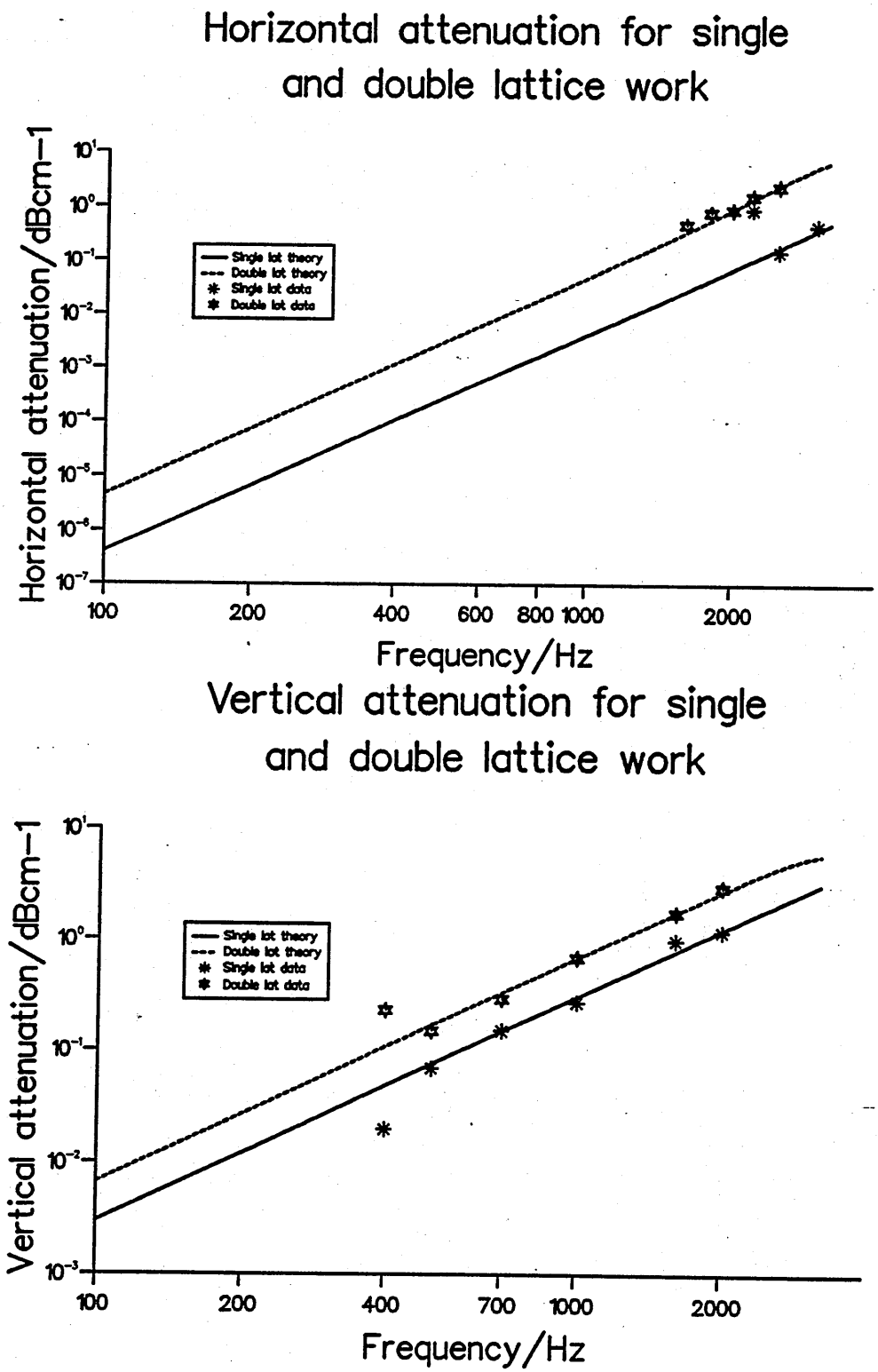


Figure 5.13 Vertical and horizontal attenuation measurements, upper line and data is for double lattice

The final experiment involves assessment of the reduced group velocity of the surface wave. The phase and group velocities given by equations 5.8 and 5.9 respectively are shown in figure 5.14. As is seen there is no discernable difference between the group and phase velocities. The reduced group velocity is measured using a technique suggested by Embleton and Daigle [185]. A 3KHz pulse was produced using the equipment shown in figure 5.19and in the photograph in appendix L. The F.F.T. is triggered to cover a twenty millisecond time window. Figures 5.15 to 5.17 show the pulses captured for a range of receiver heights and source-receiver separations. It can be seen that as the transducer separation increases the surface wave arrival becomes distinct (compare for example figure 5.15 (upper) with figure 5.15 (lower) and figure 5.16 (upper)). The surface wave magnitude decreasing rapidly with increasing receiver height due to the exponential attenuation (compare for example figure 5.16 (upper) with figures 5.17 (upper and lower)). The measured decay of the pulse with receiver height is shown in figure 5.18. The theoretical curve shown is plotted by evaluating the exponential decay coefficient in equation 5.7 the agreement is tolerably good. Table 5.2 shows the predicted and measured pulse separations. The theoretical group velocity and body wave velocity are $145ms^{-1}$ and $343ms^{-1}$ respectively. The measured and predicted pulse separations are in reasonable agreement despite the difficulties in obtaining accurate measurements. An asterisk indicates that the pulse separation cannot be determined due to the attenuation of the surface wave or the time difference between the two pulses is less than the pulse width. Again the impedance from the modified pore depth is used to calculate the theoretical values. It should be noted that this experiment may only be performed using the double lattice work, the velocities of the air (body) wave and surface wave above the single lattice are too similar to produce a detectable separation between the pulse arrivals.

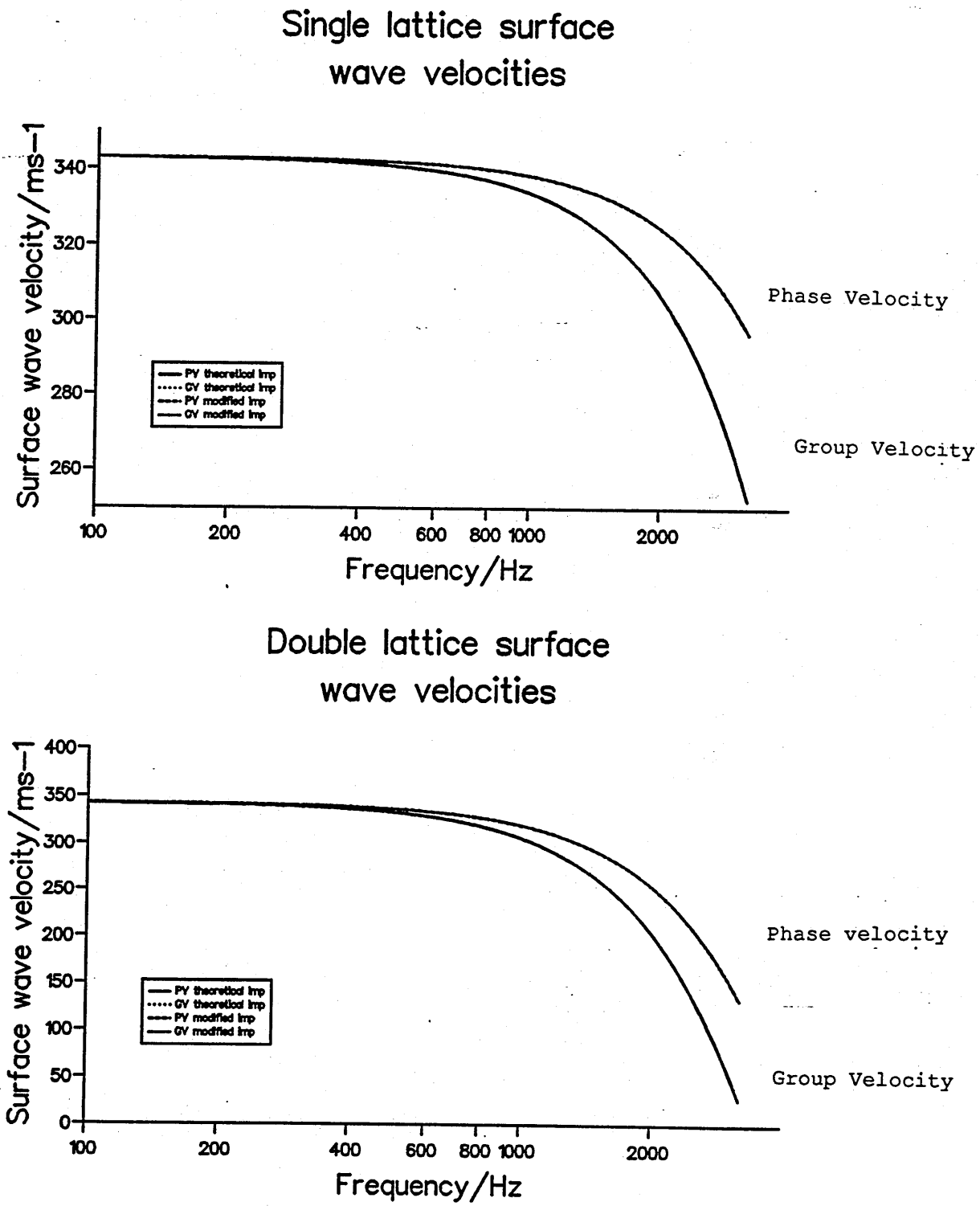


Figure 5.14 Reduced surface wave velocities

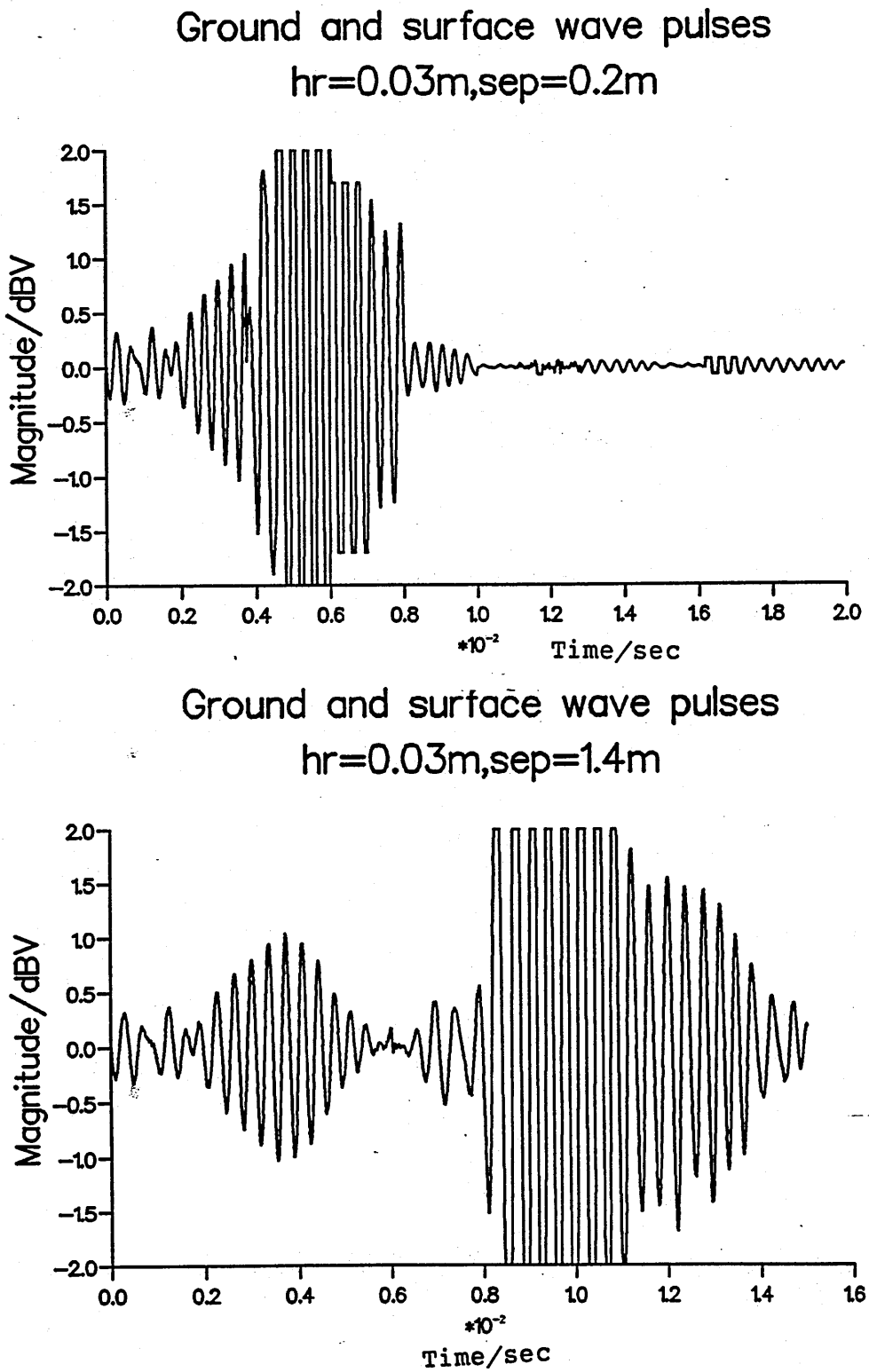


Figure 5.15 Pulse experiment results

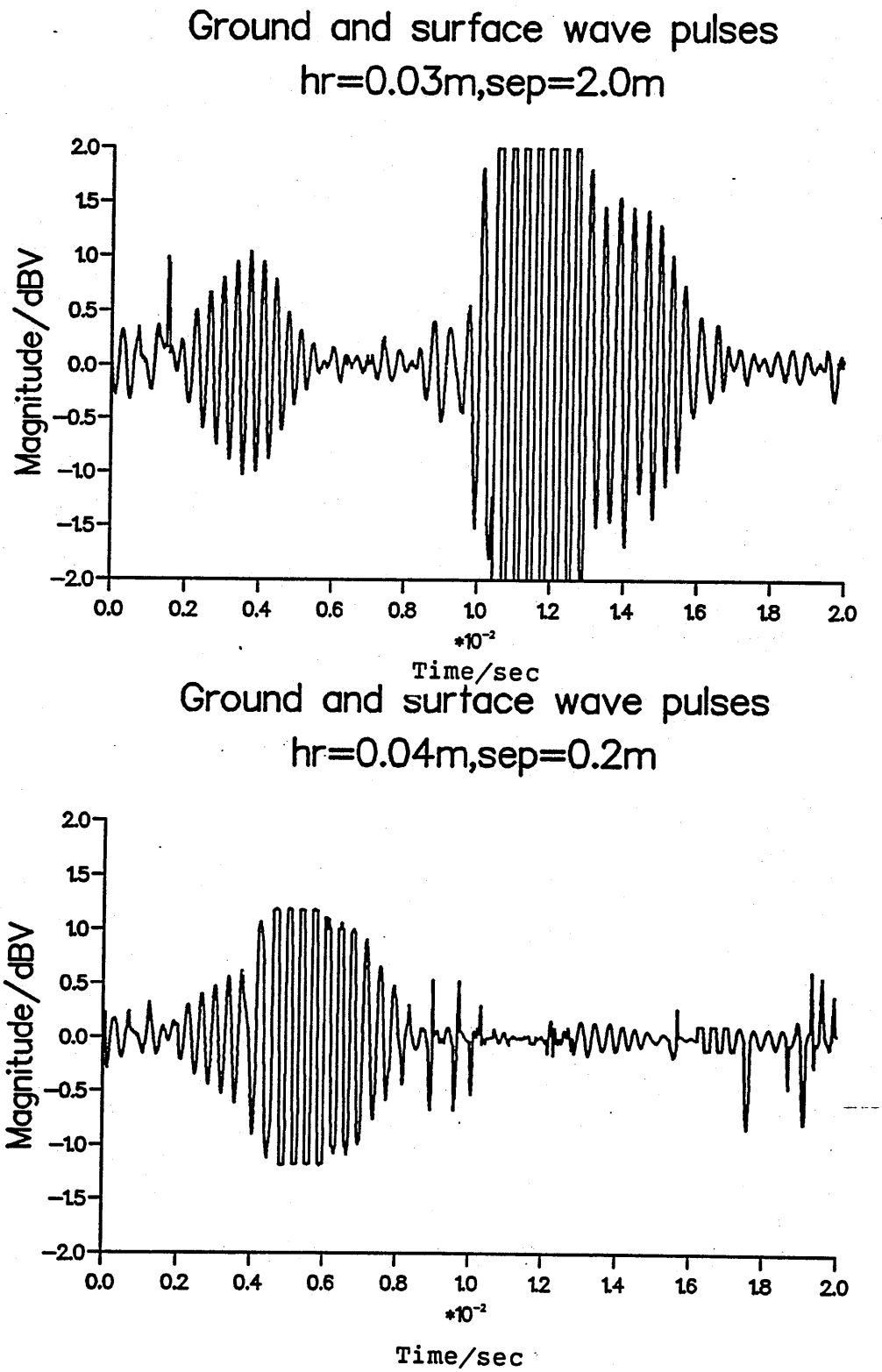


Figure 5.16 Pulse experiment results

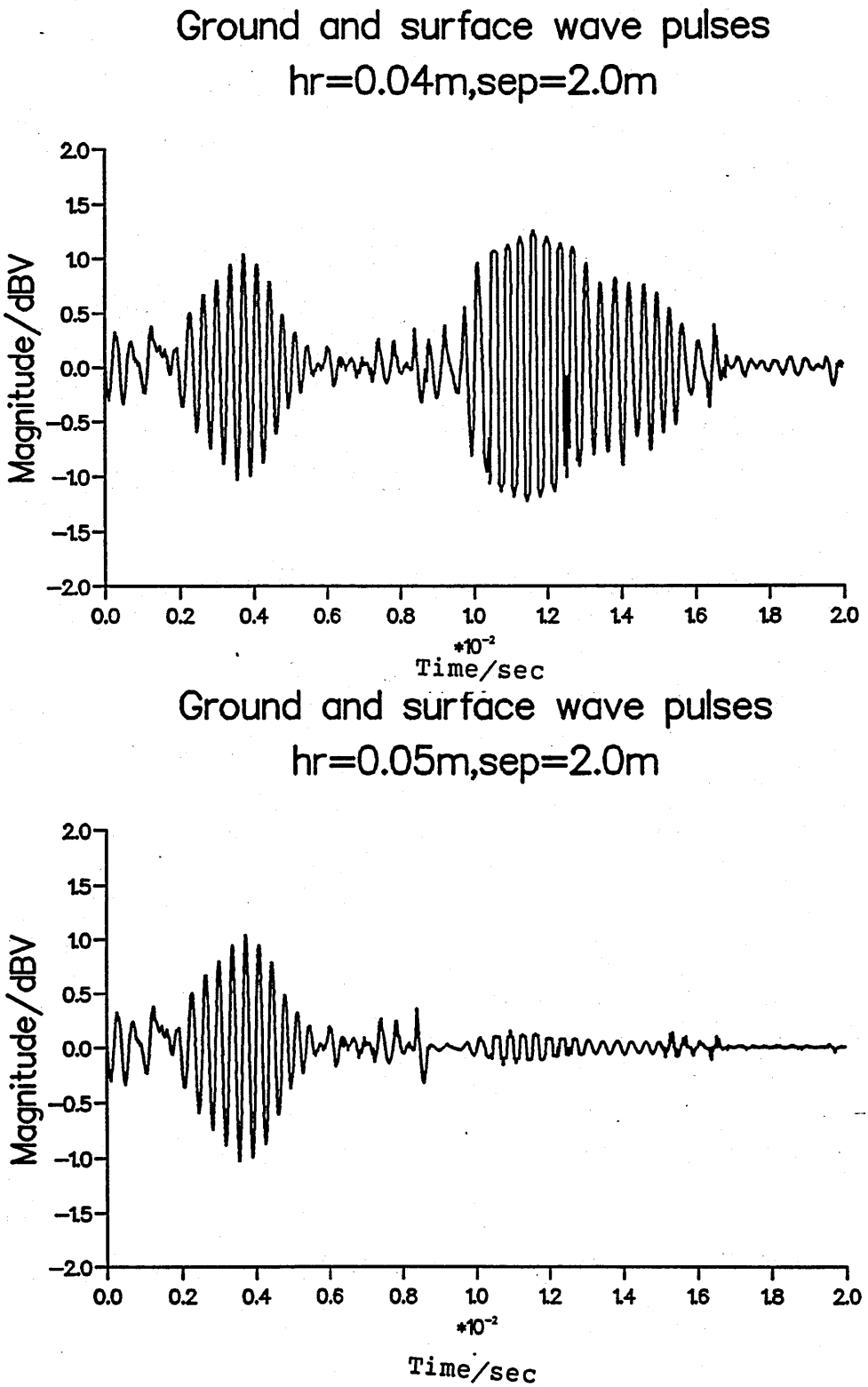


Figure 5.17 Pulse experiment results

| Separation between transducers (m) | Receiver height (m) | Theoretical pulse separation (ms) | Measured pulse separation (approx) (ms) |
|---|---|---|---|
| 2.0 | 0.03 | 7.9 | 6.7 |
| 2.0 | 0.04 | 7.9 | 6.6 |
| 2.0 | 0.05 | 7.9 | * |
| 1.4 | 0.03 | 5.5 | 6.0 |
| 0.2 | 0.03 | 0.08 | * |
| 0.2 | 0.04 | 0.08 | * |

**Table 5.2** Theoretical and measured pulse separations

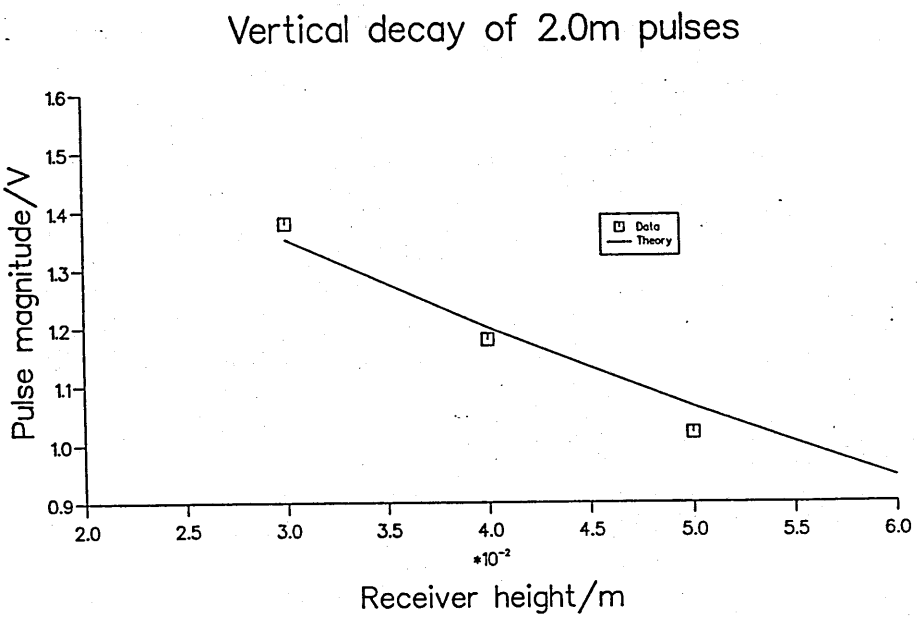


**Figure 5.18** Exponential decay of pulses above lattice for 2.0m separation

### 5.2.1 Surface waves over a porous road surface

The impedance values for a low flow resistivity road surface, ( see chapter 8 ) suggest the possibility that a surface wave may propagate over such a road. If this is the case it could contribute to the road traffic noise problem. The surface wave contribution was investigated for a typical low flow resistivity surface i.e.

- Flow resistivity=1500 Rayls/m
- Porosity=0.28
- Grain shape=1.17
- Pore shape=0.5
- Layer depth=0.05m or 0.10m

The theoretical excess attenuation was calculated for a source receiver separation of 7.0m, a receiver height of 1.2m and for two source heights. A

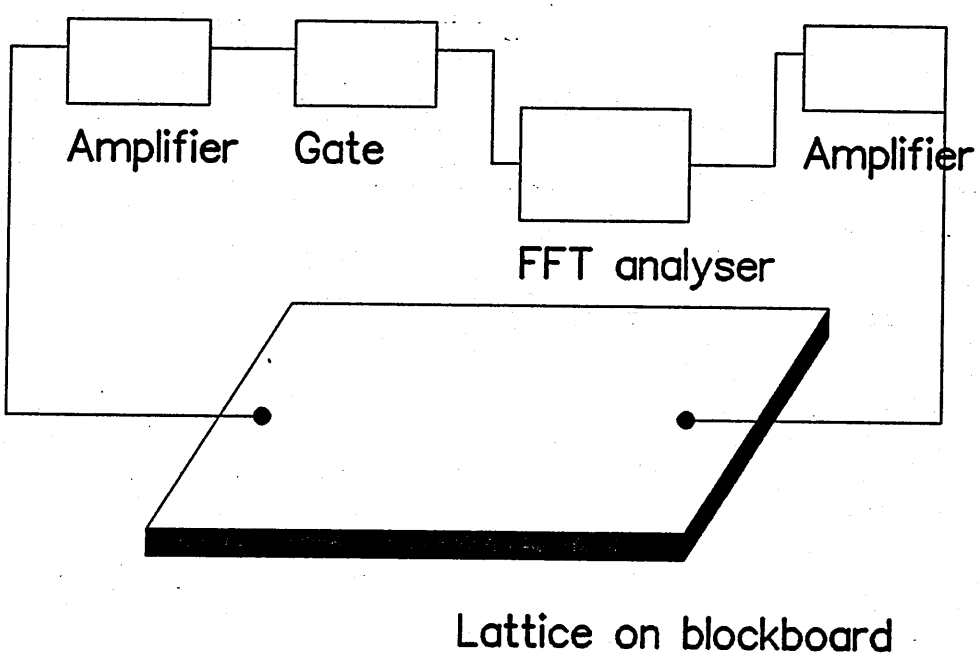


**Figure 5.19** Experimental equipment

hypothetical engine point source at a height of 1.0m and a road tyre source at a height of 0.01m. The results are shown in figures 5.20 and 5.21. Although there is some surface wave contribution for a low source height, indicated by an excess attenuation spectra greater than 6dB, the contribution to the total pressure field is not predicted to be significant.

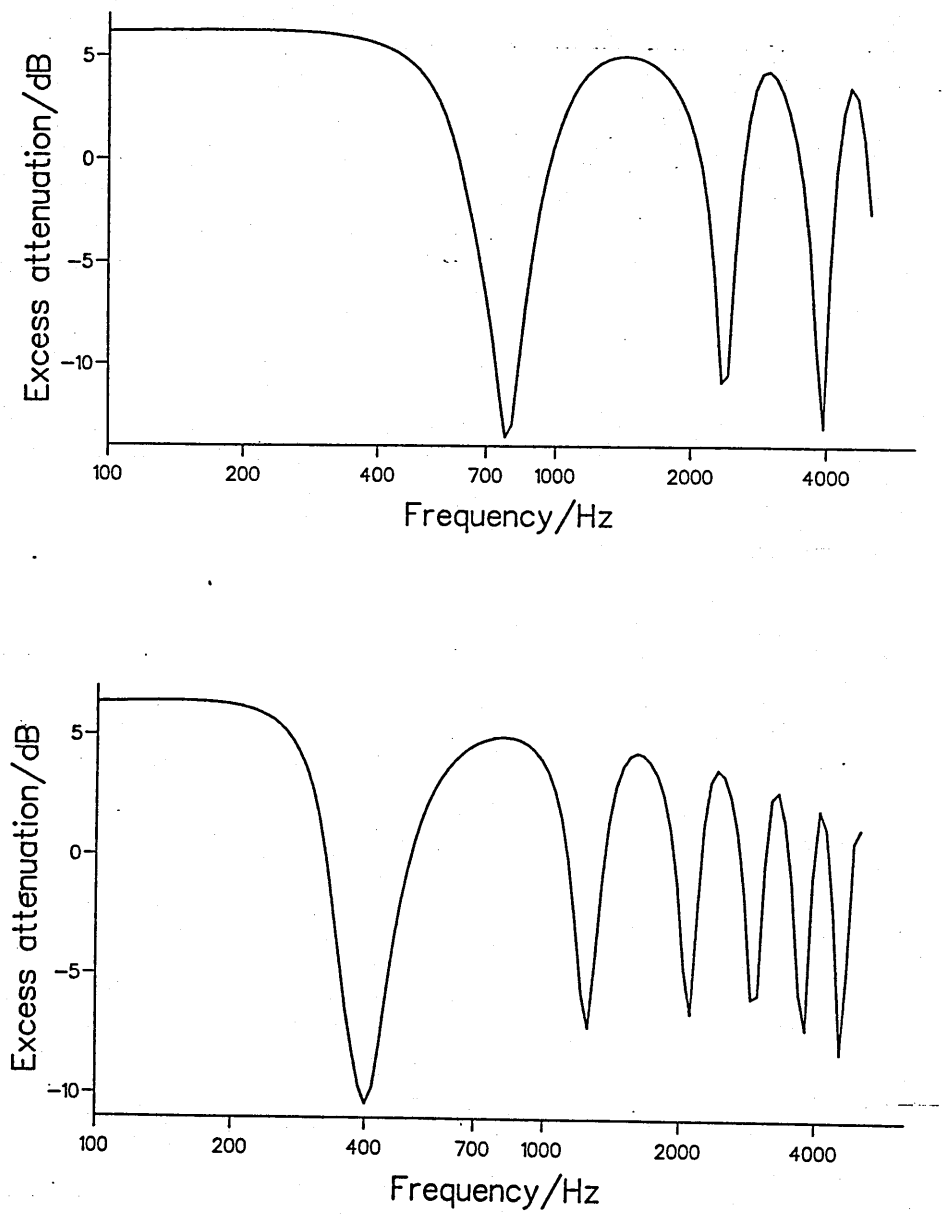


**Figure 5.20** Excess attenuation over porous road surface for engine source and 5cm (upper) or 10cm (lower) layer depths

## 5.3 Conclusions

The series of three experiments indicate that a surface wave is formed above a lattice work and that the phenomena can be explained using the theories of Attenborough and Donato. It appears that equation 5.10 does not produce an accurate impedance for a lattice work of this type mounted on a rigid backing. The anomalies may arise from the mounting of the lattice or the finite wall thickness. However use of an effective pore depth in equation 5.10 or use of the Arnott theory for the impedance of a medium composed of rectangular pores proves satisfactory. In general the results gained here are in good agreement with those shown by Donato and Embleton. There is some agreement between the results presented here and those of Embleton et al are seen by comparing lower pulse in figure 5.16 with the equivalent figure in Embleton et al's paper as seen in figure 5.22. The results presented here suggest that the pulse magnitude is decreased due to the reduction of the surface wave contribution. It is evident that the second experiment reported in this chapter may be much improved using a continuously monitored tracked receiver to increase the number of data points and by extending the frequency limits of the experimental measurements.

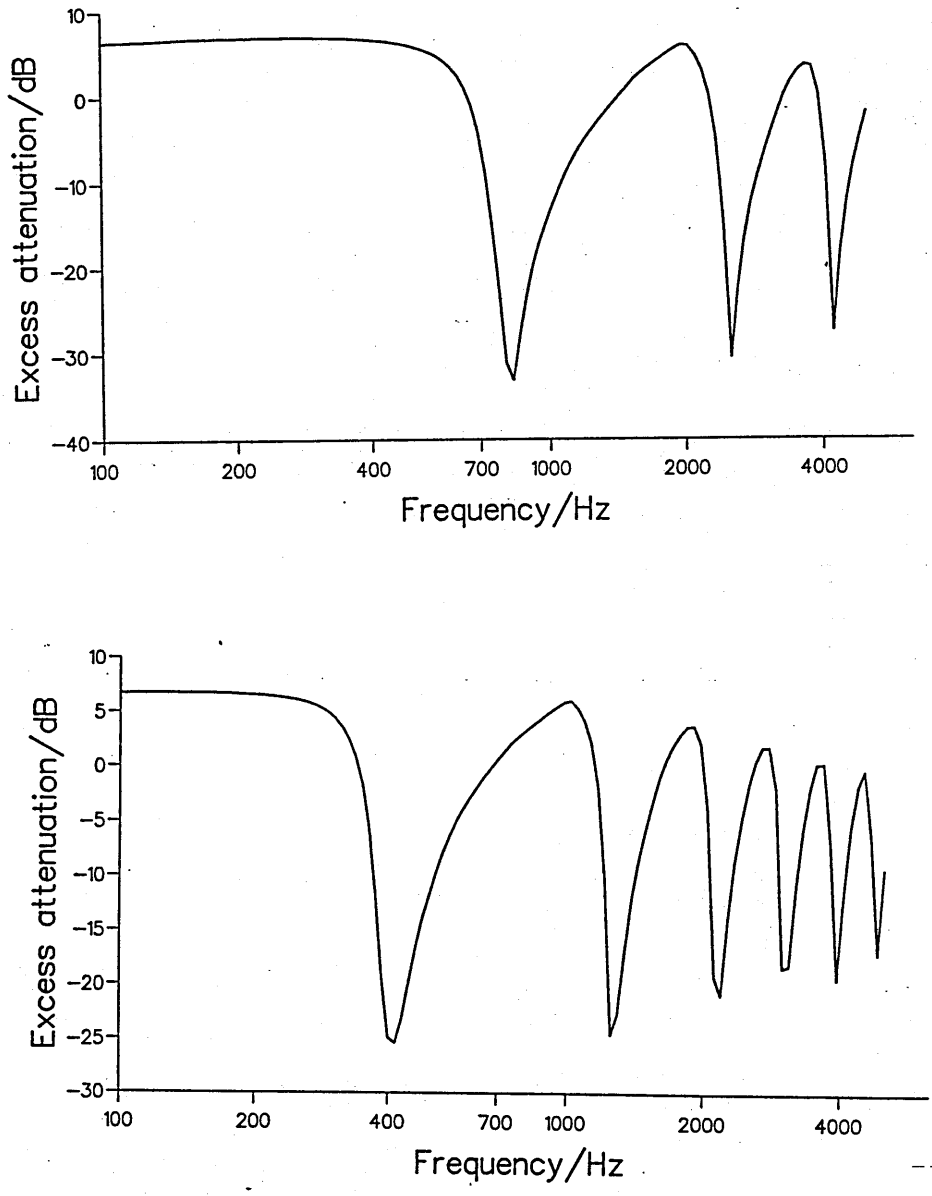


**Figure 5.21** Excess attenuation over porous road surface for road/tyre source and 5cm (upper) or 10cm (lower) layer depths

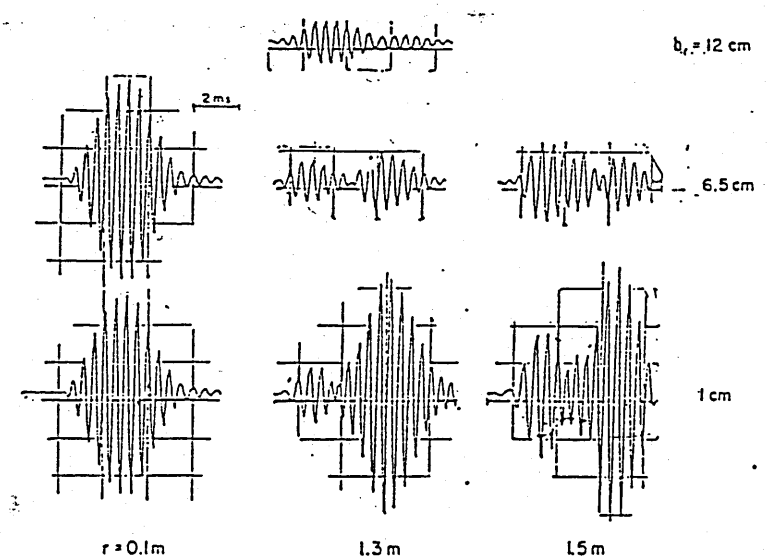


**Figure 5.22** Results of pulse propagation over lattice surface, after Embleton et al

# Chapter 6

# The indirect method of measuring impedance.

The indirect method of measuring the impedance of a surface was considered briefly in chapter 2. The indirect method may use either the components of the impedance directly ( henceforth called direct level difference fitting or the direct fitting technique ) or the parameters of an impedance model ( henceforth called parameter level difference fitting or the parameter fitting method ) as variables in order to minimize the difference between a measured and a predicted sound spectrum. The method may be applied to both locally and externally reacting surfaces and either to semi–infinite or rigidly backed media so in principle there are eight possible applications which are shown in figure 6.1.

Either method requires a sound propagation theory. It has been shown in chapter 4 that the modified Weyl van der Pol form of approximate solution is adequate for the geometries and surface impedances of interest. In the case of a parameter variation fitting an impedance model is required. An approximation of the Attenborough microstructural model has been used extensively by Hess, [82] and by Attenborough and Buser, [191] for soil and snow surfaces. In chapter 8 the microstructural model will be shown to be superior to the phenomenological model when used to model porous road surfaces.

In this chapter the sensitivity of the measurement technique is explored

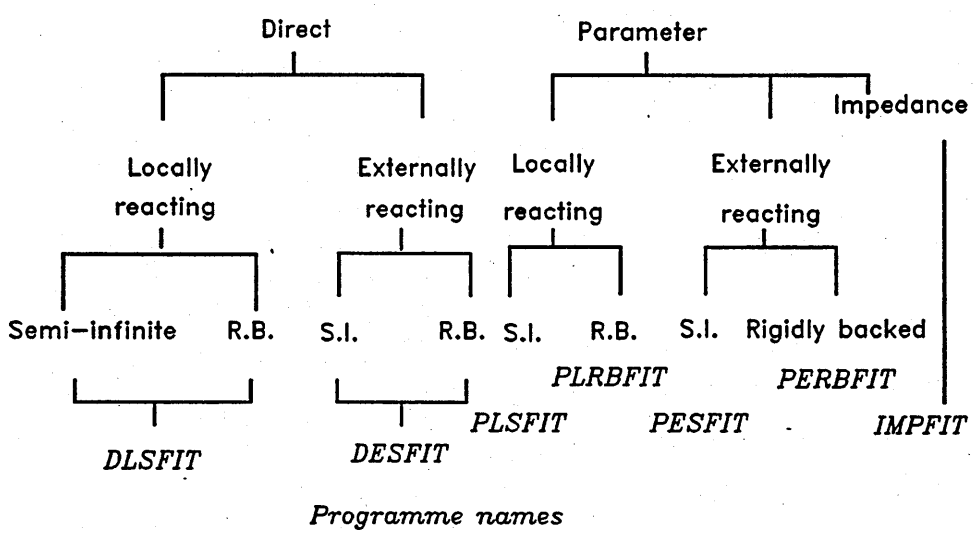


**Figure 6.1** Implementation of the indirect method for impedance measurement

and the choice of the function to be minimized is discussed. The effectiveness of the proposed method is evaluated by an error analysis method to support the analytical study of earlier researchers [72], [88] and [77]. This method involves simulation of the sound spectra which are presented as data to the minimization algorithm. Both systematic and random errors are generated and used to simulate the effects of measurement errors. The refined algorithm is applied to the acoustical characterization of various surfaces in chapter 7.

## 6.1 Formulation of the minimization algorithm.

Both the direct and parameter variation techniques exploit and fit the ground effect by using the spectrum of the difference in levels between vertically separated microphones.

### Level difference measurements.

The sound field above a surface is measured by a pair of vertically separated receivers at a short range from a point source. The lower microphone is positioned close to the surface, figure 6.2.

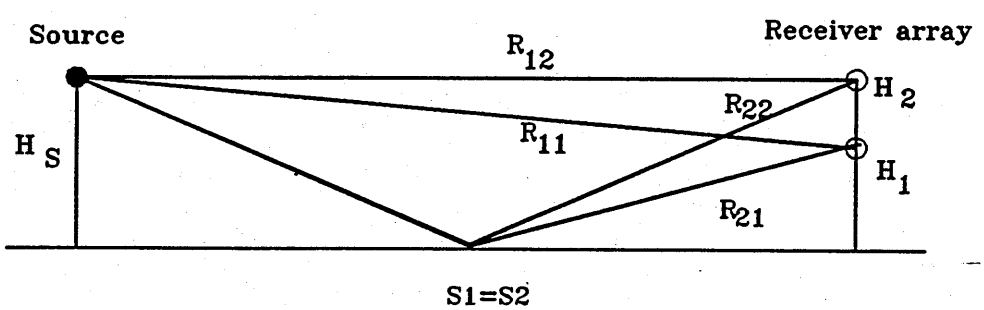


Figure 6.2 Level difference geometry

A white noise source is used and the level difference spectrum is found

| Geometry | Source height | Upper receiver height | Lower receiver height | Separation to receiver array |
|---|---|---|---|---|
| | (hs) | (h2) | (h1) | (s2=s1) |
| V1 | 0.5 | 0.5 | 0.05 | 1.5 |
| V2 | 0.3 | 0.3 | 0.05 | 1.5 |
| V3 | 0.2 | 0.2 | 0.05 | 1.0 |
| H1 | 0.5 | 0.5 | 0.5 | 1.5(0.1 closer) |

Table 6.1 Level difference geometries

from;

$$L.D. = 20.\log\left(\frac{p_2}{p_1}\right) \tag{6.1}$$

where $p_n$ is the modulus of the pressure at receiver position $n$. The lower microphone acts as a measure of the direct field if the source is conically symmetrical, i.e. the ray amplitude traced along the path $R_{11}$ is the same as that travelling along $R_{12}$, as described by Embleton [127]. Thus the level difference spectrum is independent of the frequency response and any variations in the power of the acoustic source. The contribution to the phase difference between the direct and reflected rays due to the path length difference for the lower receiver is small and hence the ground effect dip for this receiver is at a higher frequency than the upper limit of the range of interest. This means that the ground effect dips in the level difference spectra relate mainly due to the interference between the direct and reflected waves impinging on the upper receiver. The relationship between the level difference and the excess attenuation spectra for a level difference geometry of V1, table 6.1 is seen in figure 6.3, for a grassland surface with impedance S1B, see chapter 4. Excess attenuation is given by the total field at the upper receiver with respect to the direct contribution only. It should be noted that geometry H1 involves horizontal receiver separations, with receivers at 1m and 1.5m from the source and at the same height as the source.

The equipment shown in figure 6.4 is used to measure and collect the level difference spectra. The area of the sample examined by the technique has been examined in [192]. It has been shown that this area is an ellipse

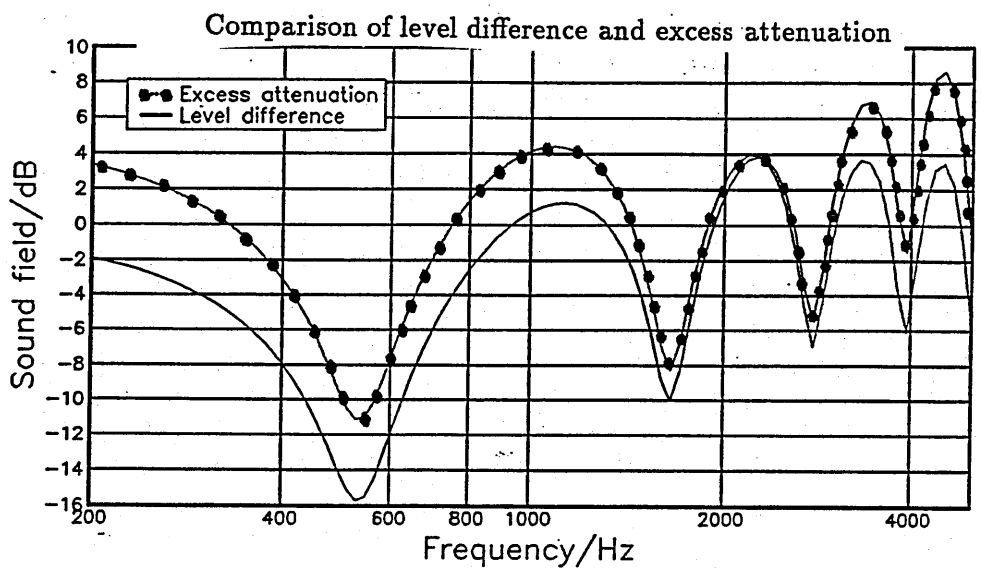


Figure 6.3 Comparison of level difference spectra and excess attenuation spectra (upper curve ) for impedance S1B (see chapter 4 ) and geometry V1 table 6.1.

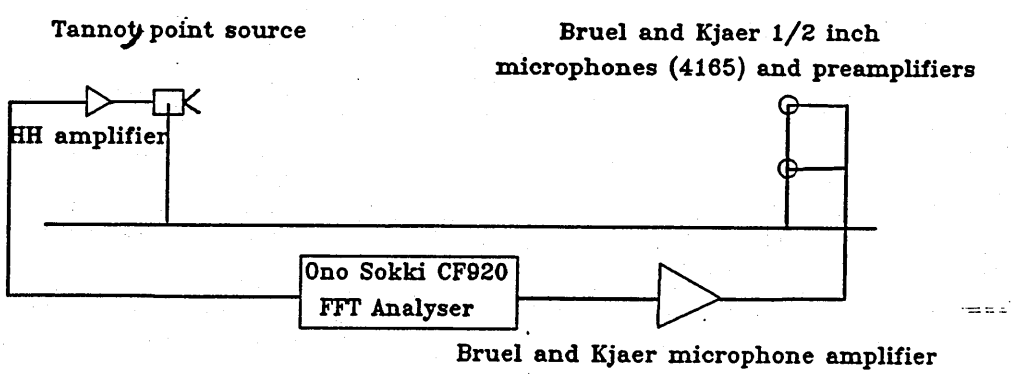


Figure 6.4 Level difference data collection

whose axes are dependent on the source receiver separation and the height of the source and upper receiver. If the source and upper receiver are at the same height the centre of the ellipse is located midway between the source and receiver array. The method used in reference [192] for measuring the sampling area of the level difference technique by gradually decreasing the area of an absorbing surface with acoustically hard material may be criticized for introducing edge effects. Indeed it is important to consider impedance discontinuities when performing the measurements. However it is expected the experiments described in [192] will have given a tolerable indication of the sampled area.

The lower microphone should be placed high enough to avoid the micro-climatic conditions i.e steep temperature gradients described by Huisman [193] and be raised clear of any vegetation while still acting as a measurement of the direct field. The separation between the source and receiver is less than three meters to reduce the effect of meteorological conditions as indicated by Tooms [177]. Figure 6.8 shows the effect of a severe temperature gradient on level difference measurements made with upper microphone and source heights of 0.5m, a lower microphone height of 0.05m and separations of either 1.5m or 50m. The effect of turbulence, [194] [195],[196],[197] on the level difference spectra and excess attenuation over a typical low flow resistivity road surface (5000 Rayls/m) is shown in figures 6.5 to 6.7. Table 6.2 shows the parameters used to calculate the turbulent conditions whilst table 6.3 shown the geometries considered. Makarewicz [198] gives for strong wind conditions $N12 \approx 15 \times 10^{-6}$ to $15 \times 25^{-6}$ and $L0 \approx 1$ to 12. The A–weighted spectral density of the mean square pressure is given by equation 6.2. This is modified by inclusion of an additional term, see equation 6.3 where the turbulence effects are contained in the term $T(f)$. The path length difference between the direct and reflected waves is given by $\delta r$, $r$ the reflected wave path length and $\alpha(f)$ is the coefficient of air absorption.

$$P_A^2(f) = \frac{P_A(f)\rho_0 c_0}{4\pi r^2}\left[1 + \left(Q_1^2 + Q_2^2\right) + 2\left[Q_1 \cos\left(\frac{2\pi f \delta r}{c_0}\right) + Q_2 \sin\left(\frac{2\pi f \delta}{c_0}\right)\right]\right] \tag{6.2}$$

$$p_A^2(f) = \frac{P_A(f)\rho_0 c_0}{4\pi r^2} e^{-2\alpha(f)r} \left[1 + \left(Q_1^2 + Q_2^2\right) + 2T(f)\left[Q_1 \cos\left(\frac{2\pi f \delta r}{c_0}\right) + Q_2 \sin\left(\frac{2\pi f \delta r}{c_0}\right)\right]\right] \quad (6.3)$$

Unless there is a considerable turbulent flow the spectrum is unchanged. The effect of turbulence at the receivers is to decrease the depth of the primary ground effect dip.

| Condition | N12 | L0 |
|---|---|---|
| No turbulence | 0 | 1 |
| Light turbulence | $5\times10^{-7}$ | 1 |
| Heavy turbulence | $1\times10^{-6}$ | 4 |

**Table 6.2** Turbulence conditions.

| Geometry | Source ht. | Upper rec. ht. | Lower rec. ht. | Separation |
|---|---|---|---|---|
| 1 | 0.5 | 0.5 | 0.05 | 1.5 |
| 2a | 0.1 | 1.2 | NA | 7.5 |
| 2b | 0.85 | 1.2 | NA | 7.5 |
| 3a | 0.1 | 1.2 | NA | 50.0 |
| 3b | 0.85 | 1.2 | NA | 50.0 |

**Table 6.3** Geometries used to study effect of turbulence of sound propagation. NA means not applicable

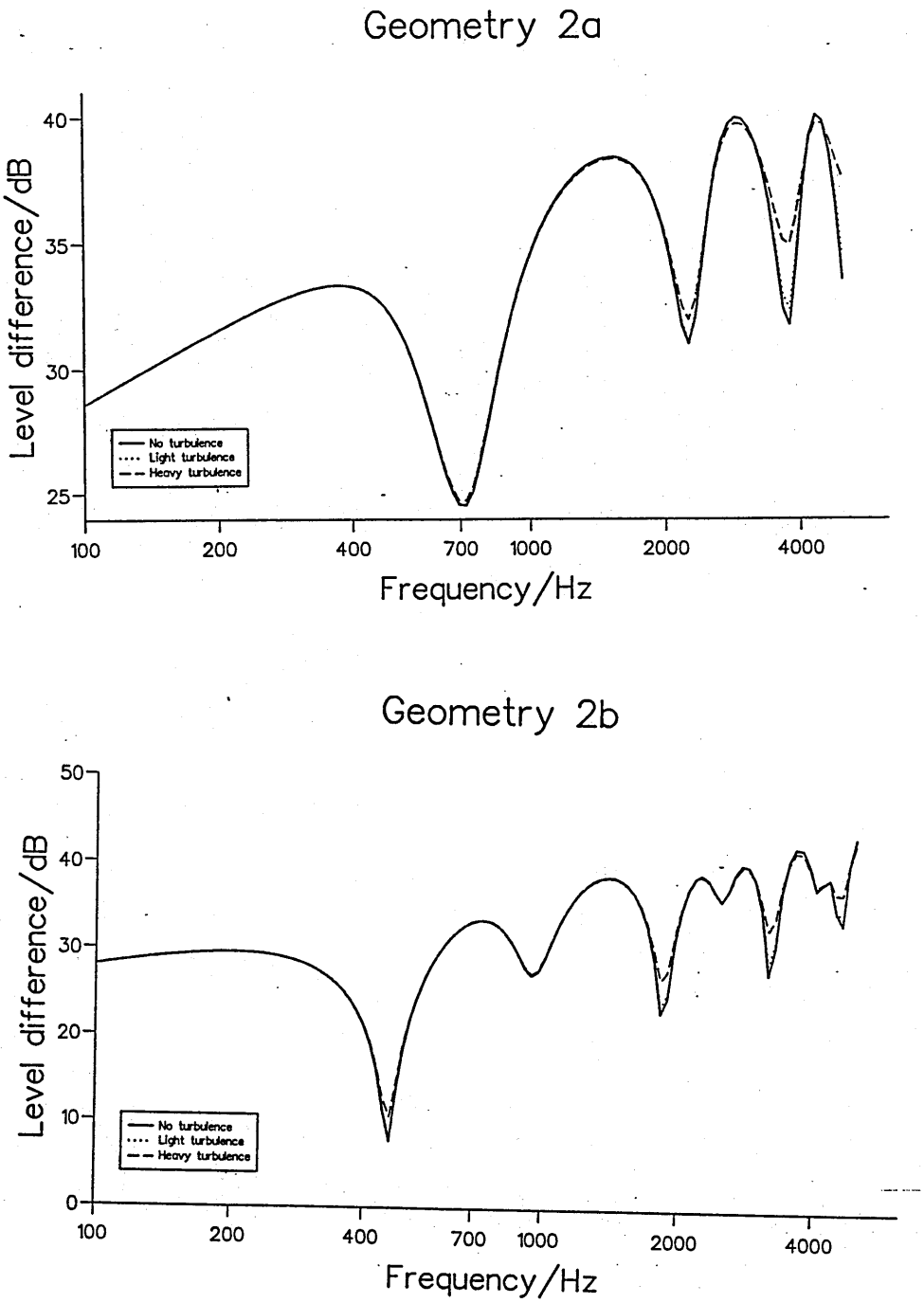


**Figure 6.5** Effect of turbulence on short range propagation from a light vehicle road/tyre or engine source

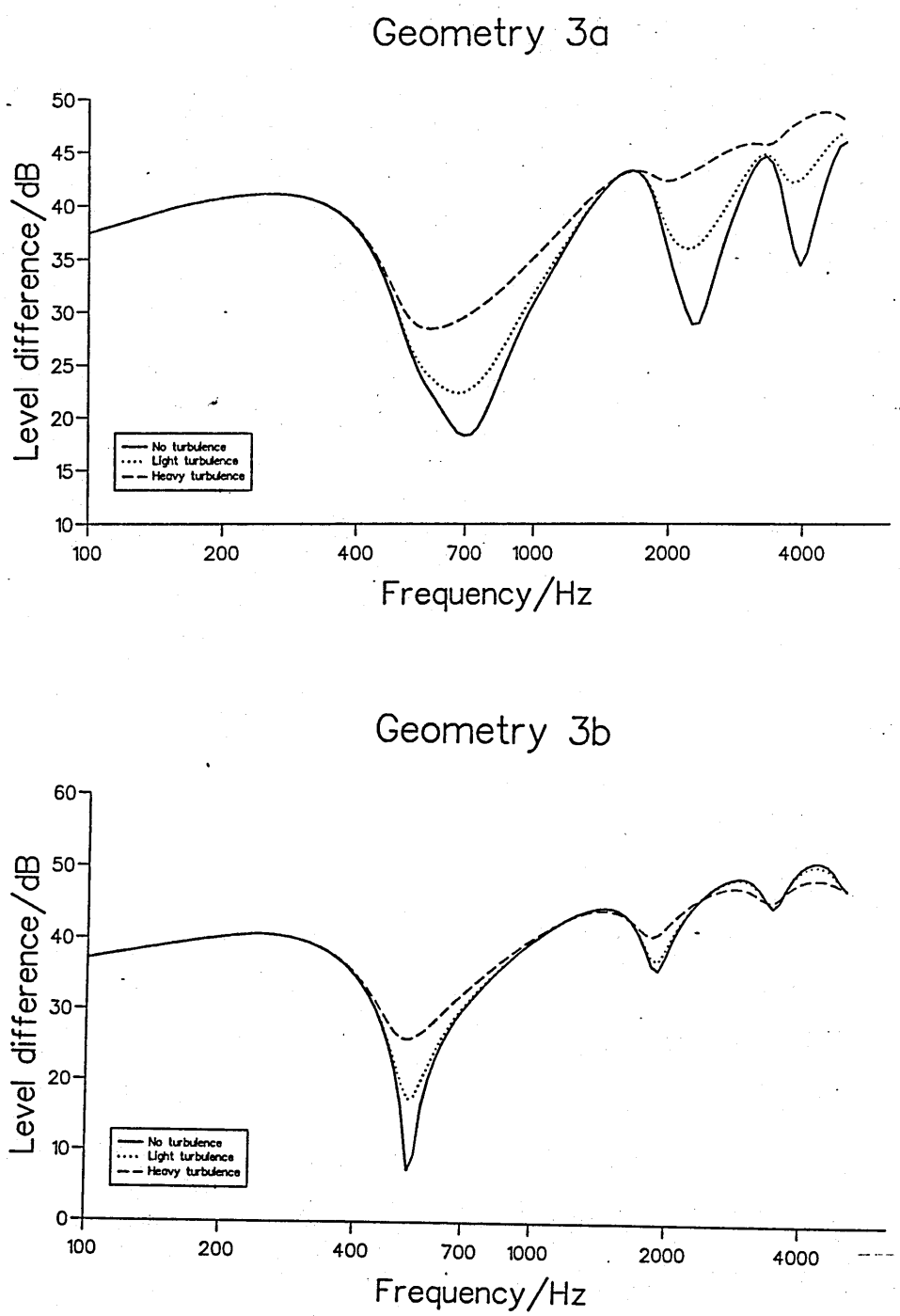


**Figure 6.6** Effect of turbulence on long range propagation from a light vehicle road/tyre or engine source

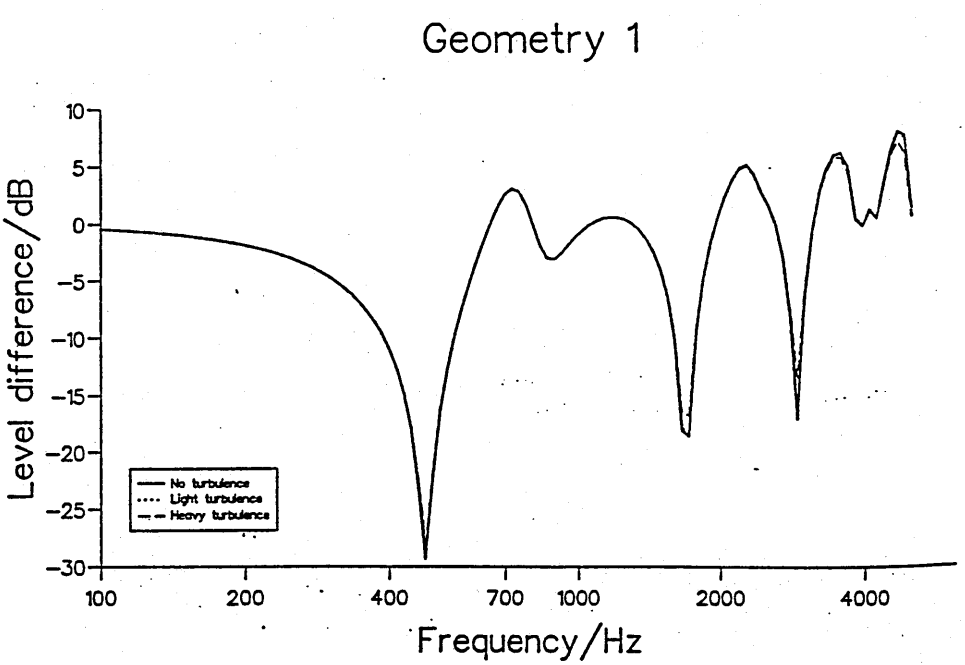


**Figure 6.7** Effect of turbulence on short range level difference measurements

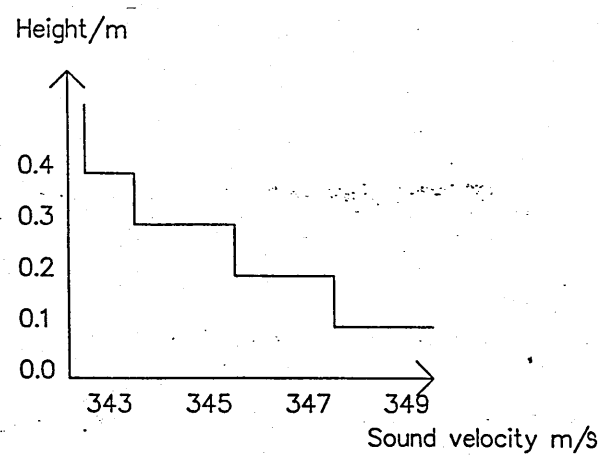


*Effect of a temperature gradient near the ground. Range=1.5 m*

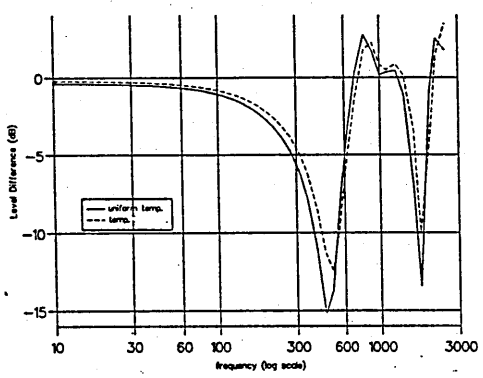


*Effect of temperature gradient near the ground. range= 50 m*

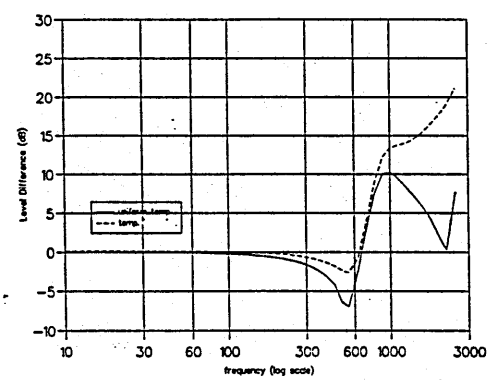


**Figure 6.8** Effect of temperature gradient on level difference.

### 6.1.1 Level difference sensitivity.

The accuracy of the direct (impedance) fitting version of the indirect method is dependent on the sensitivity of the level difference spectrum to impedance variations. Figures 6.10 and 6.11 show the changes in the spectra V1 to V3 and H1, table 6.1, when the magnitude of impedance S1B is increased over the whole frequency range, both real and imaginary parts being increased in identical manners as a result of changing the flow resistivity shown in figure 6.9, see also equation 3.94. Note all flow resistivities in figures are in Rayls/m. It may be seen that the ground effect dips are most sensitive to the impedance changes. For the geometry V1 an increase in the magnitude of the impedance of 5 (35%) is required to give a 2dB change in the level difference spectrum. The sensitivity of the system improves as the geometry is changed to shift the primary ground effect dip to higher frequencies. Similarly an impedance increase of 2 (10%) gives a 2dB change in the level difference spectrum dip for V2. Alternatives to measurement and fitting of the level difference between vertically separated microphones include van der Heijden's sloping microphone array [85] in which the interface pattern along the specular reflection path is measured, and measurement of the level difference between horizontally separated microphones. With regard to the latter technique figure 6.11 shows the sensitivity of the level difference spectra H1 to the changes in impedance in the surface S1B. It is seen that substantial changes in impedance have little effect on the spectra. A minor improvement in sensitivity may be made by placing the horizontal array close to the surface but at these grazing angles the primary ground effect dip is at high frequencies where the sensitivity obtained from the vertical level difference geometry is satisfactory.

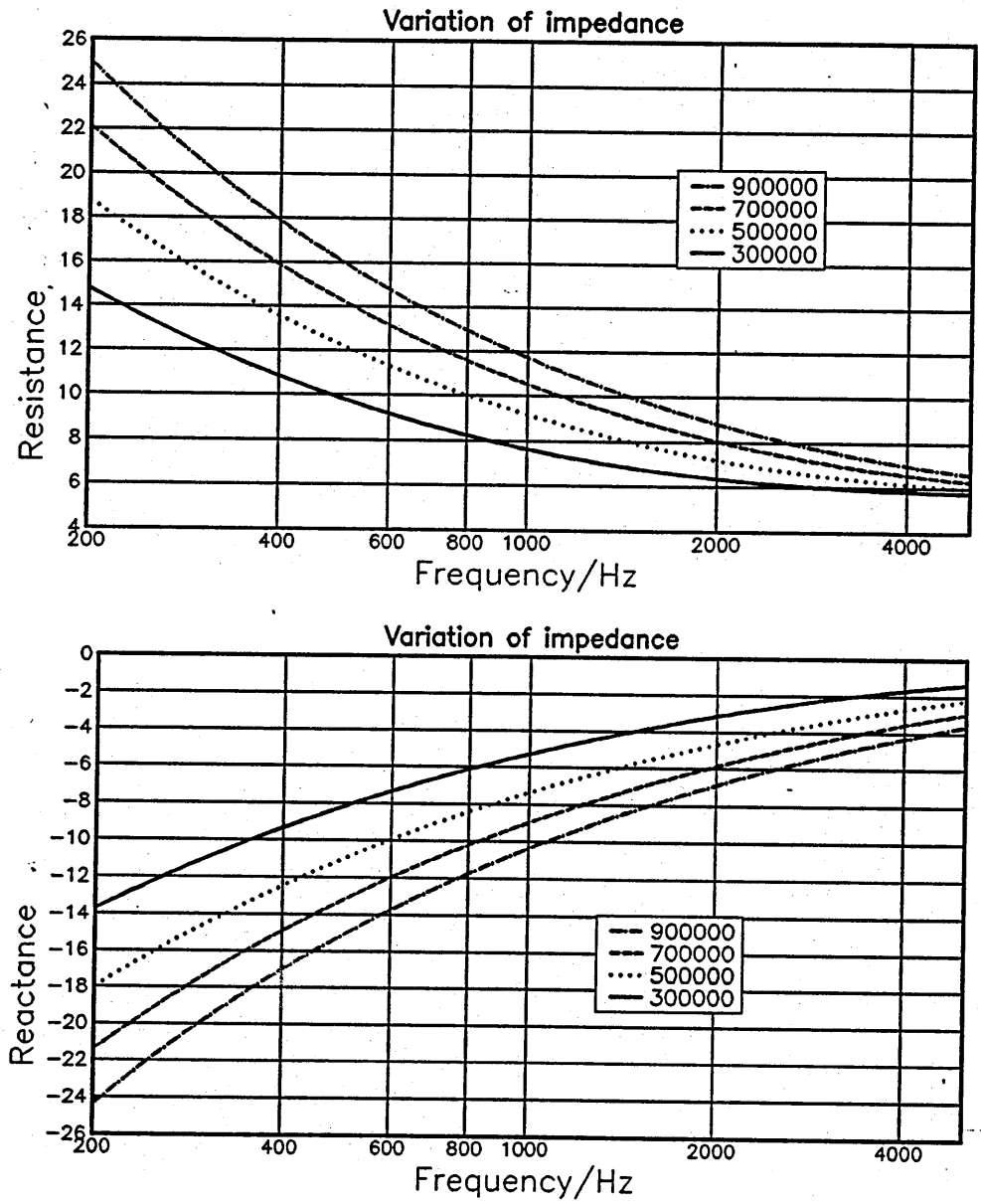


**Figure 6.9** Impedance variation in S1B

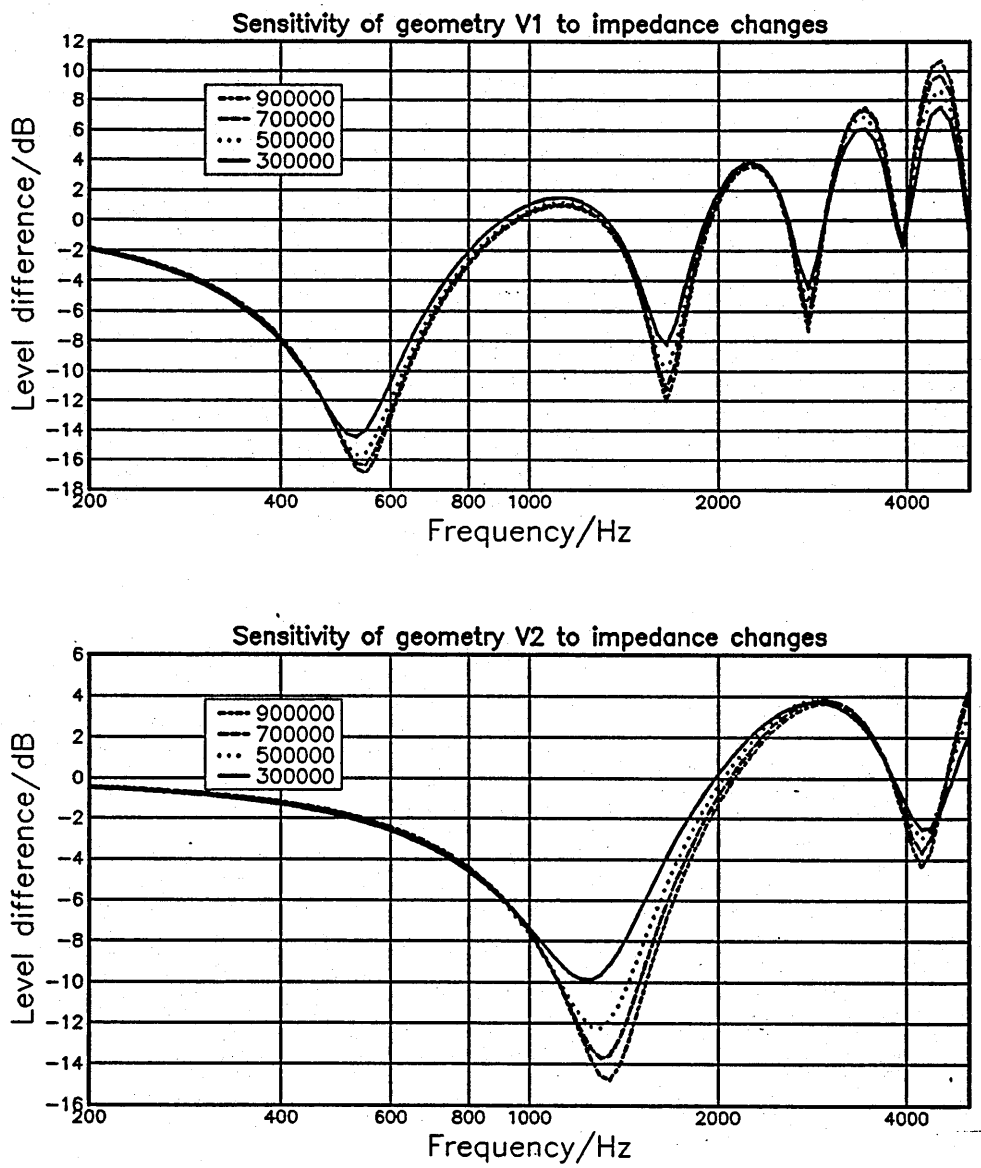


**Figure 6.10** Sensitivity of the level difference spectra for geometry V1 and V2 to increasing impedance

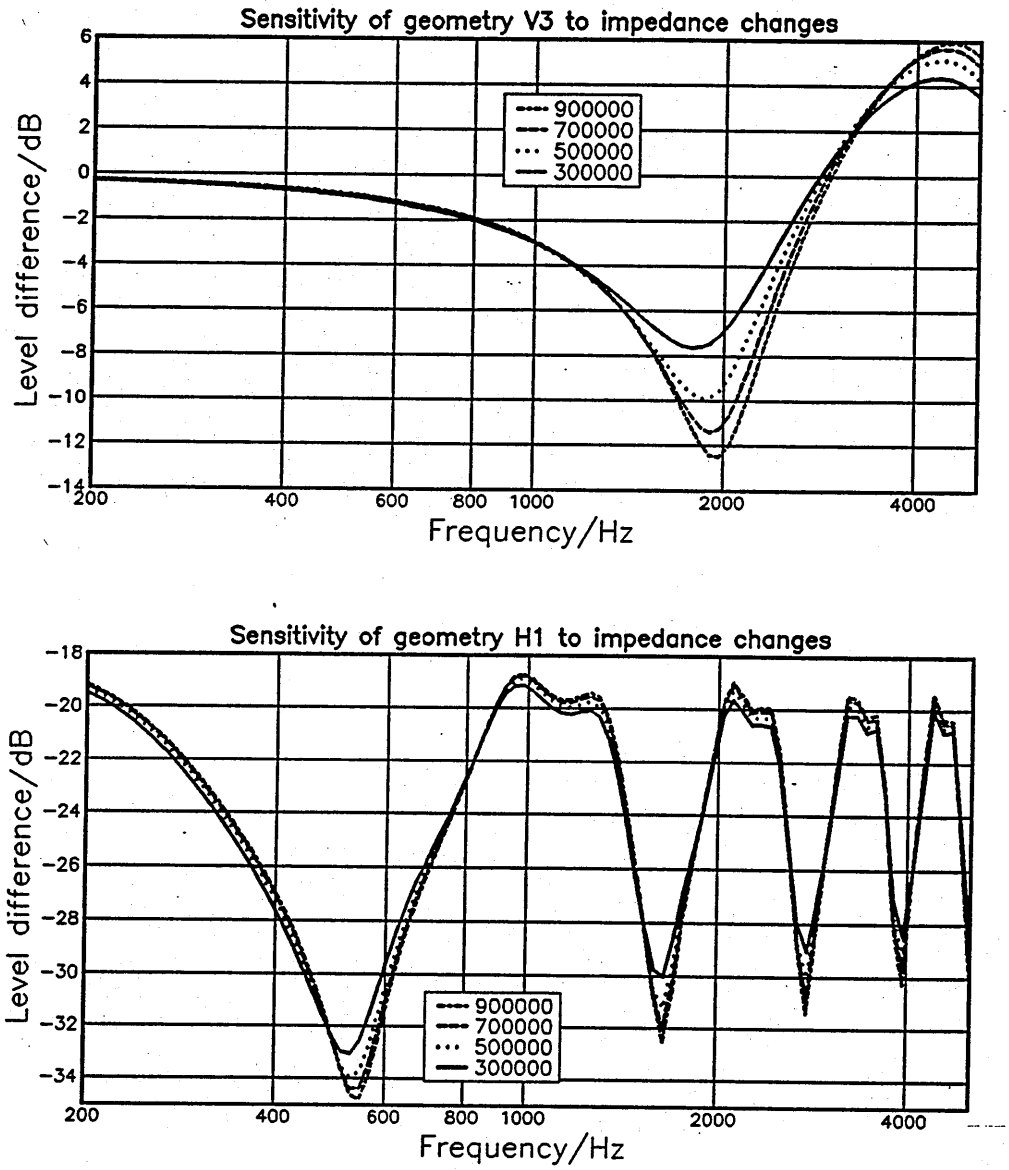


**Figure 6.11** Sensitivity of the level difference spectra for geometry V3 and H1 to increasing impedance

The primary ground effect dip becomes more sensitive to impedance variation as it is moved to higher frequencies by altering the level difference geometry. The sensitivity of the level difference spectrum V1 to changing the geometry is shown in figures 6.12, 6.13 and 6.14. In each case the parameter under study is increased by 5%, 10% and 20% respectively. Increasing either the upper microphone height or the source height lowers the frequency location of the dip and increases the magnitude. Increasing the source–receiver array separation increases the frequency location of the primary ground effect dip with little change in the magnitude. The level difference spectrum is relatively insensitive to the variations in the lower microphone height. The level difference spectrum is rather sensitive to misalignment of the vertically separated microphones. Figure 6.13 shows that in general the frequency location of the sensitive primary dip falls as the contribution to the phase difference between the direct and reflected wave due to the path length difference increases.

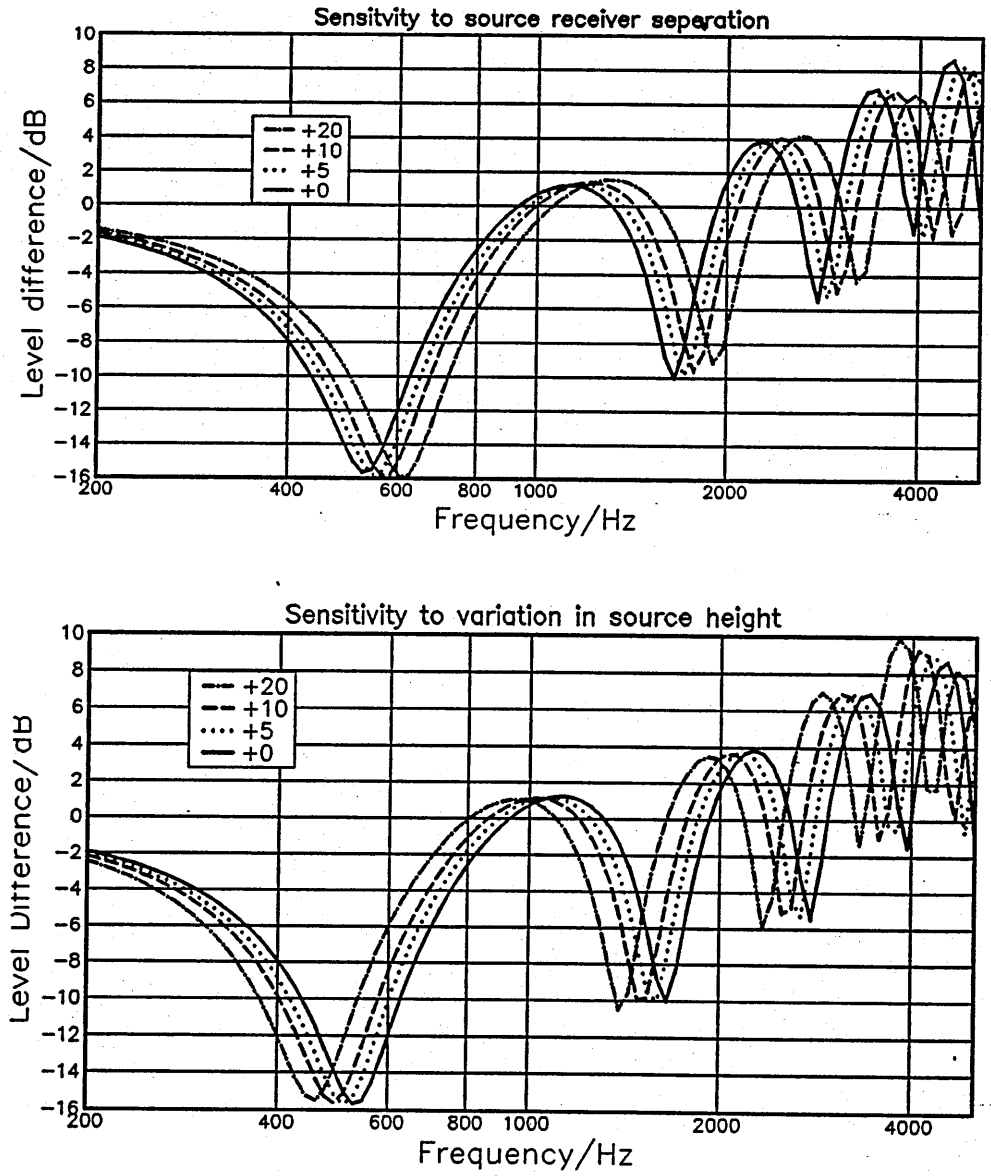


**Figure 6.12** Sensitivity of level difference spectra to changes in geometry

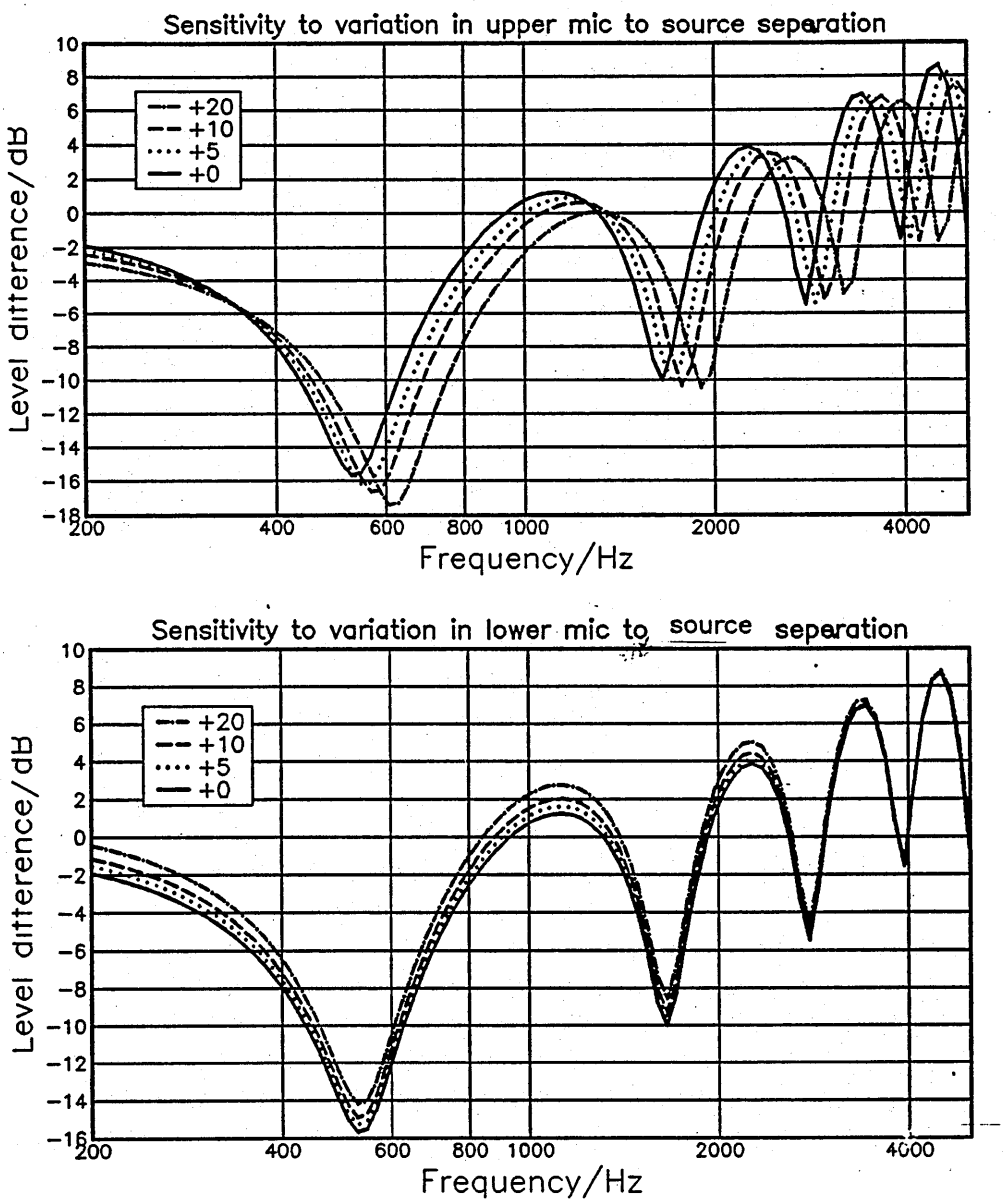


**Figure 6.13** Sensitivity of level difference spectra to changes in geometry

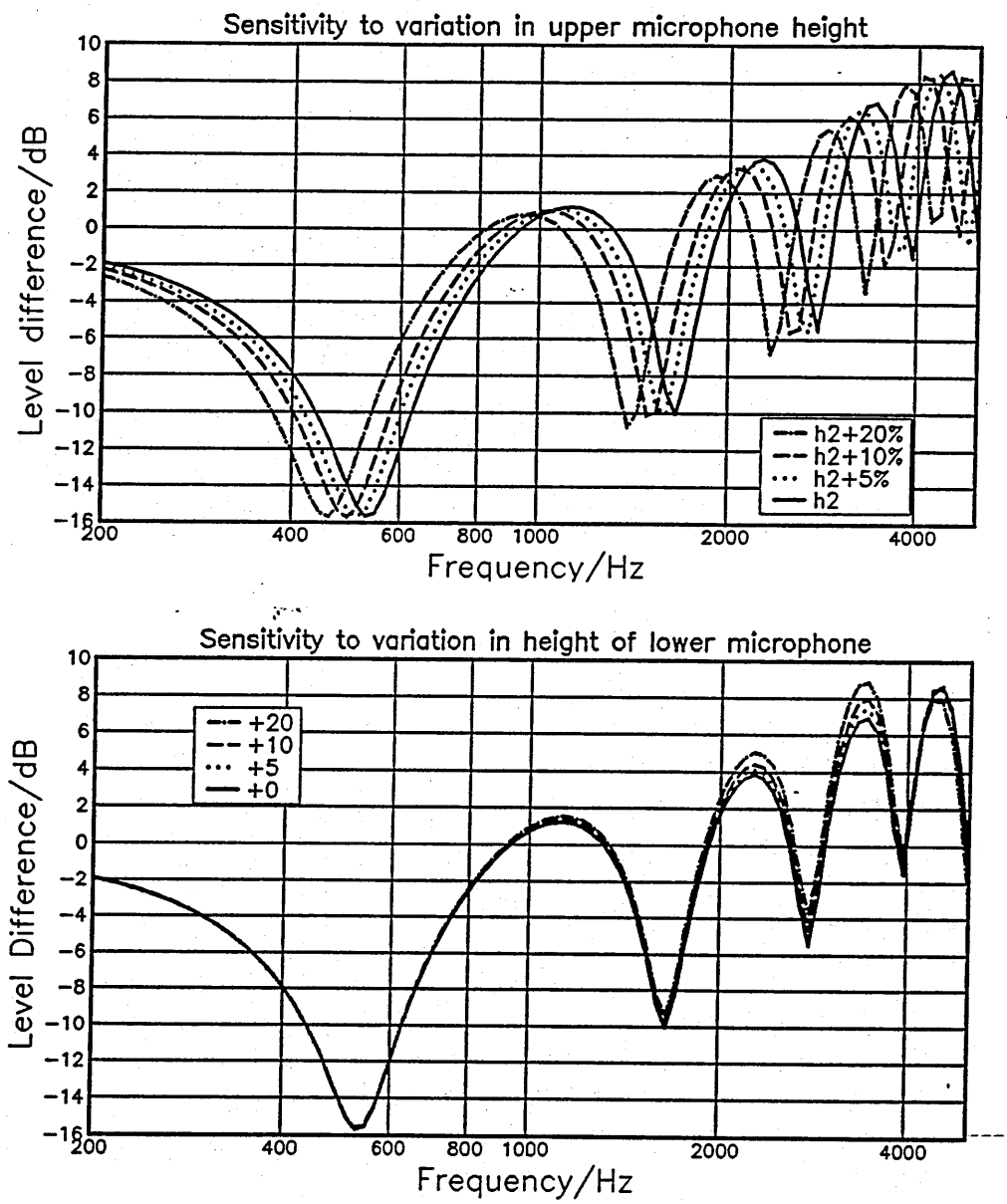


**Figure 6.14** Sensitivity of level difference spectra to changes in geometry

The sensitivity of the fitting technique is also dependent on the function to be minimized. Here an account is given of the choice of a minimization function with particular reference to the direct (i.e. impedance) fitting technique. However the same choice is used in the parameter fitting routine. The simplest function to minimize is

$$F1(R,X,f) = \sum_{f=m}^{m+l} \left( \sum_{n=1}^{3} \left[ |(LD^{n}_{meas}(R,X,f) - LD^{n}_{pred}(R,X,f))| \right] \right) \quad (6.4)$$

where $LD^{n}_{meas}(R,X,f)$ is the value at some frequency (f) of the magnitude of the measured level difference spectrum number n and $LD^{n}_{pred}(R,X,f)$ is the value predicted by inserting the variables, R the resistance and X, the reactance. The summation over $n$ indicates that three level difference spectra are recommended. The range of frequencies over which the summation is carried out is dependent on the type of indirect fitting. The direct level difference fitting technique uses three level difference spectra (i.e. n=3) over a limited frequency range whose width and location is determined by the primary ground effect dip. This only determines the impedance of the frequency of the main dip. The main problem with fitting impedance directly is that the frequency and angular dependence are not constrained. This means that the fitting process must be repeated using groups of three spectra such that the primary dip is located at adjacent frequencies until the frequency range of interest has been covered. In general this means that at least nine different spectra are required to examine a frequency range between 500Hz and 2000Hz. The parameter fitting method on the other hand imposes a frequency dependence on the corresponding impedance. Hence the parameter level difference fitting technique requires only three experimentally measured spectra to deduce the parameters, and hence the impedance over the frequency range of interest. The impedance at frequencies other than those included in the ground effect dip are evaluated via the microstructural model using the parameters deduced by fitting the ground effect dip. As a consequence of the unknown (a priori ) frequency dependency the direct method may only be used with locally reacting media the surface

impedances of which are independent of the angle of incidence, where as the parameter fitting technique may be used over both externally and locally reacting materials.

Albert [199] suggested that function F1 given above was preferable to function F2 described below which uses the more common squared function. It was suggested that a linear scale weighted the results towards high frequencies and that a logarithmic scale would be preferable.

$$F2(R,X,f) = \sum_{f=m}^{m+l} \left( \sum_{n=1}^{3} \left[ LD^{n}_{meas}(R,X,f) - LD^{1}_{pred}(R,X,f) \right]^2 \right) \quad (6.5)$$

As there are two unknowns (R and X) for a locally reacting medium at a given frequency at least two spectra are required to give a unique solution, n=2. The clarity of the minima of these functions may be found by examining F(R,X) over the expected range of R and X. Impedance S1B is used to generate the three level difference spectra V1 to V3 shown in figure 6.10 and 6.11 using the Weyl van der Pol formula see equation 4.119. The three resultant level difference spectra are substituted as if they were measured spectra in the appropriate function. The function is then plotted for a range of values of R and X at one frequency. A minimum should be apparent when the variable impedance has the same values as that given by the test impedance S1B. It should be noted that all three spectra (V1 to V3) have a ground effect dip at 1600Hz, whilst at approximately 500Hz only the spectrum given by geometry V1 is likely to be sensitive to variations in the impedance. At 200Hz level difference spectra are relatively insensitive to the surface impedance. The functions F1 and F2 at 1600Hz are plotted against the resistance and reactance giving figures 6.15 and 6.17. A minimum should be found when the resistance is approximately 7.0 and the reactance is around 5.0. The fitting routine requires specification of the range for the resistance and reactance appropriate to the expected impedance at all frequencies. Thus for impedance S1B the resistance should be varied from 6 to 18 and the reactance from 2 to 18. Over this range the minimum is not clearly detectable. Figure 6.16 shows that a smaller range of variables

has to be considered before the expected feature is visible.

The effect of taking a rather small root of the squared difference function giving function F3, see equation 6.6, is shown in figure 6.18. The location of the minimum remains unaffected but its definition is increased.

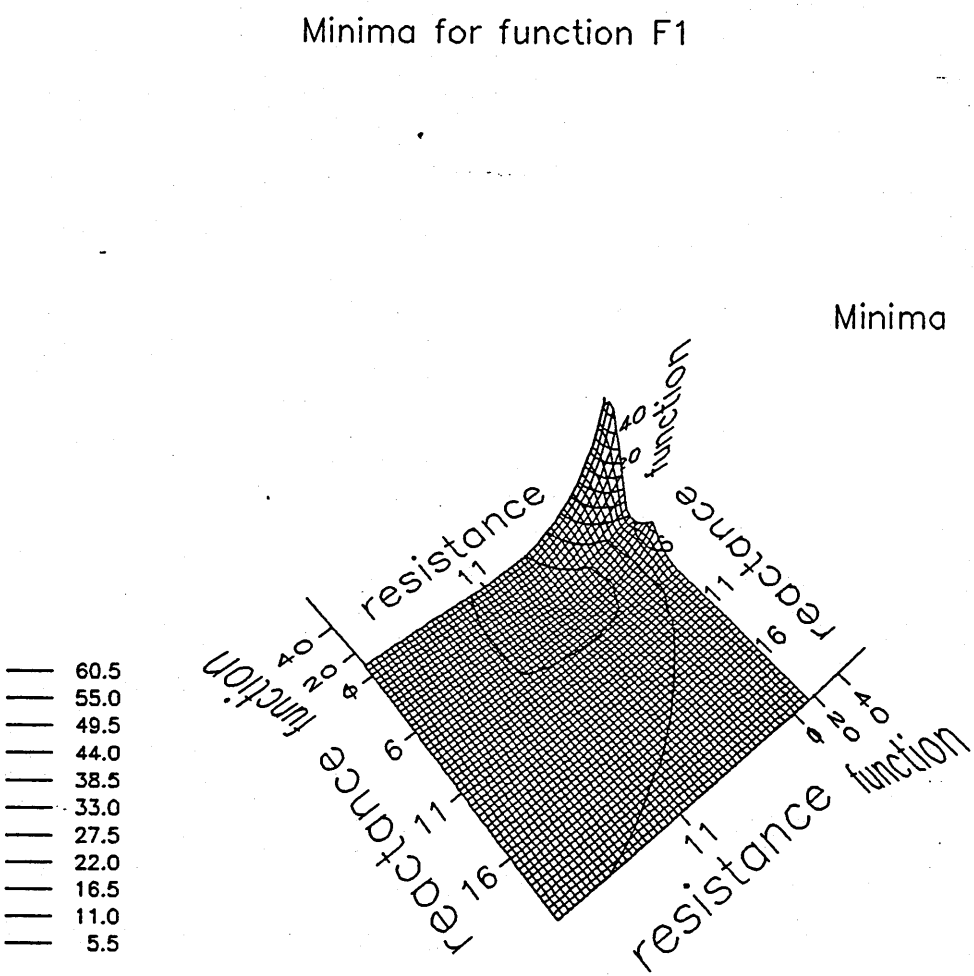


**Figure 6.15** Minima for function F1

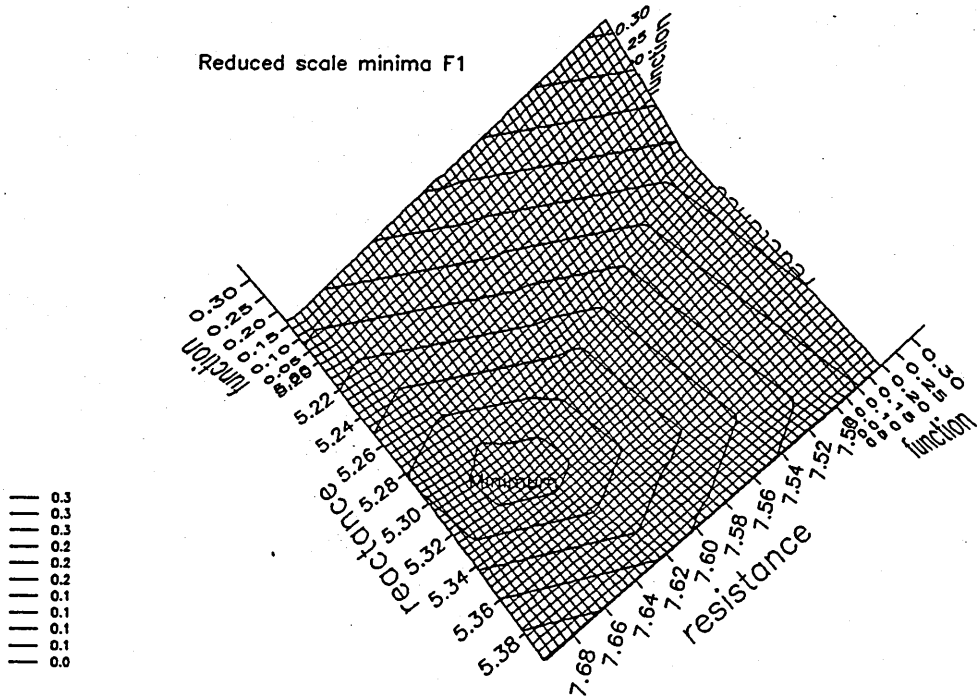


**Figure 6.16** Minima for function F1 reduced variable range

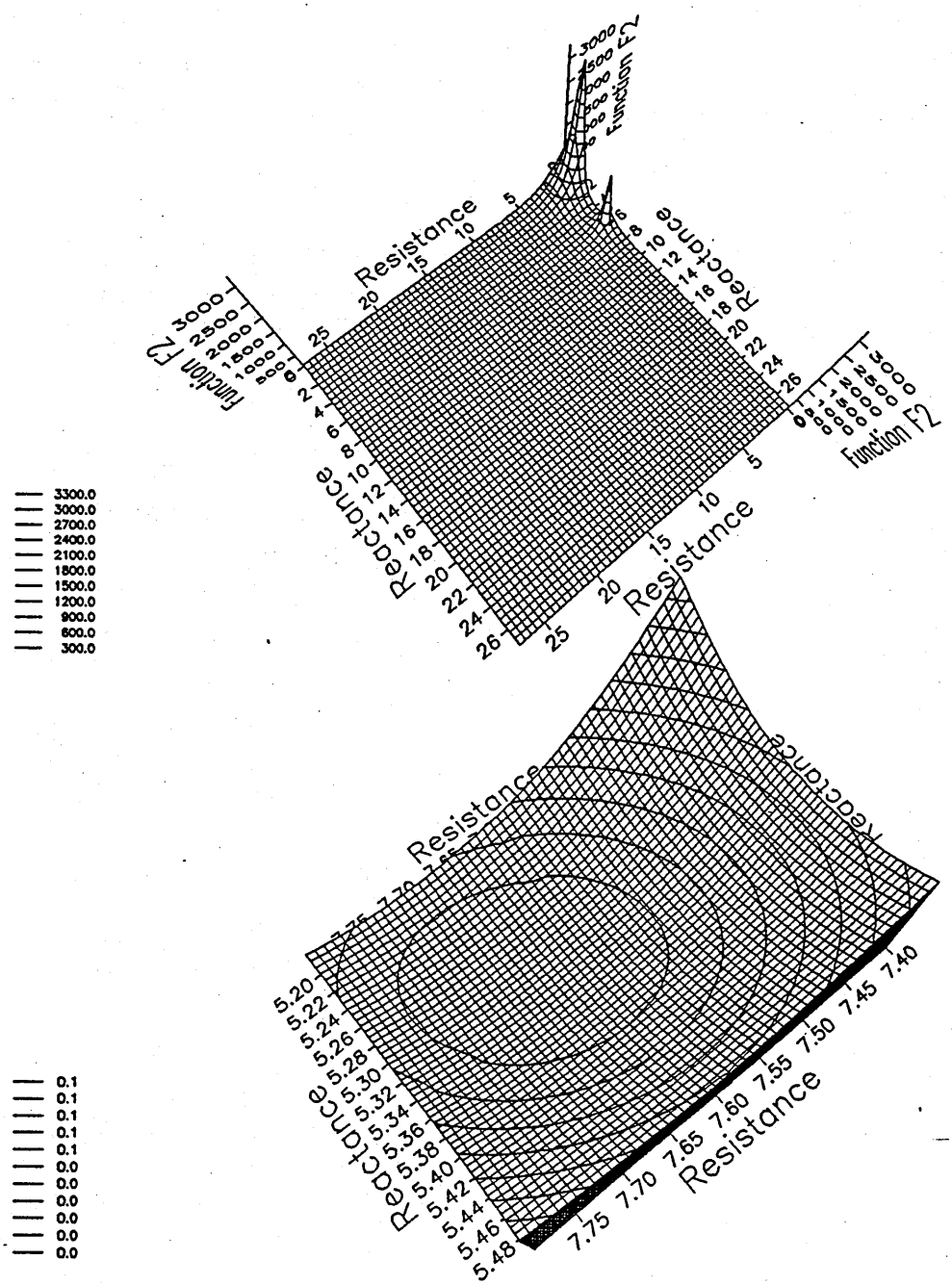


**Figure 6.17** Minima for function F2, No minimum is clearly detectable. Lower plot shows reduced scale necessary for location of minimum

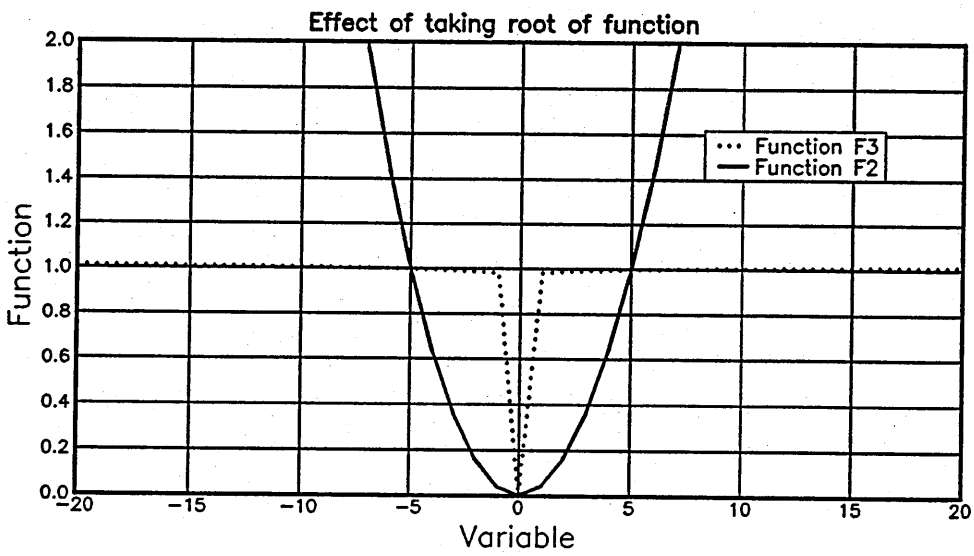


**Figure 6.18** Effect of taking roots of the function F1

Consider the function;

$$F3(R,X) = \sum_{f=m}^{m+l} \left( \sum_{n=1}^{3} \left[ (LD^{n}_{meas}(R,X,f) - LD^{n}_{pred}(R,X,f))^2 \right] \right)^{0.005} \tag{6.6}$$

The minimum becomes more clearly defined due to the compression of the vertical axis, (see figures 6.19, 6.20 and 6.21). There are several local minima obtained leading to non–uniqueness when only one level difference spectrum is used i.e. n=1. Two or more spectra enable location of the expected global minima. Hence at least two level difference spectra should be used by the fitting programs. However the geometries of the level difference spectra should be carefully chosen.

Consider the three level difference spectra (V1 to V3) at 527Hz. Only one ground effect dip is located at this point (i.e. for V1) and the minimum of the function F3 becomes less well defined, ( as shown in figure 6.22), the global minimum lies in a trough. At 200Hz there are no impedance sensitive areas of the level difference spectra. As shown in figures 6.23 and 6.24 as well as the global minimum of interest, there are several local minima. The global minimum becomes better defined if three spectra values at 200Hz are used. Sensitivity to variation in impedance is greatest if the ground effect dip were to be located at the frequency of interest.

The N.A.G. routine E04JAF locates the precise value of a local minimum. The optimum routine for finding the required global minimum uses the modified function F3, and an initial numerical search to locate region of the global minima prior to calling the N.A.G. routine. Subsequently the N.A.G. routine uses a quasi–Newton algorithm to locate the minimum of function (F3) subject to fixed upper and lower bounds and requires initial values for the variables found by the initial numerical search. Using these starting points a sequence of feasible points, which are intended to converge at the local minimum, is generated from the gradient of $F(R, X)$. This procedure is illustrated by the flow charts in figures 6.40 and 6.25. The next section discusses the performance of the optimized search routine when used for direct impedance fitting. A later section describes the use and validity of a similar routine for parameter fitting.

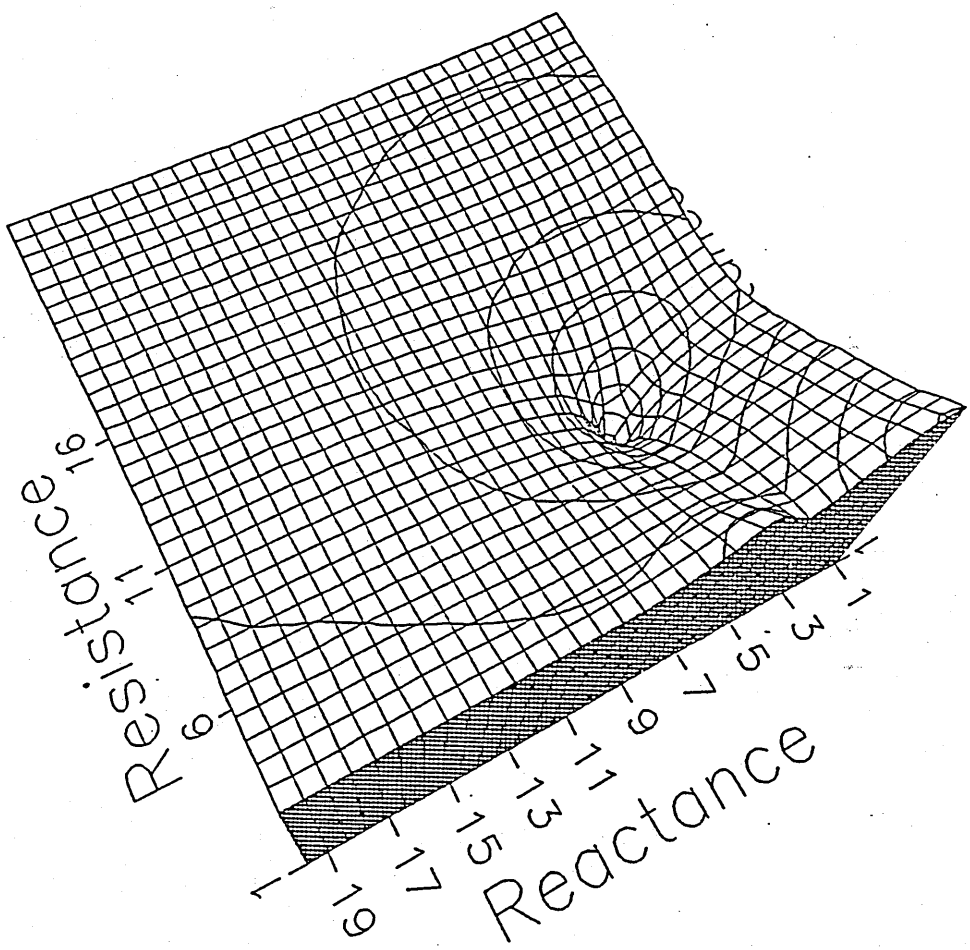


**Figure 6.19** Minima for function F3, n=3

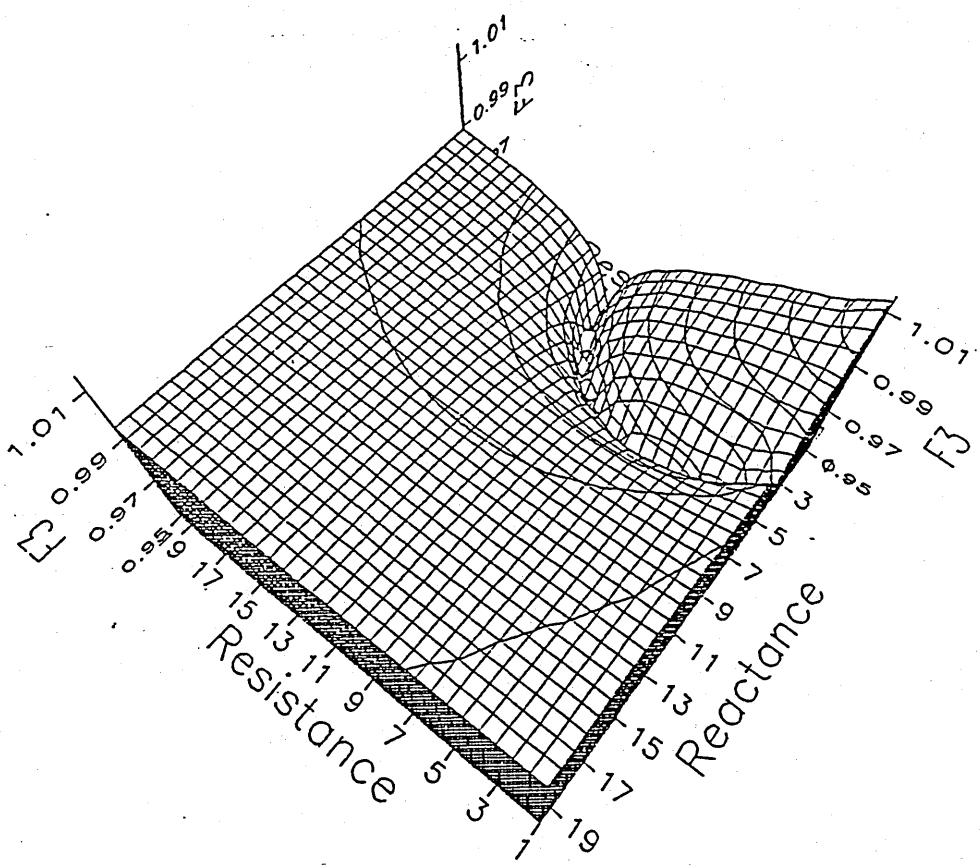


**Figure 6.20** Minima for function F3, n=1

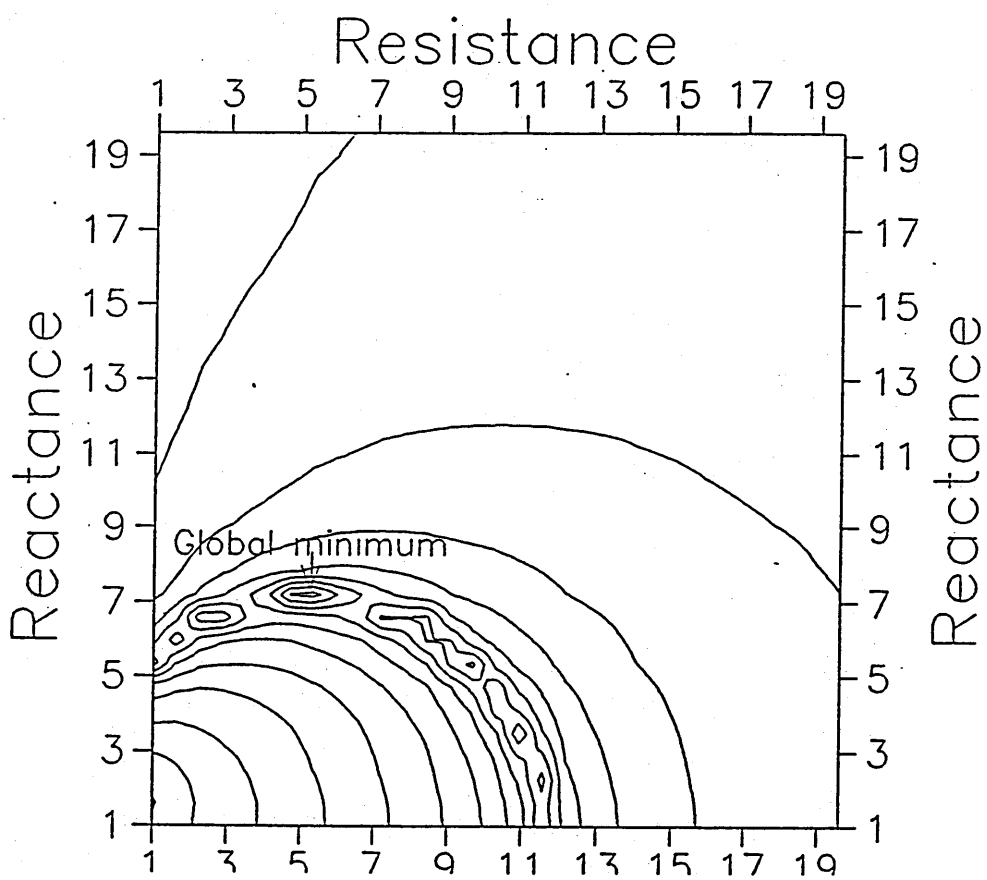


**Figure 6.21** Minima for function F3, n=1, plan

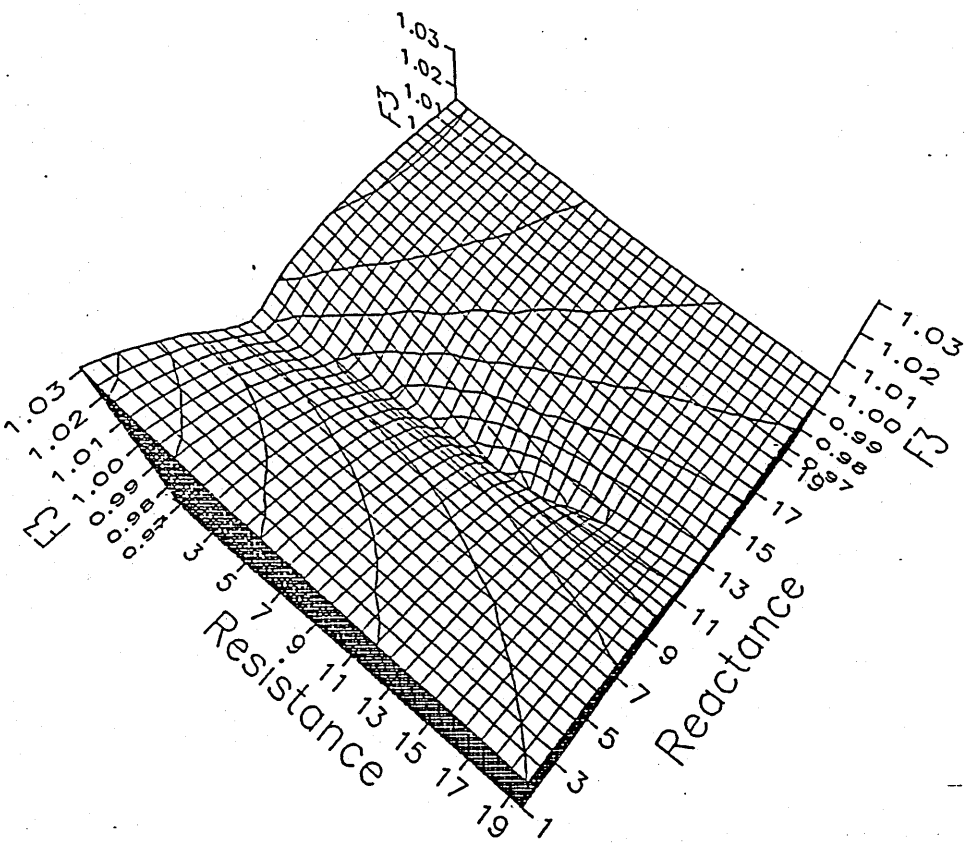


**Figure 6.22** Function F3 at 527 Hz

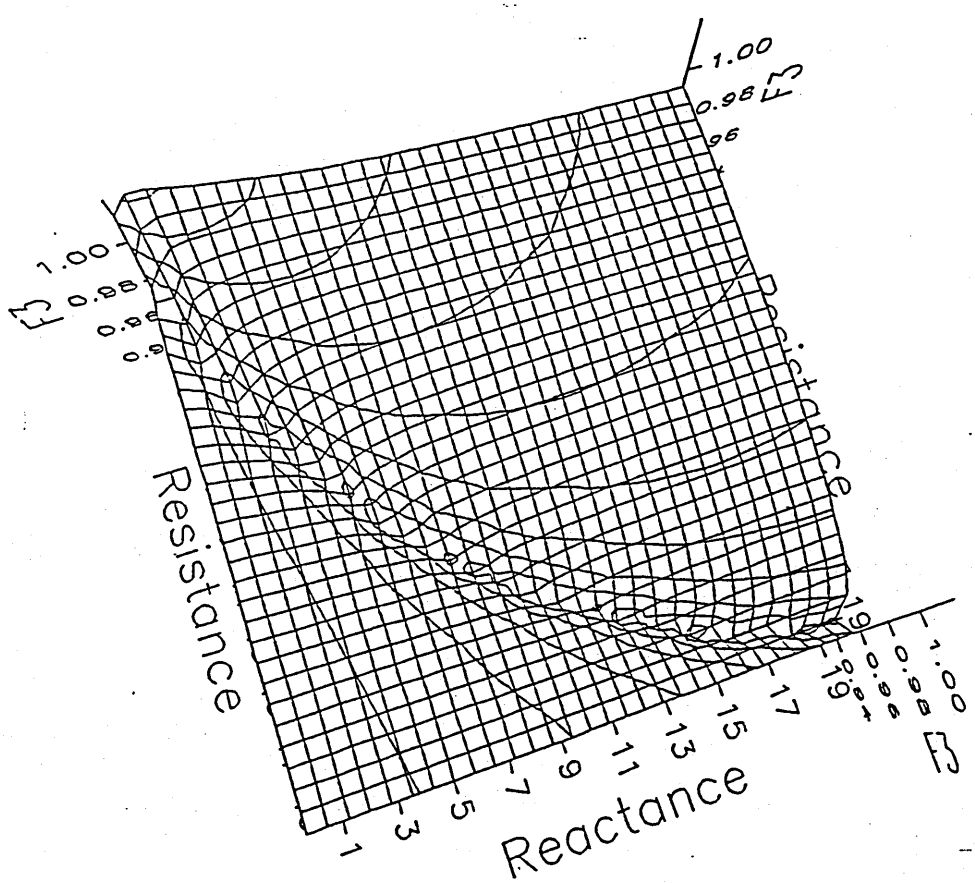


**Figure 6.23** Function F3 at 200Hz

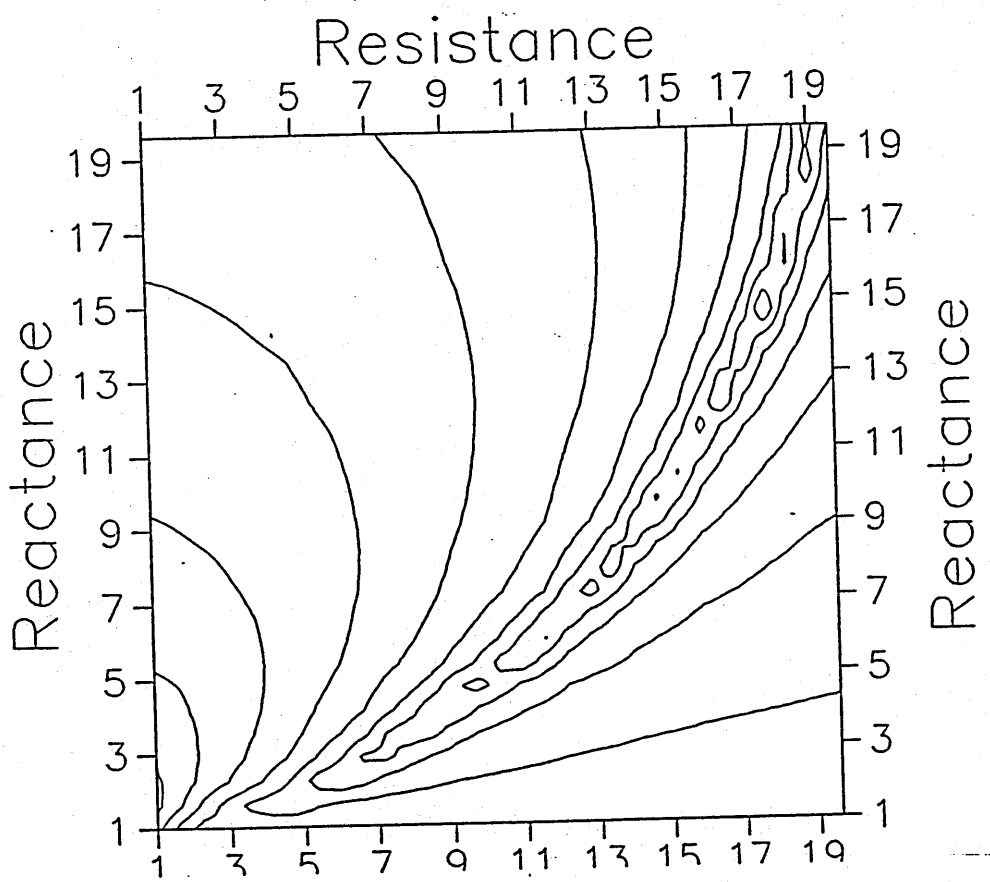


**Figure 6.24** Function F3 at 200Hz, plan

## 6.2 Direct minimization technique for locally reacting semi–infinite media.

It has been argued in the previous section that the direct level difference fitting mechanism with resistance and reactance as variables must use at least three level difference spectra for each frequency band of interest. The frequency range used is determined by the width of the primary ground effect dip. The structure of the minimization routine is shown in figure 6.25. The N.A.G. routine may possibly return an 'ifail' value which indicates that the minimum has not been found but was of the order of the returned values, in this case it often proves valuable to submit the returned parameters as new starting values to the routine.

In this section the efficiency of the program is examined using a computer generated error technique.

### 6.2.1 Systematic error.

The effect of geometrical variations on the level difference spectra has been discussed. Inaccuracies in the measurement of the level difference geometry will introduce systematic errors into the level difference spectra which in turn will produce errors in the impedance deduced from the fitting of these spectra. The impedance S1B and the Weyl van der Pol formulae is used to generate the three level difference spectra (based on V1 to V3 ) as before. These are then used as input spectra along with the appropriate geometry to the direct level difference fitting program. The errors introduced are

- An increase in the source height by 2cm
- An increase in the source–receiver separation by 2cm
- An increase in the lower receiver height by 1cm

The effect of introducing these errors into some or all of the level difference spectra are examined for fitting routines using the chosen minimization function $F3(R, X)$. The results of the error analysis are seen in figure 6.26

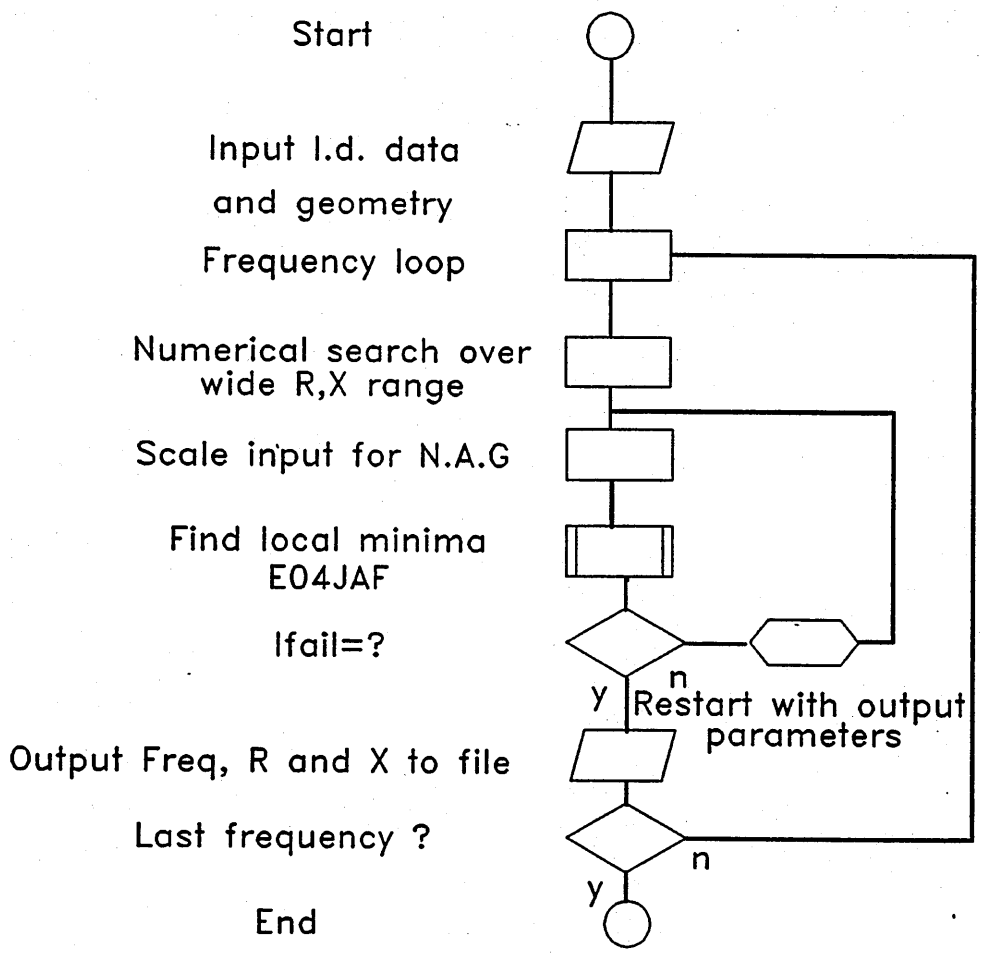


**Figure 6.25** Structure of the direct fitting algorithm

to 6.30. The errors may be introduced in up to three level difference geometries as indicated in the caption above the appropriate figure. The errors are introduced into spectra in the order of the geometries V1 to V3. For example '2 source errors' means that the source height in both geometries V1 and V2 has been increased by 2 cm. All errors are made in the positive direction. Errors made in opposite directions have similar effects depending on the total change in the path lengths. Thus the error due to reducing the receiver height by 1cm and increasing the source height by 1cm is similar to that due to increasing the height of the source by 2cm.

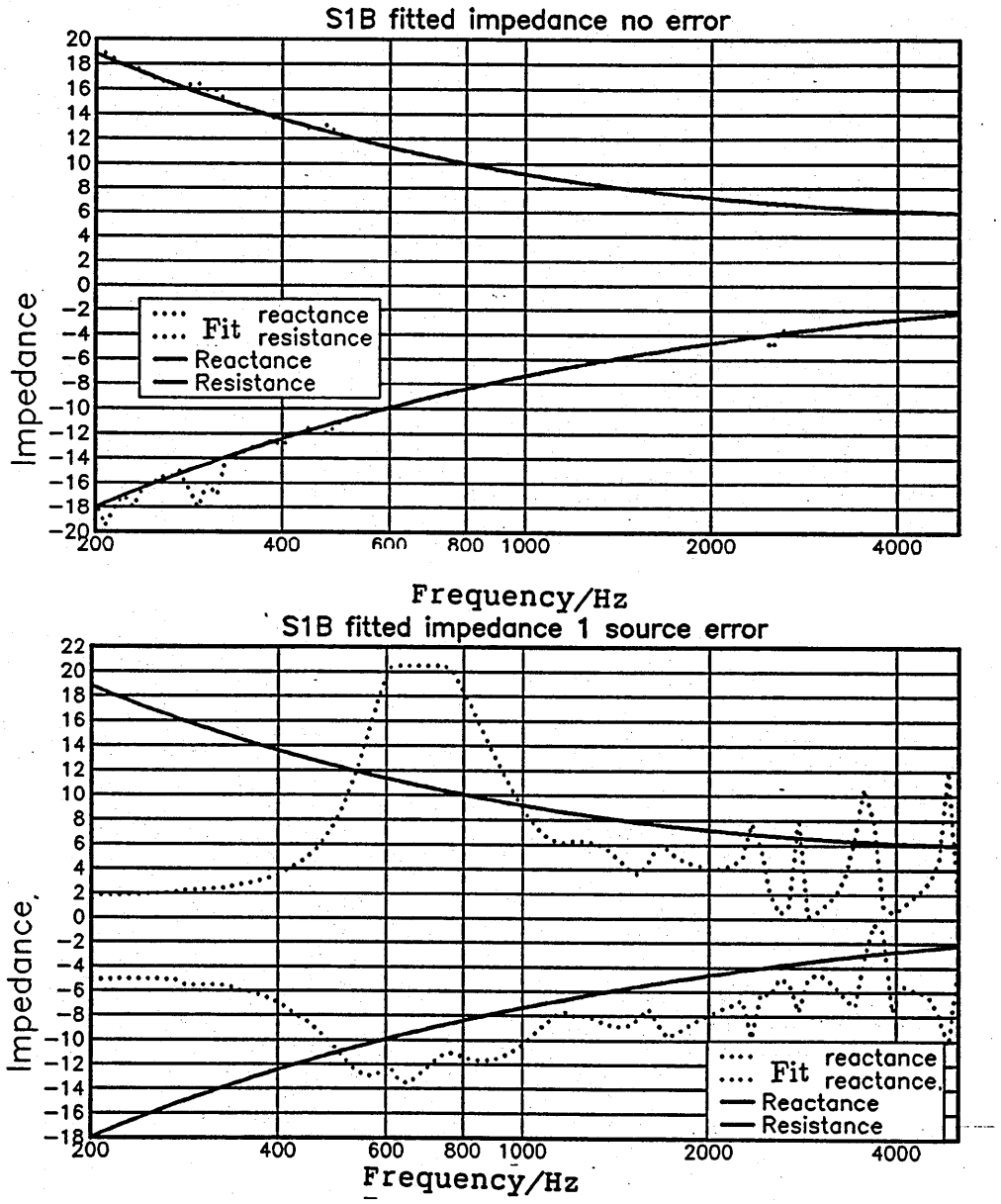


**Figure 6.26** Systematic error analysis for direct level difference fitting no and one source error

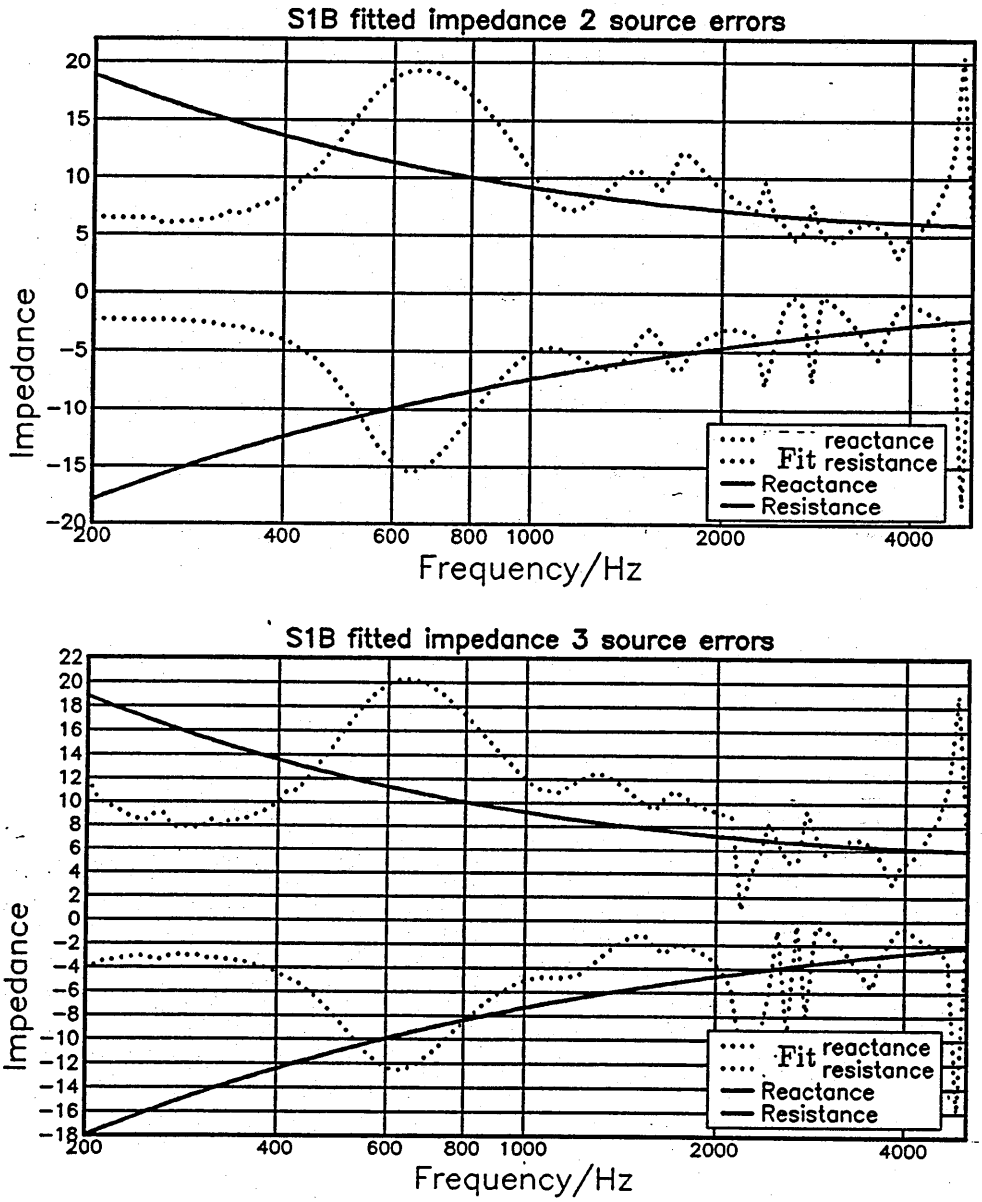


**Figure 6.27** Systematic error analysis for direct level difference fitting two and three source errors

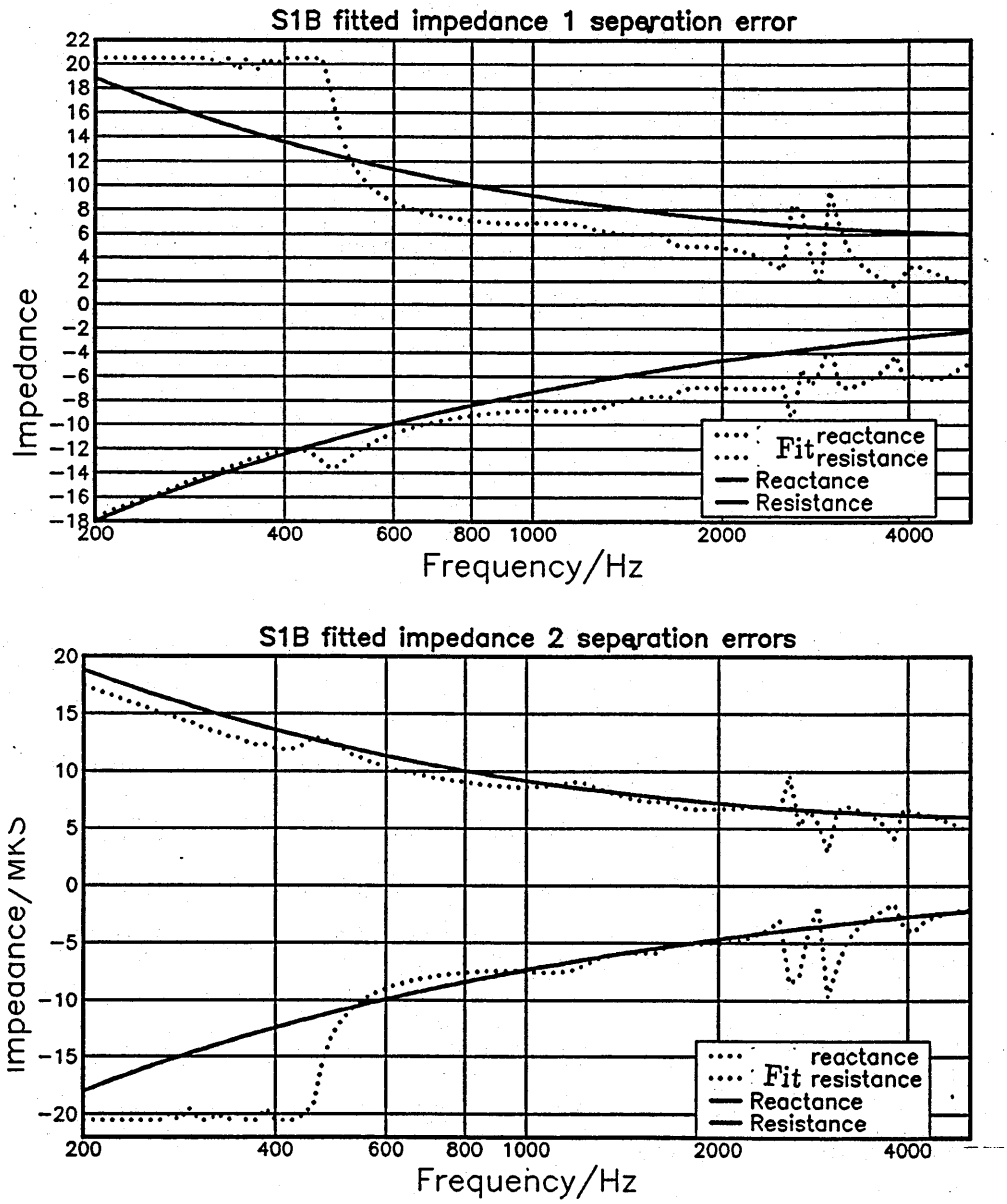


**Figure 6.28** Systematic error analysis for direct level difference fitting one and two separation errors

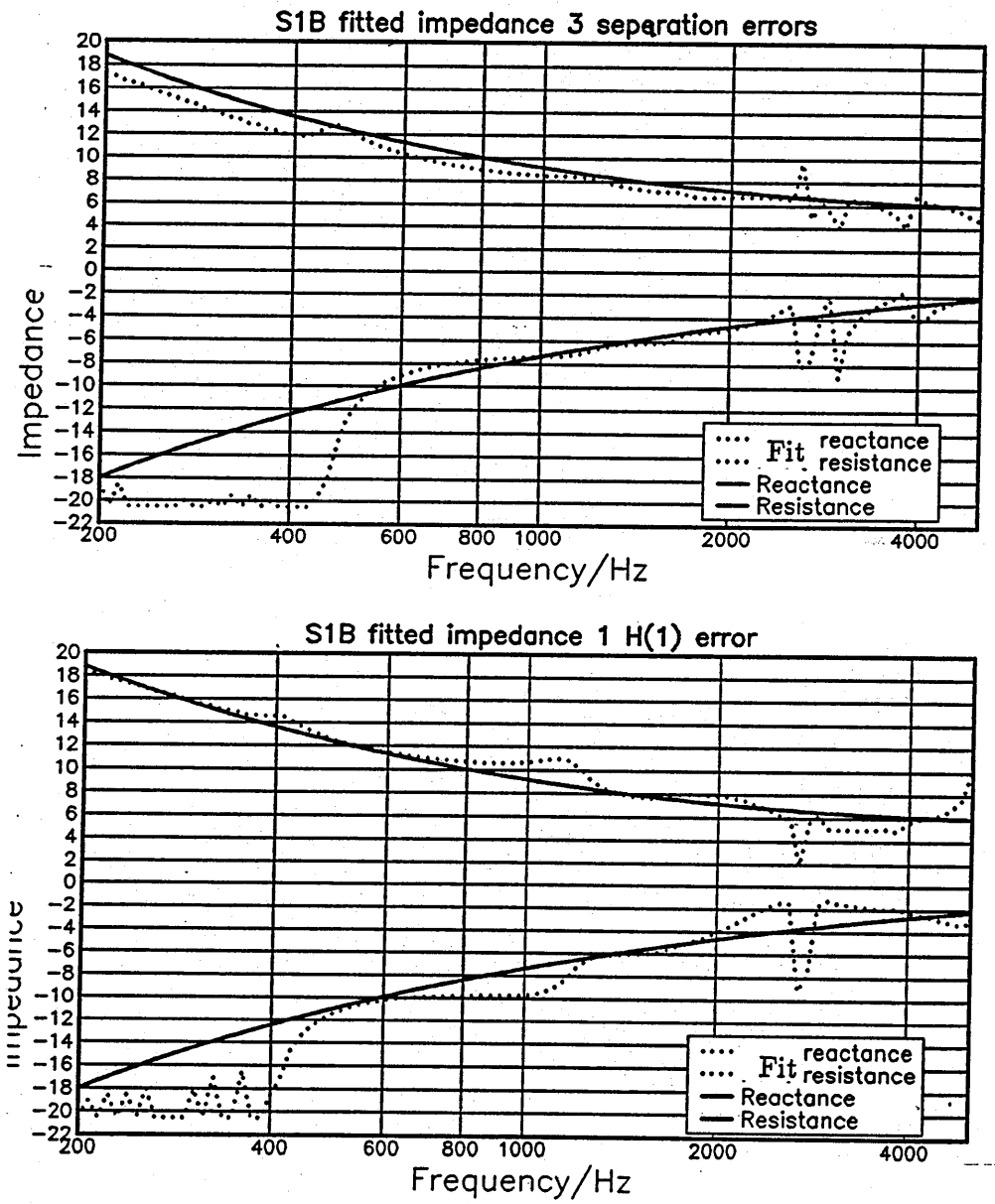


**Figure 6.29** Systematic error analysis for direct level difference fitting (note H(1) denotes lower receiver height)

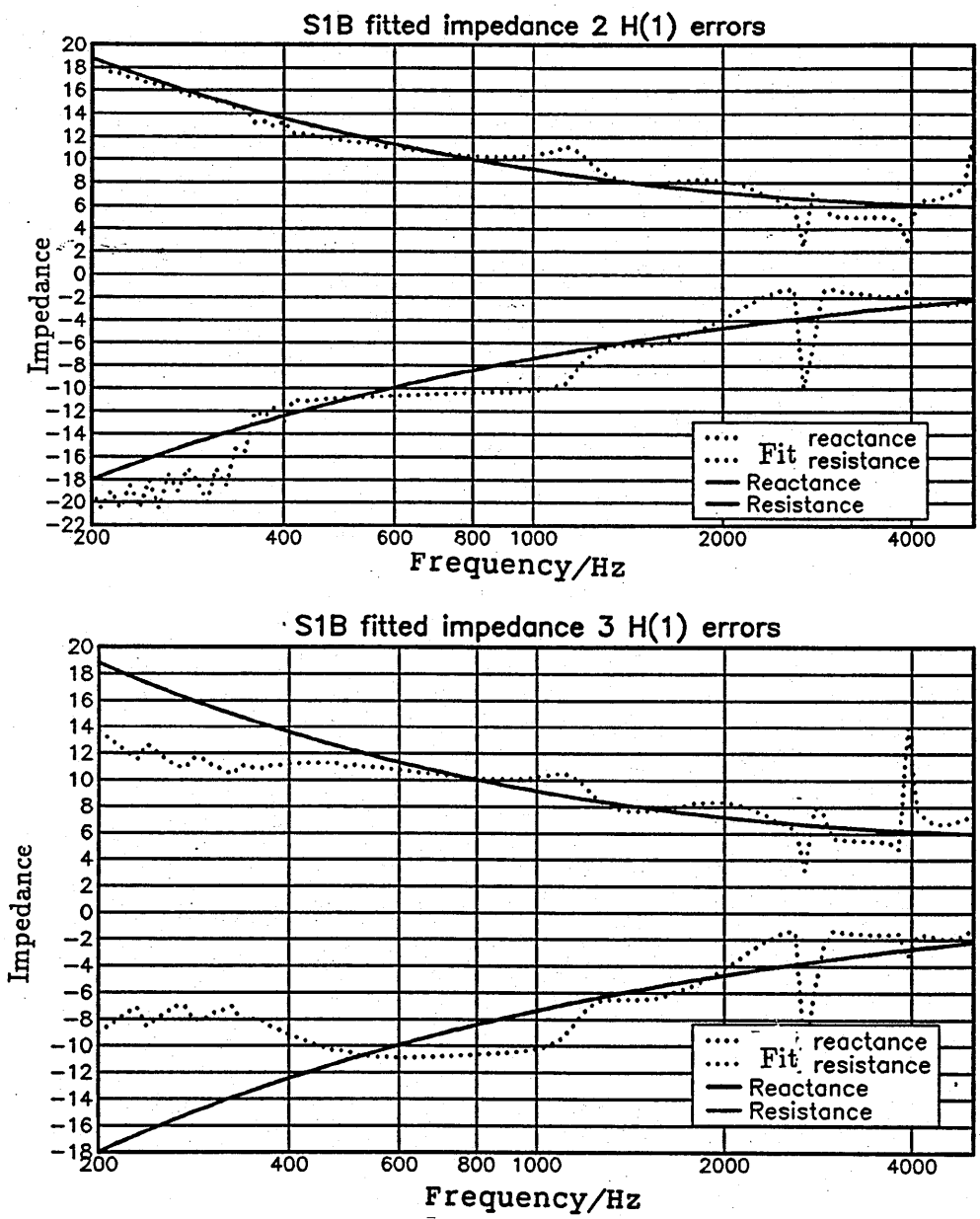


**Figure 6.30** Systematic error analysis for direct level difference fitting two and three lower receiver errors

As expected there is little error when the input spectra and geometries are correct. The error, apparent at low frequencies, is due to numerical rounding errors in the computing system. The errors are most likely to appear in the impedance at low frequencies though this tendency would be improved by arranging the geometry so that the ground effect dip is located at a lower frequency. The technique is most sensitive to errors in the source height or upper receiver height. The mirror nature of the fitted impedance is consistent with the fact that the real and imaginary parts of the impedance should be related by the Kramers–Kronig relationship cited by Daigle and Stinson [21]. The algorithm fails to give reasonable results if there is a significant error in the input measurement of the upper receiver or source height. The system is relatively insensitive to the position of the lower microphone and the source receiver separation.

### 6.2.2 Random error.

A random error may be superimposed onto the level difference spectra in order to reproduce errors due to turbulence or background noise generated acoustically, electrically or seismically. These spectra, figure 6.31, are then used as inputs to the minimization algorithm. The resulting impedance is seen in figure 6.32. Most inaccuracy is introduced at the lower frequencies. This may be recovered slightly by smoothing the level difference spectra using a sliding average technique.

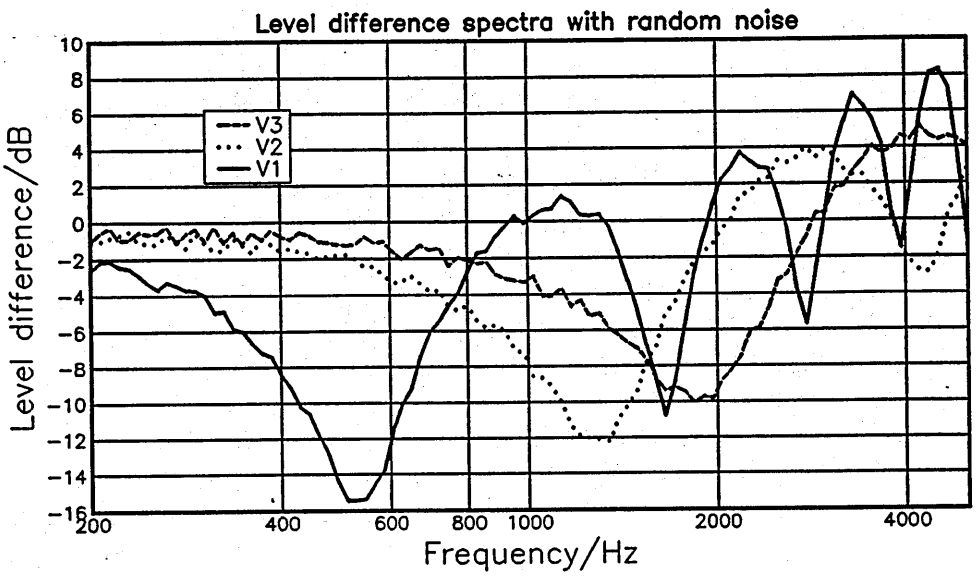


**Figure 6.31** Level difference spectra with random noise

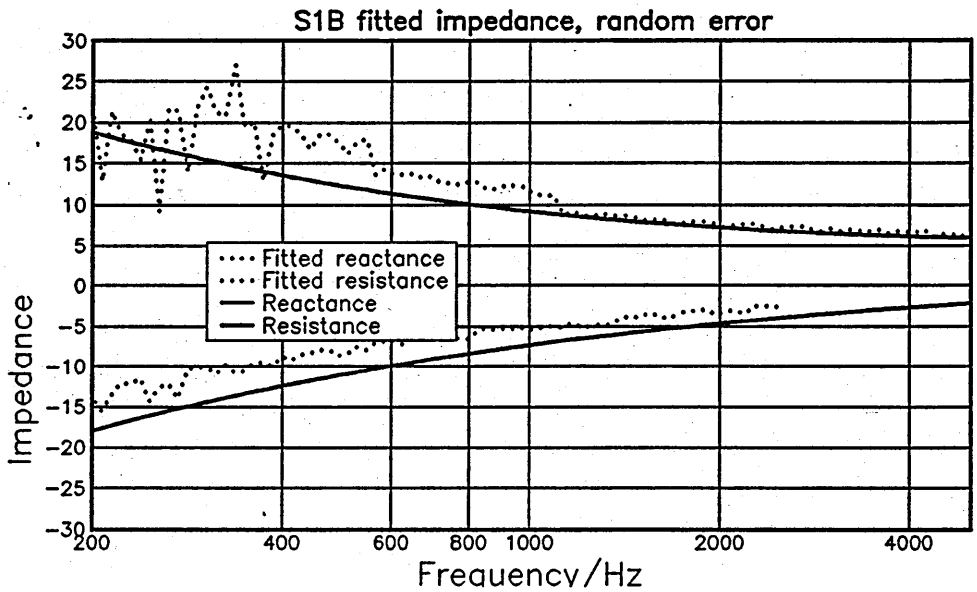


**Figure 6.32** Impedance fitted from level difference spectra with random noise

## 6.3 Parameter level difference fitting technique for locally reacting semi–infinite media.

The parameter fitting technique relies on the accuracy of the microstructural model discussed in chapter 3. The four parameters of the model are varied independently. This in turn varies the impedance which is input into the Weyl van der Pol formula to calculate the predicted level difference in function F3. As the impedance model determines the structure of the impedance spectra the program is used simultaneously for all frequencies, more than one spectrum being used to eliminate any ambiguity in the resulting parameters. Thus the frequency range of the level difference spectra considered must include the fitting–sensitive ground effect dip. In some cases better results may be gained if the smallest frequency range that encompasses the ground dip is considered in isolation.

Figures 6.33 to 6.35 show the interaction of variations in pairs of parameters of the microstructural model on the fitting process for the locally reacting type of surface S1B. It is seen that certain combinations of parameters produce a trough which contains the global minimum of interest. Both the sensitivity plot, figure 6.38 and the interaction plots indicate that although the flow resistivity and porosity values are well defined and may be easily located during the search procedure the pore shape and size distribution parameter is more difficult to determine from the parameter fitting procedure.

Figures 6.36 to 6.39 show the sensitivity of the level difference spectra ( for geometry V1 ) and the impedance to the variations of the four parameters in the impedance model. The range of parameters considered for a hypothetical locally reacting surface is given in table 6.4. This numerical experiment is repeated for an externally reacting surface in section 6.5. The sensitivity would increase if the primary ground effect dip was located at a higher frequency where the wavelength of the frequency was considerably smaller than the separation of the receivers.

| Parameter | Default | Lowest | Highest | Step |
|---|---|---|---|---|
| Flow resistivity | 500000 | 300000 | 900000 | 200000 |
| Porosity | 0.35 | 0.25 | 0.55 | 0.1 |
| Grain Shape Factor | 1.0 | 0.7 | 1.6 | 0.3 |
| (Tortuosity) | (2.85) | (2.08) | (5.36) | (1.37) |
| Pore shape factor | 0.5 | 0.3 | 0.9 | 0.3 |

**Table 6.4** Parameters for sensitivity study of the impedance of a locally reacting semi-infinite surface according to the microstructural model

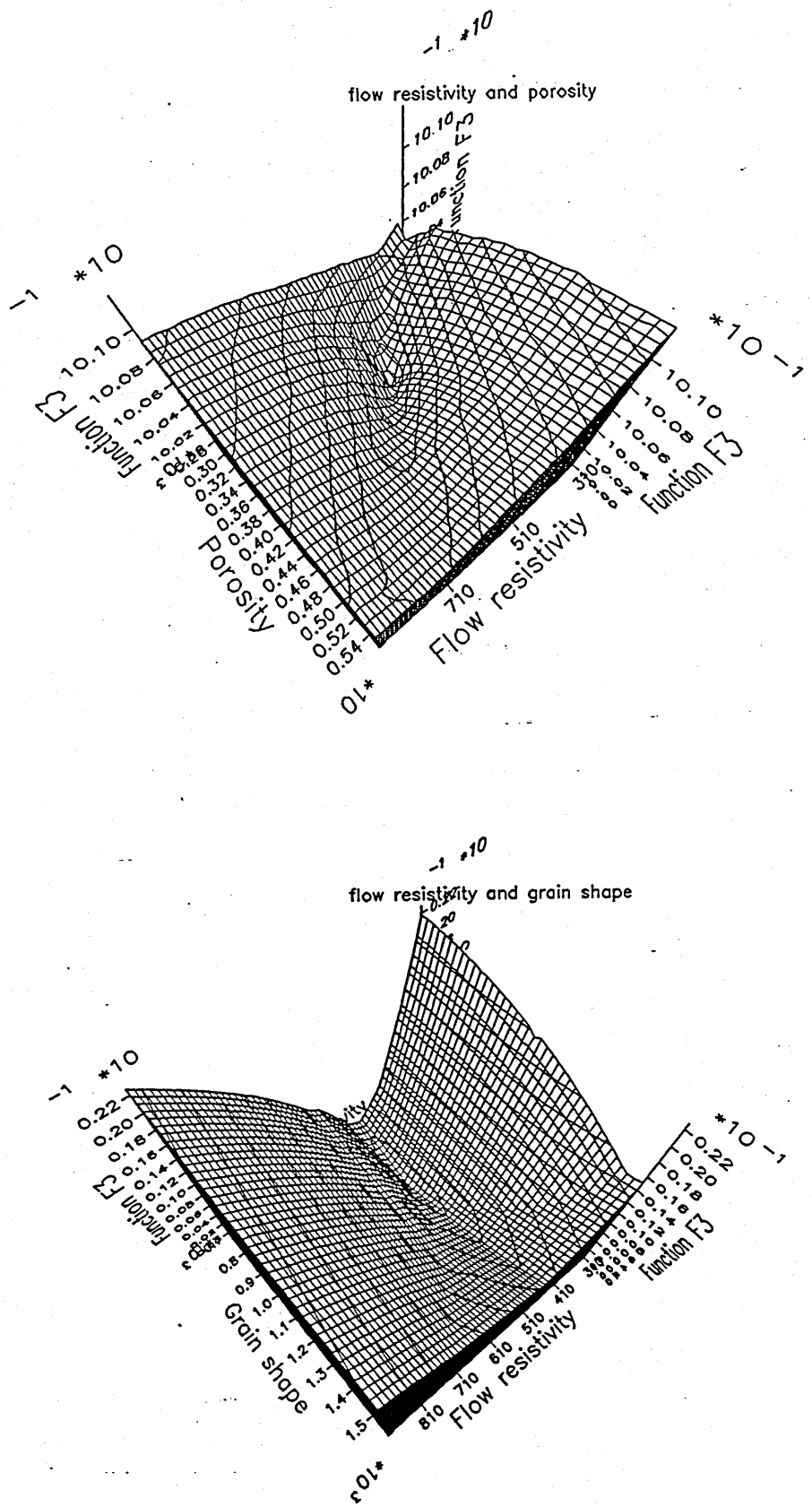


**Figure 6.33** Interaction of parameters in fitting level difference spectra .

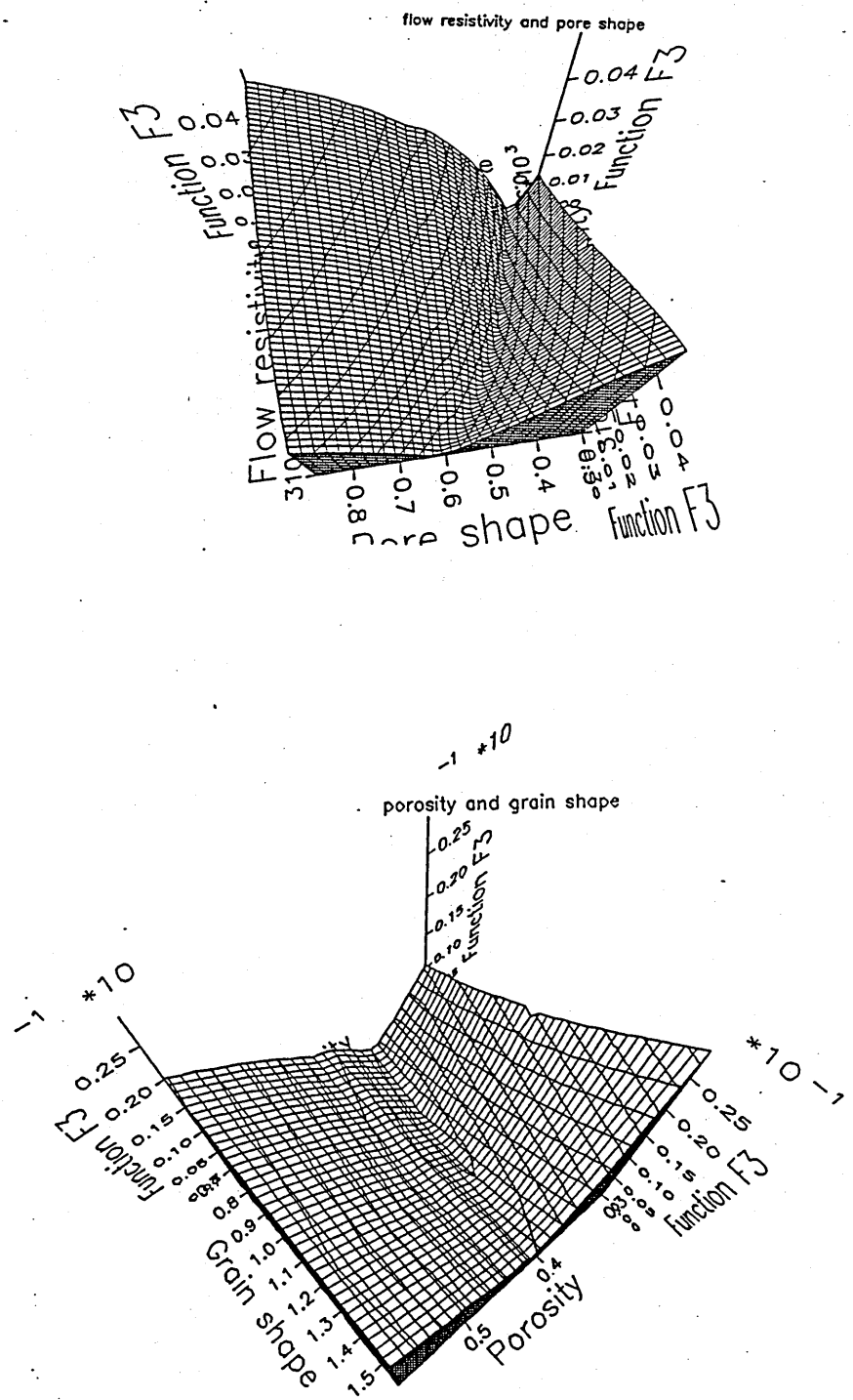


**Figure 6.34** Interaction of parameters in fitting level difference spectra.

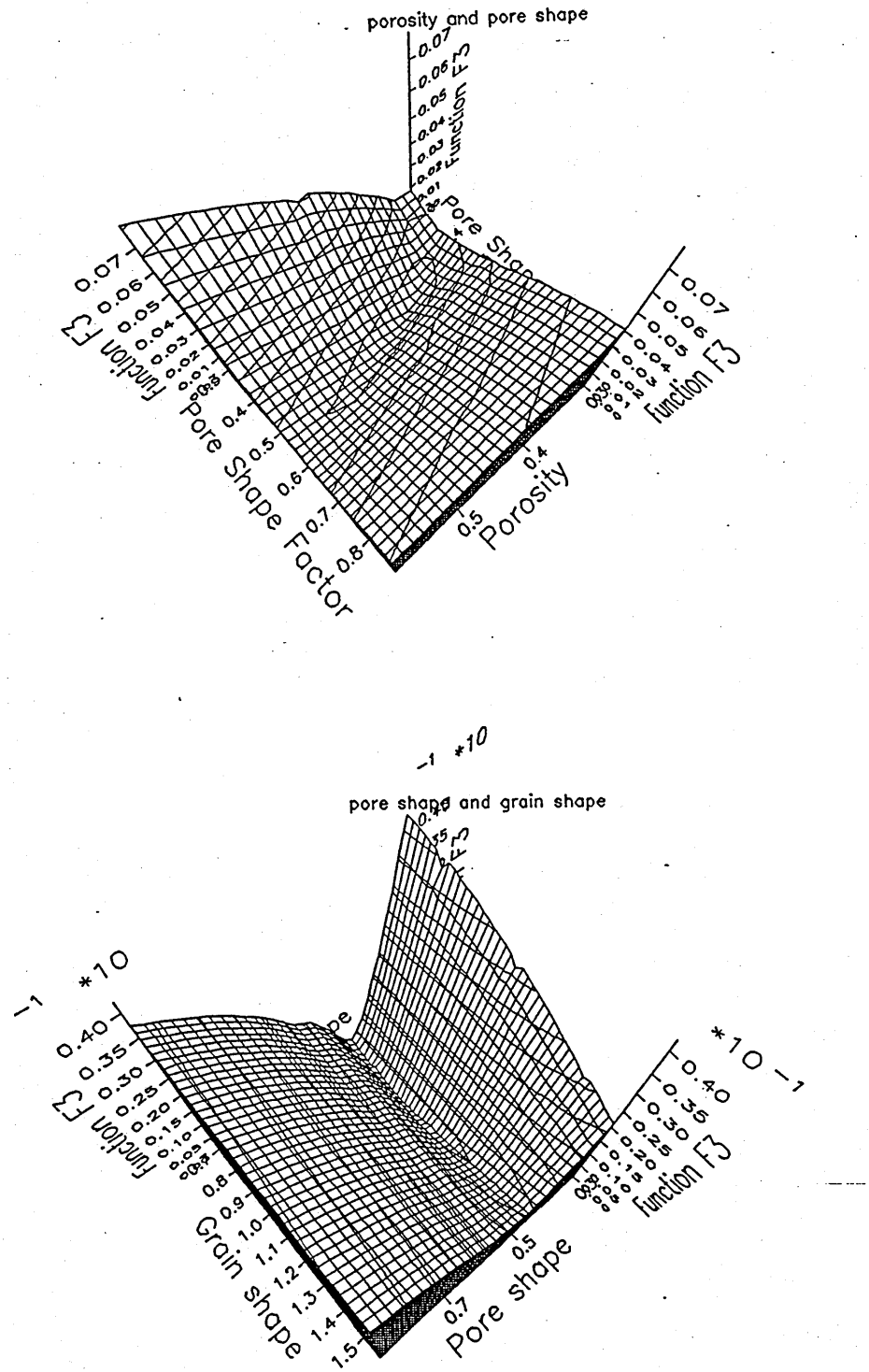


**Figure 6.35** Interaction of parameters in fitting level difference spectra.

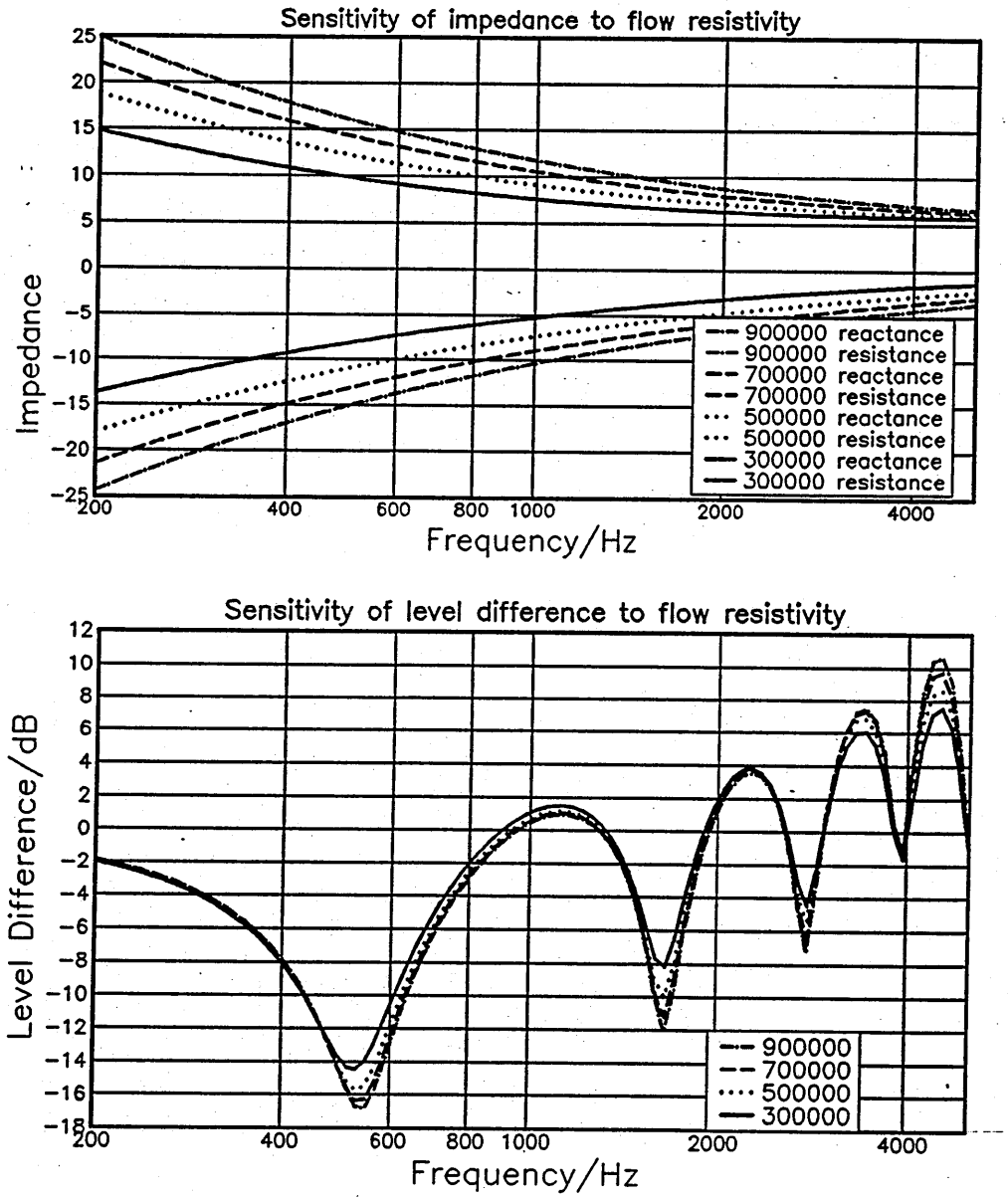


**Figure 6.36** Sensitivity of impedance and level difference to changes in flow resistivity.

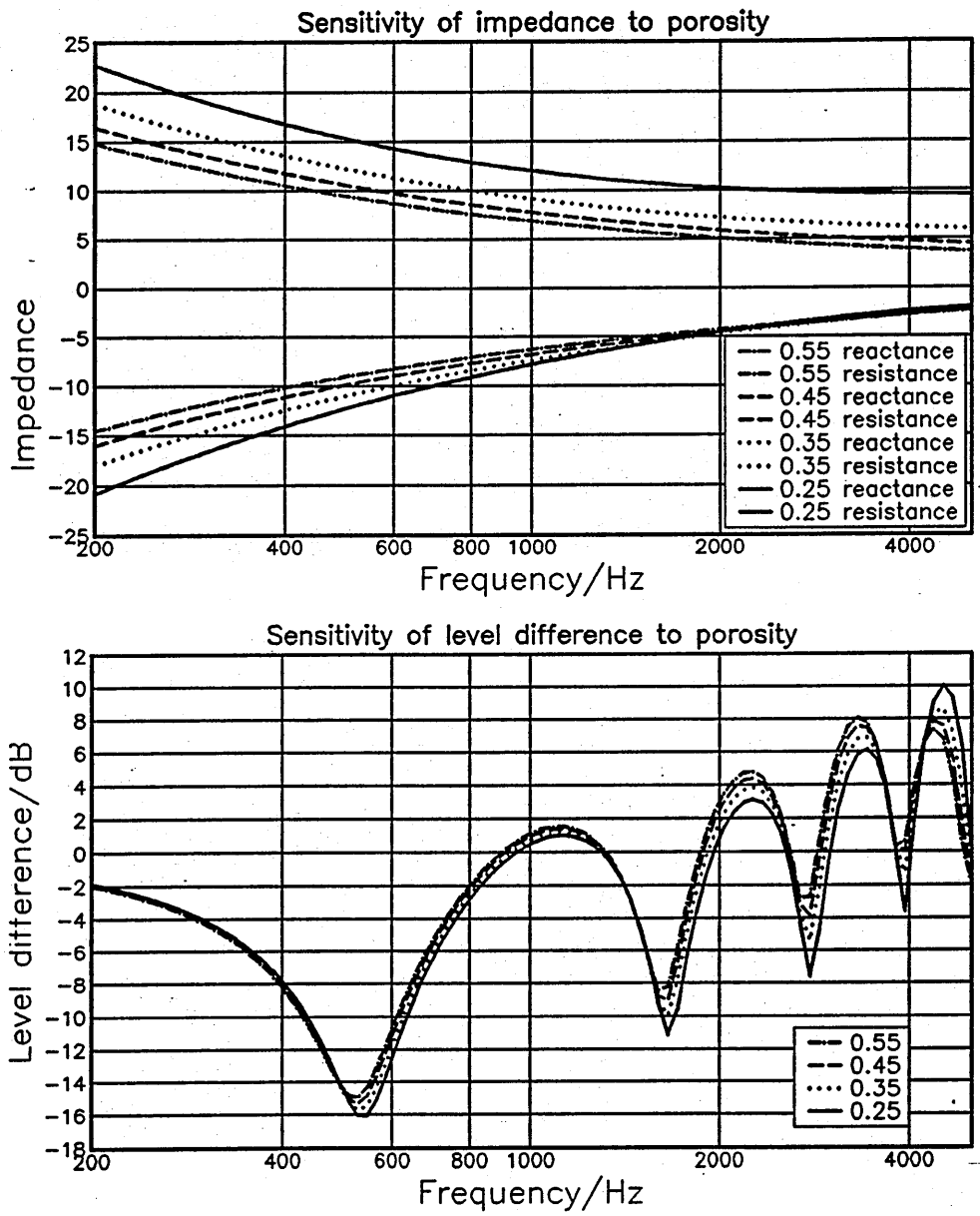


**Figure 6.37** Sensitivity of impedance and level difference to changes in porosity.

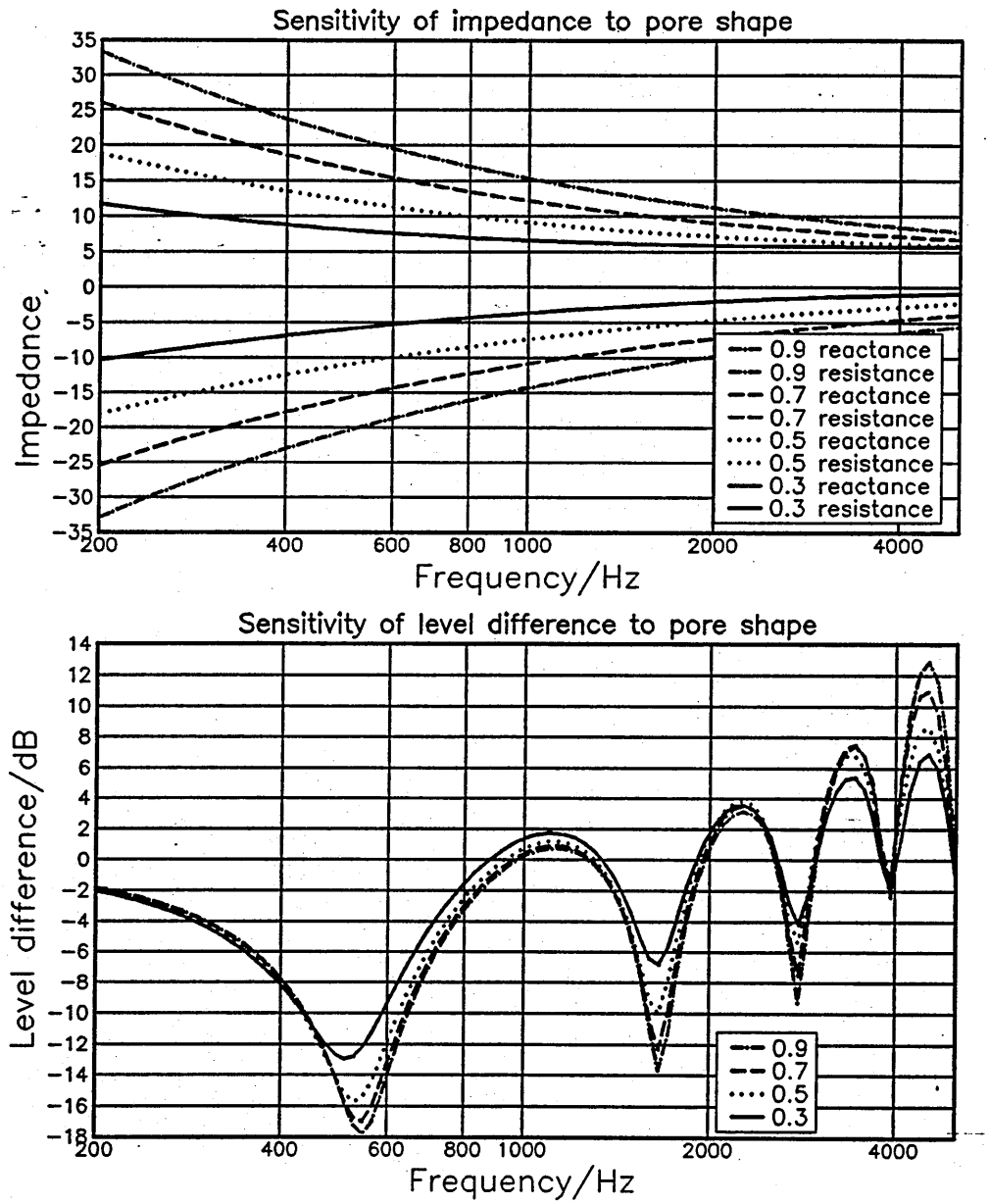


**Figure 6.38** Sensitivity of impedance and level difference to changes in pore shape factor.

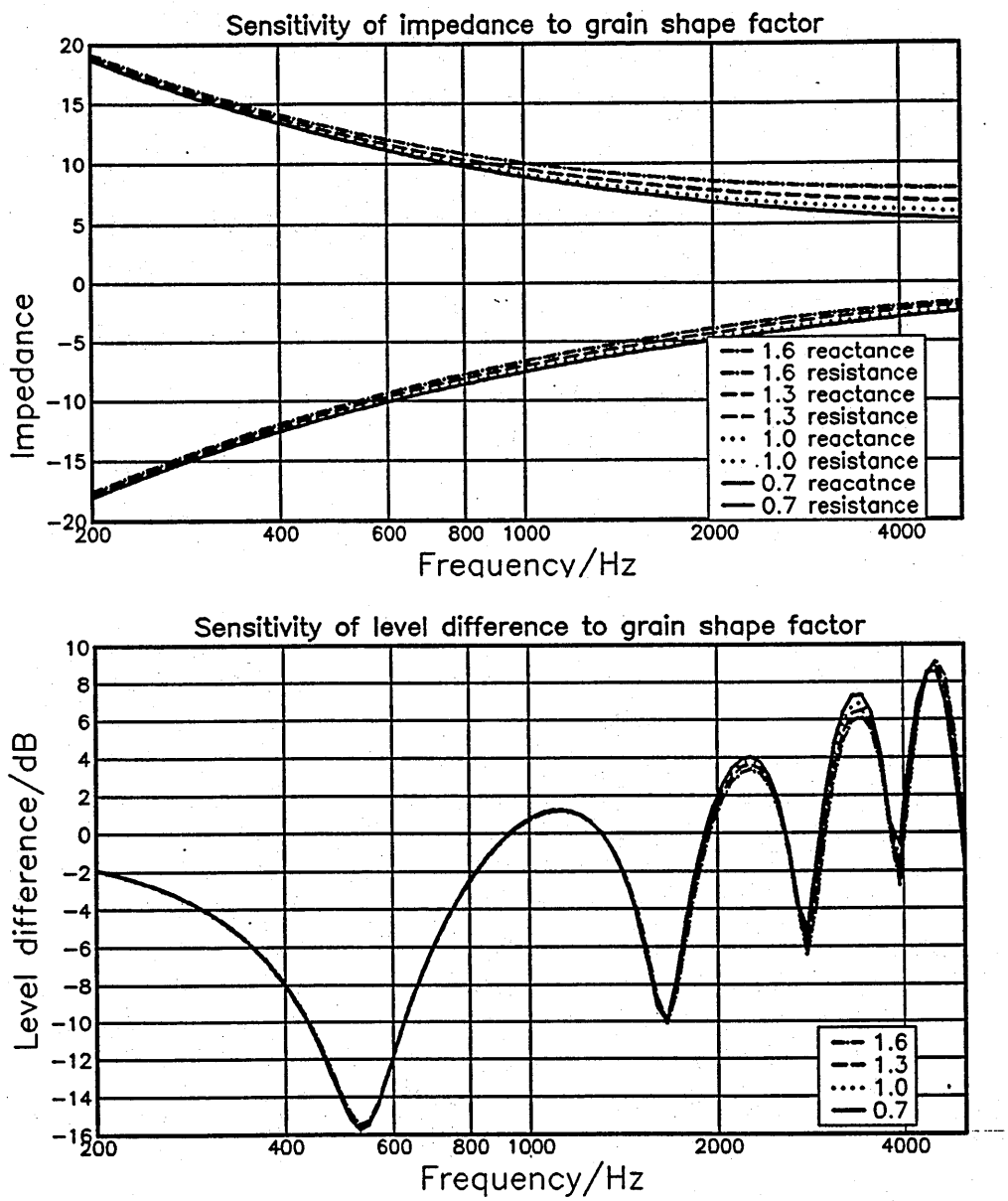


**Figure 6.39** Sensitivity of impedance and level difference to changes in grain shape factor.

The default parameters are those used to generate the impedance of surface S1B. An increase in the flow resistivity increases both the resistive and reactive parts of the impedance and the primary ground effect dip increases in magnitude with little change in the location. A similar but more marked effect is found with an increase in the pore shape factor while increasing the porosity has an inverse effect. There is little sensitivity to variation in the grain shape factor. It should be noted that this sensitivity study is for a homogeneous high flow resistivity half–space typical of grassland or soil and the effect of the parameters is dependent on the surface type (see for example the results given in table 8.6 for porous road surfaces).

The structure of the parameter level difference fitting program is given in figure 6.40. The accuracy of the result is dependent on the specified search range for the input parameters given to the routine. If this range is large it may be necessary to perform a numerical search to narrow the range prior to calling the N.A.G. routine. If the parameters of the surface have been estimated or are known from previous experience no search is required. In this case the starting parameters used are the geometric mean of the upper and lower limits specified by the user. It should be noted that with both the parameter and the direct fitting routine the input parameters and function should be scaled in accordance with the N.A.G. manual suggestion, [172]. The function and the variables to be minimized should be scaled so they are in the range (-1, +1).

Examination of the accuracy of the technique when systematic and random errors are present proceeds as before. However the output parameters of the routine which would be used to generate the impedance are studied rather than the impedance itself. The parameter variation technique is less sensitive to both random and systematic error than the direct method. Table 6.5 shows the parameters returned by the algorithm when the systematic and random errors are introduced, (reference page 196).

The default parameters are given in table 6.2. The figures in brackets are the percentage error compared to the default, a negative sign indicates the fitted value is less than the default. Most error is introduced due to

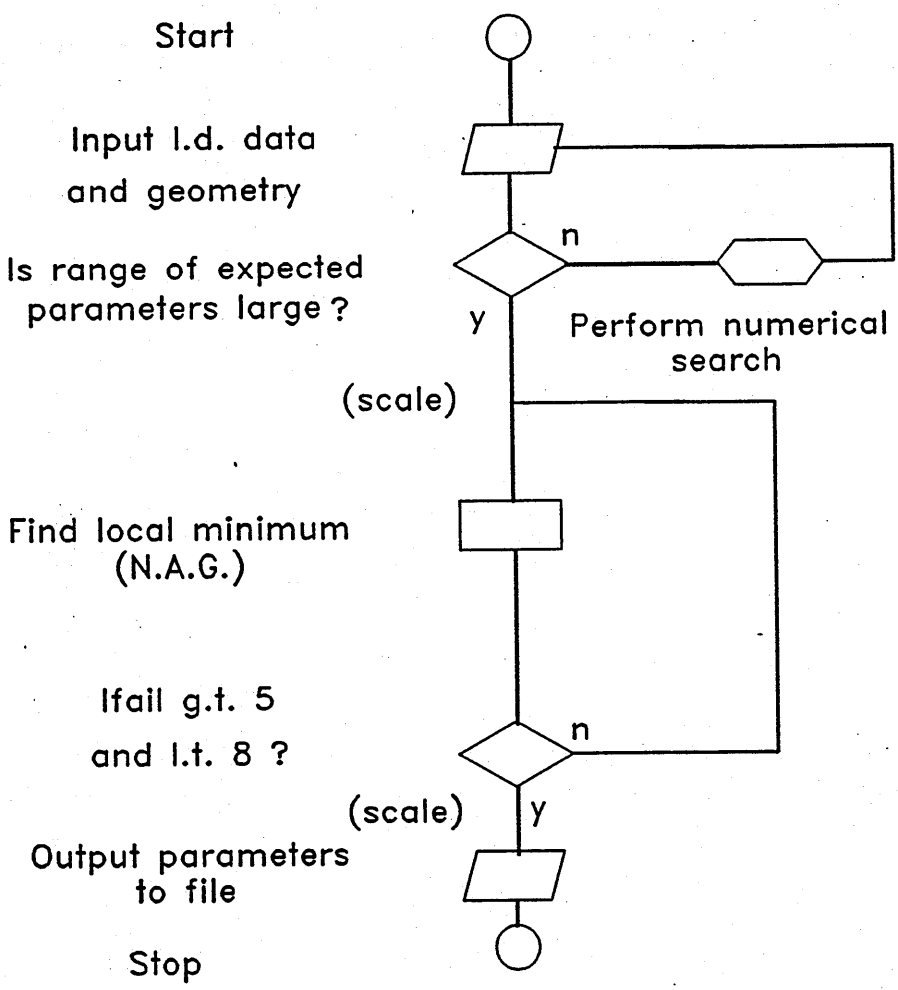


**Figure 6.40** Parameter fitting algorithm structure

| Error/Parameter | Flow resistivity | Porosity | Grain S.F. | Pore S.F |
|---|---|---|---|---|
| No error | 499519.0 | 0.35 | 1.0 | 0.55 |
| (% error) | (-0.09) | (0) | (0) | (10) |
| 1 Source height | 525138.0 | 0.37 | 0.92 | 0.46 |
| inc by 2cm | (4.78) | (5.4) | (-8.6) | (-8.6) |
| 2 source heights | 564922.0 | 0.41 | 0.86 | 0.48 |
| inc by 2cm | (11.4) | (-14.6) | (-16.2) | (-4.1) |
| 3 source heights | 565647.0 | 0.39 | 1.10 | 0.44 |
| inc by 2cm | (11.6) | (-10.2) | (9.1) | (-13.6) |
| 1 separation | 499984.0 | 0.35 | 1.0 | 0.58 |
| inc by 2cm | (0.0) | (0.0) | (0.0) | (13.7) |
| 2 separations | 499980.0 | 0.35 | 1.0 | 0.58 |
| inc by 2cm | (0.0) | (0.0) | (0.0) | (13.7) |
| 3 separations | 498391.0 | 0.348 | 1.0 | 0.58 |
| inc by 2cm | (-0.2) | (-0.57) | (0.0) | (13.7) |
| 1 lower receiver | 499999.0 | 0.35 | 1.0 | 0.5 |
| inc by 1cm | (0.0) | (0.0) | (0.0) | (0.0) |
| 2 lower receivers | 499999.0 | 0.35 | 1.0 | 0.5 |
| inc by 1cm | (0.0) | (0.0) | (0.0) | (0.0) |
| 3 lower receivers | 515867.0 | 0.34 | 0.97 | 0.51 |
| inc by 1cm | (3.1) | (-2.85) | (-3.0) | (1.96) |
| No error random | 499392.0 | 0.35 | 1.0 | 0.56 |
| noise $\simeq$1 dB | (-0.01) | (0.0) | (0.0) | (12.0) |
| Input | 200000$\rightarrow$ | 0.2$\rightarrow$ | 0.7$\rightarrow$ | 0.3$\rightarrow$ |
| parameters | 800000 | 0.5 | 1.3 | 0.7 |

**Table 6.5** Systematic and random error analysis of parameter variation technique

the inaccurate positioning of the source or upper receiver height. The pore shape factor is the parameter most likely to vary in order to account for the inaccuracies introduced into the level difference spectra. Some of the errors are introduced by the action of the N.A.G. routine and rounding errors occurring when the parameters are scaled hence the 'no error' case does not give the most accurate result. As mentioned the routine is also sensitive to the input parameters and the error will be increased if a wide range of input parameters is specified. This effect is seen in table 6.6. A wide input range often results in the location of a local minimum.

| Parameter | Flow resistivity | | Grain S. F. | | Pore S. F. | | Porosity | |
|---|---|---|---|---|---|---|---|---|
| Input range min | 300000.0 | 100000.0 | 0.2 | 0.1 | 0.7 | 0.3 | 0.3 | 0.1 |
| Input range max | 700000.0 | 900000.0 | 0.52 | 0.7 | 1.3 | 1.7 | 0.7 | 0.9 |
| Output | 500000.0 | 536420.0 | 0.35 | 0.42 | 0.95 | 1.06 | 0.5 | 0.53 |
| Error (%) | (0.0) | (7.2) | (0.0) | (-16.6) | (-5.0) | (6.0) | (0.0) | (7.2 |

**Table 6.6** Sensitivity of parameters fitting routine to input parameter range

## 6.4 Rigidly backed media.

The direct routine varies the resistance or reactance directly to obtain the normal acoustic impedance for a locally–reacting medium and may be used for either semi–infinite or rigidly backed materials. Both parameter fitting routines may be adapted to find the impedance of any rigidly backed locally reacting surface by calculating the normal acoustic impedance using:

$$Z_{rb} = Z_c coth(-\imath k_b d) \tag{6.7}$$

see [138], with $Z_c$, $k_b$ and $d$ representing the characteristic impedance, bulk propagation constant and layer depth respectively. The first two variables are calculated by the microstructural model and the layer depth is varied along with the other microstructural model parameters to give the best fit. Figure 6.41 shows the sensitivity of the impedance and level difference spectra V1 to the variation in layer depth from 0.01m to 0.05m (dotted line) in steps of 0.01m. The other parameters are the default values given in table 6.2. Surface RB1 is formed using the default parameters and a 0.03m layer depth. The level difference spectra for geometries V1 to V3 over this surface are similar to those for the semi–infinite surface.

When the three spectra are input into the rigid backed parameter fitting algorithm the parameters output are:

- Flow resistivity = 425699.0 Rayls/m (-9.5%)
- Porosity = 0.349 (0.2%)
- Grain S. F. = 0.852 (-17.3%)
- Pore S. F. = 0.055 (9.1%)
- Layer depth = 0.03m (0.0%)

The impedance produced by insertion of these parameters into the microstructural model is given in figure 6.42 along with the generation impedance RB1. The error is larger than that obtained for the comparable semi–infinite

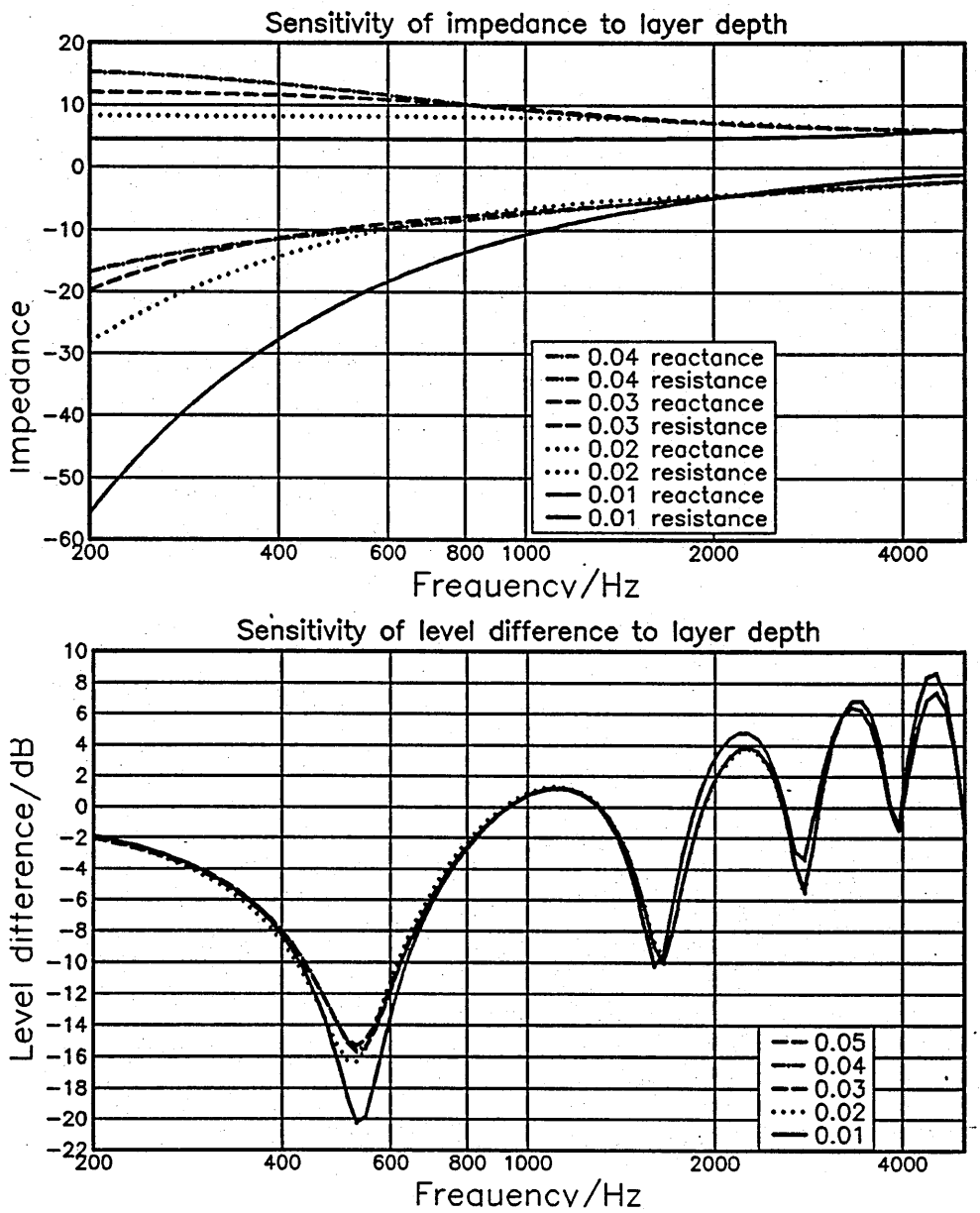


**Figure 6.41** Sensitivity of impedance and level difference to layer depth

medium ( i.e. similar flow resistivity ). This is most likely due to the addition of another variable, namely the layer depth.

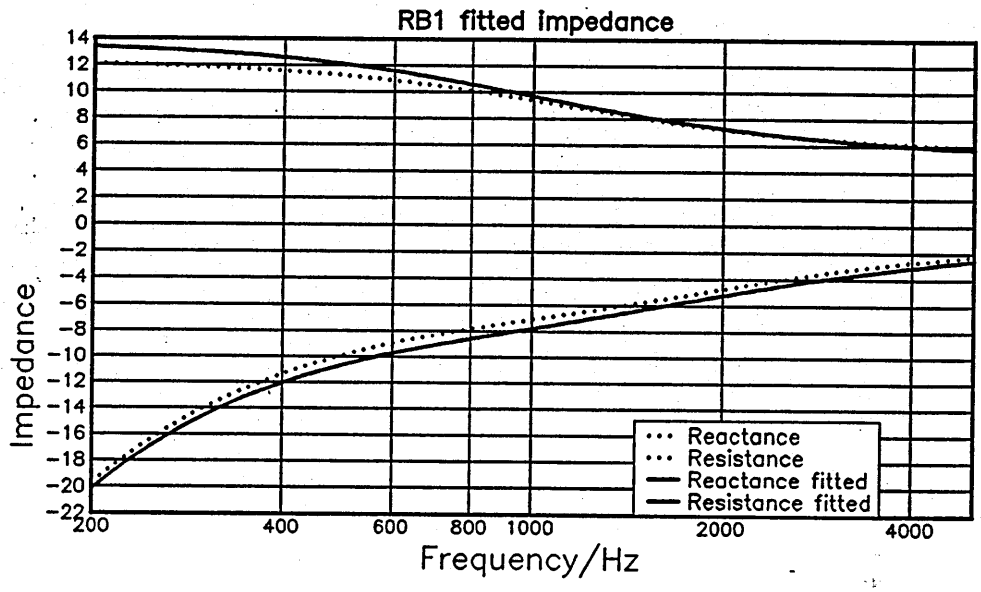


**Figure 6.42** Impedance and fitted impedance of rigidly backed locally reacting surface

## 6.5 Externally reacting media

The indirect method of impedance measurement may also be applied to externally reacting surfaces. Both the impedance and propagation constant are required to characterize the surface. Thus the same procedure is applied as before however the real and imaginary parts of the impedance and propagation constant are varied either directly or via the parameters of an impedance model. The validity of the Weyl–van der Pol form of approximation for semi–infinite and rigidly backed externally reacting surfaces has been examined in chapter 4. For the surface types and geometries examined in the thesis it has been shown to be an accurate propagation model. Surfaces S3 and S4, described in chapter 4 are used as the default surfaces for a semi infinite and rigidly backed structure respectively. In principle non–rigidly backed externally reacting media could be examined using an indirect impedance measurement technique. In practice however the number of variables required to model the upper surface and the substrate increases substantially the running time of any program. Figures 6.43 to 6.45 show the sensitivity of the level difference spectra for geometry V3 over surface S4 when the parameters of the microstructural model are varied according to the values listed in table 6.7. The sensitivity of the level difference spectra to parameter variation changes with the choice of level difference geometry and surface type.

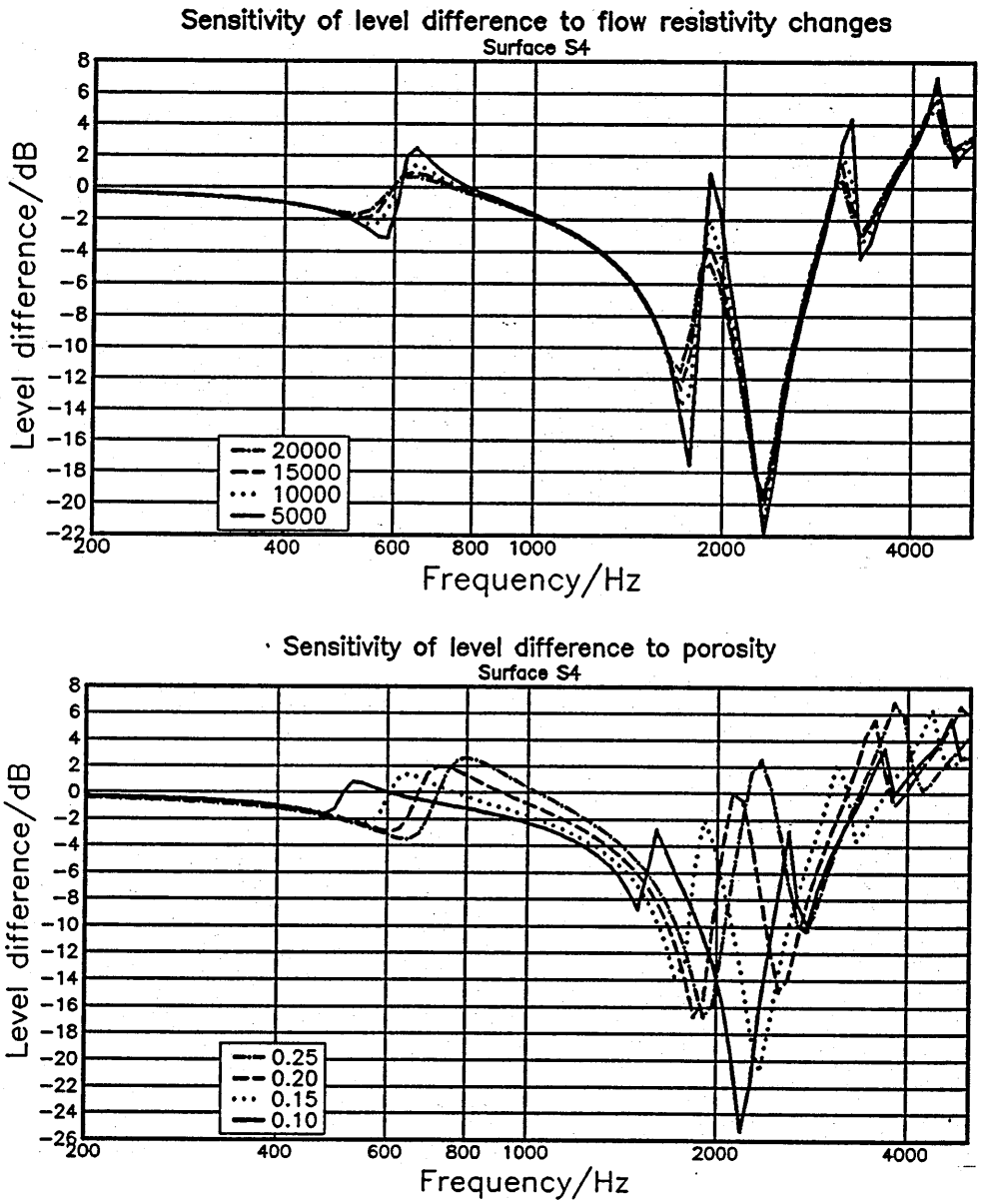


**Figure 6.43** Sensitivity of level difference spectra to variation in flow resistivity and porosity for externally reacting rigidly backed layer and geometry V3.

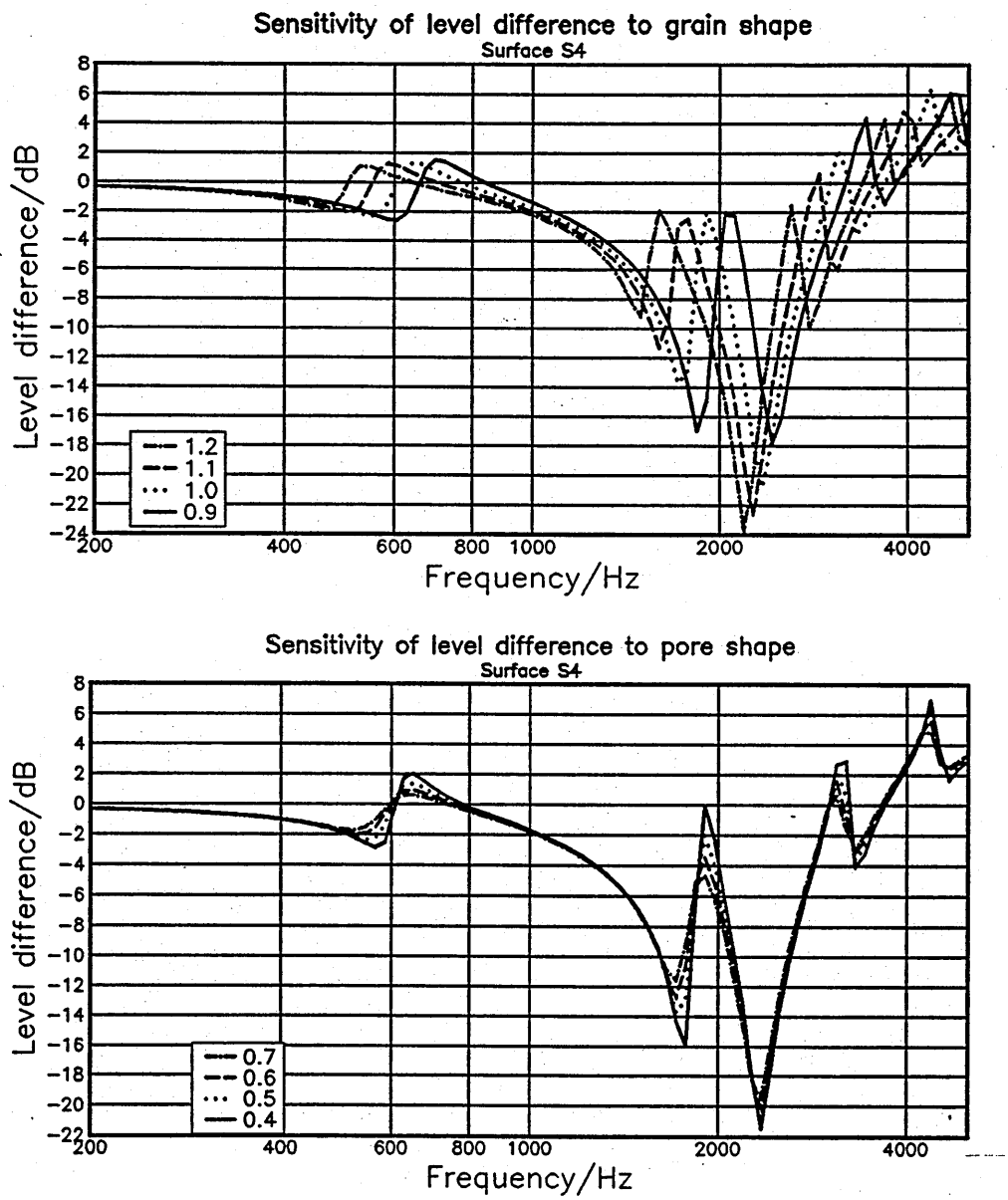


**Figure 6.44** Sensitivity of level difference spectra to variation in grain shape and pore shape factor for externally reacting rigidly backed layer and geometry V3.

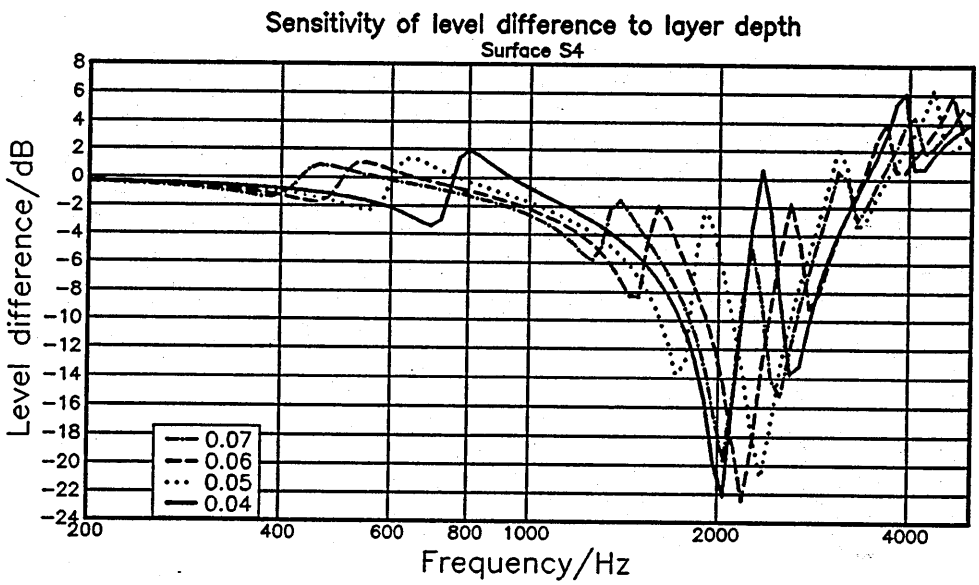


**Figure 6.45** Sensitivity of level difference spectra to variation in layer depth for externally reacting rigidly backed layer and geometry V3.

| Parameter | Default | Lowest | Highest | Increment |
|---|---|---|---|---|
| Flow resistivity | 10000 | 5000 | 20000 | 5000 |
| Porosity | 0.15 | 0.10 | 0.20 | 0.05 |
| Grain shape | 1.0 | 0.9 | 1.2 | 0.1 |
| (Tortuosity) | (6.6) | (5.5) | (9.7) | (1.2) |
| Pore shape | 0.5 | 0.4 | 0.7 | 0.1 |
| Layer depth | 0.05 | 0.04 | 0.07 | 0.01 |

**Table 6.7** Parameters for sensitivity study of externally reacting rigidly backed media.

The level difference spectrum is most sensitive in this case to porosity layer depth and grain shape. There is very little sensitivity to the pore shape parameter in level difference spectra obtained over externally reacting media. The use of a numerical search routine prior to the implementation of the N.A.G. routine is recommended to avoid large ranges in input parameters. Table 6.8 and table 6.9 shows the results of the parameter fitting routine when used with and without the initial numerical search on a semi–infinite surface. The search is best performed at the lowest point on the ground effect dip. The parameters which describe the surface considered in table 6.8 are similar to those of a deep snow surface. The ground effect dips in the level difference spectra are shallow and are not very sensitive to the variation in impedance.

The parameters of the surface examined in table 6.9 are similar to those of a porous road surface. The finite layer depth produces a much deeper primary dip and consequently the level difference technique is much more sensitive to parameter or impedance variation. This is indicated by the reduced error. The level difference amplitude spectrum used in isolation does not contain enough information about the propagation constant to make a direct fitting technique a viable method . Aa attempt to use the direct level difference fitting technique to deduce impedance of an externally reacting half–space proved unsuccessful. This is due to the increased degree of freedom introduced by two extra variables ( the real and imaginary parts of the propagation constant ).

It may be shown that the sensitivities of the externally reacting param-

eter fitting routines to systematic and random errors are similar to those of the locally reacting boundary.

| | Flow resistivity | Porosity | Grain Shape | Pore Shape | RMS Error |
|---|---|---|---|---|---|
| Maximum | 5000 | 0.95 | 7.0 | 0.3 | |
| Minimum | 1000 | 0.70 | 3.0 | 0.7 | |
| Starting | 2000 | 0.9 | 5.83 | 0.5 | |
| Result (search) | 1908.0 | 0.88 | 5.82 | 0.44 | $1.04 \times 10^{-2}$ |
| | (-4.6%) | (-2.2%) | (-0.17%) | (-12.0%) | |
| Result (no search) | 2707.0 | 0.87 | 4.59 | 0.60 | $1.06 \times 10^{-2}$ |
| | (26.1%) | (-3.3%) | (-21.2%) | (20%) | |
| Maximum | 7000 | 1.0 | 9.0 | 0.9 | |
| Minimum | 1000 | 0.50 | 1.0 | 0.1 | |
| Result (search) | 1900.0 | 0.87 | 5.78 | 0.48 | $1.04 \times 10^{-2}$ |
| | (-5.0%) | (-3.3%) | (-0.85%) | (-4.0%) | |
| Result (no search) | 3300.0 | 0.9 | 6.7 | 0.33 | $1.04 \times 10^{-2}$ |
| | (65%) | (0%) | (-14.9%) | (34%) | |

**Table 6.8** Results of parameter fitting technique for externally reacting semi infinite surface

| | Flow resistivity | Porosity | Grain Shape | Pore Shape | Layer Depth | RMS Error |
|---|---|---|---|---|---|---|
| Maximum | 12000 | 0.35 | 1.2 | 0.7 | 0.07 | |
| Minimum | 8000 | 0.05 | 0.8 | 0.3 | 0.03 | |
| Starting | 10000 | 0.15 | 1.03 | 0.5 | 0.05 | |
| Result (search) | 10200.0 | 0.145 | 1.04 | 0.48 | 0.05 | $1.02 \times 10^{-2}$ |
| | (2.0%) | (-3.3%) | (4.0%) | (-4.0%) | (-0.0%) | |
| Result (no search) | 10800.0 | 0.134 | 1.1 | 0.45 | 0.048 | $1.03 \times 10^{-2}$ |
| | (8.0%) | (-10.6%) | (10.0%) | (-10.0%) | (-4.0%) | |
| Maximum | 14000 | 0.55 | 1.4 | 0.9 | 0.09 | |
| Minimum | 6000 | 0.05 | 0.6 | 0.1 | 0.01 | |
| Result (search) | 10500.0 | 0.145 | 1.07 | 0.43 | 0.048 | $1.045 \times 10^{-2}$ |
| | (5.0%) | (-3.3%) | (7.0%) | (-14.0%) | (-4.0%) | |
| Result (no search) | 10950.0 | 0.134 | 1.12 | 0.45 | 0.043 | $1.06 \times 10^{-2}$ |
| | (9.5%) | (-10.6%) | (12.0%) | (-10.0%) | (-14.0%) | |

**Table 6.9** Results of parameter fitting technique for externally reacting rigidly backed surface

## 6.6 The use of phase in the indirect method of impedance measurement

The magnitude and phase of the level difference spectra may be measured and used to deduce the impedance rather than the magnitude of several spectra. Daigle and Stinson [21] concluded that the modulus of a signal rather than the phase was less likely to be affected by unwanted reflections. A single reflection with a signal strength 20 dB less than that of the surface reflection still contributed 10% to total the phase of the measured field. Jiří and Kříž [200], [201] rejected the use of phase as it is highly sensitive to atmospheric fluctuations and is difficult to measure in practice. The magnitude and phase of the three level difference spectra used in the semi–infinite locally reacting simulation were used as the input to the minimization algorithm. Table 6.10 shows the error introduced into the results of the parameter variation technique due to systematic and random sources of error.

Figures 6.46 to 6.51 show the results of using phase measurements in the direct fitting case for geometry V1 over a high flow resistivity surface. The results are more robust to the introduction of systematic errors but are poor when a random noise distorts the input spectra.

| Error/Parameter | Flow resistivity | Porosity | Grain S.F. | Pore S.F |
|---|---|---|---|---|
| No error | 513696.0 | 0.35 | 1.02 | 0.50 |
| (% error) | (2.73) | (-0.0) | (2.0) | (0.0) |
| 1 Source height | 500000.0 | 0.35 | 1.00 | 0.5 |
| inc by 2cm | (0.0) | (0.0) | (0.0) | (0.0) |
| 2 source heights | 5000000.0 | 0.3752 | 1.0 | 0.50 |
| inc by 2cm | (0.0) | (7.14) | (0.0) | (0.0) |
| 3 source heights | 315384.0 | 0.464 | 1.29 | 0.66 |
| inc by 2cm | (-36.9) | (32.5) | (29.0) | (32.0) |
| 1 separation | 5531288.0 | 0.33 | 0.95 | 0.47 |
| inc by 2cm | (6.25) | (-5.71) | (-5.0) | (-6.0) |
| 2 separations | 638289.0 | 0.21 | 0.77 | 0.30 |
| inc by 2cm | (27.56) | (-58.0) | (-23.0) | (-40.0) |
| 3 separations | 684615.0 | 0.23 | 0.700 | 0.34 |
| inc by 2cm | (-36.9) | (-42.8) | (-30.0) | (-32.0) |
| 1 lower receiver | 500000.0 | 0.35 | 1.00 | 0.5 |
| inc by 1cm | (0.0) | (0.0) | (0.0) | (0.0) |
| 2 lower receivers | 492403.0 | 0.34 | 1.0 | 0.49 |
| inc by 1cm | (-1.51) | (-2.8 | (0.0) | (-2.0) |
| 3 lower receivers | 487079.0 | 0.34 | 1.02 | 0.48 |
| inc by 1cm | (-2.5) | (-2.8) | (2.0) | (-4.0) |
| No error random | 535311.0 | 0.29 | 1.3 | 0.45 |
| noise $\simeq$1 dB | (7.0) | (-14.5) | (30.0) | (-10.0) |
| Input | 200000$\rightarrow$ | 0.2$\rightarrow$ | 0.7$\rightarrow$ | 0.3$\rightarrow$ |
| parameters | 800000 | 0.5 | 1.3 | 0.7 |

**Table 6.10** Systematic and random error analysis of parameter variation technique incorporating phase measurements

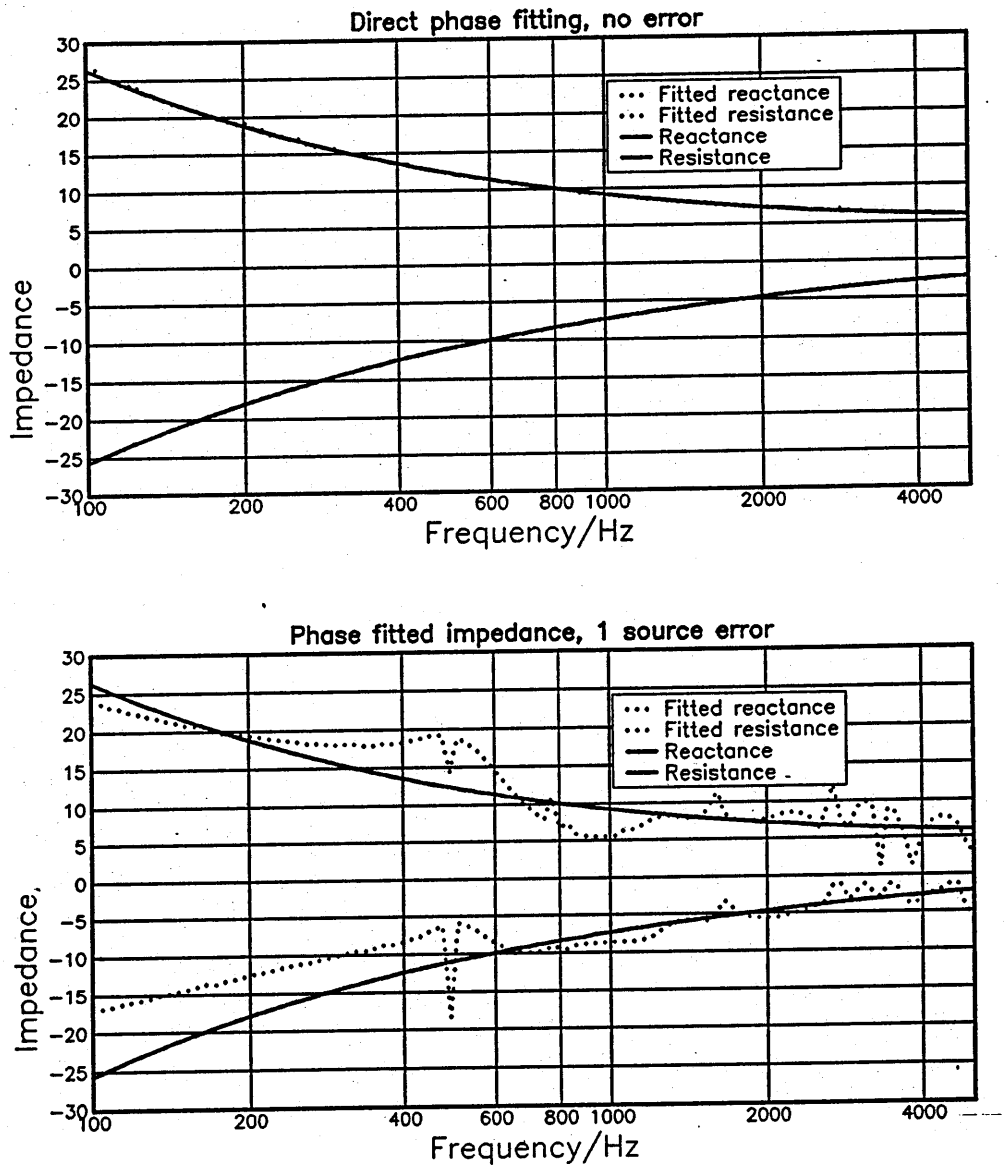


**Figure 6.46** Error analysis for direct technique incorporating phase measurements. No errors and one source error.

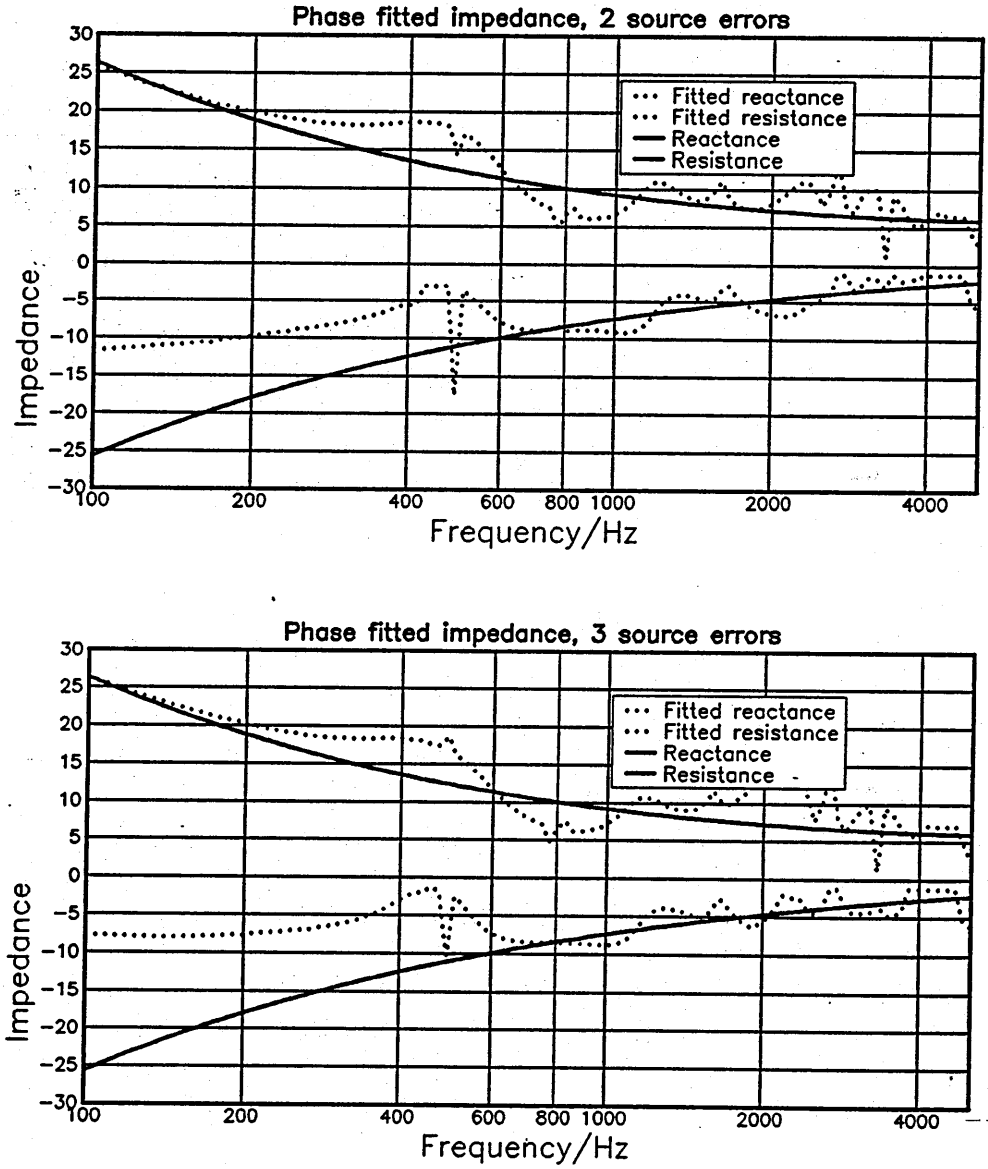


**Figure 6.47** Error analysis for direct technique incorporating phase measurements. Two and three source errors.

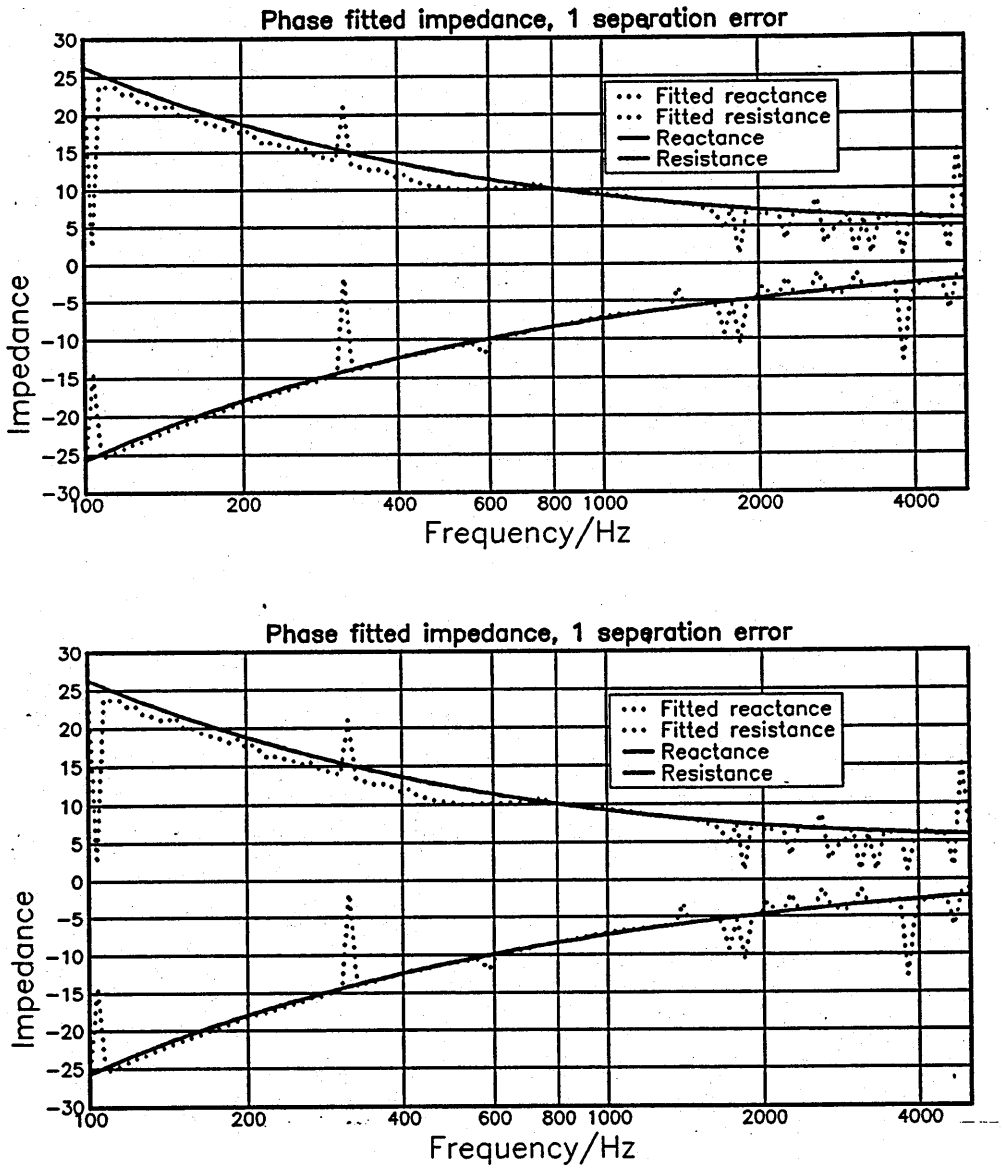


**Figure 6.48** Error analysis for direct technique incorporating phase measurements. One and two separation errors.

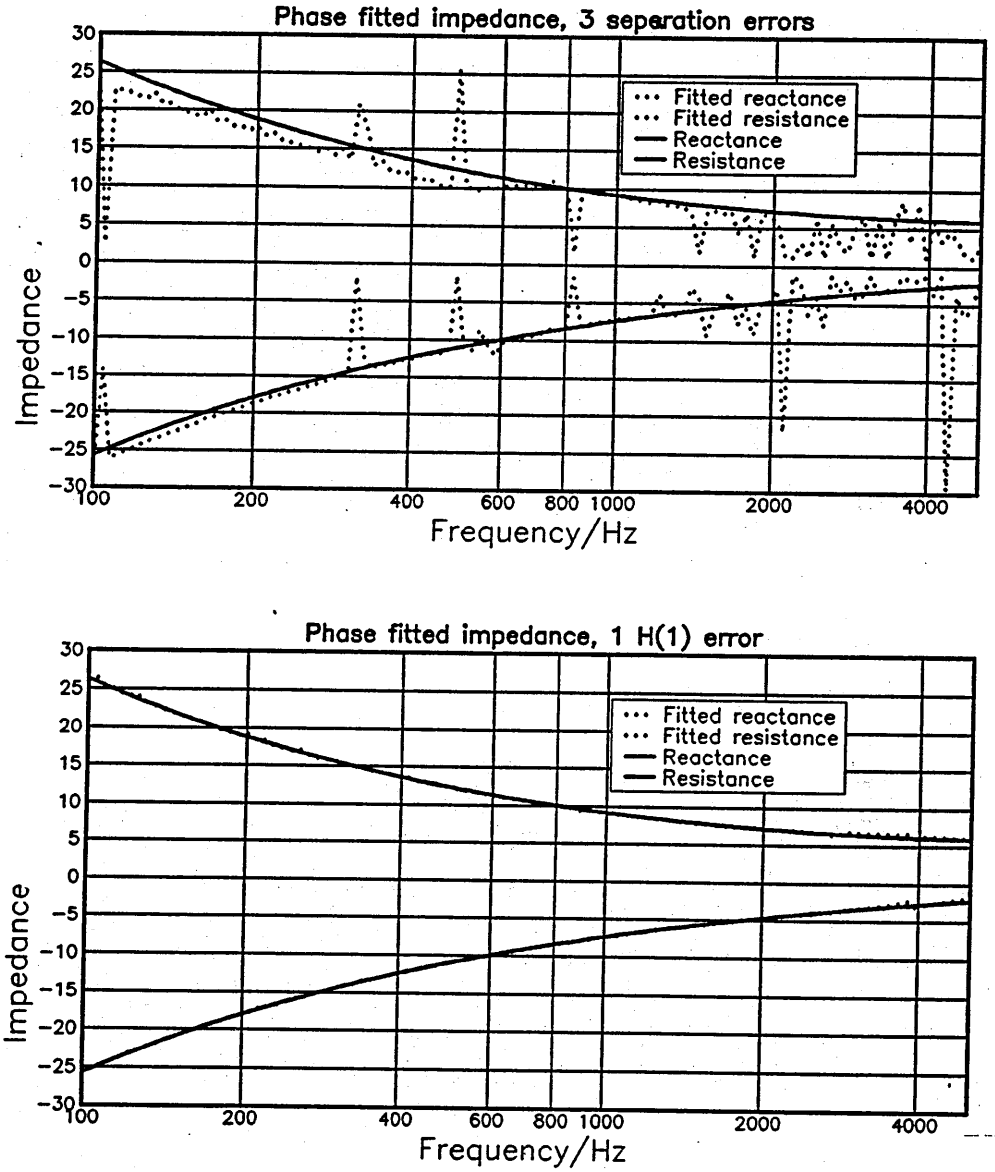


**Figure 6.49** Error analysis for direct technique incorporating phase measurements. Three separation errors and one lower receiver error.

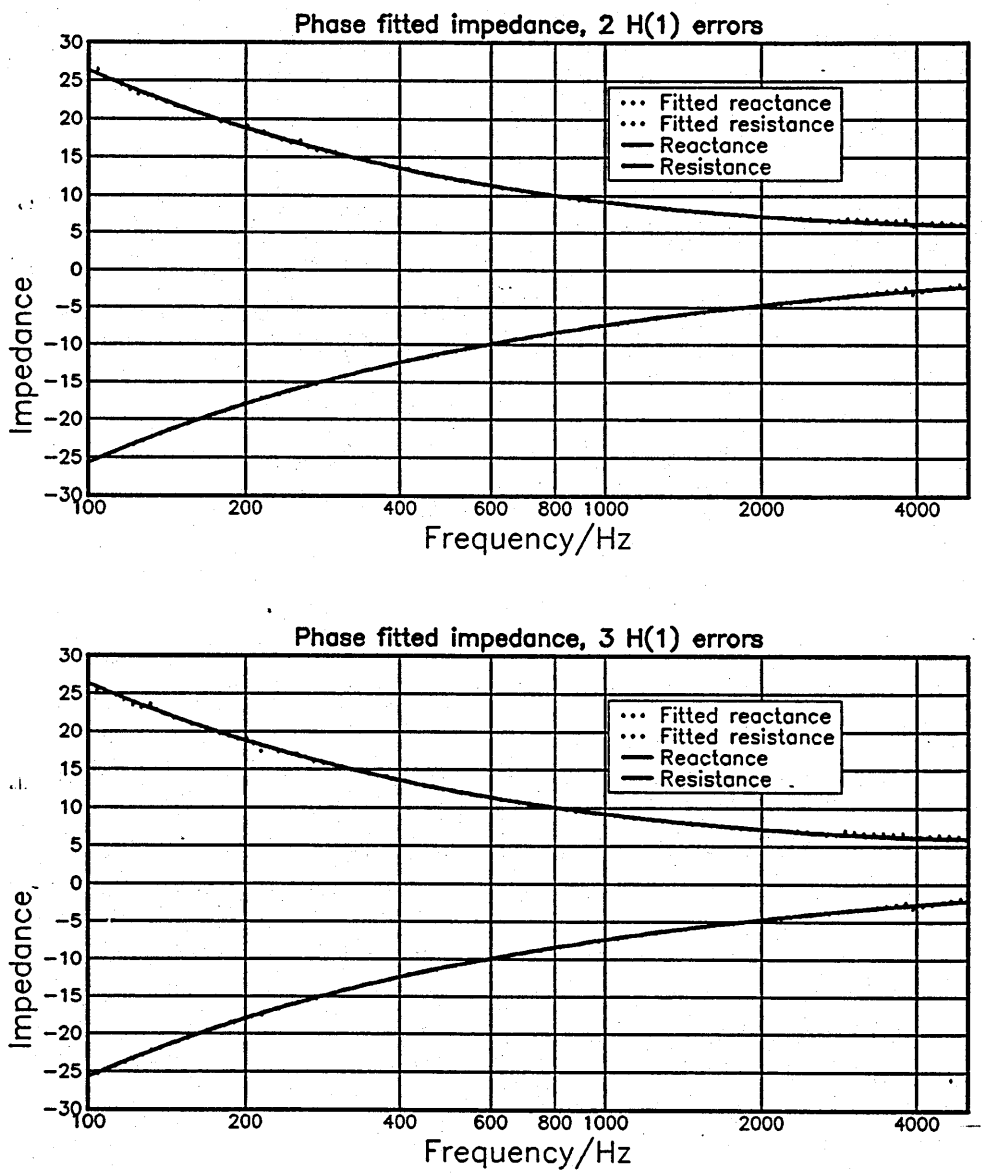


**Figure 6.50** Error analysis for direct technique incorporating phase measurements. Two and three lower receiver errors.

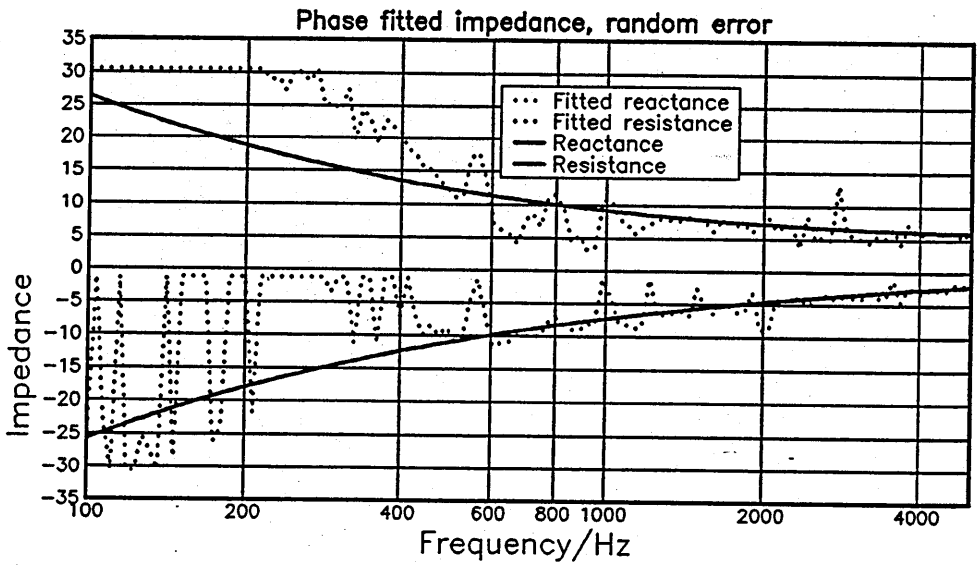


**Figure 6.51** Error analysis for direct technique incorporating phase measurements. Error due to random noise.

# Chapter 7

# Experimental comparison of indirect and pulse techniques of impedance measurement

In this chapter the surface impedances of a wide variety of materials are evaluated and compared using the indirect ( both direct and parameter fitting ) and impulse techniques. The materials include:

1. Locally reacting semi–infinite media; grass covered sportsfield, silt, clay and a sandy loam soil.
2. Locally reacting rigidly backed medium; artificial grassland
3. Externally reacting semi–infinite media; pea gravel, snow
4. Externally reacting rigidly backed media; pervious macadam surfaces, fibre glass and polyurethane foam.

### 7.0.1 Description of surfaces

Locally reacting semi–infinite media

The grass covered sportsfield consists of a compact clay base with a cover of regularly mown mixed grasses. At the time of the experimental measurements the grass was about 4cm high and the underlying soil was dry. The silt, clay and sandy loam soils were semi–natural. The soils were air dried and passed through a 6mm hole size sieve into plywood boxes

of dimensions 2m × 2m × 0.5m. The boxes which rested outdoors on a compact sandy loam soil were filled with the loose soil to prevent unwanted reflections from the edges. This sieving process ensured that the material was fairly homogeneous.

Locally reacting rigidly backed medium

The artificial grass surface consists of clumps of plastic tufts ten millimeters long and a two to three millimeters wide embedded in a six millimeter deep rubber backing, see photograph in appendix L. To ensure a rigid termination this material was closely fixed to a series of abutting concrete slabs each of dimension 0.95m × 0.60m × 0.045m using a double sided adhesive tape. The measurements were taken in an anechoic chamber.

Externally reacting semi–infinite media

A pea gravel with a nominal grain diameter of $\frac{3}{8}$ inch supplied by Erith Building Supplies of Bletchley, Milton Keynes was contained in a lined earth pit of dimension 2.5m × 4.0m × 1.3m situated outdoors. As with the soils the theoretical analysis presumes that the container is deep enough to prevent the floor of the container having any acoustical effect. Consideration of the results however indicates that this may not have been the case.

The level difference measurements over a snow field were performed at the Keeweenaw research centre, Michigan. The snow layer which was up to 1m thick was presumed deep enough and sufficiently homogeneous to act as a semi-infinite media. It is possible that the snow had a thin surface crust with a porosity less then that of the sub-surface material.

Externally reacting rigidly backed media

The two surfaces considered are porous macadam road surfaces approximately 50 millimeters deep located on a concrete base. Details of the surfaces are found in chapter 8. This data was collected from pilot experiments on the pervious 'macadam type of surface. More detailed and exhaustive measurements and results for such surfaces are given in chapter 8

The remaining externally reacting layers consisted of a Pilkington S300 crown fibreglass surface of a 1.2m × 0.9m × 0.05m fibreglass slabs fastened onto two abutting concrete slabs and a polyurethane foam.

Level difference spectra were collected for several geometries above each of the surfaces, the sites were chosen to avoid the effects of impedance discontinuities found near the edge of the sample. The level difference spectra along with the appropriate geometries are then used as the input to the indirect impedance method algorithms, figures 6.40 and 6.25. The resulting impedance values compared to impedance data obtained by the impulse technique described by Cramond and Don in [98] and in chapter 2. The angle of incidence of the impulsive source was chosen to be similar to that obtaining in the level difference geometry during measurements above the externally reacting surfaces. The impedance of the artificial grassland was measured using an impedance tube because of the reduced sample size.

The impulsive method is unreliable at low frequencies due to the poor frequency content of the impulsive source. Thus as a further check the flow resistivity and porosity of the materials were measured. In some cases the layer depth of the material and the tortuosity are determined. The techniques used to measure these parameters are explained in chapter 8. A final check has been made by varying the parameters of the microstructural model to fit the impedance data from impulsive measurements, [29].

The first of each of the following sets of graphs show the impedances of each surface deduced from the parameters obtained by 1) the parameter fitting indirect method; 2) the direct ( impedance ) fitting method and from 3) impulse measurements. The second graph in each set shows the impedance measured using the Cramond and Don impulse technique and the impedance obtained by fitting parameters of the microstructural model directly to the impedance data. For the later deductions the least squares procedure used by Buser [29] for snow impedance data has been used. The next three or four graphs in each set shows raw the level difference spectra data and the theoretical curves obtained as best fit from the parameter fitting and the direct fitting methods. The tables give summaries of the microstructural model parameters deduced from the parameter fitting of level difference spectra; parameter fitting of impedance and by direct non-acoustical measurements. Also in tabulated form is the least root mean sum

of squares (RMS) error. This is the average deviation between the measured data and the fitted curve. It is calculated using;

$$RMS = \sqrt{\sum_{n-1}^{N} \frac{(M_n - P_n)^2}{N}}$$

where $N$ is the number of frequency points on the curve,

$M_n$ is the data measured at the $n^{th}$ point and

$P_n$ is the predicted value at the $n^{th}$ point.

The RMS error is an indication of the accuracy of the fitted curve, the smaller the value the better the fit.

## 7.1 Surfaces modelled as locally reacting semi-infinite media

### 7.1.1 Grass covered sportsfield

| Parameter | Level difference fitted | Impedance fitted | Measured (non-acoustically) |
|---|---|---|---|
| Flow resistivity | 300000 | 110248 | 390000 |
| Porosity | 0.48 | 0.51 | 0.40 |
| Grain shape | 0.6 | 0.64 | |
| Pore shape | 0.4 | 0.43 | |
| Layer depth | N/A | N/A | N/A |

**Table 7.1** Deduced microstructural model parameters for sportsground

| Input data | Level difference data | | Impedance data | |
|---|---|---|---|---|
| Geometry (sportsfield) | RMS error parameter fit | RMS error direct fit | RMS error resistance fit | RMS error reactance fit |
| 1 | 1.92 | 2.23 | | |
| 2 | 1.04 | 1.56 | | |
| 3 | 2.01 | 2.21 | | |
| Impedance | | | 2.42 | 1.41 |

**Table 7.2** RMS errors for sportsfield fitted level difference

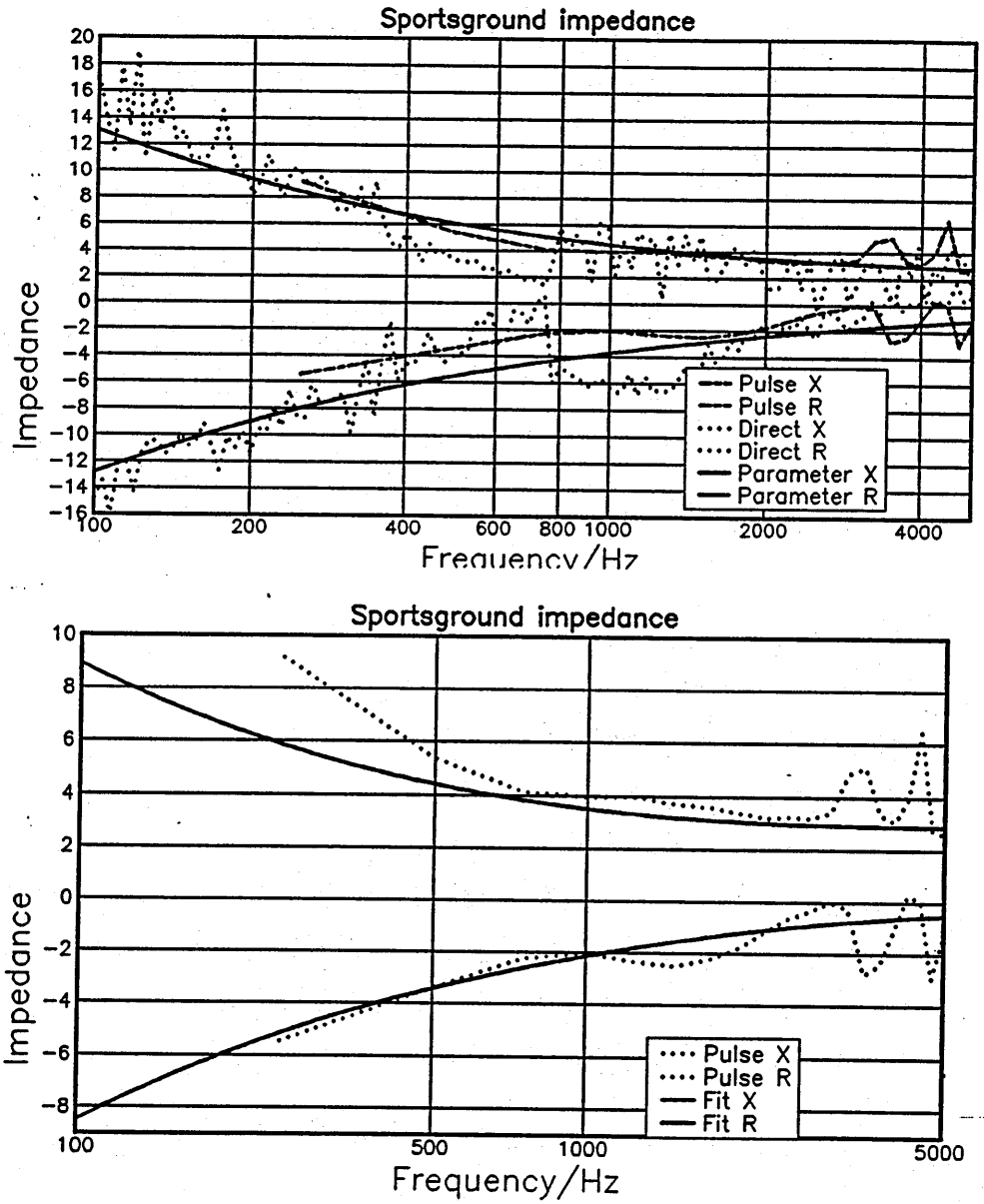


**Figure 7.1** Impedance of grass covered sportsfield

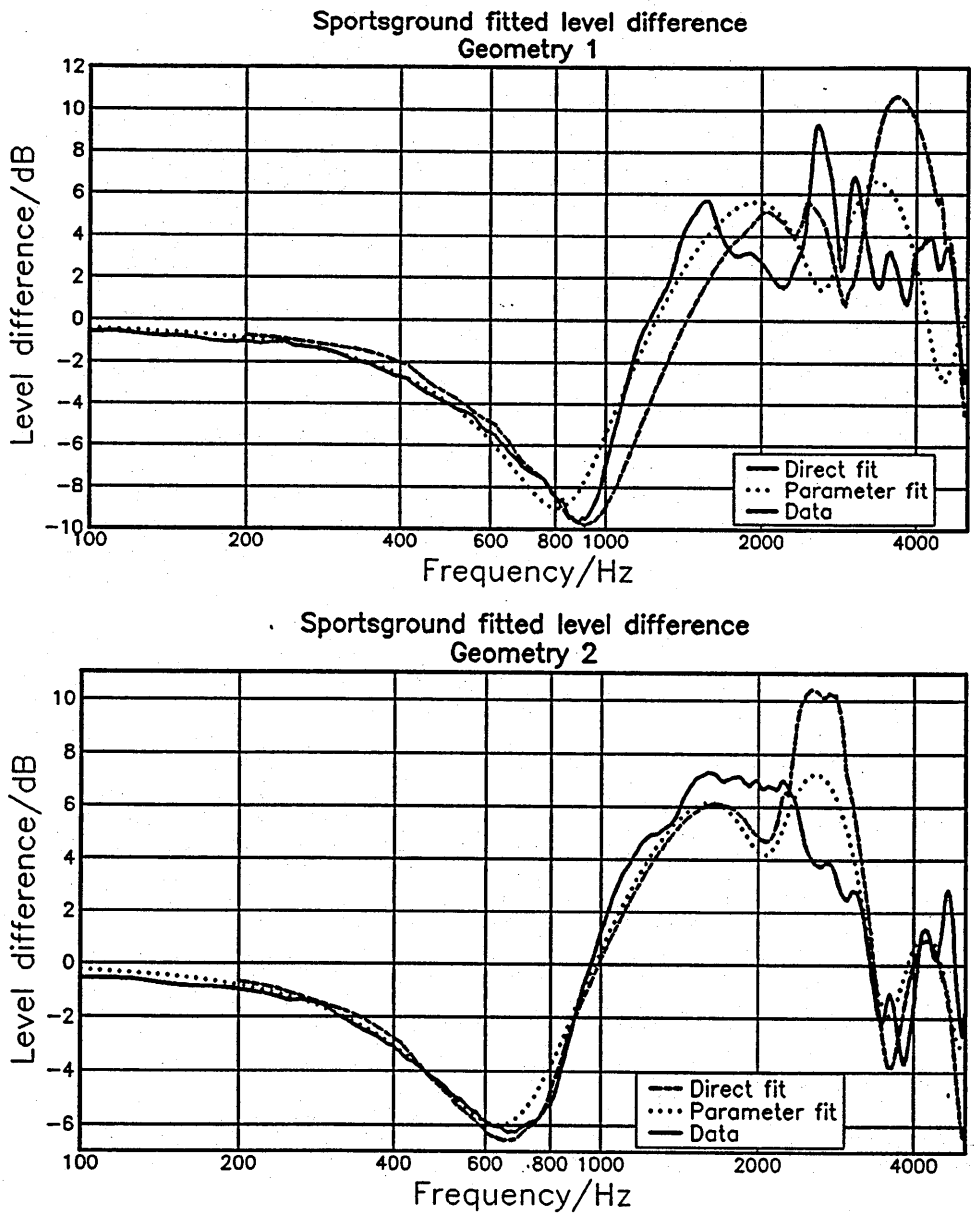


**Figure 7.2** Fitted level difference spectra for grass covered sportsfield, geometries 1 and 2.

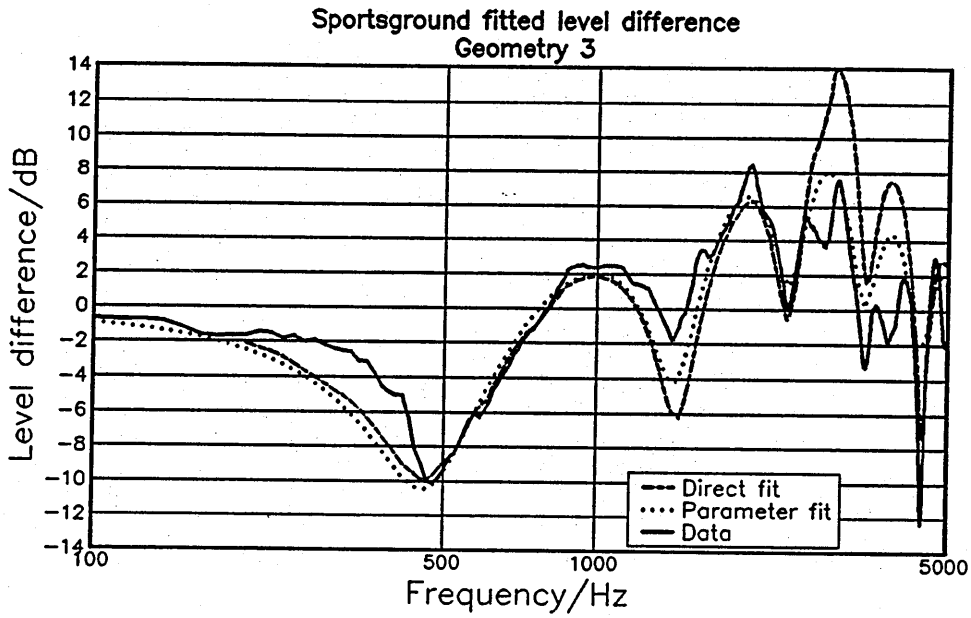


**Figure 7.3** Fitted level difference spectra for grass covered sportsfield, geometry 3.

### 7.1.2 Silt soil

| Parameter | Level difference fitted | Impedance fitted | Measured (non–acoustically) |
|---|---|---|---|
| Flow resistivity | 323000 | 300000 | 321810 |
| Porosity | 0.60 | 0.60 | 0.57 |
| Grain shape | 1.53 | 1.5 | |
| Pore shape | 0.79 | 0.59 | |
| Layer depth | N/A | N/A | N/A |

**Table 7.3** Deduced microstructural model parameters for silt soil

| Input data | Level difference data | | Impedance data | |
|---|---|---|---|---|
| Geometry (silt soil) | RMS error parameter fit | RMS error direct fit | RMS error resistance fit | RMS error reactance fit |
| 1 | 2.85 | 2.92 | | |
| 2 | 1.75 | 1.83 | | |
| 3 | 3.01 | 3.21 | | |
| Impedance | | | 0.73 | 0.91 |

**Table 7.4** RMS errors for silt soil fitted level difference

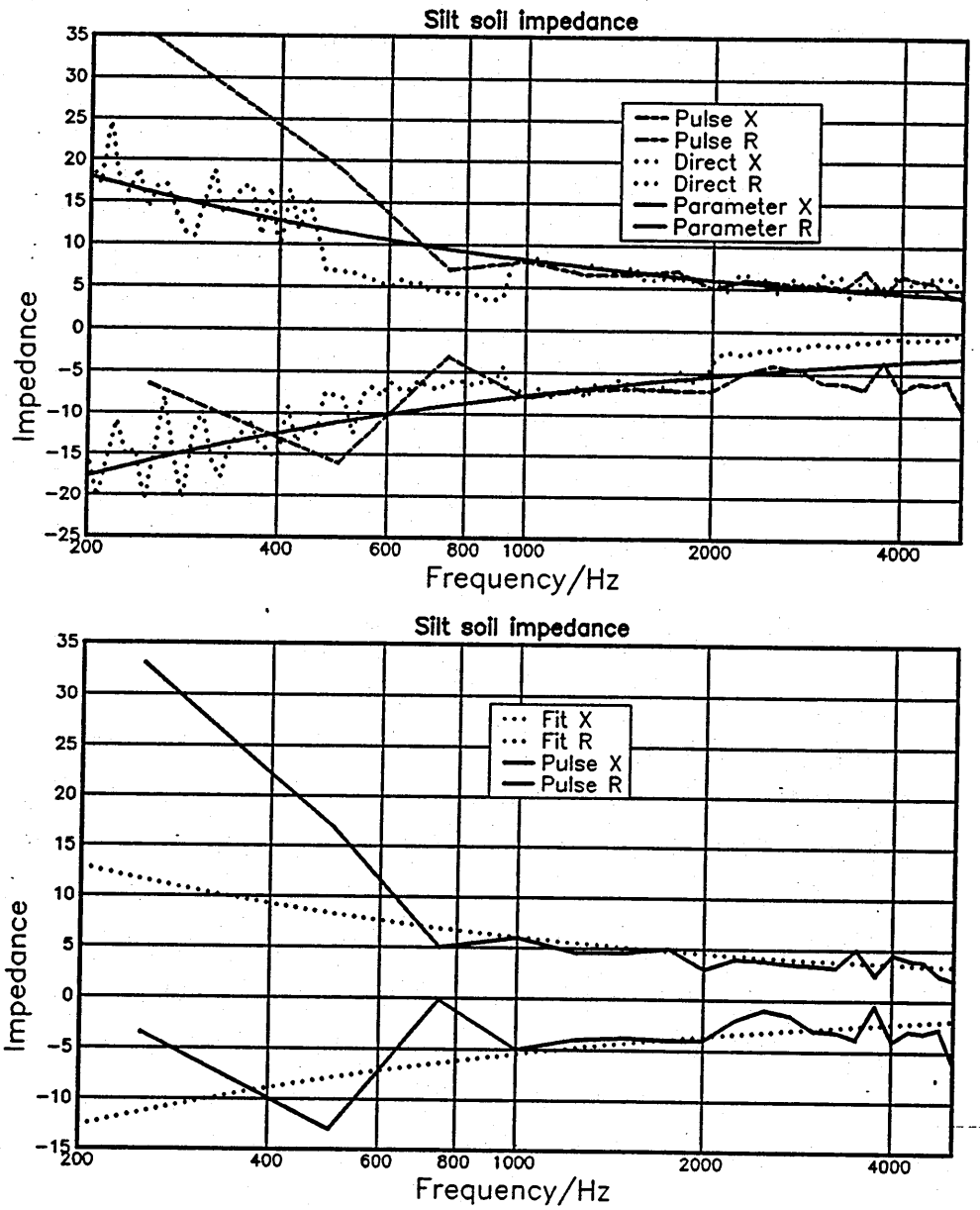


Figure 7.4 Impedance of silt soil

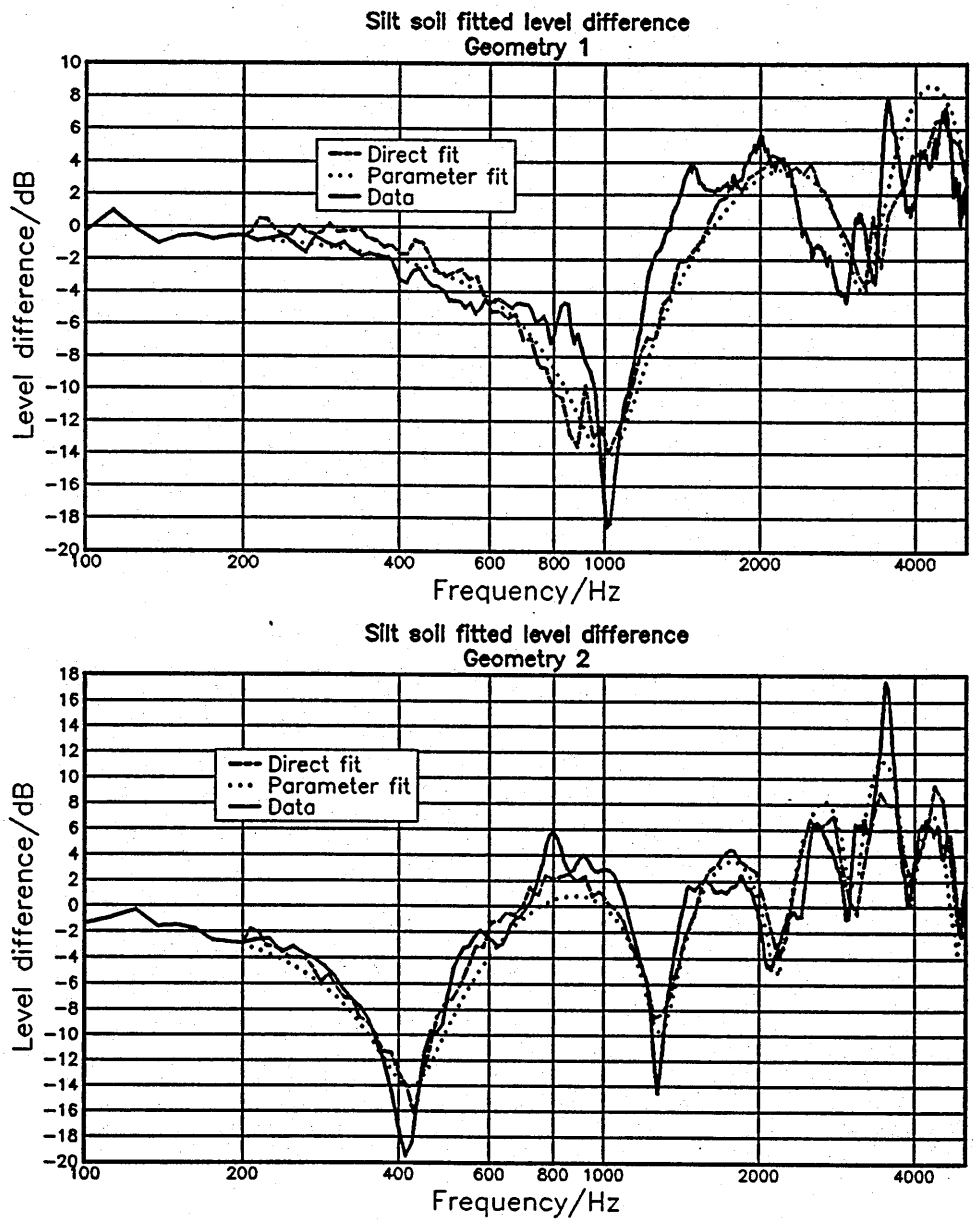


**Figure 7.5** Fitted level difference spectra for silt soil, geometries 1 and 2.

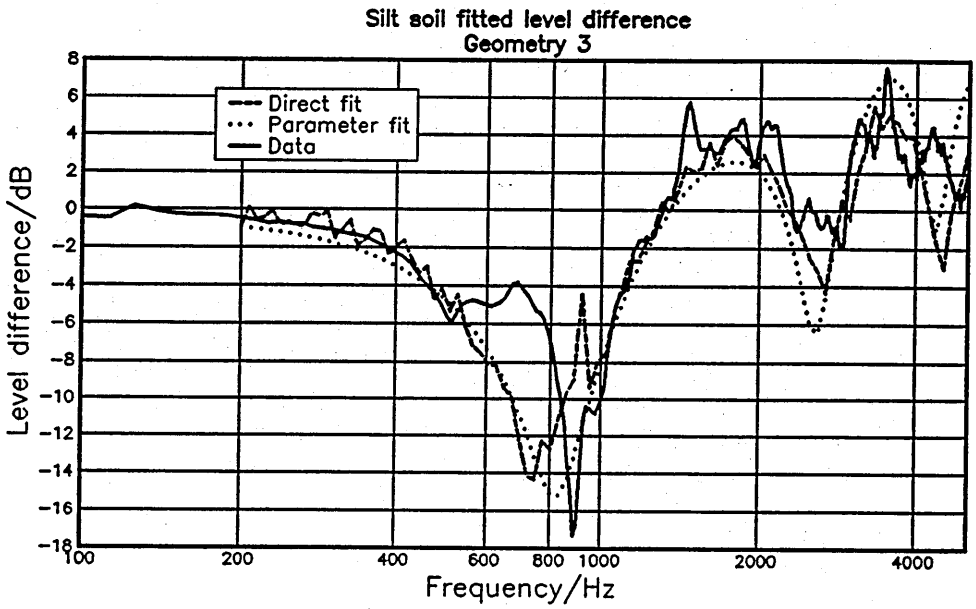


**Figure 7.6** Fitted level difference spectra for silt soil, geometry 3.

### 7.1.3 Clay soil

| Parameter | Level difference fitted | Impedance fitted | Measured (non–acoustically) |
|---|---|---|---|
| Flow resistivity | 9600 | 17800 | 10130 |
| Porosity | 0.58 | 0.58 | 0.50 |
| Grain shape | 1.0 | 1.10 | |
| Pore shape | 0.32 | 0.24 | |
| Layer depth | N/A | N/A | N/A |

**Table 7.5** Deduced microstructural model parameters for clay soil

| Input data | Level difference data | | Impedance data | |
|---|---|---|---|---|
| Geometry (clay soil) | RMS error parameter fit | RMS error direct fit | RMS error resistance fit | RMS error reactance fit |
| 1 | 1.65 | 1.43 | | |
| 2 | 1.35 | 1.29 | | |
| 3 | 1.95 | 1.72 | | |
| Impedance | | | 3.3 | 2.1 |

**Table 7.6** RMS errors for clay soil fitted level difference

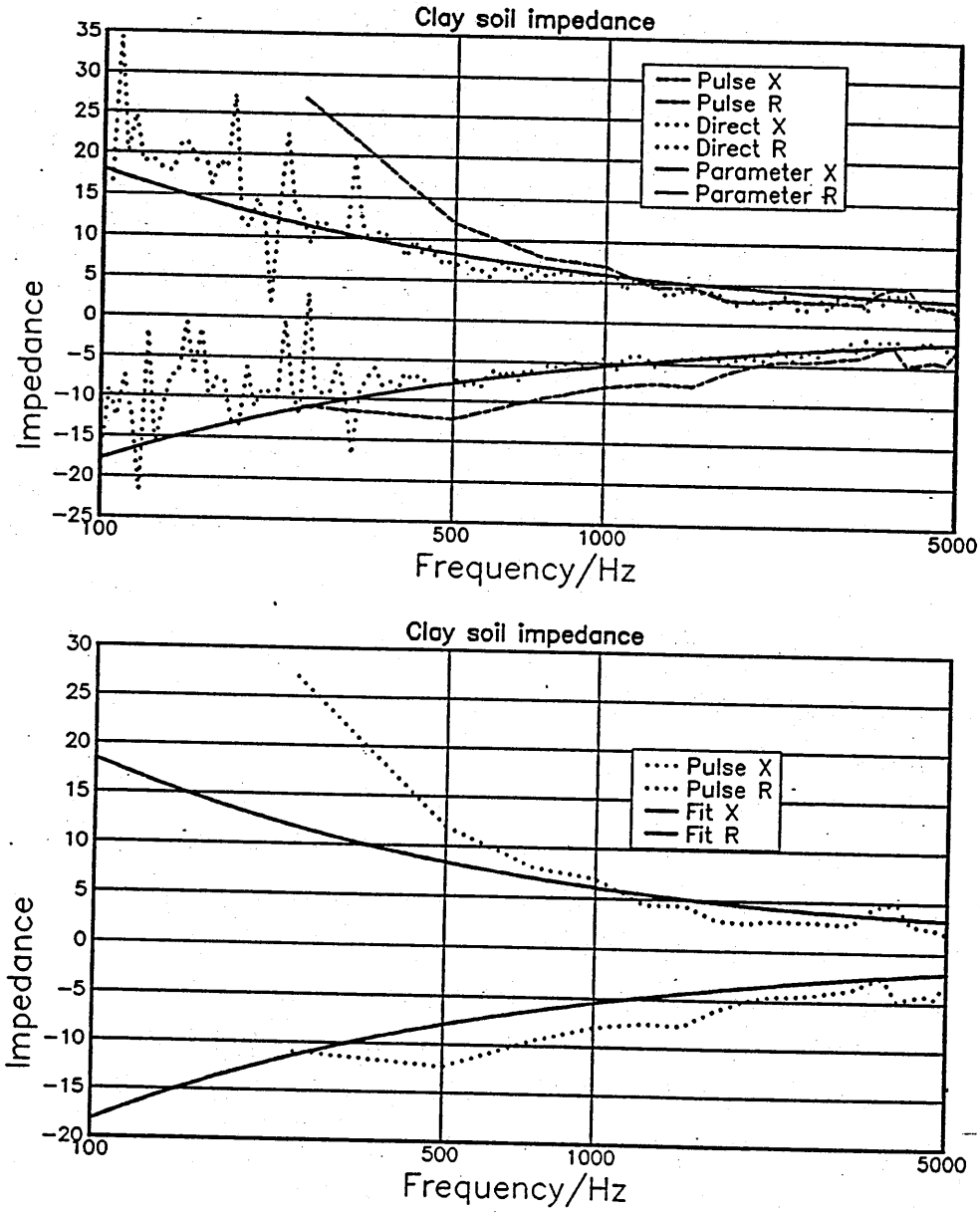


Figure 7.7 Impedance of clay soil.

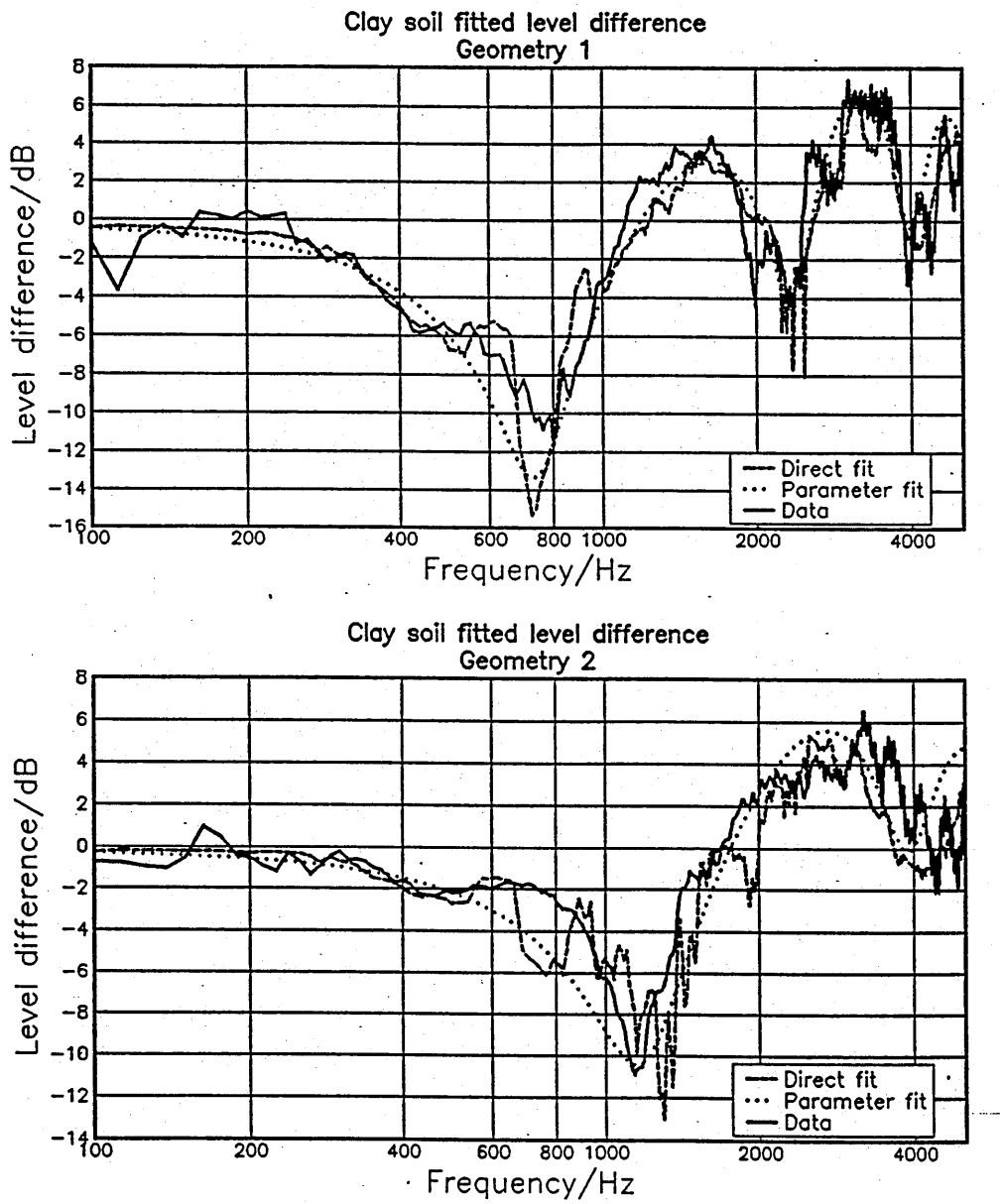


**Figure 7.8** Fitted level difference spectra for clay soil, geometries 1 and 2.

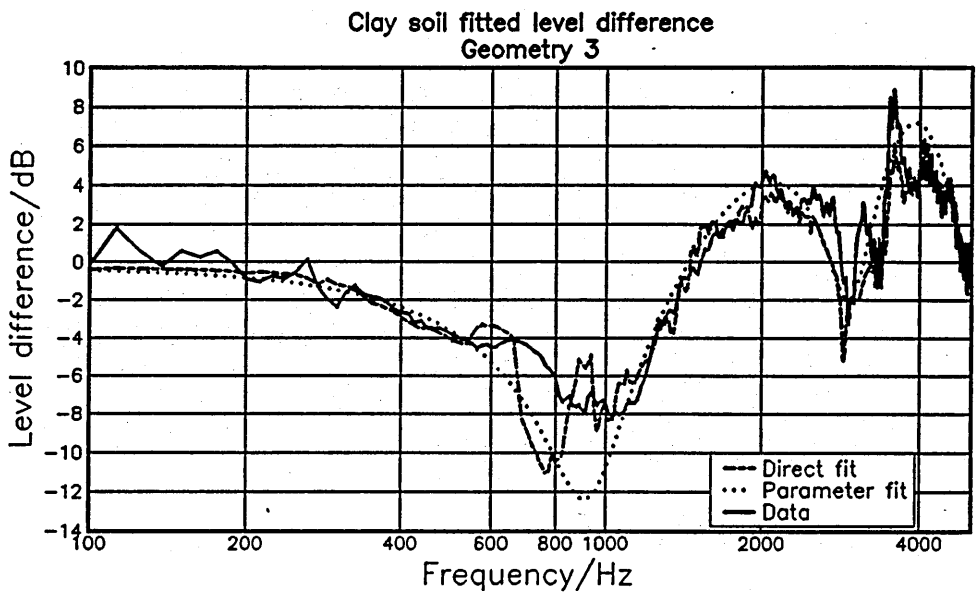


**Figure 7.9** Fitted level difference spectra for clay soil, geometry 3.

### 7.1.4 Sandy loam

| Parameter | Level difference fitted | Impedance fitted | Measured (non–acoustically) |
|---|---|---|---|
| Flow resistivity | 337100 | 100100 | 338250 |
| Porosity | 0.49 | 0.65 | 0.45 |
| Grain shape | 1.0 | 2.0 | |
| Pore shape | 0.57 | 0.20 | |
| Layer depth | N/A | N/A | N/A |

**Table 7.7** Deduced microstructural model parameters for sand loam

| Input data | Level difference data | | Impedance data | |
|---|---|---|---|---|
| Geometry (sandy loam) | RMS error parameter fit | RMS error direct fit | RMS error resistance fit | RMS error reactance fit |
| 1 | 1.36 | 1.42 | | |
| 2 | 1.67 | 1.49 | | |
| 3 | 1.71 | 1.76 | | |
| Impedance | | | 1.3 | 1.7 |

**Table 7.8** RMS errors for sandy loam fitted level difference

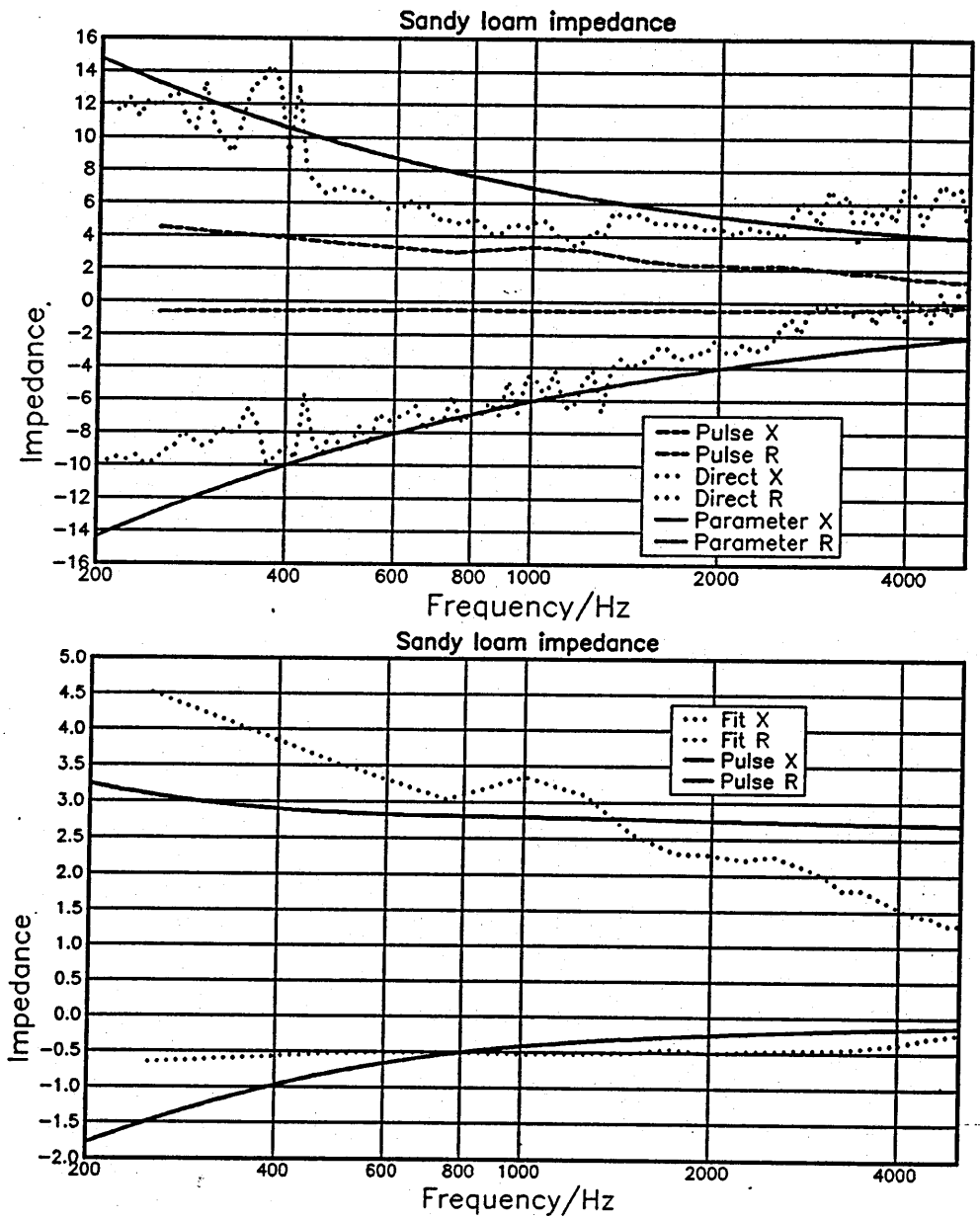


**Figure 7.10** Impedance of sandy loam

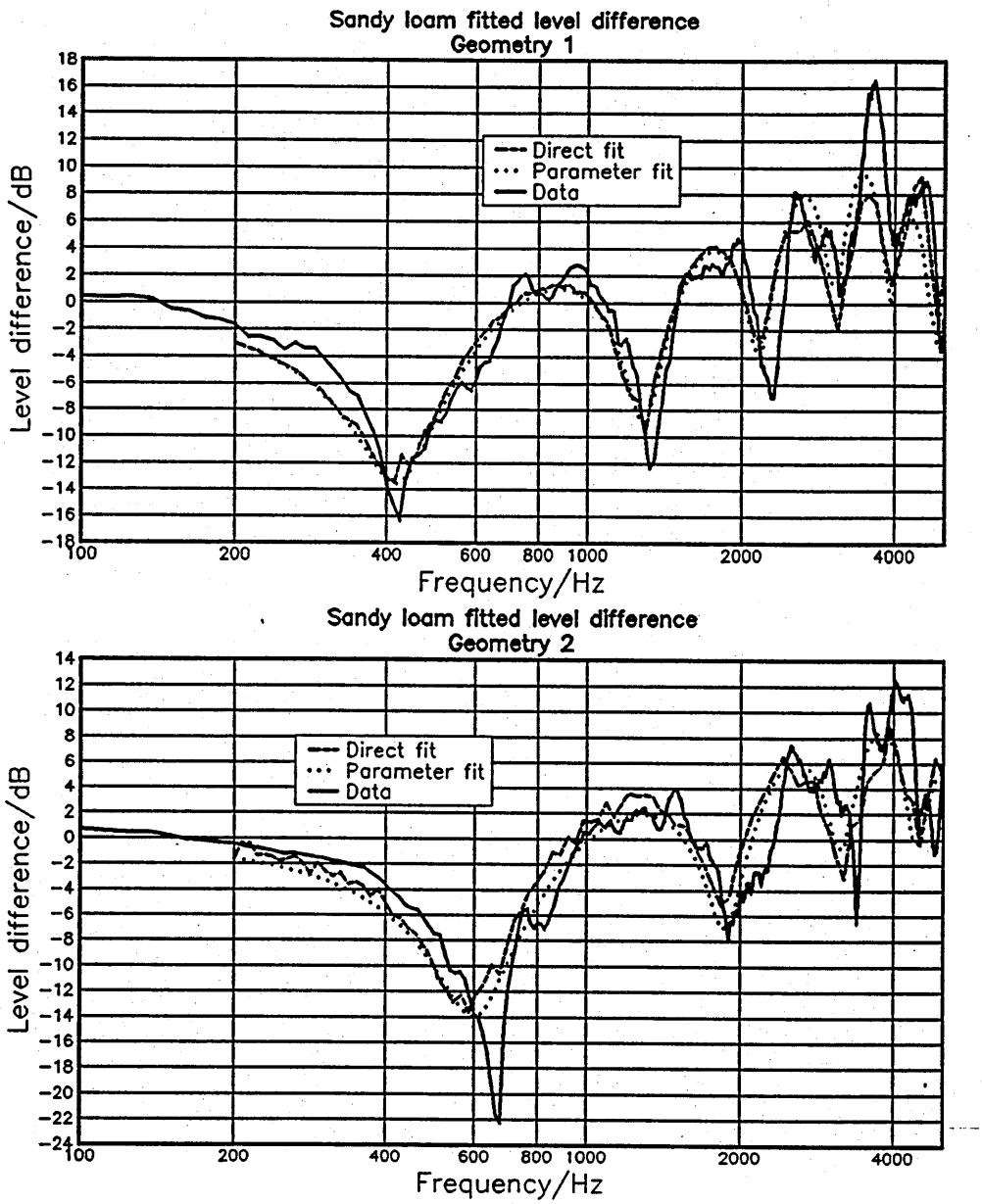


**Figure 7.11** Fitted level difference spectra for sandy loam, geometries 1 and 2.

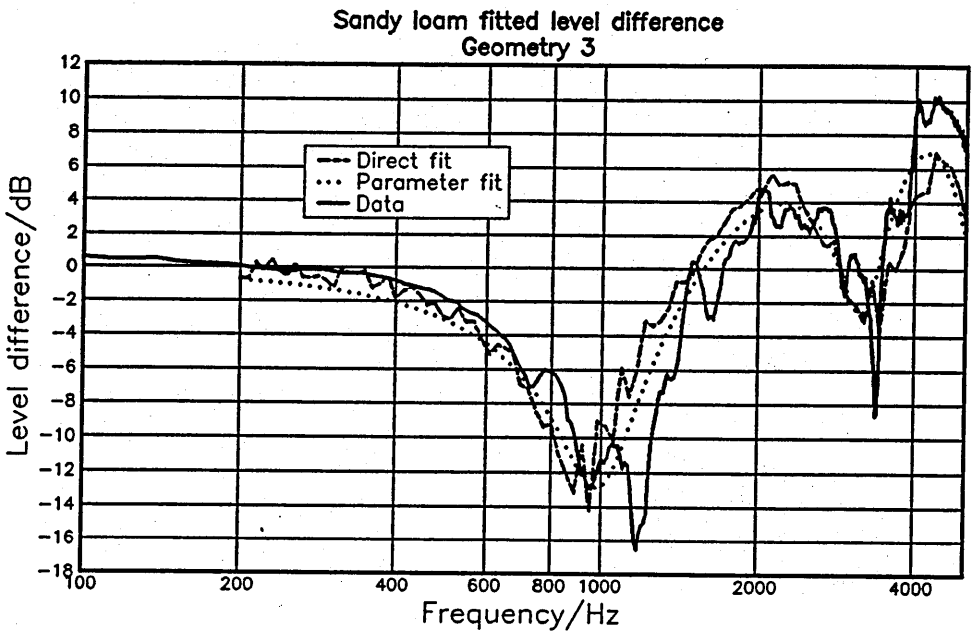


**Figure 7.12** Fitted level difference spectra for sandy loam, geometry 3.

## 7.2 Locally reacting rigidly backed media

### 7.2.1 Artificial grassland

It appears from these measurements that the artificial grassland may be better modelled as a double rigidly backed layer.

| Parameter | Level difference fitted | Impedance fitted | Measured (non–acoustically) |
|---|---|---|---|
| Flow resistivity | 300000 | 270000 | |
| Porosity | 0.48 | 0.46 | 0.41 |
| Grain shape | 0.1 | 0.1 | |
| Pore shape | 1.75 | 0.70 | |
| Layer depth | 0.007 | 0.01 | ≈0.016 |

**Table 7.9** Deduced microstructural model parameters for artificial grassland

| Input data | Level difference data | | Impedance data | |
|---|---|---|---|---|
| Geometry (artificial grassland) | RMS error parameter fit | RMS error direct fit | RMS error resistance fit | RMS err reactance |
| 1 | 2.54 | 2.98 | | |
| 2 | 3.28 | 1.76 | | |
| 3 | 2.85 | 3.52 | | |
| Impedance | | | 1.2 | 2.0 |

**Table 7.10** RMS errors for artificial grassland fitted level difference

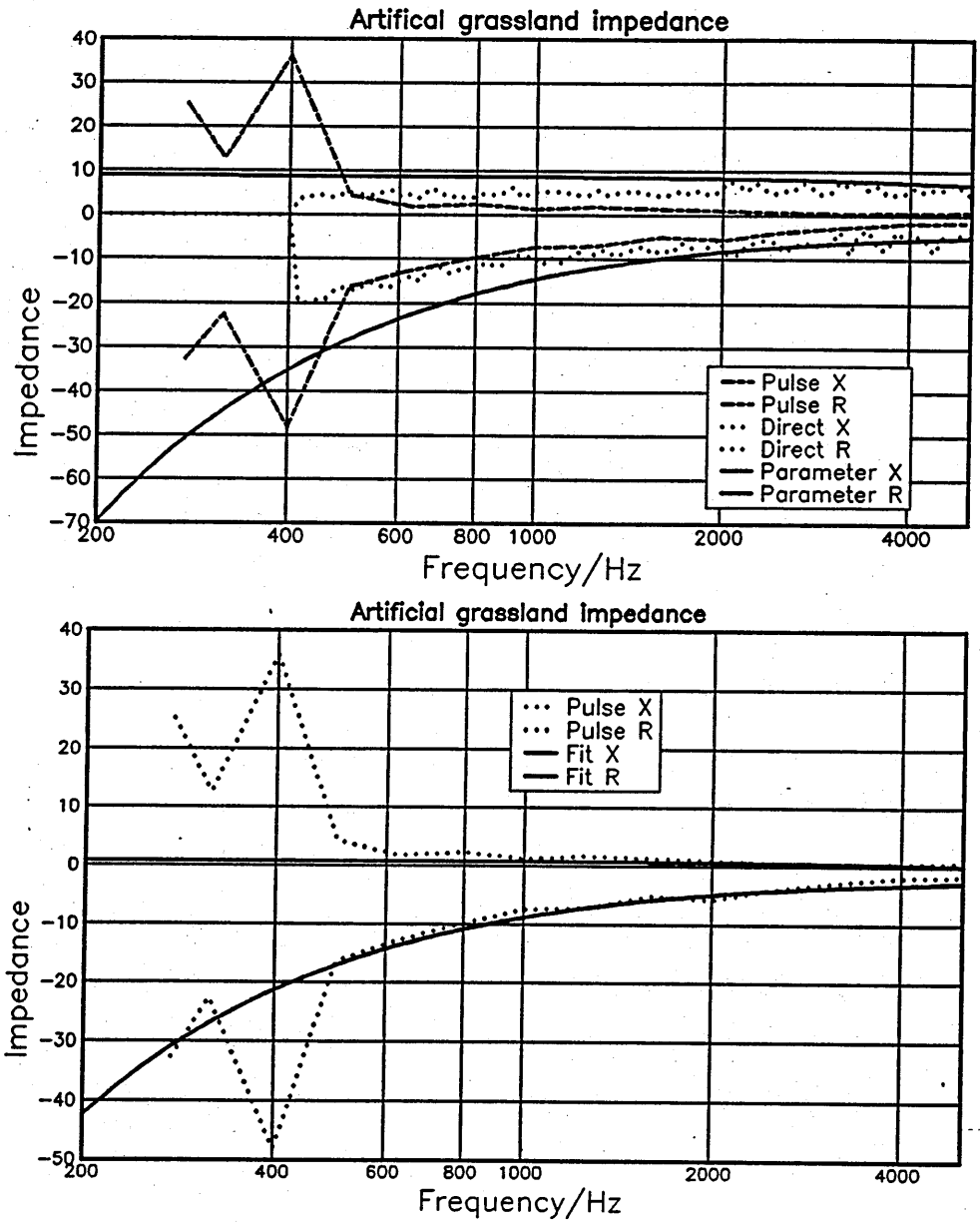


**Figure 7.13** Impedance of artificial grassland

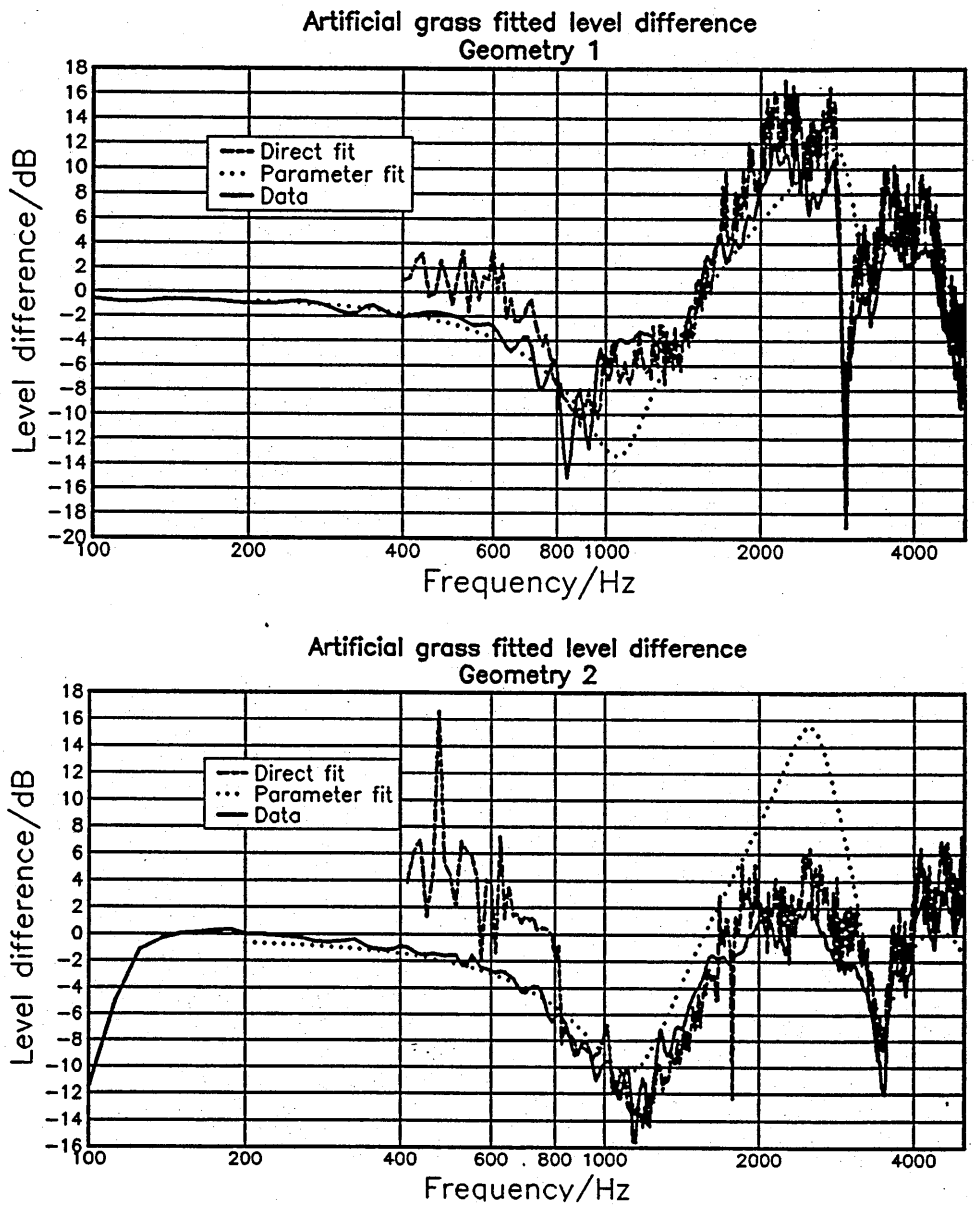


**Figure 7.14** Fitted level difference spectra for artificial grassland, geometries 1 and 2.

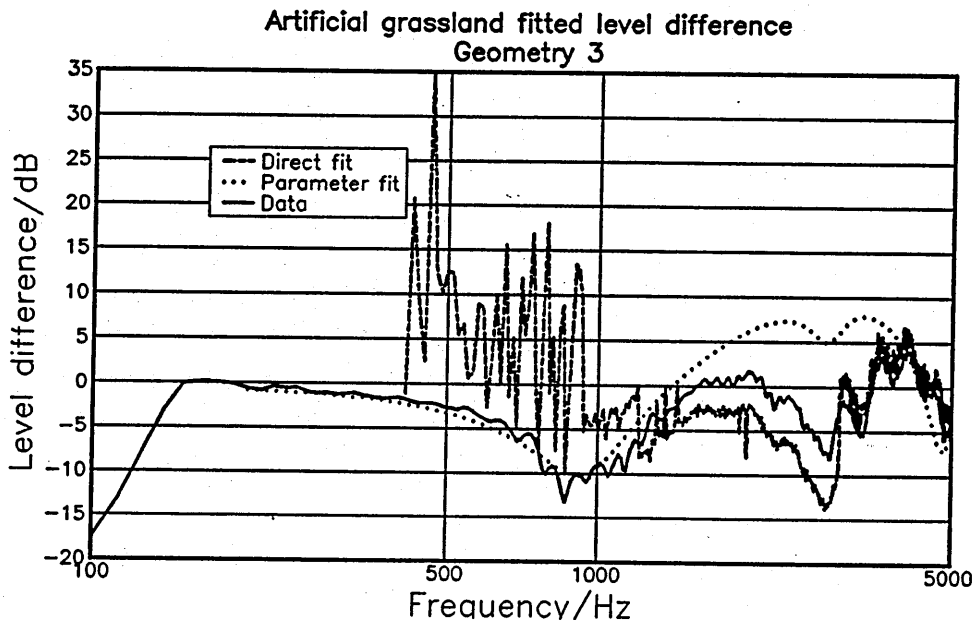


**Figure 7.15** Fitted level difference spectra for artificial grassland, geometry 3.

## 7.3 Externally reacting semi–infinite media

Note: the direct fitting routine is not used for externally reacting surfaces. The fitted curves are those obtained from fitting the impedance to give resistance and reactance.

### 7.3.1 Pea gravel

| Parameter | Level difference fitted | Impedance fitted | Measured (non–acoustically) |
|---|---|---|---|
| Flow resistivity | 9800 | 9600 | 9570 |
| Porosity | 0.42 | 0.38 | 0.40 |
| Grain shape | 1.0 | 0.10 | 0.93 |
| Pore shape | 0.4 | 1.3 | |
| Layer depth | N/A | N/A | N/A |

**Table 7.11** Deduced microstructural model parameters for peagravel

| Input data | Level difference data | Impedance data | |
|---|---|---|---|
| Geometry (pea gravel) | RMS error parameter fit | RMS error resistance fit | RMS error reactance fit |
| 1 | 3.23 | | |
| 2 | 1.51 | | |
| 3 | 1.58 | | |
| Impedance | | 1.5 | 3.2 |

**Table 7.12** RMS errors for pea gravel fitted level difference

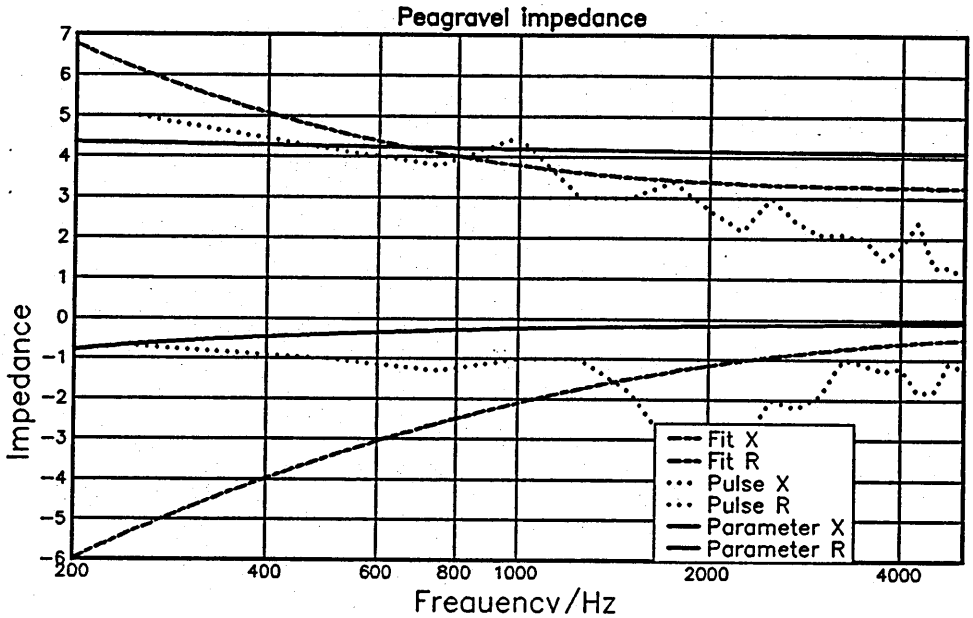


Figure 7.16 Impedance of pea gravel

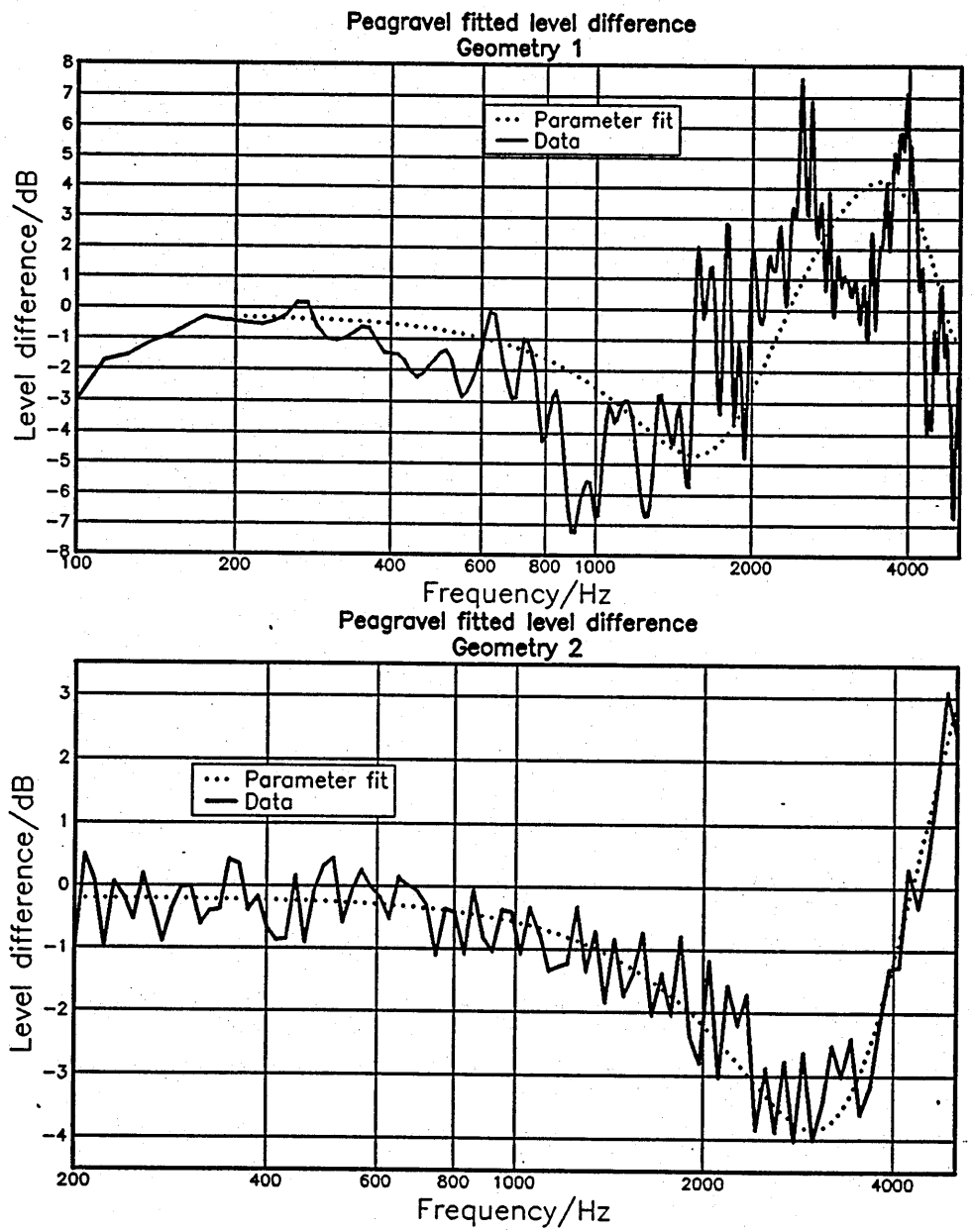


**Figure 7.17** Fitted level difference spectra for pea gravel, geometries 1 and 2.

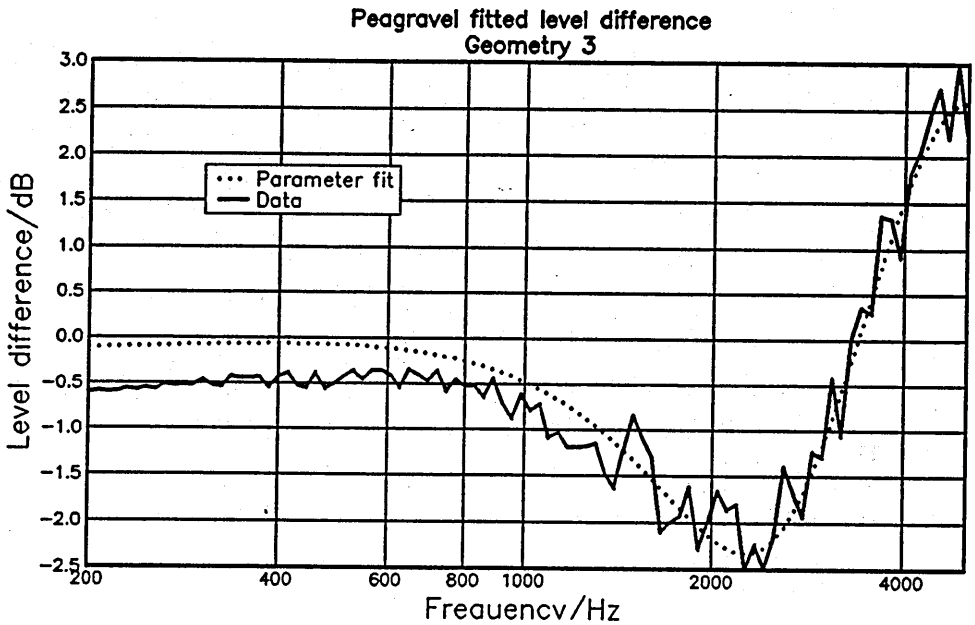


**Figure 7.18** Fitted level difference spectra for pea gravel, geometry 3.

### 7.3.2 Snow

| Parameter | Level difference fitted | Measured (non–acoustically) |
|---|---|---|
| Flow resistivity | 26000 | |
| Porosity | 0.66 | 0.61↔0.76 |
| Grain shape | 0.11 | |
| Pore shape | 0.15 | |
| Layer depth | N/A | N/A |

**Table 7.13** Deduced microstructural model parameters for snow

| Geometry (snow) | RMS error parameter fit |
|---|---|
| 1 | 7.54 |
| 2 | 6.55 |
| 3 | 4.32 |

**Table 7.14** RMS errors for snow fitted level difference

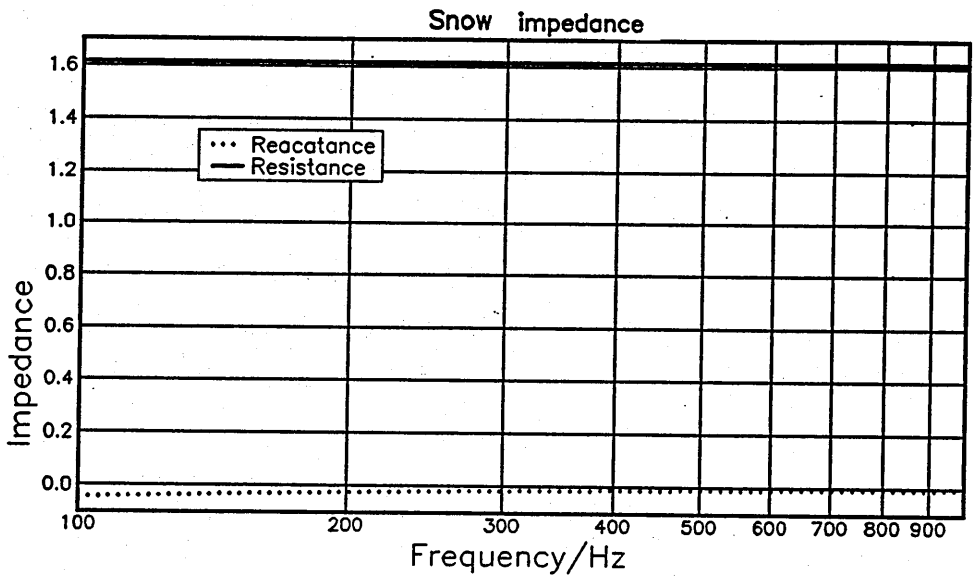


Figure 7.19 Impedance of snow

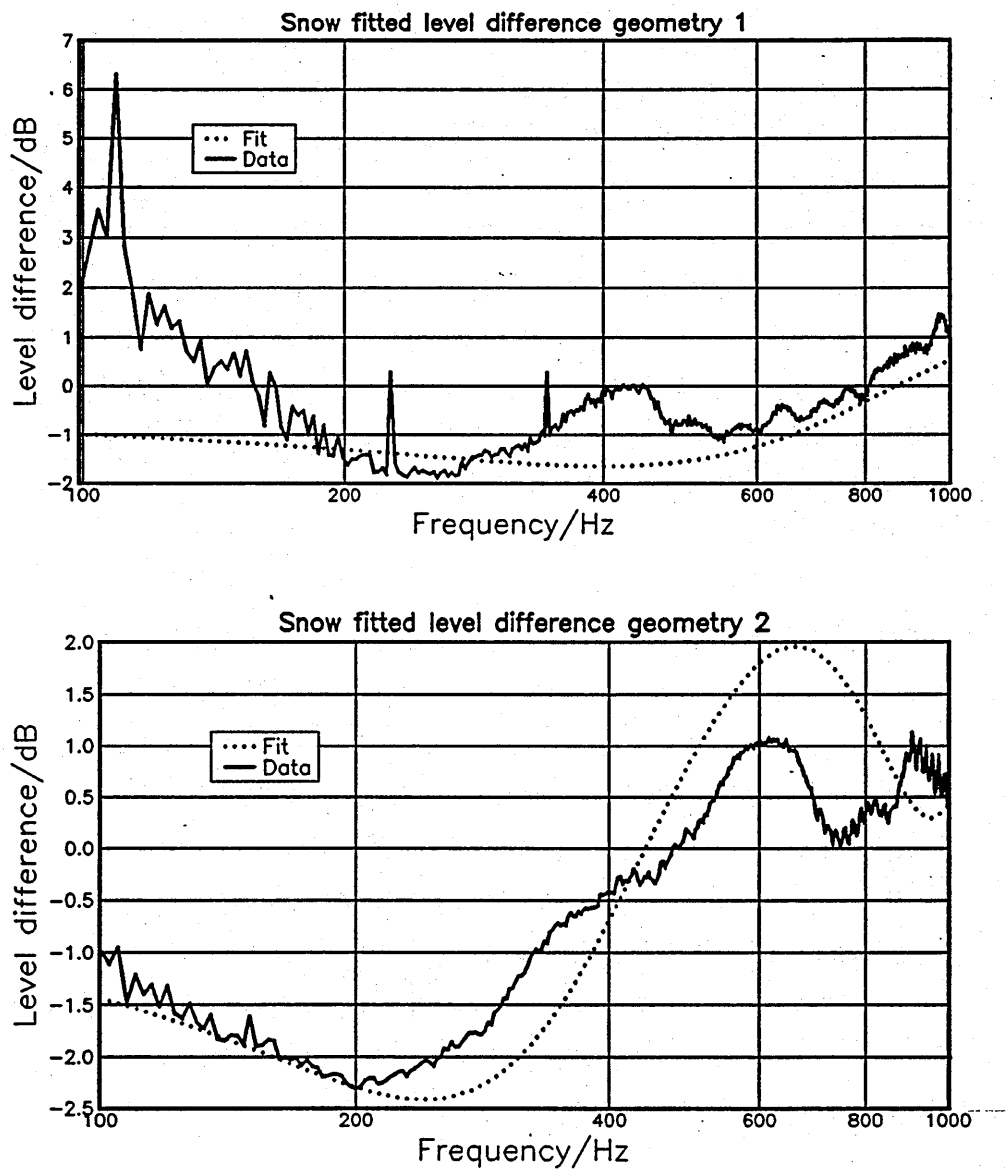


**Figure 7.20** Fitted level difference spectra for snow, geometries 1 and 2.

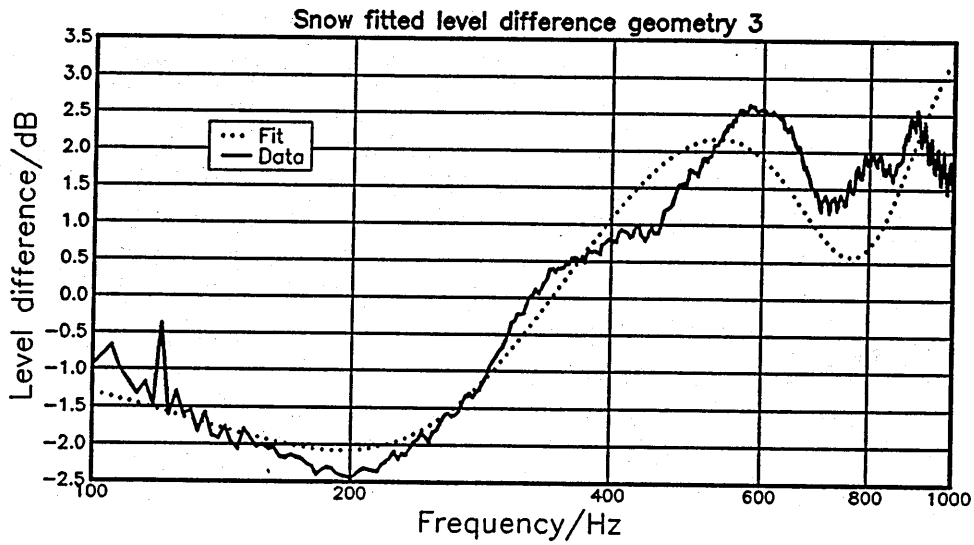


**Figure 7.21** Fitted level difference spectra for snow, geometry 3.

## 7.4 Externally reacting rigidly backed media

### 7.4.1 MIRA road surface

| Parameter | Level difference fitted | Impedance fitted | Measured (non–acoustically) |
|---|---|---|---|
| Flow resistivity | 5382 | 5472 | 5500 |
| Porosity | 0.22 | 0.23 | 0.29 |
| Grain shape | 0.51 | 0.75 | 1.3 |
| Pore shape | 1.0 | 0.50 | |
| Layer depth | 0.050 | 0.050 | 0.045 |

**Table 7.15** Deduced microstructural model parameters for MIRA road surface

| Input data | Level difference data | Impedance data | |
|---|---|---|---|
| Geometry (MIRA road surface) | RMS error parameter fit | RMS error resistance fit | RMS error reactance fit |
| 1 | 0.44 | | |
| 2 | 0.83 | | |
| 3 | 0.91 | | |
| Impedance | | 6.5 | 5.3 |

**Table 7.16** RMS errors for MIRA road surface fitted level difference

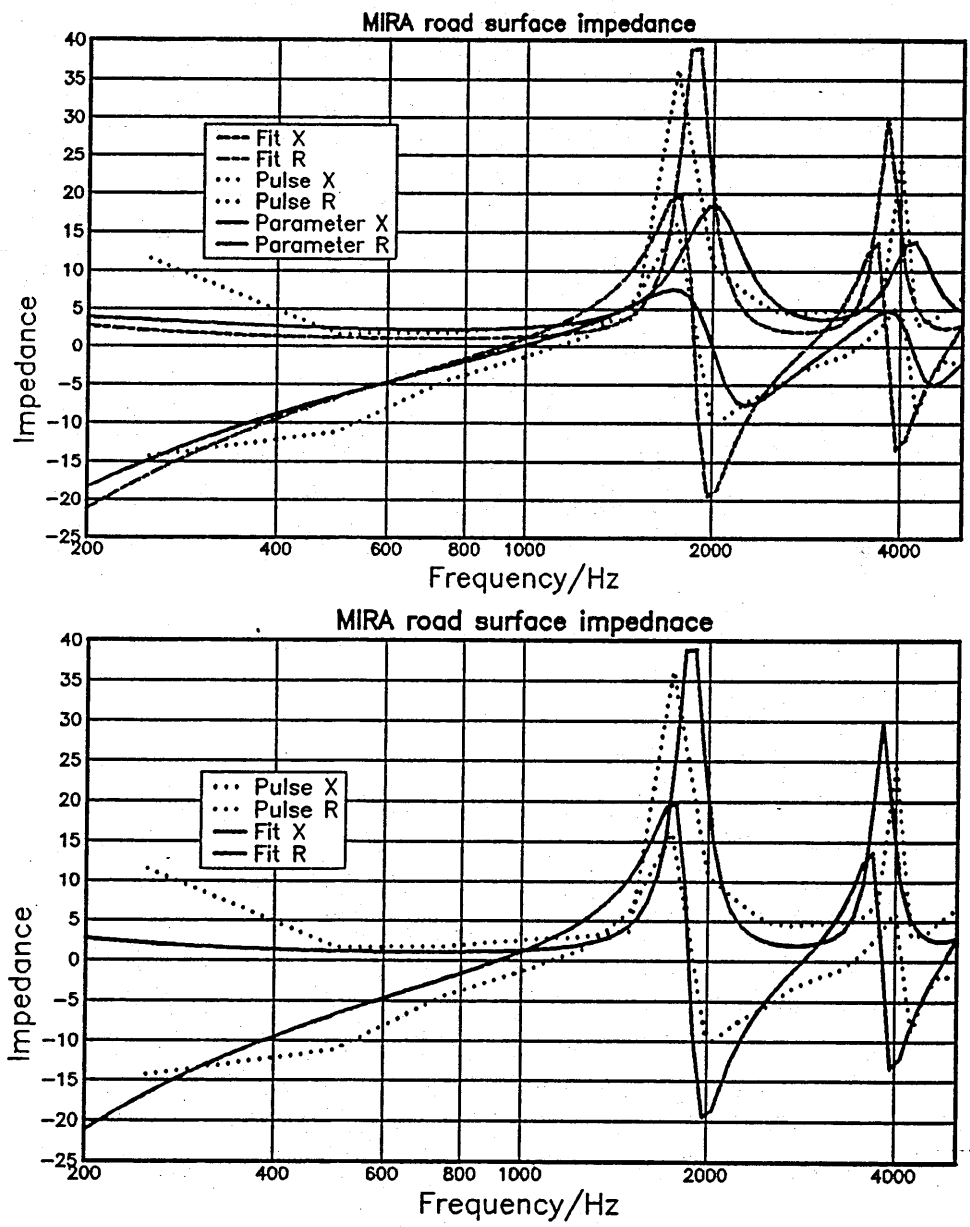


Figure 7.22 Impedance of MIRA road surface

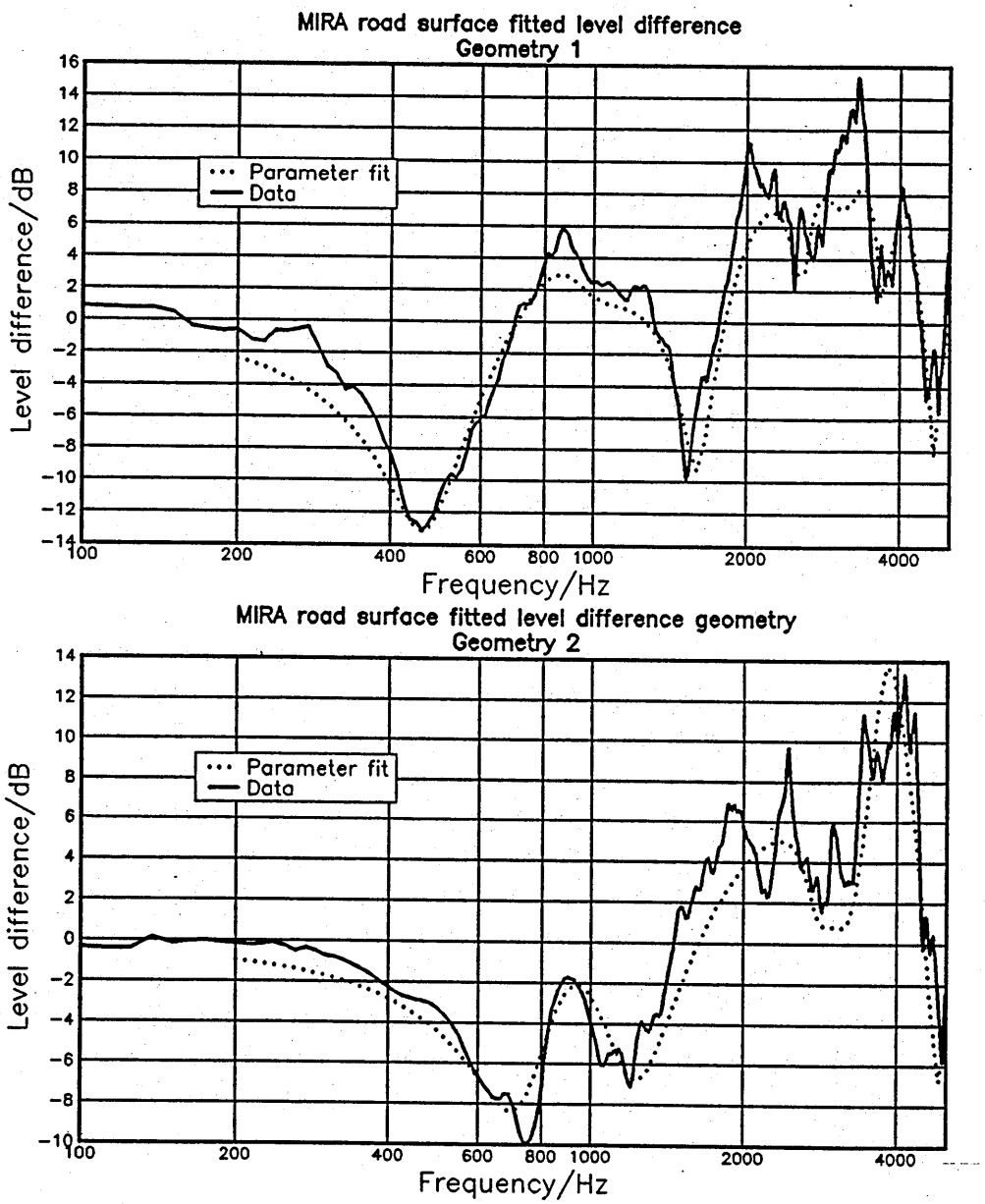


**Figure 7.23** Fitted level difference spectra for MIRA road surface, geometries 1 and 2.

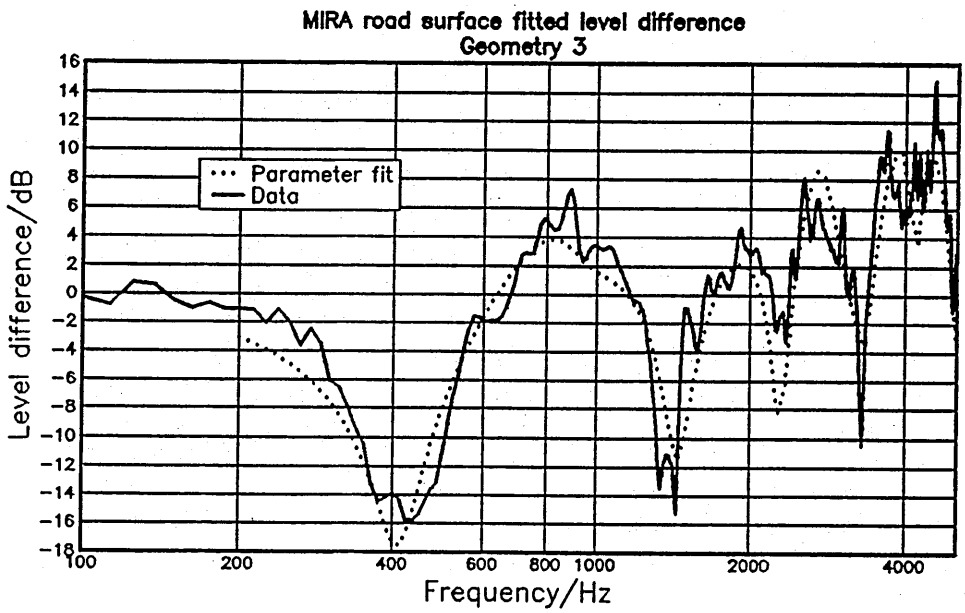


Figure 7.24 Fitted level difference spectra for MIRA road surface, geometry 3.

### 7.4.2 TRRL area L road surface

| Parameter | Level difference fitted | Impedance fitted | Measured (non–acoustically) |
|---|---|---|---|
| Flow resistivity | 3638 | 3600 | 3500 |
| Porosity | 0.214 | 0.212 | 0.204 |
| Grain shape | 0.46 | 0.46 | 0.87 |
| Pore shape | 0.24 | 0.25 | |
| Layer depth | 0.045 | 0.050 | 0.052 |

**Table 7.17** Deduced microstructural model parameters for TRRL area L road surface

| Input data | Level difference data | Impedance data | |
|---|---|---|---|
| Geometry (TRRL area L road surface) | RMS error parameter fit | RMS error resistance fit | RMS reacta |
| 1 | 0.91 | | |
| 2 | 1.13 | | |
| 3 | 2.14 | | |
| Impedance | | 3.2 | 2. |

**Table 7.18** RMS errors for TRRL area L road surface fitted level difference

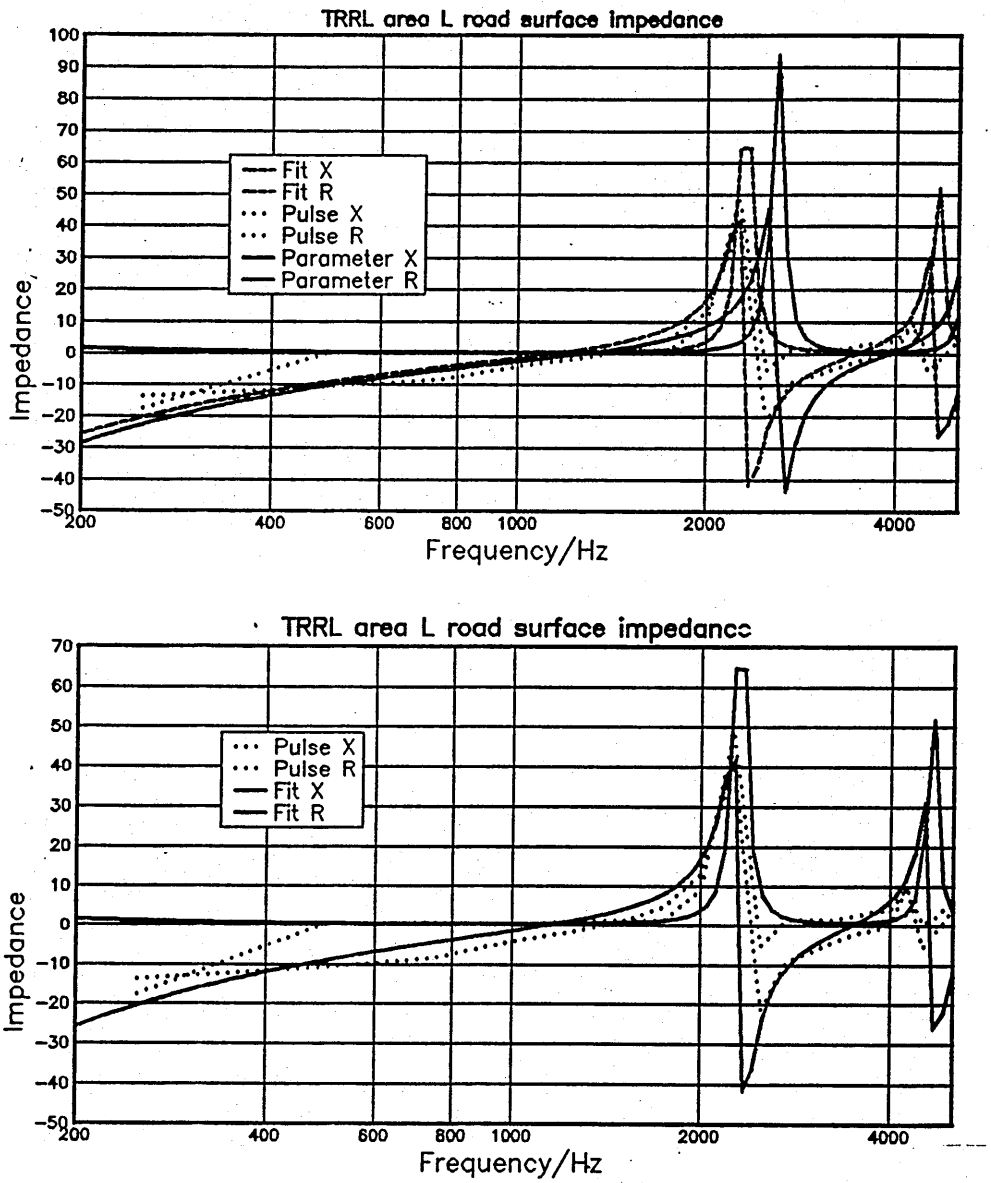


Figure 7.25 Impedance of TRRL area L road surface

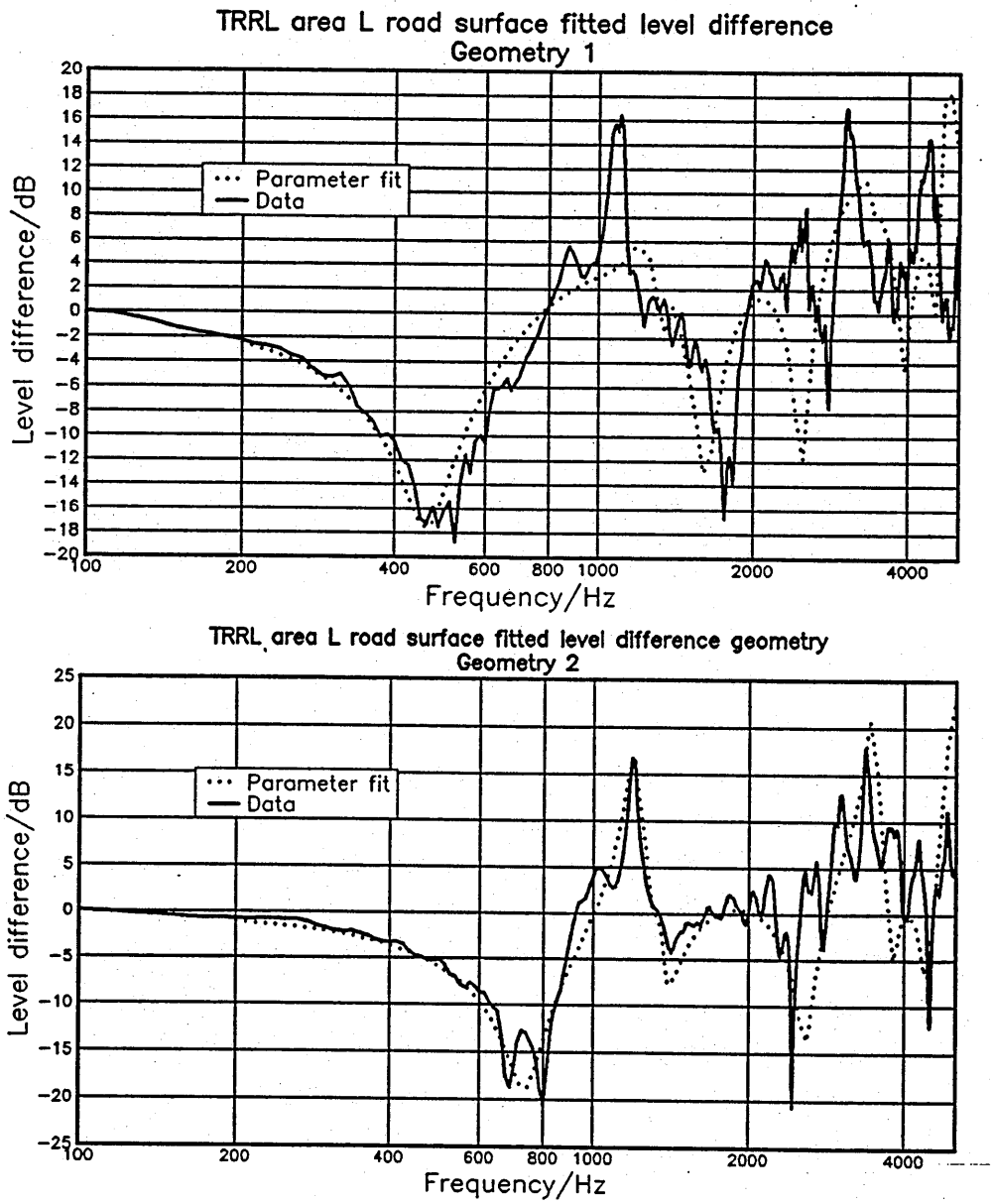


**Figure 7.26** Fitted level difference spectra for TRRL area L road surface, geometries 1 and 2.

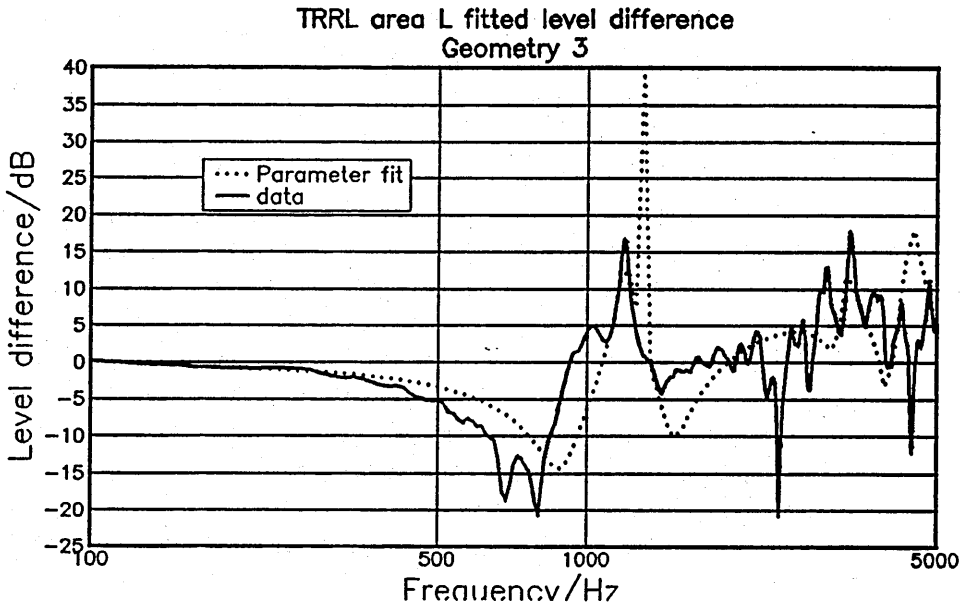


Figure 7.27 Fitted level difference spectra for TRRL area L road surface, geometry 3.

### 7.4.3 Fibreglass surface

It is suspected that the poor results arise due to the anisotropic nature of the fibre glass.

| Parameter | Level difference fitted | Impedance fitted | Measured (non–acoustically) |
|---|---|---|---|
| Flow resistivity | 29318 | 26318 | 28660 |
| Porosity | 0.59 | 0.54 | 0.72 |
| Grain shape | 1.20 | 1.10 | 0.87 |
| Pore shape | 0.46 | 0.44 | |
| Layer depth | 0.044 | 0.047 | 0.050 |

**Table 7.19** Deduced microstructural model parameters for fibreglass surface

| Input data | Level difference data | Impedance data | |
|---|---|---|---|
| Geometry (Fibreglass surface) | RMS error parameter fit | RMS error resistance fit | RMS error reactance fit |
| 1 | 0.74 | | |
| 2 | 0.63 | | |
| 3 | 0.87 | | |
| Impedance | | 0.80 | 0.78 |

**Table 7.20** RMS errors for fibreglass surface fitted level difference

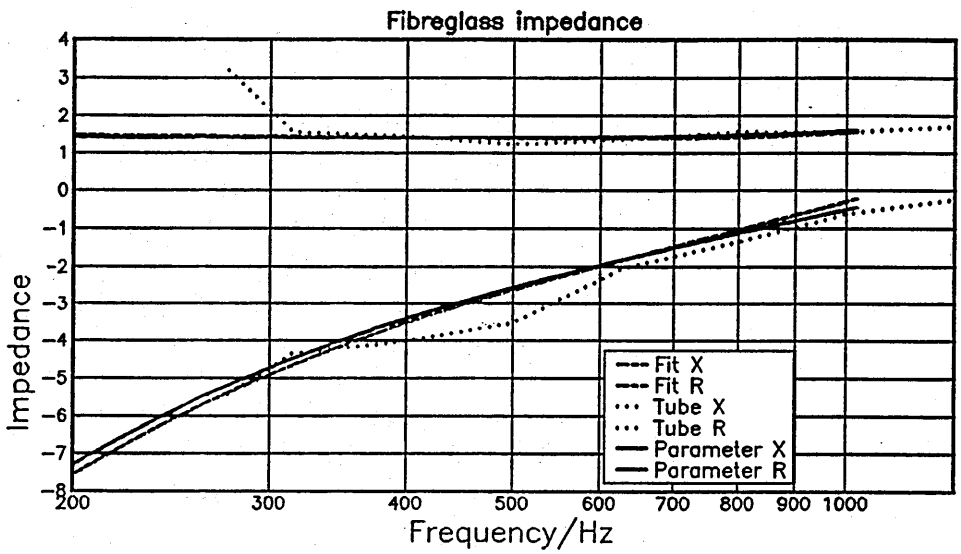


Figure 7.28 Impedance of fibreglass surface

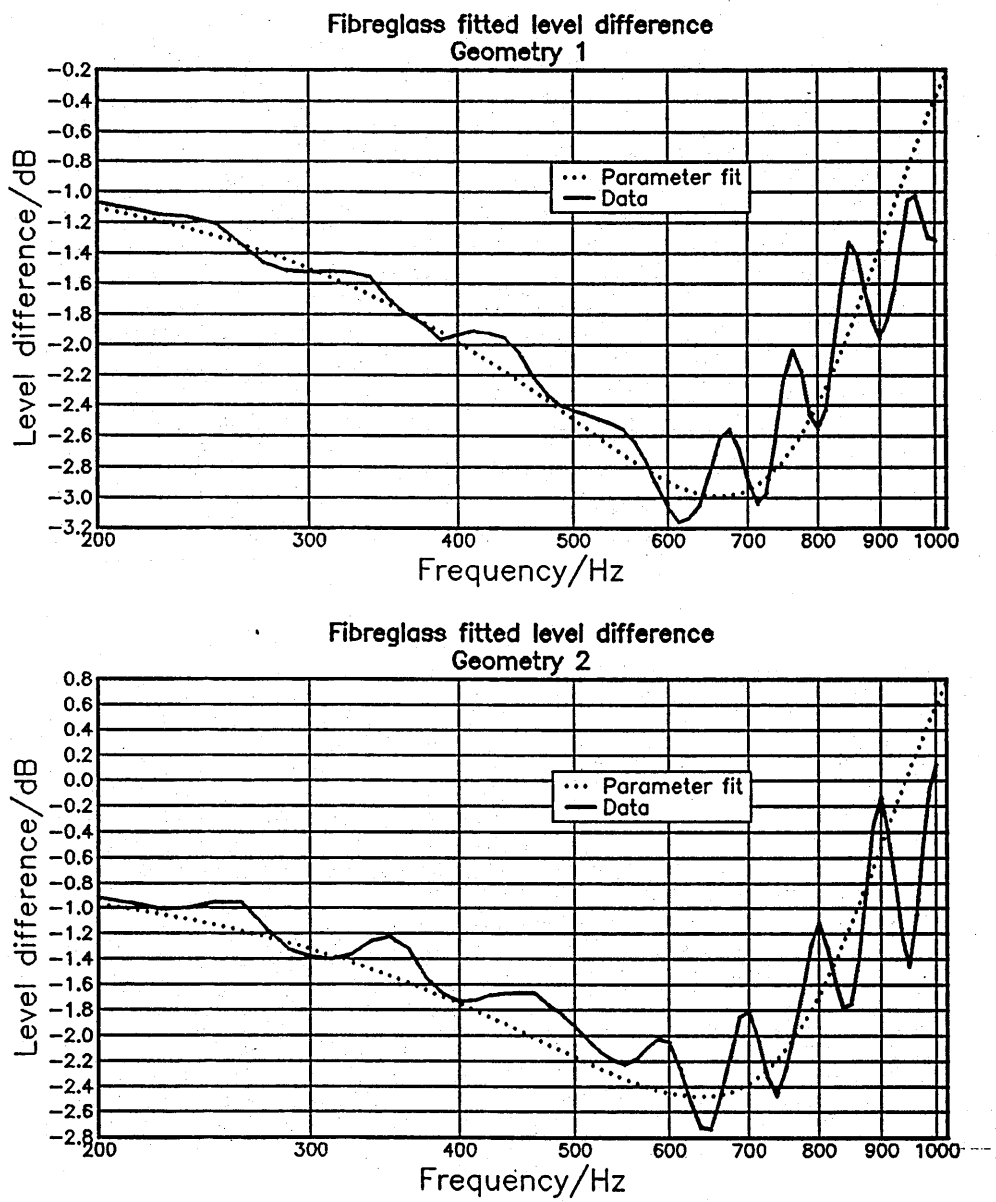


**Figure 7.29** Fitted level difference spectra for fibreglass surface, geometries 1 and 2.

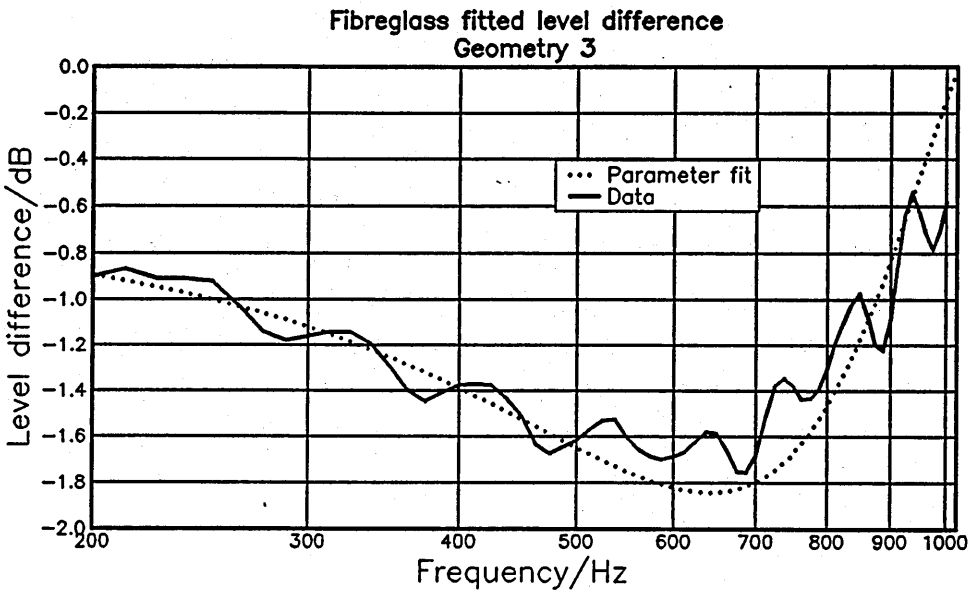


**Figure 7.30** Fitted level difference spectra for fibreglass surface, geometry 3.

### 7.4.4 Polyurethane foam

Data has been supplied for two level difference geometries. The first geometry see table 7.21, has been used twice as the program requires three level difference spectra. The results of the fitting procedure are shown in figures 7.31 and 7.32. The evaluated parameters are given in table 7.22. Figure 7.33 shows the measured data, collected using the $4^{th}$ MLSSA processing technique a maximum length sequence method [202] used for measurements in non–anechoic environments and theoretical curves evaluated using the measured and estimated data given in table 7.22. Figure 7.34 shows the impedance of the foam deduced from impedance the two–microphone free field technique and calculated using the parameters shown in table 7.22. It is suggested that the poor low frequency fit is due to the elastical properties of the material. This phenomenon has been examined by Tooms [177]. It should be noted that this example indicates that the indirect parameter fitting technique may be used with two level difference spectra.

| Geometry | Source height | Upper mic. height | Lower mic. height | Separation |
|---|---|---|---|---|
| 1 | 0.44 | 0.446 | 0.021 | 1.755 |
| 2 | 0.44 | 0.446 | 0.021 | 1.755 |
| 3 | 0.43 | 1.0 | 0.037 | 0.960 |

**Table 7.21** Geometries used for indirect impedance technique.

| Parameter | Results from fitting | Measured parameters |
|---|---|---|
| Flow resistivity | 4737.0 | 6000.0 |
| Porosity | 0.92 | 0.9 |
| Grain shape | 0.23 | 0.0* |
| (Tortuosity) | (1.01) | (1.0) |
| Pore shape | 0.56 | 0.5* |
| Layer depth | 0.038 | 0.04 |

**Table 7.22** Parameters deduced from fitting and non-acoustical techniques

Note * refers to estimated values.

## 7.5 Discussion of results

Both indirect methods have been used for a wide range of locally reacting media. Only the parameter fitting technique has been used for externally reacting media. The results of these applications have been compared to the impulse technique. It is clear that the parameter fitting indirect method is to be preferred to fitting level difference spectra by variation of the resistance and reactance alone. The imposed frequency dependence of the parameter fitting indirect method reduces the number of required level difference spectra by a factor of three to four, depending on the frequency range of interest. The computational time is reduced by a factor of six or seven. Although fewer level difference spectra are required when the microstructural model is employed to enforce a frequency dependence, the number of parameters to be varied in the fitting routine increases from two to four or five, dependent on whether or not the surface is rigidly backed.

The direct parameter fitting routine may not be used for externally reacting materials. As the impedance is angular dependent each level difference geometry at any one frequency would require two variables (resistance and reactance). Thus there are two unknowns for one solution and a series of non–unique solutions are obtained. It may be feasible to overcome this problem using the magnitude and phase of the level difference spectra however the possible problems of doing this have been mentioned briefly in chapter 6. The parameter fitting technique overcomes the angular dependence by incorporating it into the impedance model. The parameters deduced are angular independent.

The results indicate that the parameter fitting indirect method is preferable to both the impedance component fitting indirect method and the impulse technique. Additional problems may occur when using the impulse technique over rigidly backed media as two impulses, one from the surface, the other from the substrate are received rather that a single pulse indicative of the surface impedance of the layered media [98]. As a result of this study the impulse technique was not used extensively to study the characteristics of porous road surfaces in the remainder of the work described in this the-

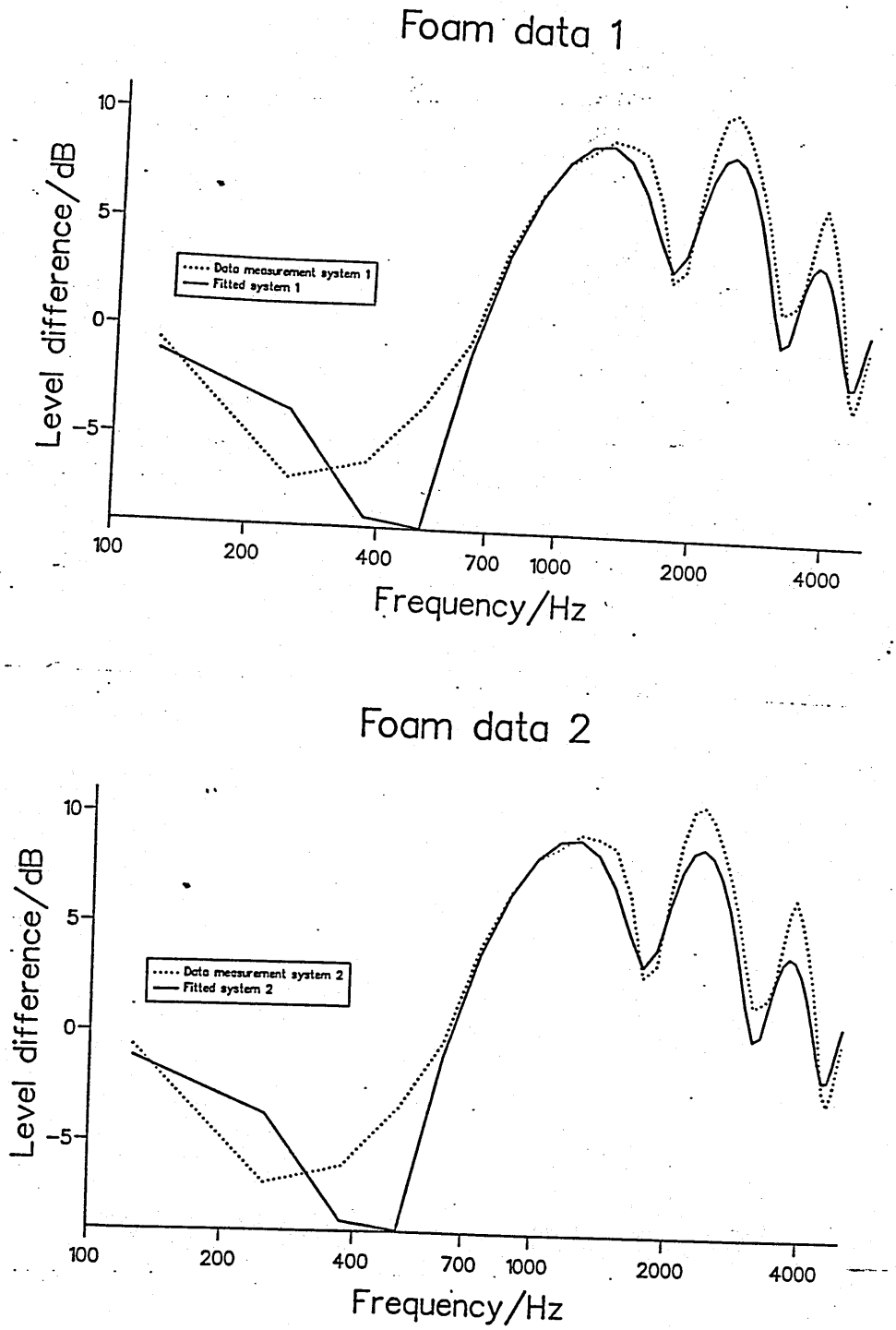


**Figure 7.31** Fitted level difference spectra for foam. Geometry 1 and 2 are identical (RMS= 2.0)

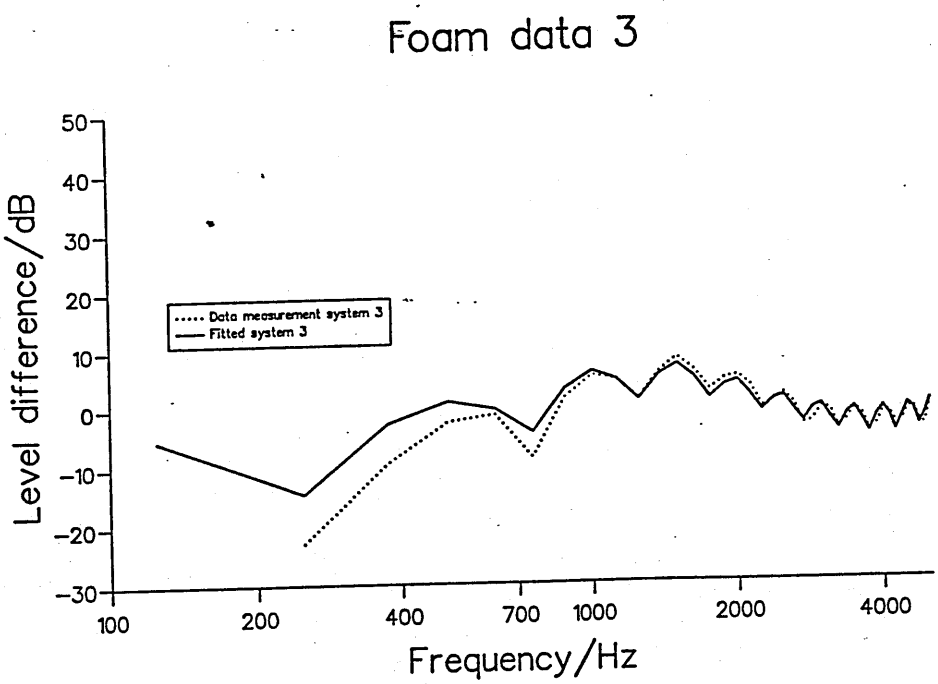


**Figure 7.32** Fitted level difference spectra for foam. Geometry 3 (RMS=1.0)

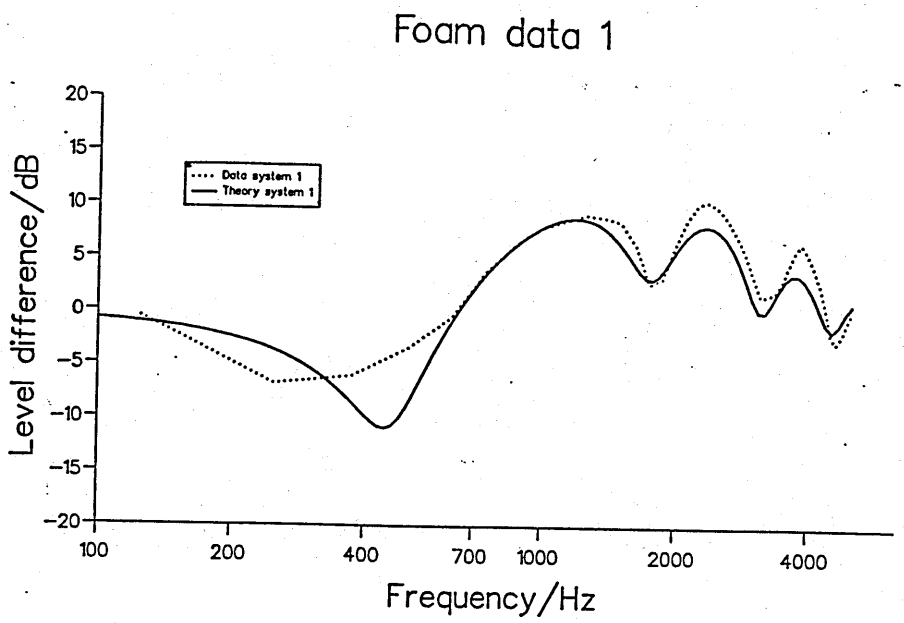


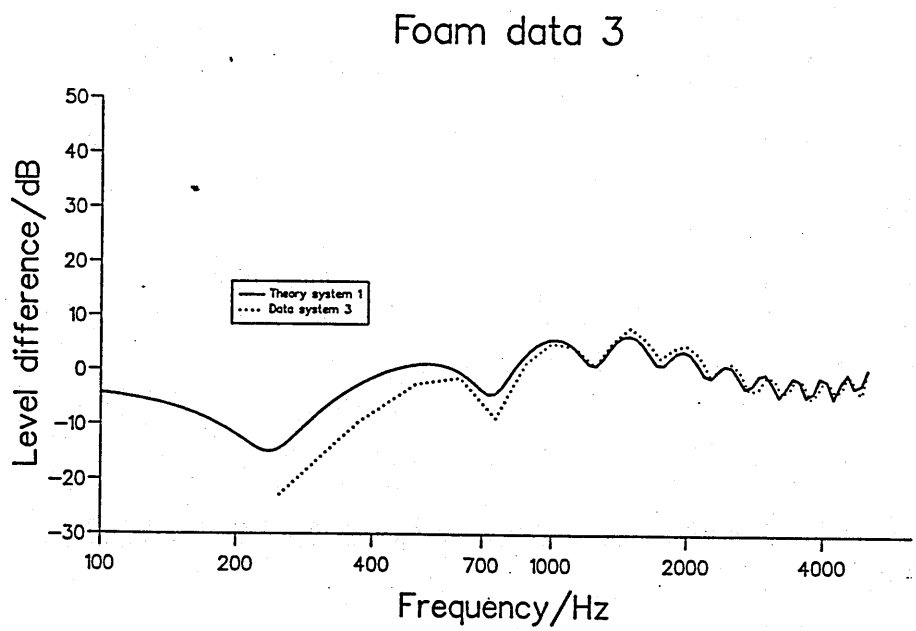


**Figure 7.33** Theoretcal level difference spectra for foam.

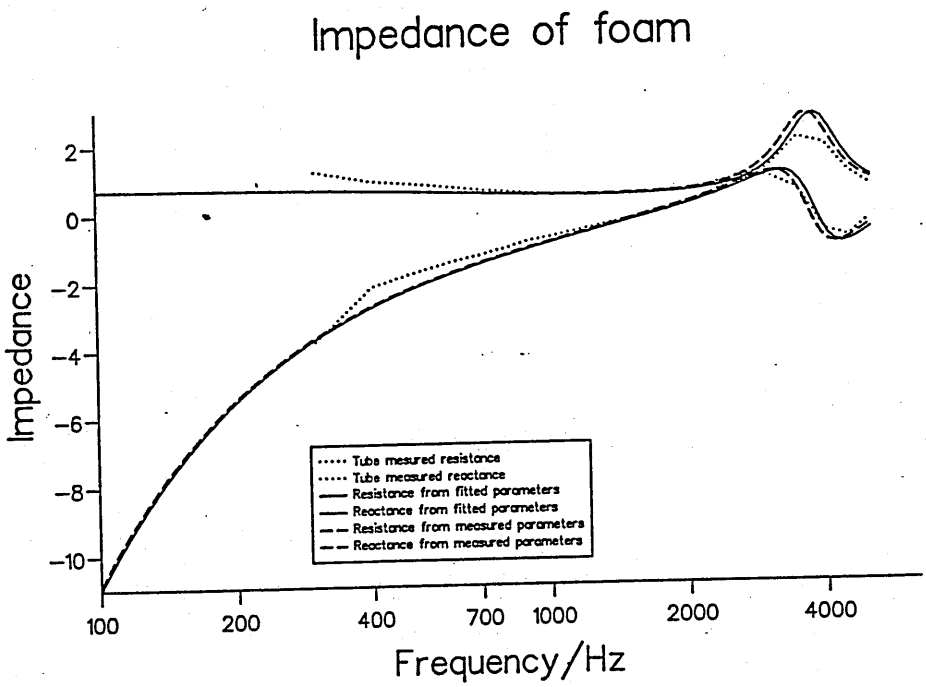


**Figure 7.34** Impedance of foam.

sis. The choice of the level difference geometries used is dependent on the surface of interest. The nine geometries listed in chapter 8 are used as a starting point. If the direct fitting technique is being used these geometries are modified to place the primary ground effect dip in the frequency band of interest. If this dip is narrow more than nine geometries may be required.

Of particular interest is the double ground effect dip as seen in figure 7.35 and the lower figure 7.23. The former spectrum is an excess attenuation spectra (receiver height 1.2m separation 7.0m) calculated for an engine source (source height 1.0m) over a typical porous road surface. Using the approximation for excess attenuation given in equations 7.2 and 7.3 then destructive interference minima will occur in the excess attenuation spectra whenever the total phase of the expression within the modulus sign in equation 7.3 is an odd number of $\pi$ radians, i.e. when;

$$\phi + k_0(R_2 - R_1) = (2n+1)\pi \tag{7.1}$$

The approximate excess attenuation spectra is derived by considering the direct and specularly reflected waves only. The total phase as calculated from equation 7.1, derived from the microstructural model using the same parameters as for figure 7.35, is given in figure 7.36 (lower). The frequencies of the first and third minima in the excess attenuation spectra correspond to total phase values of $\pi$ and $3\pi$ respectively. The second, less pronounced, minimum however is accounted for by studying the reflection from the substrate see figure 7.37. The additional phase change compared with the sound reflected from the air/road boundary is given by equation 7.4. When $\phi_t = (2n+1)\pi$ destructive interference exists between the surface and sub–strate reflected waves. Figure 7.36 (upper) shows the phase difference between the sub–strate and surface reflected wave and the substrate and direct waves. The frequency of the minor minimum coincided with the interference of the latter combination. Figure 7.38 shows the excess attenuation for a road tyre source, source height 0.05cm. The lower graph shows that the excess attenuation minima can not arise from the interference between the direct and surface reflected waves. They arise from the phase

difference between the direct and substrate reflected wave.

$$EA = 20\log|1 + R_p\frac{R_2}{R_1}e^{k_0(R_2-R_1)}| \tag{7.2}$$

$$R_p = |R_p|e^{i\phi} \tag{7.3}$$

$$\phi_t = \left|2k_b\frac{d}{\cos\theta_t}\right| \tag{7.4}$$

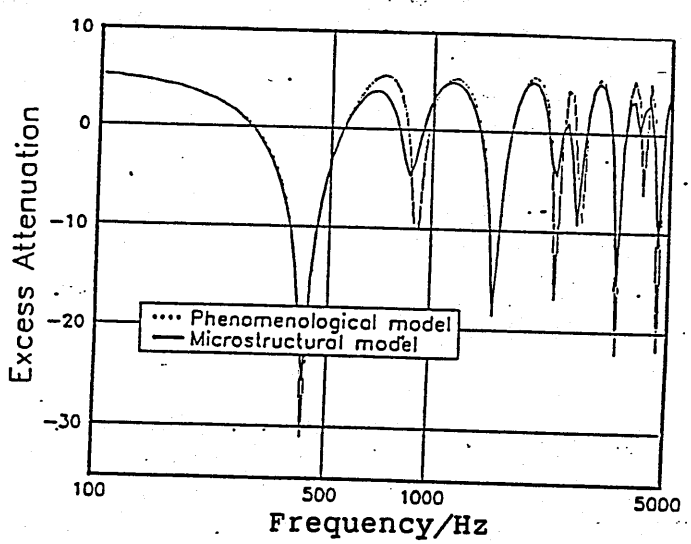


**Figure 7.35** Example excess attenuation for porous road surface

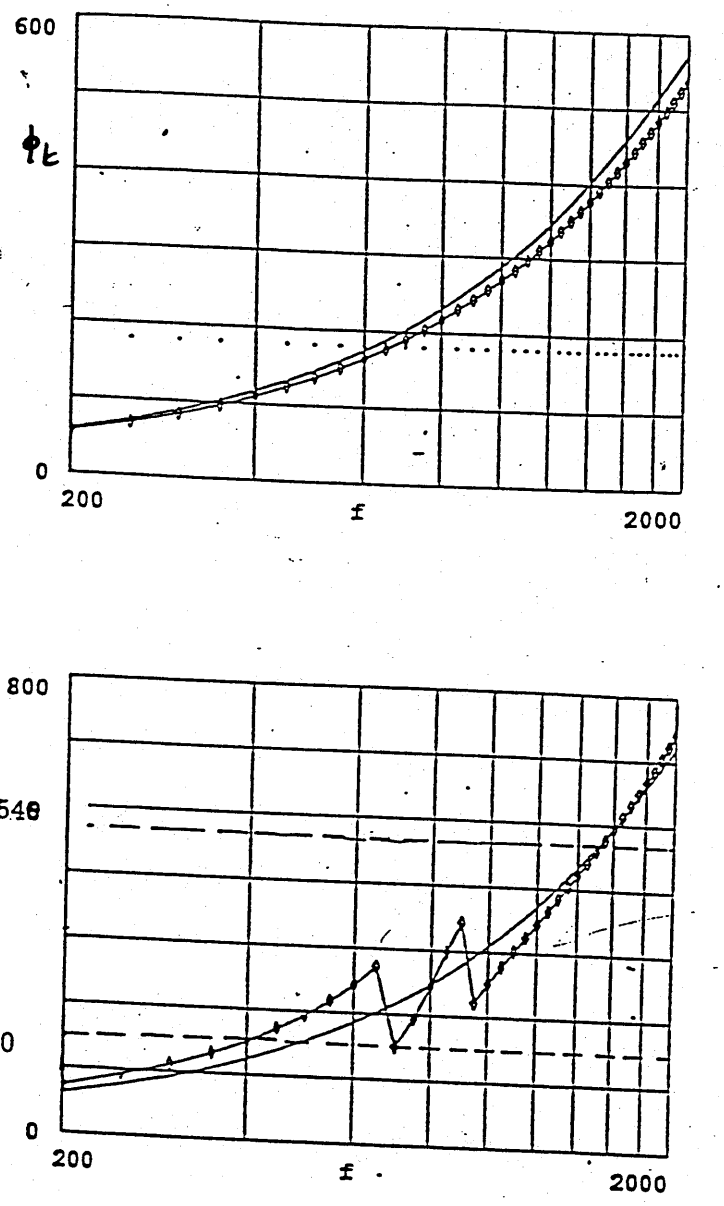


**Figure 7.36** Phase of acoustic waves reflected from single rigidly backed surface for source height 1.0m receiver height 1.2m and 7.0m separation

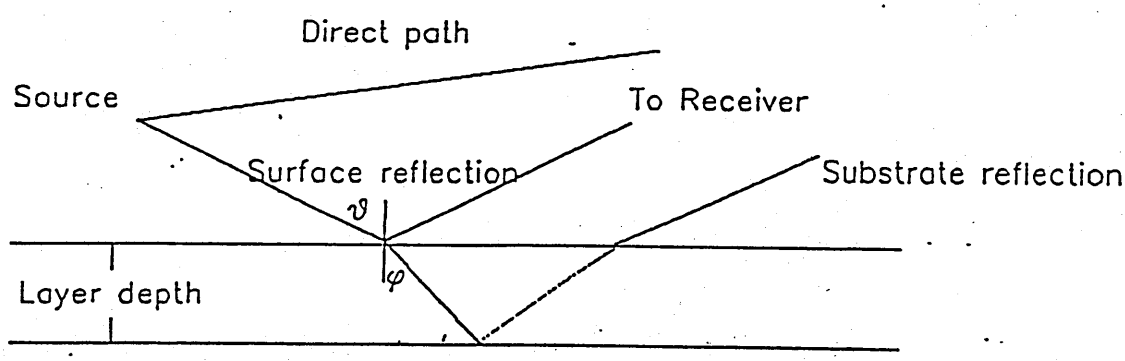


**Figure 7.37** Interference between acoustic rays reflected from surface

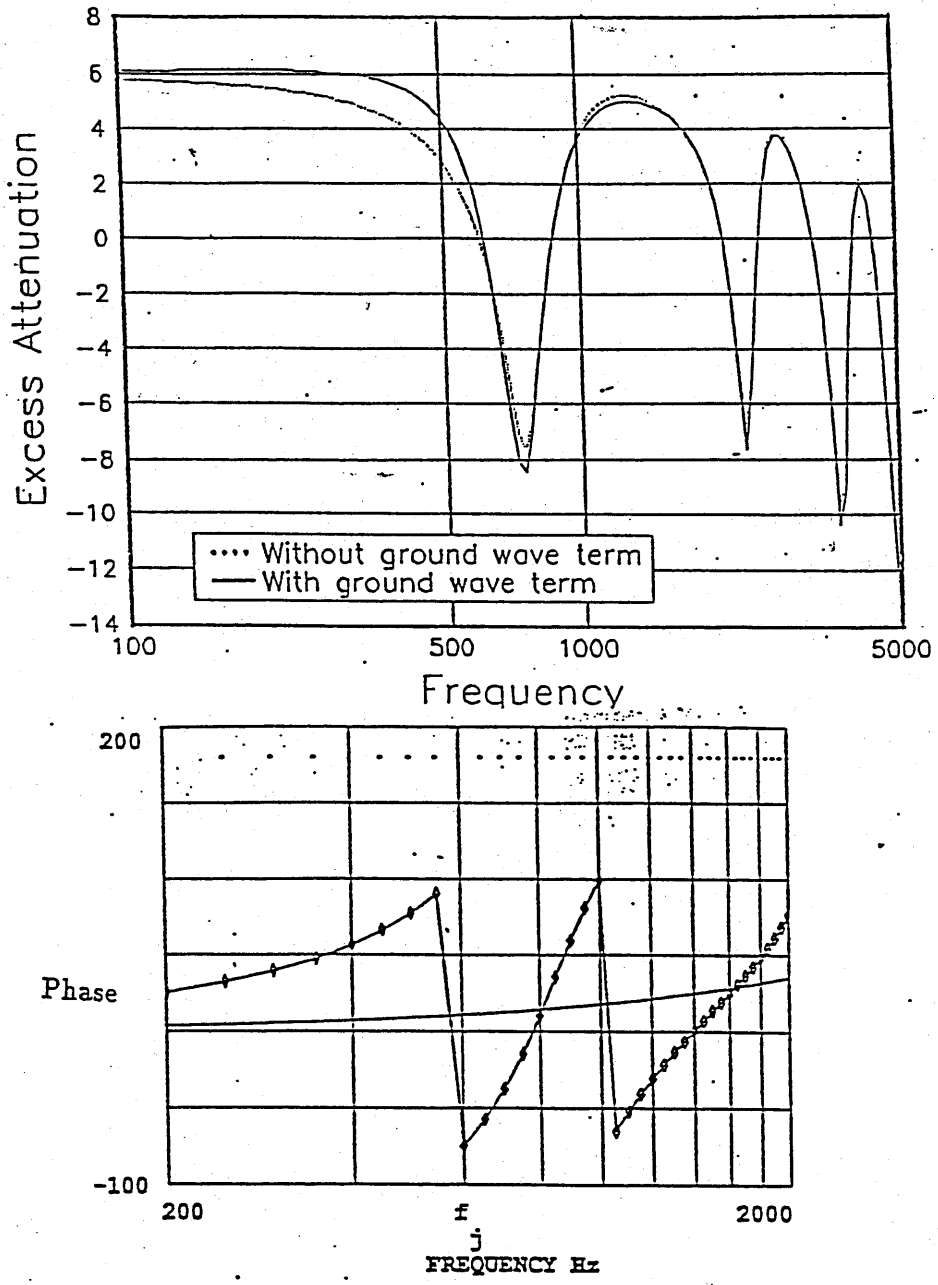


**Figure 7.38** Interference between acoustic direct and surface reflected wave fronts for road/tyre source.

# Chapter 8

# Porous Road Surfaces

This chapter is concerned with the application of the techniques developed and described earlier to the characterization and optimization of the acoustical effects of porous road surfaces. Five objectives are studied.

- The applicability of the modified Weyl van der Pol formula for spherical wave propagation above a hard–backed externally reacting layer.
- The comparative applicability of the phenomenological and microstructural impedance models to characterization of the acoustical properties of a porous road surface.
- Models of the acoustical field close to a vehicle as the results of an array of point sources.
- The porous road surface parameters that give the maximum 'A' weighted and unweighted ground effect.
- Further using tests the indirect method of impedance (parameter) measurement.

During the second world war a pervious tarmacadam was formulated with a reduced percentage of small stones. The porous nature of this surface drained water from the runway surface and thereby assisted take off and landing of aircraft in poor weather conditions. A secondary benefit was the improved acoustic performance of the material. Such surfaces when

used as roadways may produce 5 dB(A) less road traffic noise, this effect is particularly noticeable for high traffic speeds (i.e. greater than 50 km/hr) where most of the noise is generated at the road/tyre interface. This may be accounted for by two effects.

(1) The reduction of noise due to the improved sound absorbing qualities of the roadway.
(2) The reduced air pumping effect between the road/tyre interface.

This section of the thesis draws on the earlier work to study only the first phenomenon. The aim is to model the acoustical characteristics of the pervious macadam in order produce a surface optimized for noise reduction considering, only the propagation ( ground ) effect. Other sources of road/tyre noise have been detailed by Stumpf [203] are summarized in figure 8.1

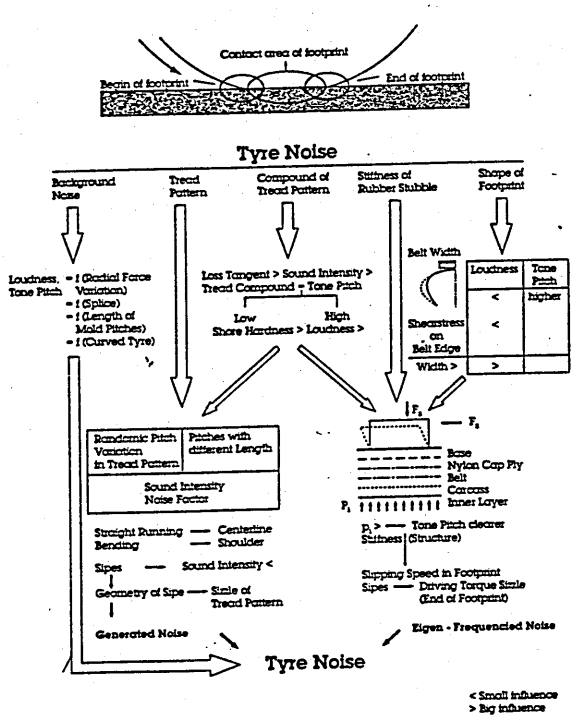


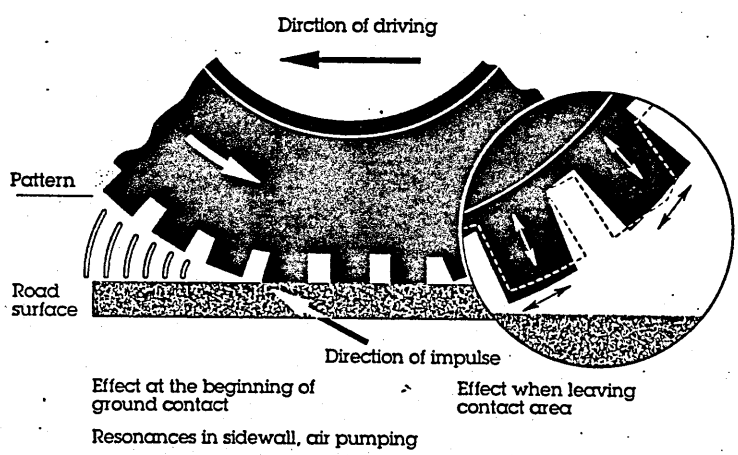


Figure 8.1 Sources of road tyre noise

The chapter commences by describing the construction and laying of the porous road surfaces. It then maps the process of validating the microstructural model (see chapter 3) as an accurate descriptor of the acoustical properties of the pervious road surface. The comparison between the microstructural model and phenomenological model started in chapter 3 is continued with particular reference to such surfaces. The chapter is concluded by examining the model parameters required to give the optimum linear and 'A' weighted noise reduction.

The validation process involved three stages. The first stage was a series of measurements made on preliminary sites that were known to have good acoustical properties. A range of binder tests were then performed on small areas, approximately 1.0m by 1.0m to determine the binder content and a range of stone sizes. The final stage followed the construction of the test track see figure 8.2 and involved a series of level difference measurements on the various bays of the track, acoustical and non–acoustical measurements on cores extracted from the test track.

## 8.1 Construction of porous road surfaces

The material specification for the pervious tarmacadam is given in appendix E. The materials were chosen to have a nominal maximum stone size grading of 20mm, 10mm and 6.3mm. Binder drainage tests were performed to determine the binder content which would ensure structural stability without significantly altering the required void content of approximately 20 %. This is determined by placing a known mass of the aggregate into a basket placed in a pre–heated oven above a drip tray. The binder is added and the amount draining through the sample into the tray is monitored over a known period of time. The process is repeated for a range of binder contents. Sample slabs of the material were constructed using the resulting binder content and examined to ensure that the lower face was not blocked by excessive binder content. The materials resulting from these trials were laid on the test track as shown in figure 8.2. The absorption coefficient was

evaluated for the sample materials and the test track cores. The results indicated that the test track material was similar to that constructed in the laboratory. The test track was constructed by placing a sheet of polypropylene over a level hardcore base onto which the pervious macadam was laid. During the construction of the test track samples of the pervious material were collected and analysed by the County engineers department of Surrey County Council. This ensured that the material laid was in accordance with the specifications. The results of these trials are shown in table 8.1

| BS sieve | 20mm material | | | 10mm material | | | 6.3mm material | | |
|---|---|---|---|---|---|---|---|---|---|
| mm | Specified grading | Lab. sample (1) | Track sample (2) | Specified grading | Lab. sample (1) | Track sample (2) | Specified grading | Lab. sample (1) | Track sample (2) |
| 28 | 100 | 100 | 100 | | | | | | |
| 20 | 95 ±5 | 95 | 99 | | | | | | |
| 14 | 65 ±10 | 65 | 67 | 100 | 100 | 100 | | | |
| 10 | 25 ±10 | 25 | 48 | 95±5 | 95 | 95 | 100 | 100 | |
| 6.3 | 20±10 | 20 | 12 | 20±5 | 20 | 60 | 95±5 | 95 | 91 |
| 3.35 | 10±5 | 10 | 7 | 10±5 | 10 | 9 | 10±5 | 10 | 23 |
| 75$\mu$m | 4.5±1 (3) | 4.5 | 3.9 | 4.5±1 (3) | 4.5 | 3.4 | 4.5±1 (3) | 4.5 | 5.4 |
| Binder Content (4) | | | | | | | | | |
| Before | 3.7±0.3 | 3.7 | | 5.2±0.5 | 5.2 | | 5.2±0.5 | 5.2 | |
| After | 3.2±0.3 | 3.2 | 3.0 | 4.0±0.3 | 4.0 | 4.1 | 5.2±0.3 | (5) | 5.1 |

**Table 8.1** Aggregate gradings and binder contents of materials

Notes for table 8.1

(1) Laboratory samples made under supervision of the Materials division T.R.R.L.

(2) Analysis carried out by the County engineers Dept. Surrey County Council

(3) To include 2 % by mass of the total aggregate of hydrated lime (4) The values refer to the binder contents of samples before and after the binder drainage tests were carried out and are expressed as a percentage by mass of the total mixture

(5) As the binder content for the sample made before the drainage tests complies with the specification further samples were not required.

## 8.2 Validation of microstructural model

The microstructural model developed by Attenborough [120] is proposed as a way of characterizing the acoustical properties of the road surface and the modified Weyl van der Pol formula as an adequate basis for calculating propagation effects. The study also acts as a further test of the indirect parameter deduction methods introduced in chapter 6. Prior to optimizing the road parameters it has to be confirmed that the model is an accurate descriptor of the acoustical characteristics of the material. This validation process is reported in five parts:

1. Acoustical procedures used for model validation
2. Non–acoustical procedures used for model validation
3. Examination of road surfaces and development of test track
4. Results of point source validation process
5. Extension to validation using vehicle source

### 8.2.1 Acoustical procedures used for model validation

Two acoustical procedures are used to survey the properties of the pervious material. These are level difference measurements on test areas and normal

| Geometry | Source height (m) | Upper receiver height (m) | Lower receiver height (m) | Separation (m) |
|---|---|---|---|---|
| 1 | 0.5 | 0.5 | 0.05 | 1.5 |
| 2 | 0.3 | 0.3 | 0.05 | 1.5 |
| 3 | 0.4 | 0.4 | 0.05 | 1.0 |
| 4 | 0.3 | 0.3 | 0.05 | 1.0 |
| 5 | 0.2 | 0.2 | 0.05 | 1.0 |
| 6 | 0.2 | 0.2 | 0.05 | 2.0 |
| 7 | 0.3 | 0.3 | 0.05 | 2.0 |
| 8 | 0.5 | 0.5 | 0.05 | 2.0 |
| 8 | 0.2 | 0.2 | 0.05 | 0.7 |

Table 8.2 Geometries used for porous road surface characterization.

incidence absorption coefficient measurements on core samples.

### Level difference measurements

The process of collecting and analysing short range level difference data was described in chapter 6. Nine geometries were chosen to produce the range of level difference spectra needed by the parameter deduction routine. These are listed in table 8.2. These source receiver configurations were maintained throughout the point source validation process.

### Normal incidence absorption coefficient data

The standing wave tube technique described in chapter 2 was used to measure the normal incidence impedance and absorption coefficient of a number of core samples taken from the test sites. The cores either 94mm or 97mm in diameter were taken following the level difference measurements from the point of specular reflection. This lies midway between the source and receiver array if the upper microphone is at the same height as the source. This method of core collection should ensure that the non-acoustical measurements are carried out on a core from the area examined by the level difference technique. For the latter measurements a 97mm core was chosen as standard as this was the internal diameter of the standing wave tube used to collect the impedance data.

### 8.2.2 Non–acoustical measurements

The non-acoustical methods used to determine the parameters of the microstructural model ( with exception of the layer depth ) have been discussed in chapter 2.

#### Layer depth

The layer depth was measured directly on the core samples taken from the road surface. This proved difficult for the preliminary sites due to the inhomogeneity of the surface material and the lack of any well defined rigid backing. This problem was overcome however by laying the test site road surfaces, described in subsection 8.2.3, onto a polypropylene layer, which was cemented to the subsurface using a tack coat, i.e. a thin layer of bituminous material. The reduction in the range of stone sizes also permitted easy visual discrimination between layers for the two–material sites when examining test cores.

### 8.2.3 Examination of road surfaces and development of test track site

The model validation process using a point source and the development of the test track may be divided into three sets of measurements:

- Measurements over preliminary sites
- Construction and measurement of binder test cores
- Construction and measurements over test track

Four preliminary sites which were known to have improved acoustic performances when compared to non-pervious 'macadams using vehicle characterization tests were surveyed using both acoustical and non–acoustical techniques. These sites are identified as

- Ricardos site

- MIRA site
- TRRL area L
- TRRL WG 27 site

The result of this initial survey are presented in section 8.2.4. The conclusions drawn from this preliminary test were three fold.

1. The microstructural model was reasonable descriptor of the acoustical characteristics of the surface and the modified Weyl van der Pol formula was an adequate descriptor of the propagation from a point source over such a surface.
2. Possible sources of error were the poorly defined layered structure due to the lack of a rigid backing and the inhomogeneity of the materials.
3. Wider ranges of stone sizes and binder contents were required to increase the range of surfaces examined.

Accordingly a series of small samples were produced using several different stone sizes and varying binder contents. This ensured that surfaces with differing acoustical properties could be developed and that the binder content was such that the structural integrity of the material was maintained without decreasing the porosity. Although these test samples were too small to allow level difference measurements test cores were collected. These were used to give absorption coefficient data and were subject to the non–acoustic tests. A further development incorporating the new test materials described above was the test track shown in figure 8.2. Consisting of ten bays 10m by 3.35m with layer depths of either 5cm or 10cm. Two bays contained a double layered structure.

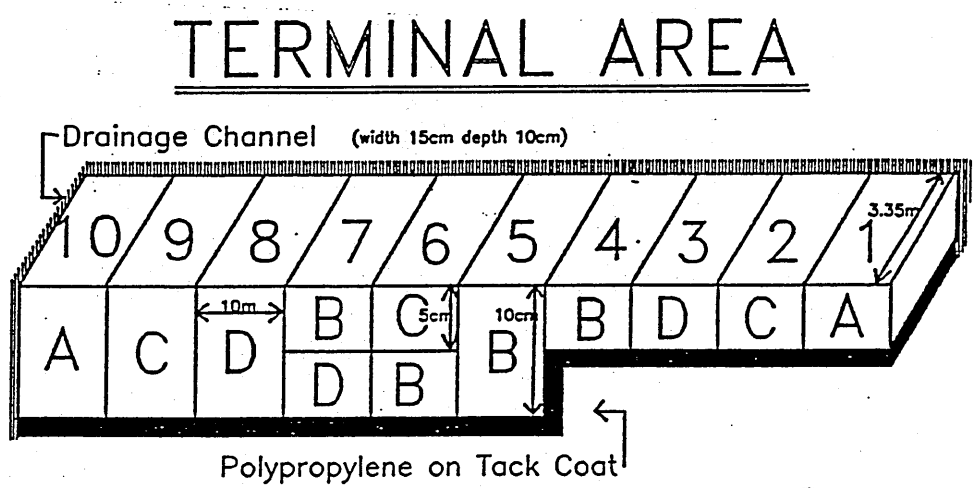


**Figure 8.2** Test track

Four material types were investigated described by the parameters in table 8.3. Table 8.3 contains information also about the other test surfaces used in the validation procedure. The material specifications are given in appendix E.

Level difference and normal incidence absorption coefficient measurements were collected over the ten test bays and the microstructural parameters were deduced using the indirect parameter fitting method described in chapter 6 for both sets of acoustical data. The non–acoustical tests were used subsequently to produce independent data of flow resistivity, porosity, tortuosity and layer depth.

### 8.2.4 Results of the point source validation process

Tables 8.4, 8.5 and 8.6 to 8.8 summarize the microstructural model parameters deduced both acoustically and non–acoustically for the test surfaces described in table 8.3. Examples of the fitted level difference spectra and absorption coefficient curves are given in appendices F and G respectively.

| Surface | Description | Location |
|---|---|---|
| Ricardos | Graded surface with 6mm stone size to 20mm stone size on earth base | Shoreham Sussex |
| MIRA | 10mm stone size in upper layer on high binder content base | Nuneaton Warwickshire |
| TRRL area L | 20mm stone size in upper layer on hard core base | Crowthorne Berkshire |
| TRRL WG 27 | Stone size less than 6mm on high binder content base | Crowthorne Berkshire |
| 6mm Binder test | 6mm stone size on rigid base | Crowthorne Berkshire |
| 10mm binder test | 10mm stone size on rigid base | Crowthorne Berkshire |
| 20mm binder test | 20mm stone size on rigid base | Crowthorne Berkshire |
| Site 1 | 5cm layer of material A (20mm high flakiness), on polypropylene layer | Crowthorne Berkshire |
| Site 2 | 5cm layer of material C (6mm), on polypropylene layer | Crowthorne Berkshire |
| Site 3 | 5cm layer of material D (20mm normal flakiness), on polypropylene layer | Crowthorne Berkshire |
| Site 4 | 5cm layer of material B (20mm high flakiness), on polypropylene layer | Crowthorne Berkshire |
| Site 5 | 10cm layer of material B (20mm high flakiness), on polypropylene layer | Crowthorne Berkshire |
| Site 6 | 5cm layer of material C on 5cm of material B, on polypropylene layer | Crowthorne Berkshire |
| Site 7 | 5cm layer of material A on 5cm of material D, on polypropylene layer | Crowthorne Berkshire |
| Site 8 | 10cm layer of material D (20mm high flakiness), on polypropylene layer | Crowthorne Berkshire |
| Site 9 | 10cm layer of material C (20mm high flakiness), on polypropylene layer | Crowthorne Berkshire |
| Site 10 | 10cm layer of material A (20mm high flakiness), on polypropylene layer | Crowthorne Berkshire |

**Table 8.3** Surfaces used in validation procedure

| Parameter/site | Ricardos | TRRL L | TRRL WG 27 | MIRA |
|---|---|---|---|---|
| Level diff fit | | | | |
| Flow resistivity | 150000 | 3638 | 170000 | 5382 |
| Porosity | 0.19 | 0.214 | 0.14 | 0.22 |
| Grain shape | 0.5 | 0.46 | 0.90 | 0.51 |
| (Tortuosity) | (2.29) | (1.44) | (5.86) | (2.16) |
| Pore shape | 0.25 | 0.24 | 0.40 | 1.0 |
| Layer depth | 0.14 | 0.045 | 0.04 | 0.05 |
| Absorption coeff. fit | | | | |
| Flow resistivity | | 3600 | | 5472 |
| Porosity | | 0.212 | | 0.23 |
| Grain shape | | 0.46 | | 0.75 |
| (Tortuosity) | | (2.04) | | (3.01) |
| Pore shape | | 0.25 | | 0.50 |
| Layer depth | | 0.05 | | 0.05 |
| Non-acoustically measured | | | | |
| Flow resistivity | 123500 | 3500 | 213000 | 5500 |
| Porosity | | 0.204 | | 0.29 |
| Grain shape | | 0.87 | | 1.3 |
| (Tortuosity) | | (3.98) | | (4.99) |
| Pore shape | | | | |
| Layer depth | 0.13 | 0.052 | 0.02 | 0.045 |

Table 8.4 Parameters deduced from preliminary site

| Parameter/Site | 6mm site | 10mm site | 20mm site |
|---|---|---|---|
| Absorption coefficient fit | | | |
| Flow resistivity | 34063 | 4282 | 4400 |
| Porosity | 0.195 | 0.24 | 0.147 |
| Grain shape | 1.33 | 1.15 | 0.77 |
| (Tortuosity) | (8.79) | (5.16) | (4.37) |
| Pore shape | 0.5 | 0.5 | 0.45 |
| Layer depth | 0.05 | 0.053 | 0.055 |
| Non-acoustically measured | | | |
| Flow resistivity | 34063 | 4282 | 4400 |
| Porosity | 0.195 | 0.224 | 0.147 |
| Grain shape | 1.4 | 1.1 | 0.71 |
| (Tortuosity) | (9.86) | (5.18) | (3.90) |
| Pore shape | | | |
| Layer depth | 0.05 | 0.053 | 0.055 |

**Table 8.5** Parameters deduced from binder tests

| Parameter/Site | Material A 20mm hf | Material B 20mm nf | Material C 10mm | Material D 6mm |
|---|---|---|---|---|
| 5cm level diff fit | | | | |
| Flow resistivity | 1976 | 1653 | 3743 | 11922 |
| Porosity | 0.28 | 0.287 | 0.238 | 0.19 |
| Grain shape | 0.74 | 0.497 | 0.75 | 0.62 |
| (Tortuosity) | (2.56) | (1.85) | (2.93) | (2.80) |
| Pore shape | 0.86 | 0.61 | 0.48 | 0.58 |
| Layer depth | 0.059 | 0.062 | 0.0609 | 0.0619 |
| 10cm level diff fit | | | | |
| Flow resistivity | 1625 | 1680 | 3270 | 32500 |
| Porosity | 0.290 | 0.292 | 0.234 | 0.146 |
| Grain shape | 1.27 | 0.859 | 1.03 | 1.12 |
| (Tortuosity) | (4.81) | (2.87) | (4.46) | (8.62) |
| Pore shape | 1.41 | 0.477 | 0.739 | 0.85 |
| Layer depth | 0.114 | 0.0984 | 0.11 | 0.105 |
| Double layer fit | | | | |
| Flow resistivity | | 1653 | 3750 | 11900 |
| Porosity | | 0.237 | 0.254 | 0.190 |
| Grain shape | | 0.497 | 0.77 | 1.00 |
| (Tortuosity) | | (2.04) | (2.87) | (5.26) |
| Pore shape | | 0.51 | 0.48 | 1.5 |
| Layer depth | | 0.06 | 0.065 | 0.041 |

**Table 8.6** Parameters deduced from test track via level difference fitting

Note: hf and nf are used as abbreviations for normal flakiness and high flakiness.

| Parameter/Site | Material A 20mm hf | Material B 20mm nf | Material C 10mm | Material D 6mm |
|---|---|---|---|---|
| 5cm absorption coeff fit | | | | |
| Flow resistivity | 1970 | 1670 | 3250 | 11900 |
| Porosity | 0.282 | 0.287 | 0.235 | 0.193 |
| Grain shape | 1.35 | 0.89 | 0.96 | 1.13 |
| (Tortuosity) | (5.52) | (3.03) | (4.01) | (6.41) |
| Pore shape | 0.83 | 0.58 | 0.47 | 0.55 |
| Layer depth | 0.058 | 0.061 | 0.061 | 0.062 |
| 10cm absorption coeff fit | | | | |
| Flow resistivity | 1425 | 1830 | 3270 | 33500 |
| Porosity | 0.285 | 0.255 | 0.238 | 0.146 |
| Grain shape | 1.21 | 0.954 | 1.03 | 1.09 |
| (Tortuosity) | (4.56) | (3.66) | (4.38) | (8.14) |
| Pore shape | 1.17 | 0.577 | 0.539 | 0.52 |
| Layer depth | 0.114 | 0.105 | 0.105 | 0.105 |
| Double layer absorption coeff fit | | | | |
| Flow resistivity | | 1650 | 3743 | 11000 |
| Porosity | | 0.29 | 0.238 | 0.20 |
| Grain shape | | 0.89 | 0.97 | 1.14 |
| (Tortuosity) | | (3.00) | (4.02) | (6.26) |
| Pore shape | | 0.50 | 0.48 | 0.48 |
| Layer depth | | 0.060 | 0.058 | 0.061 |

**Table 8.7** Parameters deduced from test track via absorption coefficient fitting

Note: hf and nf are used as abbreviations for normal flakiness and high flakiness.

| Parameter/Site | Material A 20mm hf | Material B 20mm nf | Material C 10mm | Material D 6mm |
|---|---|---|---|---|
| Measured 94/5 | | | | |
| Flow resistivity | 1900 | 1640 | 3600 | 11450 |
| Porosity | 0.229 | 0.255 | 0.242 | 0.210 |
| Grain shape | 1.37 | 0.89 | 0.97 | 1.14 |
| (Tortuosity) | (7.53) | (3.77) | (3.96) | (5.92) |
| Pore shape | | | | |
| Layer depth | 0.055 | 0.0615 | 0.059 | 0.060 |
| Measured 97/5 (1) | | | | |
| Flow resistivity | 1425 | 1475 | 3700 | 10800 |
| Porosity | 0.283 | 0.293 | 0.243 | 0.208 |
| Grain shape | 1.17 | 0.91 | 1.14 | 1.16 |
| (Tortuosity) | (4.41) | (3.07) | (5.04) | (6.21) |
| Pore shape | | | | |
| Layer depth | 0.055 | 0.0615 | 0.062 | 0.060 |
| Measured 97/10 (1) | | | | |
| Flow resistivity | 1550 | 1525 | 3300 | 33500 |
| Porosity | 0.229 | 0.255 | 0.242 | 0.146 |
| Grain shape | 0.90 | 0.91 | 0.96 | N/A |
| (Tortuosity) | (3.80) | (3.51) | (3.91) | (N/A) |
| Pore shape | | | | |
| Layer depth | 0.12 | 0.10 | 0.11 | 0.105 |
| Measured 97/5 (2) | | | | |
| Flow resistivity | 1565 | 1670 | 3200 | 9200 |
| Porosity | 0.261 | 0.208 | 0.305 | 0.208 |
| Grain shape | 1.13 | 0.85 | 1.32 | 1.08 |
| (Tortuosity) | (4.61) | (3.83) | (4.81) | (5.52) |
| Pore shape | | | | |
| Layer depth | 0.060 | 0.057 | 0.058 | 0.060 |
| Measured 97/10 (2) | | | | |
| Flow resistivity | 1360 | 1785 | 3450 | 34750 |
| Porosity | 0.279 | 0.277 | 0.262 | 0.127 |
| Grain shape | N/A | 1.06 | 1.04 | 0.89 |
| (Tortuosity) | (N/A) | (3.91) | (4.03) | (6.39) |
| Pore shape | | | | |
| Layer depth | 0.099 | 0.095 | 0.098 | 0.112 |

**Table 8.8** Parameters deduced from test track via non-acoustical measurements

The procedure used to evaluate the parameters required to fit the mixed layer data sites 6 and 7 was modified. As the minimization programme would take an unacceptable amount of time to evaluate ten parameters five parameters for the lower layer were fixed, at values obtained from fitting data for the single layer, and the algorithm used to generate the parameters for the top layer. The upper layer parameters were then kept constant and the fitting was repeated to generate the new lower layer parameters. The resulting parameters were used to generate the fitted curves given in appendix F. For reference the layer depths of the two 97mm diameter core samples taken from the mixed layer sites are given in table 8.9. The non-acoustically measured values are obtained from three sets of cores. The first 97mm diameter set (i.e 97/5 (1) and 97/10 (1) ) are taken from the point of specular reflection for the 5cm and 10cm deep layers. The second set (97/5 (2) and 97/10 (2) were collected after the vehicle validation experiments.

| Site 6(1) (upper) Material C | Site 6(1) (lower) Material B | Site 7(1) (upper) Material B | Site 7(1) (lower) Material D |
|---|---|---|---|
| 0.060 | 0.058 | 0.065 | 0.052 |
| Site 6(2) (upper) Material C | Site 6(2) (lower) Material B | Site 7(2) (upper) Material B | Site 7(2) (lower) Material D |
| 0.055 | 0.075 | 0.063 | 0.045 |

**Table 8.9** Measured layer depths for mixed layer sites

### 8.2.5 Extension to validation from vehicle sources

As the results from the point source measurements indicate that the microstructural model is an accurate description of the acoustical properties of the material under study the validation process was extended to included noise from a vehicle source. An incidental result of this work was the deduction of an effective point source array for predicting propagation from vehicles at close range (7.0m). Two vehicles were employed; an estate car and a H.G.V. tractor unit. The Vauxhall Astra estate was positioned over the test bay with engine speeds kept constant respectively at 2000 R.P.M. , 3000 R.P.M. and 4000 R.P.M.. Level difference measurements were then collected at source receiver separations of 3m, 5m and 7m. The fitting procedure used for the point source data was repeated. The single point source however was replaced by a pair of incoherent sources positioned as shown in figure 8.3. The number and location of the point sources was determined by assuming that the engine and exhaust system of the car were the main sources and using intensity measurements made at the Transport and Road Research Laboratory to indicate their approximate acoustic location. These locations needed slight adjustment to gain a best fit to the level difference spectra. The results of this validation procedure are given in table 8.10. The fitted level difference spectra are shown in appendix H. The same process was used for the tractor unit with a 1700 R.P.M. engine speed. The location of an equivalent pair of incoherent sources is shown in figure 8.4 however only the 7m distance was used. The results are shown in table 8.10 and appendix H. It is evident from the fitted spectra that the agreement between the measured and deduced spectra for the vehicle source is less satisfactory than that gained for the loudspeaker point source. It is expected however that this is due to the simplified modelling of the source characteristics of the vehicle rather than a failure of the microstructural model. The best agreement was seen at high engine speeds with a vehicle source to receiver separation of 7m.

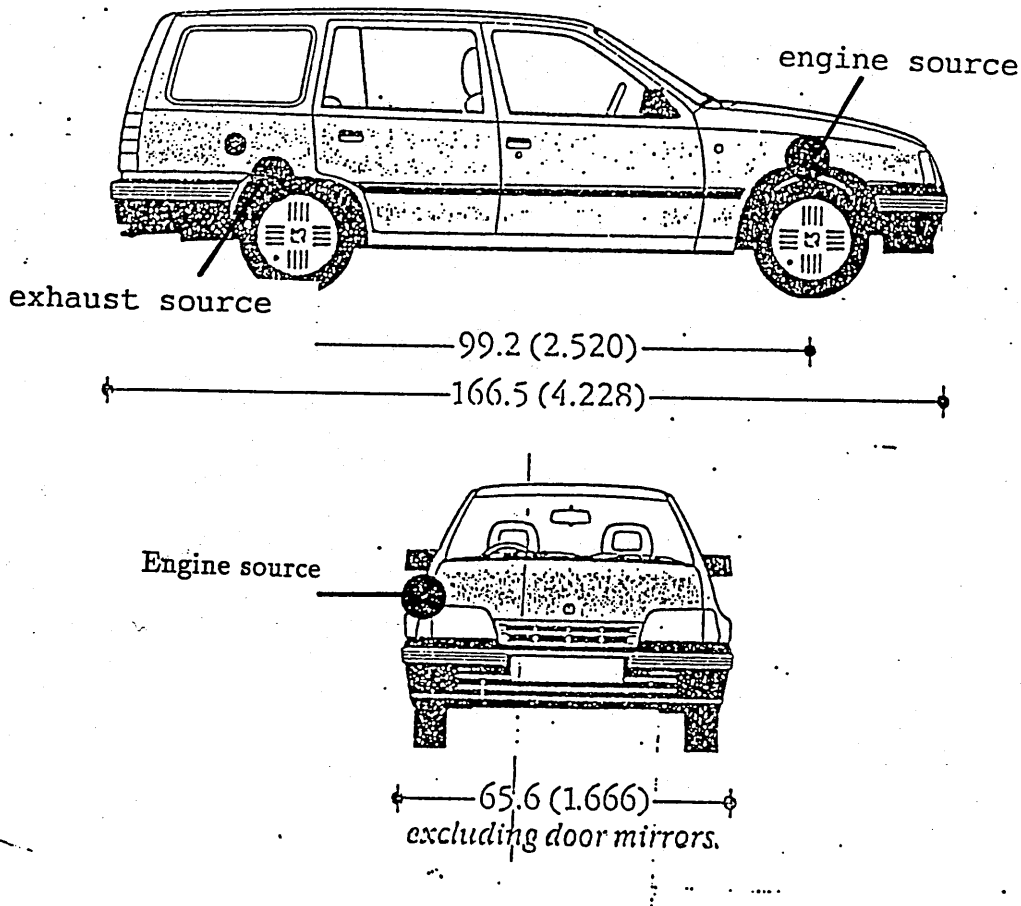


**Figure 8.3** Location of incoherent sources on light vehicle (units in brackets are meters)

| Parameter | Material | Material | Material | Material |
|---|---|---|---|---|
| Car | A | B | C | D |
| Flow resistivity | 1976 | 1600 | 3743 | 11922 |
| Porosity | 0.23 | 0.26 | 0.22 | 0.18 |
| Grain shape | 0.79 | 0.69 | 0.68 | 0.62 |
| (Tortuosity) | (3.19) | (2.53) | (2.79) | (2.89) |
| Pore shape | 0.90 | 1.49 | 0.90 | 0.88 |
| Layer depth | 0.059 | 0.0625 | 0.063 | 0.61 |
| H.G.V. | A | B | C | D |
| Flow resistivity | 1970 | 1640 | 3600 | 11800 |
| Porosity | 0.21 | 0.25 | 0.21 | 0.18 |
| Grain shape | 0.87 | 0.85 | 0.9 | 1.0 |
| (Tortuosity) | (3.88) | (3.24) | (4.07) | (5.55) |
| Pore shape | 1.7 | 0.9 | 0.8 | 0.5 |
| Layer depth | 0.048 | 0.055 | 0.055 | 0.05 |

**Table 8.10** Parameters deduced from vehicular source tests, sites 1 to 4

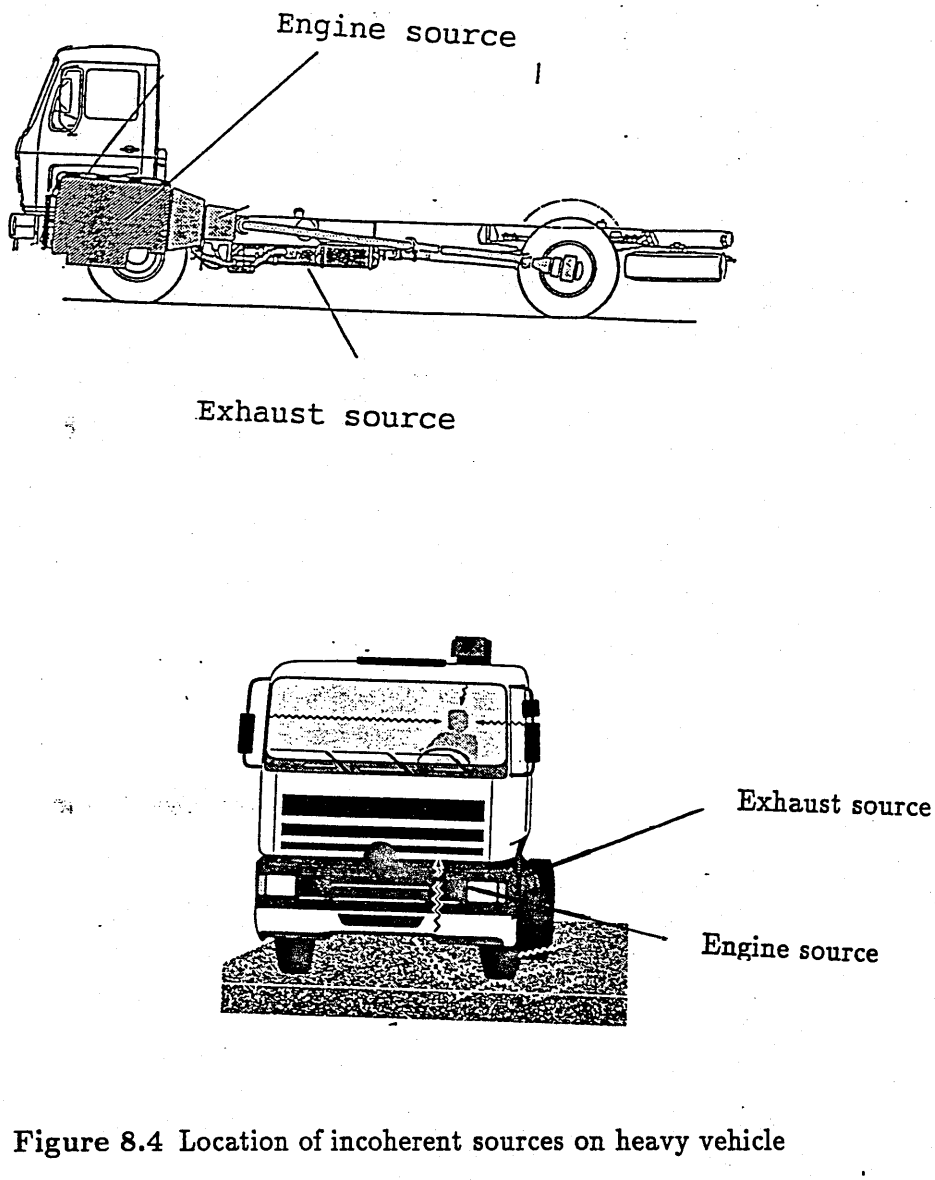


**Figure 8.4** Location of incoherent sources on heavy vehicle

## 8.3 Comparison of phenomenological and microstructural models

The phenomenological model discussed in chapter 3 has been used by French and Dutch researchers [140,204,141] to model normal incidence absorption coefficient data and to optimize the noise performance of porous road surfaces. There are considerable differences between the predictions of the two impedance models, especially for low flow resistivities , thin layers and oblique angles of incidence. This was examined previously in chapter 3 for a semi–infinite surface. In this section the ability of the two models to provide acoustical descriptors of rigidly backed externally reacting surfaces such as pervious 'macadam are compared. The theoretical formulation of each model is compared and particular attention is paid to normal and oblique incidence absorption coefficient calculations. A comparison is made between normal incidence absorption coefficient measured in an impedance tube and that predicted by the impedance models using parameters deduced acoustically and non–acoustically. This results in a statement about the relative validity of the impedance models for modelling the acoustical characteristics of pervious road surfaces.

Comparison of equations 8.1 and 8.2 ( repeated from chapter 3 ) with the low frequency and/or high flow resistivity approximation of the microstructural model, equations 8.3 to 8.5 suggests that the two models are similar if $\lambda \ll 1$, and that the structure factor is equivalent to the tortuosity. The phenomenological model does not account for the effects of pore shape or pore size distribution encompassed in the parameters $I_o$ and $s_p$ of the microstructural model.

$$Z_c = \frac{\sqrt{k}}{\Omega}\left[1 + \frac{i\Omega\sigma}{\omega\rho_0 k}\right]^{\frac{1}{2}} \tag{8.1}$$

$$k_b = \Omega Z_c \tag{8.2}$$

$$Z_c = \frac{I_o \frac{q^2}{\Omega} + \imath \frac{2s_p^2 \sigma}{\pi f \rho_0}}{k_b} \tag{8.3}$$

$$k_b = \left(\gamma \Omega^{\frac{1}{2}}\right) \left[\frac{aq^2}{\Omega} + \imath \left(\frac{2s_p^2 \sigma}{\pi f \rho_0}\right)\right]^{\frac{1}{2}} \tag{8.4}$$

$$a = I_o - \left[\frac{\gamma - 1}{\gamma}\right] N \tag{8.5}$$

$I_o$ is dependent on pore shape and is equal to 1.33 for cylindrical pores and 1.2 for slit like pores. For the two models to be in agreement for small values of $\lambda$ it would be necessary for: $I_o = 1; \gamma \left(I_o - \frac{\gamma-1}{\gamma}\right) N = 1.$ and $4s_p^2 = 1$. These conditions are unlikely. The discrepancies increase with increasing $\lambda$. The phenomenological model predicts that the second absorption coefficient resonance occurs at three times the frequency of the first and is dependent only on the layer depth and structure factor. This prediction is not in accordance with those of the 'exact' microstructural model where the resonance position may be seen to be dependent on flow resistivity and pore shape as well as layer depth and tortuosity. It is expected that the poorest agreement will occur at high frequencies and low flow resistivities corresponding to high values of $\lambda$.

Figure 8.5 shows the sensitivity of the impedance models to variation in flow resistivity. According to the phenomenological model an increase in the flow resistivity in the range 5000 MKS Rayls/m to 20000 MKS Rayls/m increases the magnitude of the first absorption coefficient peak whereas the reverse is predicted by the microstructural model. Nevertheless, for given fixed values of porosity (0.25), grain shape (1.0) and layer depth (0.05) there is an intermediate value of flow resistivity where both models will agree at normal incidence . This intermediate range includes values similar to those found in some porous road surface materials. For flow resistivities below this optimum range, i.e. less than 5000 M.K.S. Rayls/m or above 20 000 MKS Rayls/m there will be some disagreement between the models. It should also be noted that the frequency location of the first absorption coefficient peak predicted by the microstructural model is lower than that predicted by the

phenomenological model for the same values of parameter. To determine which of the impedance models is most accurate it is necessary to examine data collected from the road surfaces detailed in table 8.3. The absorption coefficient curves predicted by both models are obtained by using either parameters deduced acoustically via the level difference fitting technique or those measured non–acoustically. These curves are then compared to data obtained from measurements made using the standing wave tube. The level difference technique was applied using either the microstructural model or the phenomenological model as appropriate. The results of using the phenomenological model with the indirect method are seen in appendix F. It is clear that no suitable fit is found for low or high flow resistivity materials as is indicated by the large RMS error shown in table 8.12. The absorption coefficient curves were fitted using a method similar to that used for the level difference spectra.

| Material (Site No) | A (1) | B (4) | C (2) | D (3) |
|---|---|---|---|---|
| Flow resistivity R/m | 1449.0 | 4275.0 | 6000.0 | 117341.0 |
| Porosity | 0.21 | 0.29 | 0.30 | 0.19 |
| Structure factor | 2.19 | 6.32 | 3.13 | 3.77 |
| Layer depth (m) | 0.07 | 0.061 | 0.061 | 0.059 |

**Table 8.11** Parameters deduced from fitting level difference using Phenomenological model

| Site | Geometry | microstructural RMS error | Phen. RMS error |
|---|---|---|---|
| 1 | 1 | 2.3 | 4.5 |
| 1 | 2 | 3.3 | 4.8 |
| 1 | 3 | 2.6 | 5.1 |
| 2 | 1 | 2.7 | 2.1 |
| 2 | 2 | 2.5 | 1.5 |
| 2 | 3 | 2.6 | 1.8 |
| 3 | 1 | 2.2 | 1.9 |
| 3 | 2 | 2.1 | 1.9 |
| 3 | 3 | 2.8 | 1.8 |
| 4 | 1 | 1.9 | 3.6 |
| 4 | 2 | 3.1 | 5.3 |
| 4 | 3 | 3.2 | 5.2 |

**Table 8.12** RMS errors resulting from parameter fitting technique

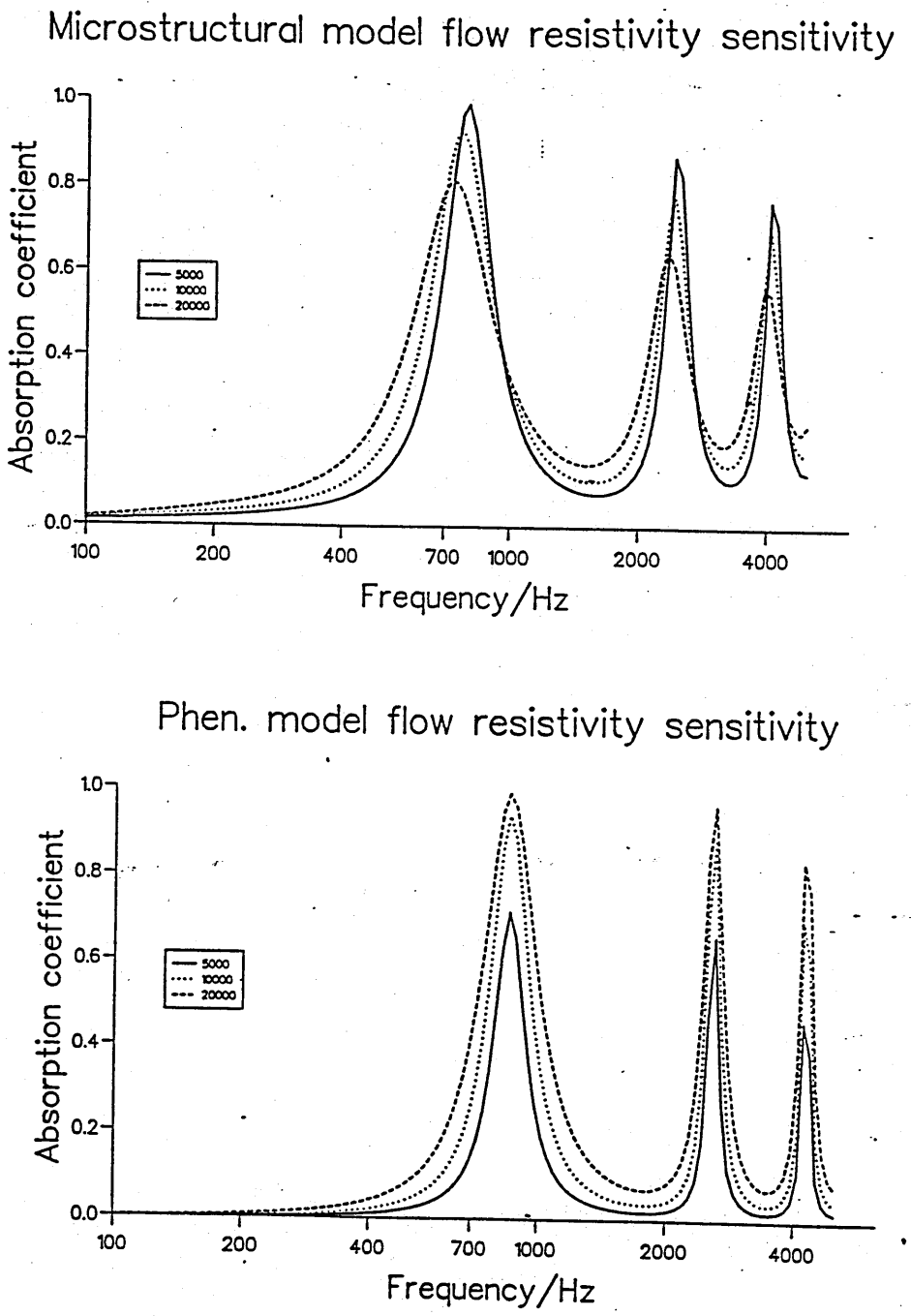


**Figure 8.5** Sensitivity of absorption coefficient to flow resistivity (other parameters given on page 316)

Figures 8.8 to 8.9 show the measured normal incidence absorption coefficient spectra and the predictions of the microstructural model for sites 1 to 4. Figures 8.10 and 8.11 show the corresponding plots for the phenomenological model the evaluated parameters are given in table 8.11. Although agreement between the measured absorption coefficient and that predicted by the microstructural model using the non–acoustically measured parameters is good, the same is not true for the phenomenological model. The frequency location of the resonant peak is predicted tolerably accurately by the phenomenological model but the magnitude of the resonant peak is underestimated particularly for the low flow resistivity materials of sites one and four . The phenomenological model gives less of an underestimate for material C on site 2. On the other hand, for the high flow resistivity material D ( site 3) the phenomenological model over predicts the magnitude of the resonant peak. This is somewhat unexpected as the sensitivity curves, figure 8.5 indicated that the flow resistivity had to be higher than the given non–acoustically measured values of approximately 12000 MKS Rayls/m before over prediction occurred. Nevertheless the comparison with data for material D emphasizes the point that there is a limited range of flow resistivities for which the phenomenological method is accurate. It should be noted that this conclusion would not be altered by adjustment of the structure factor in the phenomenological model since such adjustment alters the location but not the magnitude of the absorption coefficient resonant peak,(see for example Hamet [205] and figure 8.6).

The parameters deduced from the level difference fitting routine particularly over 5cm thick layers, ( as described in chapter 6), do not produce accurate predictions of the absorption coefficient . Primarily this is due to the lower value of the grain shape factor. Two possible explanations may be provided to account for this phenomenon. It is possible that the level difference technique only becomes sufficiently sensitive to grain shape factor for layer depths greater then 5cm. Alternatively the test site core may either have become distorted during sampling or it is not representative of the whole surface structure. The evidence to support the first explanation

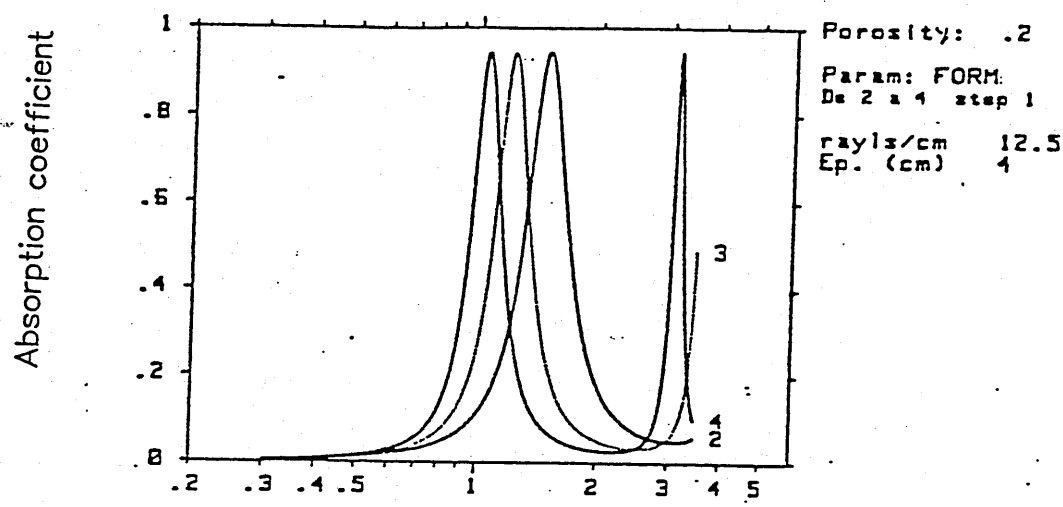


**Figure 8.6** Sensitivity of normal incidence absorption coefficient to changes in the structure factor of the phenomenological model, after Hamet

comes from studying the parameters gained from fitting level difference and absorption coefficients for the 10cm deep layers. It is seen that the two grain shape factors i.e. tortuosities are similar. This indicates that the level difference method is more accurate at predicting material characteristics when used over a deeper layer. Figure 8.7 shows the normal incidence absorption coefficient data for site 1 ( 5cm deep layer ), along with absorption coefficient curves predicted by insertion of the 5cm and 10cm layer depth level difference fitting deduced microstructural model parameters. The layer depth deduced from indirect measurement of the 10cm deep layer is set to the non-acoustically measured value of 5cm.

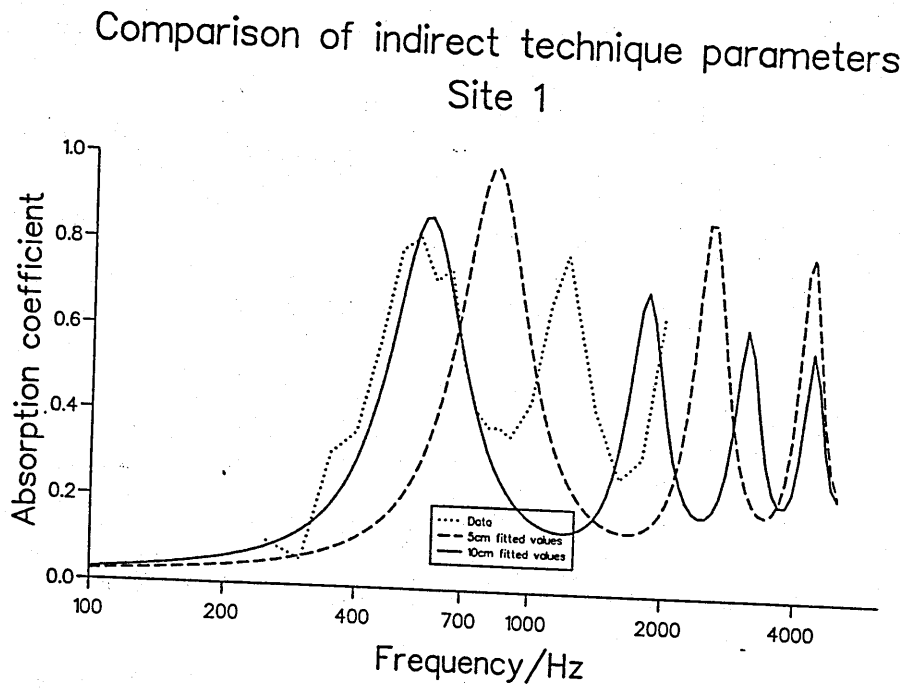


**Figure 8.7** Comparison of absorption coefficient data deduced from 5cm and 10cm level difference fitting technique

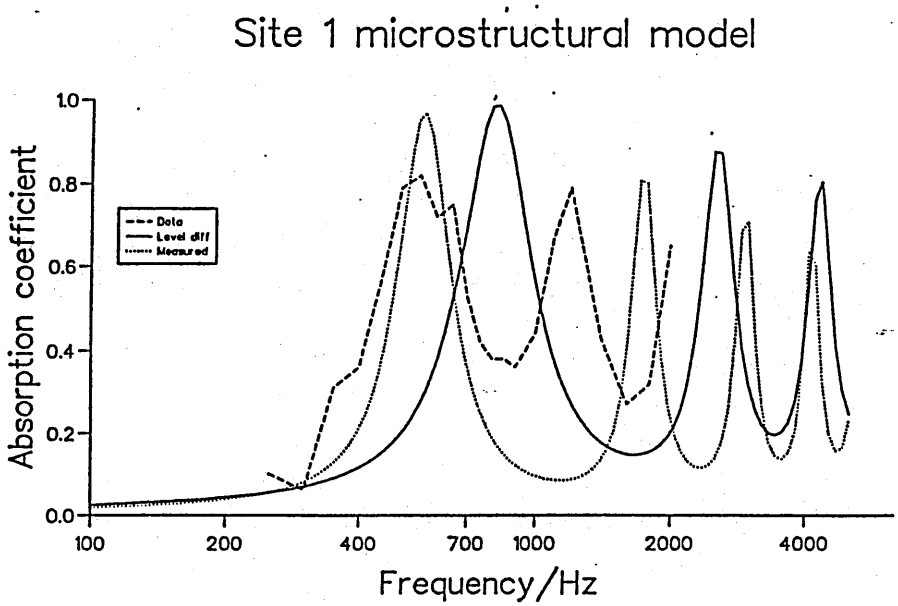


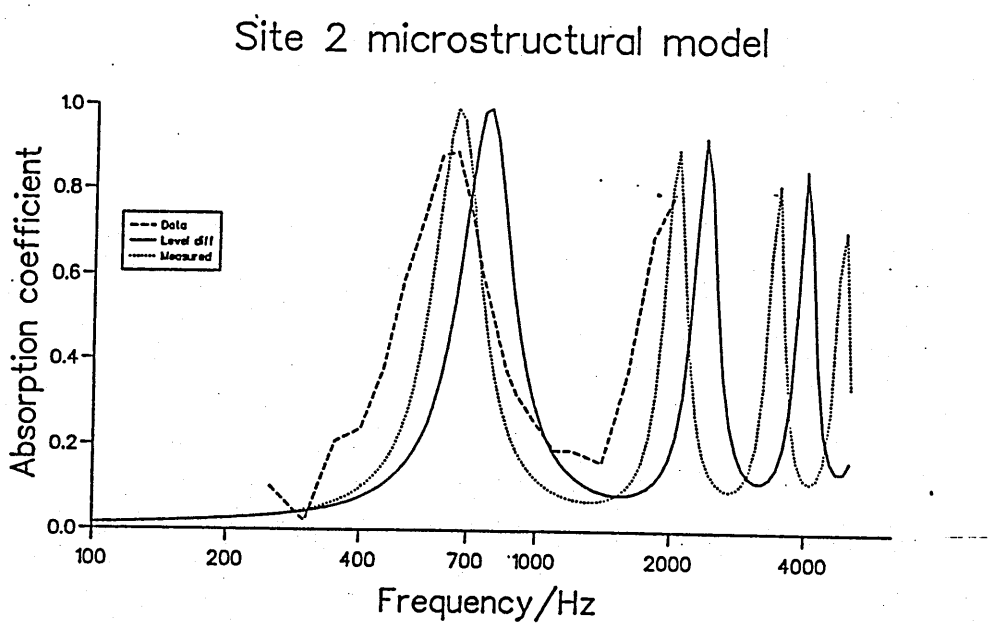


**Figure 8.8** Measured absorption coefficient site 1 (upper) and 2, c.f. microstructural model

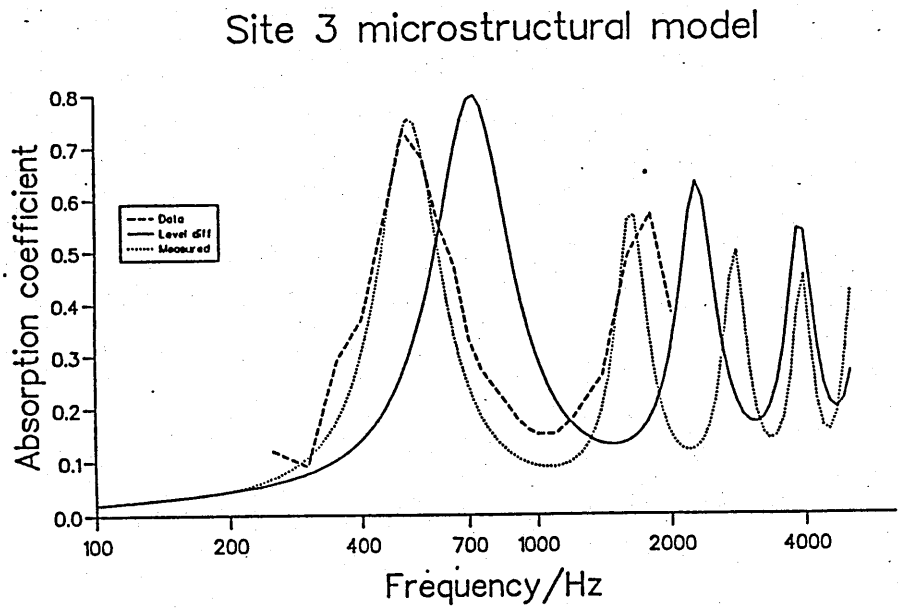


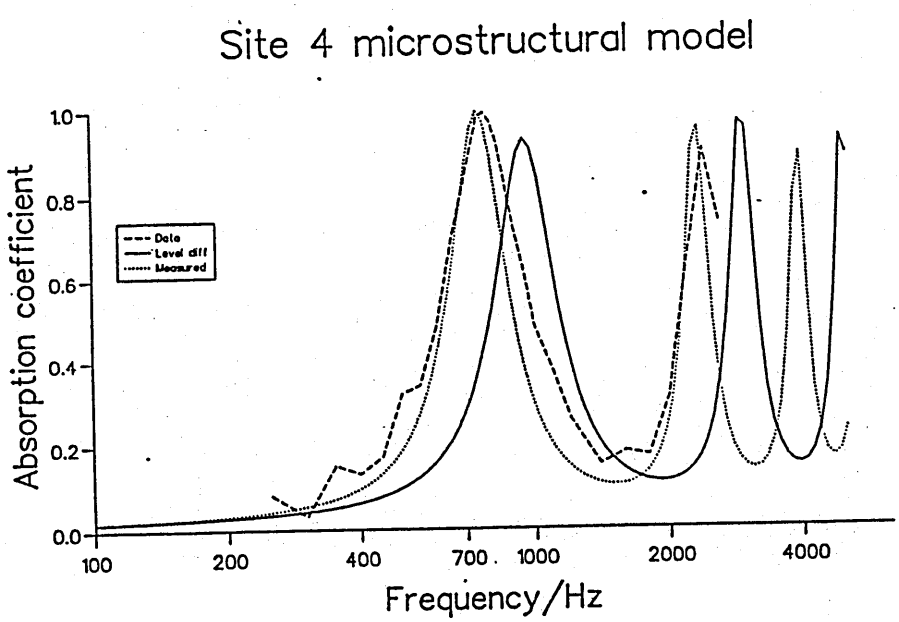


**Figure 8.9** Measured absorption coefficient site 3 (upper) and 4, c.f. microstructural model

## 8.4 Surface optimization

Having validated the applicability of the microstructural model and the modified Weyl van der Pol approximation for point and vehicle sources the model may now be used to find the acoustic properties of the road surfaces that should give maximum noise reduction ( considering only the propagation effect ). Figure 8.12 is a schematic of the optimization procedure.

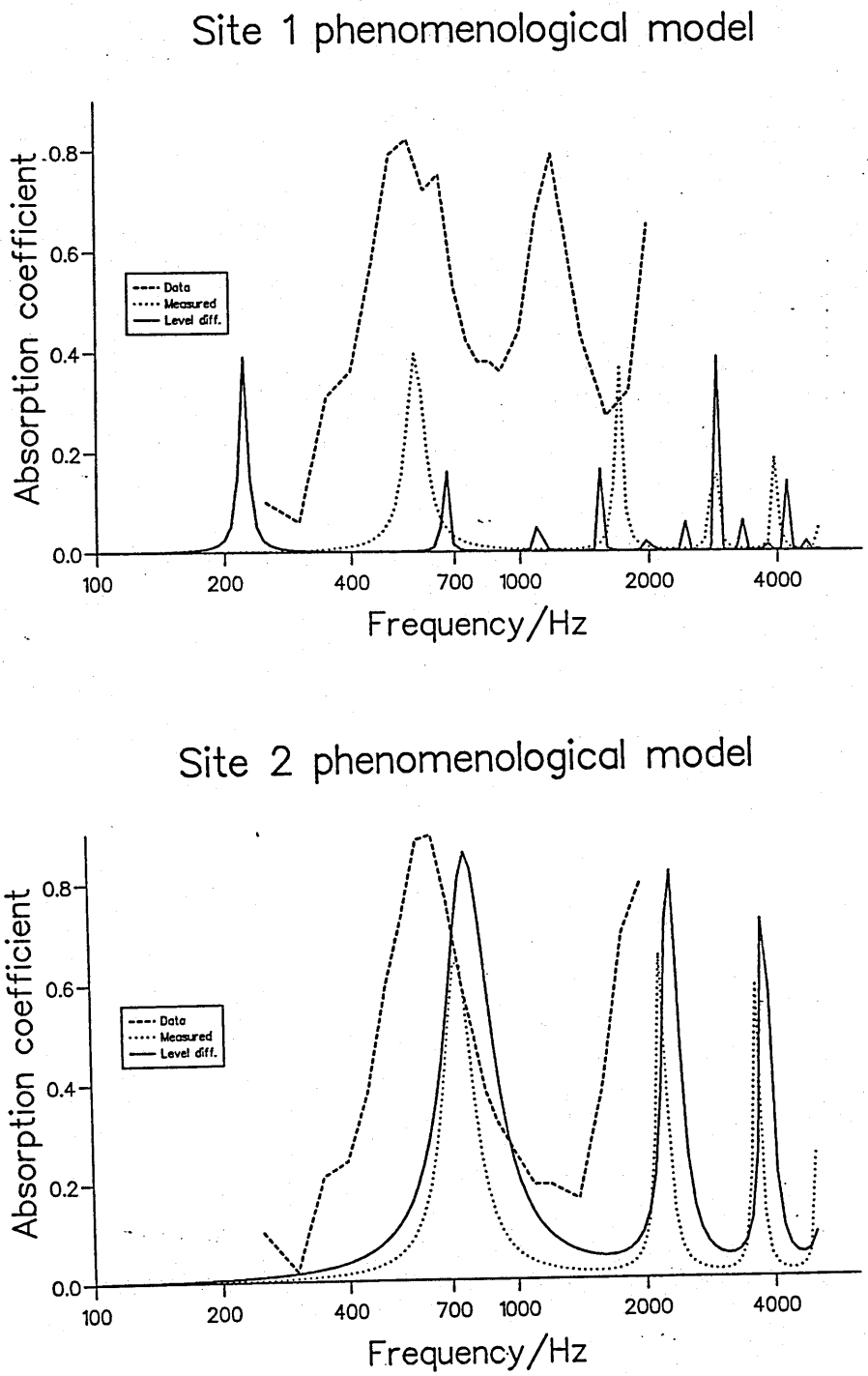


**Figure 8.10** Measured absorption coefficient site 1 (upper) and 2, c.f. phenomenological model

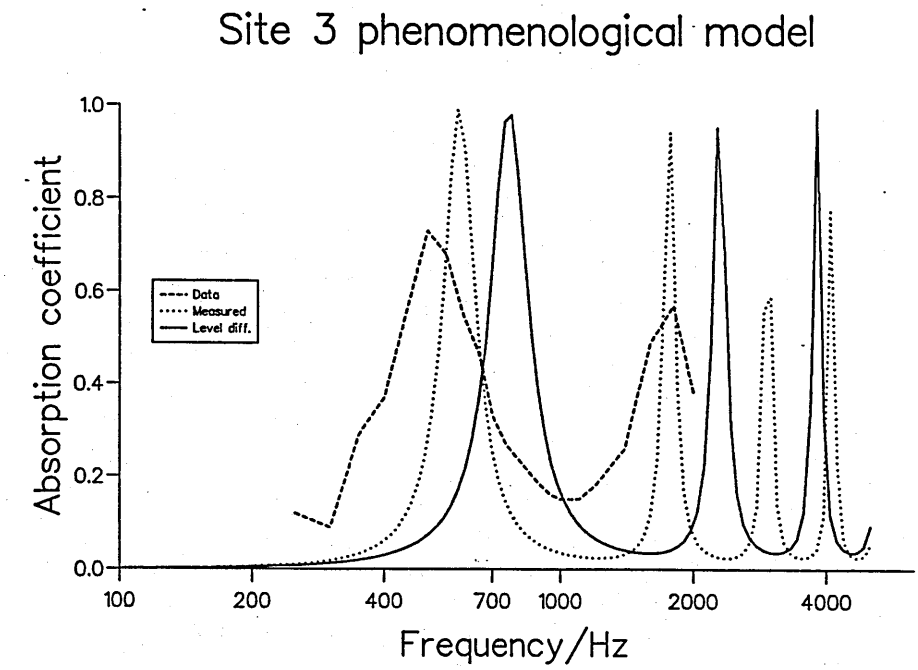


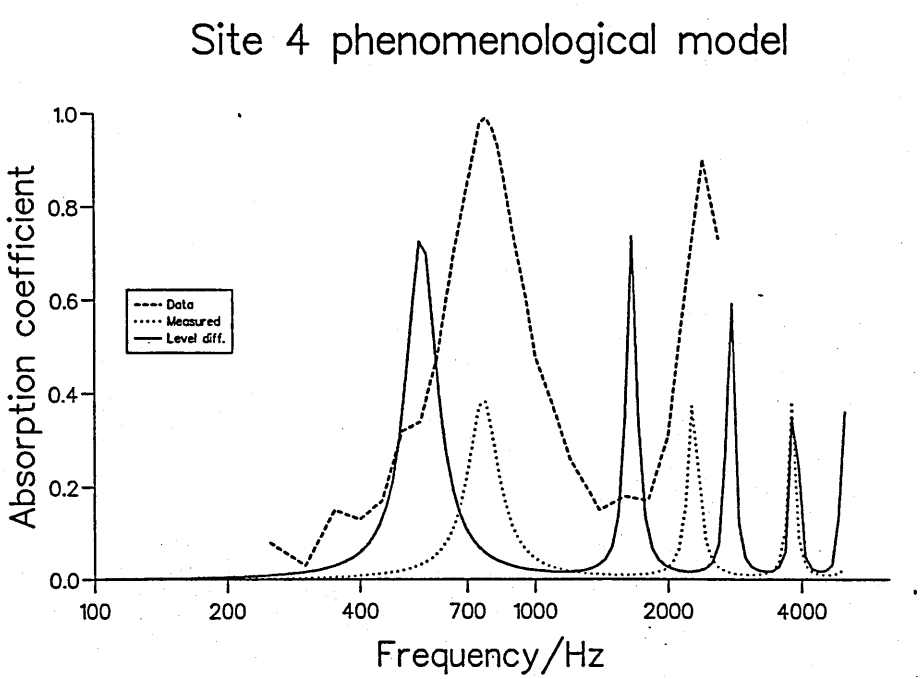


**Figure 8.11** Measured absorption coefficient site 3 (upper) and 4, c.f. phenomenological model

**Figure 8.12** Flow chart showing optimization procedure

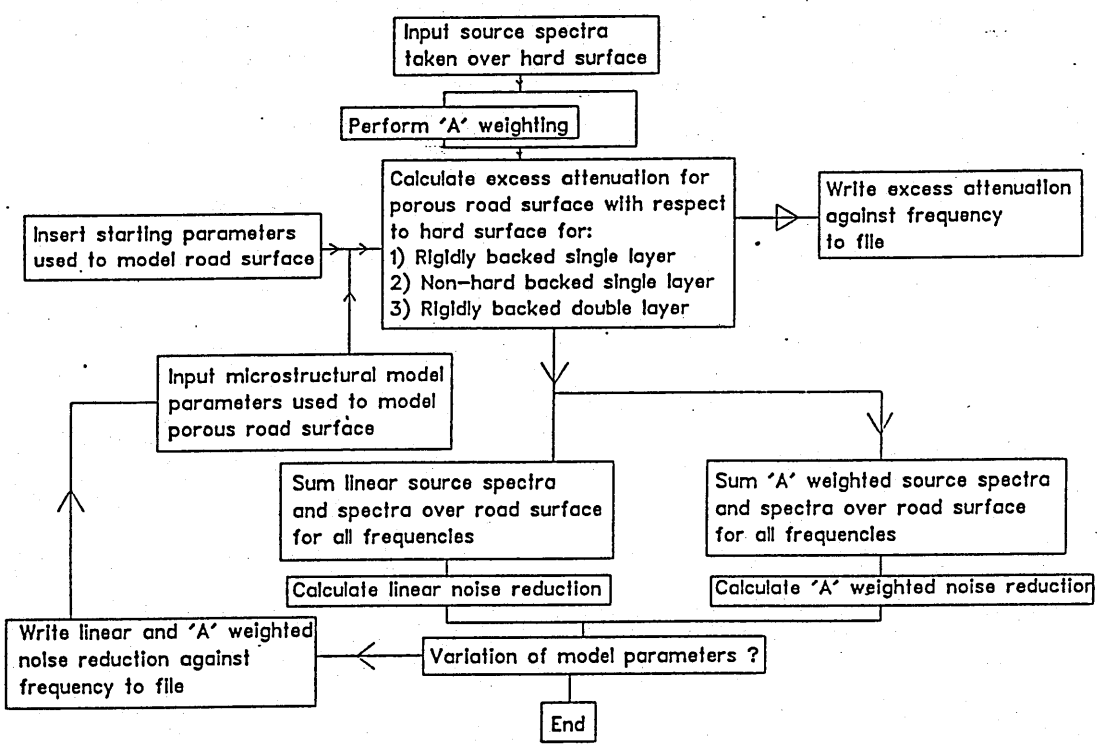

The optimum road surface characteristics depend on the source spectra. Consideration is given here to both the engine and the road/tyre interface sources and to both light and heavy vehicles. The initial spectra ($ss$) for a vehicle located above a hard, and presumed perfectly reflecting surface is input and 'A' weighted ($ssa$) using the curve shown in appendix I evaluated from the international standard [131]. The excess attenuation with respect to the hard surface $ea4$ is calculated for the road surface under consideration. This is output as a function of frequency ($f = i$ to $n$). The linear and 'A' weighted noise reduction curves are then calculated using equations 8.6 to 8.13.

$$NR = LS - MS \tag{8.6}$$

$$LS = 10\log\sum_{f=i}^{n} 10^{\left(\frac{ss_f}{10}\right)} \tag{8.7}$$

$$MS = 10\log\sum_{f=i}^{n} 10^{\left(\frac{ms_f}{10}\right)} \tag{8.8}$$

$$ms_f = ss_f + ea_f - 6 \tag{8.9}$$

$$NRA = LSA - MSA \tag{8.10}$$

$$LSA = 10\log\sum_{f=i}^{n} 10^{\left(\frac{ssa_f}{10}\right)} \tag{8.11}$$

$$MSA = 10\log\sum_{f=i}^{n} 10^{\left(\frac{msa_f}{10}\right)} \tag{8.12}$$

$$msa_f = ssa_f + ea_f - 6 \tag{8.13}$$

The linear and 'A' weighted noise reduction values are output as a function of one of the microstructural model parameters.

### Results of optimization procedure

Figure 8.13 shows an example of the reduction in sound pressure level at a range of 7.5m when a light vehicle coasts over a porous road surface rather that an acoustically hard surface assuming that the road surface only affects propagation. This also assumes that the tyres can be modelled as a pair of coherent sources of height 10cm. The input spectra used for the optimization procedure were obtained from measurements on the Vauxhall Astra and the H.G.V. tractor used for the extended source validation section 8.2.5. The parameters used are those deduced from fitting the level difference spectra for a 5cm deep layer of material B which are similar to those gained when modelling the vehicle as a pair of incoherent sources. There are significant reductions above 300Hz resulting in a linear and 'A' weighted noise reduction of 3.35 dB and 4.72 dBA respectively.

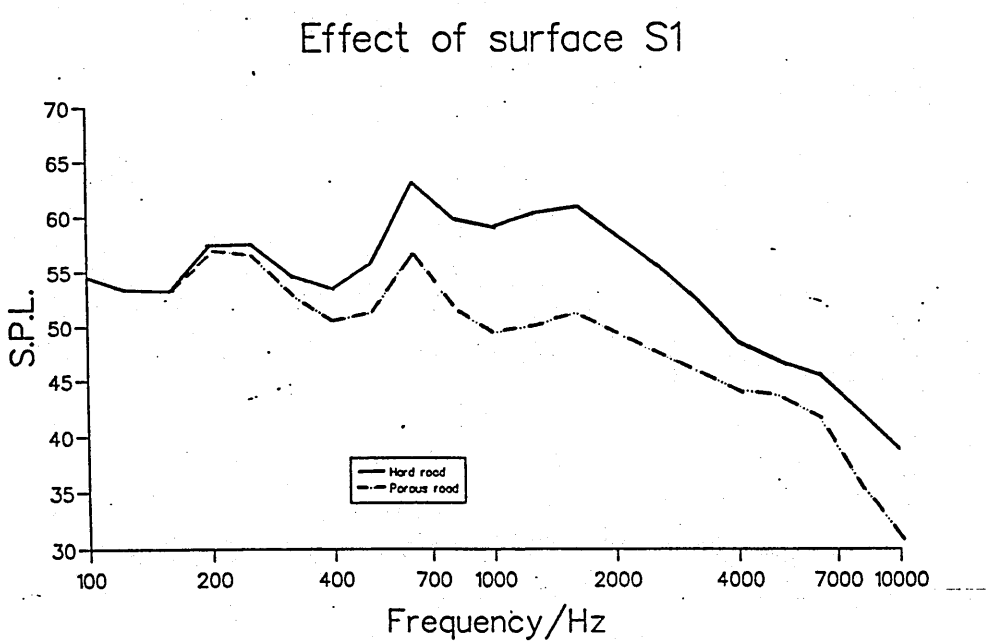


**Figure 8.13** Reduced S.P.L. optimized road surface from coasting car see table 8.16

The optimization study is divided into seven sections.

1. Optimization presuming total independence of the microstructural model parameters.
2. Optimization assuming the Bruggeman relationship, see equation 2.41, is a valid relationship between the porosity and tortuosity.
3. Optimization assuming the Bruggeman relationship and the modified Carman relationship, see equation 8.16, relating flow resistivity to porosity and tortuosity is valid.
4. Optimization presuming total independence of the microstructural model parameters and an extended source.
5. Suggested surfaces for optimum noise reduction.
6. Optimization between a range of pervious road surfaces and three tyre tread patterns for light vehicles.
7. Optimization between a range of pervious road surfaces and three tyre tread patterns for heavy vehicles.

| Source | Source height (m) | Receiver height (m) | Separation (m) |
|---|---|---|---|
| Light vehicle road/tyre noise | 0.1 | 1.2 | 7.5 |
| Light vehicle engine noise | 0.85 | 1.2 | 7.5 |
| Heavy vehicle road/tyre noise | 0.1 | 1.2 | 7.5 |
| Heavy vehicle engine noise | 1.2 | 1.2 | 7.5 |

**Table 8.13** Source receiver geometries used with optimization procedure

### Optimization with an independent variation of parameters

The 'A' weighted and linear noise reduction is evaluated for four noise sources i.e. light and heavy vehicles both for road/tyre and engine noise. The range of parameters considered in the study are given in table 8.14 The source geometry used to model the four noise sources is given in table 8.13. The results are shown in table 8.15 for a single layer road surface.

| Parameter | Maximum | Minimum | Default |
|---|---|---|---|
| Flow resistivity | 100000 | 5000 | 10000 |
| Porosity | 0.6 | 0.1 | 0.3 |
| Grain shape | 1.6 | 0.0 | 0.0 |
| (Tortuosity) | 6.8 | 1.0 | 1.0 |
| Pore shape | 0.5 | 0.25 | 0.5 |
| Layer depth | 0.3 | 0.01 | 0.075 |

**Table 8.14** Microstructural model parameters used in optimization procedure

| Source | Flow resistivity | Porosity | Tortuosity | Pore shape | Layer depth | A wt N.R. | Lin. N.R. |
|---|---|---|---|---|---|---|---|
| Light vehicle road/tyre noise | 46000(Lin.) 56000(A) | 0.6 (max) | 1.0 (min) | 0.5 (max) | 0.03(Lin.) 0.03(A) | 9.13 | 7.28 |
| Light vehicle engine noise | 96000(Lin.) 36000(A) | 0.6 (max) | 1.0 (min) | 0.45(Lin.) 0.5(A) | 0.3(Lin.) 0.27(A) | 5.80 | 3.95 |
| Heavy vehicle road/tyre noise | 81000(Lin.) 56000(A) | 0.6 (max) | 1.0 (min) | 0.49(Lin.) 0.5(A) | 0.3(Lin.) 0.25(A) | 7.89 | 3.86 |
| Heavy vehicle engine noise | 51000(Lin.) 16000(A) | 0.6(Lin.) 0.45(A) | 1.0 (min) | 0.5 (max) | 0.29(Lin.) 0.17(A) | 6.72 | 5.75 |

**Table 8.15** Optimum independent parameters for single rigid backed layer

### Bruggemann dependent optimization

The 'A' weighted and linear noise reduction is evaluated for four noise sources i.e. light and heavy vehicles both for road/tyre and engine noise sources. It is assumed that the Bruggeman relationship, equation 2.41 is valid. The results are shown in table 8.15 for single and double layer road surface. Appendix J contains the curves of noise reduction as a function of the model parameter used to evaluate the optimum values for the Bruggeman dependent optimization. A summary of the optimum parameters is found in table 8.16. A similar process has been used to evaluate the optimum parameters for double rigidly backed layers using the parameter values in table 8.14. The results of this validation procedure are given in table 8.17. Note if only one parameter value is given this indicates the A weighted and linear noise reductions were optimized to the same value.

| Source | Flow resistivity | Porosity | Grain shape (Tortuosity) | Pore shape | Layer depth | A wt N.R. | Lin. N.R. |
|---|---|---|---|---|---|---|---|
| Light vehicle road/tyre noise | 55000 ±20000 | 0.6 (max) | 0.0 (1.0) | 0.5 (max) | 0.075 (max) | 6.75 | 5.0 |
| Light vehicle engine noise | 34000 | 0.6 (max) | 0.0 (1.0) | 0.5 (max) | 0.3 (max) | 5.8 | 5.1 |
| Heavy vehicle road/tyre noise | 24000 | 0.6 (max) | 0.18 (1.09) | 0.5 (max) | 0.075 (max) | 4.95 | 2.3 |
| Heavy vehicle engine noise | 15000 | 0.6 (max) | 0.0 (1.0) | 0.5 (max) | 0.3 (max) | 6.4 | 7.4 |

**Table 8.16** Optimum Bruggeman dependent parameters for single rigid backed layer

| Parameter | Light vehicle road/tyre | Light vehicle engine | Heavy vehicle road/tyre | Heavy vehicle engine |
|---|---|---|---|---|
| Upper flow resistivity | 5000 (min) | 15000 | 10000 (min) | 12000 |
| Lower flow resistivity | 5000 (min) | 15000 | 5000 (A) 10000 (Lin.) | 15000 |
| Upper porosity | 0.6 (max) | 0.3 (A) 0.6 (Lin.) | 0.6 | 0.3 (A) 0.6 (Lin.) |
| Lower porosity | 0.6 (max) | 0.6 | 0.1(A) 0.6 (Lin.) | 0.6 |
| Upper grain shape | 0.23 (A) 0.0 (Lin.) | 0.0 (A) 1.6 (Lin.) | 0.5 | 0.0 |
| (Upper) (Tortuosity) | 1.3 (A) 1.0 (Lin.) | 1.0 (A) 7.0 (Lin.) | 1.82 | 1.0 |
| Lower grain shape | 0.0 (A) (min) | 0.0 (A) | 0.5 | 0.0 |
| (Lower) (Tortuosity) | 1.0 | 1.0 | 1.82 | 1.0 |
| Upper pore shape | 0.5 (max) | 0.5 | 0.5 | 0.5 |
| Lower pore shape | 0.5 (max) | 0.5 | 0.5 | 0.5 |
| Upper layer depth | 0.05 (A) 0.3 (Lin.) | 0.3 | 0.05 (A) 0.05 (A) | 0.3 |
| Lower layer depth | 0.00 | 0.3 | 0.02 (A) 0.3 (Lin.) | 0.1 (A) 0.1 (Lin.) |

**Table 8.17** Optimum Bruggeman dependent parameters for double rigid backed layer

### Bruggemann and Carman dependent parameters

Table 8.18 shows the results of the optimization procedure when it is presumed the Bruggeman and the modified Carman relationships between parameters of the microstructural model are valid. The Carman relationship [115] is seen in equation 8.14.

$$\sigma = \frac{2\mu q^2 s}{\Omega m^2} \tag{8.14}$$

where $\sigma$ is the flow resistivity,

$\Omega$ is the porosity,

$q^2$ is the tortuosity,

$\mu$ is the viscosity coefficient,

$s$ is the steady flow shape factor and

$m$ is the hydraulic radius. Presuming $s$, $\mu$ and $m$ remain constant and applying the Bruggeman relationship

$$\sigma \propto \Omega^{-(n'+1.0)} = F\Omega^{-(n'+1.0)} \tag{8.15}$$

The grain shape is denoted by $n'$. The constant $F$ has been evaluated by substituting parameters measured non–acoustically on the core samples into equation 8.15. The resulting equation 8.16 is derived by averaging the results, though it is apparent that $F$ is material dependent.

$$\sigma = 207.2\Omega^{-(n'+1.0)} \tag{8.16}$$

| Source | Porosity | Grain shape | Pore shape | Layer depth | A wt N.R. | Lin. N.R. |
|---|---|---|---|---|---|---|
| Light vehicle road/tyre noise | 0.6 (max) | 1.0(Lin.) 0.2(A) | 0.5 (max) | 0.22(Lin.) | 8.80 | 7.34 |
| Light vehicle engine noise | 0.6(Lin.) 0.4(A) | 1.6(Lin.) 0.3(A) | 0.5 (max) | 0.28(Lin.) 0.28(A) | 5.32 | 8.75 |
| Heavy vehicle road/tyre noise | 0.6 (max) | 1.6(Lin.) 0.2(A) | 0.5 (max) | 0.28 | 9.37 | 8.80 |
| Heavy vehicle engine noise | 0.6(Lin.) 0.37(A) | 1.6(Lin.) 1.5(A) | 0.5 (max) | 0.24(Lin.) 0.11(A) | 4.83 | 6.76 |

**Table 8.18** Optimum Bruggeman and Carman dependent parameters for single rigid backed layer

### Independent optimization using extended source

The optimization procedure was repeated using a drive by spectrum for the light vehicle, taken at 50 km/hr in second gear. However the excess attenuation spectrum was calculated using an array of four incoherent point sources rather than a single point source as used for the earlier examples. The sources were located to model the engine and exhaust source as shown in figure 8.3 with two additional sources each acoustically modelling a pair of wheels. The results are shown in table 8.19.

| Source | Flow resistivity | Porosity | Grain shape (Tortuosity) | Pore shape | Layer depth | A wt N.R. | Lin. N.R. |
|---|---|---|---|---|---|---|---|
| Light vehicle drive by | 97000(Lin.) 64000(A) | 0.6(Lin.) 0.53(A) | 0.0 (1.0) | 0.38(Lin.) 0.5(A) | 0.3 (max) | 5.55 | 4.28 |

**Table 8.19** Optimum independent parameters for single rigid backed layer using extended source calculation

### Suggested low noise road surfaces

The ideal surfaces suggested by the procedure outlined above are not realistic when practical constraints indicated by the available materials are considered. It is not possible to construct low tortuosity and high porosity road surface materials. The linear and 'A' weighted noise reductions were calculated therefore for seven possible road surfaces as listed in table 8.20. The results of this study are shown in table 8.21. Surface S6 is chosen as a small grain high flow resistivity layer over a low flow resistivity layer will be less affected by debris than a low flow resistivity large grain layer.

| Parameter | S1 | S2 | S3 | S4 | S5 | S6 | S7 |
|---|---|---|---|---|---|---|---|
| Flow resistivity | | | | | | | |
| Top | 33500 | 1500 | 1500 | 15000 | 33500 | 33500 | 1500 |
| Bottom | N/A | N/A | N/A | N/A | 1500 | 1500 | 33500 |
| Porosity | | | | | | | |
| Top | 0.15 | 0.30 | 0.30 | 0.20 | 0.15 | 0.15 | 0.30 |
| Bottom | N/A | N/A | N/A | N/A | 0.30 | 0.30 | 0.15 |
| Grain shape | | | | | | | |
| Top | 1.2 | 1.1 | 1.1 | 1.1 | 1.2 | 1.2 | 1.1 |
| Bottom | N/A | N/A | N/A | N/A | 1.1 | 1.1 | 1.2 |
| (Tortuosity) | | | | | | | |
| Top | (9.75) | (3.75) | (3.75) | (5.87) | (9.75) | (9.75) | (3.75) |
| Bottom | N/A | N/A | N/A | N/A | (3.75) | (3.75) | (9.75) |
| Pore shape | | | | | | | |
| Top | 0.5 | 0.5 | 0.5 | 0.5 | 0.5 | 0.5 | 0.5 |
| Bottom | N/A | N/A | N/A | N/A | 0.5 | 0.5 | 0.5 |
| Layer depth | | | | | | | |
| Top | 0.05 | 0.05 | 0.50 | 0.5 | 0.05 | 0.02 | 0.05 |
| Bottom | N/A | N/A | N/A | N/A | 0.05 | 0.08 | 0.05 |

**Table 8.20** Suggested porous road surfaces

| NR group | Surface | S1 | S2 | S3 | S4 | S5 | S6 | S7 |
|---|---|---|---|---|---|---|---|---|
| 1 | LVEN A | 3.94 | 3.31 | 5.14 | 4.46 | 3.92 | 3.76 | 4.84 |
| 2 | 7.5 Lin. | 2.08 | 1.88 | 3.56 | 3.10 | 2.80 | 2.58 | 2.30 |
| 3 | LVRT A | 2.31 | 4.39 | 5.39 | 3.63 | 2.17 | 2.09 | 4.55 |
| 4 | 7.5 Lin. | 1.75 | 3.29 | 4.86 | 3.12 | 1.91 | 1.89 | 3.31 |
| 5 | LVEN A | 4.68 | 3.51 | 6.10 | 6.14 | 4.97 | 4.83 | 4.10 |
| 6 | 30 Lin. | 1.22 | 0.57 | 5.87 | 4.38 | 2.63 | 1.84 | 0.78 |
| 7 | LVRT A | 4.16 | 7.78 | 11.155 | 7.64 | 3.64 | 3.56 | 9.41 |
| 8 | 30 Lin. | 3.04 | 4.64 | 9.86 | 6.69 | 3.24 | 3.37 | 5.56 |
| 9 | HVEN A | 4.81 | 4.50 | 5.43 | 5.17 | 4.84 | 4.60 | 5.25 |
| 10 | 7.5 Lin. | 3.31 | 3.28 | 4.42 | 3.91 | 3.88 | 3.99 | 3.65 |
| 11 | HVRT A | 2.67 | 3.21 | 4.98 | 3.58 | 2.63 | 2.42 | 4.46 |
| 12 | 7.5 Lin. | 1.33 | 1.02 | 3.73 | 2.54 | 2.06 | 1.92 | 1.58 |
| 13 | HVEN A | 4.68 | 3.24 | 6.27 | 5.86 | 5.26 | 5.02 | 4.15 |
| 14 | 30 Lin. | 1.74 | 0.88 | 5.97 | 4.36 | 3.33 | 3.05 | 1.42 |
| 15 | HVRT A | 4.46 | 5.52 | 9.92 | 7.24 | 4.46 | 3.87 | 8.00 |
| 16 | 30 Lin. | 1.79 | 1.05 | 7.26 | 5.38 | 3.50 | 2.94 | 1.94 |

**Table 8.21** Noise reduction for suggested surface for heavy vehicle (HV), light vehicle (LV), engine (EN) and road/tyre (RT) source. At 7.5m and 30.0m separation, other geometries given in table 8.13

Figure 8.14 shows the noise reduction for each of the sixteen cases and seven surfaces shown above.

### Optimization according to tyre type for light vehicles

An alternative method of reducing road/tyre noise involves study of the interaction of differing tyre tread patterns with the road surface. Three vehicles with different tyres were used to produce noise spectra for the vehicle coasting at 50km/hr over an acoustically hard surface. The noise reduction for these spectra was calculated for the seven road surfaces suggested earlier the results are shown in table 8.22 and figure 8.15. It is presumed that the road/tyre noise generation is independent of the surface. The vehicles and tyres used are:

- Vauxhall Astra 1.6l with Pirelli P4
- BMW 320i with Uniroyal R14

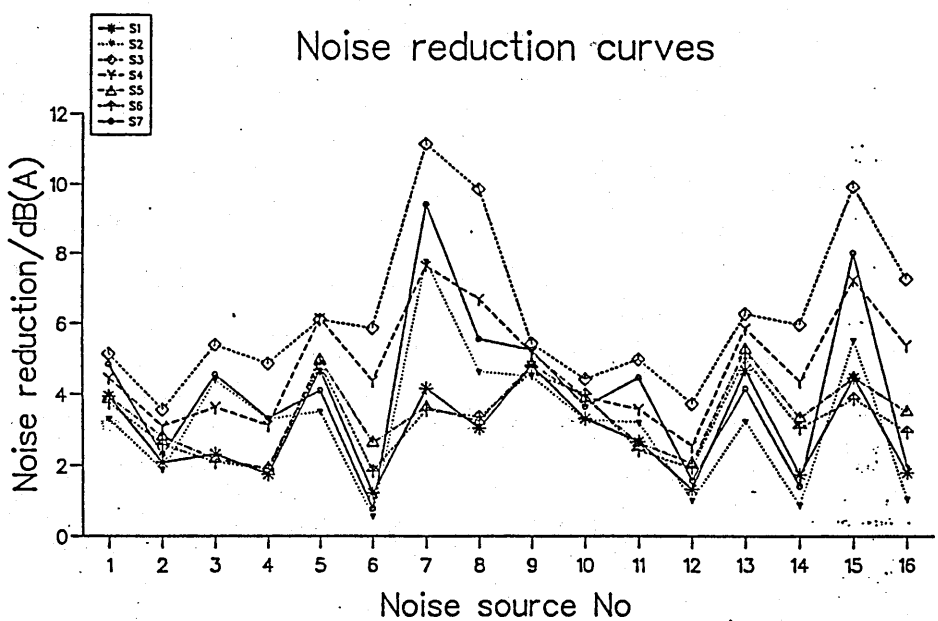


**Figure 8.14** Noise reduction for proposed surfaces and different noise sources

| Surface | S1 | S2 | S3 | S4 | S5 | S6 | S7 |
|---|---|---|---|---|---|---|---|
| Astra A | 4.97 | 4.61 | 5.68 | 5.39 | 4.87 | 4.39 | 5.32 |
| Lin. | 4.43 | 4.07 | 5.33 | 5.09 | 4.51 | 4.21 | 4.64 |
| BMW A | 1.98 | 3.25 | 4.83 | 3.13 | 2.13 | 1.34 | 5.77 |
| Lin. | 0.55 | 0.63 | 5.33 | 1.96 | 0.70 | 0.49 | 0.99 |
| Granada A | 4.76 | 5.12 | 7.42 | 6.29 | 4.25 | 3.63 | 6.79 |
| Lin. | 3.77 | 4.79 | 7.62 | 5.71 | 3.22 | 3.25 | 5.88 |

**Table 8.22** Results of tests with differing tyre patterns for light vehicles

| Surface | S1 | S2 | S3 | S4 | S5 | S6 | S7 |
|---|---|---|---|---|---|---|---|
| Ribbed/Traction A | 2.47 | 4.58 | 5.24 | 3.56 | 2.26 | 1.82 | 5.43 |
| Lin. | 2.20 | 3.76 | 4.75 | 3.05 | 1.62 | 1.62 | 5.16 |
| Smooth/Smooth A | 2.66 | 3.97 | 5.25 | 3.71 | 2.53 | 2.09 | 5.44 |
| Lin. | 1.14 | 2.73 | 4.50 | 3.03 | 1.78 | 2.03 | 5.18 |
| Ribbed/Ribbed A | 2.31 | 4.45 | 5.25 | 3.57 | 2.63 | 1.84 | 5.44 |
| Lin. | 2.20 | 3.52 | 4.85 | 3.07 | 1.87 | 1.72 | 5.18 |

**Table 8.23** Results of tests with differing tyre patterns for heavy vehicles

- Ford Granada 2.0 with Michelin MX

### Optimization according to tyre type for heavy vehicles

The process was repeated for heavy vehicles using a range of tyre tread combinations as listed below. The noise reduction for these spectra was calculated for the seven road surfaces suggested earlier the results are shown in table 8.23 and figure 8.16. The tyre types and combinations used are:

- Ribbed tyres on front and traction tyres on rear.
- Smooth tyres on front and smooth tyres on rear.
- Ribbed tyres on front and ribbed tyres on rear.

## 8.5 Conclusions

The validation procedure indicates that the microstructural model is suitable for modelling the acoustical characteristics of the pervious tarmacadam road

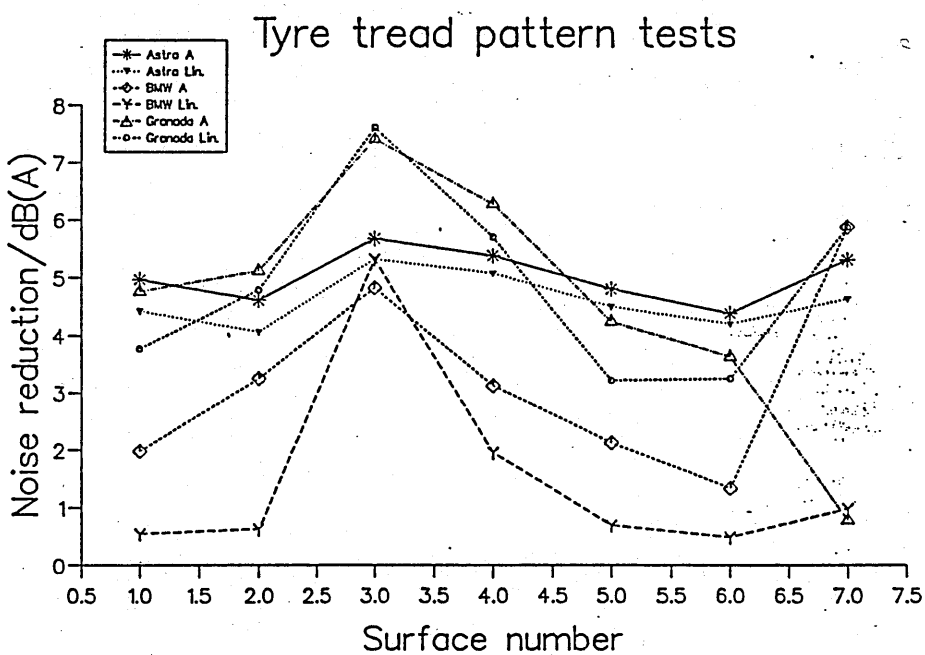


**Figure 8.15** Results of tests with differing tyre patterns for light vehicles

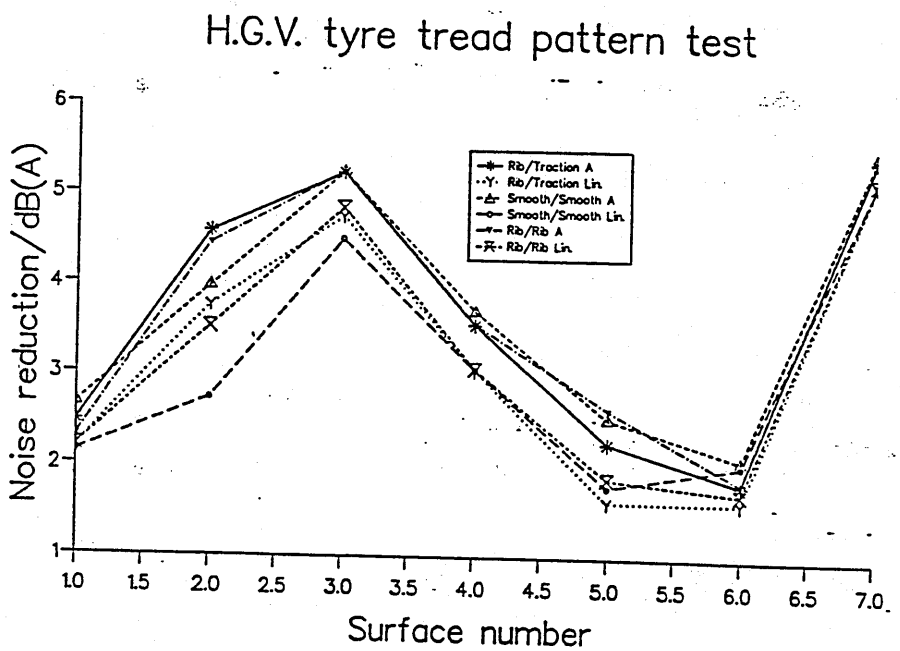


**Figure 8.16** Results of tests with differing tyre patterns for heavy vehicles

surface. The parameters gained from the level difference and absorption coefficient fitting techniques agree with those gained from non-acoustical measurements. The phenomenological model however seems applicable only to a limited range of flow resistivity values. The validation procedure had been extended to fit spectra measured from a vehicle source at 7.0m. It was found possible to model either a light or a heavy vehicle at this range as a pair of incoherent point sources. Finally optimum parameters have been presented based on calculation of linear and 'A' weighted noise reduction. As the optimum parameters are not practical seven feasible surfaces have been studied. It appears that a thick ( i.e. superthick, a large thickness compared to the 5cm deep layers laid on most road surfaces ) layer of low flow resistivity ( 1500 MKS Rayls )material would be most suitable for reducing most vehicular noise. An alternative surface is provided by placing a layer of low flow resistivity material upon a small grained surface with a flow resistivity of 30000 MKS Rayls. The study of tyre tread types indicates again that the 'superthick layer' is the preferred surface for all tyre types. There does not appear to be any optimum combination of tyre and road surface for either light or heavy vehicles.

# Chapter 9

# Conclusions and further work

## 9.1 Conclusions

The aim of this thesis has been to study sound propagation over rigid porous layers in a neutral atmosphere. The study was concerned both with the acoustical properties of the material and with the prediction of short range point to point sound propagation. Both aspects of the study were used to characterize and optimize the acoustical properties of a porous road surface.

A review of the methods of measuring impedance indicated that an indirect technique could be improved and used to generate a fast and convenient in–situ method. Two variations of the technique have been explored. The difference between measured and theoretical sound fields may be minimized for a known geometry either by varying the component parts of the surface impedance or by varying the parameters of an impedance model and hence making possible the deduction of best fit values of the variables. Either technique would require an accurate model to predict the sound propagating over a boundary from a point source. The impedance model was selected by considering three alternative rigid porous material theories. This comparison indicated that the microstructural model developed by Attenborough [83] was preferable to either an empirical model or a phenomenological model. In particular it was indicated in chapter 8 that the phenomenological model was not suitable for modelling low flow resistivity materials. The microstructural model involves parameters of porosity, flow resistivity, tortuosity and

pore shape. It was noted that predictions using the microstructural model are relatively insensitive to pore shape when parameter ranges appropriate to porous road surfaces were considered. For example constraining the pore shape to be 0.5 increased the RMS error in the level difference spectra fits by approximately 10%. Pore shape is likely to be important however when higher flow resistivity materials such as soils are considered and thus the ' acoustical ' and steady flow resistivities may differ in magnitude. In developing the microstructural model further there may be two alternative paths either the influence of pore size distribution should be studied or pore shape effect should be included using the methods proposed by Biot [144] and Allard [145].

A numerical comparison of formulae for predicting propagation from a point source over a rigid porous medium has demonstrated that for short ranges ( of the order of 5m ) the Weyl van der Pol asymptotic series solution was adequate for semi–infinite and layered locally and externally reacting surfaces. An aspect of sound propagation from a point source that had not been verified conclusively by experiment hither to is the phenomenon of the acoustic surface wave. A series of experiments using a lattice layer reported in this thesis have indicated that such a wave exists and may be modelled using the propagation theory suggested by either Attenborough [158] or by Donato [36]. Having selected accurate models for sound propagation and the acoustical behavior of the ground the indirect method of measuring ground impedance was explored further. It was seen that the spectrum of the level difference between a pair of vertically separated microphones could be used to examine the sound field above a surface of interest. Three possible minimization functions were considered. The best was found to be a small root of the squared differences. Three such spectra were required to give a non–unique solution. Computational algorithms were developed to apply the technique to a range of materials and a numerical experiment was performed to examine the effects of systematic and random errors. The refined indirect technique was then applied to a range of surfaces and the results were compared to those obtained with the impulse technique suggested by

Cramond and Don [98]. It was clear from the results of these experiments that the indirect technique incorporating a model for the acoustical properties of the material was to be preferred to fitting impedance as a result of the frequency dependence imposed by the microstructural model. The indirect impedance measurement technique however could be developed further to allow for random noise in the input spectra [206].

The indirect impedance measurement method was used to characterize acoustically the acoustical properties of a porous road surface. The method was validated by comparing the deduced parameters with those obtained from a series of non–acoustical measurements including the measurement of tortuosity. The study of the road surface characteristics also confirmed the accuracy of the modified Weyl van der Pol formulae for sound propagation. It was shown that the phenomenological impedance model suggested for use when modelling the acoustical properties of pervious 'macadams [141] had a restricted range of materials for which it was accurate. Simple point source arrays were defined for modelling the sound propagation from stationary light and heavy vehicles. The array of incoherent sources was used with the indirect fitting technique to evaluate the microstructural model parameters that describe the road surface. The results were in good agreement with values gained non-acoustically and from application of the point source based indirect impedance measurement method. Finally the optimum microstructural model parameters were deduced by calculating the 'A' weighted and linear noise reduction relative to a hard surface presuming that the propagation effect was dominant. When feasible materials were considered a superthick layer of low flow resistivity material gave the highest noise reduction for a range of noise sources and geometries. However similar levels of noise reduction have been predicted to be possible by using multilayered structures, with a low flow resistivity upper layer.

## 9.2 Further work

The work has indicated several areas which would benefit from further study. In the indirect method of impedance measurement which has been proposed no substantial use has been made of the phase information. A large surface is needed to deduce low frequency impedance due to the increase in source receiver separation and receiver height and hence the method is not suited to all types of acoustic material. No account has been made of the elastic properties of the materials under study although acoustical impedance models including the elastical properties of a material exist [177]. It has been suggested that the microstructural model may be expanded to incorporate the effect of pore size distribution and other ways of incorporating effects of pore shape. The Bruggeman relationship 2.41 has been used to relate tortuosity and porosity however the parallel equations suggested by Carmen [115] to relate flow resistivity to porosity and grain shape do not appear to be as robust. The modified Carman formulae given in equation 8.16 were tested for a series of samples by using the non–acoustical data.. The constant of proportionality was similar when evaluated for different samples of the same material but was inconsistent when different materials were considered.

If the surfaces of interest have flow resistivities that fall within a certain range, then the indirect parameter fitting technique may be applied using the phenomenological model. As this impedance model uses fewer parameters than the microstructural model the computational time falls. This would be advantageous if a vehicle mounted rapid technique was required to assess the decay and clogging of porous road surfaces.

The increased exponential decay in both the horizontal and vertical directions makes it difficult to examine the acoustical surface wave over materials with small pore sizes and high flow resistivities. Surface waves have been examined over a well defined lattice work. The study of surface waves could be extended to examine other ideal materials which may be modelled using the alternative pore shapes discussed in chapter 3.

The indirect parameter fitting impedance measurement technique has been successfully used on several different material types. It has been possi-

ble to distinguish between 'macadams incorporating low and high flakiness stones. This suggests that the technique may be used as an in–situ technique to monitor the effects of wear and the clogging of road surfaces. The technique appears less satisfactory when applied to 5cm deep layers than to 10cm deep layers. This may be a consequence of an inability to differentiate between the effects of grain shape and layer depth. If the optimum road surface suggested is too expensive to use on a large road network a multi–layered structure may be a viable alternative. A preliminary study of the use of pervious 'macadams for canyon streets has predicted considerable noise reductions for urban traffic flow [207]. Work is needed to examine whether the noise reductions predicted by the theoretical study can be achieved in practice. The work carried out here suggests that the microstructural model may be used to design absorbing materials to reduce the noise level for a specific frequency. It has been seen that the parameters may be altered to locate the absorption coefficient peak at a chosen frequency. This approach may be applied a range of materials including porous building blocks or loudspeaker cabinet damping materials. A square speaker cabinet has box resonances grouped at one frequency location. A material may be designed to reduce the effects of the resonances.

# Bibliography


[1] P. H. Parkin and W. E. Scholes. The horizontal propagation of sound from a jet engine close to the ground, at radlett. *Journal of Sound and Vibration*, 1:1–18, 1964.

[2] P. H. Parkin and W. E. Scholes. The horizontal propagation of sound from a jet engine close to the ground, at hatfield. *Journal of Sound and Vibration*, 2, 1965.

[3] Simon Neil Chandler–Wilde. *Ground effects in environmental sound propagation.* PhD thesis, University of Bradford, 1988.

[4] H. Weyl. Ausbreitung elektromagnetisher wellen uber einen ebenleiter. *Annalen der Physik*, 1919.

[5] B. Van der Pol. Theory of the reflection of the light from a point source by a finitely conducting flat mirror with an application to radiotelegraphy. *Physica*, 1935.

[6] J. E. G. M. de Bie and J. M. M. Groenewoud. *Several Manners to find Normalized Specific Impedance of an Arbitary Soil Type Pt. 1 The Inclined Track Method.* PhD thesis, Catholic University, Nijmegen, Toernooiveld, Netherlands, 1980.

[7] L. L. Beranek. Precision measurements of acoustic impedance. *Journal of the Acoustical Society of America*, 12:56–63, 1940.

[8] L. L. Beranek. *Acoustic Measurements.* J. Wiley, 1949.

[9] K. Schuster. Measurement of acoustic impedances by comparison. *Electrical Nachr. Tech.*, 13:693–699, 1936.

[10] N. W. Robinson. An acoustical impedance bridge. *Philosophical Magazine*, 23(156):665–681, 1937.

[11] W. S. Gately and R. Cohen. Methods of evaluating the performance of small acoustic filters. *Journal of the Acoustical Society of America*, 46(1), 1969.

[12] P. D. Dean. An in–situ method of wall impedance measurement in flow ducts. *Journal of Sound and Vibration*, 34(1):675–681, 1974.

[13] R. D. Kilmer. *Evaluation and prediction of Sound Absorbing Characteristics of Composite Acoustic Absorbers for Normally Incident Plane Waves.* Master's thesis, Pennsylvania State University, 1974.

[14] R. Singh. Acoustic impedance measurement methods. *Shock and Vibration Digest*, 14(2), 1982.

[15] N. W. Heap. *Sound Propagation Over Mixed Impedances.* PhD thesis, Open University, Walton Hall, Milton Keynes, England., 1982.

[16] R. K. Cook. A short tube method for measurement of impedance. *Journal of the Acoustical Society of America*, 19, 1947.

[17] O.K. Mawardi–El. Measurement of acoustic impedance. *Journal of the Acoustical Society of America*, 21, 1949.

[18] T. Salava. Continuous measurement of acoustic impedance by a signal source with constant volume velocity. *Tesla Electronics*, 1:146–153, 1975.

[19] R. L. Pratt, S. J. Elliot, and J. M. Bowsher. The measurement of acoustic impedance of brass instruments. *Acustica*, 38, 1977.

[20] A. J. Zuckerwar. Acoustic ground impedance meter. *Journal of the Acoustical Society of America*, 73(6):2180–2186, June 1983.

[21] G. A. Daigle and M. R. Stinson. Impedance of grass covered ground at low frequencies measured using a phase difference technique. *Journal of the Acoustical Society of America*, 81(1):62–68, January 1987.

[22] H. O. Taylor. A direct method for finding the values of materials as sound absorbers. *Physics Review*, 2, 1913.

[23] R. A. Scott. An apparatus for acoustic impedance of sound absorbing materials. In *Proceedings of the Physics Society*, 1946.

[24] J.N. Prout. Some measurements of the absorption coefficients of soil using the impedance tube technique. *Noise Control*, 7(6):20–23, November-December 1961.

[25] P.A. Mansbach and C. I. Holmer. Techniques for the measurement of acoustic impedance of asphalt. October 1978.

[26] Dahl M. *Sound Propagation.* PhD thesis, University of Mississippi, 1970.

[27] H. Oura. Sound waves in snow cover. *The Japan Science Review*, 2, 1952.

[28] T. Ishida. Acoustical properties of snow. In *The Intensity of Low Temperature Science*, pages 23–63, 1965. Series A Number 20.

[29] Buser O. A rigid frame model of porous media for the acoustic impedance of snow. *Journal of Sound and Vibration*, 111:71–92, 1986.

[30] L. L. Beranek, editor. *Noise Reduction and Control.* Wiley, 1968.

[31] American Society for Testing Materials. Impedance and absorption of acoustical materials by the tube method. American Standard C384–58,(88), 1958.

[32] P.M. Morse and R.H. Bolt. Sound waves in rooms. *Reviews in Modern Physics*, 16:70–150, 1944.

[33] Y. Ando. An extrapolation of measuring the reflection coefficient by an acoustic tube. *Applied Acoustics*, 2:97–99, 1969.

[34] L. Joffe. A criterion for the use of linear regression analysis in the determination of low values of absorption coefficients using the impedance tube method. *Applied Acoustics*, 7:139–146, 1974.

[35] Y. Ando. Probe microphone directivity and acoustic centre of a probe microphone. *Journal of the Acoustical Society of Japan*, 24:167–174, 1968.

[36] R. J. Donato. Model experiments on surface waves. *Journal of the Acoustical Society of America*, 63:700–703, 1978.

[37] P. J. Dickinson and P. E. Doak. Measurement of normal acoustic impedance at ground surfaces. *Journal of Sound and Vibration*, 13(3):309–322, 1970.

[38] P.M. Morse and U. Ingard, editors. *Theoretical Acoustics.* Mc Graw Hill, 1968.

[39] J. W.) Rayleigh, Lord. (Strutt. *Theory of Sound I and II.* Dover, 1945.

[40] W. E. Schmidt and J. P. Johnson. *Measurement of Acoustic Reflection from Obstructions in a Pipe with Flow.* Technical Report PD20, N.S.F., March 1975.

[41] A. F. Seybert and D. F. Ross. Experimental determination of acoustic properties using a two microphone random excitation technique. *Journal of the Acoustical Society of America*, 61(5):1362–2370, May 1977.

[42] J. Y. Chung and D. A. Blaser. Transfer function method of measuring in duct acoustic properties i. theory. *Journal of the Acoustical Society of America*, 68(3):907–913, September 1980.

[43] J. Y. Chung and D. A. Blaser. Transfer function method of measuring in duct acoustic properties ii. experiment. *Journal of the Acoustical Society of America*, 68(3):914–921, September 1980.

[44] G.M. Heisler, O.H. McDaniel, and M. Dahl . Methods for making measurements of normal impedance of forest floors. 1984.

[45] C.Y. Chung. Cross-spectral methods of measuring acoustic intensity without error caused by instrument phase mismatch. *Journal of the Acoustical Society of America*, 1978(64):6, Dec. 1978.

[46] American Society for Testing Materials. Standard test method for impedance and absorption of acoustic materials using a tube, two microphones and a digital frequency analysis system. American Standard C1050–86, 1986.

[47] W. T. Chu. Extension of the two microphone transfer function method for impedance tube measurements. *Journal of the Acoustical Society of America*, 80(1):347–349, July 1986.

[48] W. T. Chu. Transfer function technique for impedance and absorption measurement in an impedance tube using a single microphone. *Journal of the Acoustical Society of America*, 80(2):555–560, August 1986.

[49] A. F. Seybert and B. Soenarko. Error analysis of spectral estimates with application to the measurement of acoustic properties using random sound fields in ducts. *Journal of the Acoustical Society of America*, 1981.

[50] H. Boden and M. Abom. Influence of errors on the two–microphone method of measuring acoustic properties of ducts with flow. *Journal of the Acoustical Society of America*, 83:2429–2438, 1988.

[51] H. Boden and M. Abom. Influence of errors on the two–microphone method of measuring acoustic properties of ducts. *Journal of the Acoustical Society of America*, 79:541–549, 1986.

[52] P. Banks-Lee and H. Peng. Length error analysis for impedance tube measurements. *Journal of the Acoustical Society of America*, 85(4):1769–1772, April 1989.

[53] F.J. Fahy. Rapid method for the measurement of sample acoustic impedance in a standing wave tube. *Journal of Sound and Vibration*, 97(1):168–170, 1984.

[54] U. Ingard and R.H. Bolt. A free field method of measuring the absorption coefficient of acoustic materials. *Journal of the Acoustical Society of America*, 23:200–207, September 1951.

[55] Y. Ando. The interference pattern method of measuring the complex reflection coefficient of acoustic materials at oblique incidence. *Journal of the Acoustical Society of Japan*, Feb. 1966.

[56] D.J. Sides and K. A. Mulholland. The variation of normal layer impedance with angle of incidence. *Journal of the Acoustical Society of America*, 139–142, 1971.

[57] C. Klein and A. Cops. Angle dependence of the impedance of a porous layer. *Acustica*, 44(4):258–264, 1980.

[58] T. Legouis and J. Nicholas. Phase gradient method of measuring acoustic impedance of materials. *Journal of the Acoustical Society of America*, 44–50, 1987.

[59] J. Nicholas and G. Lemire. Precision of active sound intensity measurements in a progressive and a non-progressive field. *Journal of Acoustical Society of America*, 78, 1985.

[60] Y. Miki. Application of the synchronized correlation method to the measurement of sound propagation over a ground surface. *Journal of the Acoustical Society of Japan*, 1(3):157–166, 1980.

[61] I. Yamada. Cross spectral method for the estimation of ground reflection characteristics and free-field spectrum of noise. *Journal of the Acoustical Society of Japan*, 1(4):249–259, 1980.

[62] M Watanabe and S. Kotabe. A correlation method of ground reflection effect on sound pressure spectra. In *Meeting Acoustical Society of Japan*, 1975. In Japanese.

[63] J. F. Allard and A. Akine. Acoustic impedance measurements with a sound intensity meter. *Applied Acoustics*, 18:69–75, 1985.

[64] J. F. Allard and P. Delage. Free field measurement of absorption coefficients of square panels of absorbing media. *Journal of Sound and Vibration*, 101(2):161–170, 1985.

[65] J. F. Allard and B. Seiben. Measurements of acoustic impedance in a free field with two microphones and a spectrum analyser. *Journal of the Acoustical Society of America*, 77(4):230–256, April 1985.

[66] J. F. Allard, R. Bourdier, and A. M. Bruneau. The measurements of acoustic impedance at oblique incidence with two microphones. *Journal of Sound and Vibration*, 101(1):130–131, 1985.

[67] J.F. Allard, A. Akine, and C. Depollier. Acoustical properties of partially reticulated foams with high and medium flow resistance. *Journal of the Acoustical Society of America*, 79(6):1734–1740, June 1986.

[68] J. F. Allard, R. Bourdier, and A. L'Esperance. Anisotropy effect in glass wool on normal impedance at oblique incidence. *Journal of Sound and Vibration*, 114(2):233–238, 1987.

[69] J. F. Allard and Y. Champoux. In situ free field measurements of the surface acoustic impedance of materials. *Journal of Noise Control and Engineering*, 134–146, 1989.

[70] J. F. Allard, C. Depollier, and C. Guignouard. Free field surface impedance measurements of sound absorbing materials with surface coatings. *Applied Acoustics*, 26:199–207, 1989.

[71] Y. Champoux, J. Nicolas, and J. F. Allard. Measurement of an acoustic impedance in a free field at low frequencies. *Journal of Sound and Vibration*, 125(2):313–323, 1988.

[72] Y. Champoux and A. L'Esperence. Numerical evaluation of errors associated with the measurement of acoustical impedance in a free field using two microphones and a spectrum analyser. *Journal of the Acoustical Society of America*, 84(1):30–38, July 1988.

[73] M. Minten, A. Cops, and W. Laurikis. Absorption characteristics of an acoustical material at oblique incidence measured with the two microphone technique. *Journal of Sound and Vibration*, 129(3):499–510, 1988.

[74] M. A. Nobile. Measurement of absorption coefficient and acoustic impedance in a hemi–anechoic space using a transfer function method. *Journal of the Acoustical Society of America*, Oct 1978.

[75] T. E. Vigran. Measuring the acoustic properties of ducts. *Applied Acoustics*, 18:7–10, 1985.

[76] T. E. Vigran. Free field measurements of acoustic impedance, a simplified approach. In $13^{th}$ *International Congress on Acoustics*, 1989.

[77] D. C. Waddington and R. J. Orlwoski. A two microphone technique for measuring acoustic impedance in the free field: effects of the sample area and measurement errors. In *Proceeding Institute of Acoustics*, pages 521–531, 1989.

[78] D. C. Waddington. *Acoustic Impedance Measurement using a Two Microphone Transfer Function technique.* PhD thesis, University of Salford, 1990.

[79] M. Tamura. Spatial fourier transform method of measuring acoustical reflection coefficient at oblique incidence. In *2nd Joint meeting of the Acoustical Society of America and The Acoustical Society of Japan*, pages 2259–2264, November 1988. Paper EE6.

[80] E. Luzzato, A. Adobes, and Bossehut D. An original method for in–situ impedance measurement. In *International Congress on Acoustics*, pages 315–318, 1989.

[81] S.I. Thomasson. Reflection of waves from a point source by an impedance boundary. *Journal of the Acoustical Society of America*, 59(4):780–785, April 1976.

[82] H. M. Hess. *Determination of the Acoustical Properties of Soils,*. PhD thesis, The Open University, Walton Hall, Milton Keynes, Great Britain, June 1988.

[83] K . Attenborough. Acoustical impedance models for outdoor ground surfaces. *Journal of Sound and Vibration*, 99(4):521–544, 1985.

[84] H. E. Bass and L. N. Bolen. *Propagation of Sound through the Atmosphere: Effects of Ground Cover.* Interim Report, University of Mississippi, June 1976–1978.

[85] L.A.M. Van der Heijden. Impedance measurements of natural soils with an inclined track method. In *Internoise '81*, pages 265–270, 1981.

[86] C. Glaretas. *A New Method for Measuring the Acoustic Impedance of the Ground.* PhD thesis, Pennsylvania State University, 1981.

[87] C. Glaretas. *Acoustic Properties of the Ground.* Master's thesis, Pennsylvania State University, 1981.

[88] D. Habault and C. Corsain. Identification of acoustical properties of a ground surface. *Journal of Sound and Vibration*, 169–180, 1985.

[89] C. I. Chessel. Propagation of noise along a finite impedance boundary. *Journal of the Acoustical Society of America*, 62:825–834, 1977.

[90] D. A. Bies and C. H. Hanson. Flow resistance information for acoustical design. *Applied Acoustics*, 13:357–391, 1980.

[91] H. M. Hess, K. Attenborough, and N. W. Heap. Ground characterization by short range propagation measurements. *Journal of the Acoustical Society of America*, 87:1975–1985, 1990.

[92] M. M. Loudon. The single pulse method for measuring the transmission characteristics of acoustic system. *Acustica*, 25, 1971.

[93] Z. Kintsl. Investigation of the sound absorption of wall sections by a pulse technique. *Soviet Physical Acoustics*, 21(1):30–32, July – August 1975.

[94] J. C. Davies and K. A. Mullholland. An impedance method of measuring normal impedance at oblique incidence. *Journal of Sound and Vibration*, 67(1):135–149, 1979.

[95] R. Singh and T. Katra. Development of an impulse technique for measurement of muffler characteristics. *Journal of Sound and Vibration*, 56, 1978.

[96] L.A.M. Van der Heijden, J.G.E.M. de Bie, and J. Groenewoud. A pulse method to measure the impedance of semi natural soils. *Acustica*, 51(3):193–197, 1982.

[97] M. Yuzawa. A method of obtaining the oblique incident sound absorption coefficient through an on the spot measurement. *Applied Acoustics*, 8:27–41, 1975.

[98] A. J. Cramond and C. G. Don. Reflection of impulses as a method of determining acoustic impedance. *Journal of the Acoustical Society of America*, 75(2):382–389, February 1984.

[99] J.S. Bolton and E. Gold. The determination of acoustic reflection coefficients by using cepstral techniques: i: experimental procedures and measurements of polyurethane foam ii: extensions of the technique and considerations of accuracy. *Journal of Sound and Vibration*, 110(2):179–202, 1986.

[100] J. S. Bolton and P. E. Doak. Acoustical models of the ground. In *G.A.R.T.E.U.R. 5, Atmospheric and Ground Effects on Sound Propagation*, pages 1–8, R.A.E., Farnborough, England, 1978.

[101] J.S. Bolton and E. Gold. The application of cepstral techniques to the measurement of transfer functions and acoustical reflection coefficients. *Journal of Sound and Vibration*, 93(2), 1984.

[102] M.A. Ferrero and G.G. Sacerdote. The acoustic impedance of thin layers of porous material. *Acustica*, 10:336–339, 1960.

[103] J. S. Pyett. The acoustical impedance of a porous layer at oblique incidence. *Acustica*, 3:375–382, 1953.

[104] J. Rybner. Nomograms of complex hyperbolic functions. Cojellerups Forlag, July 1955. Copenhagen.

[105] J. I. Dunlop. Specific acoustic impedance measurement by a protruding tube method. *Journal of the Acoustical Society of America*, 79(4):1177–1180, April 1986.

[106] J. I. Dunlop. An open tube technique for the measurement of the acoustic parameters of porous absorbing materials. *Journal of the Acoustical Society of America*, 77(6):2173–2178, June 1985.

[107] C. Zwikker and C.W. Kosten. Sound absorbing materials. *Elesevier*, 99, 99 1949.

[108] R.W. Leonard. Simplified flow resistance measurements. *Journal of the Acoustical Society of America*, 17(3), 1946.

[109] E. H. Wall. *Measurement of Air Permeability in Soils.* Master's thesis, Silsoe College, Cranfield Institute of Technology, Silsoe, Bedfordshire, 1986.

[110] M. A. Stanton. *Determination of Pore Continuity by a Measurement of Air Permeability.* Master's thesis, Silsoe College, Cranfield Institute of Technology, Silsoe, Bedfordshire, 1985.

[111] Y. Champoux, M. R. Stinson, and G. A. Daigle. Air-based system for the measurement of porosity. *Journal of the Acoustical Society of America*, 89(2), February 1991.

[112] L. L. Beranek. Acoustic impedance of porous materials. *Journal of the Acoustical Society of America*, 13:534–568, 1942.

[113] R. J. S. Brown. Connection between formation factor for electrical resistivity and fluid–solid coupling factor in biot's equations for acoustics waves in fluid–fitted porous media. *Geophysics*, 45:152–159, 1980.

[114] P.N. Sen, C. Scala, and Cohen M.H. A self–similar model for sedimentary rocks with application to the dielectric constant of fused glass beads. *Geophysics*, 46:781–794, 1981.

[115] P. C. Carman. *Flow of Gasses Through Porous Media.* Academic Press, 1956.

[116] P.D. Jackson, D. Taylor–Smith, and P.N. Stanford. Sound propagation. *Geophysics*, 43, 1978.

[117] Champoux Y. and Stinson M. R. Measurement of tortuosity of porous materials and the implications for acoustic modelling. In *Proceeding of the Acoustical Society of America*, 1990. Supplement 1 (87).

[118] Y. Champoux. Details of tortuosity measurement equipment. December 1990. Private Communication.

[119] P. H. Nye and P. B. Tinkler. *Solute Movement in the Soil Root Systems.* Blackwell, 1977. London.

[120] K. Attenborough. Acoustical characteristics of porous materials. *Physics Reports*, 1981.

[121] M. E. Delany and E. N. Bazely. Acoustical properties of fibrous absorbent materials. *Applied Acoustics*, 3:309–322, 1970.

[122] F. P. Mechel. Ausweitung der absorberformel von delany and bazley zu tiefen frequenzen. *Acustica*, 35, 1976.

[123] M.E. Delany and Bazley E. N. *A Note on the Effect of Ground Absorption in the Measurement of Aircraft Noise.* Aero report AC 41, National Physics Laboratories, 1969.

[124] T.F.W. Embleton, J.E. Piercy, and N. Olson. Outdoor sound propagation over ground of finite impedance. *Journal of the Acoustical Society of America*, 59(2):267–277, 1976.

[125] J. E. Piercy, Embleton T. F. W., and Sutherland L. C. Review of noise propagation in the atmosphere. *Journal of the Acoustical Society of America*, 61:1403–1418, 1977.

[126] H.G. Jonasson. What a load of stuff. *Journal of Sound and Vibration*, 22, 1972.

[127] T.F.W. Embleton, J.E. Piercy, and G. A. Daigle. Effective flow resistivity of ground surfaces determined by acoustical measurements. *Journal of the Acoustical Society of America*, 74(4):1239–1244, 1983.

[128] R. H. Talaske. *The Acoustic Impedance of a Layered Forest Floor.* Master's thesis, Pennsylvania State University, 1980.

[129] A. A. Soom and J. C. Bollinger. Snowmobile noise emission and propagation. In *Proceedings of the Third Interagency Symposium on University Research in Transportation Noise*, 1975.

[130] Raspet R., Bass H. E., and Ezell J. Effect of finite ground impedance on the propagation of acoustic pulses. *Journal of the Acoustical Society of America*, 74(1), 1983.

[131] International Standard. DIS 46-38.

[132] P.M. Morse, R.H. Bolt, and R.C. Brown. Acoustic impedance and sound absorption. *Journal of Acoustical Society of America*, 12(2), 1940.

[133] L.L. Beranek. Acoustic impedance of commercial materials and the performance of rectangular rooms with one treated surface. *Journal of the Acoustical Society of America*, 12:23–30, 1940.

[134] K. Attenborough. Acoustical characteristics of rigid fibrous absorbents and granular materials. *Journal of the Acoustical Society of America*, 73(3):785–799, 1983.

[135] J. F. Hamet. *Acoustic Modelling of a Drained Overlay, Theoretical Study Relating to Perpendicular Incidence on the Surface.* Technical Report 59, I.N.R.E.T.S., January 1988.

[136] S.I. Thomasson. Sound propagation above a layer with a large refraction index. *Journal of the Acoustical Society of America*, 61(3):659–674, March 1977.

[137] R.J. Donato. Impedance models for grass covered ground. *Journal of the Acoustical Society of America*, 61(6):1449–1452, June 1977.

[138] L. M. Brekhovskikh. *Waves in Layered Media.* Academic Press, 1960.

[139] K Attenborough. Near grazing sound propagation over open flat continuous terrain. *Acoustics Autumn Bulletin*, 23–29, 1984.

[140] A. Von Meier. *A Noise Absorbing Road Surface Made of Poro-Elastic Asphaltic Concrete.* Technical Report, Ministerie van V.R.O.M., Postbus 450, 2260 DB Leidschendam, The Netherlands, January 19866.

[141] M. Berengier, J. F. Hamet, and P. Bar. Acoustical properties of the porous asphalts: theoretical and experimental aspects. In *TRB–AJPCR Congress*, Washington, D.C., 1989.

[142] K. Attenborough and C. Howorth. *Models for the Acoustical Characteristics of Porous Road Surfaces.* Preliminary report for TRRL contract, Open University Walton Hall Milton Keynes.

[143] K. Attenborough and C. Howorth. Models for the acoustical characteristics of porous road surfaces. In Ulf Sandberg, editor, *Introc 90*, Gothenburg, Sweden, August 1990.

[144] M.A. Biot. Theory of propagation of elastic waves in a fluid saturated porous solid. *Journal of the Acoustical Society of America*, 28:168–178, 1956.

[145] J. F. Allard. Acoustical properties of porous materials. 1992.

[146] M. R. Stinson. The propagation of plane sound waves in narrow and wide circular tubes, and generalization to uniform tubes of arbitrary cross–sectional shape. *Journal of the Acoustical Society of America*, 89(2):550–558, February 1991.

[147] P.G. Smith and R.A. Greenkorn. Theory of acoustical wave propagation in porous media. *Journal of the Acoustical Society of America*, 52:247–250, 1972.

[148] A. R. P. Janse. *Sound Absorption at the Soil Surface.* Technical Report, Centre for Agricultural Publishing and Documentation, 1969.

[149] K. Attenborough. Influence of pore shape distribution on porous absorber properties. In *Proceedings of the Institute of Acoustics*, pages 355–364, 1990.

[150] A. N. Norris. On the viscodynamic operator in biot's equations of poroelasticity. *Journal of Wave Material Interaction*, 1(4), 1986.

[151] T. Yamamoto and A. Turgout. Acoustics wave propagation through porous media with arbitrary pore size distributions. *Journal of the Acoustical Society of America*, 83(5), 1988.

[152] Rudnick I. The propagation of an acoustic wave along a boundary. *Journal of the Acoustical Society of America*, 19(2):348–356, March 1947.

[153] U. Ingard. On the reflection of spherical sound from an infinite plane. *Journal of the Acoustical Society of America*, 23(3):329–335, May 1951.

[154] A. Sommerfeld. Propagation of waves in wireless telegraphs. *Annalen der Physik*, 1909.

[155] J.R. Wait. *Electromagnetic Waves in Stratified Media.* Pergammon Press, 1970.

[156] R.B. Lawhead and I. Rudnick. Acoustic wave propagation along a constant normal impedance boundary. *Journal of the Acoustical Society of America*, 23, 1951.

[157] R. J. Donato. Propagation of a spherical wave near a plane boundary with a complex impedance. *Journal of the Acoustical Society of America*, 60(1):34–39, July 1976.

[158] K. Attenborough, S.I. Hayek, and J.M. Lawther. Propagation of sound above a porous half–space. *Journal of the Acoustical Society of America*, 68(5):1493–1501, November 1980.

[159] C.F. Chein and W.W. Soroka. Sound propagation along an impedance plane. *Journal of Sound and Vibration*, 43:9–20, 1975.

[160] C.F. Chein and W.W. Soroka. A note on the calculation of sound propagation along an impedance surface. *Journal of Sound and Vibration*, 69:340–343, 1980.

[161] D.I. Paul. Acoustical radiation from a point source in the presence of two media. *Journal of the Acoustical Society of America*, 29:1102–1109, 1957.

[162] L.R. Quartarraro. *A Theoretical Investigation of Sound Propagation above a Half–space of Extended Reaction.* Master's thesis, Pennsylvania State University, 1983.

[163] S.I. Thomasson. A powerful asymptotic solution for sound propagation above an impedance boundary. *Acustica*, 45:122–152, 1980.

[164] T. Kawai, T. Hidaka, and T. Nakajima. Sound propagation above an impedance boundary. *Journal of Sound and Vibration*, 83(1):125–138, 1982.

[165] M. Abramowitz and A.G. Stegun, editors. *Handbook of Mathematical Functions.* Dover Publications Inc., 1970.

[166] M.A. Nobile and S.I. Hayek. Acoustic propagation over an impedance plane. *Journal of the Acoustical Society of America*, 78(4):1325–1336, October 1985.

[167] D. Habault and P. J. T. Filippi. Ground effect analysis: surface wave and layer potential representations. *Journal of Sound and Vibration*, 79(4):529–550, 1981.

[168] D. Habault. Diffraction of a spherical wave by different models of ground: approximate formulas. *Journal of Sound and Vibration*, 68, 1978.

[169] T.L. Richards, K. Attenborough, N.W. Heap, and A.P. Watson. Penetration of sound from a point source into a rigid porous media. *Journal of the Acoustical Society of America*, 78:956–963, 1985.

[170] A.D. Rawlins. The field of a spherical wave reflected from a plane absorbent surface expressed in terms of an infinite series of legendre polynomials. *Journal of Sound and Vibration*, 89:359–363, 1983.

[171] D. Habault. *Etude de L'Influence es Sols sur la Propagation Sonore.* PhD thesis, Universite d'Aix Marseille, 1984.

[172] Numerical Algorithms Group Ltd., editor. *NAG ForTran Library Manual.* Volume 13, Numerical Algorithms Group Ltd., 1988.

[173] E.T. Copson. *An Introduction to the Theory of Functions of a Complex Variable.* Oxford University Press, 1935.

[174] H. Ott. Die sattelpunktsmethode in der umegebung eines pols. *Annalen der Physik*, 43, 1943.

[175] P.C. Clemmow. Some extensions to the method of integration by steepest descents. *Quarterly Journal of Mechanics and Applied Mathematics*, 3, 1950.

[176] C. Howorth. Calculation of sound propagation from a point source over an impedance boundary. In *Proceedings Institute of Acoustics*, pages 2157–263, 1989. Vol 2, part 5.

[177] Tooms S. *Sound Propagation Over Porous Elastic Media*. PhD thesis, Open University, Walton Hall, Milton Keynes, United Kingdom, 1990.

[178] J. Nicolas, J. L. Berry, and G. A. Daigle. Propagation of sound above a finite layer of snow. *Journal of Acoustical Society of America*, 77(1):67–73, 1985.

[179] F. P. Mechel. Analysis of spherical wave propagation over absorbing ground. In *Proceedings of the Institute of Acoustics*, pages 231–256, Institute of Acoustics, 1989. Volume 2, part 5.

[180] T. Embleton and G. Daigle. Experiments with surface waves. In *Internoise 1990*, 1990.

[181] Brekhovskikh L. M. Surface waves in acoustics. *Acoustics Journal (U.S.S.R.)*, 5(1):3–12, 1959.

[182] Ivanov–Shits K. M. and Rozhin F. V. Investigation of surface waves in air. *Acoustics Journal (U.S.S.R.)*, 5(4), 1959.

[183] Raspet R., Bass H. E., and Ezell J. Additional comments on and erratum for "effect of finite ground impedance on the propagation of acoustic pulses". *Journal of the Acoustical Society of America*, 77(5), 1985.

[184] L.A.M. Van der Heijden and Martens M. J. M. Traffic noise reduction by means of surface wave exclusion above parallel grooves in the roadside. *Applied Acoustics*, 15:329–339, 1982.

[185] Daigle G. A., Piercy J. E., Embleton T. F. W., and Donato R. J. Surface waves. In *The Symposium on Long Range Sound Propagation*, Diamondhead, Mississippi, November 1981.

[186] Raspet R. and Baird G. E. The acoustic surface wave above a complex impedance ground surface. *Journal of the Acoustical Society of America*, 1988.

[187] Tolstoy I. *Wave Propagation.* McGraw Hill, 1973.

[188] Daigle G. A. Surface waves above porous ground surfaces. In *117 th of the Acoustical Society of America*, Acoustical Society of America, Syracuse, May 1989.

[189] Arnott. P. Measurement and calculation of acoustic propagation constants in arrays of small air–filled rectangular tubes. *Journal of the Acoustical Society of America*, 1–12, 1991.

[190] K. B. Rasmussen. Sound propagation over grass covered ground. *Journal of Sound and Vibration*, 247–255, 1981.

[191] K Attenborough and O. Buser. On the application of rigid porous models to the impedance data for snow. *Journal of Sound and Vibration*, 124(2):315–327, 1988.

[192] D. L. Berry. Location of buried objects. In *Proceedings of the Third Symposium on Long Range Propagation*, Jackson, Mississippi, 1989.

[193] Huisman W. H. T., Martens M. J. M., and van Asseldonk W. Measured and modelled temperature effects on outdoor sound transmission. In *Institute of Acoustics*, 1987. Number 9.

[194] U. Ingard. A review of the influence of meterological conditions on sound propagation. *Journal of the Acoustical Society of America*, 1953.

[195] R. Grosse, V. Mellert, M Schultz-von Glahn, and A. Sill. Sound propagation in the turbulent atmosphere a comparison of approximation methods. In *8th Symposium Fase 89*, 1989.

[196] S. F. Clifford and R. J. Lataitis. Turbulence effects on acoustic wave propagation over a smooth surface. *Journal of the Acoustical Society of America*, 73, 1983.

[197] M. A. Johnson, R. Raspet, and M. K. Bobak. A turbulence model for sound propagation from an extended source above level ground. *Journal of the Acoustical Society of America*, 81, 1980.

[198] R. Makerarewicz. Reply to "comment on: near–grazing propagation above a soft ground". To be published in Journal of the Acoustical Society of America.

[199] D. Albert. Private Communication, 1990.

[200] Jiří C. and Kříž M. Measurements of acoustic properties of real absorptive surfaces. In *Internoise 1988*, 1990.

[201] Jiří C. and Kříž M. Measurements of acoustic properties of absorptive surfaces at scale modeling of traffic noise propagation. In *Internoise 1988*, 1990.

[202] Mees P. and Verhagen C. Private Communication. Catholic University of Leuven, Belgium.

[203] H. W. Stumpf. Linking evaluation of heavy truck tyre noise, measured by iso 362, with scale factors for sound intensity. In *International tire/road noise conference¿*, 1990.

[204] J. F. Hamet. *Modélisation Acoustique dun Enrobé Drainant, La super épaisseur.* Technical Report NNB 890 1, I.N.R.E.T.S., 1989.

[205] J. F. Hamet, M. Berengier, and M. Jacques. Acoustic performance of pervious surfaces. In U. Sandberg, editor, *I.N.T.R.O.C.*, page 345ff, 1990.

[206] D. Sprung. Least square fits with sharp and fuzzy constraints. November 1990. Talk given at the Open University.

[207] Attenborough K. Private Communication. Open University.

[208] *VAX ForTran User Manual.* Digital Equipment Corporation, Maynard, Mass., 1989. Edition 5.0.

[209] *VAX DCL Concepts Manual.* Digital Equipment Corporation, Maynard, Mass., 1988.

# Appendix A

# Glossary of symbols

This appendix lists the commonly used symbols and their meanings. In some cases one symbol has more than one meaning, which definition is to be used should be clear from the context.

| Symbol | Meaning |
|---|---|
| $A$ | Constant |
| $b$ | Semi–width of pore in the form of a parallel slit |
| $c_0$ | adiabatic speed of sound in air |
| $c_e$ | Probe end correction |
| $C(\omega)$ | Frequency dependent compressibility of air in a pore |
| $d$ | Layer thickness |
| $f$ | Frequency |
| $F$ | Formation factor |
| $h_s$ | Source height |
| $h_r$ | Receiver height |
| $H$ | Hankel function |
| $Hz$ | Hertz |
| $H_{ij}$ | Transfer function i.e. quotient of function $i$ and function $j$ |
| $I$ | Electrical current |
| $\Im(x)$ | Imaginary part of $x$ |
| $J_n$ | $n^{th}$ order Bessel function |
| $k_0$, $k$ | Wave number in air |
| $k_b$ | Propagation constant |
| $K_P$, $K_T$, $K_S$ | Compressibility (general, adiabatic and isothermal) |
| $K$ | Shape factor |
| $K_M$ | Bulk modulus |
| $L$ | Standing wave ratio |
| $M$ | Mass |
| $N_{PR}$ | Prandtl number |
| $p$ | Acoustic pressure |
| $P_0$ | Pressure amplitude |
| $q^2$ | Tortuosity |
| $Q$ | Spherical wave reflection coefficient |
| $Q$ | Flow rate |
| $r$, $d$, $x$, $a$, $s$ | Measurements of distance |
| $\Re(x)$ | Real part of $x$ |
| $R_p$ | Plane wave reflection coefficient |
| $R_N$ | Reflection coefficient |
| $R1$, $R2$ | Propagation paths between source and receiver |
| $R_s$, $R$, $R'$ | Resistance |
| $R$ | Flow resistivity |
| $s$ | Entropy |
| $SPL$ | Sound pressure level |

| | |
|---|---|
| $t$ | Time |
| $T$ | Temperature |
| $V$ | Electrical voltage |
| $x(\tau)$ | Time waveform |
| $X_s$, $X$, $X'$ | Reactance |
| $Z$ | Impedance |
| $Z_c$ | Characteristic impedance |
| $Z_s$ | Surface impedance |
| $\alpha$ | Standing wave tube attenuation |
| $\beta$ | Grain shape |
| $\gamma$ | Ratio of specific heats |
| $\Delta\varphi$ | Phase gradient |
| $\theta$ | Angle of incidence with respect to normal |
| $\lambda$ | Wavelength of sound |
| $\mu$ | Coefficient of dynamic viscosity of air |
| $\nu$ | Coefficient of kinematic viscosity of air |
| $\nu_{ij}$ | Coherence function |
| $\rho_0$ | Static density of air |
| $\rho$ | Dynamic density of air |
| $\sigma$ | Flow resistivity |
| $\sigma_f$, $\sigma_s$ | Electrical conductivity |
| $\phi$ | Phase change on reflection |
| $\phi$ | Field potential |
| $\Omega$ | Porosity |
| $\omega$ | Angular frequency |

# Appendix B

# Glosary of commonly use terms

This section lists some of the more commonly encountered acoustical terms and their meanings.

**Absorption coefficient** the ratio of sound energy absorbed by a surface to the total sound energy impinging on the surface.
**Acoustics** the science of sound.
**Acoustical** relating to acoustics.
**Amplitude** the magnitude of a variable.
**Anechoic** totally sound–absorbent i.e. without reflections.
**Attenuation** the reduction in a sound pressure or other level usually in dB
**Audio frequency** a frequency between 20Hz and 20KHz
**Band** a section of a frequency spectrum
**Characteristic impedance** a measure of the reflective properties of a material. The ratio of the root mean square sound pressure level to the root mean square particle velocity.
**Decibel (dB)** One tenth of a Bel. Evaluated from $dB = 20.\log\frac{a}{b}$ where $b$ is a reference value; i.e. $2 \times 10^{-5}$ when evaluating sound pressure.
**Diffraction** the diversion of the direction of travel of a wave other than by reflection or refraction.
**Excess attenuation** the ratio of the total field and direct field impinging on a receiver.
**Field** region of air put into motion by an acoustic wave.
**Free field** a region free from and reflections.
**Flow resistance** the ratio of the pressure gradient to the induced flow velocity across a given porous sample. **Flow resistivity** the flow resistance per unit length.
**Frequency** the number of times a vibrating particle oscillates in one second, expressed in hertz.
**Level difference** the difference between the sound level in decibels measured at two separated microphones above a ground surface.
**Phase** a measurement of a point in time of an oscillatory motion with respect to a fixed point.

**Plane wave** a wave in which the wave fronts are parallel to each other and perpendicular to the direction of travel.
**Random noise** a fluctuating quantity whose amplitude distribution with time is a Gaussian function.
**Refraction** the change in direction of a sound ray when passing across a temperature or other physical gradient.
**Resonant frequency** a preferred frequency of oscillation of a system.
**Root mean square value** (rms) the values of a variable are squared, averaged and then the square root is evaluated.
**Sine wave** a wave which has an amplitude varying in a sinusoidal fashion.
**Sound** the wave motion in an elastic medium due to the passage of an acoustic wave.
**Sound pressure level** the rms values of acoustically induced pressure fluctuations expressed in decibels.
**Spherical wave** a wave in which the wave fronts are concentric spheres.
**Wave front** a theoretical surface constructed by joining points at which the phase of a wave is the same.
**Wavelength** the perpendicular wavefront between two wave fronts in which the phases differ by one cycle.
**White noise** noise of a statistically random nature, having equal energy at all frequencies.

# Appendix C

# Graphical comparison of spherical wave propagation solutions

The comparison of the level difference is given in graphical form the frequency range of interest is compared to the magnitude of the difference between the two level difference spectra. The following tables detail the propagation model reference numbers.

Table C.1 Summary of local reaction propagation models

| Solution | Equation number | Programme name | Reference number |
|---|---|---|---|
| P.W.R.C | 4.24,4.25,4.23 | PLN | M1 |
| Weyl–van der Pol | 4.27,4.28,4.29, 4.30 | WVP | M2 |
| Thomasson | 4.54 | THM | M3 |
| Attenborough *et al* | 4.32 | AHL | M4 |
| Kawai,Hidaka and Nakajima | 4.60 | KHN | M5 |
| Nobile and Hayek | 4.67 | NAH | M6 |
| Habault and Fillippi | 4.81 | HAF | M7 |
| Adaptive quadrature | 4.110 | TCW | M8 |
| Chandler Wilde | 4.116 | CHW | M9 |

## C.1 Locally reacting media

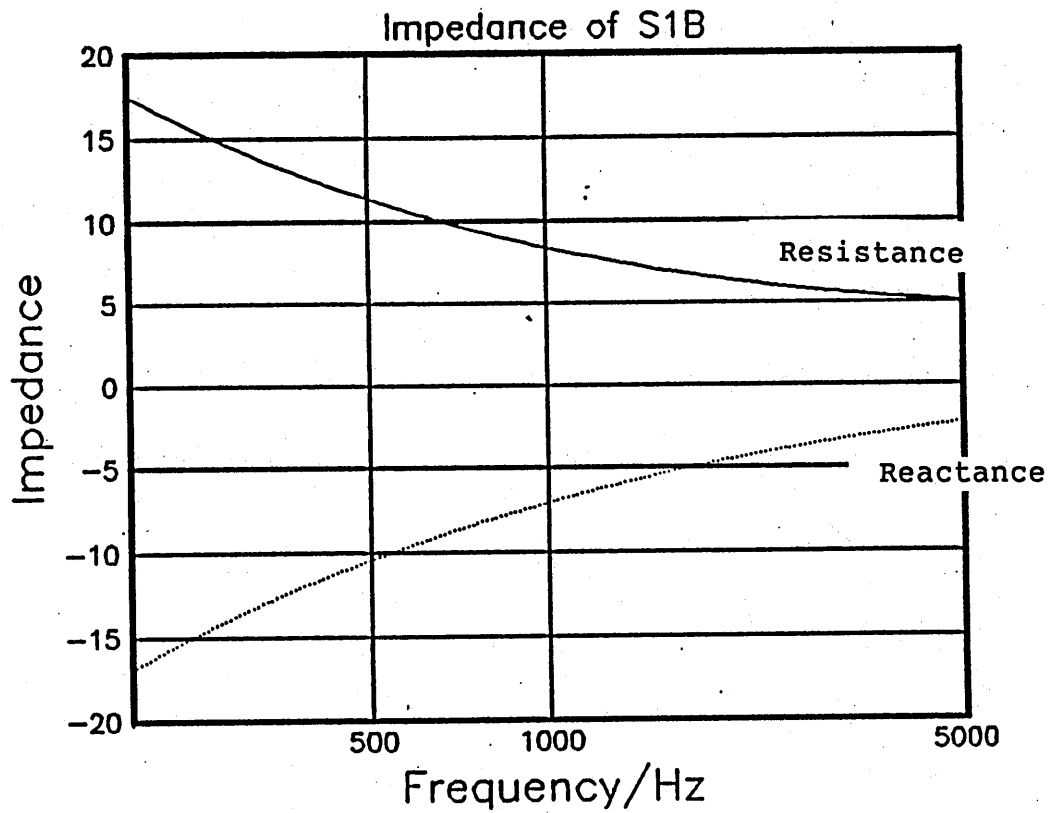


Figure C.1 Impedance of surface S1

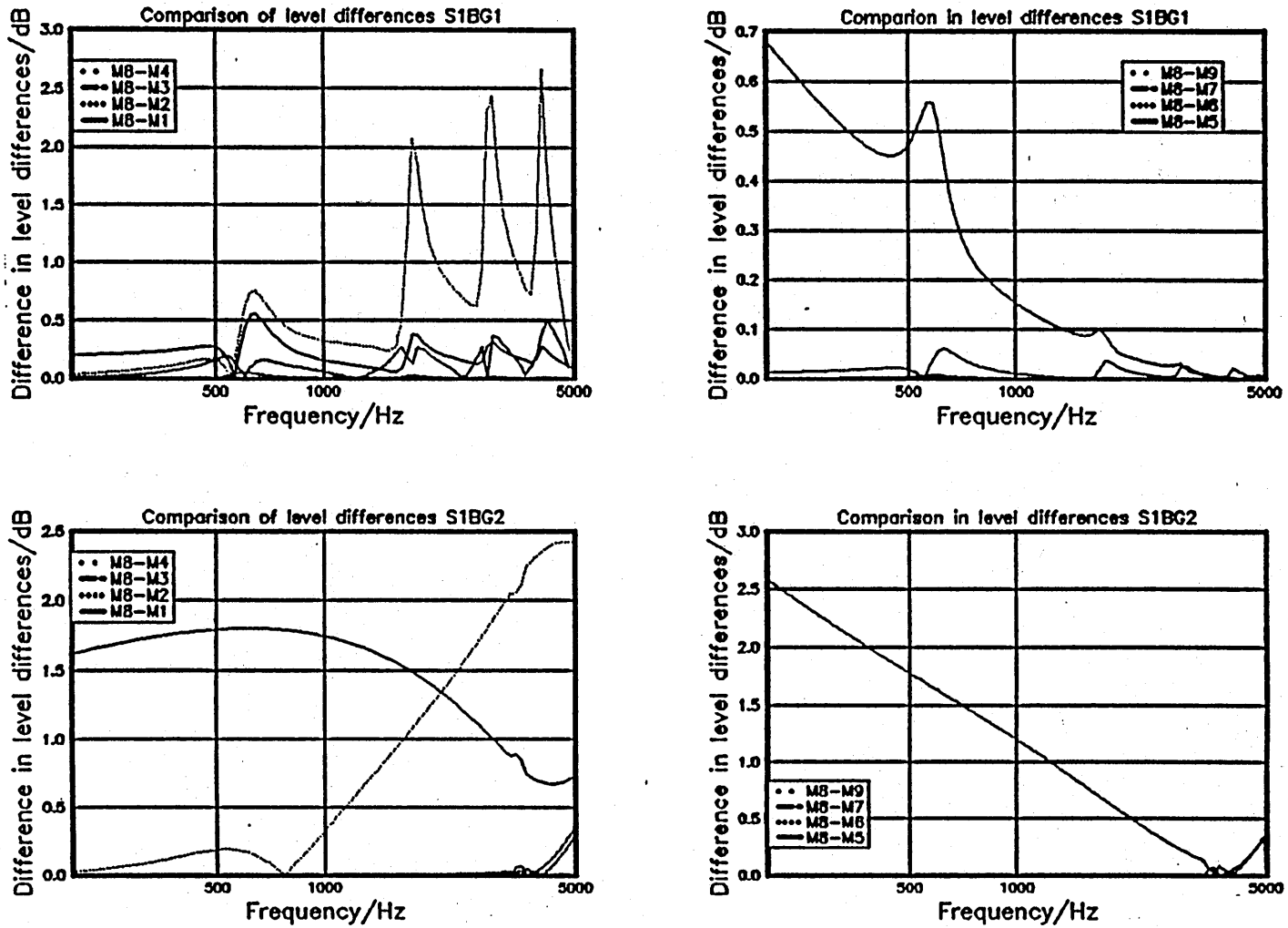


Figure C.2 Comparison of level difference for locally reacting half space

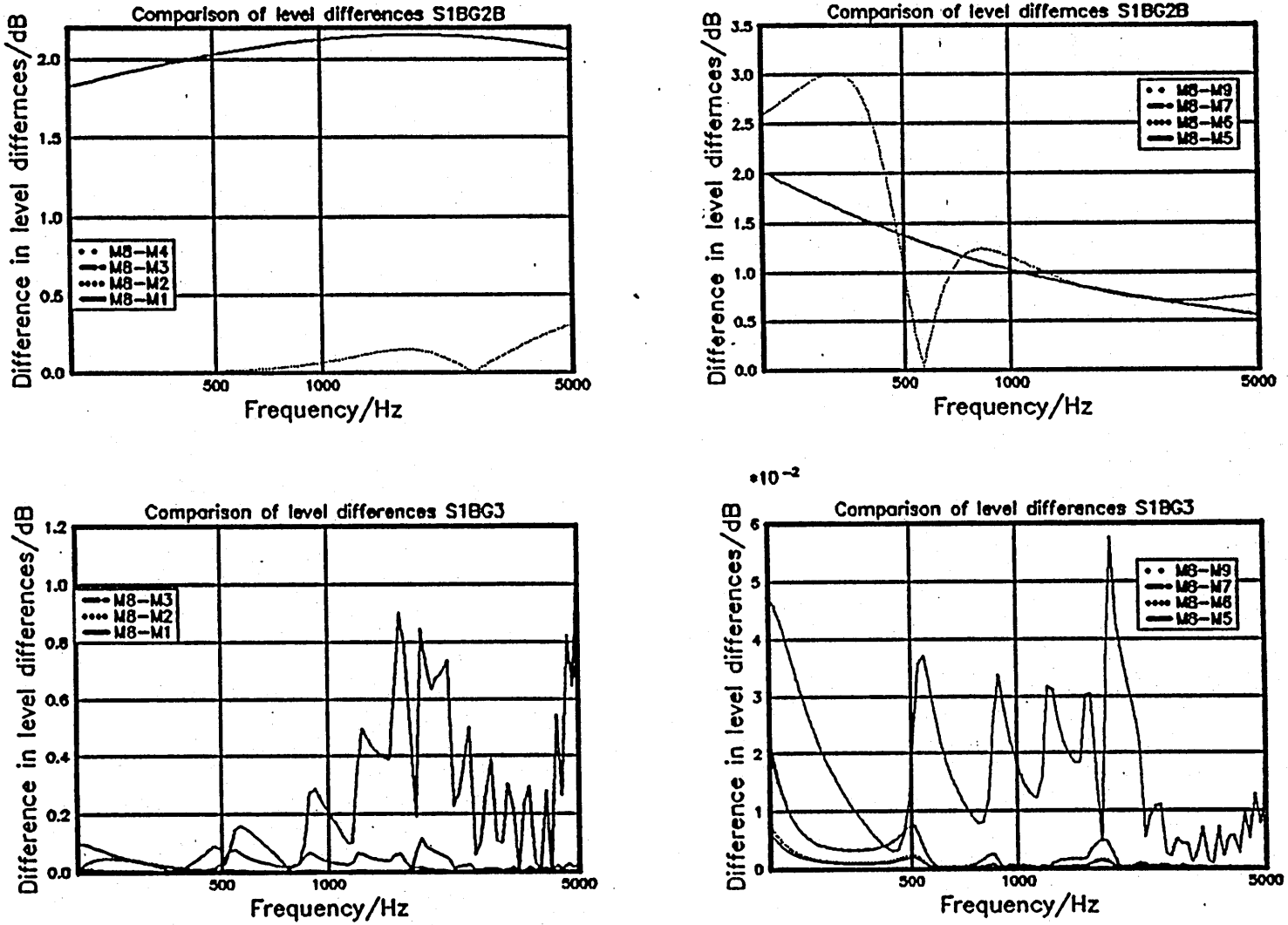


Figure C.3 Comparison of level difference for locally reacting half space

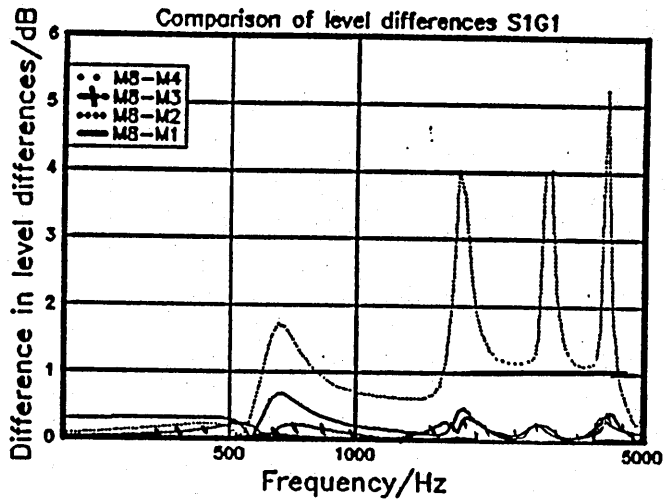


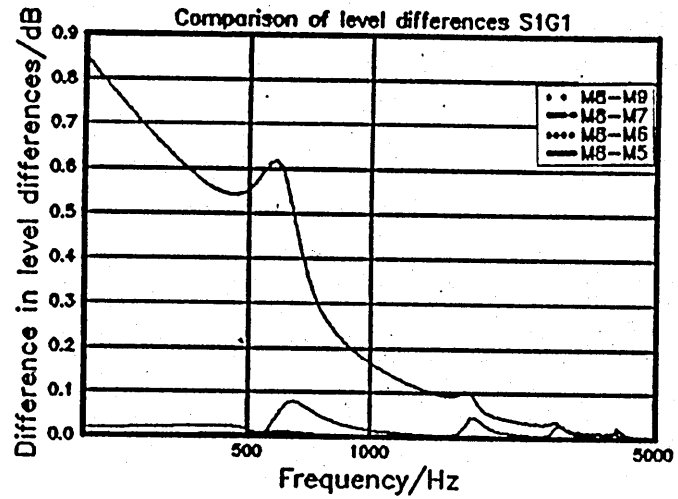


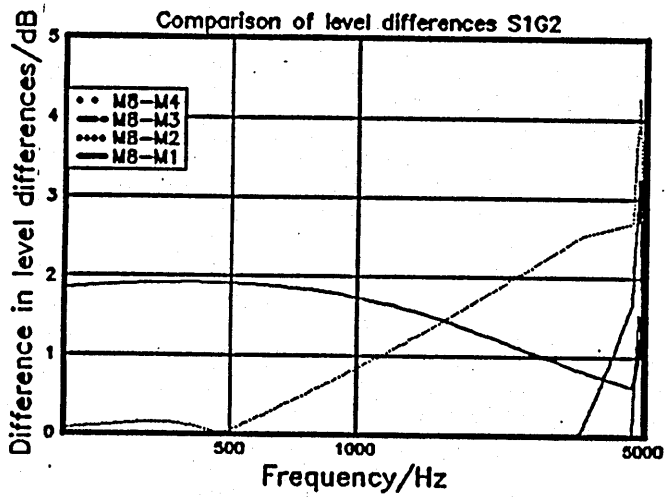


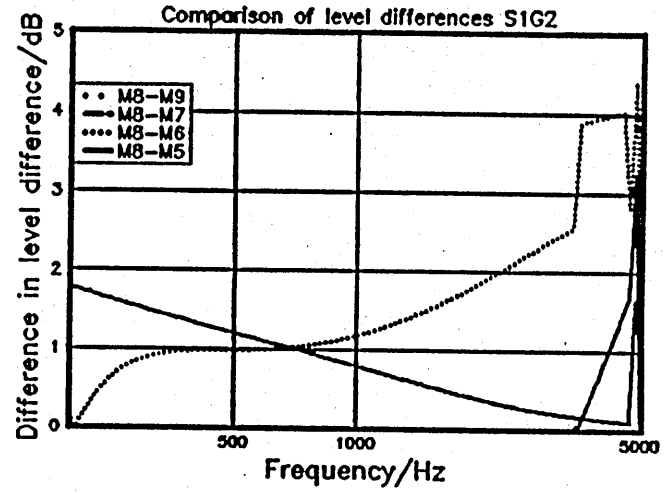


Figure C.4 Comparison of level difference for locally reacting rigidly backed medium

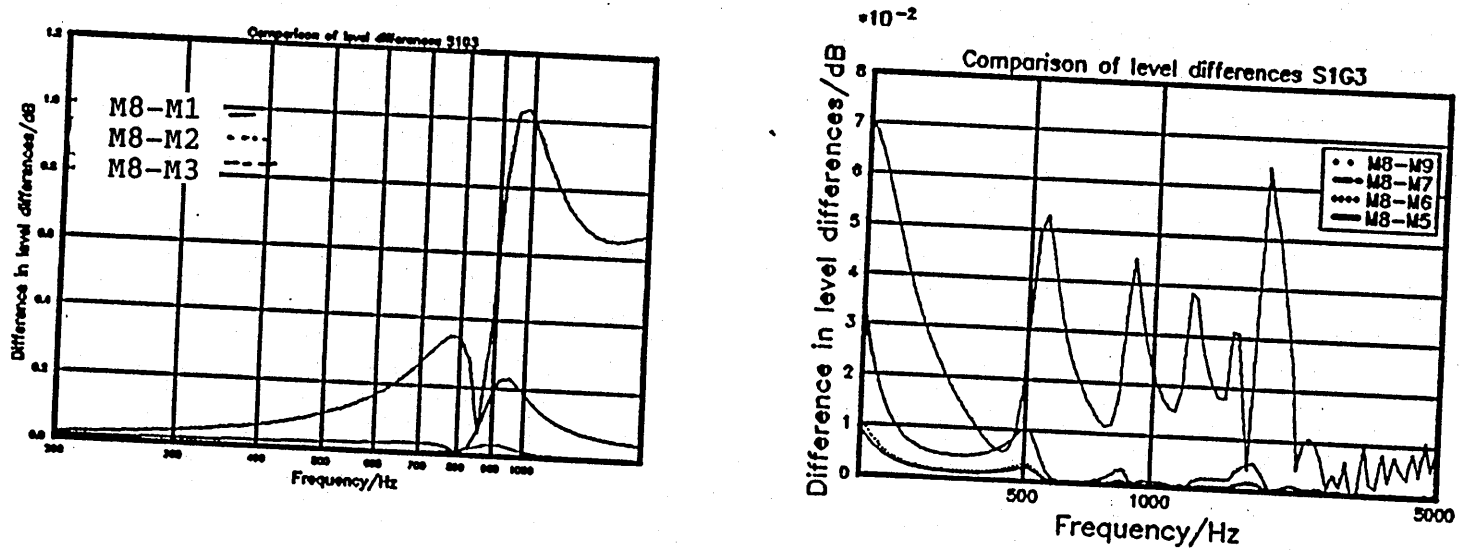


**Figure C.5** Comparison of level difference for locally reacting rigidly backed medium

## C.2 Externally reacting media

1. Weyl van der Pol solution (M10)
2. Attenborough, Hayek and Lawther solution (M11)
3. Attenborough, Hayek and Lawther approximate solution (M12)
4. Habault and Fillipi solution (M13)
5. FFP solution (M14)

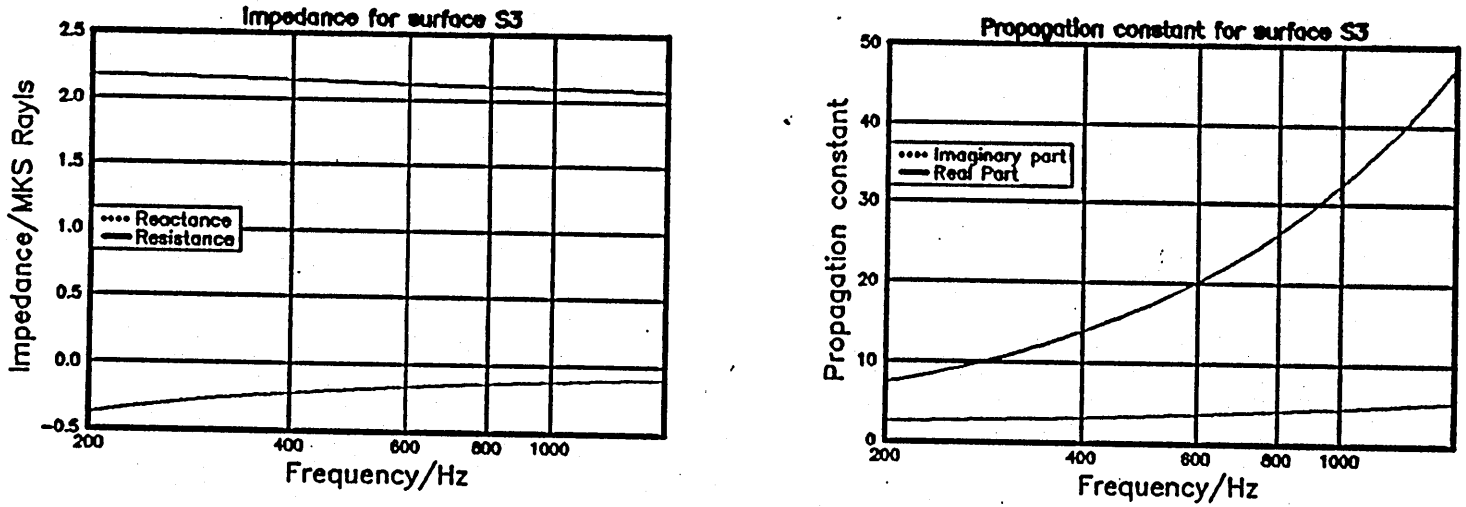


Figure C.6 Acoustical parameters for surface S3

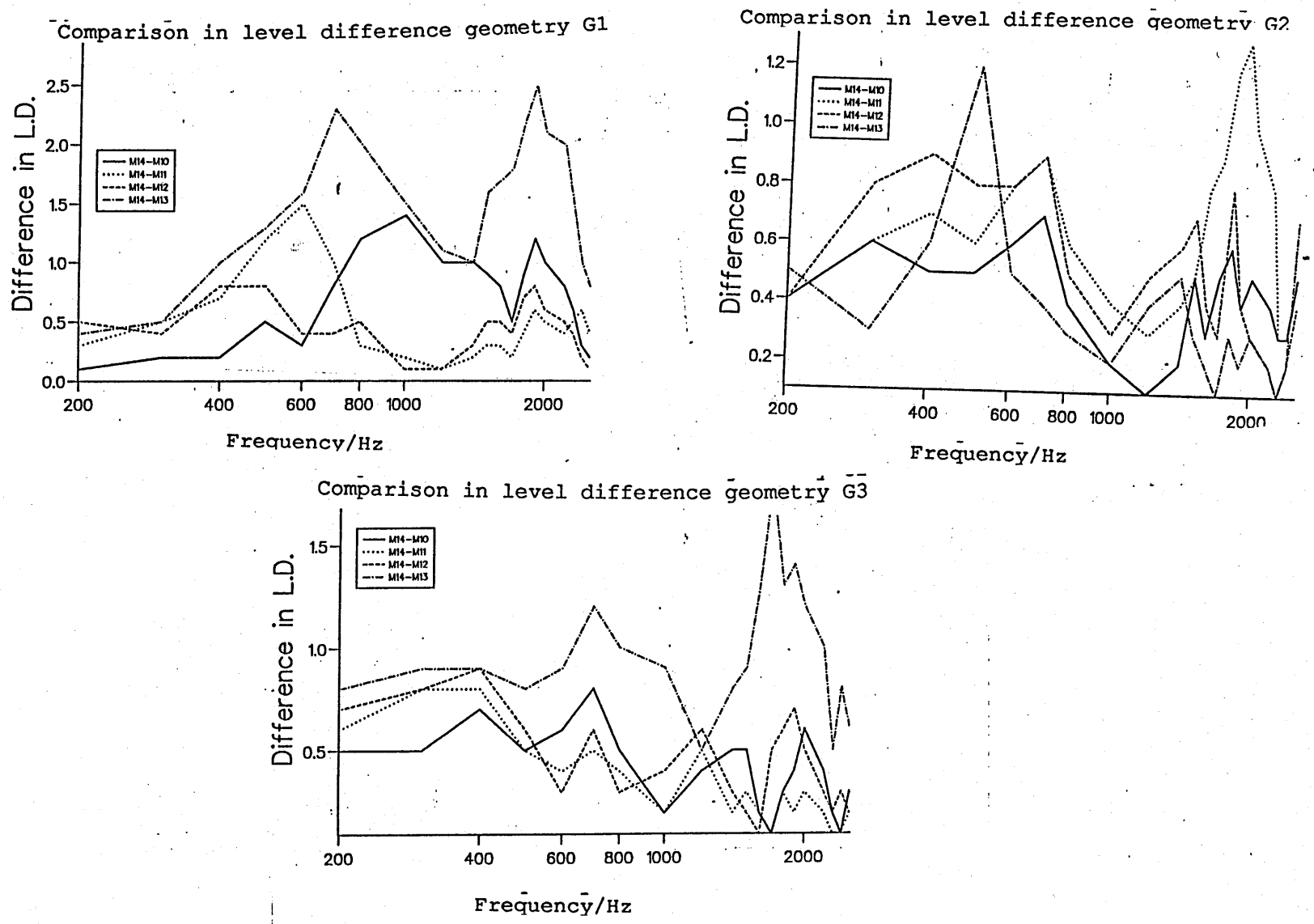


**Figure C.7** Comparison of level difference for externally reacting half space

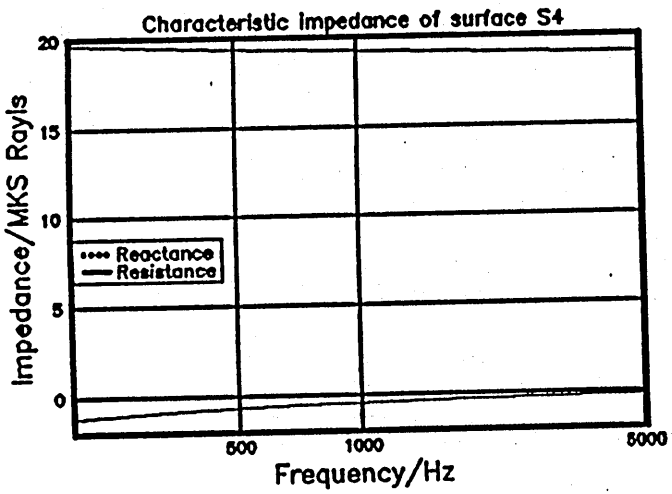


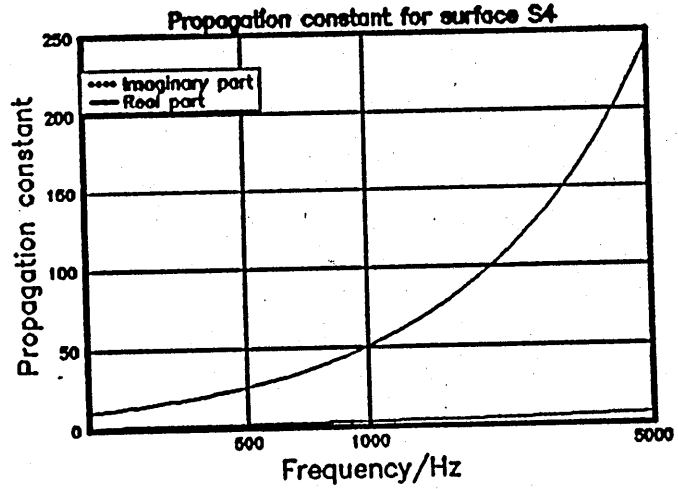


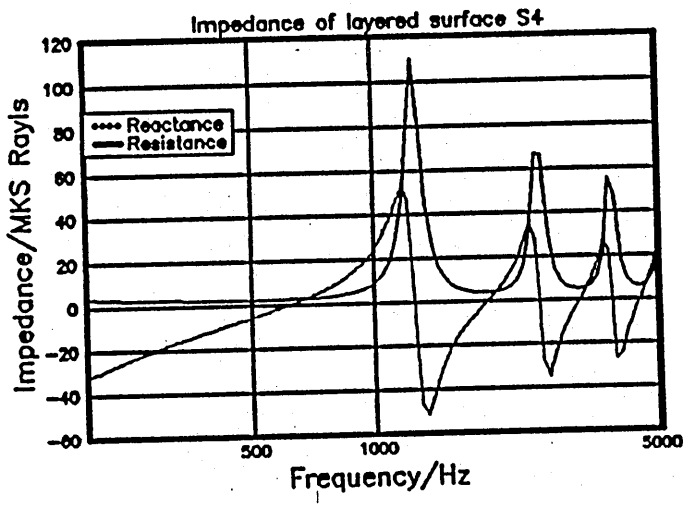


Figure C.8 Acoustical parameters for surface S4

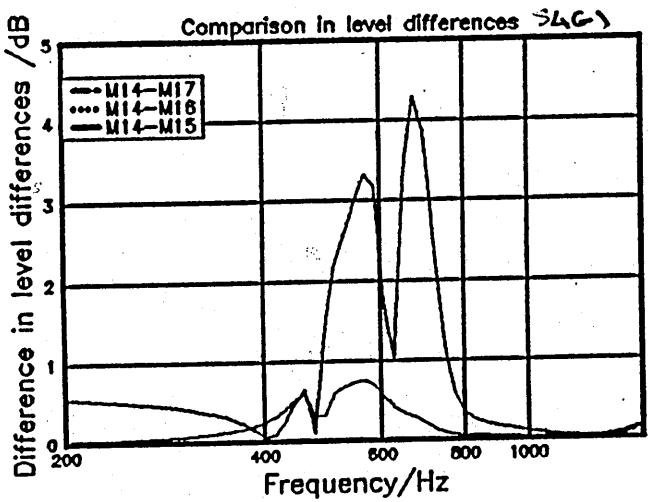


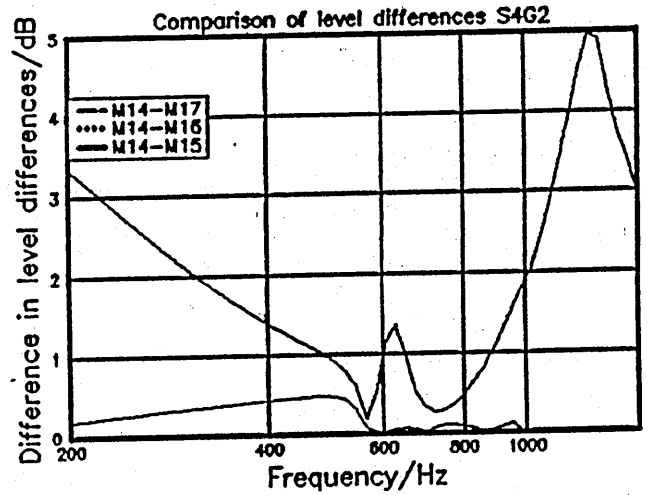


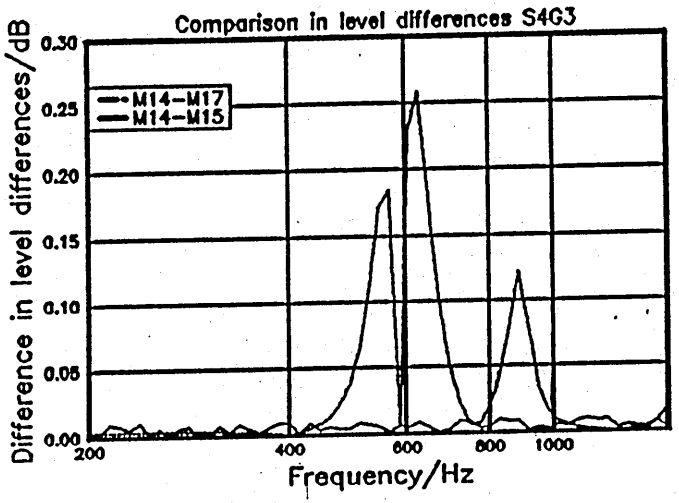


Weyl van der Pol M15
Habault and Fillippi M16
Fast Field program M17

Figure C.9 Comparison of level difference for externally reacting rigidly backed medium

# Appendix D

# Flow resistivity curves for test track sites 1 to 10

Shown below are the results of the non-acoustic measurement of flow resistivity. The plots show the flow resistivity against flow rate. As can be seen a consistent value is obtained when low flow rates are used.

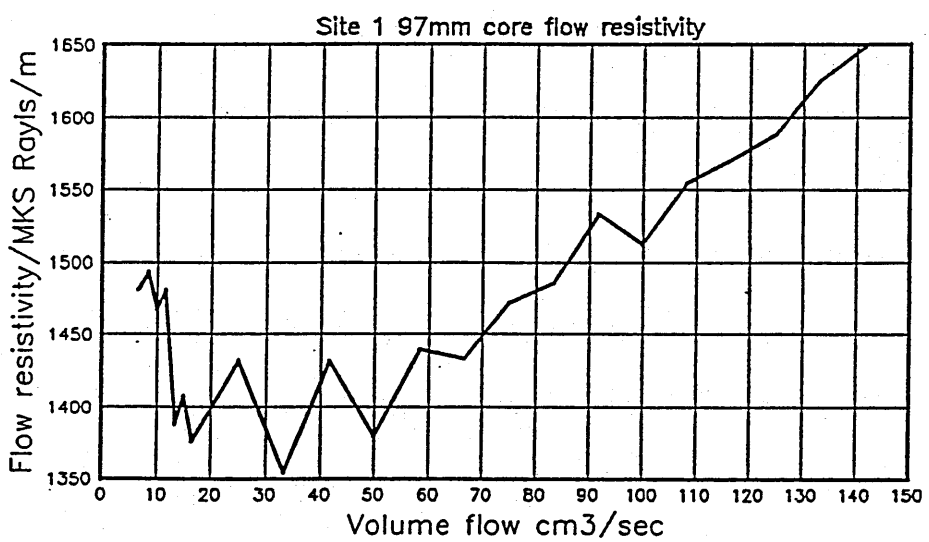


**Figure D.1** Flow resistivity evaluation for site 1

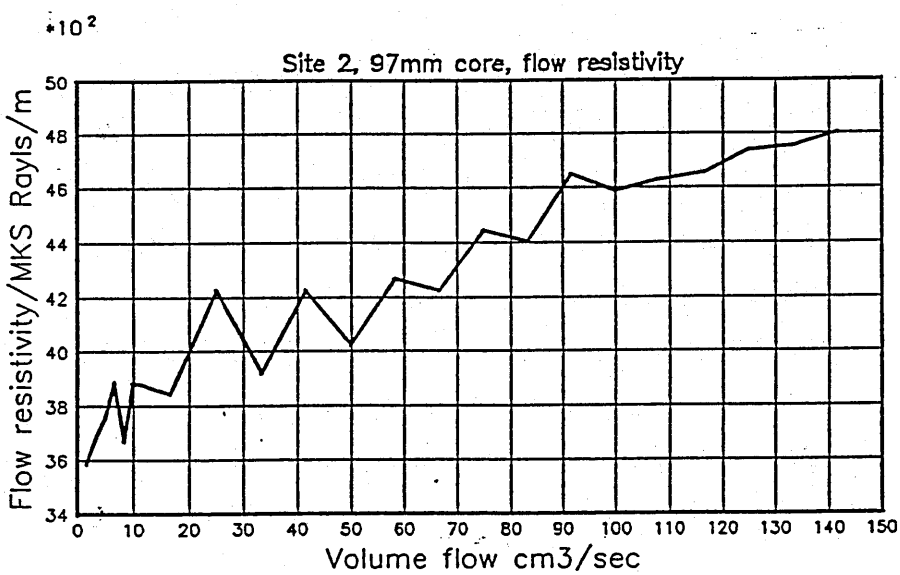


**Figure D.2** Flow resistivity evaluation for site 2

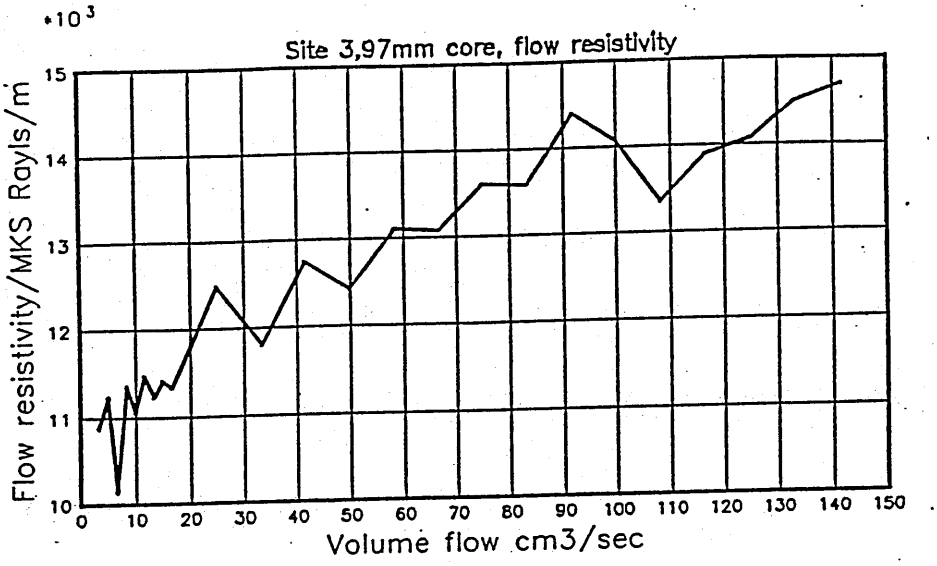


**Figure D.3** Flow resistivity evaluation for site 3

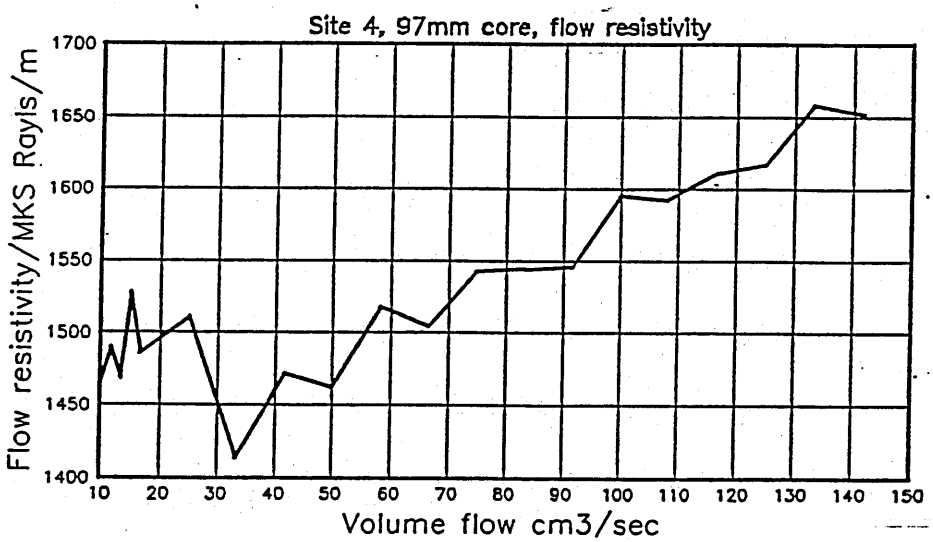


**Figure D.4** Flow resistivity evaluation for site 4

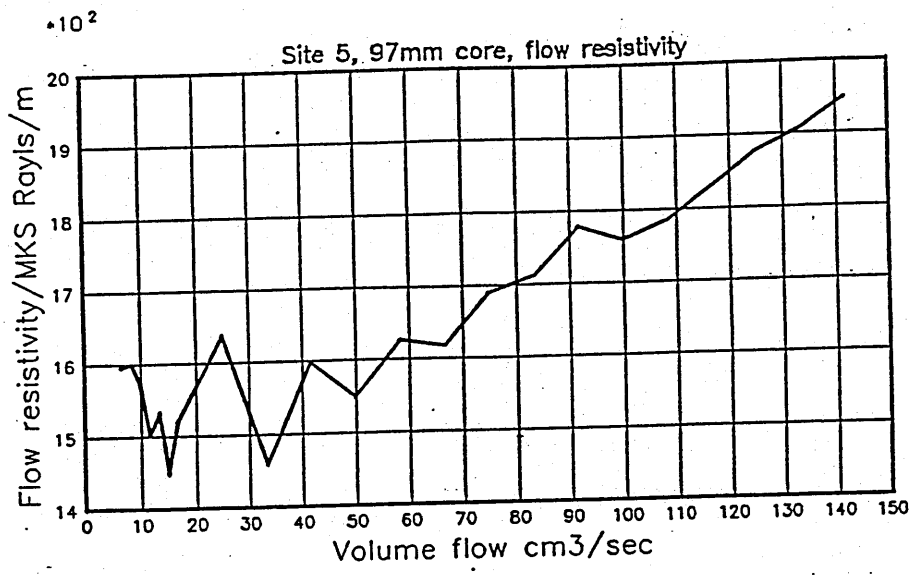


**Figure D.5** Flow resistivity evaluation for site 5

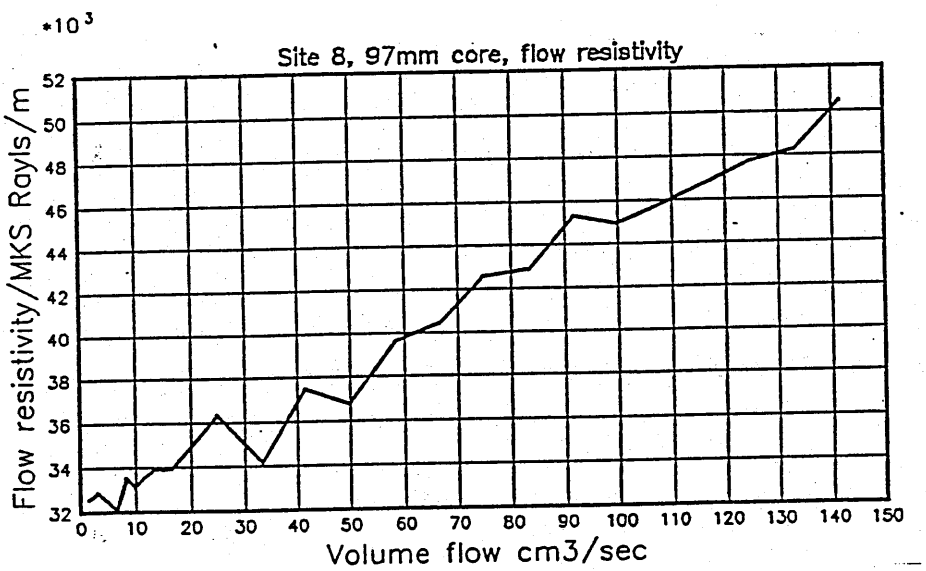


**Figure D.6** Flow resistivity evaluation for site 8

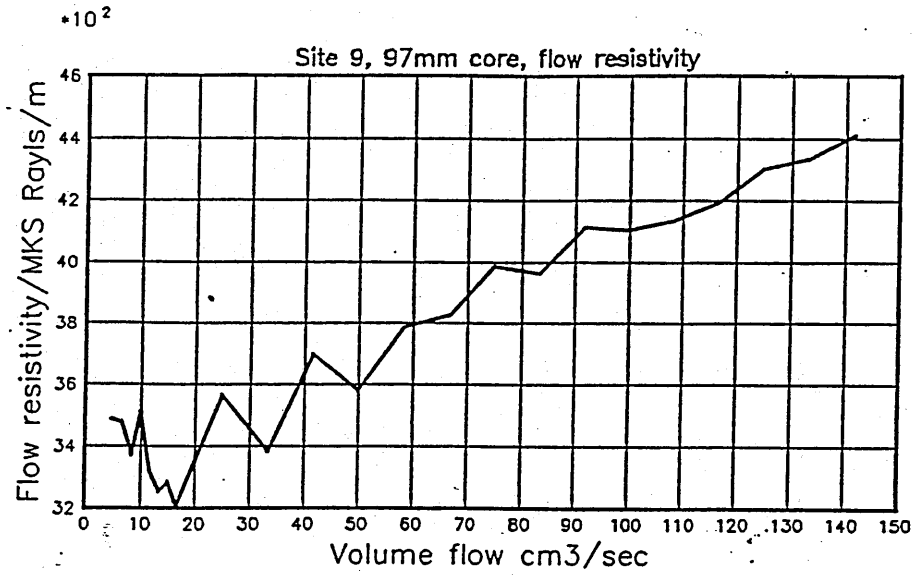


**Figure D.7** Flow resistivity evaluation for site 9

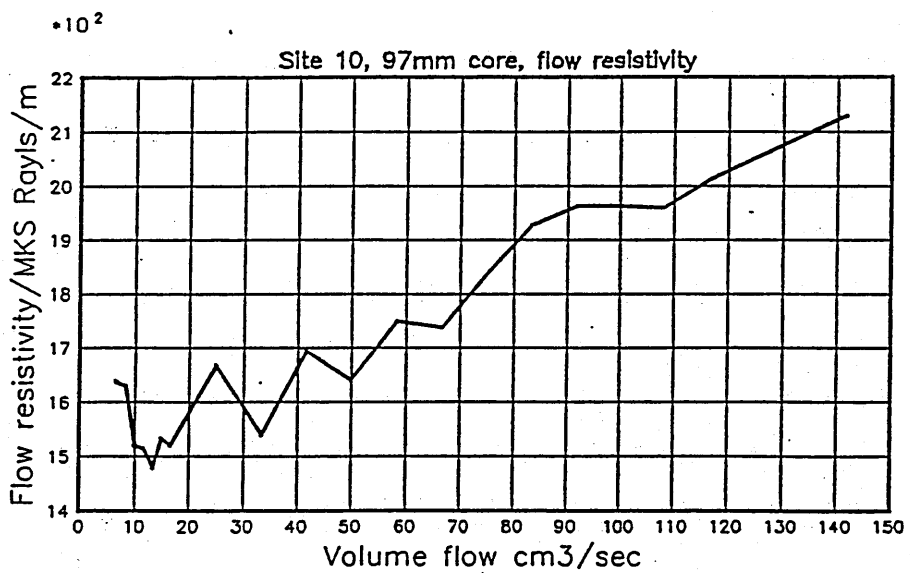


**Figure D.8** Flow resistivity evaluation for site 10

# Appendix E

# Material specifications for test track site

## E.0.1 Material A

This appendix list the specifications to which materials A to D were composed for laying on the test track site.

1) Material A will be laid in sections 1 and 10 according to
the schedule attached
2) The material will be as follows:
2.1) The aggregate shall be Porphyry with the following properties:
a) Minimum polished stone value (PSV) - 58
b) Maximum aggregate crushing value (ACV) - 15
c) Maximum aggregate abrasion value (AAV) - 12
d) Flakiness range - 30 to 35 %
These properties shall be as determined by the method in the relevant current part of BS 812.
2.2) The aggregate grading on analysis shall comply with table E.0.1

* At least 2 per cent by mass of the total aggregate shall by hydrated lime filler.

2.3) The binder shall be 200 pen grade bitumen to BS 3690: Part 1: 1982
The binder content shall be 3.2 ± 0.3 per cent by mass of the total mix

| BS Sieve mm | Per cent by mass passing |
|---|---|
| 28 | 100 |
| 20 | 95 ± 5 |
| 14 | 65 ± 10 |
| 10 | 25 ± 10 |
| 6.3 | 20 ± 10 |
| 3.35 | 10 ± 5 |
| 75 | 4.5 ±1.0* |

Table E.1 Table A1

| BS Sieve mm | Per cent by mass passing |
|---|---|
| 28 | 100 |
| 20 | 95 ± 5 |
| 14 | 65 ± 10 |
| 10 | 25 ± 10 |
| 6.3 | 20 ± 10 |
| 3.35 | 10 ± 5 |
| 75 | 4.5 ±1.0* |

Table E.2 Table B1

3) The contractor should allow for a sufficient sample of the material to be taken from the site for subsequent grading and binder analysis.
4) The material shall be mixed at a temperature not exceeding 125°C

## E.0.2 Material B

1) Material B will be laid in sections 4, 5 the lower 50mm of section of 6 and the upper 50mm of section 7 according to the schedule attached
2) The material will be as follows:
2.1) The aggregate shall be Porphyry with the following properties:
a) Minimum polished stone value (PSV) - 58
b) Maximum aggregate crushing value (ACV) - 15
c) Maximum aggregate abrasion value (AAV) - 12
d) Flakiness range - 15 to 20 %
These properties shall be as determined by the method in the relevant current part of BS 812.
2.2) The aggregate grading on analysis shall comply with table E.0.2

* At least 2 per cent by mass of the total aggregate shall by hydrated lime filler.

2.3) The binder shall be 200 pen grade bitumen to BS 3690: Part 1: 1982
The binder content shall be 3.2 ± 0.3 per cent by mass of the total mix
3) The contractor should allow for a sufficient sample of the material to be taken from the site for subsequent grading and binder analysis.
4) The material shall be mixed at a temperature not exceeding 125°C

## E.0.3 Material C

1) Material C will be laid in sections 2, 9 and the upper 50mm of section 6 according to the schedule attached
2) The material will be as follows:
2.1) The aggregate shall be Porphyry with the following properties:
a) Minimum polished stone value (PSV) - 58
b) Maximum aggregate crushing value (ACV) - 15

| BS Sieve mm | Per cent by mass passing |
|---|---|
| 14 | 100 |
| 10 | 95 ± 5 |
| 6.3 | 20 ± 5 |
| 3.35 | 10 ± 5 |
| 75 | 4.5 ±1.0* |

Table E.3 Table C1

c) Maximum aggregate abrasion value (AAV) - 12
d) Flakiness range - 15 to 20 %
These properties shall be as determined by the method in the relevant current part of BS 812.
2.2) The aggregate grading on analysis shall comply with table E.0.3

* At least 2 per cent by mass of the total aggregate shall by hydrated lime filler.

2.3) The binder shall be 200 pen grade bitumen to BS 3690: Part 1: 1982
The binder content shall be 4.0 ± 0.3 per cent by mass of the total mix
3) The contractor should allow for a sufficient sample of the material to be taken from the site for subsequent grading and binder analysis.
4) The material shall be mixed at a temperature not exceeding 125°C

## E.0.4 Material D

1) Material D will be laid in sections 3, 8 and the lower 50mm of section 7 according to the schedule attached
2) The material will be as follows:
2.1) The aggregate shall be Porphyry with the following properties:
a) Minimum polished stone value (PSV) - 58
b) Maximum aggregate crushing value (ACV) - 15
c) Maximum aggregate abrasion value (AAV) - 12
d) Flakiness range - 15 to 20 %
These properties shall be as determined by the method in the relevant current part of BS 812.
2.2) The aggregate grading on analysis shall comply with table E.0.4

* At least 2 per cent by mass of the total aggregate shall by hydrated lime filler.

2.3) The binder shall be 200 pen grade bitumen to BS 3690: Part 1: 1982
The binder content shall be 5.2 ± 0.3 per cent by mass of the total mix
3) The contractor should allow for a sufficient sample of the material to be taken from the site for subsequent grading and binder analysis.
4) The material shall be mixed at a temperature not exceeding 125°C

| BS Sieve mm | Per cent by mass passing |
|---|---|
| 10 | 100 |
| 6.3 | 95 ± 5 |
| 3.35 | 10 ± 5 |
| 75 | 4.5 ±1.0* |

Table E.4 Table D1

# Appendix F

# Level difference data fitted to derive rigid porous material model parameters

## F.1 Microstructural model fitted curves

Below are examples of the level difference data taken over the test track sites and the curves fitted using the procedure described in chapter 6. The results of the fitting process are shown in table 8.6 of chapter 8. Curves are shown for sites 1 to 4 i.e. for each material type; one curve for site 5 a double thickness layer and curves fitted from the mixed double layers sites.

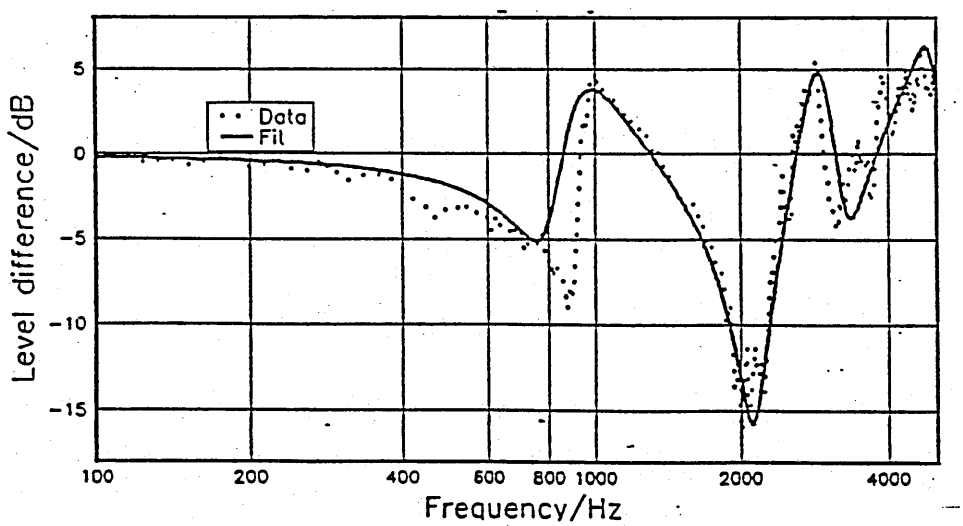


**Figure F.1** Site 1 geometry 1 (A), RMS=2.3

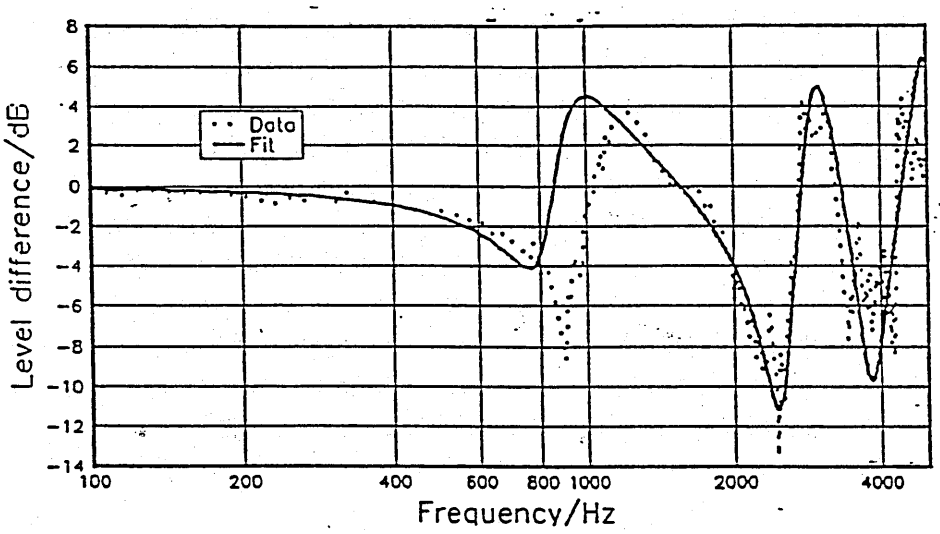


**Figure F.2** Site 1 geometry 2 (A), RMS=3.3

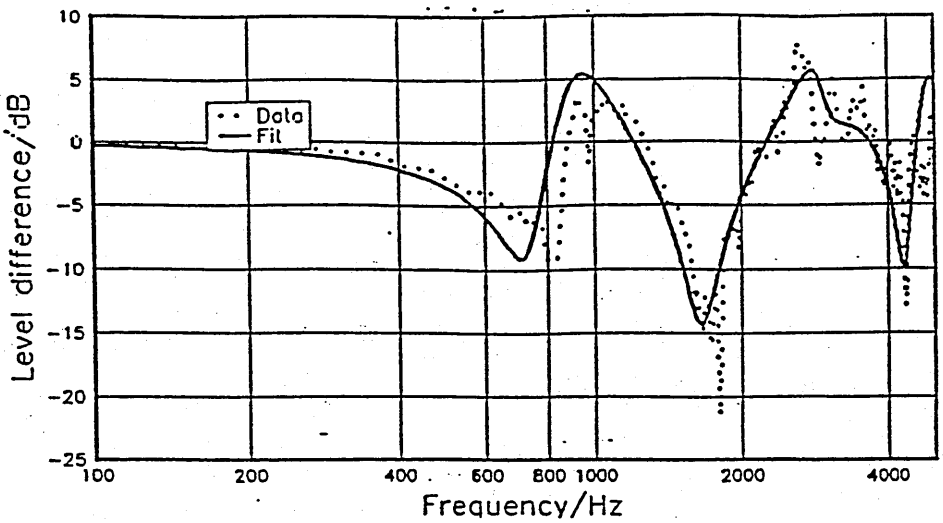


**Figure F.3** Site 1 geometry 3 (A), RMS=2.6

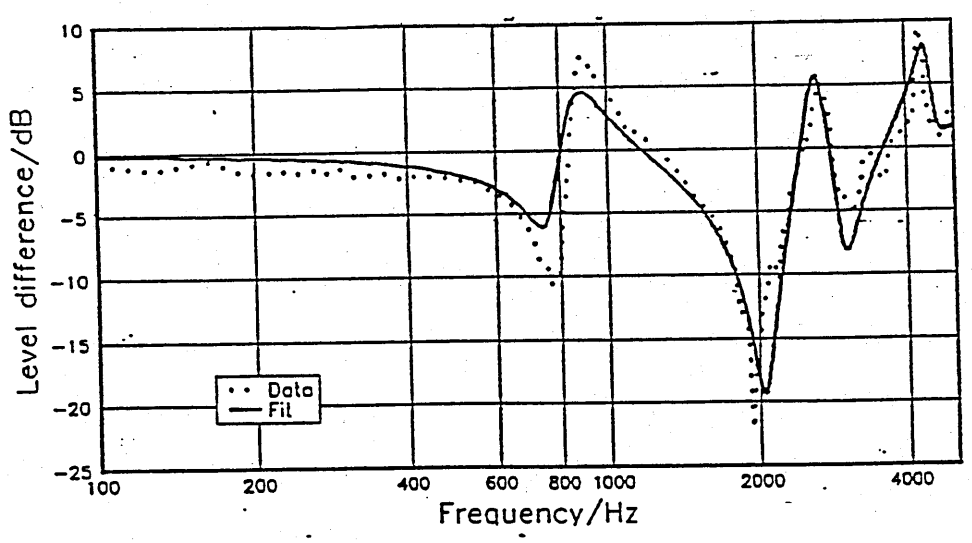


**Figure F.4** Site 2 geometry 1 (C), RMS=2.7

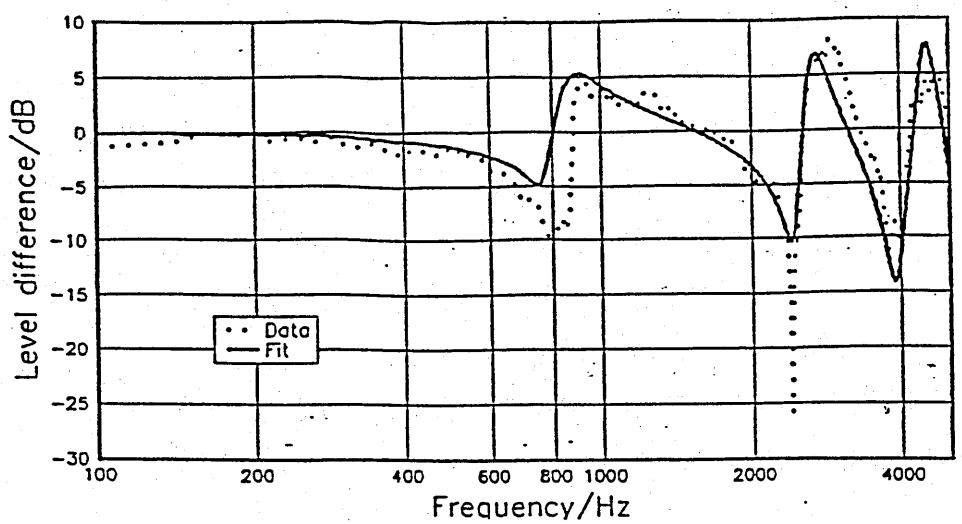


**Figure F.5** Site 2 geometry 2 (C), RMS=2.5

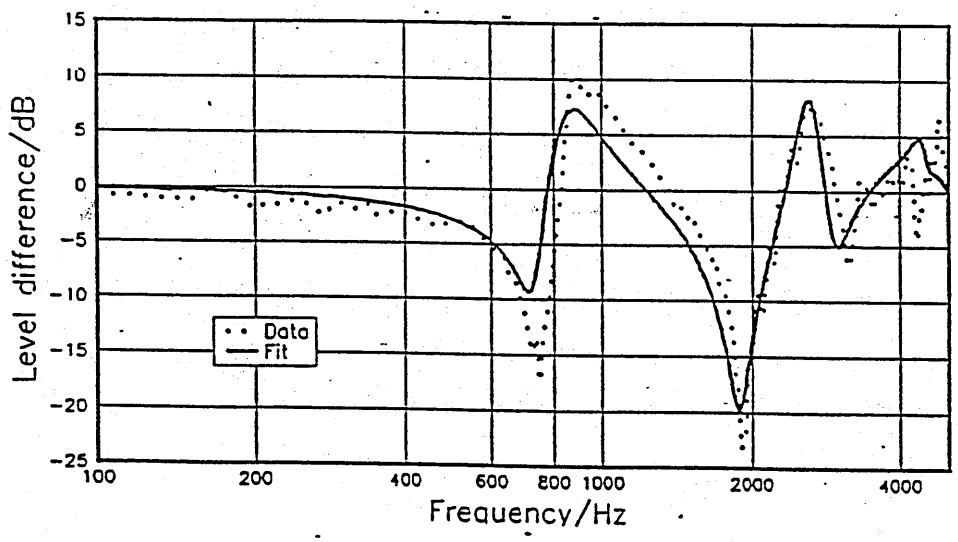


**Figure F.6** Site 2 geometry 3 (C), RMS=2.6

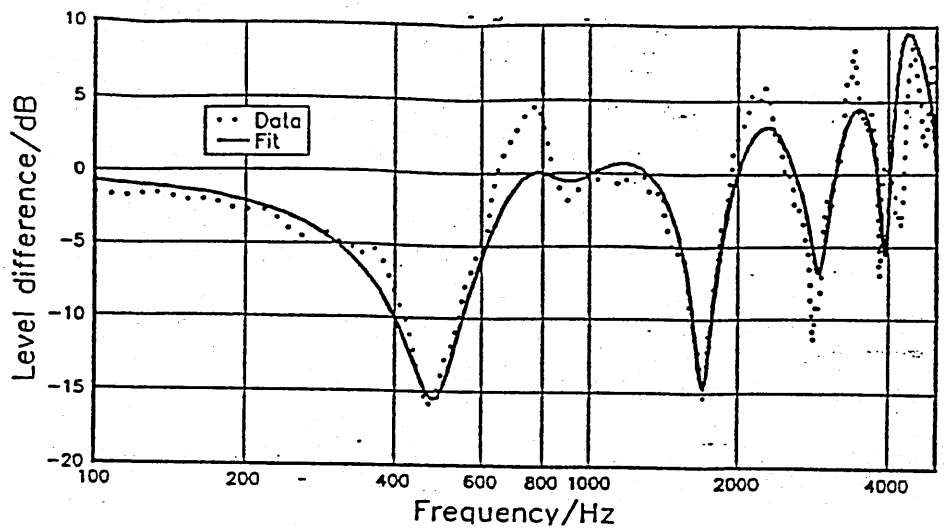


**Figure F.7** Site 3 geometry 1 (D), RMS=2.2

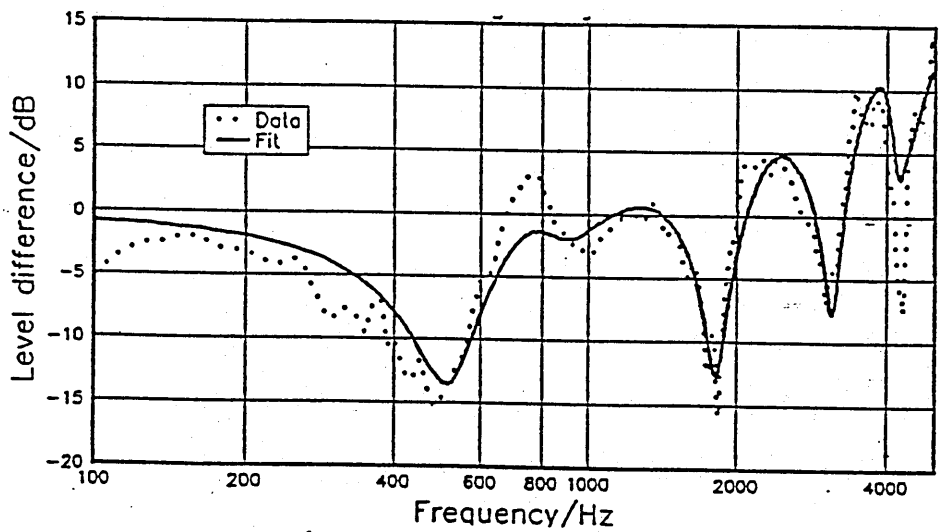


**Figure F.8** Site 3 geometry 2 (D), RMS=2.1

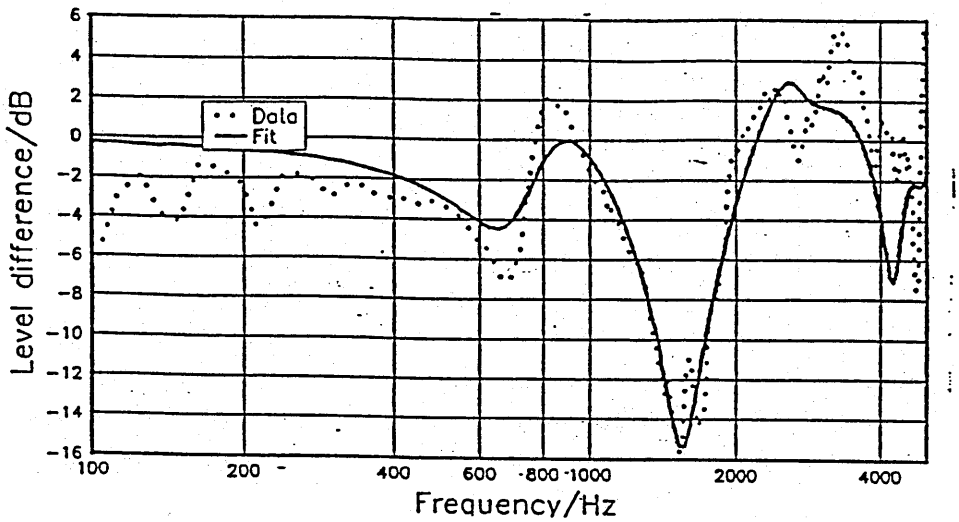


**Figure F.9** Site 3 geometry 3 (D), RMS=2.8

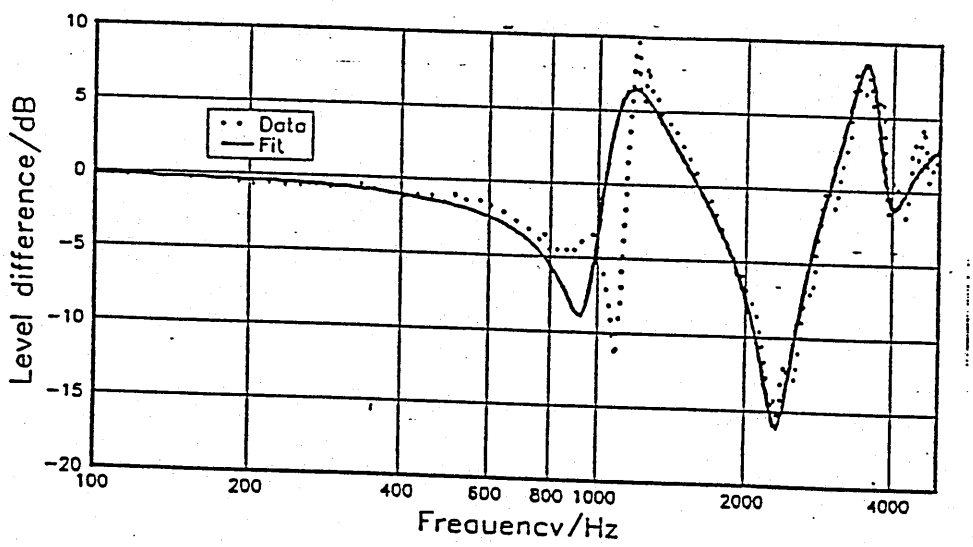


**Figure F.10** Site 4 geometry 1 (B), RMS=1.9

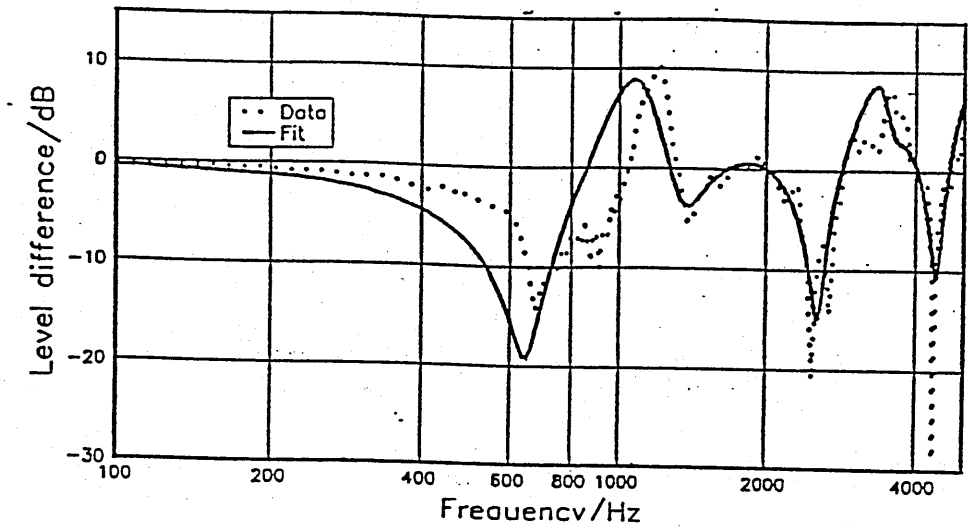


**Figure F.11** Site 4 geometry 2 (B), RMS=3.1

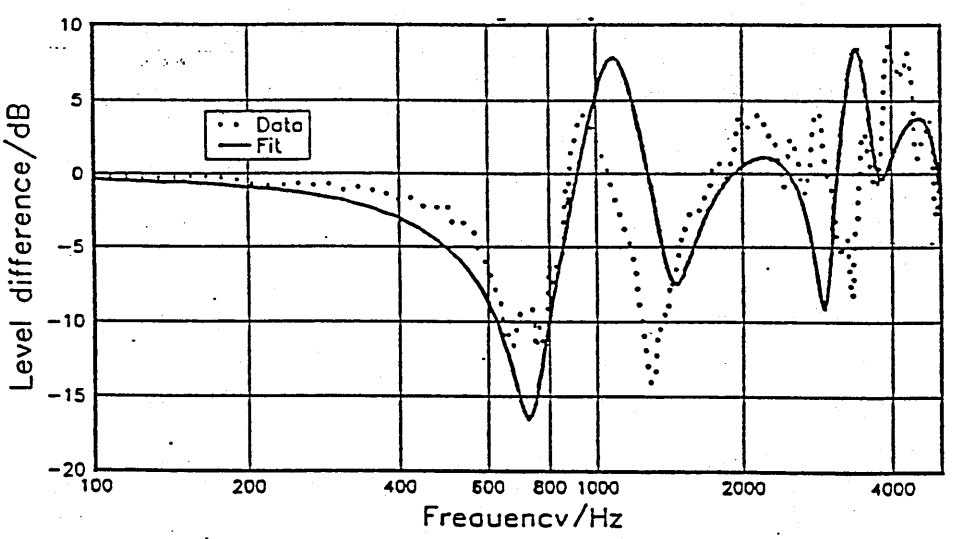


**Figure F.12** Site 4 geometry 3 (B), RMS=3.2

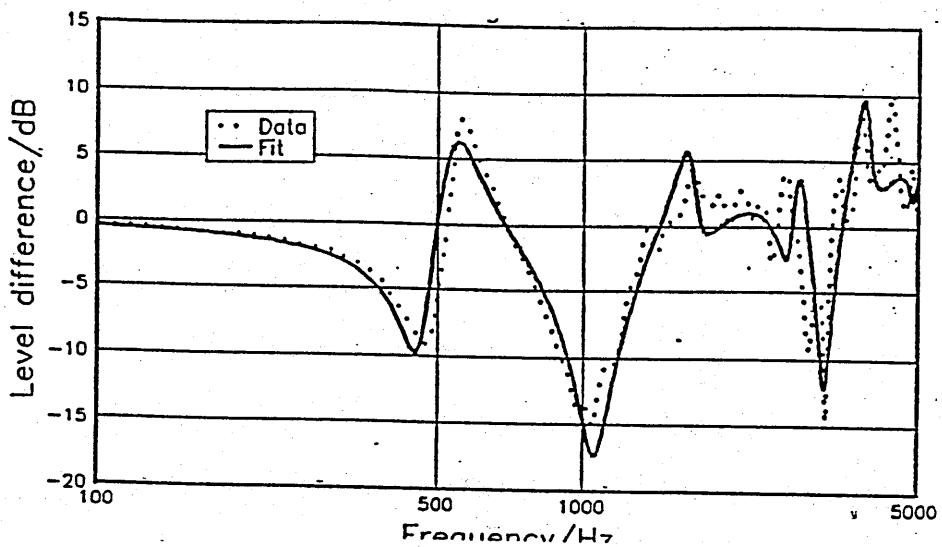


**Figure F.13** Site 5 geometry 2, 10cm deep layer (B), RMS=1.5

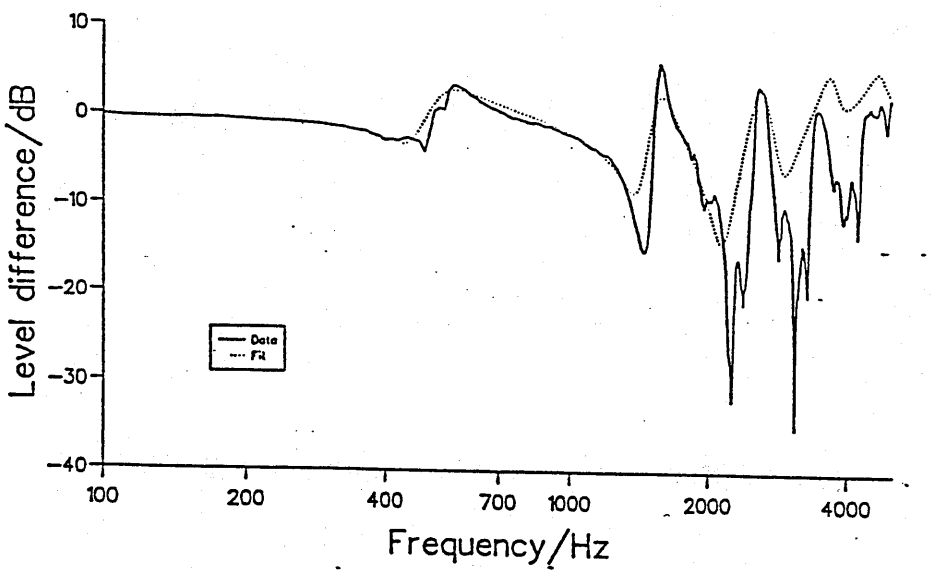


**Figure F.14** Site 6 geometry 1, double layer site (C/B), RMS=2.5

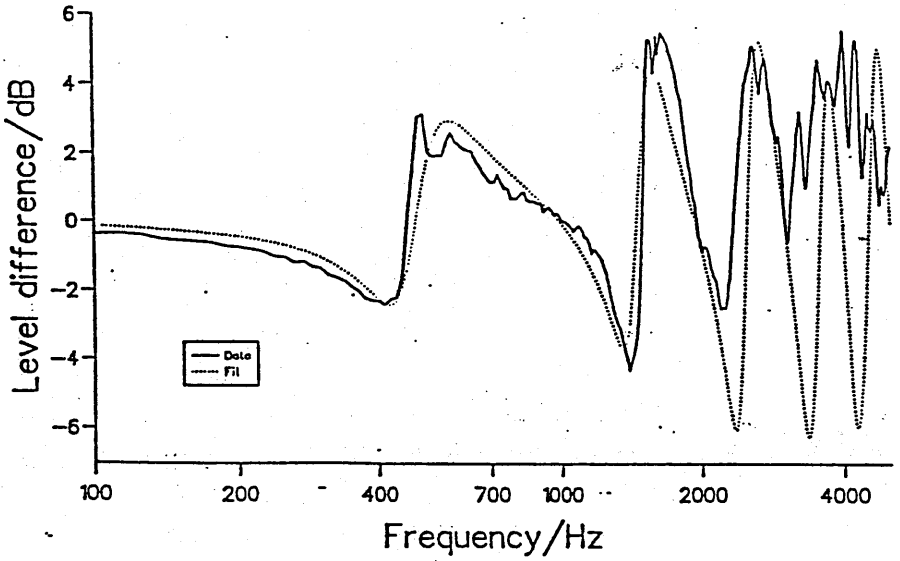


**Figure F.15** Site 6 geometry 2, double layer site (C/B), RMS=3.5

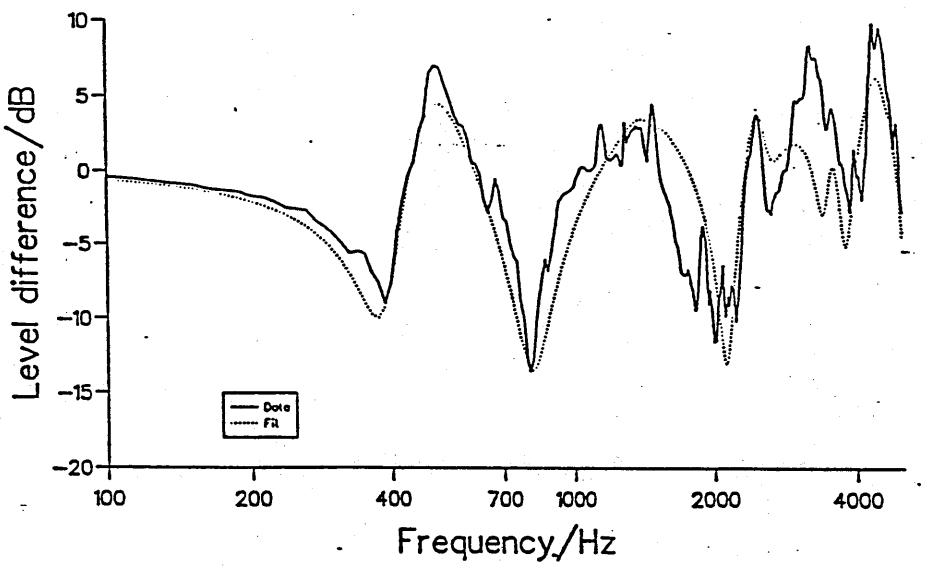


**Figure F.16** Site 6 geometry 3, double layer site (C/B), RMS=2.8

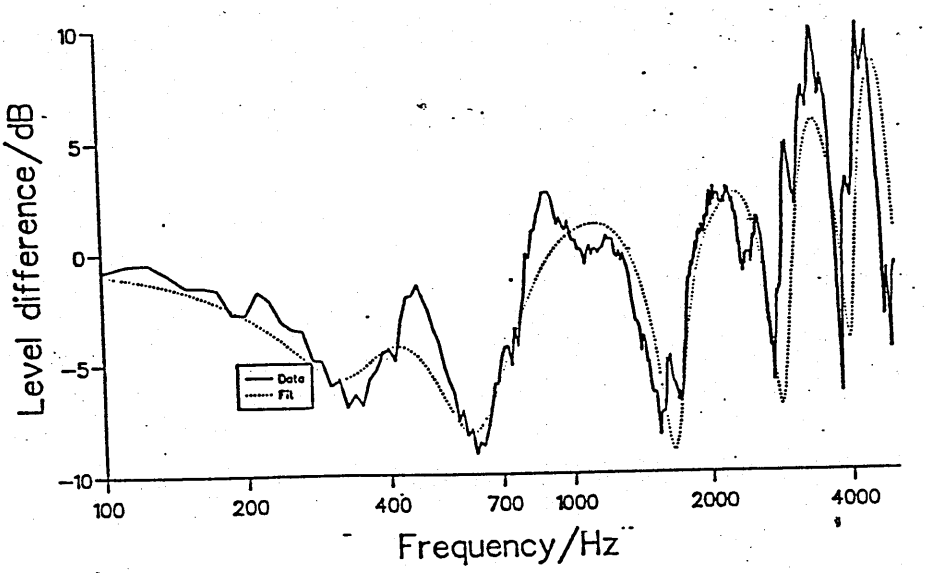


**Figure F.17** Site 7 geometry 1, double layer site (B/D), RMS=3.2

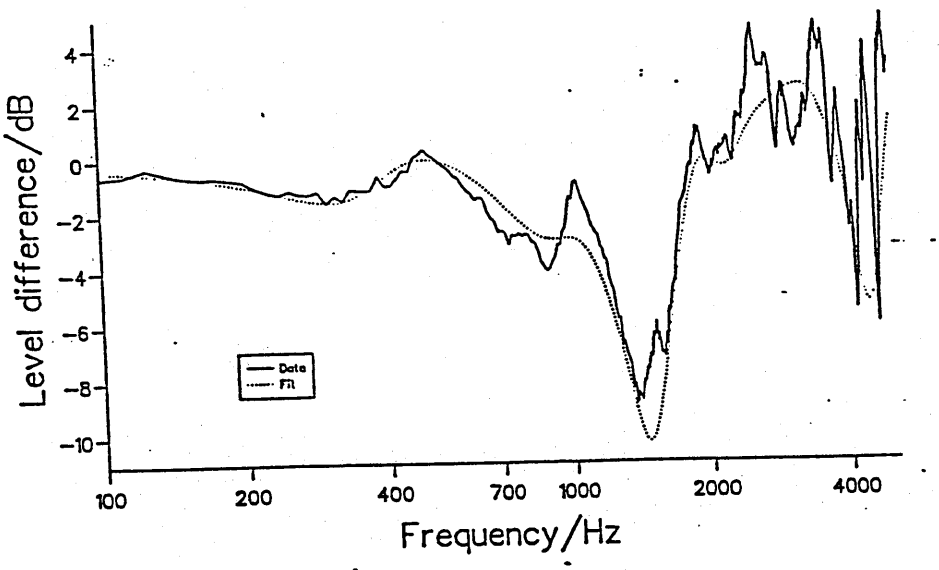


**Figure F.18** Site 7 geometry 2, double layer site (B/D), RMS=2.7

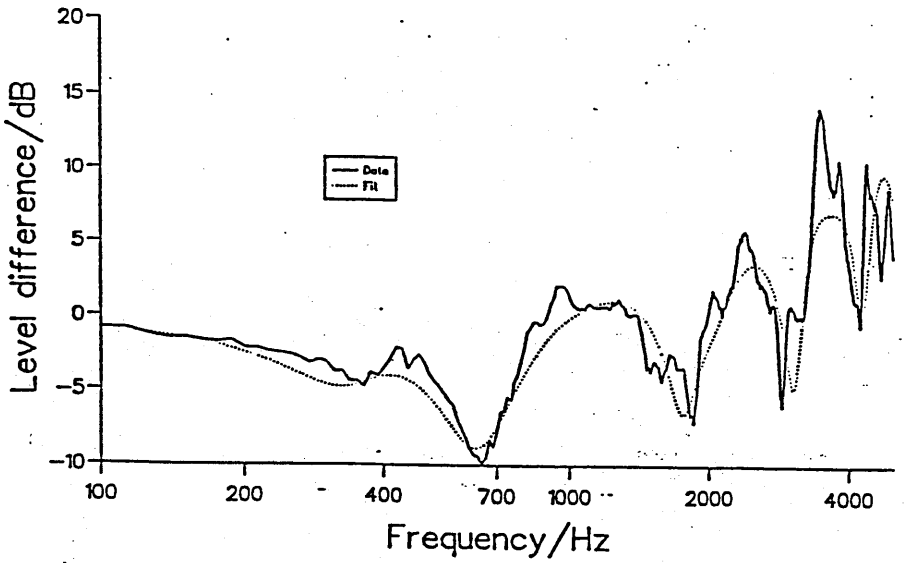


**Figure F.19** Site 7 geometry 3, double layer site (B/D), RMS=2.0

## F.2 Phenomenological model fitted curves

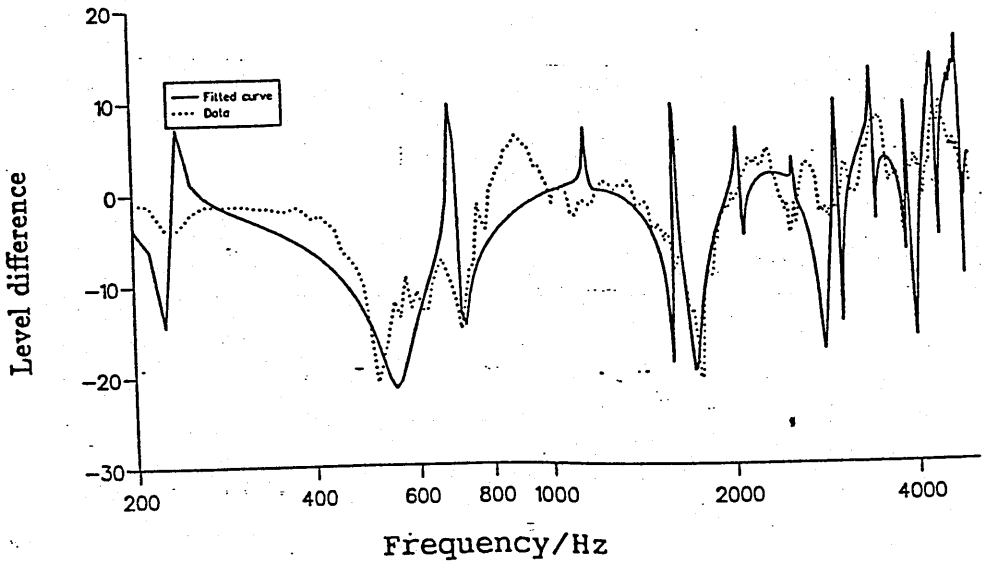


**Figure F.20** Site 1 geometry 1 (A), RMS=4.5

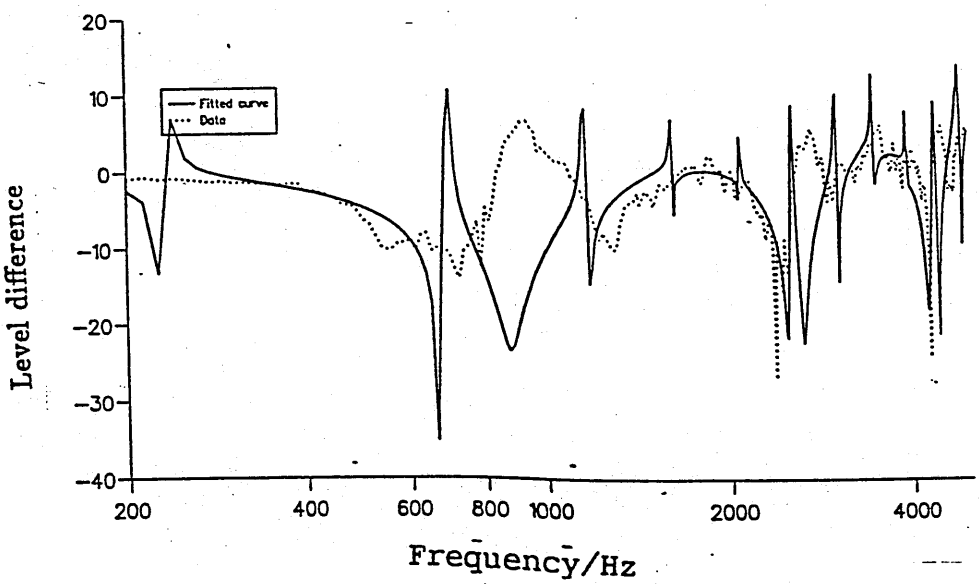


**Figure F.21** Site 1 geometry 2 (A), RMS=4.8

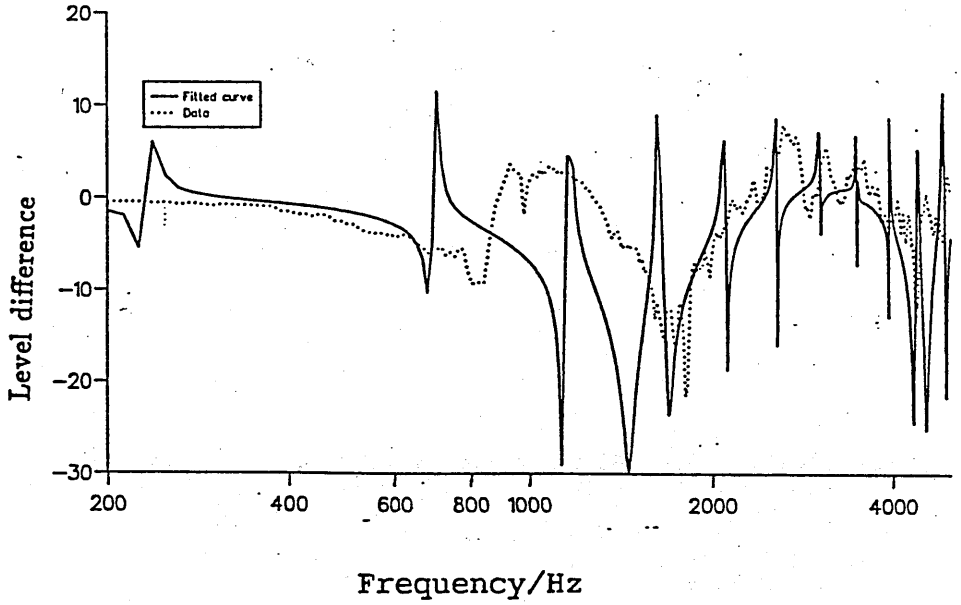


**Figure F.22** Site 1 geometry 3 (A), RMS=5.1

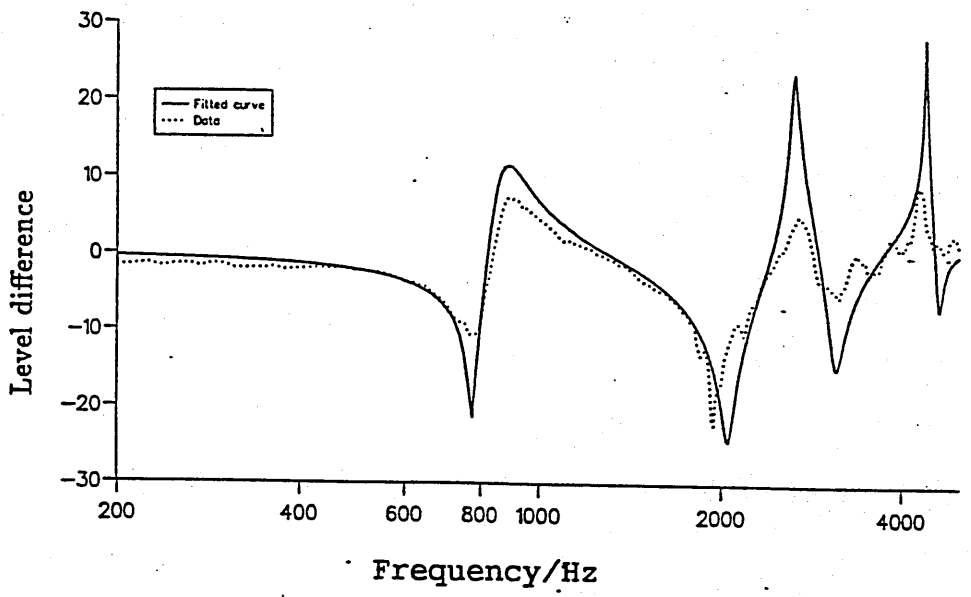


**Figure F.23** Site 2 geometry 1 (C), RMS=2.1

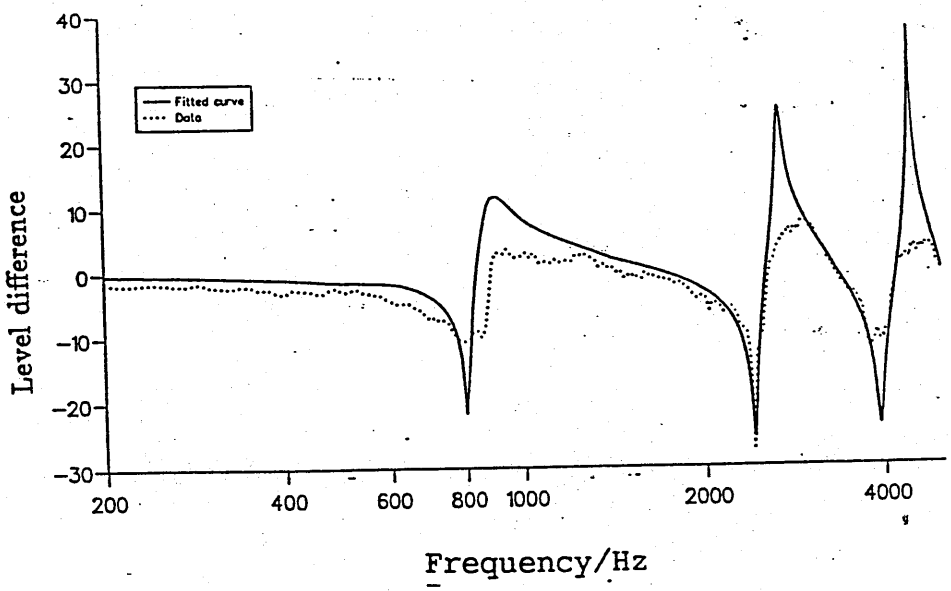


**Figure F.24** Site 2 geometry 2 (C), RMS=1.5

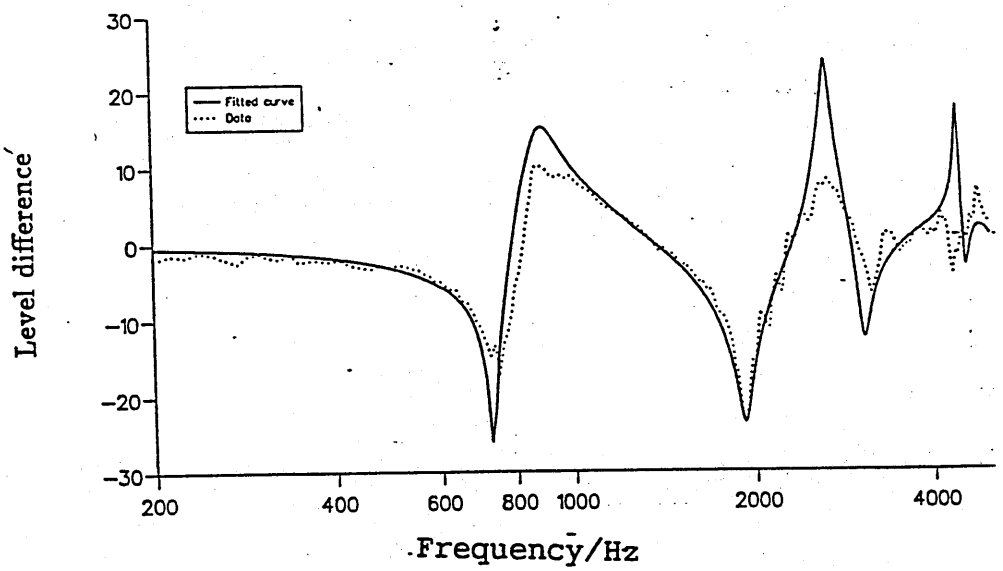


**Figure F.25** Site 2 geometry 3 (C), RMS=1.8

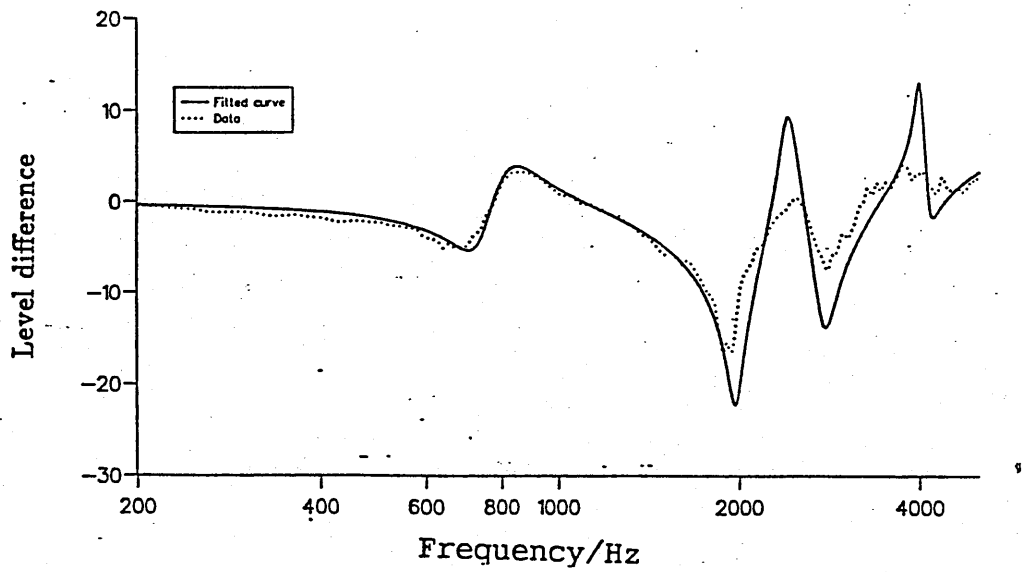


Figure F.26 Site 3 geometry 1 (D), RMS=1.9

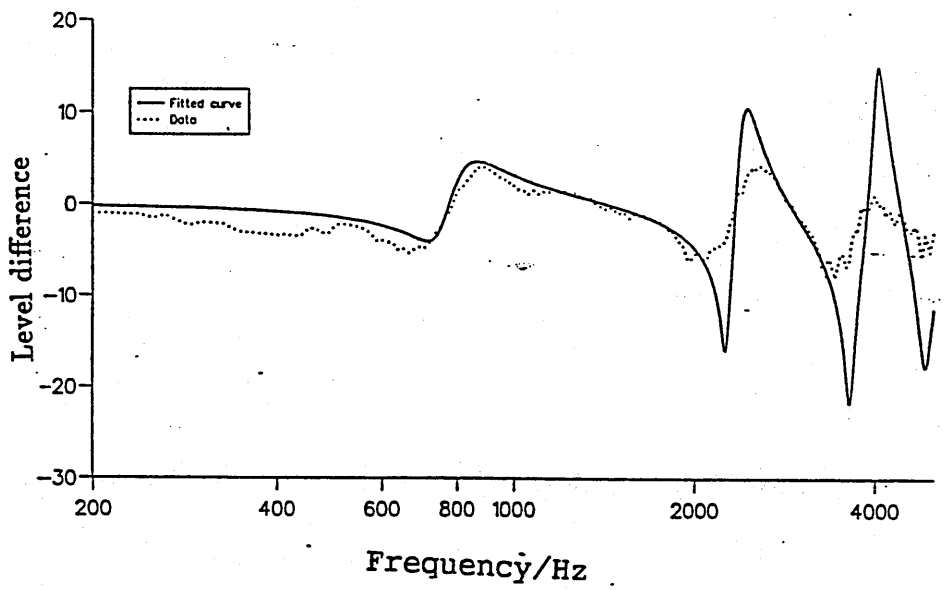


Figure F.27 Site 3 geometry 2 (D), RMS=1.9

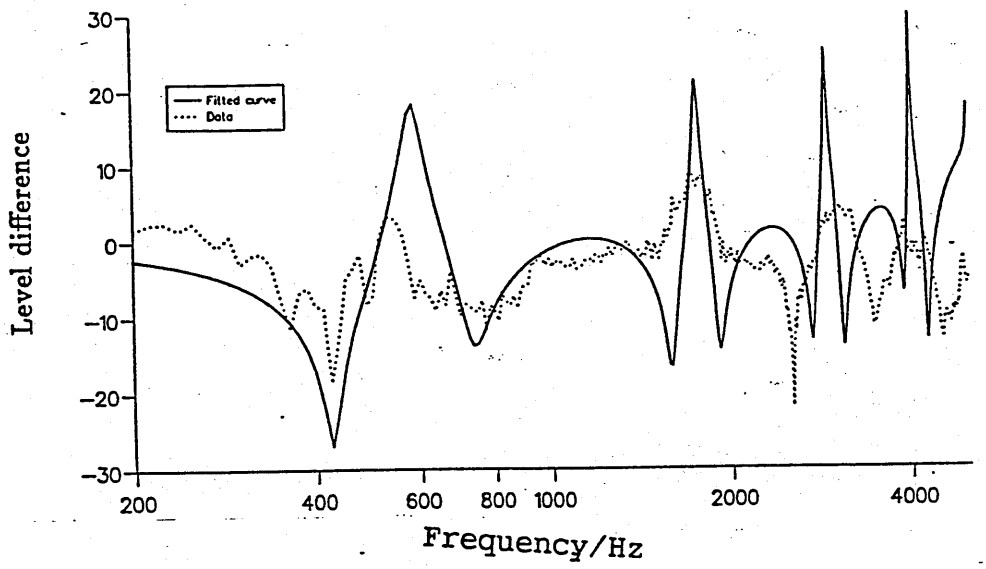


Figure F.28 Site 3 geometry 3 (D), RMS=1.8

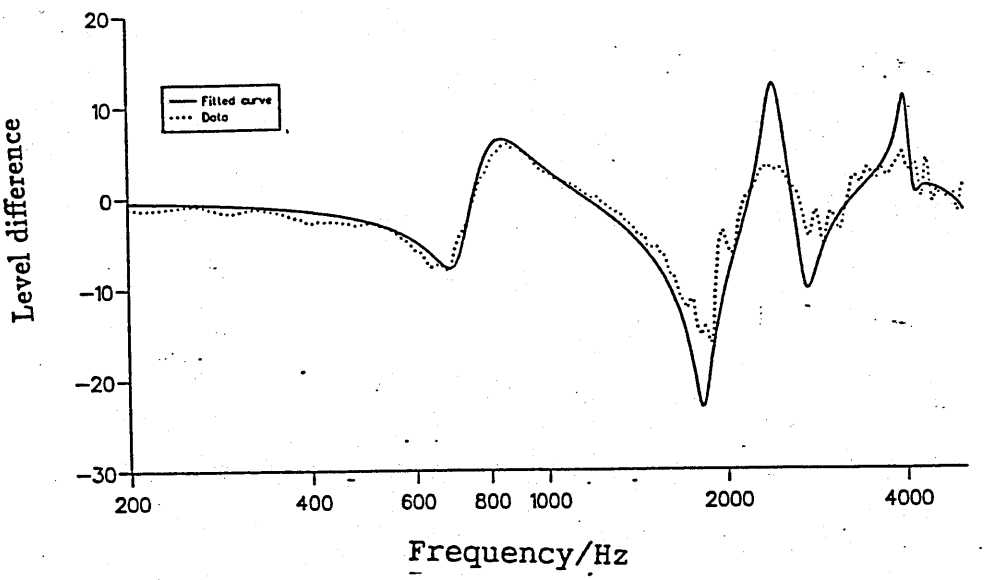


Figure F.29 Site 4 geometry 1 (B), RMS=3.6

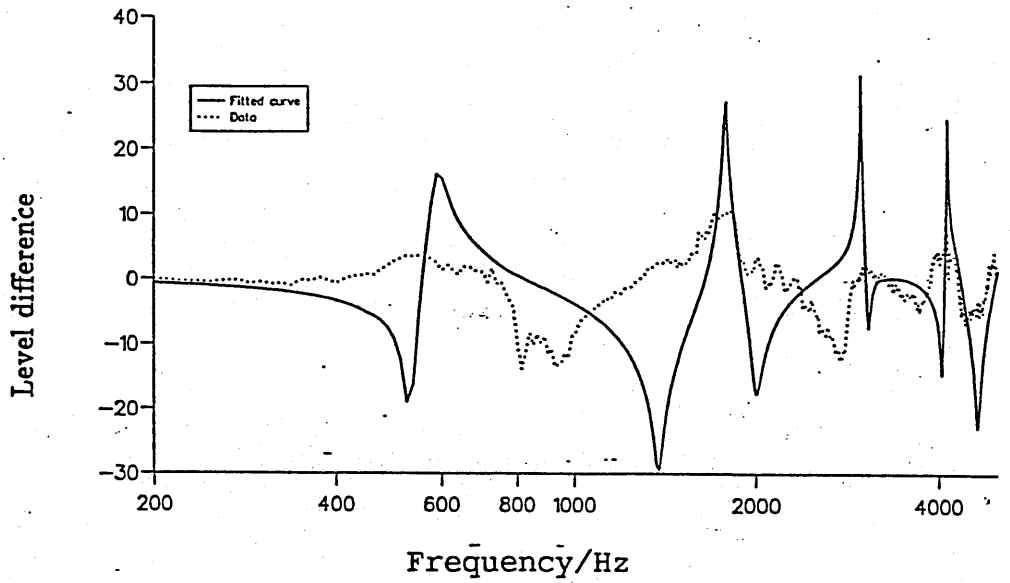


**Figure F.30** Site 4 geometry 2 (B), RMS=5.3

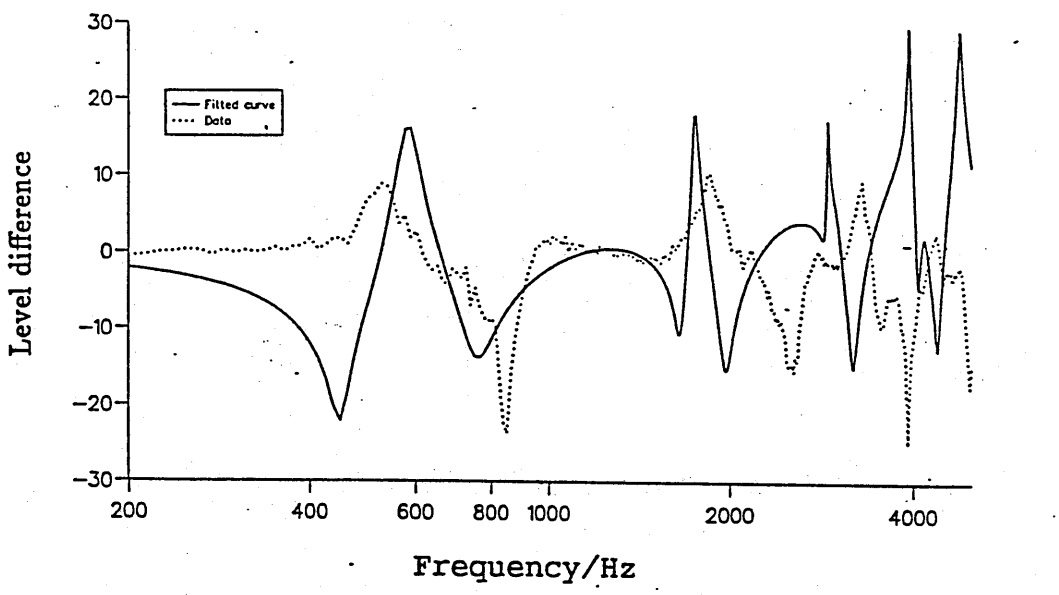


**Figure F.31** Site 4 geometry 3 (B), RMS=5.2

# Appendix G

# Absorption coefficient data fitted to derive microstructural model parameters

Below are examples of fitted level difference curves used to deduce the microstructural model parameters given in chapter 8. Examples are given for the four different materials and for the double layers both with single and mixed materials.

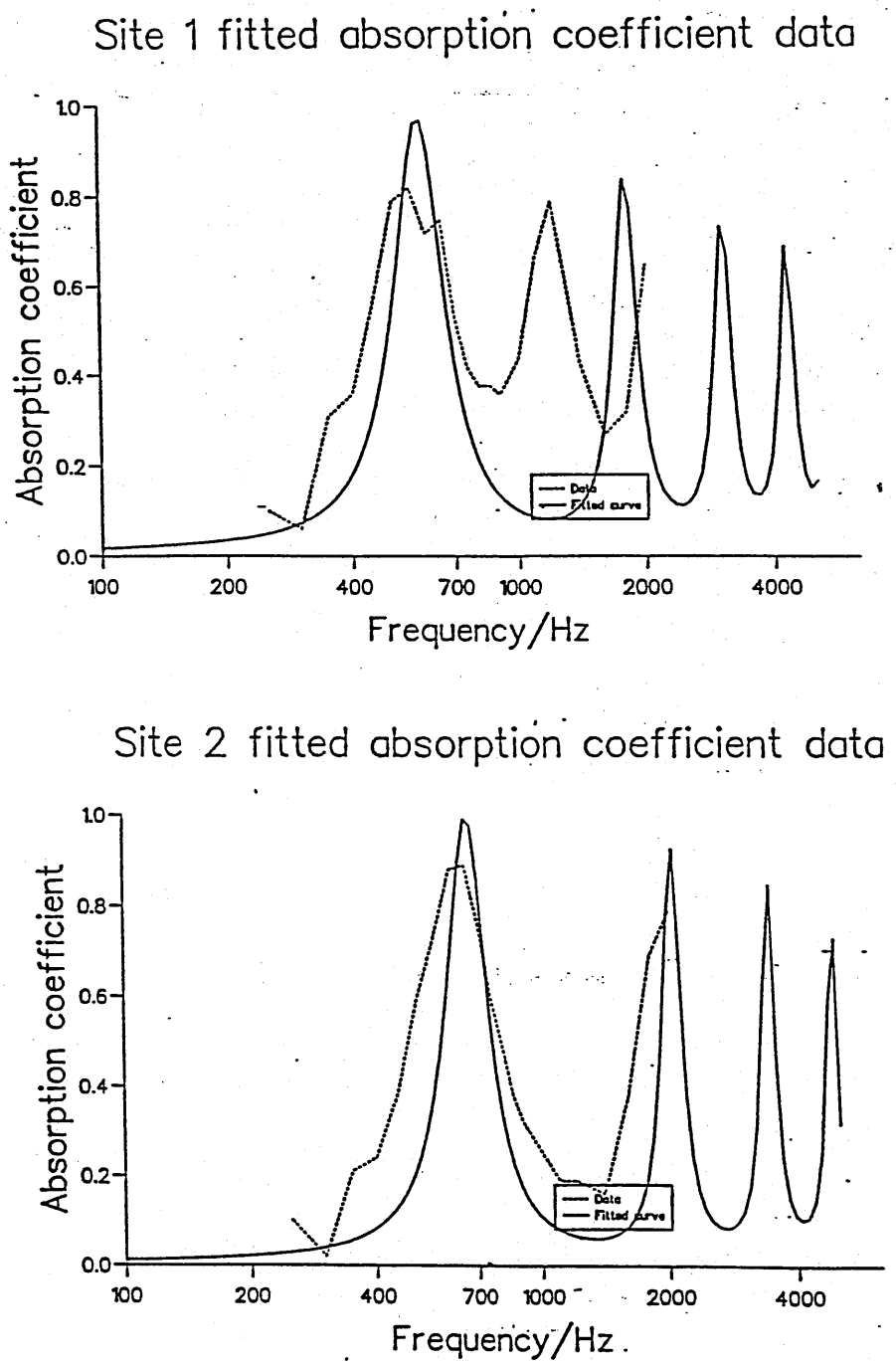


**Figure G.1** Fitted absorption coefficient curves for sites 1 and 2

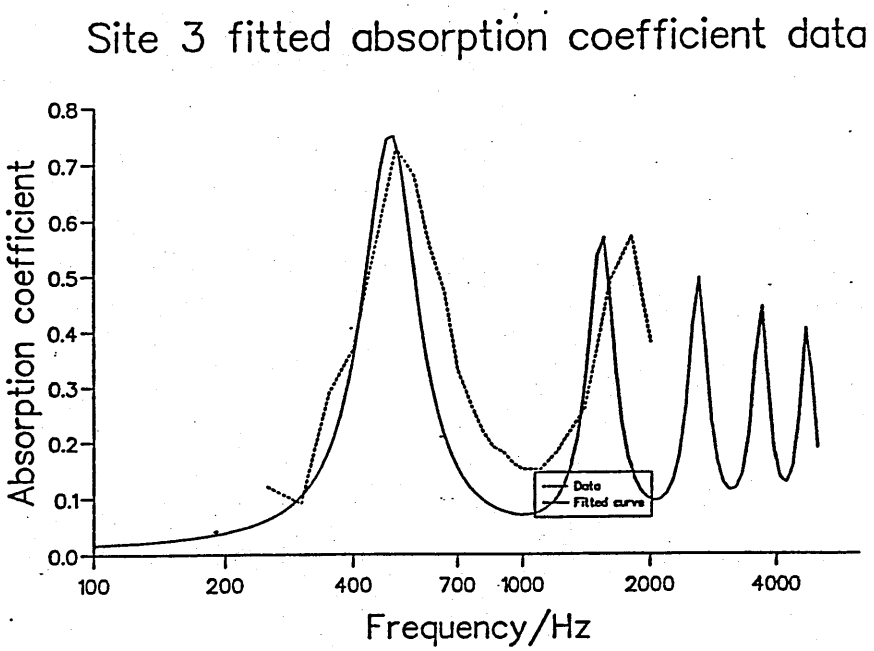


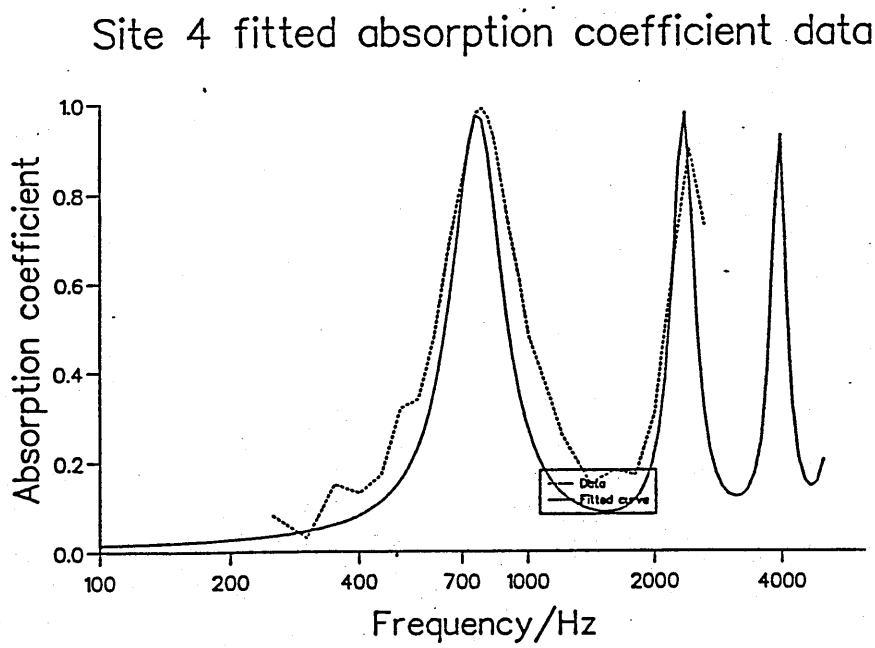


**Figure G.2** Fitted absorption coefficient curves for sites 3 and 4

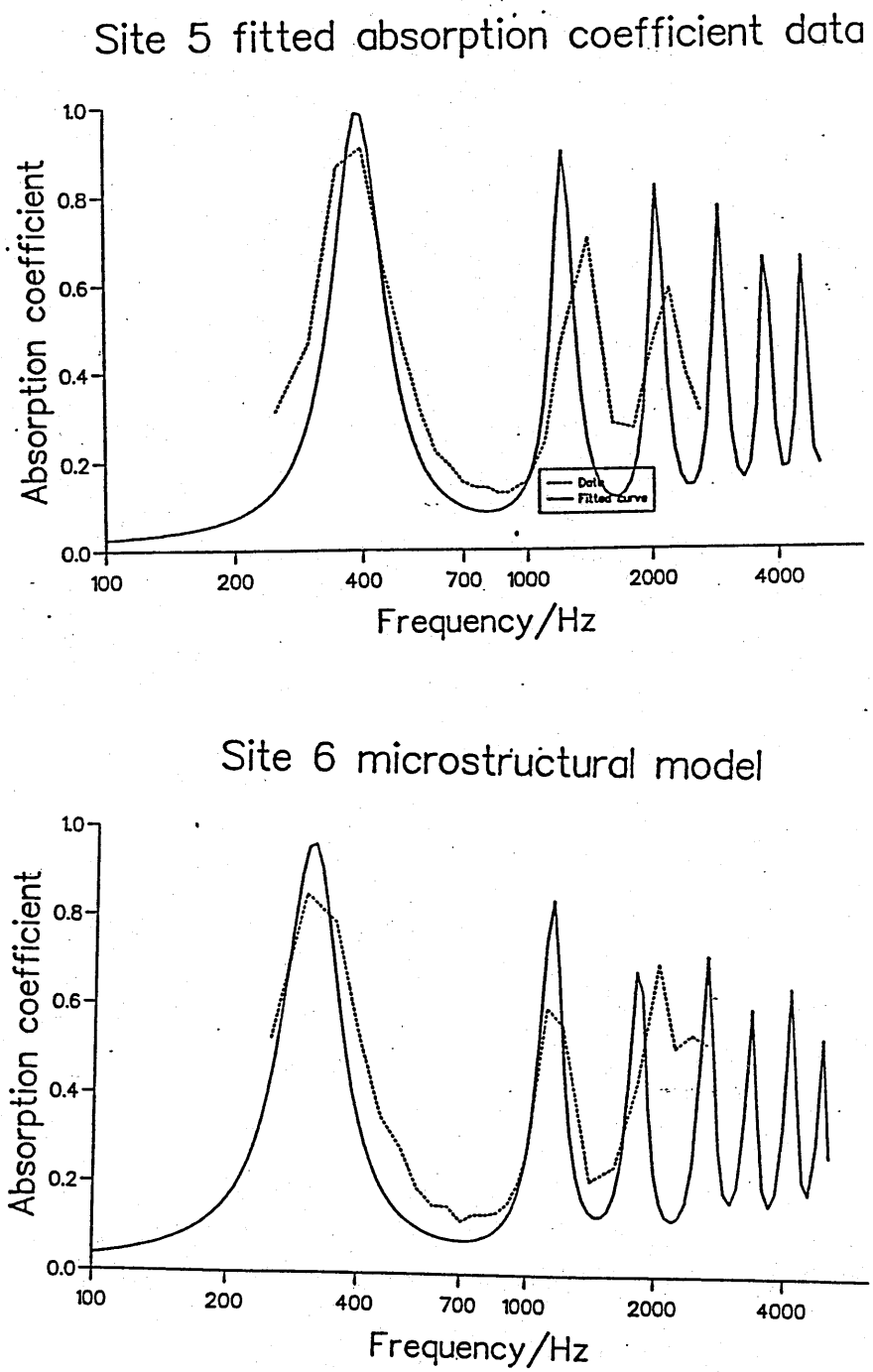


**Figure G.3** Fitted absorption coefficient curves for sites 5 and 6

# Appendix H

# Fitted level difference curves using vehicular source

The level difference curves given in these section result from fitting data collected using a light vehicle and a heavy good vehicle tractor unit as a noise source, as detailed in chapter 8. Examples curves are given for site 1,2,3,4,5, and 6,for the car and sites 1 to 4 for the H.G.V.. Although as for the point source three spectra are used see appendix F only single examples are presented here.

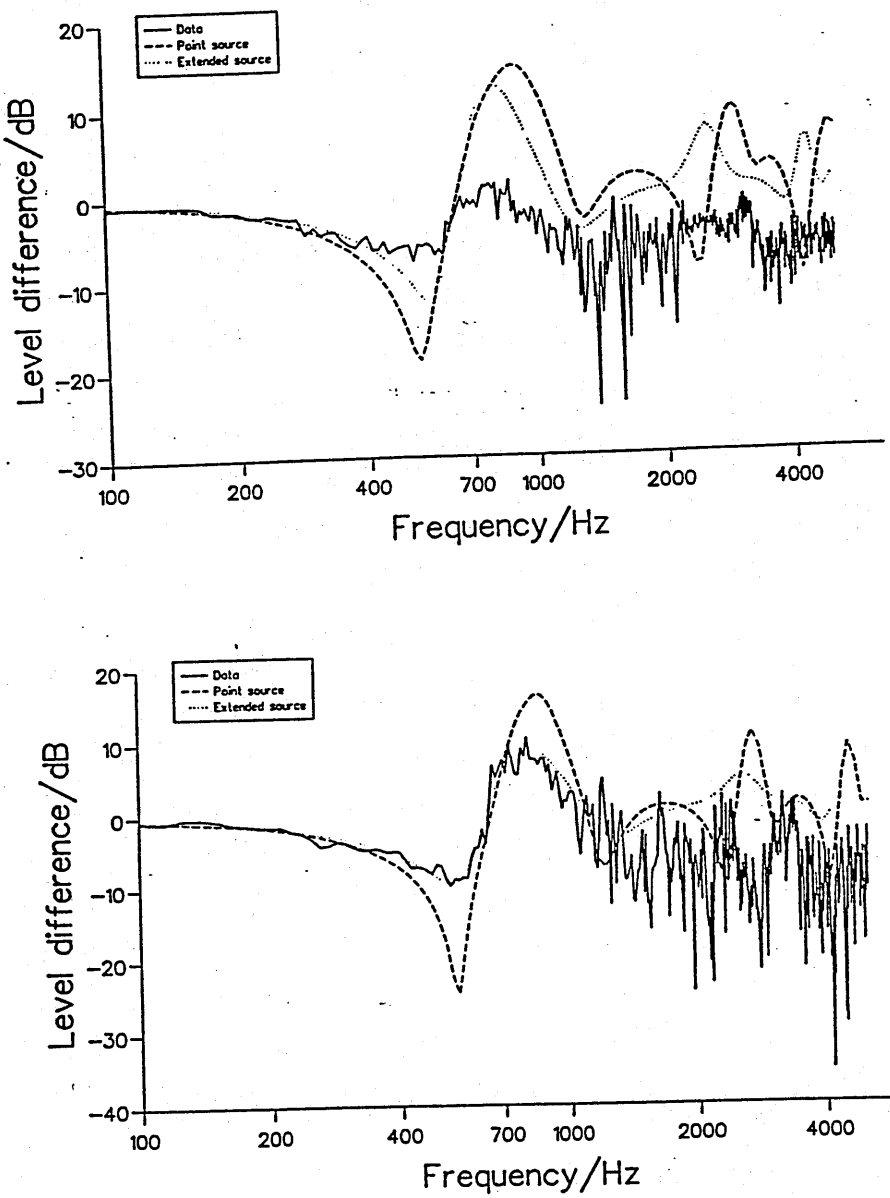


**Figure H.1** Fitted level difference spectra for sites 1 and 2, Car

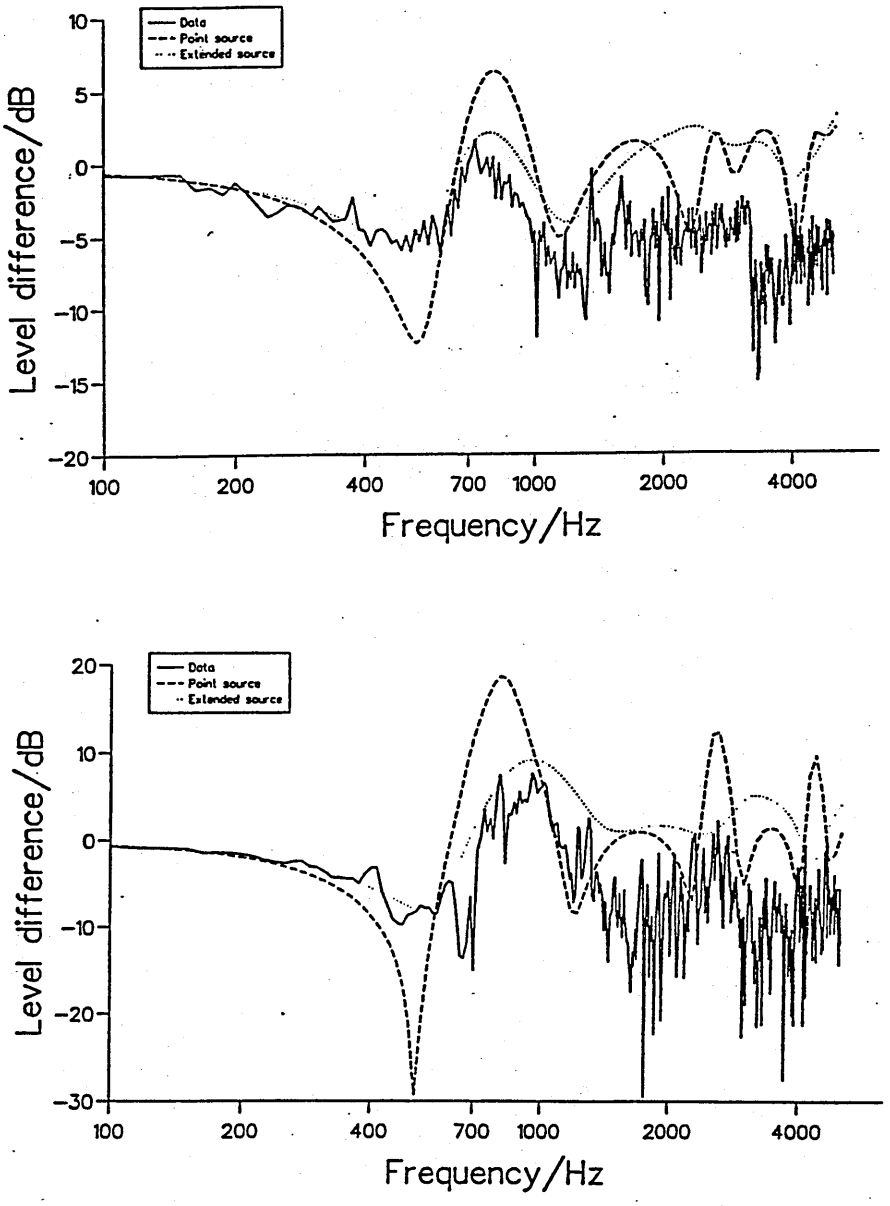


**Figure H.2** Fitted level difference spectra for sites 3 and 4, Car

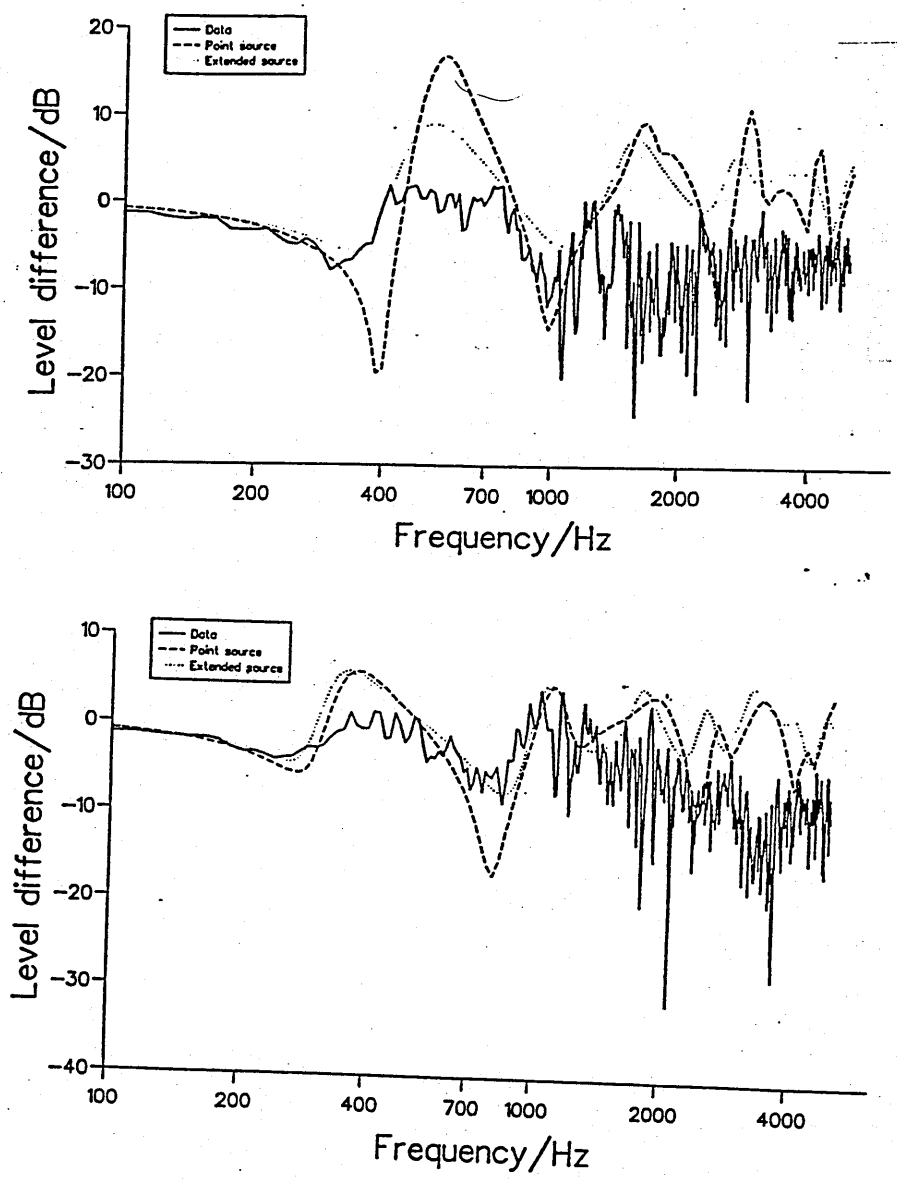


**Figure H.3** Fitted level difference spectra for sites 5 and 6, Car

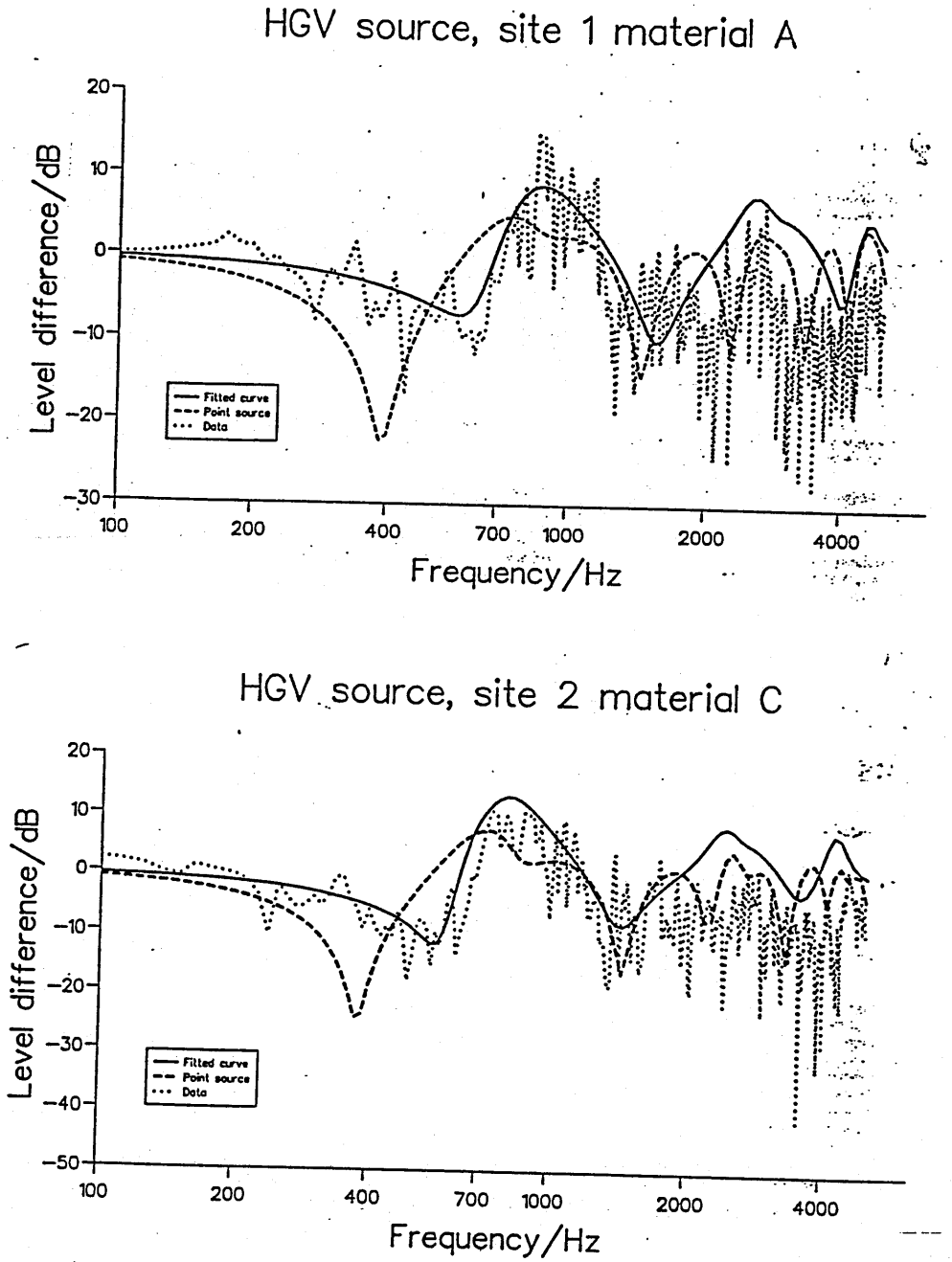


**Figure H.4** Fitted level difference spectra for sites 1 and 2, H.G.V.

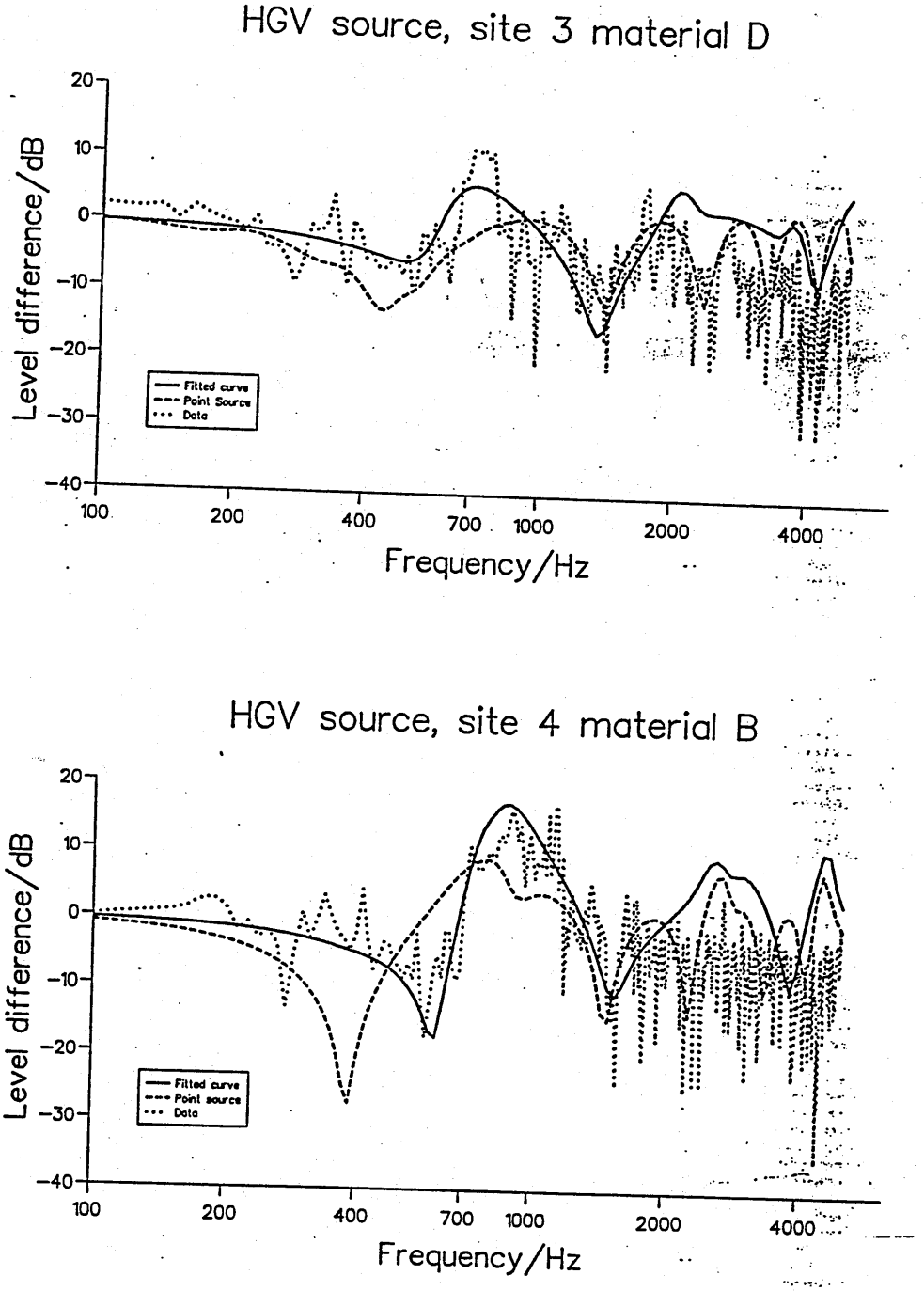


**Figure H.5** Fitted level difference spectra for sites 3 and 4, H.G.V.

# Appendix I

# 'A' weighting curve

Listed here is the 'A' weighting curve applied to the road vehicle spectra during the optimization procedure.

| Frequency | 'A' weighting |
|---|---|
| 100.0 | -19.1 |
| 125.9 | -16.1 |
| 158.7 | -13.4 |
| 200.0 | -10.9 |
| 251.9 | -8.6 |
| 317.4 | -6.6 |
| 400.0 | -4.8 |
| 503.9 | -3.2 |
| 634.9 | -1.9 |
| 800.0 | -0.8 |
| 1007.9 | 0.0 |
| 1269.9 | 0.6 |
| 1600.0 | 1.0 |
| 2015.8 | 1.2 |
| 2539.8 | 1.3 |
| 3200.0 | 1.2 |
| 4013.7 | 1.0 |
| 5079.6 | 0.5 |
| 6400.0 | -0.1 |
| 8063.4 | -1.1 |
| 10159.3 | -2.5 |

# Appendix J

# Optimization curves

This appendix shows plots of linear and 'A' weighted noise reduction used to calculate the optimum microstructural parameters for the road surface. Plots are shown for single and double rigidly backed layers and for four vehicle spectra also given in this chapter. Example spectra are shown. A summary of the optimum parameters evaluated from these curves is given in tables 8.16 and 8.17 of chapter 8.

## J.1 Vehicle spectra used in optimization procedure

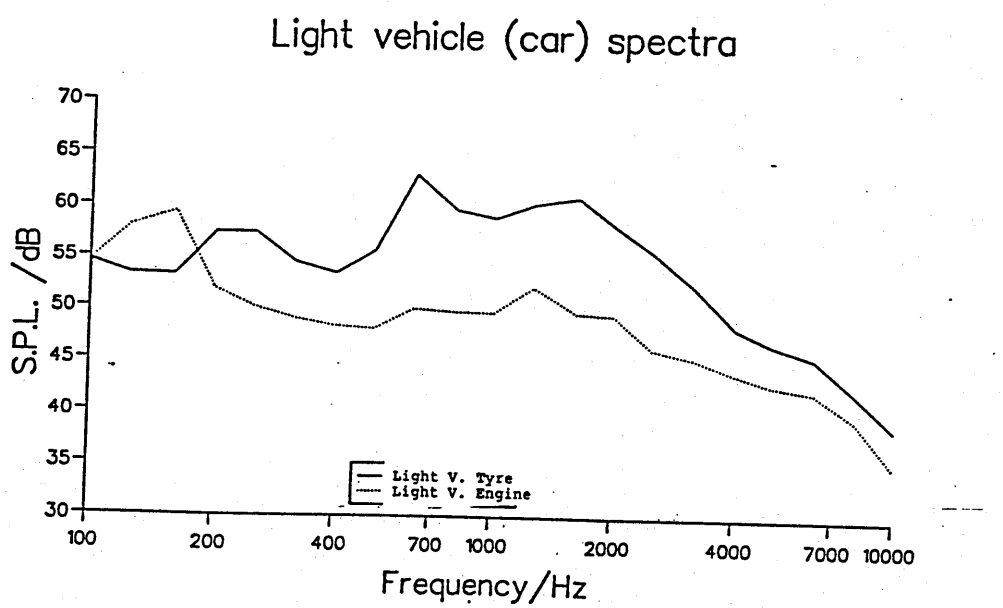


Figure J.1 Light vehicle coasting at 70 km/hr and stationary with 3000 rpm engine speed

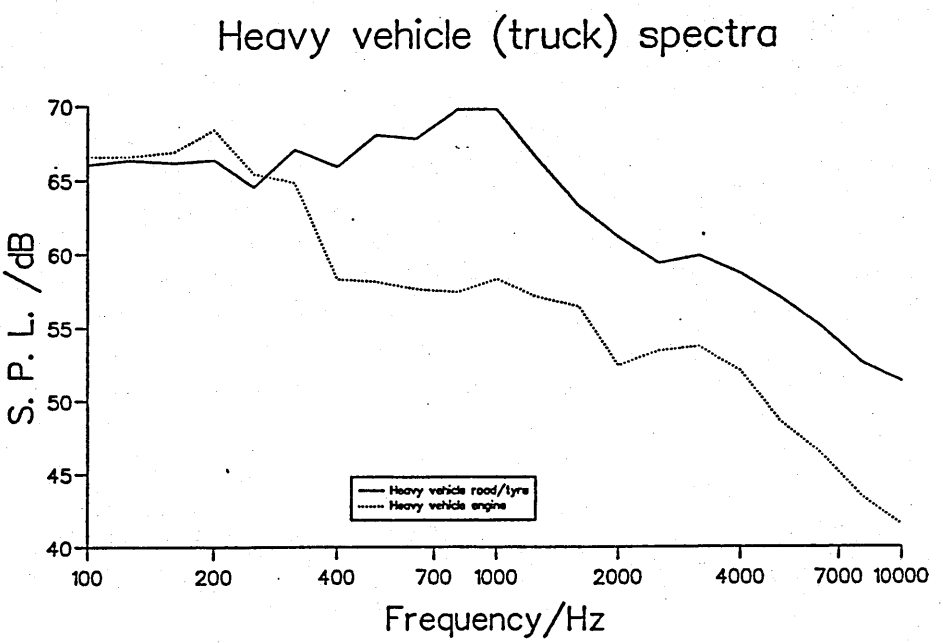


**Figure J.2** Heavy vehicle coasting at 50 km/hr and stationary with 1500 rpm engine speed

## J.2 Optimization curves for single rigid backed layer

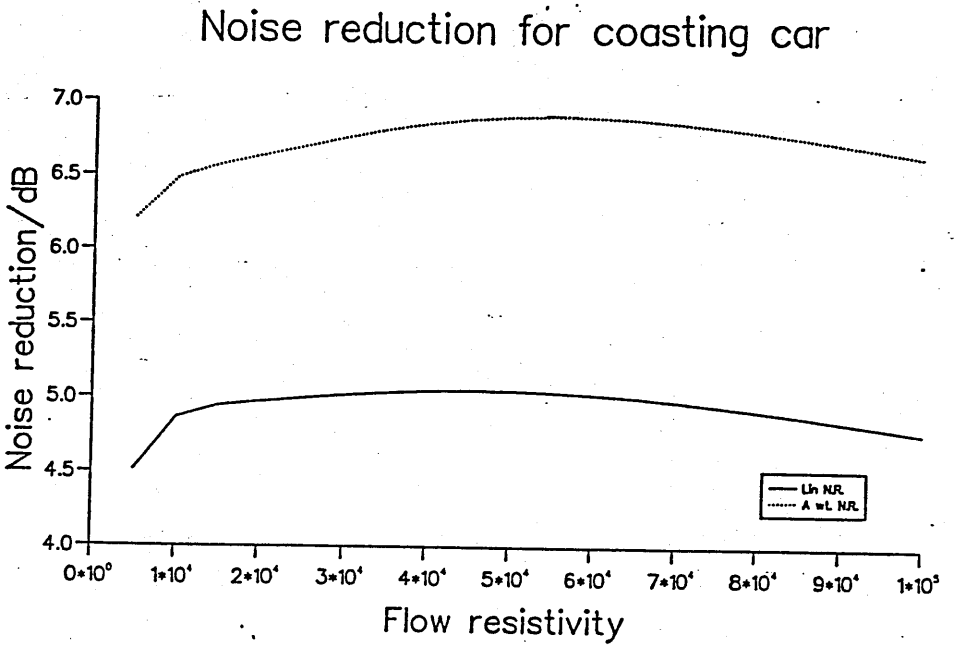


**Figure J.3** Light vehicle coasting optimization for flow resistivity

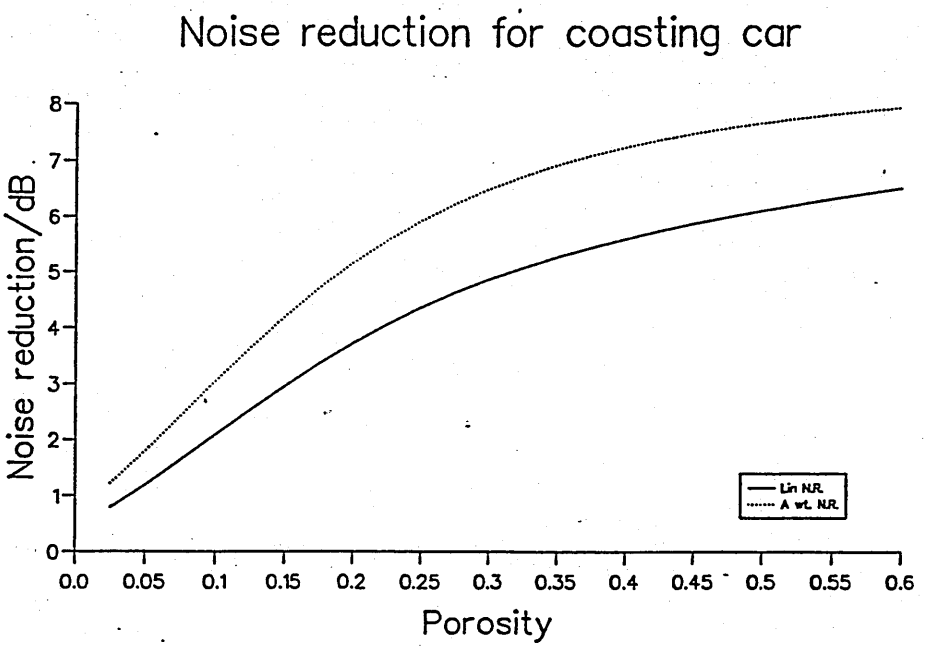


**Figure J.4** Light vehicle coasting optimization for porosity

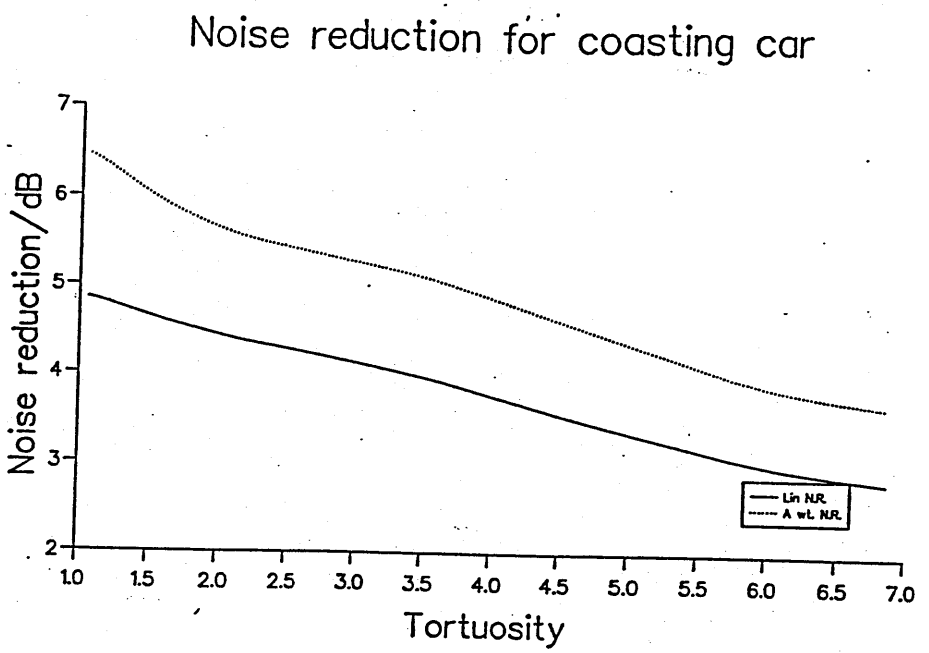


**Figure J.5** Light vehicle coasting optimization for tortuosity

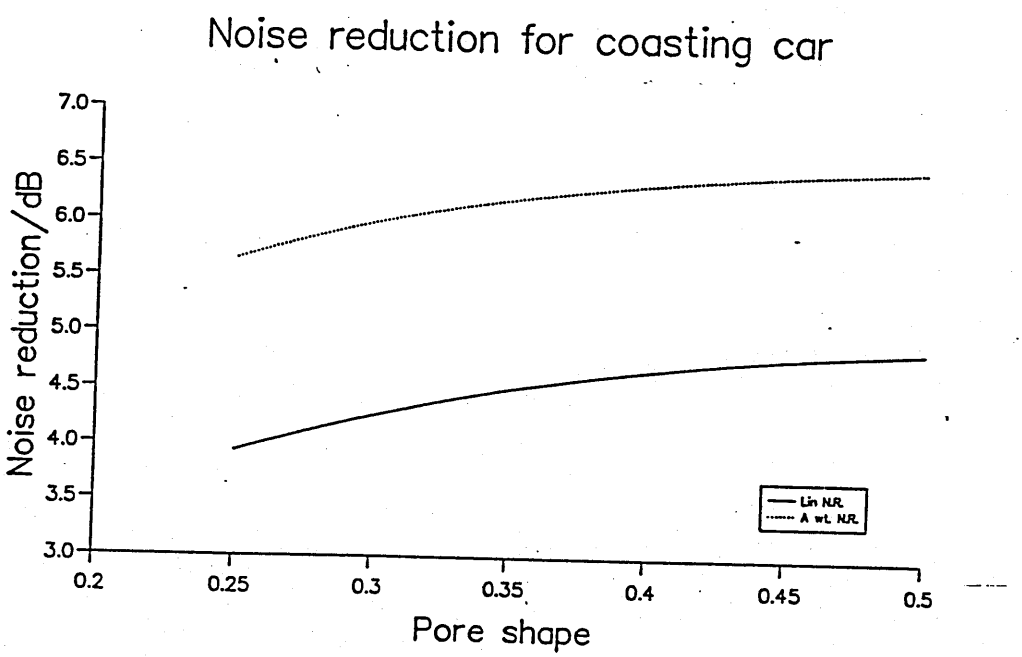


**Figure J.6** Light vehicle coasting optimization for pore shape

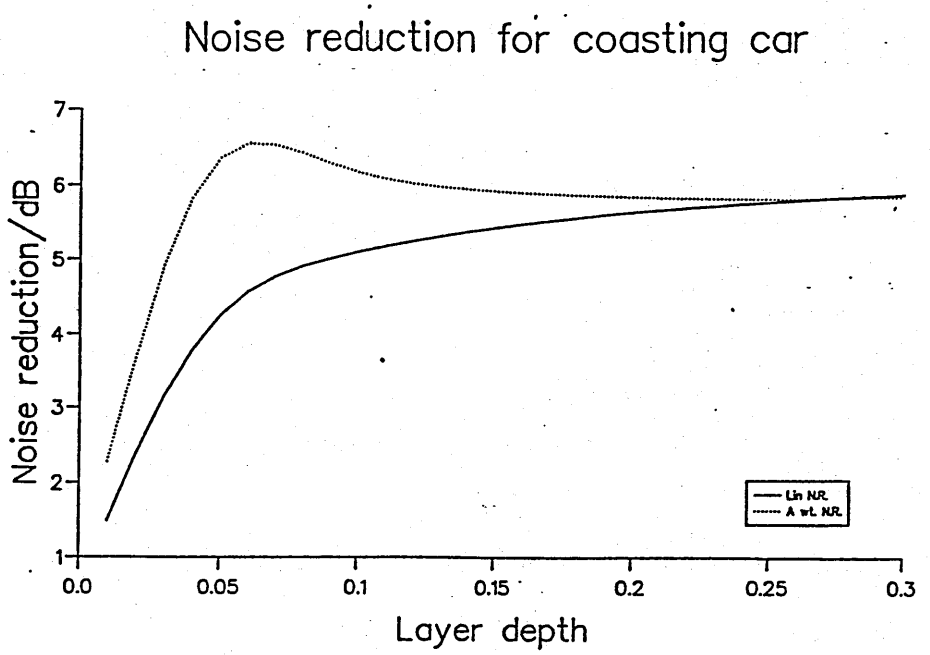


**Figure J.7** Light vehicle coasting optimization for layer depth

## J.3 Optimization curves for double rigid backed layer

### J.3.1 Upper layer parameters

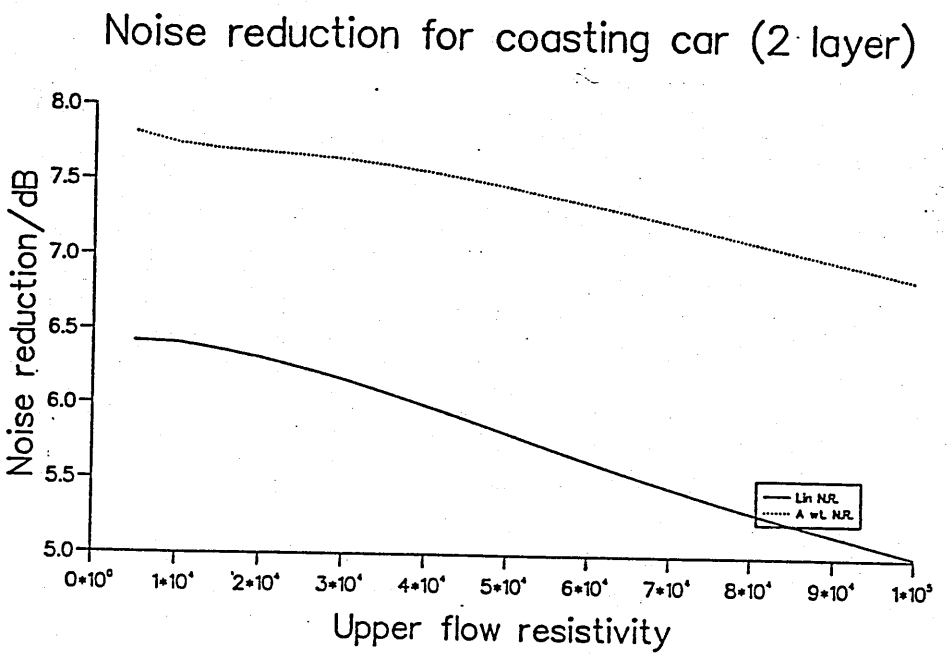


**Figure J.8** Light vehicle coasting optimization for flow resistivity

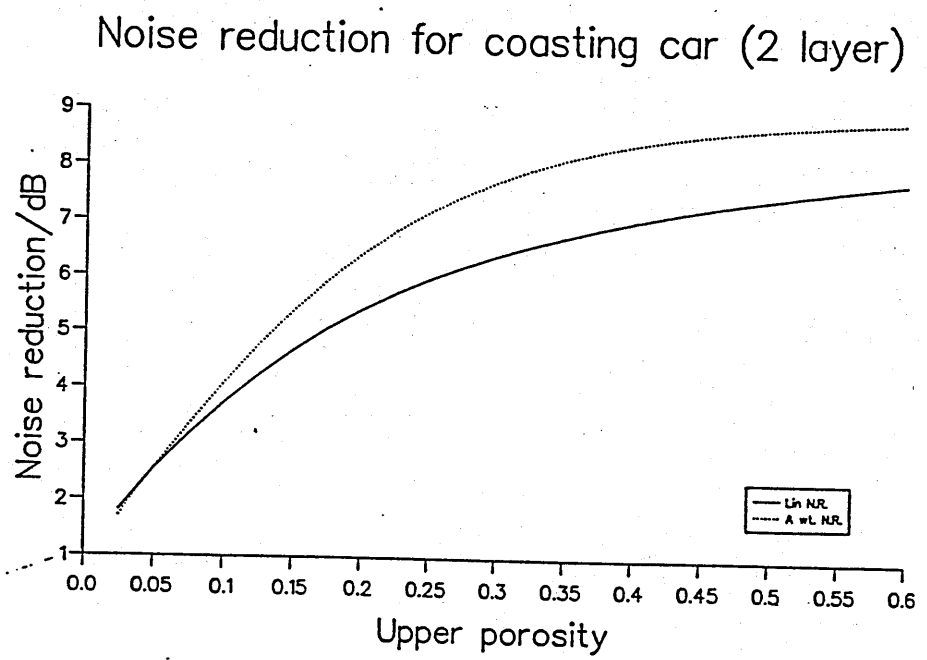


**Figure J.9** Light vehicle coasting optimization for porosity

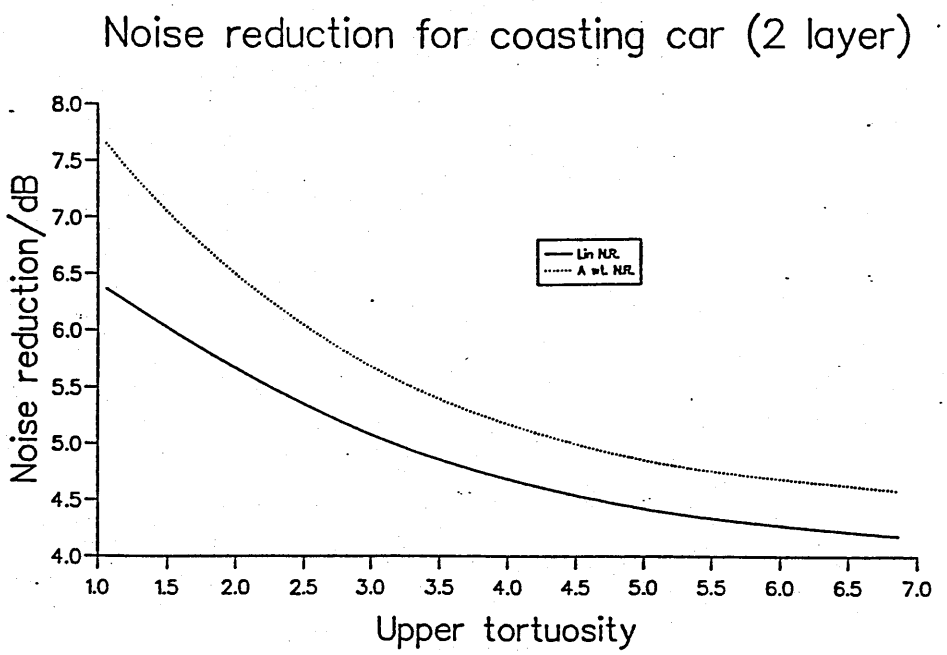


**Figure J.10** Light vehicle coasting optimization for tortuosity

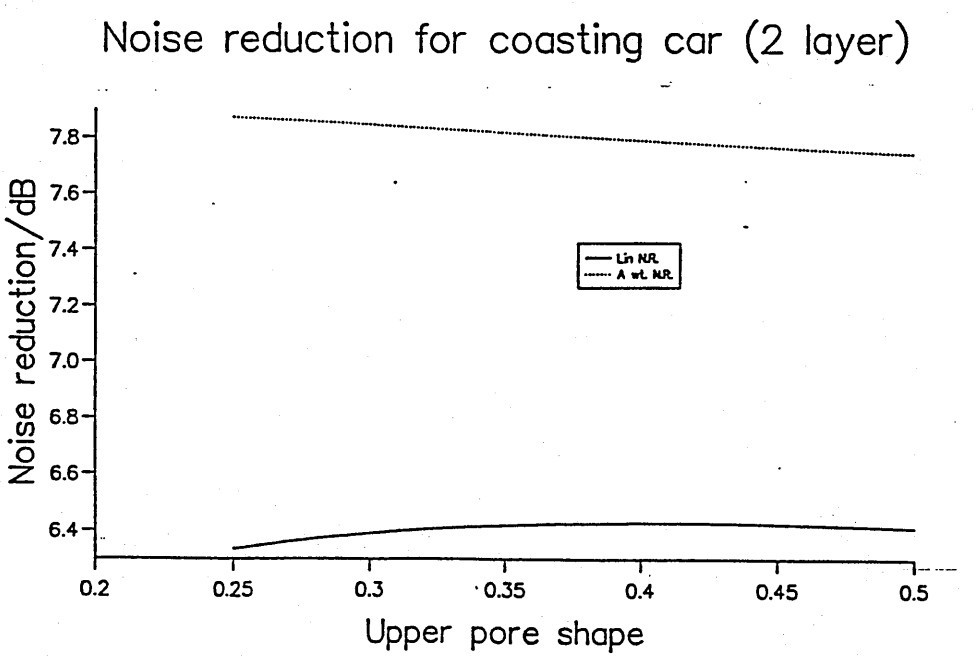


**Figure J.11** Light vehicle coasting optimization for pore shape

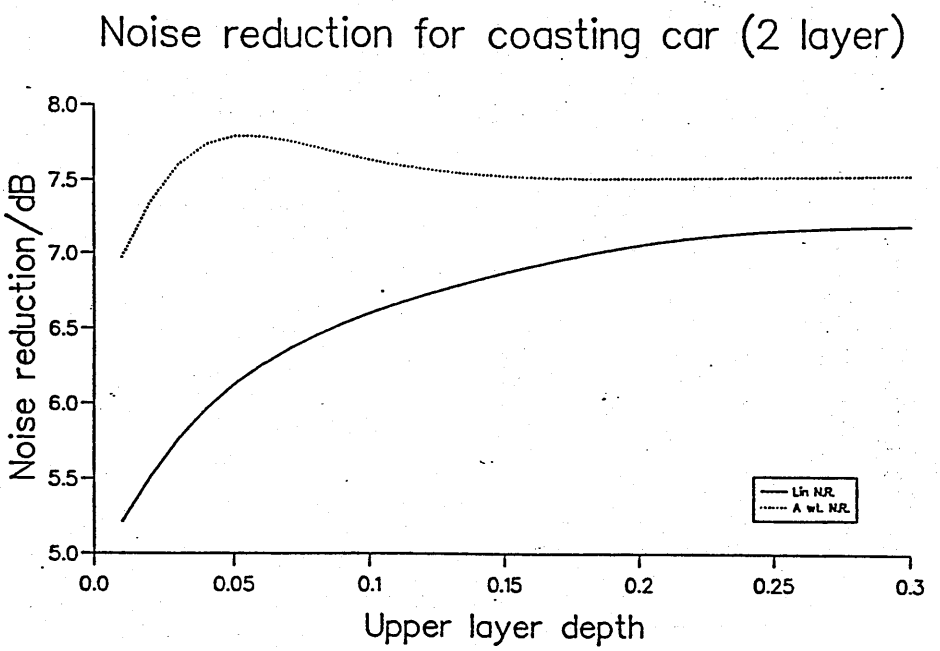


**Figure J.12** Light vehicle coasting optimization for layer depth

### J.3.2 Lower layer parameters

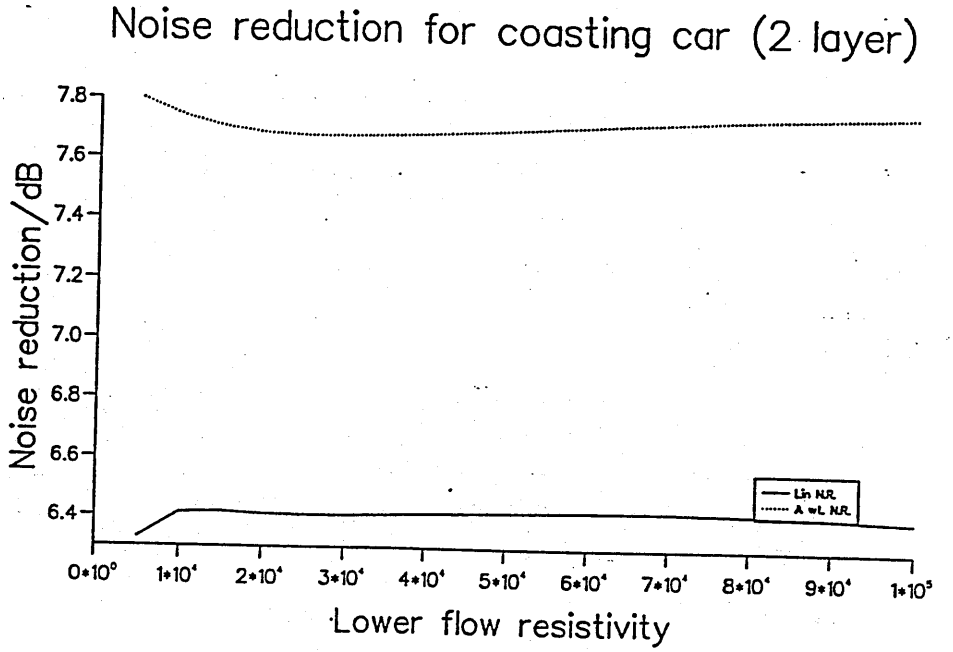


**Figure J.13** Light vehicle coasting optimization for flow resistivity

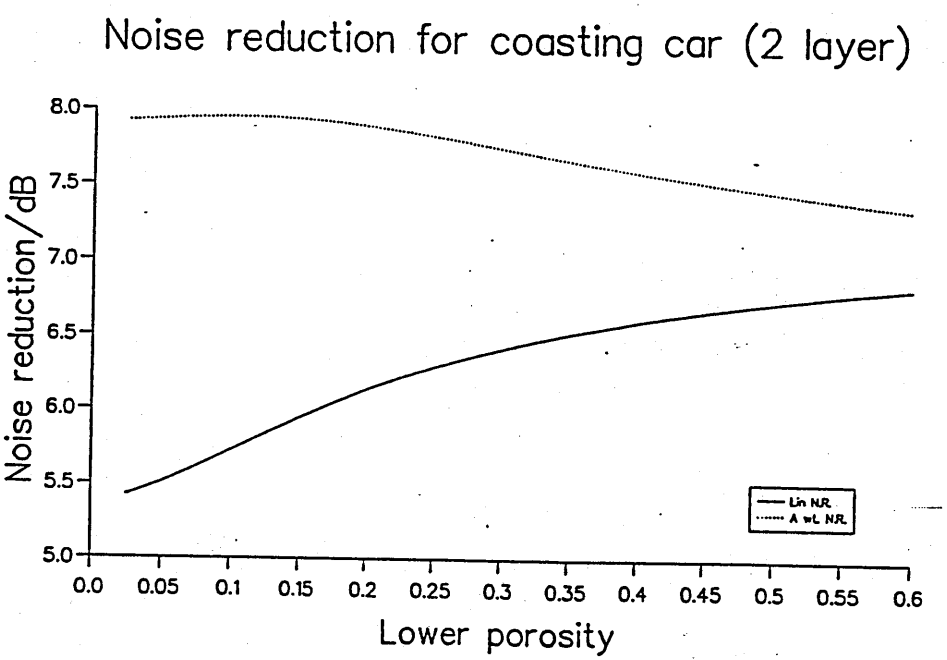


**Figure J.14** Light vehicle coasting optimization for porosity

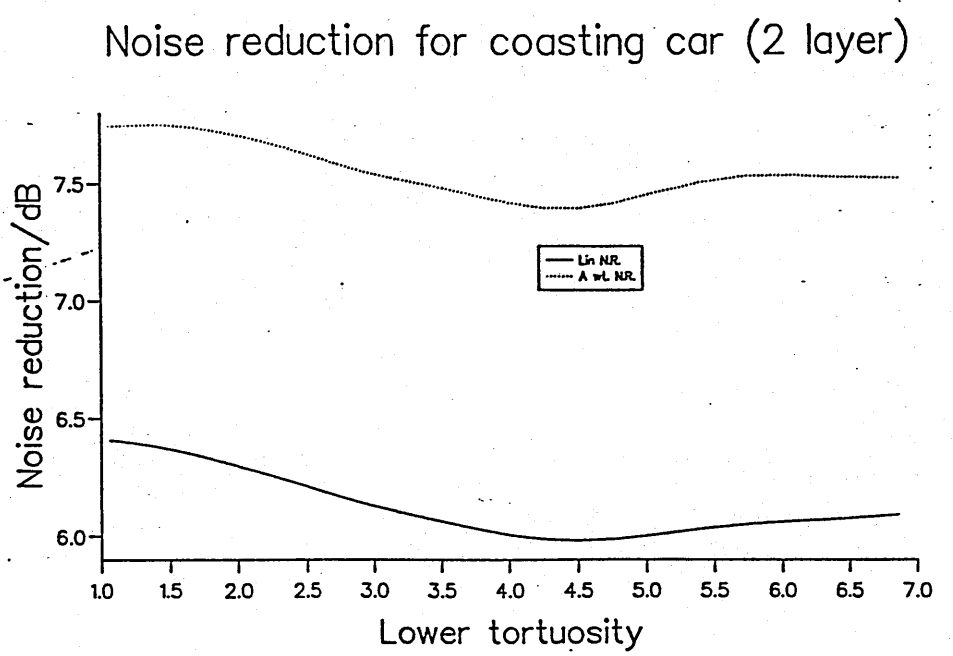


**Figure J.15** Light vehicle coasting optimization for tortuosity

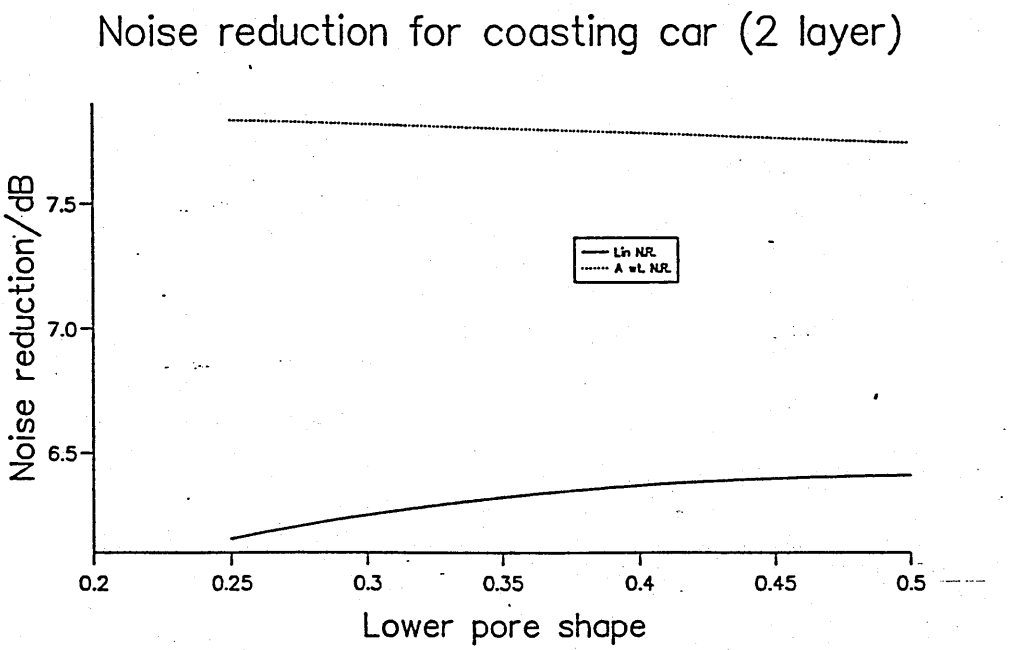


**Figure J.16** Light vehicle coasting optimization for pore shape

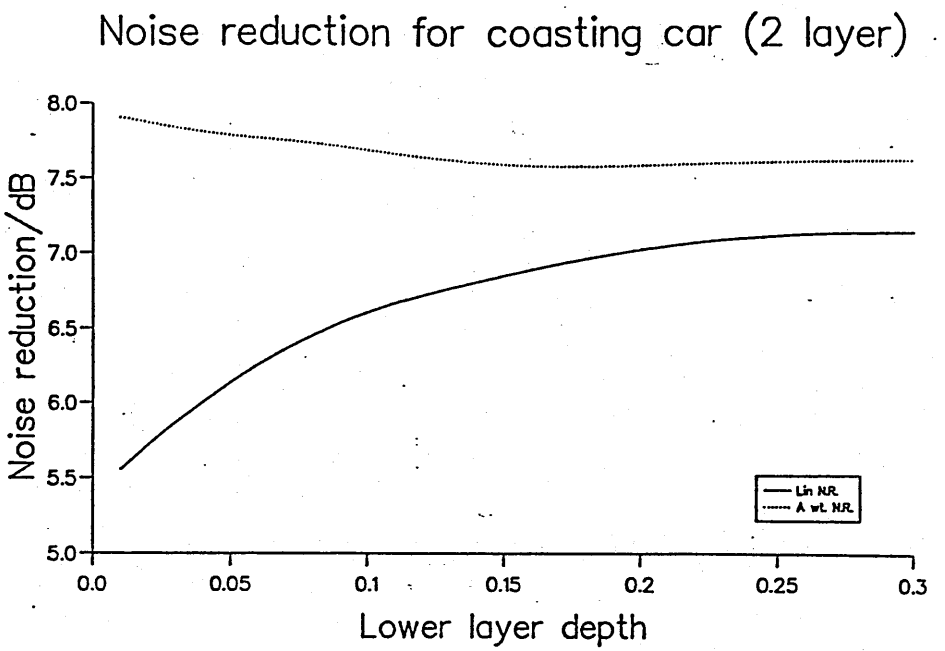


**Figure J.17** Light vehicle coasting optimization for layer depth

# Appendix K

# Programmes

The following appendix contains the ForTran subroutines used in the development of this work. The programmes are written in VAX ForTran which is similar to ForTran 77 any variations are detailed in the VAX ForTran user manual [208]. In general the programmes were run using Dec command language [209]. It should be noted that in general only the driver programmes are included here in order to minimize the length of the thesis. The sections are divided into work in relation to the chapters.

## K.1 Programmes used in conjunction with rigid porous material theory

The first programme used in this section of the work, calculated the complex propagation constant and complex density according to the microstructural, phenomenological and empirical models. These models are used elsewhere and hence are not given in this section. The second programme calculated the effects of different pore shapes and is detailed below.

### K.1.1 Programme to compare pore shape theories

This programme calculates the complex density and compressibility for a rigid porous media with, slit, circular, square and triangular pores. Note the listing does not include the subroutines used to calculate the mathematical functions.

```
DIMENSION FR(200)
COMPLEX CI,CDR,CCR,CDC,CCC,CDS,CCS,CDT,CCT
     1  ,ZS,ZC,ZR,ZT,PS,PC,PR,PT
CHARACTER*64 SLI,CIR,REC
COMMON/PYS/ RHOO,CO,CI,GAMMA,RNU,PI,B,R,AS,BS,D,PRAN
        COMMON/MED/ TORT,POROS
PRINT*,'INPUT NAME OF FILES TO CONTAIN OUTPUT FOR
     1  SLIT,CIRCULAR, AND RECTANGULAR PORES'
READ123,SLI
READ123,CIR
READ123,REC
OPEN(11,FILE=SLI,STATUS='UNKNOWN')
OPEN(12,FILE=CIR,STATUS='UNKNOWN')
OPEN(13,FILE=REC,STATUS='UNKNOWN')
PRINT*,'INPUT HALF WIDTH OF SLIT,RADIUS OF CAPILLARY,
     1  AND HALF SIDES OF RECTANGLE'
READ*,B,R,AS,BS
PRINT*, 'INPUT TORTUOSITY AND POROSITY'
READ*, TORT,POROS
PI=4.*ATAN(1.)
RHOO=1.21
CO=343.
GAMMA=1.402
RNU=1.49E-5
CI=CMPLX(0.0,1.0)
PRAN=0.76
DO 10 IRI=1,143
IF (IRI.EQ.1) THEN
FR(IRI)=100.
ELSE
FR(IRI)=FR(IRI-1)*2.**0.05
ENDIF
OMEG=2.*PI*FR(IRI)
CALL SLIT(OMEG,RLAM1,CDS,CCS,ZS,PS)
CALL CIRC(OMEG,RLAM2,CDC,CCC,ZC,PC)
CALL RECT(OMEG,RLAM3,CDR,CCR,ZR,PR)
WRITE(11,*) RLAM1,REAL(CDS),-AIMAG(CDS),
     1  REAL(CCS),-AIMAG(CCS)
WRITE(12,*) RLAM2,REAL(CDC),-AIMAG(CDC),
     1  REAL(CCC),-AIMAG(CCC)
WRITE(13,*) RLAM3,REAL(CDR),-AIMAG(CDR),
     1  REAL(CCR),-AIMAG(CCR)
 10 CONTINUE
 123 FORMAT(A)
END


        SUBROUTINE SLIT(OMEG,RLAM,CDS,CCS,ZS,PS)
COMPLEX CDS,CCS,CI,F,FT,ARG,ZS,PS,CTANH
COMMON/PYS/ RHOO,CO,CI,GAMMA,RNU,PI,B,R,AS,BS,D,PRAN
RLAM=B*(SQRT(OMEG/RNU))
ARG=RLAM*CSQRT(-CI)
        F=(CTANH(ARG))/ARG
F=1-F
FT=SQRT(PRAN)*F
CALL CD(F,CDS)
CALL CC(FT,CCS)
CALL IMP(OMEG,CDS,CCS,ZS,PS)
END
```

```
      SUBROUTINE CIRC(OMEG,RLAM,CDC,CCC,ZC,PC)
      COMPLEX CI,CDC,CCC,F,ARG,FT,ZC,PC
      COMPLEX*16 ARGD,RJ1D,RJOD
      COMMON/PYS/ RHOO,CO,CI,GAMMA,RNU,PI,B,R,AS,BS,D,PRAN
      RLAM=R*(SQRT(OMEG/RNU))
      ARG=RLAM*CSQRT(CI)
      ARGD=DCMPLX(ARG)
      CALL CMPBJ(ARGD,1,RJ1D)
      CALL CMPBJ(ARGD,0,RJOD)
      F=CMPLX(RJ1D)/CMPLX(RJOD)
      F=(2*F)/(ARG)
      F=1.-F
      FT=SQRT(PRAN)*F
      CALL CD(F,CDC)
      CALL CC(FT,CCC)
      CALL IMP(OMEG,CDC,CCC,ZC,PC)
      END


      SUBROUTINE RECT(OMEG,RLAM,CDR,CCR,ZR,PR)
      COMPLEX CI,F,CDR,CCR,FT,YMN,ZR,PR
      COMMON/PYS/ RHOO,CO,CI,GAMMA,RNU,PI,B,R,AS,BS,D,PRAN
      RLAM=(2*AS*BS)/(AS+BS)
      RLAM=RLAM*(SQRT(OMEG/RNU))
      F=CMPLX(0.,0.)
      DO 5  IJ=1,41,2
      DO 55 II=1,41,2
      F=F+(1./(REAL(II)*REAL(II)*REAL(IJ)*REAL(IJ)*YMN(RLAM,II,IJ)))
       55 CONTINUE
       5      CONTINUE
      FT=SQRT(PRAN)*F
      CALL CD(F,CDR)
      CALL CC(F,CCR)
      CALL IMP(OMEG,CDR,CCR,ZR,PR)
      END

      COMPLEX FUNCTION YMN(RLAM,M,N)
      COMPLEX CI
      COMMON/PYS/ RHOO,CO,CI,GAMMA,RNU,PI,B,R,AS,BS,D,PRAN
      YMN=(CI*PI*PI)/(RLAM*RLAM)
      YMN=YMN*(((BS*BS*M*M)+(AS*AS*N*N))/((AS+BS)**2.))
      YMN=1+YMN
      RETURN
      END

      SUBROUTINE CD(F,CDENS)
      COMPLEX F,CDENS,CI
        COMMON/PYS/ RHOO,CO,CI,GAMMA,RNU,PI,B,R,AS,BS,D,PRAN
      CDENS=RHOO/F
      END


      SUBROUTINE CC(FT,CCOMP)
      COMPLEX FT,CCOMP,CI
      COMMON/PYS/ RHOO,CO,CI,GAMMA,RNU,PI,B,R,AS,BS,D,PRAN
      CCOMP=1.-GAMMA
      CCOMP=(CCOMP*FT)+GAMMA
      CCOMP=CCOMP/(RHOO*CO*CO)
```

```
END

SUBROUTINE IMP(OMEG,CD,CC,ZC,PC)
COMMON/MED/ TORT,POROS
COMPLEX CD,CC,ZC,PC,CI
CI=CMPLX(0.,1.)
ZC=SQRT(TORT)/POROS
ZC=ZC*((CD/CC)**.5)
PC=CI*OMEG*SQRT(TORT)*((CD*CC)**.5)
END
```

## K.2 Programmes used in conjunction with sound propagation from a point source

The programmes listed here were used to compare the formulae which predict the sound propagation from a point source.

### K.2.1 Programme used to calculate sound propagation from a point source using the plane wave reflection coefficient formula

The listings include only the driver programmes and subroutines unique to each programme.

```
c
c Program description:
c
c  Programme to calculate the pressure or level difference above
c  an impedance boundary using the plane wave coefficient model
c
c
c ********************************************************
c Initialization and input of geometry

DIMENSION AFREQ(500),RFREQ(500),R(500),X(500)
DIMENSION H(2),PTOT(2,500),OUT(500)
COMPLEX PTOT
CHARACTER*32 DIN,DOUT
PRINT*, 'INPUT NAME OF INPUT AND OUTPUT FILE'
READ 123,DIN,DOUT
PRINT *,'INPUT LOWER AND HIGHER RECEIVER HEIGHT
     1  SOURCE HEIGHT AND SEPARATION'
READ*, H(1),H(2),HS,SEP
PRINT*,'INPUT NUMBER OF DATA POINTS'
READ*,IN
OPEN(11,FILE=DOUT,STATUS='UNKNOWN')
OPEN(1,FILE=DIN,STATUS='UNKNOWN')
PI=4.*ATAN(1.)

C Frequency loop
DO 10 I=1,IN
READ (1,*) RFREQ(I),R(I),X(I)
c use to change log to linear frequency if required
AFREQ(I)=RFREQ(I)
DO 5 II=1,2
HR=H(II)
c Call subroutine to calculate specific solution
CALL PLANE(AFREQ(I),R(I),X(I),HR,HS,SEP,PTOT(I,II))
 5 CONTINUE
c Calculate level difference
OUT(I)=20.*LOG10(CABS(PTOT(I,2))/CABS(PTOT(I,1)))
WRITE (11,*)AFREQ(I),OUT(I)
 10 CONTINUE
 123 FORMAT (A/A)
END


c Subroutine to calculate propagation from pwrc solution

SUBROUTINE PLANE(AFREQ,R,X,HR,HS,SEP,PTOT)
COMPLEX PTOT,REFC,BETA,CI,TE1,TE2
CI=CMPLX(0.,1.)
PI=4.*ATAN(1.)
RK=(2.*PI*AFREQ)/343.
R1=SQRT((SEP)**2.+(HS-HR)**2.)
R2=SQRT((SEP)**2.+(HS+HR)**2.)
COST=(HS+HR)/R2
BETA=1./CMPLX(R,X)
REFC=(COST-BETA)/(COST+BETA)
TE1=CEXP(CI*RK*R1)/R1
TE2=CEXP(CI*RK*R2)/R2
PTOT=TE1+REFC*TE2
 10 CONTINUE
```

### K.2.2 Programme to calculate sound propagation from a point source using the Weyl van der Pol formula

```
c Programme to calculate pressure from Weyl van del Pol solution
SUBROUTINE WV(AFREQ,R,X,HR,HS,SEP,PTOT)
COMPLEX RP,P1,P2,WIZ,PE,PE2,F,P3,PTOT,J,BETA
REAL KO
H=HS+HR
R1=SQRT((HS-HR)**2.+SEP*SEP)
R2=SQRT(H*H+SEP*SEP)
COST=H/R2
PI=4.*ATAN(1.)
J=CMPLX(0.,1.)
BETA=1./(CMPLX(R,X))
KO=(2.*PI*AFREQ)/343.
RP=(COST-BETA)/(COST+BETA)
P1=CEXP(J*KO*R1)/(4.*PI*R1)
P2=CEXP(J*KO*R2)/(4.*PI*R2)
PE=CSQRT((J*KO*R2)/2.)*(COST+BETA)
PE2=-J*PE
CALL AW(PE2,WIZ)
F=1+J*SQRT(PI)*PE*WIZ
P3=RP+(1.-RP)*F
PTOT=P1+P2*P3
END
```

### K.2.3 Programme to calculate the sound propagation from a point source using the Thomasson formula

```
C Routine to calculate field above an impedance boundary
C using Thomassons iterative technique
SUBROUTINE THOME(AFREQ,R,X,HR,HS,SEP,PTOT)
COMPLEX TE1,TE2,PH1,PH2,PTOT
PI=4.*ATAN(1.)
RK=(2.*PI*AFREQ)/343.
CALL AR1(HS,HR,SEP,RK,TE1)
CALL AR2(HS,HR,SEP,RK,TE2)
CALL PHI1(HS,HR,SEP,RK,R,X,PH1)
CALL PHI2(AFREQ,HS,HR,SEP,RK,R,X,PH2)
PTOT=TE1+TE2+PH1+PH2
END

SUBROUTINE PHI1(HS,HR,SEP,RK,R,X,PHI)
DIMENSION CII(0:20),CO3(0:20)
COMMON C
REAL MOD1,MOD2
COMPLEX CI1,CI2,CIH,CMPI,CR2,CRK,CCOST,CSINT,BETA,ADMIT
COMPLEX CI,GAMO,GAM1,C,CA,CB,CO1,ERA,CI4,CII,CO2,RM,CO3
COMPLEX RN,RME2,RNN,PHI
PI=4.*ATAN(1.)
R2=SQRT(SEP**2+(HS+HR)**2)
CI1=CMPLX(1.,0.)
CI4=CMPLX(4.,0.)
CI2=CMPLX(2.,0.)
CIH=CMPLX(0.5,0.)
CI=CMPLX(0.,1.)
CMPI=CMPLX(PI,0.)
CR2=CMPLX(R2,0.)
CRK=CMPLX(RK,0.)
COST=(HS+HR)/R2
SINT=SQRT(1.-COST**2.)
CSINT=CMPLX(SINT,0.)
CCOST=CMPLX(COST,0.)
BETA=CMPLX(R,X)
ADMIT=1/BETA
GAMO=-ADMIT*CCOST+((CI1-ADMIT**CI2)**CIH)*CSINT
GAM1=-ADMIT*CCOST-((CI1-ADMIT**CI2)**CIH)*CSINT
CA=(CI*CRK*CR2*(GAMO-CI1))**CIH
CB=(CI*CRK*CR2*(CI1-GAM1))**CIH
AA=ATAN(AIMAG(CA)/REAL(CA))
        IF (AA.LT.(PI/4.)) THEN
       C=CMPLX(+1.,0.)
       ELSE
       C=CMPLX(-1.,0.)
       ENDIF
CO1=(C*CRK*ADMIT*CEXP(CI*CRK*CR2))/(CI2*CMPI*CB)
CA1=REAL(CA)
CA2=AIMAG(CA)
        IF (CA2.LT.0.)CA2=CA2*-1
CA=CMPLX(CA1,CA2)
CALL W(CA,ERA)
ERA1=REAL(ERA)
ERA2=AIMAG(ERA)
ERA=CMPLX(ERA1,ERA2)
CII(0)=CSQRT(CMPI)*ERA
CII(1)=CA+((CIH-CA**CI2)*CII(0))
 DO 30 M=2,10,1
 RM=CMPLX(M,0)
```

```
 CII(M)=(RM-CIH-CA**CI2)*(CII(M-1))+(RM-CI1)*(CA**CI2)*CII(M-2)
 30  CONTINUE
C02=CMPLX(0.,0.)
DO 40 N=0,6,1
C03(0)=CMPLX(0.,0.)
RNN=CMPLX(N,0)
ME=2*N
CALL FACT(ME,ME2)
CALL FACT(N,N2)
RN=CMPLX(N2,0)
RME2=CMPLX(ME2,0)
C03(N)=(RME2*CII(N))/((RN**CI2)*(CI4*(CB**CI2))**RNN)
    IF (N.GE.3) THEN
    MOD1=CABS(C03(N-3)-C03(N-2))
    MOD2=CABS(C03(N-2)-C03(N-1))
IF (MOD1.GT.MOD2) THEN
CONTINUE
ELSE
GOTO 75
ENDIF
    ELSE
    CONTINUE
    ENDIF
C02=C02+C03(N)
 40 CONTINUE
 75 PHI=C01*C02
END


SUBROUTINE PHI2(AFREQ,HS,HR,SEP,RK,R,X,PH2)
COMMON C
COMPLEX CI1,CI2,CIH,CMPI,CR2,CRK,CCOST,CSINT,BETA,ADMIT
COMPLEX CI,GAM0,GAM1,CB,PH2,CSEP,HA,HAA,CHR,CHS,CIQ,C
PI=4.*ATAN(1.)
CHR=CMPLX(HR,0.)
CHS=CMPLX(HS,0.)
R2=SQRT(SEP**2+(HS+HR)**2)
CIQ=CMPLX(0.25,0.)
CSEP=CMPLX(SEP,0.)
CI1=CMPLX(1.,0.)
CI2=CMPLX(2.,0.)
CIH=CMPLX(0.5,0.)
CI=CMPLX(0.,1.)
CMPI=CMPLX(PI,0.)
CR2=CMPLX(R2,0.)
CRK=CMPLX(RK,0.)
COST=(HS+HR)/R2
SINT=SQRT(1.-COST**2)
CSINT=CMPLX(SINT,0.)
CCOST=CMPLX(COST,0.)
BETA=CMPLX(R,X)
ADMIT=1/BETA
GAM0=-ADMIT*CCOST+((CI1-ADMIT**CI2)**CIH)*CSINT
GAM01=REAL(GAM0)
IF (GAM01.GT.1.) THEN
GOTO 60
ELSE
  GOTO 70
ENDIF
```

```
 60 GAM1=-ADMIT*CCOST-((CI1-ADMIT**CI2)**CIH)*CSINT
HA=CRK*CSEP*(CI1-ADMIT**CI2)**CIH
IF (ABS(REAL(HA)).GT.154.)THEN
CALL HANKELA(HA,0,1,HAA)
ELSE
CALL HO1(HA,HAA)
ENDIF
PH2=HAA*CEXP(-CI*CRK*(CHR+CHS)*ADMIT)*CIQ*(CI1-C)
     1  *CRK*ADMIT
GOTO 80
 70  PH2=CMPLX(0.,0.)
 80 END


SUBROUTINE AR1(HS,HR,SEP,RK,TE1)
COMPLEX TE1,CRK,C4,CPI,CR1,CI
PI=4.*ATAN(1.)
R1=SQRT(SEP**2+(HS-HR)**2)
CRK=CMPLX(RK,0.)
CPI=CMPLX(PI,0.)
CR1=CMPLX(R1,0.)
CI=CMPLX(0.,1.)
C4=CMPLX(4.,0.)
TE1=CEXP(CRK*CI*CR1)/(-CR1*C4*CPI)
END


SUBROUTINE AR2(HS,HR,SEP,RK,TE2)
COMPLEX TE2,CRK,CPI,C4,CR2,CI
PI=4.*ATAN(1.)
R2=SQRT(SEP**2+(HS+HR)**2)
CPI=CMPLX(PI,0.)
C4=CMPLX(4.,0.)
CRK=CMPLX(RK,0.)
CR2=CMPLX(R2,0.)
CI=CMPLX(0.,1.)
TE2=CEXP(CRK*CI*CR2)/(-CR2*CPI*C4)
END

SUBROUTINE FACT(N,NN)
NN=1.
DO 40 M=N,1,-1
NN=NN*M
 40 CONTINUE
END
```

## K.2.4 Programme to calculate sound propagation from a point source using the Attenborough et al formula

```
C Subroutine to calculate field from attenborough hayek and lawther model
SUBROUTINE ATHALA(AFREQ,R,X,HR,HS,SEP,PTOT)
COMPLEX TE1,TE2,B,V,REFC,PTOT
   PI=4.*ATAN(1.)
RK=(2.*PI*AFREQ)/343.
CALL LRAHL(AFREQ,HS,HR,SEP,R,X,RK,V,B)
CALL AR1(HS,HR,SEP,RK,TE1)
CALL AR2(HS,HR,SEP,RK,TE2)
CALL RTH(HS,HR,SEP,R,X,RK,REFC)
PTOT=TE1+(REFC*TE2)+V-B
END


SUBROUTINE LRAHL(AFREQ,HS,HR,SEP,R,X,RK,V,B)
COMPLEX CSINT,CCOST,CI1,CI2,CI3,CI4,CI,BETA,ADMIT
COMPLEX CI8,CIH,CIT,CR2,B,Z,WIZ,RX,BET
COMPLEX LR1,LR2,LR4,RLR1,CRK,CSEP,CMPI,VET
COMPLEX V,V1,V2,V3,V4,V5,V6,BET2,BET3,CRR2
R2=SQRT(SEP**2.+(HS+HR)**2.)
PI=4.*ATAN(1.)
CMPI=CMPLX(PI,0.)
COST=(HS+HR)/R2
SINT=SEP/R2
CSINT=CMPLX(SINT,0.)
CCOST=CMPLX(COST,0.)
CRK=CMPLX(RK,0.)
CI1=CMPLX(1.,0.)
CI2=CMPLX(2.,0.)
CI=CMPLX(0.,1.)
CRR2=CI1/CSQRT(CI2)
CSEP=CMPLX(SEP,0.)
BETA=CMPLX(R,X)
ADMIT=1/BETA
CI3=CMPLX(3.,0.)
CI8=CMPLX(8.,0.)
CIH=CMPLX(0.5,0.)
AN=1.50
CIT=CMPLX(AN,0.)
CI4=CMPLX(4.,0.)
CR2=CMPLX(R2,0.)
BET=ADMIT*CCOST
BET2=CI1+BET
BET3=ADMIT+CCOST
VET=CSINT*CSQRT(CI1-ADMIT**CI2)
V1=(ADMIT*CEXP(CI*CRK*CR2))/(CI2*CMPI*CR2*BET3)
V2=CSQRT((BET2/VET)+CI1)
V3=CI1/(CI*CR2*CRK*CSQRT(BET3))
V4=(VET)/(CI8*CSQRT(CI2))
      V5=(CI1+(BET2/VET))**CIT
V6=(BET2/VET)+CI3
V=V1*((CRR2*V2)+(V3*((V4*V5*V6)-BET2)))
RX=CI*CRK*CR2*(CI1+(ADMIT*CCOST)-((CI1-ADMIT**CI2)**CIH)*CSINT)
RX1=REAL(RX)
RX2=AIMAG(RX)
IF (RX1.LT.0.)RX1=RX1*-1.
RX=CMPLX(RX1,RX2)
Z=-CI*CSQRT(RX)
c Error function routine
CALL W(Z,WIZ)
```

```
WIZ1=REAL(WIZ)
WIZ2=AIMAG(WIZ)
IF (WIZ1.LT.0.)WIZ1=WIZ1*-1.
IF (WIZ2.LT.0.)WIZ2=WIZ2*-1.
WIZ=CMPLX(WIZ1,WIZ2)
LR2=CEXP(CI*CRK*CR2)
LR1=CRK*CSEP*CSQRT(CI1-ADMIT**2.)
c Hankel function routine
CALL HANAP(LR1,RLR1)
LR4=(RK*ADMIT)/CI4
B=LR4*WIZ*RLR1*LR2
END
```

## K.2.5 Programme to calculate the sound propagation from a point source using the Kawai et al formula

```
C Routine to calculate field from Kawai, Hidaka and Nakajima solution
SUBROUTINE KAHINA(AFREQ,R,X,HR,HS,SEP,PTOT)
COMPLEX TE1,TE2,REFC,TOTJ,CSINT,BETA,ADMIT,CA,PTOT
COMPLEX CCOST,CI1,CI2,CI,CR2,SW1,CI3,CI4,FER,CMPI
HT=HS+HR
R2=SQRT(SEP**2.+HT**2.)
PI=4.*ATAN(1.)
RK=(2.*PI*AFREQ)/343.
CMPI=CMPLX(PI,0.)
COST=(HT/R2)
SINT=SQRT(1.-COST**2.)
CSINT=CMPLX(SINT,0.)
CCOST=CMPLX(COST,0.)
CI1=CMPLX(1.,0.)
CI2=CMPLX(2.,0.)
CI3=CMPLX(3.,0.)
CI4=CMPLX(4.,0.)
CI=CMPLX(0.,1.)
CR2=CMPLX(R2,0.)
  CALL ERFC(AFREQ,R,X,HR,HS,SEP,N,RK,FER)
CALL AR1(HS,HR,SEP,RK,TE1)
  CALL AR2(HS,HR,SEP,RK,TE2)
CALL RTH(HS,HR,SEP,R,X,RK,REFC)
BETA=CMPLX(R,X)
ADMIT=CI1/BETA
CA=CI1+(ADMIT*CCOST)-(SQRT(CI1-ADMIT**CI2)*CSINT)
ADMIT2=AIMAG(ADMIT)
CA1=REAL(CA)
         IF (ADMIT2.LT.0..AND.CA1.LT.0.) THEN
        CALL SFJ(R,X,RK,HS,HR,SEP,SW1)
        SW1=CMPLX(0.,0.)
GOTO 50
ELSE
  SW1=CMPLX(0.,0.)
ENDIF
  50 PTOT=TE1+TE2*REFC-TE2*FER+SW1
END


SUBROUTINE ERFC(AFREQ,R,X,HR,HS,SEP,N,RK,FER)
COMPLEX CI1,T,CI,CSINT,CCOST,CR2,CFR,BETA,CRK,CI3
COMPLEX ADMIT,CA,CZ,Z,WIZ,CFS1,CI2,FER,CMPI,FER1
HT=HS+HR
R2=SQRT((SEP)**2.+(HS+HR)**2.)
PI=4.*ATAN(1.)
COST=(HT/R2)
SINT=SQRT(1.-COST**2.)
CI1=CMPLX(1.,0.)
CI2=CMPLX(2.,0.)
CI3=CMPLX(3.,0.)
CMPI=CMPLX(PI,0.)
CI=CMPLX(0.,1.)
CSINT=CMPLX(SINT,0.)
CCOST=CMPLX(COST,0.)
CR2=CMPLX(R2,0.)
CFR=CMPLX(4.,0.)
CRK=CMPLX(RK,0.)
BETA=CMPLX(R,X)
ADMIT=1/BETA
```

```
 T=CSQRT(CI1-ADMIT**CI2)
 CA=CI1+(ADMIT*CCOST)-(T*CSINT)
 CZ=CR2*CA*CRK
 RCZ=REAL(CZ)
 RICZ=AIMAG(CZ)
 IF(RICZ.LT.0.)RICZ=0.
 CZ=CMPLX(RCZ,RICZ)
 Z=CSQRT(-CI*CZ)
 CALL W(Z,WIZ)
 WIZ1=REAL(WIZ)
 WIZ2=AIMAG(WIZ)
      IF (WIZ1.LT.0.)WIZ1=WIZ1*-1
 IF (WIZ2.LT.0.)WIZ2=WIZ2*-1
 WIZ=CMPLX(WIZ1,WIZ2)
 CFS1=CSQRT(CMPI*CZ)
        FER1=WIZ*CFS1*CEXP((-CI*CMPI)/CFR)
 FER=(FER1-CI1)*CA*((CFR*ADMIT*(CI1+ADMIT*COST))
     1  /((ADMIT+COST)**CI3))
 END


 SUBROUTINE SMALL(AFREQ,R,X,HR,HS,SEP,N,RK,FER)
 COMPLEX CCOST,CSINT,CI1,CI2,CI3,CI4,CMPI,CI,ADMIT,BETA
 COMPLEX CR2,T,CA,CZ,CFS1,FER1,FER,WIZ,WIZ1,CRK
 R2=SQRT((SEP)**2.+(HS+HR)**2.)
 PI=4.*ATAN(1.)
 HT=HS+HR
 COST=(HT/R2)
 SINT=SQRT(1.-COST**2.)
 CI1=CMPLX(1.,0.)
 CI2=CMPLX(2.,0.)
 CMPI=CMPLX(PI,0.)
 CI=CMPLX(0.,1.)
 CSINT=CMPLX(SINT,0.)
 CCOST=CMPLX(COST,0.)
 CR2=CMPLX(R2,0.)
 CI4=CMPLX(4.,0.)
 CI3=CMPLX(3.,0.)
 CRK=CMPLX(RK,0.)
 BETA=CMPLX(R,X)
 ADMIT=1/BETA
 T=CSQRT(CI1-ADMIT**CI2)
 CA=CI1+(ADMIT*CCOST)-(T*CSINT)
 CZ=CR2*CA*CRK
 WIZ1=CMPLX(0.,0.)
 DO 20 L=1,10
 WIZ=((-CI2*CI*CZ)**(L+CI1))/(CI2*L+CI1)
 WIZ1=WIZ1+WIZ
  20 CONTINUE
 CFS1=CSQRT(CPI*CZ)
        FER1=WIZ1*CFS1*CEXP(((-CI*CPI)/CI4)-(CI*CZ))
 FER=(FER1-1.)*CA*((CI4*ADMIT*(CI1+ADMIT*COST))
     1  /((ADMIT+COST)**CI3))
 END


 SUBROUTINE LARGE (AFREQ,R,X,HR,HS,SEP,N,RK,FER)
 COMPLEX CCOST,CSINT,CI1,CI2,CI3,CI4,CMPI,CI,ADMIT,BETA
```

```
COMPLEX CR2,T,CA,CZ,FER1,FER,WIZ,WIZ1,CRK
R2=SQRT((SEP)**2.+(HS+HR)**2.)
PI=4.*ATAN(1.)
COST=(HT/R2)
SINT=SQRT(1.-COST**2.)
CI1=CMPLX(1.,0.)
CI2=CMPLX(2.,0.)
CMPI=CMPLX(PI,0.)
CI=CMPLX(0.,1.)
CSINT=CMPLX(SINT,0.)
CCOST=CMPLX(COST,0.)
CR2=CMPLX(R2,0.)
CI4=CMPLX(4.,0.)
CI3=CMPLX(3.,0.)
CRK=CMPLX(RK,0.)
BETA=CMPLX(R,X)
ADMIT=1/BETA
T=CSQRT(CI1-ADMIT**CI2)
CA=CI1+(ADMIT*CCOST)-(T*CSINT)
CZ=CR2*CA*CRK
WIZ1=CMPLX(0.,0.)
DO 20 L=1,10
WIZ=(CI2*L-1)/((CI2*CI*CZ)**L)
WIZ1=WIZ1+WIZ
 20 CONTINUE
FER1=1+WIZ1
FER=(FER1-1.)*CA*((CI4*ADMIT*(CI1+ADMIT*COST))
     1  /((ADMIT+COST)**CI3))
END


  SUBROUTINE SFJ(R,X,RK,HS,HR,SEP,SW1)
COMPLEX BETA,ADMIT,HANA,H,SW1,CI,CRK,CI2,CMPI,CI1,CSEP
COMPLEX CIH
CSEP=CMPLX(SEP,0.)
CI1=CMPLX(1.,0.)
PI=4.*ATAN(1.)
CMPI=CMPLX(PI,0.)
CI2=CMPLX(2.,0.)
CIH=CMPLX(0.5,0.)
CRK=CMPLX(RK,0.)
BETA=CMPLX(R,X)
ADMIT=1/BETA
CI=CMPLX(0.,1.)
  HANA=CSQRT(CI1-(ADMIT**CI2))*CRK*CSEP
PRINT *,HANA
IF (REAL(HANA).GT.154.) THEN
CALL HANKELA(HANA,0,1,H)
ELSE
CALL HO1(HANA,H)
ENDIF
SW1=-CI2*CRK*ADMIT*H*(CEXP(CI*CRK*(HS+HR)*ADMIT))*
     1  CEXP(CI*CRK*CSEP*((CI1-ADMIT**CI2)**CIH))
  END
```

### K.2.6 Programme to calculate the sound propagation from a point source using the Nobile et al. formula

```
c Routine to calculate field using Nobile and Hayek solution
SUBROUTINE NOHA(AFREQ,R,X,HR,HS,SEP,PTOT)
COMPLEX CI4,CMPI,F,PTOT,TE1,TE2,CI1,R1,R2
PI=4.*ATAN(1.)
CI4=CMPLX(4.,0.)
CI1=CMPLX(1.,0.)
CMPI=CMPLX(PI,0.)
RK=(2.*PI*AFREQ)/343.
CALL NOEX(AFREQ,R,X,HR,HS,SEP,N,RK,F)
CALL AR1(HS,HR,SEP,RK,TE1,R1)
CALL AR2(HS,HR,SEP,RK,TE2,R2)
PTOT=TE1+TE2*F
END

SUBROUTINE NOEX(AFREQ,R,X,HR,HS,SEP,N,RK,TOT)
DIMENSION TT(0:10)
REAL MOD1,MOD2
COMPLEX CMPI,BETA,ADMIT,CI,COE
COMPLEX SQ1,SQ2,B,G,H,TTL,TN,EN,BKN,E1,TT,TOT
COMPLEX CI1,CI2,CSINT,CCOST,CR2,CRK,C4
PI=4.*ATAN(1.)
CRK=CMPLX(RK,0.)
CMPI=CMPLX(PI,0.)
CI=CMPLX(0.,1.)
C4=CMPLX(4.,0.)
CI1=CMPLX(1.,0.)
CI2=CMPLX(2.,0.)
R2=SQRT((SEP)**2.+(HS+HR)**2.)
CR2=CMPLX(R2,0.)
COST=(SEP/R2)
SINT=SQRT(1.-COST**2.)
CSINT=CMPLX(SINT,0.)
CCOST=CMPLX(COST,0.)
BETA=CMPLX(R,X)
ADMIT=CMPLX(1.,0.)/BETA
SQ1=CSQRT(CI1-ADMIT**CI2)
ASQ1=REAL(SQ1)
c Ensure sq1 and sq2 positive
IF (ASQ1.LT.0.) THEN
SQ1=SQ1*-1
ELSE SQ1=SQ1
ENDIF
SQ2=CSQRT(CI1+(ADMIT*CSINT)-(SQ1*CCOST))
ASQ2=REAL(SQ2)
IF (ASQ2.LT.0.) THEN
SQ2=SQ2*-1
ELSE
SQ2=SQ2
ENDIF
B=-CI*SQ2
G=-CI1*(B**CI2)
H=CI1+ADMIT*CSINT+SQ1*CCOST
COE=CI1
     TTL=CMPLX(0.,0.)
CALL EOH(CI,RK,R2,ADMIT,SINT,COST,SQ1,E1)
DO 10 NN=0,10,1
TT(0)=CMPLX(0.,0.)
c Calculates Taylor coefficients
CALL TCN(NN,B,G,H,TN)
```

```
 CALL TCE(NN,G,CI,RK,R2,EN)
 CALL TCK(NN,CI,RK,R2,G,BKN)
 TT(NN)=TN*(E1*EN+BKN)
     IF (NN.GE.3) THEN
     MOD1=CABS(TT(NN-3)-TT(NN-2))
     MOD2=CABS(TT(NN-2)-TT(NN-1))
 IF (MOD1.GT.MOD2) THEN
 CONTINUE
 ELSE
 GOTO 75
 ENDIF
     ELSE
     CONTINUE
     ENDIF
 TTL=TTL+TT(N)
 10 CONTINUE
 75 TOT=COE+(CI2*ADMIT)/(ADMIT+CSINT)*TTL
 END


 SUBROUTINE TCN(NN,B,G,H,TN)
 DIMENSION A(0:300)
 COMPLEX SU,SUT,CBINC,CAM,TR,G,H,B,TN,C1,C2,C4
 C1=CMPLX(1.,0.)
 C2=CMPLX(2.,0.)
 C4=CMPLX(4.,0.)
 A(0)=1.
 DO 70 J=1,8
 A(J)=((0.5-J)/J)*A(J-1)
  70 CONTINUE
 SUT=CMPLX(0.,0.)
 DO 50 KN=0,9,1
        SU=CMPLX(0.,0.)
 TT=NN-2*KN
 IF (TT.LT.0.) THEN
 GOTO 60
 ELSE
 CONTINUE
 ENDIF
   M=NN-KN
 TR=((C4*G)/H)**M
 BAM=A(M)
 CAM=CMPLX(BAM,0.)
 CALL FACT(M,FIM)
 CALL FACT(KN,FIKN)
 MM=M-KN
 CALL FACT(MM,FIMM)
 BINC=FIM/(FIKN*FIMM)
 CBINC=CMPLX(BINC,0.)
 SU=TR*CAM*CBINC
 SUT=SUT+SU
  50 CONTINUE
  60 TN=SUT
 END


 SUBROUTINE TCK(NN,CI,RK,R2,G,BKN)
 DIMENSION BK(0:500)
 REAL RI
```

```
COMPLEX B,BK,BKN,CI,CR2,CRK,C1,C2,CIH,CI8,G,CBI
CRK=CMPLX(RK,0.)
CR2=CMPLX(R2,0.)
CIH=CMPLX(0.5,0.)
CI8=CMPLX(8.,0.)
C1=CMPLX(1.,0.)
C2=CMPLX(2.,0.)
BK(0)=CMPLX(0.,0.)
BK(1)=-C1/C2
DO 80 I=2,6
RI=REAL(I)
CBI=CMPLX(RI,0.)
BK(I)=CIH*BK(I-1)-(((CBI-CI1)/(CI8*CI*CRK*CR2*G))*BK(I-2))
 80 CONTINUE
BKN=BK(NN)
END

SUBROUTINE TCE(NN,G,CI,RK,R2,EN)
DIMENSION E(0:500)
REAL RI
COMPLEX E,EN,G,CI,CR2,CRK,C1,C2,CI8,CIH,CEI
CR2=CMPLX(R2,0.)
CIH=CMPLX(0.5,0.)
CI8=CMPLX(8.,0.)
CRK=CMPLX(RK,0.)
C1=CMPLX(1.,0.)
C2=CMPLX(2.,0.)
E(1)=-C1/C2
E(0)=CMPLX(1.,0.)
DO 70 I=2,6
RI=REAL(I)
CEI=CMPLX(RI,0.)
E(I)=CIH*E(I-1)-(((CEI-CI1)/(CI8*CI*CRK*CR2*G))*E(I-2))
 70 CONTINUE
EN=E(NN)
END


SUBROUTINE EOH(CI,RK,R2,ADMIT,SINT,COST,SQ1,E1)
COMPLEX CI1,CR2,CLAM1,WIZ,E1,ADMIT,CI,CMPI,CRK
COMPLEX CSINT,CCOST,CLAM2,CI2,SQ1
PI=4.*ATAN(1.)
CMPI=CMPLX(PI,0.)
CI1=CMPLX(1.,0.)
CI2=CMPLX(2.,0.)
CR2=CMPLX(R2,0.)
CRK=CMPLX(RK,0.)
CSINT=CMPLX(SINT,0.)
CCOST=CMPLX(COST,0.)
CLAM1=CSQRT(CI*CRK*CR2)*CSQRT(CI1+ADMIT*CSINT-
     1  (SQ1*CCOST))
AICLAM1=AIMAG(CLAM1)
RECLAM1=REAL(CLAM1)
IF (AICLAM1.LT.0.) THEN
  AICLAM1=AICLAM*-1
ELSE
AICLAM1=AICLAM1
ENDIF
CLAM1=CMPLX(RECLAM1,AICLAM1)
```

```
CLAM2=-CI*CLAM1
CALL W(CLAM2,WIZ)
WIZ1=REAL(WIZ)
WIZ2=AIMAG(WIZ)
IF (WIZ1.LT.0.)WIZ1=WIZ1*-1.
IF (WIZ2.LT.0.)WIZ2=WIZ2*-1.
WIZ=CMPLX(WIZ1,WIZ2)
E1=CI*CLAM1*CSQRT(CMPI)*WIZ
END
```

## K.2.7 Programme to calculate the sound propagation from a point source using the Adaptive quadrature formula

```
C Routine to calculate field from adaptive quadrature
SUBROUTINE UN(AFREQ,R,X,HR,HS,SEP,PTOT)
IMPLICIT REAL*8(A-H)
IMPLICIT REAL*8(O-Z)
COMPLEX*16 TE1,TE2,PB,PTOT,RR1,RR2
PI=4.*ATAN(1.)
RK=(2.*PI*AFREQ)/343.
CALL AR1(HS,HR,SEP,RK,TE1)
CALL AR2(HS,HR,SEP,RK,TE2)
CALL RINT(R,X,RK,HS,HR,SEP,PB,RAP)
PTOT=-TE1-TE2+PB
END

SUBROUTINE RINT(R,ZX,RK,HS,HR,SEP,PB,RAP)
IMPLICIT REAL*8(A-H)
IMPLICIT REAL*8(O-Z)
COMMON BET,CCOST,CRK,CR2,AP,AN
DIMENSION W(3000),IW(500),W2(3000),IW2(500)
INTEGER IFAIL,IFAIL2
EXTERNAL WTI1,WTR1,WTI2,WTR2
COMPLEX*16 CI2,CMPI,CI,CR2,Z,BET,AP,AN,CRK,CO1,CO2,CCOST
COMPLEX*16 SWVE,WAT,CO,PB,RAP
PI=4.0D0*DATAN(1.0D0)
CMPI=DCMPLX(PI,0.0D0)
CI2=DCMPLX(2.0D0,0.0D0)
CI=DCMPLX(0.0D0,1.0D0)
R2=DSQRT((HS+HR)**2.0D0+SEP**2.0D0)
CR2=DCMPLX(R2,0.0D0)
COST=(HS+HR)/R2
CCOST=DCMPLX(COST,0.0D0)
Z=DCMPLX(R,ZX)
BET=DCMPLX(1.0D0,0.0D0)/Z
AP=(1.0D0+BET*CCOST)-(CDSQRT(DCMPLX(1.0D0,0.D0)-BET**CI2))*
     1  (CDSQRT(DCMPLX(1.0D0,0.0D0)-CCOST**CI2))
RAP=DREAL(AP)
AN=(1.0D0+BET*CCOST)+(CDSQRT(DCMPLX(1.0D0,0.D0)-BET**CI2))*
     1  (CDSQRT(DCMPLX(1.0D0,0.0D0)-CCOST**CI2))
CRK=DCMPLX(RK,0.0D0)
CO1=((DCMPLX(0.0D0,1.0D0)*CRK*BET)/(CI2*CMPI))*(CDEXP(CI*CR2*CRK))
CO2=((CRK*BET)/(CI2*CMPI))*(CDEXP(CI*CR2*CRK))
IF (DIMAG(BET).LT.0.0D0.AND.DREAL(AP).LT.0.0D0)THEN
IFAIL=0
IFAIL2=0
CALL D01AMF(WTR1,0.0D0,1,1.0D-1,
     1  1.0D-1,WAR,WARE,W,2000,IW,252,IFAIL)
  CALL D01AMF(WTI1,0.0D0,1,
     1  1.0D-1,1.0D-1,WAI,WAIE,W2,2000,IW2,252,IFAIL2)
WRITE (6,*) 'SURFACE WAVE HERE', (RK*343.)/6.28
CALL SW(R,ZX,HS,HR,RK,SEP,SWVE)
CO=CO1
ELSE
IFAIL=0
IFAIL2=0
CALL D01AMF(WTR2,0.0D0,1,
     1  1.0D-2,1.0D-2,WAR,WARE,W,2000,IW,252,IFAIL)
CALL D01AMF(WTI2,0.0D0,1,
     1  1.0D-2,1.0D-2,WAI,WAIE,W2,2000,IW2,252,IFAIL2)
CO=CO2
SWVE=DCMPLX(0.0D0,0.0D0)
```

```
ENDIF
WAT=DCMPLX(WAR,WAI)
PB=CO*WAT+SWVE
END


SUBROUTINE SW(R,ZX,HS,HR,RK,SEP,SWVE)
IMPLICIT REAL*8(A-H)
IMPLICIT REAL*8(O-Z)
COMPLEX*8 HI1,HO1
COMPLEX*16 Z,BET,CRK,CO,HI,HO
Z=DCMPLX(R,ZX)
BET=DCMPLX(1.0DO,0.0DO)/Z
CRK=DCMPLX(RK,0.0DO)
CO=((CRK*BET)/(DCMPLX(2.0DO,0.0DO)))
     1  *CDEXP(DCMPLX(0.0DO,-1.0DO)*
     1  CRK*BET*(DCMPLX(HS,0.0DO)+DCMPLX(HR,0.0DO)))
HI=CRK*DCMPLX(SEP,0.0DO)*CDSQRT(DCMPLX(1.0DO,0.0DO)
     1  -BET**DCMPLX(2.0DO,0.0DO))
HI1=CMPLX(HI)
IF (ABS(HI1).GT.154) THEN
CALL HANKELA(HI1,0,1,HO1)
ELSE
CALL HO1(HI1,HO1)
ENDIF
HO=DCMPLX(HO1)
SWVE=CO*HO
END


DOUBLE PRECISION FUNCTION WTR1(X)
IMPLICIT REAL*8(A-H)
IMPLICIT REAL*8(O-Z)
COMMON BET,CCOST,CRK,CR2,AP,AN
COMPLEX*16 WT,COE,BET,CR2,CRK,CCOST,CI,AP,AN,WTIN
CI=DCMPLX(0.0DO,1.0DO)
COE=CDEXP(-CRK*CR2*DCMPLX(X,0.0DO))
WT=DCMPLX(-1.0DO,0.0DO)*(X-CI*AP)*(X-CI*AN)
WTIN=COE/CDSQRT(-WT)
WTR1=DREAL(WTIN)
END


DOUBLE PRECISION FUNCTION WTI1(X)
IMPLICIT REAL*8(A-H)
IMPLICIT REAL*8(O-Z)
COMMON BET,CCOST,CRK,CR2,AP,AN
COMPLEX*16 WT,BET,CCOST,CRK,CR2,COE,CI,AP,AN,WTIN
CI=DCMPLX(0.0DO,1.0DO)
WT=DCMPLX(-1.0DO,0.0DO)*(X-CI*AP)*(X-CI*AN)
COE=CDEXP(-CRK*CR2*DCMPLX(X,0.0DO))
WTIN=COE/CDSQRT(-WT)
WTI1=DIMAG(WTIN)
END

DOUBLE PRECISION FUNCTION WTR2(X)
IMPLICIT REAL*8(A-H)
IMPLICIT REAL*8(O-Z)
COMMON BET,CCOST,CRK,CR2,AP,AN
```

```
COMPLEX*16 WT,COE,BET,CCOST,CRK,CR2,CI,AP,AN,WTIN
CI=DCMPLX(0.0D0,1.0D0)
WT=DCMPLX(-1.0D0,0.0D0)*(X-CI*AP)*(X-CI*AN)
COE=CDEXP(-CRK*CR2*DCMPLX(X,0.0D0))
WTIN=COE/CDSQRT(WT)
WTR2=DREAL(WTIN)
END

DOUBLE PRECISION FUNCTION WTI2(X)
IMPLICIT REAL*8(A-H)
IMPLICIT REAL*8(O-Z)
COMMON BET,CCOST,CRK,CR2,AP,AN
COMPLEX*16 WT,BET,CCOST,CRK,CR2,COE,CI,AP,AN,WTIN
CI=DCMPLX(0.0D0,1.0D0)
WT=DCMPLX(-1.0D0,0.0D0)*(X-CI*AP)*(X-CI*AN)
COE=CDEXP(-CRK*CR2*DCMPLX(X,0.0D0))
WTIN=COE/CDSQRT(WT)
WTI2=DIMAG(WTIN)
END
```

## K.2.8 programme to calculate the sound propagation from a point source using the Chandler–Wilde formula

```
C Routine to calculate field from Chandler Wilde solution
SUBROUTINE CW(AFREQ,R,X,HR,HS,SEP,PTOT,PTOT2)
COMPLEX CI,BETA,REFC,TE1,TE2,A1,A2,W,WIZ,
     1  F,T1,PS,PTOT,T2,PTOT2,WW
CI=CMPLX(0.,1.)
PI=4.*ATAN(1.)
RK=(2.*PI*AFREQ)/343.
R1=SQRT((SEP)**2.+(HS-HR)**2.)
R2=SQRT((SEP)**2.+(HS+HR)**2.)
COST=(HS+HR)/R2
BETA=1./CMPLX(R,X)
REFC=(COST-BETA)/(COST+BETA)
TE1=CEXP(CI*RK*R1)/(4.*PI*R1)
TE2=CEXP(CI*RK*R2)/(4.*PI*R2)
A1=1.+BETA*COST-CSQRT(1-BETA**2.)*SQRT(1-COST**2.)
A2=1.+BETA*COST+CSQRT(1-BETA**2.)*SQRT(1-COST**2.)
W=CSQRT(CI*A1*RK*R2)
WW=-CI*W
WW1=REAL(WW)
WW2=AIMAG(WW)
IF (WW1.LT.0.)WW1=WW1*-1.
WW=CMPLX(WW1,WW2)
CALL AW(WW,WIZ)
WIZ1=REAL(WIZ)
WIZ2=AIMAG(WIZ)
IF (WIZ1.LT.0.)WIZ1=WIZ1*-1.
IF (WIZ2.LT.0.)WIZ2=WIZ2*-1.
WIZ=CMPLX (WIZ1,WIZ2)
C 1+?
F=SQRT(PI)*W*WIZ*CI
T1=((CI)/(8.*RK*R2))
     1  +((1+(A1/A2)-(A1/4.)-(CI/(8.*RK*R2)))*F)
T2=(BETA*CEXP(CI*RK*R2))/(2.*PI*R2*(BETA+COST))
IF (AIMAG(BETA).LT.0..AND.REAL(A1).LT.0.)THEN
CALL SURF(AFREQ,R,X,HR,HS,SEP,PS)
ELSE
 IF (AIMAG(BETA).LT.0..AND.REAL(A1).EQ.0.)THEN
 CALL SURF(AFREQ,R,X,HR,HS,SEP,PS)
 PS=PS/2.
 ELSE
 CONTINUE
 ENDIF
PS=CMPLX(0.,0.)
ENDIF
PTOT=-TE1-(TE2*REFC)-T2*T1+PS
PTOT2=-TE1-(TE2*REFC)-(T2*((1.+(A1/A2))*F))+PS
END


C Routine to calculate surface wave term for Chandler Wilde series
C solution
SUBROUTINE SURF(AFREQ,R,X,HR,HS,SEP,PS)
COMPLEX CI,BETA,ARG,HAN,PS
CI=CMPLX(0.,1.)
PI=4.*ATAN(1.)
RK=(2.*PI*AFREQ)/343.
R1=SQRT((SEP)**2.+(HS-HR)**2.)
R2=SQRT((SEP)**2.+(HS+HR)**2.)
```

```
COST=(HS+HR)/R2
BETA=1./CMPLX(R,X)
ARG=RK*SEP*CSQRT(1.-BETA**2.)
CALL HO1(ARG,HAN)
PS=HAN*CEXP(-CI*RK*BETA*(HS+HS))
END
```

## K.3 Indirect method of impedance measurement

Listed here are five programmes. The first three programmes were used to calculate the impedance using the impulse technique. These are followed by example programmes used with the indirect impedance measurement technique. The second of these programmes is that used for evaluating the acoustical properties of the porous road surface.

### K.3.1 Programme to calculate impedance from pulse waveforms

This programme uses the basic Crammond and Don technique to [98] to calculate the impedance of a semi–infinite locally reacting material.

```
c
c      calculate impedance from two pulse waveforms
c
c  assumes pulses already conditioned -using "sum" program
c
c  may require a calibration file giving the ratio, in freq. domain,
c   of reflected/direct mics. receiving identical pulses.
c
c  the rp file may be used as a cal file if two "directs" are
c                       used as the input.
c
c
CHARACTER DIR*8,REF*8,RP*17,IMP*17,CAL*23
COMPLEX*16 AT(1024),BT(1024),CX(1024),RP(512),Z(512),CALIB(512)
DIMENSION A(1024),B(1024)
REAL*8 SIGNI
c
c  geometry of measuring system
c
PRINT*,' INPUT SOURCE RECEIVER DISTANCE'
READ(5,74)D
PRINT*,' INPUT SOURCE HEIGHT (ASSUMED SAME AS REC. HEIGHT)'
READ(5,74)HS
HR=HS
HYP=SQRT(D*D+(HR+HS)*(HR+HS))
S=(HR+HS)/HYP
c
c  input direct (a) and reflected (b) pulses
c
PRINT*,' INPUT DIRECT FILE NAME (NO ".DAT")'
READ(5,70) DIR
PRINT*,' INPUT REFLECTED FILE NAME (NO ".DAT")'
READ(5,70) REF
PRINT*,' IF WANT TO HAVE CAL. FILE INPUT 1, ELSE INPUT 3'
READ(5,73) MM
IF (MM.GT.1) GOTO 32
PRINT*,' INPUT MIC. CALIBRATION FILE NAME (NO ".DAT")'
READ(5,70) CAL
CAL=CAL//'.DAT'
32 IMP=DIR//'IMP.DAT'
RP=DIR//'RP.DAT'
DIR=DIR//'.DAT'
REF=REF//'.DAT'
OPEN(1,FILE=DIR,STATUS='UNKNOWN')
OPEN(2,FILE=REF,STATUS='UNKNOWN')
OPEN(3,FILE=IMP,STATUS='UNKNOWN')
OPEN(4,FILE=RP,STATUS='UNKNOWN')
OPEN(8,FILE=CAL,STATUS='UNKNOWN')
c
NB=1024
LX=1024
DO 10 I=1,512
READ(1,*) ZZ,A(I)
READ(2,*) ZX,B(I)
IF (MM.GT.1) THEN
CALIB(I)=(1.,0.)
ELSE
    IF (I.LT.100) THEN
    READ(8,*) CALIB(I)
```

```
 ELSE
 CALIB(I)=(1.,0.)
 ENDIF
 ENDIF
 10      CONTINUE
 c
 c   perform fourier transform on waveforms
 c
 SIGNI=1DO
 DO 20 I=1,512
 CX(I)=DCMPLX(A(I),0.)
 CX(I+512)=(0.,0.)
 20      CONTINUE
 CALL FORK(LX,CX,SIGNI)
 DO 30 I=1,512
 AT(I)=CX(I)
 CX(I)=DCMPLX(B(I),0.)
 CX(I+512)=(0.0,0.0)
 30      CONTINUE
 CALL FORK(LX,CX,SIGNI)
 c
 c  calculate impedance values
 c
 DO 40 I=2,100
 WRITE(6,*)I,CX(I)
 RP(I)=CX(I)/(AT(I)*CALIB(I))
 Z(I)=DCONJG(1./(S*(1-RP(I))/(1+RP(I))))
 F=250.*(I-1)
 WRITE(3,78) F, Z(I)
 WRITE(4,79) RP(I)
 40      CONTINUE
 WRITE(6,76) IMP,RP
 DO 42 I=2,5
 WRITE(6,75) RP(I),Z(I)
 42 CONTINUE
 C
 70 FORMAT(A)
 73 FORMAT(I5)
 74 FORMAT(F12.4)
 75 FORMAT(4F10.2)
 76 FORMAT( 'IMP DATA STORED IN ',A,' WHILE RP (ie. CAL) IN ',A)
 78 FORMAT(F7.1,2F8.3)
 79 FORMAT(2F8.3)
 END
 C
 C


        SUBROUTINE FORK(LX,CX,SIGNI)
 c
 c  fft as given by j.f.claerbout, "fundamentals of geophysical
 c  data processing" PAGE 12.
 c
 c cx(lx) : the variable being processed
 c lx     : a whole power of two
 c
 c
 IMPLICIT REAL*8(A-H,O-Z)
 COMPLEX*16 CX(LX),CARG,CW,CTEMP
```

```
c TYPE *, 'FORK: LX=', LX, '  SIGNI=', SIGNI
PI= 2*DASIN(1D0)
WRITE(6,*)LX,CX(1)
       J=1
       SC=DSQRT(1D0/LX)
       DO 30 I=1,LX
    IF(I.GT.J)GO TO 10
       CTEMP=CX(J)*SC
       CX(J)=CX(I)*SC
       CX(I)=CTEMP
   10       M=LX/2
   20       IF(J.LE.M)GO TO 30
       J=J-M
       M=M/2
    IF(M.GE.1)GO TO 20
   30       J=J+M
       L=1
   40       ISTEP=2*L
       DO 50 M=1,L
       CARG=(0d0,1D0)*(PI*SIGNI*(M-1))/L
       CW=CDEXP(CARG)
       DO 50 I=M,LX,ISTEP
       CTEMP=CW*CX(I+L)
       CX(I+L)=CX(I)-CTEMP
   50       CX(I)=CX(I)+CTEMP
       L=ISTEP
    IF(L.LT.LX)GO TO 40
       RETURN
       END
```

### K.3.2 Programme to process pulses for use with impedance programme

Programme inputs number of files to be processed. A time file is created and a set of pulse only files are created from combined time/pulse files.

```
DIMENSION A(2000),T(2000)
CHARACTER CAT*10,DOG*15,Z1*15,Z2*15,Z3*15,Z4*15
CHARACTER TIM*15,CA*2,FRED*2,BIN*6,FRE*3

PRINT*, 'INPUT NUMBER OF FILES TO BE PROCESSED'
READ(5,71) NM
PRINT*, 'INPUT FIRST TWO LETTERS OF REQD. OUTPUT FILE'
READ(5,70)CA
PRINT*, 'INPUT STARTING INTEGER OF REQD. OUTPUT FILE'
READ(5,71)NAN
PRINT*, 'INPUT STARTING PART OF INPUT FILE'
READ(5,70)BIN
DO 101 LL=1,NM
PRINT*, 'INPUT FILE NUMBER (NO START OR ".DAT") '
READ(5,71) NIB
WRITE(FRE,98)NIB
CAT=BIN//FRE
WRITE(FRED,81)NAN+LL-1
DOG=CA//FRED//'A'//'.DAT'
CAT=CAT//'.DAT'
OPEN(1,FILE=CAT,STATUS='UNKNOWN')
OPEN(2,FILE=DOG,STATUS='UNKNOWN')
READ(1,72)Z1,Z2,Z3,Z4

DO 5 I=1,512
READ (1,74)T(I),A(I)
A(I)=A(I)*1000.
5 CONTINUE
DO 80 I=2,500
W=(A(I)-A(15))*(A(I)-A(15))
IF (W.GT.3800.) GOTO 85
80 CONTINUE
85 CONTINUE
DO 82 J=1,20
WRITE(6,79) A(I+J-29),I+J-10,A(I+J-10),A(I+J+11)
82 CONTINUE
PRINT*,'START OF PULSE IS ?'
WRITE(6,75) CAT,DOG
C
DO 60 I=1,499
ZZ=REAL(I)
WRITE(2,*) ZZ,A(I)
60 CONTINUE
101 CONTINUE
C
70 FORMAT(A)
71 FORMAT(I20)
72 FORMAT(2A,/,2A)
74 FORMAT(2E15.10)
75 FORMAT(' THIS FILE IS ',A,' STORED AS FILE ',A)
76 FORMAT(I3,F12.5)
78 FORMAT(2E12.4)
79 FORMAT(F12.2,I6,2F12.2)
81 FORMAT(I2)
98 FORMAT(I3)
END
```

### K.3.3 Programme to sum pulses for impulse impedance measurement technique

```
C             SHIFTS ANS SUMS PULSE FILES
C
C  INPUT NUMBER OF FILES TO BE ADDED. PRODUCES A SINGLE
C  FILE OF LENGTH 512 POINTS, WITH PULSE AT 50 AND BEGINNING
C  AND END SET TO ZERO.
C
C  A SECOND FILE OF ONLY 499 POINTS IS ALSO PRODUCED FOR USE
C  WITH UNIGRAPH IF DESIRED.
C
C  THERE IS AN OPTION FOR INCLUDING A "PREPULSE" IN THE SUM FILE.
C
DIMENSION A(2000),T(2000),B(1000)
CHARACTER CAT*10,DOG*15,Z1*15,Z2*15,Z3*15,Z4*15
CHARACTER DAG*15,CA*5

NN=1
PRINT*, 'INPUT NUMBER OF FILES TO BE PROCESSED'
READ(5,71) NM
PRINT*,' DO YOU WANT ANY PREPULSE ? TYPE 1 FOR YES, 3 FOR NO'
READ(5,71) NLL
C INITIALLY ZERO SUM FILE
DO 88 I=1,512
T(I)=0.
88  CONTINUE
C ADJUSTMENT AND SUMMATION LOOP
DO 101 LL=1,NM
PRINT*, 'INPUT FILE NAME (NO "A.DAT") '
READ(5,70) CA
IF(NN.GT.1) GOTO 99
DOG=CA//'S'//'.DAT'
DAG=CA//'P'//'.DAT'
OPEN(2,FILE=DOG,STATUS='UNKNOWN')
OPEN(3,FILE=DAG,STATUS='UNKNOWN')
99  CONTINUE
NN=NN+1
CAT=CA//'A.DAT'
OPEN(1,FILE=CAT,STATUS='UNKNOWN')
DO 5 I=1,499
READ (1,*)ZZ,A(I)
5 CONTINUE
C ADJUST PULSE SO STARTS AT 50TH DATA WORD
PRINT*,' START OF PULSE IS ?  (DONT FORGET DECIMAL POINT)'
READ(5,72) P1
IF(NLL.GT.1) THEN
P2=P1
ELSE
PRINT*,' ZERO INPUT UP TO ?'
READ(5,72) P2
ENDIF
DO 80 I=1,512
B(I)=0.
80 CONTINUE
D=P1-P2
DO 82 I=1,400+D
B(I+49-D)=A(I+P2-1)
82 CONTINUE
```

```
C MAKES TAIL OF PULSE COME TO ZERO SMOOTHLY
DO 83 I=1,20
B(I+448)=B(448)-(B(448)*I/20)
83 CONTINUE
C SUMS PULSES
DO 85 I=1,512
T(I)=T(I)+B(I)
85 CONTINUE
C
101 CONTINUE
C PUTS AN AVERAGE PULSE INTO FILE
DO 60 I=1,512
ZZ=REAL(I)
WRITE(2,*) ZZ,T(I)/NM
60 CONTINUE
DO 61 I=1,499
WRITE(3,*) T(I)/NM
61 CONTINUE
WRITE(6,75) DOG,DAG
C
70 FORMAT(A)
71 FORMAT(I200)
72 FORMAT(F12.2)
73 FORMAT(I4,F12.5)
74 FORMAT(E15.10)
75 FORMAT(' DATA STORED IN ',A,' FOR CALC., IN ',A,' FOR VIEWING')
76 FORMAT(' PULSE END = ',)
78 FORMAT(2E12.4)
79 FORMAT(F12.2,I6,2F12.2)
END
C
C
```

### K.3.4 Example indirect parameter fitting programme used to deduce impedance of porous road surfaces

This programme is complete and includes the routines for calculating the mathematical functions. A similar programme is to determine the microstructural model parameters from the absorption coefficient.

```
C+
C
C ABSTRACT:
C
C Programme to deduce microstructural model parameters
C  from fitted level difference spectra.
C Programme inputs three level difference spectra and their
C associated geometries and outputs the microstructural model
C parameters which correspond to the best fitted curves
C
C The programme also requires the point of the primary ground effect
C       dip for the first spectra and the starting and finishing points
C       of the areas to be fitted. These locations are indicated by using
C       the unit number. Unit 1 being the first frequency.
C
C AUTHOR(S):
C
C  Craig Howorth (Open University 1989)
C
C CREATION DATE:
C
C  December 1989
C
C COMMON BLOCKS:
C
C COMMON /PARAM/HS,SEP,H,FLMAX,PORMAX,IFLAGW
C       ,PSFRMAX,GSFMAX,DMAX,M,RLD,RLD2,RLD3,RFREQ,FACT,
C       IS,IE,CS
C
C
C DESIGN:
C
C     {tbs}
C
C
C MODIFICATION HISTORY:
C
C  Date      | Name   | Description
C ----------------+-------+-----------------------------------------------------
C 10-10-1990     |  Craig Howorth  | Commented for passing to TRRL
C ----------------+-------+-----------------------------------------------------
C [change_entry]
C-


C ***********************************************************************
C * Main programme, reads in file names and initial parameter values *
C ***********************************************************************

IMPLICIT REAL*8(A-H)
IMPLICIT REAL*8(O-Z)
DIMENSION BL(5),BU(5),XO (5),RFREQ(400),RLD(400),H(3,2),W(80),IW(7)
DIMENSION OUT(5),RLD2(400),RLD3(400),SEP(3),HS(3),IS(3),IE(3)
COMMON /PARAM/HS,SEP,H,FLMAX,PORMAX,IFLAGW
     1 ,PSFRMAX,GSFMAX,DMAX,M,RLD,RLD2,RLD3,RFREQ,FACT,
     1  IS,IE,CS
CHARACTER*32 FILEIN,OUT,FILE2IN,FILE3IN,OUT2
  PRINT*,'INPUT NAME OF FILES WITH DATA TO BE FITTED'
READ123,FILEIN,FILE2IN,FILE3IN
```

```
PRINT *,'INPUT OUTPUT FILE NAMES ONE FOR OUTPUT PARAMETERS OTHER FOR
     1  FITTED CURVE'
READ123, OUT
READ123, OUT2
OPEN(21,FILE=OUT2,STATUS='UNKNOWN')
OPEN(2,FILE=FILEIN,STATUS='UNKNOWN')
OPEN(3,FILE=FILE2IN,STATUS='UNKNOWN')
OPEN(4,FILE=FILE3IN,STATUS='UNKNOWN')
OPEN(11,FILE=OUT,STATUS='UNKNOWN')
CALL CLEAR
PRINT*,'INPUT NUMBER OF DATA POINTS ?'
READ*,M
READ (3,*) (RFREQ(I),RLD2(I), I=1,M)
READ (4,*) (RFREQ(I),RLD3(I), I=1,M)
READ (2,*) (RFREQ(I),RLD(I), I=1,M)
C LOOP TO READ IN GEOMETRY FOR EACH LD SET UP GEOMETRY
    DO 5 I=1,3
    PRINT*, 'READ IN SOURCE HEIGHTS,SEPARATIONS,LOWER
     1     AND UPPER MIC HTS FOR FILE',I
    READ*,HS(I),SEP(I),H(I,1),H(I,2)
 5     CONTINUE
CALL CLEAR
PRINT*,' INPUT TEMPERATURE IN CELSIUS'
READ*,TEMP
CS=20.05*SQRT(273.2+TEMP)
CALL CLEAR
PRINT*, 'READ IN MAXIMUM MINIMUM VALUES OF'
PRINT*, 'FLOW RESISTIVITY'
READ*, FLMAX,FLMIN
FLOPT=(FLMAX+FLMIN)/2.
FLMAXC=FLMAX/FLMAX
FLMINC=FLMIN/FLMAX
FLOPTC=FLOPT/FLMAX
CALL CLEAR
PRINT*, 'READ IN MAXIMUM MINIMUM VALUES OF'
PRINT*, 'POROSITY'
READ*, PORMAX,PORMIN
POROPT=(PORMAX+PORMIN)/2.
PORMAXC=PORMAX/PORMAX
PORMINC=PORMIN/PORMAX
POROPTC=POROPT/PORMAX
CALL CLEAR
PRINT*, 'READ IN MAXIMUM MINIMUM VALUES OF'
PRINT*, 'PORE SHAPE FACTOR RATIO'
READ*, PSFRMAX,PSFRMIN
PSFROPT=(PSFRMAX+PSFRMIN)/2.
PSFRMAXC=PSFRMAX/PSFRMAX
PSFRMINC=PSFRMIN/PSFRMAX
PSFROPTC=PSFROPT/PSFRMAX
CALL CLEAR
PRINT*, 'READ IN MAXIMUM MINIMUM VALUES OF'
PRINT*, 'GRAIN SHAPE FACTOR'
READ*, GSFMAX,GSFMIN
GSFOPT=(GSFMAX+GSFMIN)/2.
GSFMAXC=GSFMAX/GSFMAX
GSFMINC=GSFMIN/GSFMAX
GSFOPTC=GSFOPT/GSFMAX
CALL CLEAR
PRINT*, 'READ IN MAXIMUM MINIMUM VALUES OF'
```

```
 PRINT*, 'LAYER DEPTH'
 READ*, DMAX,DMIN
 DOPT=(DMAX+DMIN)/2.
 DMAXC=DMAX/DMAX
 DMINC=DMIN/DMAX
 DOPTC=DOPT/DMAX
 CALL CLEAR
 BL(1)=FLMINC
 BU(1)=FLMAXC
 BL(2)=PORMINC
 BU(2)=PORMAXC
 BL(3)=PSFRMINC
 BU(3)=PSFRMAXC
 BL(4)=GSFMINC
 BU(4)=GSFMAXC
 BL(5)=DMINC
 BU(5)=DMAXC
 XO(1)=FLOPTC
 XO(2)=POROPTC
 XO(3)=PSFROPTC
 XO(4)=GSFOPTC
 XO(5)=DOPTC

 c The numerical search should be used if the input range of
 c expected parameters is large. The resolution of the output
 c of the search routine may be increased by incrementing the
 c order of the loops in the STARTFIND routine

 PRINT*, 'NUMERICAL SEARCH? (1,0)=(Y,N)'
 READ*, ICH
     IF (ICH.EQ.1) THEN
     PRINT*, 'ENTER UNIT NUMBER FOR SEARCH IN FIRST FILE'
     READ*, IST
            CALL STARTFIND(IST,BL,BU,XO)
     WRITE(11,*) 'STARTING FREQ IS', RFREQ(IST),'PARAMS ARE',XO
             XO(1)=XO(1)/FLMAX
     XO(2)=XO(2)/PORMAX
     XO(3)=XO(3)/PSFRMAX
     XO(4)=XO(4)/GSFMAX
     XO(5)=XO(5)/DMAX
     BL(1)=FLMINC
     BU(1)=FLMAXC
     BL(2)=PORMINC
     BU(2)=PORMAXC
     BL(3)=PSFRMINC
     BU(3)=PSFRMAXC
       BL(4)=GSFMINC
     BU(4)=GSFMAXC
             BL(5)=DMINC
     BU(5)=DMAXC
     ELSE
     CONTINUE
     ENDIF

 DO 67 ISTR=1,3
 PRINT*,'ENTER START AND STOP UNITS FOR FILE',ISTR
 READ*, IS(ISTR),IE(ISTR)
  67 CONTINUE
```

```
FACT=1.

c The next call to FUNCT1 ensures that the scaling of the returned
c function is optimized, ref NAG library manual

CALL FUNCT1(N,XO,FC)
FACT=(FC)

c Sets up initial parameters for NAG routine

IFLAG=0
 27 N=5
IFAIL=1
IBOUND=0
LIW=7
LW=80
CALL E04JAF(N,IBOUND,BL,BU,XO,F,IW,LIW,W,LW,IFAIL)
IFLAG=IFLAG+1.

C     Rerun NAG routine with returned parameters if number of
c     iterations exceeded

    IF (IFAIL.EQ.2.AND.IFLAG.EQ.1) THEN
    GOTO 27
    ELSE
    CONTINUE
    ENDIF

DO 45 L=1,5
OUT(L)=SNGL(XO(L))
 45 CONTINUE
WRITE(11,*) SNGL(FLMAX*OUT(1)),SNGL(PORMAX*OUT(2))
     1  ,SNGL(PSFRMAX*OUT(3))
     1  ,SNGL(GSFMAX*OUT(4)),SNGL(DMAX*OUT(5)),SNGL(F),IFAIL
IFLAGW=1

c Final call to FUNCT1 to write out fitted curve

CALL FUNCT1(N,XO,FC)

 123 FORMAT(A)
END
```

```
C ************************************************************************
C * Subroutine required by NAG library inputs range of parameters       *
C * to be varied XG, and number of parameters, N and returns            *
C * minimized function FC, ie difference between measured and predicted *
C * level differences and optimized parameters, XG. Note: the routine   *
C * only finds  a local minimum.                                        *
C ************************************************************************
      SUBROUTINE FUNCT1(N,XG,FC)
      IMPLICIT REAL*8(A-H),(O-Z)
      REAL*4 AE,CCCR,X,SHR,SHS,SSEP,SRK,SEXATTO,SPH
      DIMENSION H(3,2),EXATTO(3,2),SEXATTO(3),FCI(3)
      DIMENSION XG(5),SXG(5),HS(3),SEP(3),OUT(3)
      DIMENSION RLD(400),RLD2(400),RLD3(400),RFREQ(400)
      DIMENSION ZR(3,2),R(3,2),X(3,2),IS(3),IE(3),FCT(3)
      COMMON /PARAM/HS,SEP,H,FLMAX,PORMAX,IFLAGW
     1 ,PSFRMAX,GSFMAX,DMAX,M,RLD,RLD2,RLD3,RFREQ,FACT,
     1  IS,IE,CS
      COMPLEX*8 PROPC,CDENS,ZR,Y,CCC,B,P1
      COMPLEX*16 DZR,DY,DPROPC,DCDENS,PTOT
      PI=4.0D0*ATAN(1.)

      c Scales functions for use in calculating level difference

      SXG(1)=SNGL(XG(1))*FLMAX
      SXG(2)=SNGL(XG(2))*PORMAX
      SXG(3)=SNGL(XG(3))*PSFRMAX
      SXG(4)=SNGL(XG(4))*GSFMAX
      SXG(5)=SNGL(XG(5))*DMAX

      c Minimizes function for first level difference file

      DO 100 MM=1,3
      FCI(MM)=0.
      FCT(MM)=0.
      DO 201 I=IS(MM),IE(MM)
      SFREQ=SNGL(RFREQ(I))

      c Calculates complex propagation constant

      CALL PCALL(SFREQ,SXG(4),SXG(3),SXG(1),SXG(2),AE,Y,CCC,PROPC,CS)
      DPROPC=DBLE(PROPC)
      DY=DBLE(Y)
      DAE=DBLE(AE)
      DCCC=DBLE(CCC)

      c Calculates complex density

      CALL CDALL(SFREQ,SXG(4),SXG(3),SXG(1),SXG(2),CDENS,CS)
      DCDENS=DBLE(CDENS)
      RRK=REAL(PROPC)
      XK=AIMAG(PROPC)
      RK=(2.0D0*SFREQ*PI)/DBLE(CS)
      SRK=SNGL(RK)
      DO 15 II=1,2

      c Calculates impedance of rigidly backed layer

      CALL ZLRIGPOR(SFREQ,PROPC,CDENS,SXG(5)
```

```
     1   ,H(MM,II),HS(MM),SEP(MM),ZR(MM,II),CS)
R(MM,II)=REAL(ZR(MM,II))
X(MM,II)=AIMAG(ZR(MM,II))
SHR=SNGL(H(MM,II))
SHS=SNGL(HS(MM))
SSEP=SNGL(SEP(MM))

c Calculates field at receiver from modified Weyl van der Pol
c equation


CALL EXTEND(SFREQ,R(MM,II),X(MM,II)
     1   ,RRK,XK,SHR,SHS,SSEP,B,P1,PTOT,AP1,SEXATTO(MM),CS)
EXATTO(MM,II)=DBLE(SEXATTO(MM))
 15 CONTINUE
  OUT(MM)=20.0DO*DLOG10(EXATTO(MM,2)/EXATTO(MM,1))
FCI(MM)=(RLD(I)-OUT(MM))**2.
FCT(MM)=FCT(MM)+FCI(MM)
 201 CONTINUE
 100 CONTINUE

c Function to be minimized

FC=FCT(1)+FCT(2)+FCT(3)
FC=FC**0.005

c Writes out fitted level difference spectra on last call

IF (IFLAGW.EQ.1) THEN
DO 207 I=1,M
SXG(1)=SNGL(XG(1))*FLMAX
SXG(2)=SNGL(XG(2))*PORMAX
SXG(3)=SNGL(XG(3))*PSFRMAX
SXG(4)=SNGL(XG(4))*GSFMAX
SXG(5)=SNGL(XG(5))*DMAX
SFREQ=SNGL(RFREQ(I))
CALL PCALL(SFREQ,SXG(4),SXG(3),SXG(1),SXG(2),AE,Y,CCC,PROPC,CS)
DPROPC=DBLE(PROPC)
DY=DBLE(Y)
DAE=DBLE(AE)
DCCC=DBLE(CCC)
CALL CDALL(SFREQ,SXG(4),SXG(3),SXG(1),SXG(2),CDENS,CS)
DCDENS=DBLE(CDENS)
RRK=REAL(PROPC)
XK=AIMAG(PROPC)
RK=(2.0DO*SFREQ*PI)/DBLE(CS)
SRK=SNGL(RK)
DO 557 MP=1,3
DO 157 II=1,2
CALL ZLRIGPOR(SFREQ,PROPC,CDENS,SXG(5)
     1   ,H(MP,II),HS(MP),SEP(MP),ZR(MP,II),CS)
R(MP,II)=REAL(ZR(MP,II))
X(MP,II)=AIMAG(ZR(MP,II))
SHR=SNGL(H(MP,II))
SHS=SNGL(HS(MP))
SSEP=SNGL(SEP(MP))
CALL EXTEND(SFREQ,R(MP,II),X(MP,II)
     1   ,RRK,XK,SHR,SHS,SSEP,B,P1,PTOT,AP1,SEXATTO(MP),CS)
EXATTO(MP,II)=DBLE(SEXATTO(MP))
```

```
 157 CONTINUE
  OUT(MP)=20.0D0*DLOG10(EXATTO(MP,2)/EXATTO(MP,1))
 557 CONTINUE
WRITE(21,*) SNGL(SFREQ),SNGL(OUT(1)),SNGL(OUT(2)),SNGL(OUT(3))
 207 CONTINUE
ELSE
CONTINUE
ENDIF
END
```

```
c  .This programme uses the Weyl van der Pol formulae modified by Nicolas,
c    Daigle and Berry to calculate the sound propagation over a rigid
c    porous externally reacting rigidly backed layer. The inputs are the
c    frequency (f), the resistance (r) and reactance (x) of the rigidly backed
c    layer, the phase and attenuation coefficients (rrk, xk), and the level
c    difference geometry (hr, hr, sep). The pressure and magnitude of pressure
c    are returned for the direct (ap1, p1) and total waves (aptot,ptot)


SUBROUTINE EXTEND(FREQ,R,X,RRK,XK,HR,HS,SEP,B,P1,PTOT
     1  ,AP1,APTOT,CS)
COMPLEX J,CK,CG,CR1,CR2,CPI,RP,BETA,P1,P2,P3,PTOT,REFLIND
COMPLEX PE,PE2,WIZ,F,C1,C2,C4,CSSQTH,KTHETA,KTHETAM,A
COMPLEX NUMA,DENA,BNUM1,BNUM2,BDEN1,BDEN2,ZKKB1,B,WSQUARED
COMPLEX Z
REAL KO,SSQTH
BETA=CMPLX(1.0,0.0)/CMPLX(R,X)
ZKKB1=CMPLX(RRK,XK)
PI=3.141592653
KO=(2.0*PI*FREQ)/DBLE(CS)
H=HS+HR
R1=SQRT((HS-HR)**2+SEP*SEP)
R2=SQRT(H*H+SEP*SEP)
CTH=H/R2
J  =CMPLX(0.0,1.0)
C1=(1.0,0.0)
C2=(2.0,0.0)
C4=(4.0,0.0)
CG=CMPLX(CTH,0.0)
CK=CMPLX(KO,0.0)
CR1=CMPLX(R1,0.0)
CR2=CMPLX(R2,0.0)
CPI=CMPLX(PI,0.0)
Z=CMPLX(R,X)
RP=(z*cth-1.)/(z*cth+1.)
P1=CEXP(J*CK*CR1)/(C4*CPI*CK*CR1)
P2=RP*CEXP(J*CK*CR2)/(C4*CPI*CK*CR2)
WSQUARED=0.5*(J*CR2*KO)*((CTH+(1/Z))**2.)
WTESTR=REAL(WSQUARED)
WTESTI=AIMAG(WSQUARED)
IF(WTESTI.LT.0.0)WTESTI=0.0
WSQUARED=CMPLX(WTESTR,WTESTI)
PE2    =  -J*CSQRT(WSQUARED)

c Calculates complex complementary error function

CALL AW(PE2,WIZ)

F      =  C1+J*CSQRT(CPI)*CSQRT(WSQUARED)*WIZ
P3=(C1-RP)*F*CEXP(J*CK*CR2)/(C4*CPI*CK*CR2)

PTOT=P1+P2+P3
AP1=CABS(P1)
APTOT=CABS(PTOT)

RETURN
END
c
c    This programme calculates the complex complementary error function.
```

```
c   Using the solution given in Abramowitz and Stegun. The complex
c     argument is read in and the error function multiplied by $e^{z^{2}}$ is
c     returned (wiz).
c
      SUBROUTINE AW(Z,WIZ)
      LOGICAL LX,LY
      COMPLEX*8 Z,WIZ,CEFW,S,T1,T2,T3
      DATA CONS/1.128379167095/
      X=-AIMAG(Z)
      Y=REAL(Z)
      X1=Y
      Y1=-X

c Determine quadrant for z

   10 LX=X.GE.0.0
      LY=Y.GE.0.0
      IF(LX.AND.LY)IQ=1
      IF(.NOT.LX.AND.LY)IQ=2
      IF(.NOT.LX.AND..NOT.LY)IQ=3
      IF(LX.AND..NOT.LY)IQ=4

c Convert to 1st quadrant

      X=ABS(X)
      Y=ABS(Y)
      S=CMPLX(X,Y)
      XS=X
      YS=Y
  100 IF(Y.GE.4.29.OR.X.GE.5.33)GOTO 110
      S=(1.0-Y/4.29)*SQRT((1.0-(X*X)/28.41))
      H=1.6*S
      H2=2.0*H
      NCAP=6.5+23.0*S
      ALAMDA=H2**NCAP
      NU=9.5+21.0*S
      GOTO 120
  110 T1=4.613135E-1/(S*S-1.901635E-1)
      T2=9.999216E-2/(S*S-1.7844927)
      T3=2.883894E-3/(S*S-5.5253437)
      WIZ=S*(T1+T2+T3)
      V=REAL(WIZ)
      U=-AIMAG(WIZ)
      GOTO 180
  120 R1=0.0
      R2=0.0
      S1=0.0
      S2=0.0
      N=NU
  130 IF(N.LT.0)GOTO 150
      P1=N+1
      T1=Y+H+P1*R1
      T2=X-P1*R2
      C=0.5/(T1*T1+T2*T2)
      R1=C*T1
      R2=C*T2
      IF(H.EQ.0.0.OR.N.GT.NCAP)GOTO 140
      T1=ALAMDA+S1
      S1=R1*T1-R2*S2
```

```
S2=R2*T1+R1*S2
ALAMDA=ALAMDA/H2
140 N=N-1
GOTO 130
150 IF(ALAMDA.EQ.0.0)GOTO 160
U=CONS*S1
V=CONS*S2
GOTO 180
160 U=CONS*R1
V=CONS*R2
180 CEFW=CMPLX(U,V)

c Test for underflow and overflow

TEST=-XS*XS+YS*YS
IF(TEST.LT.-85.0)TEST=-85.0
IF(TEST.GT.87.)TEST=87.0

c       Test for quadrant

GOTO(230,220,210,210),IQ
210 CEFW=2.0*CEXP(CMPLX(TEST,-2.*XS*YS))-CEFW
IF(IQ.EQ.3)GOTO 230
IF(IQ.EQ.4)GOTO 220
c for 2nd and 4th quads conjugate cefw
c
220 CEFW=CONJG(CEFW)
C
C
230 WIZ=CEFW
RETURN
END
```

```
c     ************************************************************************
c     * Subroutine PCALL(f, npr, sfr, sigma, poros, ae, y, ccc, propc, cs)   *
c     * Calculates a single value of complex propagation constant (propc)using *
c     * the Rayleigh-Attenborough model, given the frequency(f),             *
c     * the tortuosity q2 (only if aq=1), grain shape factor (n prime - npr), *
c     * pore shape factor ratio (sfr), flow resistivity (sigma) and          *
c     * porosity (poros).                                                    *
c     * The functions ae, y and ccc are also returned by this subroutine in  *
c     * case they are required.                                              *
c     ************************************************************************

      SUBROUTINE PCALL(F, NPR, SFR, SIGMA, POROS, AE, Y, CCC, PROPC, CS)
      REAL MU,NUF,NPR,LAMBDAP
      COMPLEX I,Y,T,YP,TP,ZKKB,J0,J1,CCC,PROPC
      Q2 = POROS**-NPR
      Q=SQRT(Q2)
      PI=3.141592653
      I=CMPLX(0.0,1.0)
      CF=CS
      GAMMA=1.4
      PRANDTL=0.76
      SQRTNP=SQRT(PRANDTL)
      MU=181E-9
      RHOF=1.2
      NUF=MU/RHOF
      AE=8*MU*(Q**2)/(POROS*SIGMA)
      AE=AE**0.5

      OMEGA=2*PI*F
      LAMBDAP=(AE/(2.*SFR))*((OMEGA/NUF)**0.5)
      Y=SQRTNP*LAMBDAP*(I**0.5)
c
c calls Bessel function routine CMPBJ
c
      N1=0
      CALL CMPBJ(Y,N1,J0)
      N1=1
      CALL CMPBJ(Y,N1,J1)
      T=J1/J0
      CCC=1+2*((GAMMA-1)/Y)*T
      YP=LAMBDAP*(I**0.5)
      N1=0
      CALL CMPBJ(YP,N1,J0)
      N1=1
      CALL CMPBJ(YP,N1,J1)
      TP=J1/J0
      ZKKB=CCC/(1-(2/YP)*TP)
      ZKKB=ZKKB*(Q*OMEGA/CF)**2
      PROPC=ZKKB**0.5
      RETURN
      END


c     ************************************************************************
c     * Subroutine CDALL(f, npr, sfr, sigma, poros, cdens,cs)                *
c     * Calculates a single value of complex density (cdens) using the       *
c     * Rayleigh-Attenborough model given the frequency(f),                  *
c     * the tortuosity q2 (only if aq=1), grain shape factor (n prime - npr), *
```

```
c  _ * pore shape factor ratio (sfr), flow resistivity (sigma) and          *
c    * porosity (poros).                                                    *
c    ***************************************************************************

SUBROUTINE CDALL(F, NPR, SFR, SIGMA, POROS, CDENS, CS)
REAL MU,NUF,NPR,LAMBDAP
COMPLEX I,YP,TP,J0,J1,CDENS
Q2 = POROS**-NPR
Q=SQRT(Q2)
PI=3.141592653
I=CMPLX(0.0,1.0)
CF=CS
GAMMA=1.4
PRANDTL=0.76
MU=171E-7
RHOF=1.317
NUF=MU/RHOF
AE=8*MU*(Q**2)/(POROS*SIGMA)
AE=AE**0.5
OMEGA=2*PI*F
LAMBDAP=(AE/(2.*SFR))*((OMEGA/NUF)**0.5)
YP=LAMBDAP*(I**0.5)

c Calls Bessel function routine CMPBJ

N1=0
CALL CMPBJ(YP,N1,J0)
N1=1
CALL CMPBJ(YP,N1,J1)  .
TP=J1/J0
CDENS=Q**2*RHOF/((1-(2/YP)*TP)*POROS)
RETURN
END
```

```
c     ************************************************************************
c     * Subroutine ZLRIGPOR( f, propc, cdens, d, h, hs, sep, zr, cs)         *
c     * Calculates a single value of the surface impedance of a rigid-backed *
c     * layer(zr), given the frequency (fr), propagation constant(propc)     *
c     * and complex density(cdens) of the top layer and the layer depth.     *
c     ************************************************************************
SUBROUTINE ZLRIGPOR( F, PROPC, CDENS, D,
     1  H, HS, SEP, ZR, CS)
COMPLEX I,CDENS,PROPC,ZC,IKD,IKD1,ZR,CCOTH
COMPLEX ZR1,DK,CFCOST,ZR2
PI=3.141592653
I=CMPLX(0.0,1.0)
RHOF=1.2
FCOST=(SEP)/(SQRT(SEP**2.+(HS+H)**2.))
CFCOST=CMPLX(FCOST,0.)
OMEGA=2*PI*F
CF=CS
DK=OMEGA/CF
ZC=(CDENS*OMEGA)/(PROPC*RHOF*CF)

c Characteristic impedance from attenborough 4 param model
c propc is propagation constant from attenborough model
c put into nicolas daigle and berry model for rigid backed
c layer, ref: JASA 77 (1) 1985

ZR1=CSQRT(1.-(((DK**2.)/(PROPC**2.))*(CFCOST**2.)))
ZR=((ZC/ZR1)*CCOTH(-1*I*D*PROPC*ZR1))
RETURN
END

c *********************************************************
c *  Subroutine clear                                     *
c *  Clears the screen of a VT100 or VT220 type terminal. *
c       *********************************************************

subroutine clear
byte esc
data esc /"33/
write(6,20)esc,esc
20 format('+',a1,'[2J',a1,'[1;1f')
return
end

c     ***************************************************************
c     * Subroutine CMPBJ( Z,N,VAL )                                 *
C     * .... computes complex bessel function for any               *
c     * .... argument, using CBESJ.FOR and CBJ.FOR                  *
c     * Calls Subroutine CBJ or CBESJ depending on the size of the  *
c     * argument.                                                   *
c     ***************************************************************
c Test for argument
SUBROUTINE CMPBJ( Z,N,VAL )
COMPLEX Z,VAL
CABSZ = CABS( Z )
IF( CABSZ .LT. 7.0 ) THEN
CALL CBESJ( Z,N,VAL )
ELSE
CALL CBJ( Z,N,VAL )
```

```
ENDIF
RETURN
END


c     ***************************************************
c     * subroutine cbesj(x,n,cbj)                       *
c     * routine to compute complex Bessel Function Jn(x) *
c     * where x is a complex argument                   *
c     ***************************************************
SUBROUTINE CBESJ(X,N,CBJ)
COMPLEX X,CBJ,FM1,FM,BMK,ALPHA,CBPREV
CBPREV=(0.0,0.0)
D=1.0E-4
AX=CABS(X)
NTEST=20.0+10.0*AX-AX**2/3
IF(AX.GT.15.0)NTEST=90.0+AX/2.0
IF(N.LT.NTEST)GOTO 20
WRITE(6,1001)
1001 FORMAT(1X,'RANGE OF X AND N IS INCORRECT')
RETURN
20 N1=N+1
MA=AX+6.0
IF(AX.GE.5.0)MA=1.4*AX+60.0/AX
IX=AX
MB=N+IX/4+2
MO=MAXO(MA,MB)
MMAX=NTEST
DO 90 M=MO,MMAX,3
FM1=1.0E-28
FM=0.0
ALPHA=0.0
J1=1
IF(M.EQ.M/2*2)J1=-1
M2=M-2
DO 160 K=1,M2
MK=M-K
XMK=MK*2
BMK=XMK*FM1/X-FM
FM=FM1
FM1=BMK
IF(MK-N-1.EQ.0.0)CBJ=BMK
J1=-J1
S=1+J1
160 ALPHA=ALPHA+BMK*S
BMK=2.0*FM1/X-FM
IF(N.EQ.0)CBJ=BMK
ALPHA=ALPHA+BMK
CBJ=CBJ/ALPHA
IF(CABS(CBJ-CBPREV).LT.(CABS(D*CBJ)))GOTO96
90 CBPREV=CBJ
96 RETURN
END
```

```
c     ************************************************************
c     * Subroutine CBJ(x,n,j)                                    *
C     * Routine to compute complex bessel function JN(X)         *
C     * where x is complex                                       *
c     * the routine CBESSEL is used                              *
c     * if cabs(x) is greater than 7.0,otherwise CBESJ is used.  *
c     ************************************************************

c Zero and first order bessel functions of complex arguments are
c computed.
c N = 0; Zero order bessel function.
C N = 1; First order bessel function.

      SUBROUTINE CBJ(X,N,J)
      COMPLEX X,J,FM1,FM,BMK,ALPHA,CBPREV
      COMPLEX Z,CHI,EZ,T0,T1,T2,T3,T4,T5,T6,T7,P0,Q0
      COMPLEX*16 DCHI
      REAL JR,JI
      AX = CABS(X)
      IF(AX.GT.7.0) GO TO 100
      CBPREV = (0.0,0.0)
      D = 1.0E-04
      NTEST = 20.0 + 10.0*AX - AX**2/3
      IF(AX.GT.15.0) NTEST = 90.0 + AX/2.0
      IF(N.LT.NTEST) GO TO 20
      WRITE(6,1001)

 1001 FORMAT(1X,'RANGE OF X AND N IS INCORRECT' )
      RETURN
   20 N1 = N + 1
      MA = AX + 6.0
      IF(AX.GE.5.0) MA = 1.4*AX + 60.0/AX
      IX = AX
      MB = N + IX/4 + 2
      M0 = MAX0(MA,MB)
      MMAX = NTEST
      DO 90 M = M0,MMAX,3
      FM1 = 1.0E-28
      FM = 0.0
      ALPHA = 0.0
      J1 = 1
      IF(M.EQ.M/2*2) J1 = -1
      M2 = M - 2
      DO 160 K = 1,M2
      MK = M - K
      XMK = MK*2
      BMK = XMK*FM1/X - FM
      FM = FM1
      FM1 = BMK
      IF(MK-N-1.EQ.0) J = BMK
      J1 = -J1
      S = 1 + J1
  160 ALPHA = ALPHA + BMK*S
      BMK = 2.0*FM1/X - FM
      IF(N.EQ.0) J = BMK
      ALPHA = ALPHA + BMK
      J = J/ALPHA
      IF(CABS(J-CBPREV).LT.(CABS(D*J)))GO TO 200
   90 CBPREV = J
```

```
      GO TO 200

c Begin calculation using large argument series
c a. and s. equ.9.2.5 ( 8 terms are used )

  100 Z = X
      EZ = 8.0*Z
      IF(N.EQ.0) GO TO 189

c First order calculation.

      CHI = Z - 3.0*3.14159265359/4.0

c Terms in p0 and q0 series are formed by
c chain multiplication

      T0  = 1.0
      T1 = T0*(3.0/EZ)
      T2 = T1*(5.0/(2.0*EZ))
      T3 = T2*(21.0/(3.0*EZ))
      T4 = T3*(45.0/(4.0*EZ))
      T5 = T4*(77.0/(5.0*EZ))
      T6 = T5*(117.0/(6.0*EZ))
      T7 = T6*(165.0/(7.0*EZ))

c Form P0 = 1.0+T2-T4+T6

      P0 = T6 - T4
      P0 = P0 + T2
      P0 = P0 + T0

c Form Q0 = T1-T3+T5-T7

      Q0 = T5 - T7
      Q0 = Q0 - T3
      Q0 = Q0 + T1
      GO TO 199

c Zero order calculation

  189 CHI = Z - 3.14159265359/4.0

c Terms in P0 and Q0 series are formed by
c chain multiplication.

      T0  = 1.0
      T1 = T0/EZ
      T2 = T1*(9.0/(2.0*EZ))
      T3 = T2*(25.0/(3.0*EZ))
      T4 = T3*(49.0/(4.0*EZ))
      T5 = T4*(81.0/(5.0*EZ))
      T6 = T5*(121.0/(6.0*EZ))
      T7 = T6*(169.0/(7.0*EZ))

C Form P0 = 1.0-T2+T4-T6

      P0 = T4 - T6
      P0 = P0 - T2
      P0 = P0 + T0
```

```
C Form Q0 = -T1+T3-T5+T7

Q0 = T7 - T5
Q0 = Q0 + T3
Q0 = Q0 - T1
199 CONTINUE
DCHI=DCMPLX(CHI)
J = CSQRT( 2.0/(3.14159265359*Z))*(P0*CDCOS(DCHI)-
     & Q0*CDSIN(DCHI) )

c End of calculation using series expression.

200 CONTINUE
XR = REAL( X )
XI = AIMAG( X )
JR = REAL( J )
JI = AIMAG( J )

c For zeroth order function:
c - IF XR=0.0 OR XI=0.0 THEN J IS REAL.
c - Thus set imag. result to zero.

IF(((XR.EQ.0.0).OR.(XI.EQ.0.0)).AND.(N.EQ.0))JI = 0.0

c For first order function
c - IF XI = 0.0 THEN J IS REAL
c - Thus set imag. result to zero

c - IF XR = 0.0 THEN J IS IMAGINARY
c - Thus set real result to zero

IF((XI.EQ.0.0).AND.(N.EQ.1)) JI = 0.0
IF((XR.EQ.0.0).AND.(N.EQ.1)) JR = 0.0
J = CMPLX(JR,JI)
RETURN
END
```

```
c     ****************************************************************
c     * complex function ccoth(z)                                    *
c     * calculates coth of a complex number if the real part of z is *
c     * large then ccoth(z) is equal to 1 + i0                       *
c     ****************************************************************
      COMPLEX FUNCTION CCOTH(Z)
      COMPLEX Z,I
      I=CMPLX(0.0,1.0)
      IF (REAL(Z) .GT. 44.3) THEN
        CCOTH=(1.0,0.0)
      RETURN
      ELSE
      RZ2=2.*REAL(Z)
      AZ2=2.*AIMAG(Z)
      C1=COSH(RZ2)-COS(AZ2)
      CCOTH=(SINH(RZ2)-I*SIN(AZ2))/C1
      END IF
      RETURN
      END

c ****************************************************************
c       * Routine uses simple numerical search to locate global minima. *
c * Resolution of search can be found by incrementing loops.      *
c       * Search is carried out at primary dip of first spectra.        *
c       ****************************************************************
      SUBROUTINE STARTFIND(IST,BL,BU,XO)
      IMPLICIT REAL*8(A-H)
      IMPLICIT REAL*8(O-Z)
      DIMENSION BL(5),BU(5),RFREQ(400),XO(5)
      DIMENSION XG(5),BVAR(5),HS(3),H(3,2),SEP(3)
      DIMENSION RLD(400),RLD2(400),RLD3(400),IS(3),IE(3)
      COMMON /PARAM/HS,SEP,H,FLMAX,PORMAX,IFLAGW
           1 ,PSFRMAX,GSFMAX,DMAX,M,RLD,RLD2,RLD3,RFREQ,FACT
           1  ,IS,IE,CS
      IFR=IST
      DFREQ=RFREQ(IST)
      BU(1)=BU(1)*FLMAX
      BL(1)=BL(1)*FLMAX
      BU(2)=BU(2)*PORMAX
      BL(2)=BL(2)*PORMAX
      BU(3)=BU(3)*PSFRMAX
      BL(3)=BL(3)*PSFRMAX
      BU(4)=BU(4)*GSFMAX
      BL(4)=BL(4)*GSFMAX
      BU(5)=BU(5)*DMAX
      BL(5)=BL(5)*DMAX
      BVAR(1)=(BU(1)-BL(1))/30.
      BVAR(2)=(BU(2)-BL(2))/15.
      BVAR(3)=(BU(3)-BL(3))/15.
      BVAR(4)=(BU(4)-BL(4))/15.
      BVAR(5)=(BU(5)-BL(5))/8.
       10 CONTINUE
      DMIN=999.99
      DO 11 I=1,30
      RI=REAL(I)
      XG(1)=BL(1)+(RI*BVAR(1))
      DO 11 II=1,15
      RII=REAL(II)
```

```
XG(2)=BL(2)+(RII*BVAR(2))
DO 11 III=1,15
RIII=REAL(III)
XG(3)=BL(3)+(RIII*BVAR(3))
DO 11 IIII=1,15
RIIII=REAL(IIII)
XG(4)=BL(4)+(RIIII*BVAR(4))
DO 11 IIIII=1,8
RIIIII=REAL(IIIII)
XG(5)=BL(5)+(RIIIII*BVAR(5))
CALL DIFF(DFREQ,XG,IST,FC)
IF (FC.LT.DMIN) THEN
DMIN=FC
XO(1)=XG(1)
XO(2)=XG(2)
XO(3)=XG(3)
XO(4)=XG(4)
XO(5)=XG(5)
ELSE
CONTINUE
ENDIF
 11 CONTINUE
END


c *******************************************************
c       * Calculates minima of function for first spectra only. *
c       *******************************************************
SUBROUTINE DIFF(SFREQ,XB,IST,FC)
IMPLICIT REAL*8(A-H),(O-Z)
REAL*4 AE,CCCR,X,SHR,SHS,SSEP,SRK,SEXATTO,SPH
REAL *4 SXG,SFREQ
DIMENSION HS(3),EXATTO(2),RFREQ(400),ZR(2),R(2),X(2)
DIMENSION XB(5),SXG(5),RLD(400),RLD2(400),RLD3(400)
DIMENSION SEP(3),H(3,2),IS(3),IE(3)
COMMON /PARAM/HS,SEP,H,FLMAX,PORMAX,IFLAGW
     1  ,PSFRMAX,GSFMAX,DMAX,M,RLD,RLD2,RLD3,RFREQ,FACT
     1  ,IS,IE,CS
COMPLEX*8 PROPC,CDENS,ZR,Y,CCC,B,P1
COMPLEX*16 DZR,DY,DPROPC,DCDENS,PTOT
PI=4.0DO*ATAN(1.)
DO 25 II=1,5
SXG(II)=SNGL(XB(II))
 25 CONTINUE
SFREQ=SNGL(SFREQ)
CALL PCALL(SFREQ,SXG(4),SXG(3),SXG(1),SXG(2),AE,Y,CCC,PROPC,CS)
DPROPC=DBLE(PROPC)
DY=DBLE(Y)
DAE=DBLE(AE)
DCCC=DBLE(CCC)
CALL CDALL(SFREQ,SXG(4),SXG(3),SXG(1),SXG(2),CDENS,CS)
DCDENS=DBLE(CDENS)
RRK=REAL(PROPC)
XK=AIMAG(PROPC)
RK=(2.0DO*SFREQ*PI)/DBLE(CS)
DO 15 II=1,2
CALL ZLRIGPOR(SFREQ,PROPC,CDENS,SXG(5)
     1  ,H(1,II),HS(1),SEP(1),ZR(II),CS)
R(II)=REAL(ZR(II))
```

```
X(II)=AIMAG(ZR(II))
  SHR=SNGL(H(1,II))
SHS=SNGL(HS(1))
SSEP=SNGL(SEP(1))
SRK=SNGL(RK)
CALL EXTEND(SFREQ,R(II),X(II)
     1   ,RRK,XK,SHR,SHS,SSEP,B,P1,PTOT,AP1,SEXATTO,CS)
EXATTO(II)=DBLE(SEXATTO)
 15 CONTINUE
OUT=20.0D0*DLOG10(EXATTO(2)/EXATTO(1))
FC=(RLD(IST)-OUT)**2.
FC=FC**0.005
END
```

## K.3.5 Example of indirect, resistance and reactance fitting, impedance measurement programme

```
C
C ABSTRACT:
C
C  Indirect fitting routine for variation of R and X externally
C  reacting medium
C
C AUTHOR(S):
C
C  Craig Howorth
C
C CREATION DATE:
C
C  30/5/1990
C
C
C MODIFICATION HISTORY:
C
C  Date      | Name  | Description
C ----------------+-------+-----------------------------------------------------
C [change_entry]
C-
IMPLICIT REAL*8(A-H),(O-Z)
  DIMENSION FREQ(3,500),RLD(3,500),HS(3),HR(3,2),SEP(3)
     1  ,IW(8),W(80),BL(4),BU(4),XG(4)
     1  ,RRES(500),XRES(500),SC(4),RRK2(500),XRK2(500)
COMMON NF,HS,HR,SEP,FREQ,RLD,FACTOR,SC
       COMMON /C2/LNP,RS,XS,RH,XH,RL,XL,RK2H,RK2L,XK2H,XK2L
CHARACTER*32 FILEI(3),FILEOUT,FILEOUT2
PRINT*,'INPUT NAME OF QUTPUT FILE'
READ100,FILEOUT
OPEN(10,FILE=FILEOUT,STATUS='UNKNOWN')
PRINT*, 'INPUT NUMBER OF FILES TO BE PROCESSES AND NUMBER
     1  OF POINTS IN EACH FILE'
READ*, NF,NP
DO 10 I=1,NF
PRINT*,'INPUT NAME OF FILE',I
READ 100, FILEI(I)
OPEN(I,FILE=FILEI(I),STATUS='UNKNOWN')
READ(I,*)(FREQ(I,J),RLD(I,J), J=1,NP)
PRINT*, 'INPUT SOURCE HEIGHT, LOWER AND UPPER RECEIVER HEIGHTS
     1  AND SOURCE RECEIVER SEPARATION FOR L.D.',I
READ*, HS(I),HR(I,1),HR(I,2),SEP(I)
 10 CONTINUE
PRINT*,'INPUT HIGHEST AND LOWEST RESISTANCE'
READ*,RH,RL
PRINT*,'INPUT HIGHEST AND LOWEST REACTANCE'
READ*,XH,XL
PRINT*,'INPUT HIGHEST AND LOWEST REAL PART
     1  OF PROPAGATION CONSTANT'
READ*,RK2H,RK2L
PRINT*,'INPUT HIGHEST AND LOWEST IMAGINARY PART
     1   OF PROPAGATION CONSTANT'
READ*,XK2H,XK2L
 200 DO 50 LNP=83,83,1
         CALL RXSTART(LNP,RH,XH,RL,XL,RK2H,RK2L
     1    ,XK2H,XK2L,NF,HS,HR,SEP,FREQ,RLD,FACTOR,RS,XS,RK2,
     1  XK2)
  SC(1)=RH
  SC(2)=XH
```

```
      SC(3)=RK2H
      SC(4)=XK2H
      BU(1)=SC(1)/SC(1)
      BL(1)=RL/SC(1)
      BU(2)=SC(2)/SC(2)
      BL(2)=XL/SC(2)
      BU(3)=SC(3)/SC(3)
      BL(3)=RK2L/SC(3)
      BU(4)=SC(4)/SC(4)
      BL(4)=XK2L/SC(4)
      XG(1)=RS/SC(1)
      XG(2)=XS/SC(2)
      XG(3)=RK2/SC(3)
      XG(4)=XK2/SC(4)
    FACTOR=1.
    N=4
    CALL FUNCT1(N,XG,FC)
    FACTOR=FC
    NU=4
    IBOUND=0
    LIW=8
    LW=80
    IFAIL=1
    CALL E04JAF(NU,IBOUND,BL,BU,XG,F,IW,LIW,W,LW,IFAIL)
    RRES(LNP)=XG(1)*SC(1)
    XRES(LNP)=XG(2)*SC(2)
    RRK2(LNP)=XG(3)*SC(3)
    XRK2(LNP)=XG(4)*SC(4)
    WRITE(10,*) FREQ(1,LNP),RRES(LNP),XRES(LNP),RRK2(LNP),XRK2(LNP)
     50 CONTINUE
     100 FORMAT(A)
    END


    C ***************************************************************
    SUBROUTINE RXSTART(LNP,RH,XH,RL,XL,RK2H,RK2L,XK2H,
         1  XK2L,NF,HS,HR,SEP,FREQ,RLD,FACTOR,RS,XS,RK20,XK20)
    IMPLICIT REAL*8(A-H),(O-Z)
    DIMENSION FREQ(3,500),HS(3),HR(3,2),RLDIFF(3)
         1  ,SEP(3),RLD(3,500),DIFF(3)
    COMPLEX*16 PTOT(2)
    COMPLEX*8 PTOT1(2)
    DMIN=99.D20
    SFREQ=FREQ(1,LNP)
     67 IFLAG=IFLAG+1.
    STEP=10.
    ISTEP=INT(STEP)
    PRK2INC=(RK2H-RK2L)/STEP
    PXK2INC=(XK2H-XK2L)/STEP
    RINC=(RH-RL)/STEP
    XINC=(XH-XL)/STEP
    R=RL-RINC
    DO 30 II=1,ISTEP
    R=R+RINC
    X=XL-XINC
    PRK2=RK2L-PRK2INC
    PXK2=XK2L-PXK2INC
    DO 40 JJ=1,ISTEP
```

```
X=X+XINC
PRK2=RK2L-PRK2INC
PXK2=XK2L-PXK2INC
DO 45 III=1,ISTEP
PRK2=PRK2+PRK2INC
PXK2=XK2L-PXK2INC
DO 46 JJJ=1,ISTEP
PXK2=PXK2+PXK2INC
DO 75 INF=1,NF
DO 50 KK=1,2
SH=HS(INF)
HRH=HR(INF,KK)
SP=SEP(INF)
CALL EWVP(SNGL(SFREQ),SNGL(R),SNGL(X),SNGL(PRK2),SNGL(PXK2)
     1   ,SNGL(HRH),SNGL(SH),SNGL(SP),PTOT1(KK))
PTOT(KK)=DCMPLX(PTOT1(KK))
 50 CONTINUE
RLDIFF(INF)=20.*DLOG10(CDABS(PTOT(2))/CDABS(PTOT(1)))
DIFF(INF)=(RLD(INF,LNP)-RLDIFF(INF))**2.
 75     CONTINUE
DIFFT=DIFF(1)+DIFF(2)+DIFF(3)
DIFFT=(DIFFT)**0.005
    IF (DIFFT.LT.DMIN) THEN
    DMIN=DIFFT
    RS=R
    XS=X
    RK20=PRK2
    XK20=PXK2
    ELSE
    CONTINUE
    ENDIF
 46 CONTINUE
 45 CONTINUE
 40 CONTINUE
 30 CONTINUE
IF (IFLAG.LE.2) THEN
RH=RS+RINC
RL=RS-RINC
RK2H=RK20+PRK2INC
XK2H=XK20+PXK2INC
XH=XS+XINC
XL=XS-XINC
RK2L=RK20-PRK2INC
XK2L=XK20-PXK2INC
GOTO 67
ELSE
CONTINUE
ENDIF
END



SUBROUTINE FUNCT1(N,XC,FC)
IMPLICIT REAL*8 (A-H),(O-Z)
COMMON NF,HS,HR,SEP,FREQ,RLD,FACTOR,SC
       COMMON /C2/LNP,RS,XS,RH,XH,RL,XL,RK2H,RK2L,XK2H,XK2L
DIMENSION XC(4),HS(3),HR(3,2),SEP(3),DIFF(3),FREQ(3,500)
     1   ,RLD(3,500),SFREQ(500),SC(4)
COMPLEX*16 PTOT(2)
```

```
FCST=0.
DO 20 I=1,NF
SFREQ(I)=FREQ(I,LNP)
DO 30 J=1,2
SH=HS(I)
HRH=HR(I,J)
SP=SEP(I)
R=XC(1)*SC(1)
X=XC(2)*SC(2)
RK2=XC(3)*SC(3)
AK2=XC(4)*SC(4)
CALL EWVP(SFREQ(I),R,X,RK2,XK2,HRH,SH,SP,PTOT(J))
 30 CONTINUE
DIFF(I)=20.*DLOG10(CDABS(PTOT(2))/CDABS(PTOT(1)))
FCST= FCST+((RLD(I,LNP)-DIFF(I))**2.)
FC=((FCST)**0.005)/FACTOR
 20 CONTINUE
END
```

## K.4 Programmes used in conjunction with study of porous road surfaces

This section includes the programmes used when studying the acoustical properties of porous road surfaces. It contains only the driver programmes as the subroutines used to calculate, for example the microstructural model values, have been listed previously.

### K.4.1 Programme to calculate the characteristic impedance using the phenomenological model

The is programme uses the phenomenological model to calculate characteristic impedance. The input parameters are the frequency (f), the flow resistivity (fres) the porosity (poros) and the structure factor or grain shape (gsf) depending on whether the Bruggeman relationship is applied. The characteristic impedance (zpca) and the impedance of a rigid backed layer (zpa) are returned.

```
SUBROUTINE PHEN(F,FRES,POROS,GSF,D,H,SEP,HS,PKA,ZPA,ZPCA)
COMPLEX ZPA,ZPCA,CGAM,CKK,PKA,W2,W3
COMPLEX CPOROS,CFRES,CO,I,ZPC1,CIKD
COMPLEX CCIKD,CCOTH,ZR1,CFCOST
RKK=(POROS)**(-1.*GSF)
CKK=CMPLX(RKK,0.)
RO=2.0*3.141592653*F
CO=CMPLX(RO)
CPOROS=CMPLX(POROS,0.)
CFRES=CMPLX(FRES,0.)
I=CMPLX(0.0,1.0)
W2=(CFRES*CPOROS)/(CO*CMPLX(1.2,0.)*CKK)
W3=CSQRT(cmplx(1.,0.)+I*W2)
DK=RO/343.
      ZPCA=((CSQRT(CKK)/CPOROS)*W3)
PKA=DK*(CPOROS*ZPCA)
c
c characteristic impedance zpca
c propagation constant pka
c
FCOST=(SEP)/(SQRT((SEP**2.)+((HS+H)**2.)))
CFCOST=CMPLX(FCOST)
ZR1=CSQRT(1.-(((DK**2.)/(PKA**2.))*(CFCOST**2.)))
ZPA=((ZPCA/ZR1)*CCOTH(-1*I*D*PKA*ZR1))
END
```

### K.4.2 Programme to calculate sound field from extended source

This programme is used to calculate the level difference from an extended source using nicolas daigle and berry, the 5 parameter model and an extended source. Specific point source locations are required.

```
c
c Summation of total sound pressure due to an extended source
c
      IMPLICIT REAL*8 (A-H,O-Z)
      REAL*8 KO,LD1,LD2,LD3
      REAL*4 SHP,SSEP,SRLD,SFREQ,SPOROR,SFRES,SGS,SPS,SHR
      COMPLEX*8 PROPC,CCC,Y,CDENS,ZR,PTOT
      COMPLEX*16 PD,PR,BETA,RP,RPTERM,PE,PE2,WIZ,F,RTPI,PD1,PR1,ZRD
     1           ,DPROPC,PTOTT
      CHARACTER*20 OFILE,IFILE
      DIMENSION R1(20,2),R2(20,2),CTH(20,2),TOTAL(2),HR(2),
     1          P1(2),P2(2),XS(10),YS(10),ZS(10),SEP(10),FREQ(200)
      PARAMETER (PI2V0=1.82651D-2,RTPI=(0.0,1.77245D0),
     1           PI = 3.14159265358979D0)
c
c   pi = 3.1415926    and     v0 = 344.0 m/s
c   rtpi = sqrt(pi)   and  pi2v0 = 2*pi/v0
c
      PRINT*,' NAME OF OUTFILE FILE?'
      READ(5,'(A20)')OFILE
      PRINT*,' NAME OF INPUT FILE?'
      PRINT*,' '
      PRINT*,' Press RETURN if you want interactively'
      READ(5,'(A20)')IFILE
      IF(IFILE .NE. ' ')THEN
       OPEN(5,FILE=IFILE,STATUS='OLD')
      ELSE
       PRINT*,' DO YOU WANT TO SAVE COMMANDS (Y/N)?'
       READ(5,'(A1)')ANS
       IF(ANS .EQ. 'Y')THEN
        PRINT*,' '
        PRINT*,' INPUT FILE NAME TO SAVE COMMANDS NOW!'
        READ(5,'(A20)')ICOM
        OPEN(3,FILE=ICOM,STATUS='NEW')
       ENDIF
      ENDIF
1     CONTINUE
      PRINT*,' iNPUT FLOW RESISTIVITY,POROSITY,GRAIN SHAPE,PORE SHAPE
     1 AND LAYER DEPTH'
      READ(5,*) FRES,POROS,GS,PS,RLD
      IF(ANS .EQ. 'Y')WRITE(3,'(1P5E15.7)')FRES,POROS,GS,PS,RLD
      PRINT*,' WHAT IS THE LOWER AND UPPER RECEIVER HEIGHTS?'
      READ(5,*)HR(1),HR(2)
      IF(ANS .EQ. 'Y')WRITE(3,'(1PE15.7)')HR(1),HR(2)
c
c Set up the direct and reflected path lengths for individual element.
c
      PRINT*,' TOTAL NO. OF POINT SOURCES ?'
      READ(5,*)ITL
      IF(ANS .EQ. 'Y')WRITE(3,'(I7)')ITL
      DO 10 I1 = 1 , ITL
        PRINT*,'WHAT IS THE RANGE,HEIGHT
     1  AND LATERAL DISPLACEMENT OF SOURCE',I1
        READ(5,*) XS(I1),YS(I1),ZS(I1)
        IF(ANS .EQ. 'Y')WRITE(3,'(1P2E15.7)')XS(I1),YS(I1),ZS(I1)
c
c Set up the path length for upper and lower receivers
c i2 = 1  : lower receiver    ; i2 = 2  : upper receiver
c
```

```
SEP(I1)=SQRT(XS(I1)*XS(I1)+ZS(I1)*ZS(I1))
        RSQ = XS(I1)*XS(I1)+ZS(I1)*ZS(I1)
        DO 10 I2 = 1, 2
          HH = YS(I1) + HR(I2)
          R1(I1,I2) = DSQRT(RSQ+(YS(I1)-HR(I2))**2)
          R2(I1,I2) = DSQRT(RSQ+HH*HH)
          CTH(I1,I2)= HH/R2(I1,I2)
10     CONTINUE
      OPEN(2,FILE=OFILE,STATUS='NEW')
C
C Calculate the total sound pressure due to the contributions from each
c point source.
c
      DO 50 KK = 1, 114
if (KK.eq.1) THEN
FREQ(KK)=100.
ELSE
FREQ(KK)=FREQ(KK-1)*2.**0.05
ENDIF
       FTEMP=FREQ(KK)
       KO=PI2VO*FTEMP
c
c Loop through each element.
c
       DO 55 I2 = 1, 2
         PTOTT=0.0D0
c Calculate the acoustical characteristics of the surface material
c at each frequency given the microstructural model parameters
SFREQ=SNGL(FTEMP)
SGS=SNGL(GS)
SPS=SNGL(PS)
SPOROS=SNGL(POROS)
SFRES=SNGL(FRES)
CALL PCALL(SFREQ,SGS,SPS,SFRES,SPOROS,AE,YY,CCC,PROPC)
        CALL CDALL(SFREQ,SGS,SPS,SFRES,SPOROS,CDENS)
         DO 60 I1 = 1, ITL
c
c     Calculate angular dependant impedance for each point source
c
         SRLD=SNGL(RLD)
 SHR=SNGL(HR(I2))
 HP=YS(I1)+HR(I2)
 SHP=SNGL(HP)
 SSEP=SNGL(SEP(I1))
 CALL ZLRIGPOR(SFREQ,PROPC,CDENS,SRLD,SHP,SSEP,ZR)
         ZRD=CMPLX(ZR)
 RR=DREAL(ZRD)
 RX=DIMAG(ZRD)
 DPROPC=CMPLX(PROPC)
 RRK=DREAL(DPROPC)
 XK=DIMAG(DPROPC)
 CALL EXTEND(SFREQ,RR,RX,RRK,XK,SHR,SNGL(YS(I1)),SSEP,PTOT)
 PTOTT=PTOTT+CABS((PTOT)**2.)
 60     CONTINUE
       TOTAL(I2)=CDABS(PTOTT)
 55    CONTINUE
       LD1=10.0D0*DLOG10(TOTAL(2)/TOTAL(1))
       WRITE(2,'(1P6E15.4)')FTEMP,LD1
50    CONTINUE
```

### K.4.3 Road surface optimization programme

This section includes the driver programme for the optimization routine. The other subroutines used are listed in the other sections.

```
DIMENSION FR(100),SP(100),SPA(100),FRES(2),POROS(2)
    1  ,GS(2),PS(2),RLD(2),EA(100),RS(100),RSA(100)
CHARACTER*58 SPIN,SPOUT,DAOUT
PRINT*, 'PROGRAMME CAN BE USED FOR DOUBLE RIGID BACKED LAYER
     1  DOUBLE LAYER WITH SEMI INFINITE BACKING, MAKE RLD(2) LARGE
     1  OR SINGLE BACKED LAYER. IF WANT SINGLE BACKED LAYER ENTER 1'
READ*, ICH
PRINT*, 'INPUT NAME OF FILE WITH INPUT SPECTRA'
READ123, SPIN
OPEN(11,FILE=SPIN,STATUS='UNKNOWN')
PRINT*, 'INPUT NAME OF FILE FOR OUTPUT SPECTRA'
READ123,SPOUT
OPEN(13,FILE=SPOUT,STATUS='UNKNOWN')
PRINT*, 'INPUT NAME OF FILE FOR OUTPUT DATA'
READ123, DAOUT
OPEN(12,FILE=DAOUT,STATUS='UNKNOWN')
PRINT*, 'INPUT FLOW RESISTIVITY, POROSITY,GRAIN SHAPE,PORE SHAPE
     1  AND LAYER DEPTH OF TOP LAYER'
READ*, FRES(1),POROS(1),GS(1),PS(1),RLD(1)
PRINT*, 'INPUT FLOW RESISTIVITY, POROSITY,GRAIN SHAPE,PORE SHAPE
     1  AND LAYER DEPTH OF BOTTOM LAYER'
READ*, FRES(2),POROS(2),GS(2),PS(2),RLD(2)
PRINT*, 'INPUT SOURCE HEIGHT, RECEIVER HEIGHT AND SEPARATION'
READ*, HS,HR,SEP
DO 30 II= 1,15
READ (11,*) FR(II),SP(II)
 30 CONTINUE
RLS=0.
RMS=0.
RLSA=0.
RMSA=0.
DO 10 I=1,15
        CALL WA(I,FR(I),SP(I),SPA(I))
CALL MICRO(FR(I),ICH,FRES,POROS,GS,PS,RLD,HS,HR,SEP,EA(I))
RS(I)=SP(I)+EA(I)-6
c
c   Performs A weighting
c
CALL WA(I,FR(I),RS(I),RSA(I))
c
c   Calculates linear and A' weighted sound reduction
c
RLS=RLS+(10.**(SP(I)/10.))
RMS=RMS+(10.**(RS(I)/10.))
RLSA=RLSA+(10.**(SPA(I)/10.))
RMSA=RMSA+(10.**(RSA(I)/10.))
c WRITE (13,*) FR(I),SP(I),RS(I)
 10  CONTINUE
RLS=10.*LOG10(RLS)
RLSA=10.*LOG10(RLSA)
RMS=10.*LOG10(RMS)
RMSA=10.*LOG10(RMSA)
WRITE (6,*) FRES(1),GS(1),'Linear',RLS-RMS,'A wt',RLSA-RMSA
 123 FORMAT(A)
END


SUBROUTINE WA(I,FR,SP,SPA)
c
```

```
c   Subroutine to calculate 'A' weighting
c
IF (I.EQ.1) SPA=SP-19.1
IF (I.EQ.2) SPA=SP-16.1
IF (I.EQ.3) SPA=SP-13.4
IF (I.EQ.4) SPA=SP-10.9
IF (I.EQ.5) SPA=SP-8.6
IF (I.EQ.6) SPA=SP-6.6
IF (I.EQ.7) SPA=SP-4.8
IF (I.EQ.8) SPA=SP-3.2
IF (I.EQ.9) SPA=SP-1.9
IF (I.EQ.10) SPA=SP-0.8
IF (I.EQ.11) SPA=SP-0.0
IF (I.EQ.12) SPA=SP+0.6
IF (I.EQ.13) SPA=SP+1.0
IF (I.EQ.14) SPA=SP+1.2
IF (I.EQ.15) SPA=SP+1.3
IF (I.EQ.16) SPA=SP+1.2
IF (I.EQ.17) SPA=SP+1.0
IF (I.EQ.18) SPA=SP+0.5
IF (I.EQ.19) SPA=SP-0.1
IF (I.EQ.20) SPA=SP-0.1
IF (I.EQ.21) SPA=SP-2.5
END
```

# Appendix L

# Photographic section

This appendix contains photographs of some of the measurement techniques used in the thesis

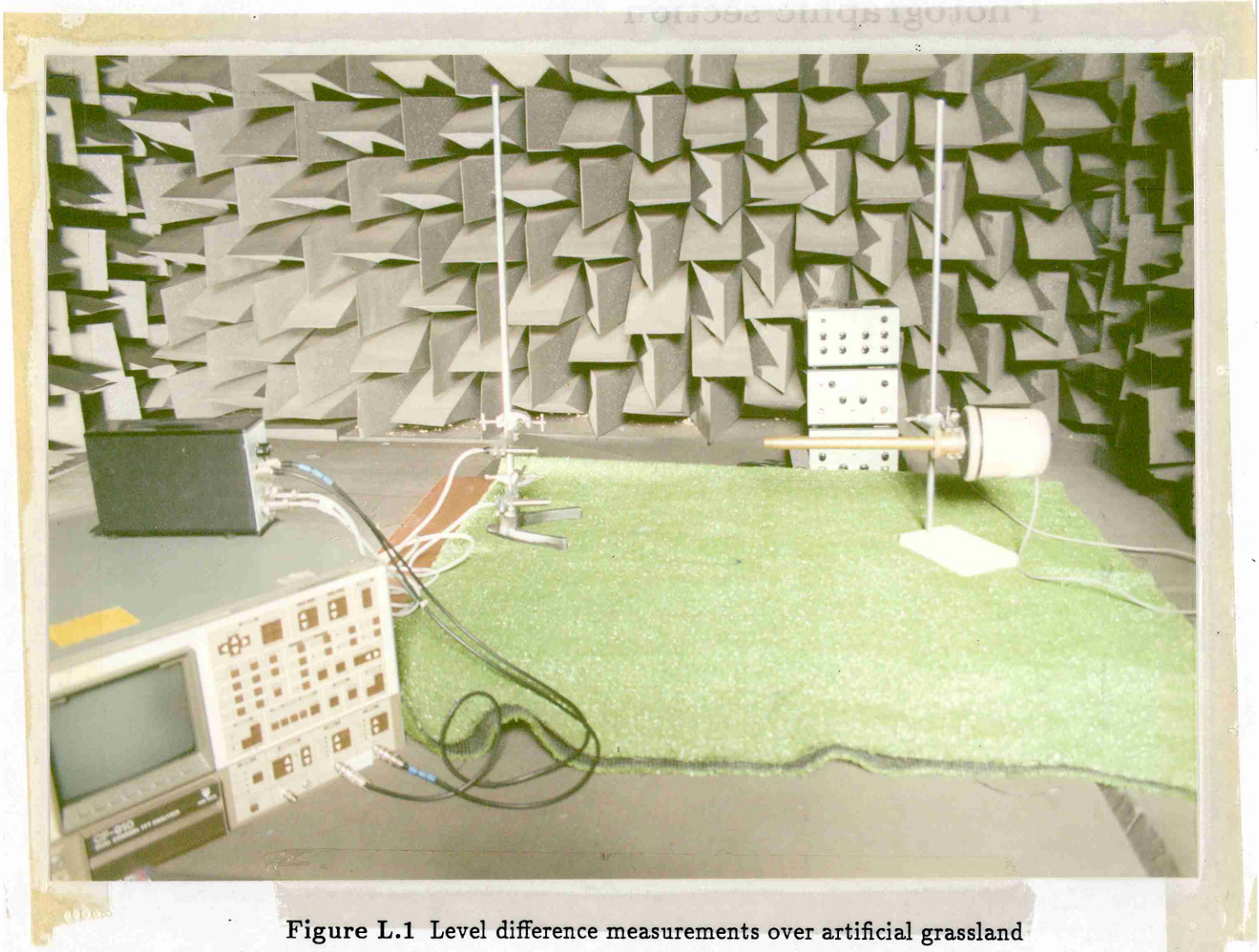

**Figure L.1** Level difference measurements over artificial grassland

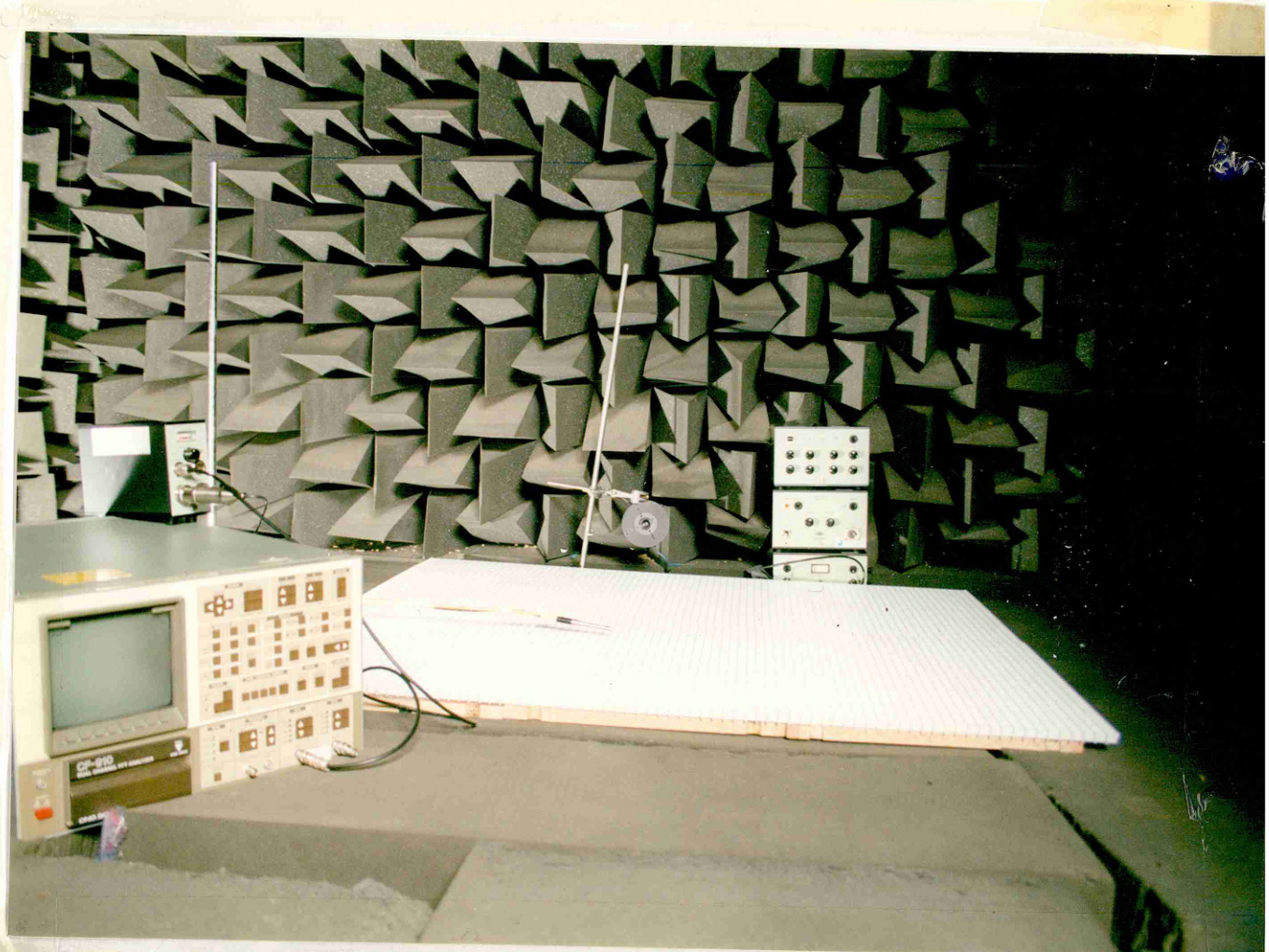

**Figure L.2** Surface wave experiments over lattice work

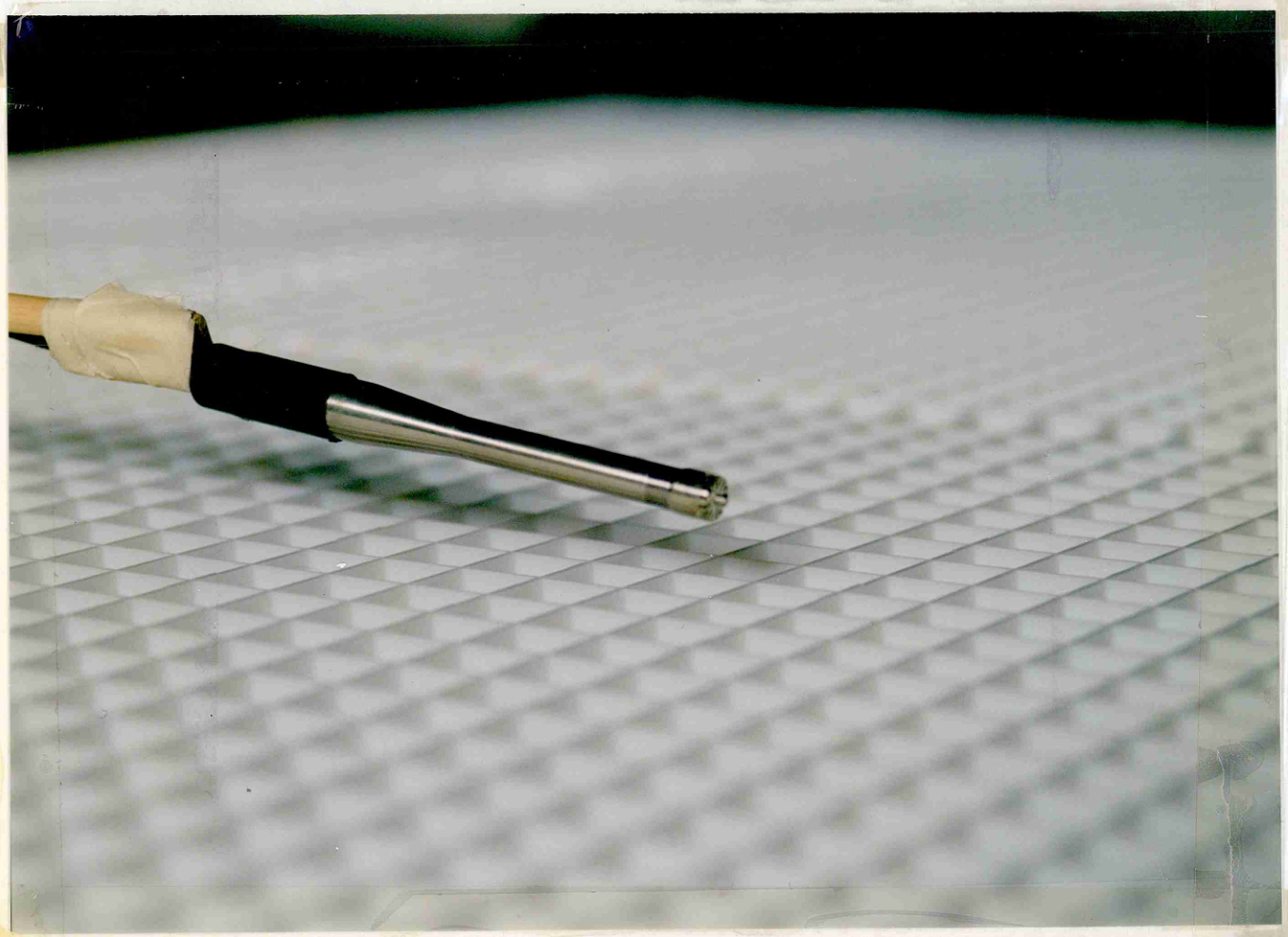

**Figure L.3** Details of surface wave experiments over lattice work

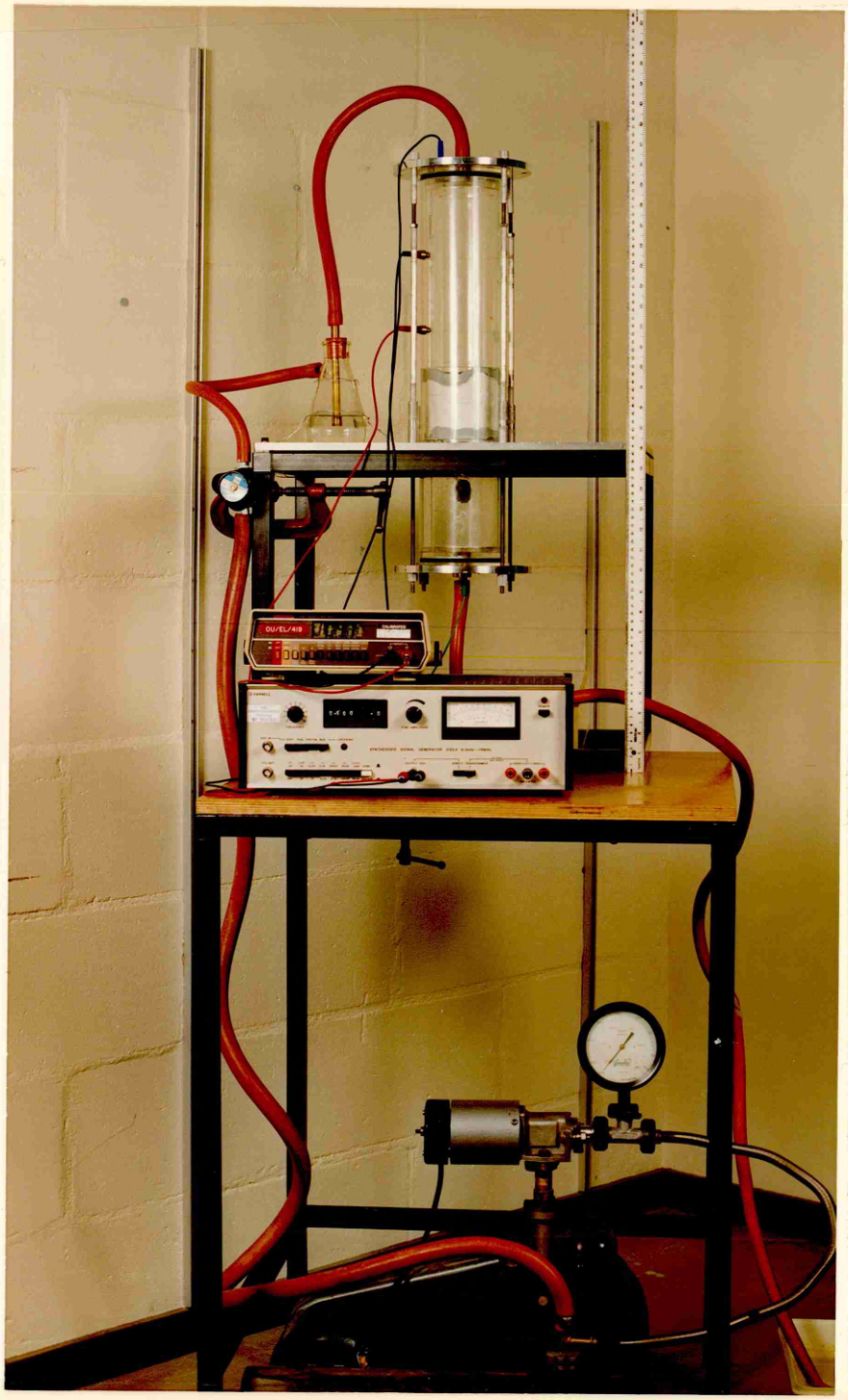

Figure L.4 Tortuosity rig

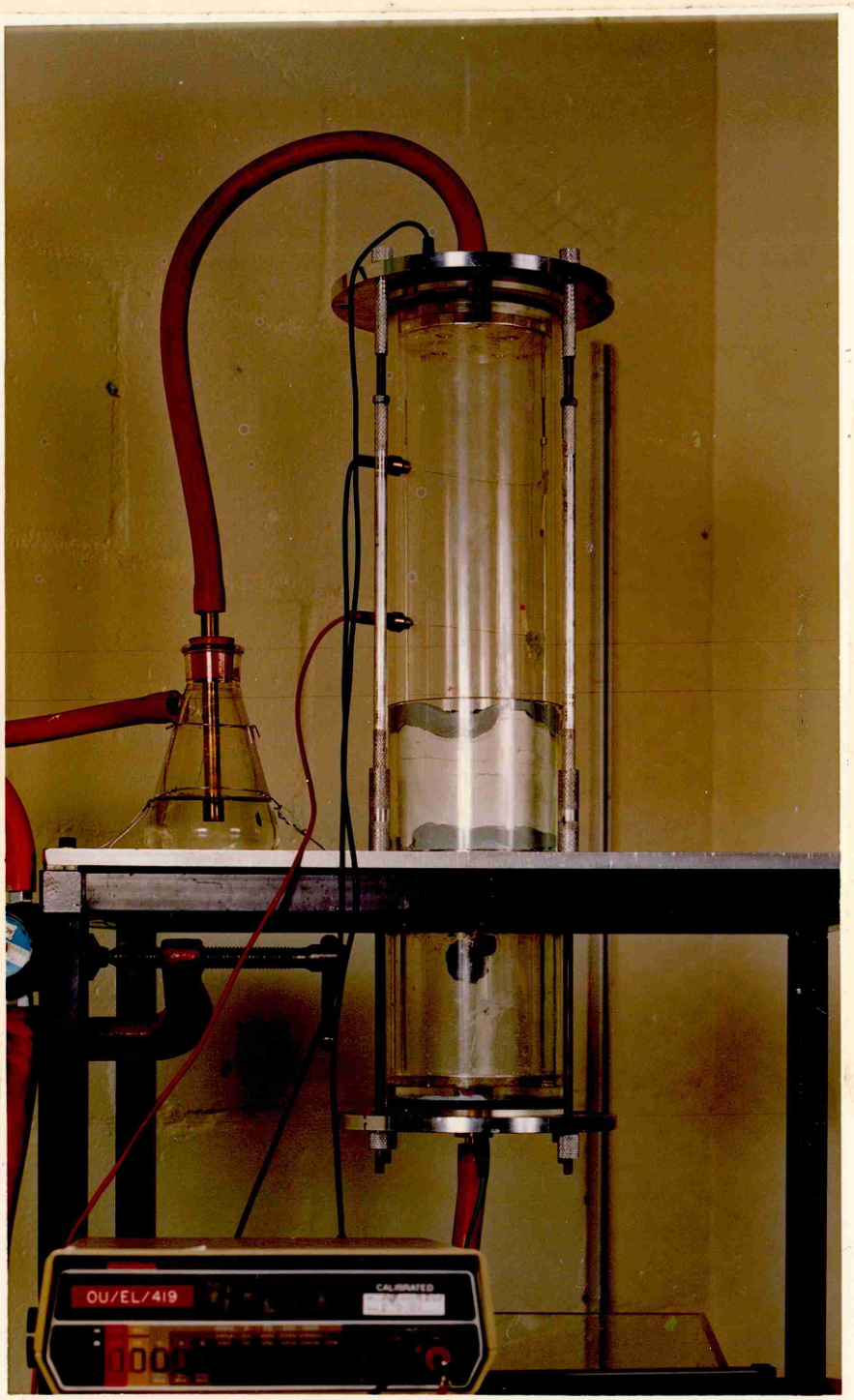


**Figure L.5** Details of sample holder of tortuosity rig

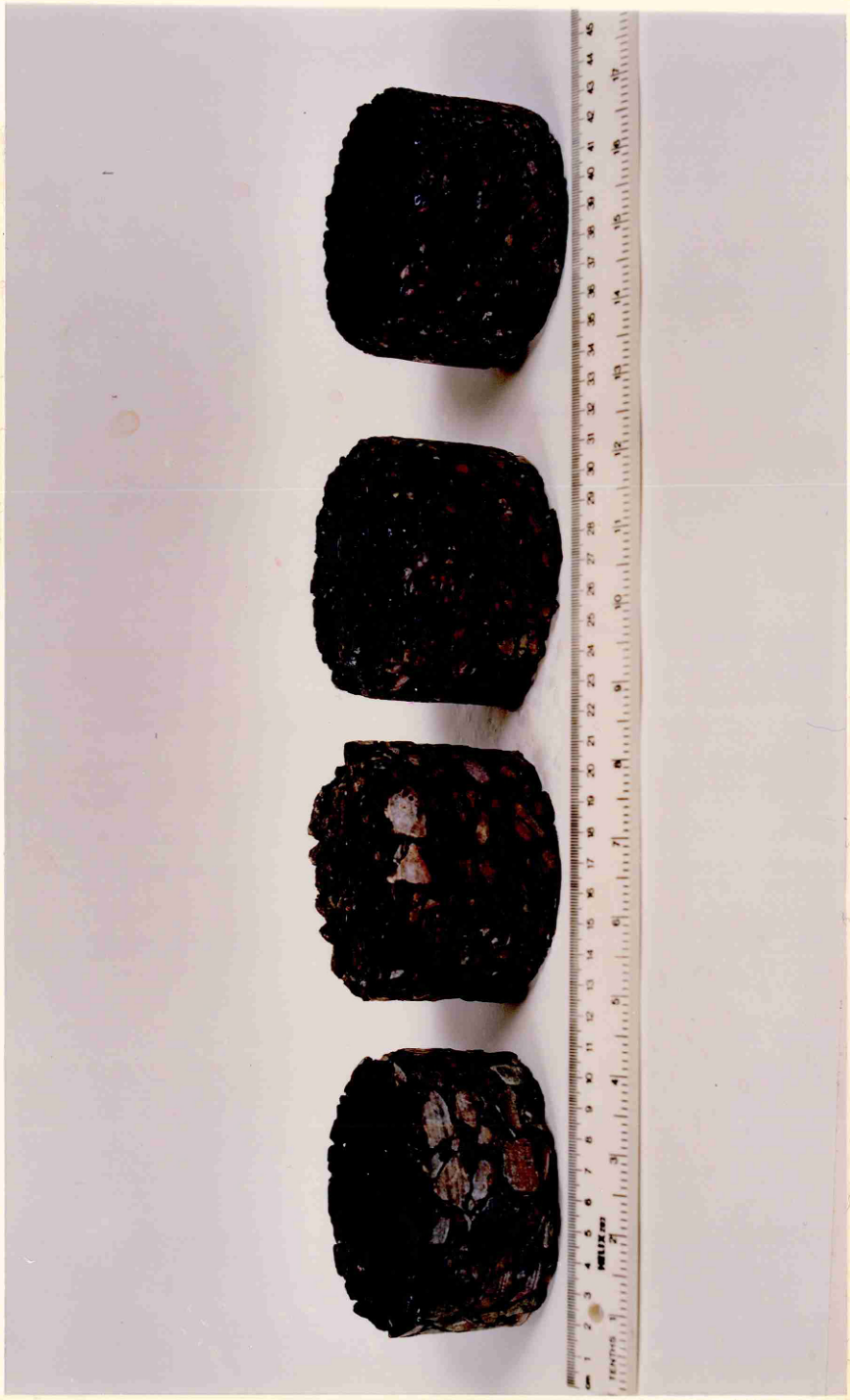

**Figure L.6** Cores from four materials used for road surfaces, highest stone size on left